Imperial College London
Department of Earth Science and Engineering

The Impact of Capillary Heterogeneity on Subsurface Carbon Dioxide Storage

Nele Mareike Wenck

Supervisors:

Dr. Samuel Krevor, Prof. Ann Muggeridge and Dr. Samuel Jackson

A doctoral thesis submitted in fulfilment of the requirements for the degree of

Doctor of Philosophy
of
Imperial College London

August 2023

Copyright Declaration

The copyright of this thesis rests with the author. Unless otherwise indicated, its contents are licensed under a Creative Commons Attribution-Non Commercial 4.0 International Licence (CC BY-NC).

Under this licence, you may copy and redistribute the material in any medium or format. You may also create and distribute modified versions of the work. This is on the condition that: you credit the author and do not use it, or any derivative works, for a commercial purpose.

When reusing or sharing this work, ensure you make the licence terms clear to others by naming the licence and linking to the licence text. Where a work has been adapted, you should indicate that the work has been changed and describe those changes.

Please seek permission from the copyright holder for uses of this work that are not included in this licence or permitted under UK Copyright Law.

Nele Mareike Wenck

August 2023

Declaration of Originality

I declare that this thesis titled, The Impact of Capillary Heterogeneity on Subsurface Carbon Dioxide Storage, and the work presented in it are my own, performed under the supervision of Dr. Samuel Krevor, Prof. Ann Muggeridge and Dr. Samuel Jackson, at the Department of Earth Science and Engineering, Imperial College London. All published and unpublished material used in the thesis has been given full acknowledgement. This thesis has not been previously submitted in whole or in part for a degree or any other qualification at this University or any other institution.

Nele Mareike Wenck

August 2023

Abstract

Rock heterogeneity can be observed at a range of scales and can result in the spatial variation of capillary pressure, termed 'capillary heterogeneity'. Over centimetre to metre length scales, studies have shown that capillary heterogeneity is one of the dominant fluid distribution mechanisms. On larger scales, recent literature indicates that capillary heterogeneity can lead to anisotropy and flow rate dependency in the observed relative permeability, which is one of the key parameters controlling fluid behaviour. Albeit these findings, there remain significant gaps in our understanding, characterisation and modelling of capillary heterogeneity and its impact on multiphase flow. This poses challenges to the predictive modelling of subsurface CO_2 flow and other scientific and engineering processes where multiphase fluid flow in porous media is central.

We examined the importance of, and the challenges associated with, characterising core-scale rock heterogeneities. We applied a capillary heterogeneity characterisation workflow to five rock cores (two sandstones and three carbonates) with varying degrees of heterogeneity to systematically evaluate the inversion approach against a systematic variation in rock structures. For the carbonates, we found the success of the workflow to correlate with the size of the controlling heterogeneous features resolved by the scanner. Strongly-heterogeneous rocks such as carbonates introduce complexities that warrant further advancements in core characterisation approaches. Utilising the successful digital core model of a carbonate, we also discovered that isotropic heterogeneity results in non-monotonic rate dependency behaviour of the relative permeability.

Following these discoveries, we focused our work on the proposed Endurance CCS site in the UK to evaluate the potential impacts of capillary heterogeneity on CO_2 plume migration at this site. We conducted an experimental and characterisation study on reservoir samples from the site. We successfully obtained capillary pressure and relative permeability characteristics, which were subsequently used as input into modelling studies. We discovered that the Endurance site exhibits strong capillary heterogeneity on a range of 10s metres along the proposed injection interval.

This motivated the investigation into the impact of rock heterogeneity on CO_2 plume migration at the metre scale varying flow rate, heterogeneity structure and tilt, using fine-scale simulations incorporating these experimental observations. Capillary heterogeneity can lead to a noticeable increase or decrease in the CO_2 migration speed depending on the orientation of heterogeneity relative to the flow axis. In a tilted domain the impact of unfavourable heterogeneities aligned perpendicular to the flow axis is enhanced. We also discovered that the effects of capillary heterogeneity decreased in a 2D model, which suggests that reduced-dimensionality models under-predict the importance of capillary heterogeneity.

Based on these findings, we explored the upscaled impact of capillary heterogeneity on the multiphase flow properties, capillary pressure and relative permeability, by developing a novel 3D, capillary-limit, steady-state upscaling scheme. Using the algorithm, we built a 3D reservoir model of the Endurance site and simulated CO_2 injection. Our work demonstrated that capillary heterogeneity has a significant impact on 3D CO_2 plume migration. Near the injector, it enhances the formation of CO_2 channels, which significantly improves sweep efficiency and may result in an increase in capillary trapping and dissolution. At distance from the injector, the gravity tongue is thinned and the plume travels faster as a result of capillary heterogeneity. These are novel insights and underpin the importance of characterising capillary heterogeneity in reservoir models of geological carbon storage sites.

Acknowledgements

I have had immense support over the last few years, for which I will be eternally grateful and without which I would have not come this far.

First and foremost I wish to thank my supervisors, Dr. Samuel Krevor, Prof. Ann Muggeridge and Dr. Sam Jackson, for their continuous support, mentorship and guidance throughout my PhD.

To Sam K.: you have been a superb primary PhD supervisor, who ensured my experience of doing a PhD during a pandemic runs as smoothly as possible. It has been great to dive into the world of CCS and I have learnt a lot from you. You have always been a tremendous support and provided guidance whenever needed. I also very much appreciate the experiences that you enabled outside of my PhD including the various internships and conferences. This truly had a huge impact on me and I thank you for that.

To Ann: I am so grateful to have had you as one of my supervisors. You have taught me so much over the years, which has made me a better scientist. Your level of patience, understanding and kind words in times of need have also been greatly appreciated - thank you for always responding to yet another of my email queries. Perhaps one day I will be as patient with CMG and Eclipse as you are. I will also truly miss the uplifting squirrel-GTAing sessions.

To Sam J: thank you for your continuous support albeit your growing family! Every meeting, in the early hours of the morning or late hours at night, have been an immense help. Your attention to detail and the breadth of knowledge you hold is impressive and has had a huge impact on the work I produced over the years.

Special thanks also to Prof. Martin Blunt, through whom I discovered my interest in flow in porous media, which subsequently led me to do a PhD! I wish to also thank Mike Spearing for his mentorship and scientific insights throughout my PhD. My thanks also go to Kate Flynn, who helped me embark on the journey of studying Physics.

To my parents, Hans and Violetta. Thank you for absolutely everything. Thank you for providing the opportunity to move to the UK for my undergraduate. Thank you for consistently supporting me, I know it was not easy. Dad, thank you for believing in me - I still remember our first visit to Imperial for my undergraduate interview. Also, thank you for invoking my interest in science from an early age, although this was not always effortless... Mum, thank you for constantly looking after me - your caring nature truly is a gift and without your continuous support, I certainly would not have come this far.

To Alena, my better half. Words cannot describe how lucky and grateful I am to have you in my life. Thank you for always having my back (sometimes literally), for listening and for lifting my spirits after yet another failed experiment. And thank you for opening your home to me during the pandemic, it made the first year of my PhD forever memorable ("Dann hebt er ab und völlig losgelöst...")

My thanks also go out to Sam's research group, who have been extremely supportive over the years. Special thanks to Flowra, Catrin and Nihal. Flowra, I will cherish our adventures in Chicago forever... Catrin, thanks for always listening and being a great support in the lab. Nihal, thank you for being remarkably kind and for preparing me for my journey outside of academia.

I wish to thank the two postdocs in Sam's group, Sojwal and Senyou. Sojwal, I really appreciate all the time you took (weekdays, weekends, evenings) throughout my PhD to explain the ins and outs of the lab to me, you have been an immense help. Senyou, it has been amazing working with you. Your work ethic and breadth of knowledge is inspiring and I can't wait to see what milestones are next for you (Prof. An!). Thank you for everything!

Thanks also to Vincenzo, Ed B., Francois and Gareth for your guidance on the lab and IT side, which has enabled me to complete my PhD. I would like to especially thank Vincenzo for his tremendous help during my time in the lab - I appreciated your high spirits even in difficult times. Special thanks also to Francois for his continuous efforts during my final year - I would not have been able to run all these simulations without your help.

To my friends - you know who you are, thank you for your support over the years and equilibrating my work-life balance. Special thanks to Sneha, Sam and Theo. I cherish our 8-year friendships that all began in the RSM - you truly have been a big part of my time here at Imperial and have made this journey unforgettable! I appreciate you all very, very much.

And last but certainly not least, thank you Andy. Having you in my life has made the last few years so very special. I thank you dearly for always keeping up with me and my thoughts (going at a million miles an hour). Early alarms, weekend laboratory sessions, yet another failed simulation, and so much more...You have been extraordinarily supportive and it means the world to me. Thank you for always listening and being the support I so very much need(ed).

Finally: here's to all the Dr. Wencks, past, present and future!

Funding Acknowledgements

We gratefully acknowledge the Engineering and Physical Sciences Research Council and BP Exploration for providing funding for this project [Project reference: EP/T517690/1 2383679].

We also thank the Computer Modelling Group and Schlumberger for providing access to CMG IMEX and ECLIPSE, respectively.

List of Publications and Conference Proceedings

List of Publications

Wenck, N., Jackson, S.J., Manoorkar, S., Muggeridge, A. and Krevor, S., 2021. Simulating core floods in heterogeneous sandstone and carbonate rocks. Water Resources Research, 57(9), p.e2021WR030581.

An, S., **Wenck, N.**, Manoorkar, S., Berg, S., Taberner, C., Pini, R., Krevor, S., May 2023. Inverse modelling of core flood experiments for predictive models of sandstone and carbonate rocks. Authorea. DOI:10.22541/essoar.168298704.44298407/v1

Conference Proceedings

- AGU Fall Meeting, December 2020, online - poster presentation
- Interpore, September 2020, online - oral presentation
- EGU General Assembly, April 2021, online presentation
- The Society of Core Analysts, September 2021 - online presentation
- AGU Fall Meeting, December 2021, New Orleans, United States - presentation
- Gordon Carbon Capture, Utilization and Storage Research Conference, April 2022, Ventura, United States - poster
- Gordon Flow and Transport in Permeable Media Research Seminar, July 2022, Les Diablerets, Switzerland - presentation
- Gordon Flow and Transport in Permeable Media Research Conference, July 2022, Les Diablerets, Switzerland - poster
- AGU Fall Meeting, December 2022, Chicago, United States - poster
- Interpore, May 2023, Edinburgh, Scotland - presentation
- SCCS Bunter Sandstone webinar, June 2023 - online presentation

Nomenclature

Symbol	Description
A	Cross-sectional area [L^2]
A_f	Plume footprint area [L^2]
f_p	Fractional flow of phase p [-]
g	Acceleration due to gravity [$L{\cdot}t^{-2}$]
H	Length scale associated with the heterogeneity [L]
J	Leverett-J function [-]
K	Permeability [L^2]
K_{abs}	Absolute permeability [L^2]
K_{arith}	Arithmetic average of permeability [L^2]
K_{harm}	Harmonic average of permeability [L^2]
K_{geom}	Geometric average of permeability [L^2]
$k_{eff,p}$	Effective/phase permeability [L^2]
k_{rp}	Relative permeability of phase p [-]
L	Length [L]
N	Number of coarse grid blocks [-]
N_c	Capillary Number [-]
n	Number of fine scale grid blocks [-]
q	Darcy velocity [$L{\cdot}t^{-1}$]
P	Pressure [$mL^{-1}t^{-2}$]
P_b	Macroscopic boundary pressure [$mL^{-1}t^{-2}$]
P_c	Capillary Pressure [$mL^{-1}t^{-2}$]
P_e	Entry pressure [$mL^{-1}t^{-2}$]
P_{max}	Capillary pressure at the irreducible water saturation [$mL^{-1}t^{-2}$]
Q	Volumetric flow rate [m^3s^{-1}]
R^2	Correlation coefficient [-]
r	Radius [L]
r_x,r_y,r_z	Correlation lengths in each dimension (x,y,z) [L]
S_{gc}	Critical gas saturation [-]
S_p	Saturation of phase p [-]

S_{wirr}	Irreducible water saturation [-]
t	Time, [t]
t_0	Breakthrough time of the uncorrelated base model [t]
t_i	Breakthrough time of a specific model [t]
V_r	Relative migration speed [-]
V_s	Plume swept volume [L^3]
V_t	Volume of a coarse grid block [L^3]
1D	One-dimensional
2D	Two-dimensional
3D	Three-dimensional
4D	Four-dimensional
Greek Letters	
α	$P_e/P_{\max}$ [-]
ΔP	Pressure difference [$mL^{-1}t^{-2}$]
ΔP_c	Capillary pressure difference [$mL^{-1}t^{-2}$]
θ	Contact angle [°]
κ	Capillary pressure scaling factor [-]
λ	Brooks Corey pore size distribution factor [-]
μ	Viscosity [$mL^{-1}t^{-1}$]
ρ	Density [$m{\cdot}L^{-3}$]
σ	Interfacial tension [mt^{-2}]
ϕ	Porosity [-]
Subscripts	
g	Gas
inj	Injected
nw	Non-wetting
p	Phase
t	Total
w	Water/Wetting
I	Upscaled coordinate in the x-axis
i	Fine-scale coordinate in the x-axis
J	Upscaled coordinate in the y-axis

j	Fine-scale coordinate in the y-axis
K	Upscaled coordinate in the z-axis
k	Fine-scale coordinate in the z-axis
x	Upscaled property in the x dimension
y	Upscaled property in the y dimension
z	Upscaled property in the z dimension
Superscripts	
$*$	Effective
Acronyms	
PV	Pore volumes
PV_{inj}	Pore volumes injected

Contents

Copyright Declaration ii

Declaration of Originality iii

Abstract iv

Acknowledgements vi

Funding Acknowledgements viii

List of Publications and Conference Proceedings ix

Nomenclature x

1 Introduction and Motivation 1

1.1 Global Decarbonisation 1

1.2 Geologic Carbon Storage 3

1.3 Unexpected Flow Behaviour at CCS Sites 5

1.3.1 Sleipner 5

1.3.2 Otway 7

1.3.3 Decatur 9

1.3.4 In Salah . . . 10
1.3.5 Snøhvit . . . 12
1.4 Summary, Challenges and Implications for CCS . . . 14
1.5 Aims and Objectives . . . 16
1.6 Outline of the thesis . . . 17

2 Scientific Background **18**

2.1 Theory for Multiphase Flow in Porous Media . . . 18
2.1.1 Capillary Pressure . . . 19
2.1.2 Relative Permeability . . . 21
2.1.3 Phase Mobility and Fractional Flow Theory . . . 23
2.2 Rock Heterogeneity . . . 25
2.2.1 Definition . . . 25
2.2.2 Micrometres . . . 26
2.2.3 Millimetres to Centimetres . . . 27
2.2.4 Metres to Kilometres . . . 28
2.3 The Impact of Rock Heterogeneity on Multiphase Flow Properties . . . 30
2.3.1 Rate Dependence of Relative Permeability . . . 30
2.3.2 Capillary Pressure Heterogeneity . . . 31
2.4 Flow Processes Resulting from Capillary Heterogeneity . . . 34
2.4.1 Capillary Crossflow . . . 34
2.4.2 Cross-Layer Flow and Capillary Trapping . . . 36
2.4.3 Connected Pathway Flow, Fingering and Channeling . . . 36

2.5 Characterising and Modelling the Impact of Capillary Heterogeneity 38

2.5.1 Elementary Volumes 38

2.5.2 Pore-Scale Capillary Heterogeneity 40

2.5.3 Core-Scale Capillary Heterogeneity 42

2.6 Upscaling the Impact of Rock Heterogeneity to the Field Scale 48

2.6.1 Single Phase Upscaling 50

2.6.2 Two Phase Upscaling 53

2.6.3 Issues and Considerations 56

3 Experimental Methods **58**

3.1 Centimetre-Scale Corefloods with Medical CT X-Ray Imaging 58

3.1.1 Sample Preparation 58

3.1.2 Flow-Rig and Experimental Design 59

3.1.3 Measuring Absolute Permeability 61

3.1.4 Measuring Porosity and Saturation 61

3.1.5 Measuring Steady-State Drainage Relative Permeability 65

3.1.6 Experimental Procedure 66

3.2 Micro-CT Dry Scans 68

3.2.1 Image Acquisition 68

3.2.2 Image Processing 69

4 Characterising and Simulating Corefloods in Heterogeneous Rocks **71**

4.1 Objectives 71

4.2 Materials and Methods 72

4.2.1 Heterogeneous Rock Types 72
4.2.2 Experimental Conditions and Fluids 73
4.2.3 Capillary Number 74
4.2.4 Image Coarsening 75
4.2.5 Building Digital Core Models 78
4.2.6 History Match of the Numerical Models 82
4.3 Results and Discussion 86
4.3.1 Heterogeneous Porosity Distribution 86
4.3.2 Measures to Evaluate the Workflow Success 88
4.3.3 Characterisation of Heterogeneous Sandstones 90
4.3.4 Characterisation of Heterogeneous Carbonates 93
4.3.5 Evaluation of the Extended Approach 100
4.3.6 Discussion of the Workflow Applicability 104
4.3.7 Rate-Dependant Behaviour of Relative Permeability 106
4.4 Conclusions 110

5 Advanced Experimental Study for Reservoir Characterisation 112

5.1 Objectives 112
5.2 The Endurance Proposed CCS Site 113
5.2.1 White Rose Project 113
5.2.2 Net Zero Teesside Project 113
5.2.3 Geological Setting 114
5.2.4 Storage Complex 115

5.2.5 Wells . . . 118

5.3 Results . . . 119

5.3.1 MICP to Characterise Reservoir Heterogeneity . . . 120

5.3.2 Steady-State Coreflood Experiment to Obtain the Relative Permeability 124

5.3.3 Digital Rock Analysis of Micro X-Ray CT Imagery from a Bunter Sandstone147

5.4 Conclusions . . . 160

6 Impact of Capillary Heterogeneity on CO_2 Flow at the Metre Scale 161

6.1 Objectives . . . 161

6.2 Methods . . . 162

6.2.1 Geostatistical Approach to Create Heterogeneous Domains . . . 164

6.2.2 Simulator . . . 166

6.3 Results and Discussion . . . 167

6.3.1 Impact of Capillary Heterogeneity at Typical Reservoir Flow Rates . . . 167

6.3.2 The Importance of Representing Flow in 3D . . . 188

6.3.3 Impact of Capillary Heterogeneity at Varying Flow Rate . . . 191

6.3.4 Tilted Domain . . . 196

6.3.5 Modelling Assumptions . . . 200

6.4 Conclusions . . . 202

7 The Impact of Capillary Heterogeneity on CO_2 Flow at the Field Scale 204

7.1 Objectives . . . 204

7.2 Methods . . . 205

7.2.1 Building a Fine-Scale Reservoir Model . . . 205

7.2.2 A 3D Capillary-Limit Upscaling Workflow 209

7.3 Results and Discussion 222

7.3.1 The Impact of Capillary Heterogeneity in 2D 222

7.3.2 Simulating the Impact of Capillary Heterogeneity in 3D 232

7.3.3 The Importance of Building a 3D Reservoir Model 252

7.3.4 Changes in Behaviour with Well Placement 255

7.3.5 The Impact of Multi-Point Injection 260

7.3.6 Modelling Assumptions 271

7.3.7 Implications for Endurance Operations 274

7.3.8 Implications for CCS Operations 275

7.4 Conclusions 277

8 Conclusions and Future Work **278**

8.1 Summary of Thesis Achievements 278

8.2 Conclusions 279

8.3 Recommendations for Future Research 281

8.3.1 Geochemical and Phase Mixing Effects 281

8.3.2 Geologically-Based Reservoir Modelling Approach 281

8.3.3 Unsteady-State Versus Steady-State Behaviour 282

8.3.4 Representative Relative Permeability Measurements 283

8.3.5 Application to Operational CCS Site 283

8.3.6 Impact of Geological Uncertainty 284

8.3.7 Reservoir Pressure 284

8.3.8 Near Wellbore Upscaling 285

8.3.9 Improvement of Numerical Methods 285

8.3.10 Bridging the Gap Between Pore-Scale Observations and Field-Scale Modelling 285

Bibliography **286**

Appendices **325**

A Fractional Flows of Carbonates and Sandstones Experiments **325**

B Percentage Errors of Simulated Corefloods **328**

C Error Surfaces **331**

D Rate Dependency Tabular Data **333**

E Experimental Pressure Drop **336**

F Permissions **337**

Chapter 1

Introduction and Motivation

1.1 Global Decarbonisation

Since the beginning of the industrial era, anthropogenic greenhouse gas (GHG) emissions have been rising continuously. As shown in Figure 1.1, the concentration of GHGs in the atmosphere has not only seen a sharp rise compared with pre-industrial levels, but also with levels on a geological timescale. GHGs trap solar radiation in the atmosphere leading to a rise in atmospheric temperatures, Figure 1.2. Although all GHGs are potent, CO_2 has been identified as the main driver of global warming: "Each 1000 Gt of cumulative CO_2 emissions is assessed to likely cause a 0.27°C to 0.63°C increase in global surface temperature with a best estimate of 0.45°C" (IPCC, 2021).

Following these discoveries, climate change was recognised as a major threat by 196 countries and resulted in the adoption of the Paris Agreement in 2015. The agreement is an international treaty on climate change, primarily focused on limiting the global temperature increase to 1.5°C relative to pre-industrial levels. In 2022, the Intergovernmental Panel on Climate Change (IPCC) found that global temperatures have increased to 1.1°C above pre-industrial levels, Figure 1.2. Studies have found that this human-induced climate change has led to adverse impacts to nature and people such as weather extremes, increased mortality, loss of ecosystems and reduced water security (IPCC, 2022).

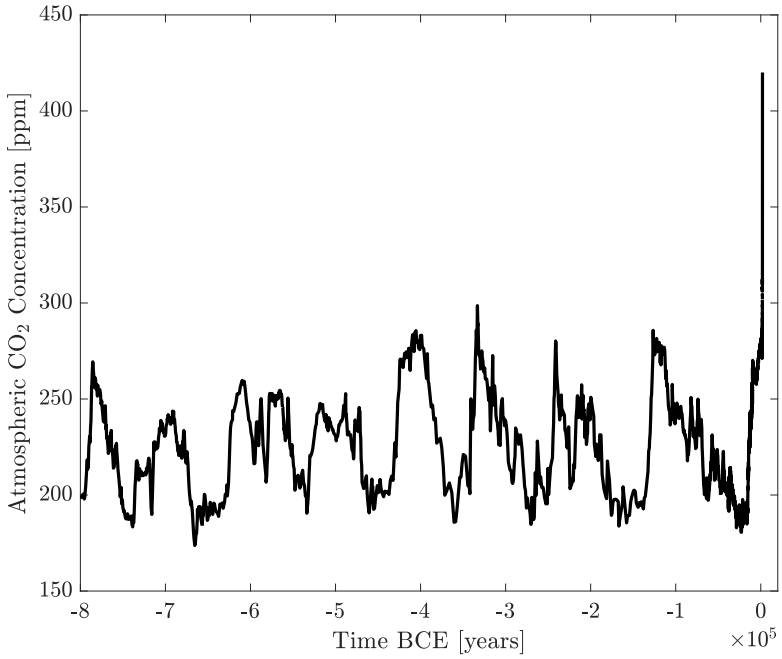


Figure 1.1: Post-industrial increase in global atmospheric CO_2 concentration relative to the average level on geological timescales. Data from Ritchie et al. (2020).

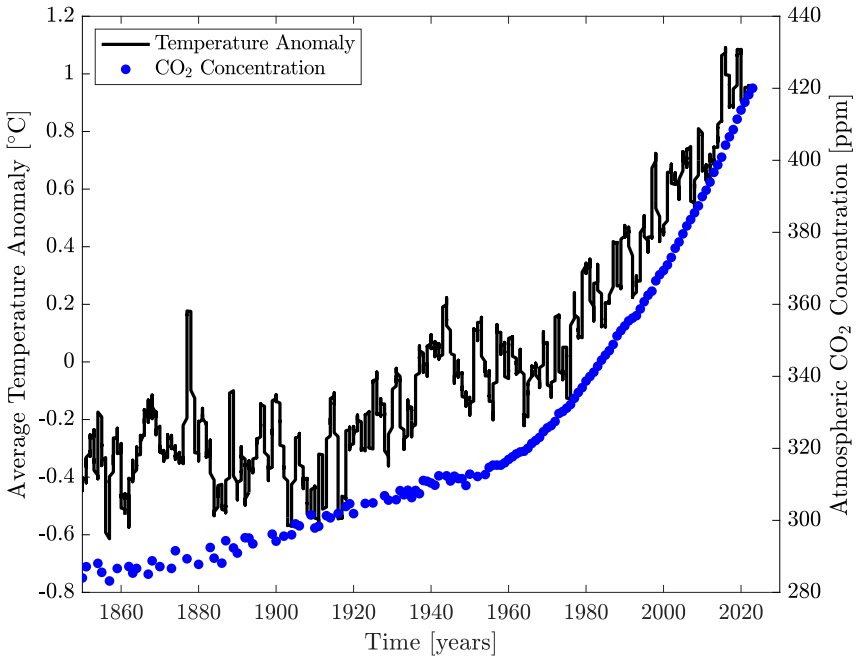


Figure 1.2: Increase in the average temperature anomaly (relative to the 1850-1900 average temperature) and in the global atmospheric CO_2 concentration from 1850 until present. The data presents a strong positive correlation between the two measures. Temperature data from Rohde and Hausfather (2020), CO_2 data from Ritchie et al. (2020).

To combat climate change and limit global warming to 1.5°C, innovative engineering solutions need to be implemented that reduce GHG emissions in all sectors including transport, industry and energy. In the energy sector, the transition from fossil-fuel based energy sources to renewable energies has been widely promoted, with 28% of the world's electricity production in 2021 being attributed to renewables (IEA, 2022). The industrial sector is the third largest emitter of GHGs, yet many of the subsectors, including steel and cement production, face challenges reducing their emissions and are therefore called hard-to-abate sectors. In these sectors, carbon capture and storage (CCS) has been identified as a key player in the net zero transition.

CCS involves the capture of CO_2 emissions at industrial point sources or from the atmosphere (direct air capture) using a range of technologies such as adsorption, absorption or chemical looping, after which the CO_2 is transported and stored. There are various CO_2 storage solutions such as mineral, ocean and geological storage. However, geological carbon storage is at the highest technology readiness level (IEA, 2020). As of 2021, 14 countries, including China, Saudi Arabia and South Africa, had incorporated CCS in their nationally determined contributions (Turan et al., 2021). The most recent IPCC report also highlighted the importance of CCS in the net zero transition. It was found that technical geological CO_2 storage capacity exceeds the storage requirements needed to limit global warming to 1.5°C above pre-industrial levels through 2100 (IPCC, 2022).

1.2 Geologic Carbon Storage

CO_2 can be stored in various geological formations including saline aquifers and depleted hydrocarbon reservoirs. The CO_2 is injected as a supercritical fluid into the formation and trapped via four key mechanisms: 1) structural trapping due to the presence of a caprock, 2) mineral trapping due to the reaction of the CO_2 with the host rock to form carbonate minerals, 3) solubility trapping due to the CO_2 dissolving in the host fluid and 4) capillary trapping, whereby the CO_2 residing in the pore space becomes immobile due to capillary forces.

Saline aquifers represent the greatest storage potential, however extensive geo-scientific characterisation studies have to be completed to reduce uncertainties and propose a robust storage development plan prior to injection. As such, storing CO_2 in depleted hydrocarbon reservoirs has the added benefit, beyond enhanced oil recovery (EOR), of having been characterised previously for exploration purposes. Nevertheless, there are big differences between producing hydrocarbons from reservoirs and/or performing EOR versus injecting CO_2 for geological carbon storage, namely 1) the CO_2 needs to be stored permanently, 2) the chemical and physical properties of CO_2 differ to hydrocarbons.

Geologic carbon storage began in 1996 at the Sleipner site in Norway and has since seen a significant rise to 26 projects worldwide with a total storage rate of 28 Mt $CO_2 \cdot yr^{-1}$ in 2019 (Zhang et al., 2022; Krevor et al., 2023), Figure 1.3. However, many of these sites have displayed unexpected CO_2 behaviour upon injection, discussed in Section 1.3.

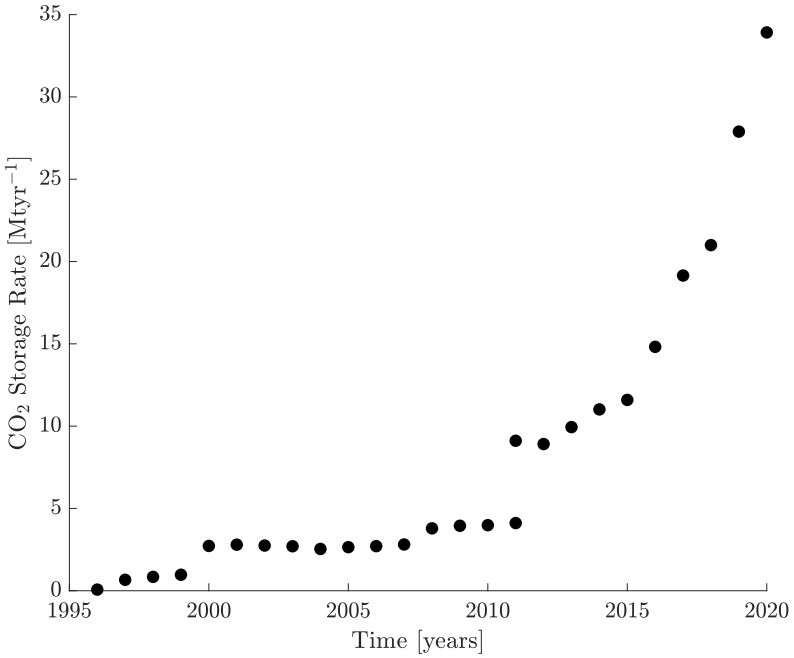


Figure 1.3: Increase in the yearly CO_2 storage rate from 1996 to 2020. Data from Zhang et al. (2022).

1.3 Unexpected Flow Behaviour at CCS Sites

Many CCS sites around the world have displayed unexpected flow behaviour, where the CO_2 once injected, migrated away from injection wells at much higher rates and in different directions to what had been predicted previously with reservoir flow simulations. It has also been challenging to history match field observations made at these sites. The following sections summarise key uncertainties and challenges encountered during CO_2 injection at five storage sites.

1.3.1 Sleipner

Sleipner is the most widely studied CCS site, having been operational since 1996 (Arts et al., 2004). Due to the introduction of a carbon tax by the Norwegian government, Statoil and its partners chose to capture the CO_2 produced from the Sleipner Vest and Sleipner Ost gas fields in the mid 1990s (Furre et al., 2017). The injection interval at Sleipner, the Utsira formation, consists of basin-restricted marine lowstand deposits with predominantly high porosities averaging to 0.3-0.4 and permeabilites of several Darcys, and interbedded, thin (1 m) low-porous shales (Eiken et al., 2011; Furre et al., 2019). Wet CO_2 is injected at around 1000 m below sea level, which is roughly 200 m below the top of the reservoir (Chadwick et al., 2009). An average of 0.9 Mt of CO_2 were injected during the first years. However, this rate was later reduced corresponding to a reduction in CO_2 volume output from the Sleipner Vest gas field (Furre et al., 2017).

Since CO_2 injection has commenced, the plume has been closely monitored using primarily seismic (2D, 3D and 4D) and gravity surveys. Overall, the observed flow behaviour differs significantly from flow predictions and is described by some as “striking” (Chadwick et al., 2009). The CO_2 plume is characterised by a distinct “Christmas tree” shape (Chadwick and Noy, 2010) consisting of 9 separate layers each with high CO_2 saturations. The lateral extent and thickness of the CO_2 layers vary. Between 1999 and 2006, seismic data revealed that

the topmost layer formed an elongated tongue towards the North, characterised by a 1 m·d^{-1} advance rate between 2001 and 2004 (Chadwick et al., 2009). Comparing this trend with the local topography derived from seismic data, it appears that the CO_2 plume closely follows the topography of the top seal, and as of 2019 reached a lateral extent of over 5 km in the NE-SW direction (Furre et al., 2019), Figure 1.4.

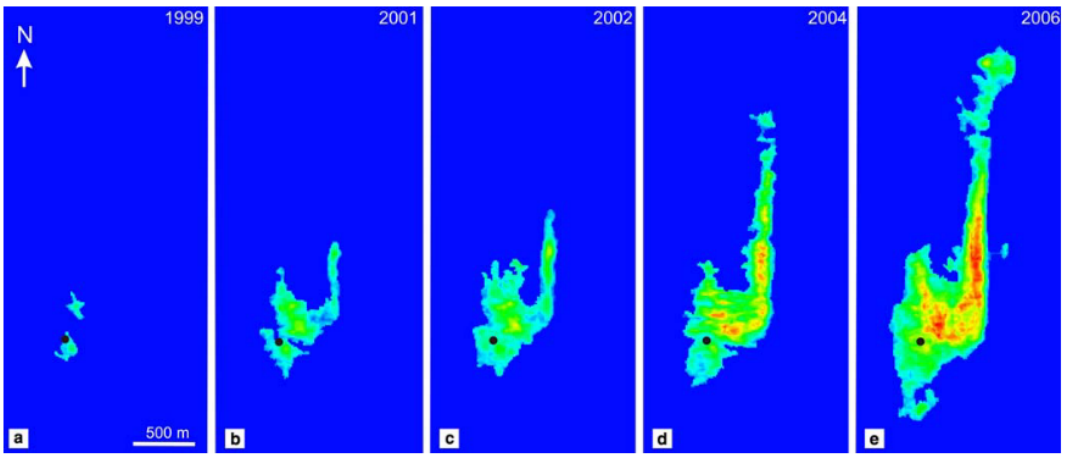


Figure 1.4: Amplitude maps of the topmost CO_2 layer through time derived from seismic data at the Sleipner site. The black spot denotes the location of the CO_2 injection well. From Chadwick and Noy (2010).

Using a combination of field observations and laboratory measurements, reservoir models of the Sleipner site were built to better understand the CO_2 behaviour. The studies experienced significant challenges to match the observations and/or predict the CO_2 flow pathways. "Unpredicted geological factors" (Eiken et al., 2011) and incomplete understanding of the underlying physics (Furre et al., 2017) were identified as the main attributing factors. Interestingly, the majority of reservoir models such as Arts et al. (2004) and Chadwick et al. (2009), resulted in a dome or circular-shaped CO_2 plume rather than the elongated tongue observed at Sleipner. Good matches were only obtained when geologically unconstrained properties were assigned to the model, such as the high-contrast permeability distribution in Chadwick et al. (2009) or the low entry pressures of mud baffles in Cavanagh and Nazarian (2014). Studies have concluded that the most important factors driving the CO_2 behaviour at this site are 1) temperature variations affecting the CO_2 density, 2) seal topography, 3) CO_2 flow properties, especially the entry pressure of the shale baffles and 4) the interplay of viscous, capillary and gravity forces (Alnes et al., 2011; Cavanagh and Nazarian, 2014; Furre et al., 2017; Ringrose, 2020; Akai et al., 2021; Williams and Chadwick, 2021; Nazarian and Furre, 2022).

1.3.2 Otway

The Otway CCS site is located within the onshore part of the Otway basin in Victoria, Australia (Dance, 2013). In 2008, CO_2 capture from the Buttresss CO_2 and Naylor gas fields began and the gas was subsequently injected at a depth of 1500 m TVDSS (Dance, 2013; Jackson et al., 2022a). The site serves as a small-scale project, having injected only 95 kt of CO_2 between 2008 and 2020 (CO2CRC, 2022). Classed as a demonstration project, considerable focus has been placed on undertaking scientific studies to improve the understanding of CO_2 plume migration, reduce geological uncertainties, reduce leakage risks and test new monitoring technologies (Dance, 2013; Yavuz et al., 2021; Sidenko et al., 2022).

The Paaratte formation, part of the Sherbrook group, serves as the injection interval at Otway and consists of a high quality sandstone with a high porosity averaging to 0.25 and a permeability between 1-2 D, as well as interbedded, low quality silt and mudstones (Mehin and Constantine, 1999; Dance, 2013; Dance et al., 2019). The interbedded low porosity layers, associated with high entry pressures, are expected to act as baffles and impede CO_2 plume migration, which poses modelling challenges. Characteristic to this site is the gently dipping slope towards the North with dip angles ranging between 2-5° (Shao et al., 2022) as well as various splay faults striking NW-SE (Feitz et al., 2018; Jenkins et al., 2022).

In 2007, the first characterisation well was drilled and the resultant 24 m of core underwent thorough laboratory analysis (Dance, 2013). The core testing confirmed the high quality nature of the sandstone in the injection interval. However, it also emerged that the reservoir rock was highly heterogeneous with a variable grain size distribution as well as thick shale baffles with 1-3 m thicknesses (Dance, 2013). Overall, a large permeability range was measured from 8 mD to 6 D, which underpins the presence of strong heterogeneity in the target interval (Dance, 2013).

Two separate injection cycles took place, stage 2 and stage 3, where the former focused on understanding seismic techniques and mitigation strategies and the latter focused on borehole-based, cost-effective monitoring solutions (Jackson et al., 2022a; Sidenko et al., 2022). During

stage 3, the CO_2 was injected down dip of the stage 2 injection location (Jackson et al., 2022a). Interestingly, the plumes from both stages merged into one and formed an elongated-shaped plume orientated NW-SE (Popik et al., 2020; Jenkins et al., 2022), Figure 1.5. Dance et al. (2019) proposed that this migration trend is indicative of CO_2 preferentially flowing via the splay faults. However, studies have found it challenging to replicate the flow behaviour. Reservoir models were only able to match the fast spreading plume by incorporating additional splay faults invisible on seismic data.

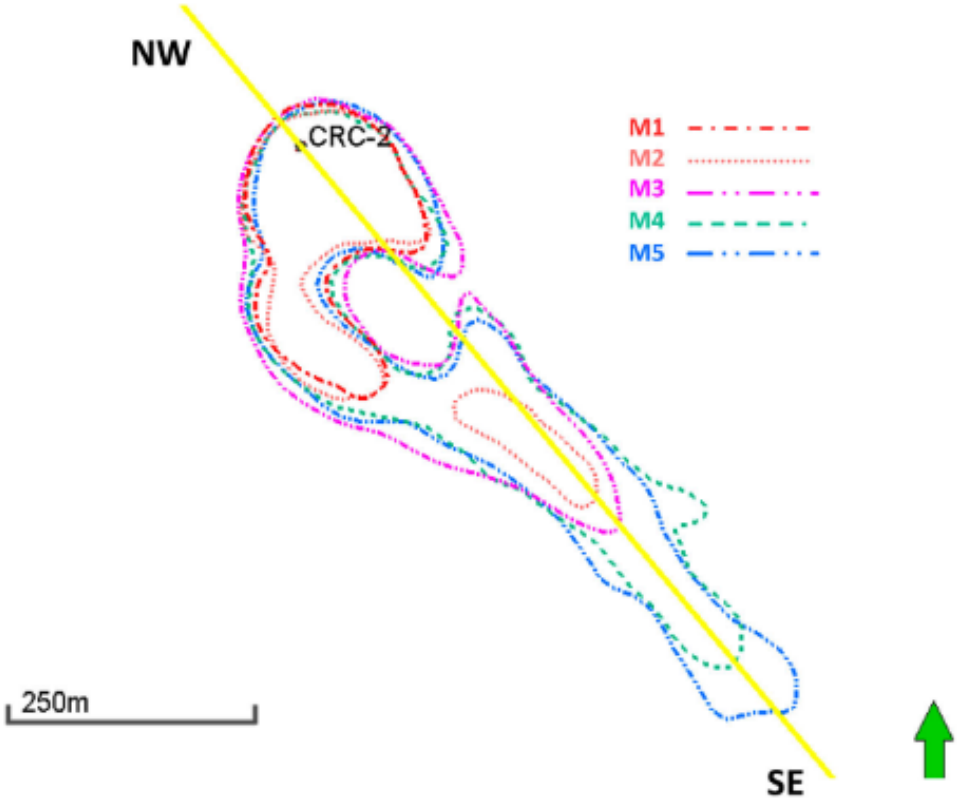


Figure 1.5: Evolution of the CO_2 plume at the Otway site derived from 4D seismic data. The yellow line indicates the orientation trend of the plume. The dashed lines indicate the outlines from different seismic surveys. "The M1, M2 and M3 seismic datasets were recorded after injection of 5, 10, and 15 kt (end of injection) respectively (...) M4 was acquired nine months and M5 was acquired 23 months after the end of injection." (Popik et al., 2020). The plume length along the NW-SE axis increased from 150 m in M1 to 780 m in M5. From Popik et al. (2020).

1.3.3 Decatur

The Decatur site in the Illinois basin in the United States also serves as a site for CO_2 injection, which commenced in 2011 (Finley et al., 2013). The injection interval forms part of the Mt. Simon formation, characterised by medium porosity averaging to 0.2 and permeability approximated at 183 mD (Couëslan et al., 2014). However, well and seismic data have indicated the presence of very low permeability (< 1 mD) layers towards the base of the injection interval. These have small correlation lengths, but were identified as potential controls on the plume migration (Couëslan et al., 2014; Leetaru and Freiburg, 2014; Dando et al., 2021).

During the first project phase (2011-2014), 1 Mt of CO_2 were injected into the subsurface at a depth of roughly 1900 m and at an average rate of 1000 $tCO_2 \cdot d^{-1}$ (Gollakota and McDonald, 2014; Dando et al., 2021). Upon injection, monitoring techniques were implemented, including time-lapse logging, pressure monitoring, seismic and deep fluid sample analyses, to track the plume and the reservoir response (Couëslan et al., 2014; Kaven et al., 2014). Micro-seismicity was detected, with epicentres scattered around the injection site (Dando et al., 2021). The CO_2 was first detected by a verification well in early 2012 and later that year by an additional well further away (Strandli et al., 2014).

Strandli et al. (2014) focused their work on using multilevel pressure monitoring data to track the plume through time. Although they successfully matched the reservoir pressure data at early times, the deviation between their model and the field observations increased significantly as more CO_2 was injected, requiring "further investigation" (Strandli et al., 2014). Later studies focused on calibrating the original reservoir model that was built prior to CO_2 injection. Subsequently, the calibrated models were used for predictive analyses using dynamic data collected during the injection period (Senel et al., 2014; Bauer et al., 2019). The results displayed a significant contrast in plume shape between the original and calibrated models, where the latter incorporated revised petrophysical properties such as permeability, relative permeability and the $\frac{K_v}{K_h}$ ratio. This indicates the challenges and uncertainties associated with building a reservoir model without calibration and dynamic field data. Similarly, the work by Bauer et al.

(2019) calibrated a reservoir model by modifying the reservoir quality and incorporating a flow barrier, unconstrained by geological observations. The results are presented in Figure 1.6 and exhibit a strong deviation between the field observation and the simulation output.

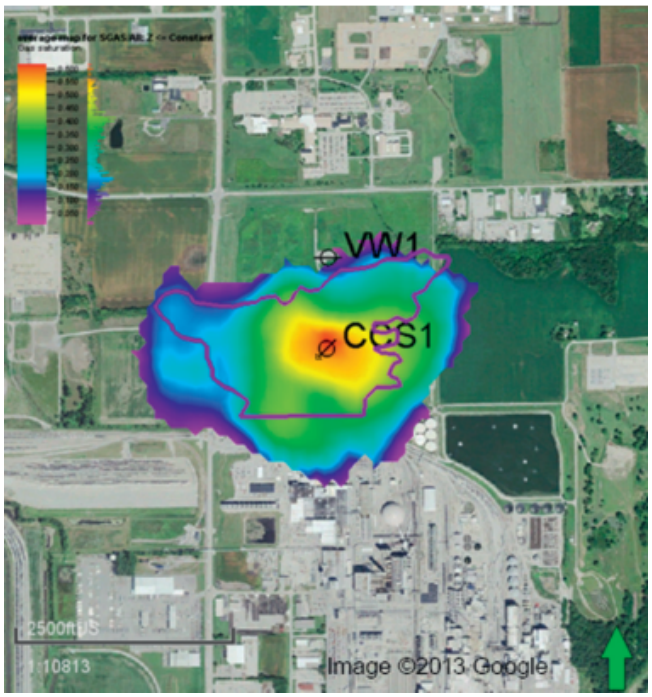


Figure 1.6: Comparison of the plume outline plotted as a purple line (obtained from surface seismic time-lapse NRM attribute data collected between 2001-2015) with the plume distribution from a numerical simulation at the Decatur site. From Bauer et al. (2019).

1.3.4 In Salah

The In Salah CCS site is located in onshore Algeria, where CO_2 is captured from the In Salah oil field (Ringrose et al., 2013). 4 Mt of CO_2 were injected between 2004 and 2011, after which injection was ceased due to concerns regarding caprock integrity indicated from seismic and pressure data (Aminu et al., 2017). The target reservoir is a depleted hydrocarbon reservoir, the Krechba field, with CO_2 having been injected downdip into the water leg at a depth of 1800 m (Pamukcu et al., 2011). The injection interval is characterised by a high quality "fracture-influenced, matrix-dominated" (Ringrose et al., 2009) carboniferous sandstone, exhibiting permeability variations of 0.1-300 mD, with an average of 10 mD (Ringrose et al., 2009). The site is characterised by fractures predominantly orientated NW-SE.

During injection, a range of monitoring techniques were implemented, including seismic and InSAR (Eiken et al., 2011), which allowed for the plume to be tracked. This data showed the fast migration speed of the plume, 3 times faster than a simulated homogeneous, cylindrical plume (Ringrose et al., 2009) and orientated parallel to the fracture orientation (Ringrose et al., 2009; Pamukcu et al., 2011). Modelling efforts focused on matching the field observations have been challenging. For instance Pamukcu et al. (2011), who used a multi-phase, multi-component compositional simulator to model the plume behaviour, was only able to achieve a satisfactory history match by reducing the permeability of matrix and fractures by up to several orders of magnitudes, unconstrained by geological data. Even then, the model was unable to replicate pressure responses for the entire injection period and the authors state that the observed behaviour "could not be fully explained by fluid dynamics only" (Pamukcu et al., 2011). Similarly, the modelling approach in Deflandre et al. (2013) fails to replicate the surface ground displacement field observations as presented in Figure 1.7. Ringrose et al. (2009) describe the plume development at In Salah as "complex" and call for "further analysis" to address "remaining uncertainties in modelling".

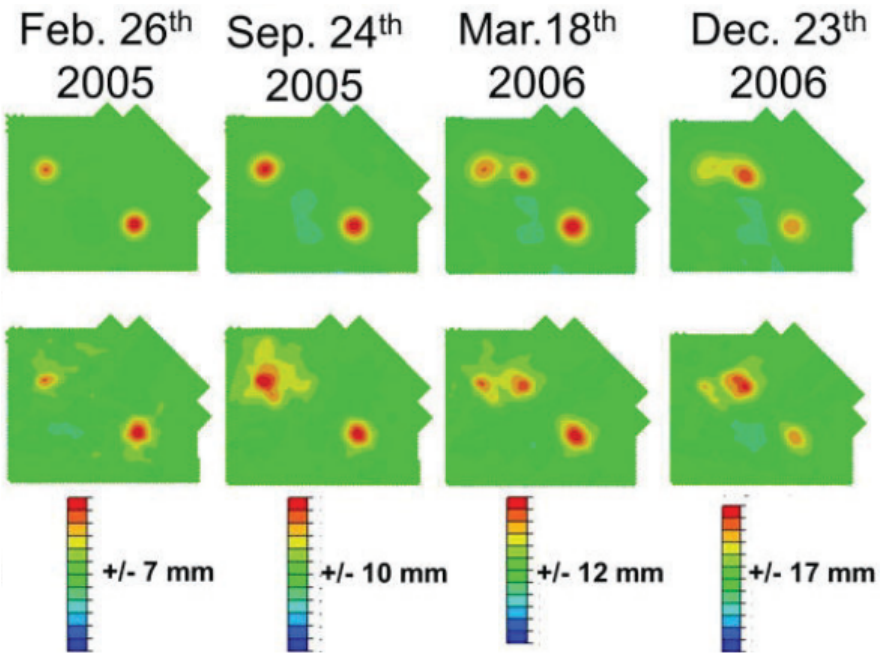


Figure 1.7: Comparison of the simulated (top) and observed (bottom) surface ground displacements at the Decatur site. At later times, the deviation between the observations and simulation results increases significantly, suggesting that the model is unable to capture the CO_2 flow behaviour. From Deflandre et al. (2013).

1.3.5 Snøhvit

The Snøhvit site is located 150 km offshore in the Barents Sea (Aminu et al., 2017). Similarly to Sleipner, Snøhvit is a producing gas field. Operated by Statoil and partners, the CO_2 is separated from the produced natural gas and re-injected into the subsurface (Sweatman et al., 2011). Injection of CO_2 commenced in April 2008 and was directed into the Tubåen formation at a depth of 2600 m (Hansen et al., 2013). This formation is a saline sandstone aquifer and is overlain by a shale caprock, which acts as the primary seal (Hansen et al., 2013). The injection interval consists of a deltaic to fluvial sandstone sequence, characterised by interbedded, high-permeability fluvial sand channels with low-permeability silt and mudstones (Buscheck et al., 2016).

From April 2008 to April 2011, 1.09 Mt of CO_2 were injected into the Tubåen formation (Buscheck et al., 2016). The injector was equipped with temperature and pressure gauges at the well head and downhole, which monitored any reservoir changes during the injection operations (Hansen et al., 2013). These indicated a significant buildup of reservoir pressure. This buildup was thought to be caused by 1) salt precipitation near the injector reducing well injectivity and 2) reservoir compartmentalisation (Birkholzer et al., 2015).

The initial reservoir characterisation undertaken by Statoil overpredicted the storage efficiency and permeability of the formation (Buscheck et al., 2016). The data collected during injection showed that the reservoir is characterised by limited hydraulic communication due to the complex, interbedded rock type sequence (Buscheck et al., 2016). Concerns were raised regarding the increase in reservoir pressure towards the fracture pressure. Studies indicated that fracture pressure could be reached in merely 6 months although the exact duration was largely uncertain due to the unknown sealing ability of faults in the reservoir (Hansen et al., 2013).

Ultimately, the pressure buildup required a re-design of the injection plan. From April 2011, the injection was diverted into the shallower Stø formation with increased layer conductivity expected. By the end of 2019, 6.5 Mt of CO_2 have been injected into this interval (Ringrose and Sæther, 2020). A pressure profile over the entire injection period is shown in Figure 1.8.

Near the onset of injection, the pressure spikes from injectivity losses can be identified (region a in Figure 1.8). The increasing pressure due to reservoir compartmentalisation whilst gas is injected into the Tubåen formation in the first part of operations is also visible (region b in Figure 1.8). This highlights the importance of considering the injection of dry versus wet CO_2 and potential impacts on well injectivity. The transition of injecting into the Stø formation is also clearly visible and is associated with a reduction in reservoir pressure (region c in Figure 1.8). Overall, the Snøhvit case study demonstrates the importance of implementing a flexible injectivity design, which can easily be adapted based on data collected during CCS operations.

Buscheck et al. (2016) built a reservoir model of the Tubåen formation to investigate the leading controls on pressure buildup. They combined the initial reservoir characterisation studies with 4D seismic data collected during injection to construct an updated reservoir model. The seismic data provided useful insights into the confinement of the CO_2 plume, from which the spatial reservoir quality could be better constrained. Using the updated model, the authors achieved a good match between the simulated and observed build-up of reservoir pressure. This demonstrates the value of implementing data collected during injection in a reservoir model. The work by Buscheck et al. (2016) also highlights the potential of pre-injection brine production to increase storage efficiency and enhance reservoir characterisation.

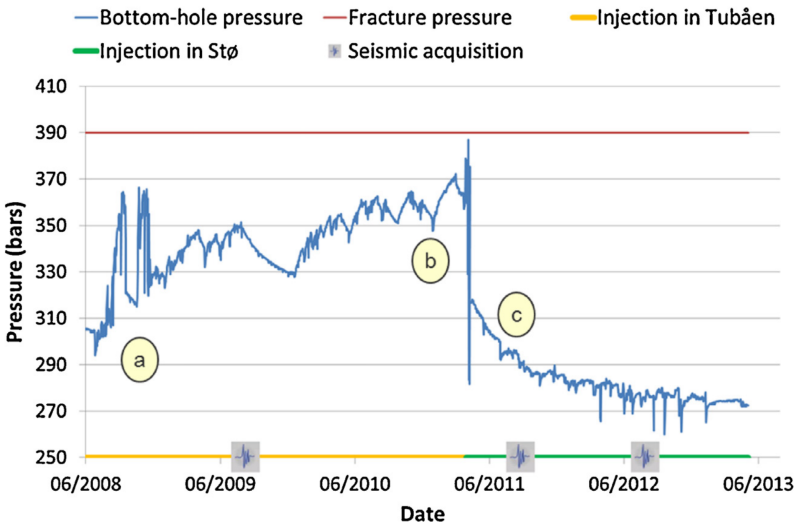


Figure 1.8: Downhole pressure data collected during CO_2 injection. The annotations refer to regions of the pressure trend discussed in the main text. From Pawar et al. (2015).

1.4 Summary, Challenges and Implications for CCS

Section 1.3 provided a summary of key uncertainties and challenges encountered at five carbon storage sites. The case studies emphasized that there are longstanding difficulties with the characterisation and predictive modelling of subsurface CO_2 flow. These observations suggest that field scale flow simulations are missing some of the leading order mechanisms governing fluid flow.

Rock heterogeneity can be observed at a range of scales (μm - 100s m) and can result in the spatial variation of capillary pressure, termed 'capillary heterogeneity'. Studies have found that capillary heterogeneity is one of the dominant fluid distribution mechanisms over centimetre to metre length scales (Chang and Yortsos, 1992; Ringrose et al., 1993; Chaouche et al., 1994; Huang et al., 1995; Krause, 2012; Jackson et al., 2018). On larger scales, this heterogeneity can lead to variations in the effective relative permeability, which is one of the key parameters controlling fluid behaviour (Krevor et al., 2019). Even though the impact of capillary heterogeneity is less well understood, recent research indicates that it is one of the leading causes of anisotropy and flow rate dependency in observed relative permeability and thus can have a significant impact on upscaled properties (Krishnamurthy et al., 2017, 2019; Jackson et al., 2018; Boon and Benson, 2021; Ershadnia et al., 2021).

It follows that heterogeneity in the multiphase flow properties resulting from variations in capillary pressure may be an equal or more important control than porosity or permeability heterogeneity on CO_2 plume migration. Furthermore, the injection of supercritical CO_2 is significantly more complex than traditional hydrocarbon exploration processes, a result of its geo-chemical and physical properties, leading to complex multiphase flow processes including advection, diffusion, dissolution, mixing and precipitation (Yamamoto, 2009; Teletzke and Lu, 2013). This poses additional challenges to understanding and predicting the fluid flow.

One area of active research in geological carbon storage is the impact of rock heterogeneity on CO_2 trapping as this ensures long-term storage and reduces leakage risks. Research has found that trapping can significantly increase in the presence of strong heterogeneity (Ide et al., 2007;

Han et al., 2010; Saadatpoor et al., 2010; Elenius et al., 2010; Krevor et al., 2011; Gershenzon et al., 2014; Krevor et al., 2015; Park et al., 2016; Gershenzon et al., 2016, 2017; Al-Khdheeawi et al., 2017, 2018; Singh et al., 2021). As such, storage capacity is also largely controlled by heterogeneity and its orientation relative to the dominant plume migration orientation (Hovorka et al., 2004; Ambrose et al., 2008; Frailey and Leetaru, 2009). Studies have confirmed that tortuosity, footprint, vertical and horizontal migration distance, flow pulsations and migration speed of the plume vary depending on the strength, correlation length and orientation of the rock heterogeneity (Flett et al., 2007; Green and Ennis-King, 2010; Han et al., 2010; Doughty, 2010; Li and Benson, 2015; Trevisan et al., 2015; Guo et al., 2016; Al-Khdheeawi et al., 2017, 2018; Onoja and Shariatipour, 2019; Wen and Benson, 2019; Mishra et al., 2020; Ershadnia et al., 2021; Seyyedi et al., 2022; Ni and Meckel, 2022).

Whilst these discoveries have enhanced our knowledge of the impact of rock heterogeneity on fluid flow, the resultant impact on the multiphase flow properties, the relative permeability and capillary pressure characteristics, is less well understood. Therefore, it has been challenging to develop appropriate heterogeneity characterisation and modelling approaches that represent the impact of small-scale (mm-m) heterogeneity on multiphase flow (Jackson and Krevor, 2020). Thus, most CO_2 reservoir models fail to account for this flow behaviour. We hypothesise this is a major driver behind the unexpected flow observed at numerous CCS sites.

1.5 Aims and Objectives

There remain significant gaps in our understanding, characterisation and modelling of capillary heterogeneity and its impact on multiphase flow, which have yet to be addressed.

Thus far, the majority of research has focused on relatively simple rock structures, spanned limited length scales less than metres and considered only two dimensional (2D) vertical cross sections. The main aim of this thesis is to understand the impact of capillary heterogeneity on fluid flow, in complex rock systems, in three dimensions, and at scales ranging from the laboratory to the field. The topics identified are primarily focused on applications for CCS. However, the issues tackled also have relevance for other scientific and engineering processes where multiphase fluid flow in porous media is central, including hydrocarbon production, geological hydrogen storage or geothermal energy.

The objectives of this thesis are:

1. Evaluate a state-of-the-art characterisation approach to modelling capillary heterogeneity at the core scale in complex systems.

2. Investigate the impact of capillary heterogeneity on multiphase flow properties in complex rock systems.

3. Develop a procedure for upscaling the impact of capillary heterogeneity on multiphase flow in three dimensions at the reservoir scale.

4. Apply the upscaling procedure to a CCS case study to evaluate the impact of capillary heterogeneity on CO_2 flow at the field scale in three dimensions under the influence of gravity and topography.

1.6 Outline of the thesis

In this thesis, the aforementioned objectives are addressed by means of experimental and numerical methods.

Chapter 2 provides an overview on the scientific background and literature, which is followed by an introduction to the experimental methods in Chapter 3.

In Chapter 4, we evaluate a state-of-the-art workflow that characterises capillary heterogeneity on the core-scale using coreflood experimental data. We apply the workflow to five rock types with varying heterogeneity complexity to systematically evaluate the approach. This is followed by an extensive discussion on the limitations of the method. We also present the impact of heterogeneity on multiphase flow properties in these heterogeneous rocks and analyse the observed flow patterns.

In Chapter 5, we present the results from an experimental study conducted on reservoir samples from a proposed CCS site (Endurance) in the UK. We apply a novel workflow to a reservoir sample to characterise the capillary heterogeneity on a core scale. We also present pore-scale imaging results. We conclude by discussing the limitations associated with the experimental procedures and imaging technologies.

Chapter 6 focuses on applying the methods and approaches to a case study. First, the impact of capillary heterogeneity in three dimensions at the metre scale is investigated, varying flow rate, dip and heterogeneity.

A novel upscaling procedure is developed in Chapter 7 to conduct a CO_2-injection simulation study on a kilometre scale reservoir model of the case study. The impact of capillary heterogeneity on field-scale fluid flow in three dimensions as well as the importance of topography and well location is discussed.

We conclude our study, summarise our findings and discuss areas of future work in Chapter 8.

Chapter 2

Scientific Background

2.1 Theory for Multiphase Flow in Porous Media

Subsurface multiphase fluid flow is central to a number of scientific and engineering processes of major societal importance including energy resource use, environmental contaminant remediation, and climate change mitigation. Initially, the motivation behind multiphase flow research was driven by the hydrocarbon industry, where advances in our understanding have led to the development of enhanced oil recovery schemes, increased hydrocarbon production efficiency as well as more accurate recovery predictions.

Understanding and predicting the flow of fluids is thus of vital importance and has led to intensive research over the last decades. Early work by Darcy (1856) established Darcy's Law, which is often considered to mark the onset of comprehensive studies in the field of fluid flow. It is an empirical relationship describing the single-phase flow of fluids in sand filters. This empirical relationship can be written in its general form by averaging the steady-state Stokes equation and describes the resulting volumetric flow rate of a fluid in a medium as a function of absolute permeability, viscosity, pressure changes and gravitational forces (Nutting, 1930; Wyckoff and Botset, 1936; Blunt, 2017). As it is only applicable to single phase flow, it was later extended to describe fluid flow of multiple phases (Muskat and Meres, 1936; Muskat et al., 1937):

$$q_p = -\frac{Kk_{rp}}{\mu_p}(\frac{dP}{dx} - \rho_p g) \quad , \tag{2.1}$$

where q is the Darcy velocity [m·s^{-1}], K is the permeability [m^2], μ is the viscosity [Pa·s], $\frac{dP}{dx}$ is the pressure gradient in the direction of flow [Pa·m^{-1}], ρ is the density [kg·m^{-3}] and g is the component of gravity in the direction of flow [m·s^{-2}]. k_{rp} is the relative permeability of phase p. Equation 2.1 is termed the multiphase Darcy law.

2.1.1 Capillary Pressure

Capillary pressure, P_c , is defined as the pressure difference across an interface that separates two fluid phases in mechanical equilibrium, which simplifies to the following for a gas-water system:

$$P_c = P_g - P_w \quad , \tag{2.2}$$

where P_g and P_w are the gas and water phase pressures [Pa], respectively. Capillary pressure represents the ability of a formation to retain water and as such, it is a key control on the initial saturation distribution observed within a formation (McPhee et al., 2015). It is related to other rock and fluid properties through the Young-Laplace equation:

$$P_c(S_w) = \frac{2\sigma cos\theta}{r} \quad , \tag{2.3}$$

where σ is the interfacial tension [N·m^{-1}], θ is the contact angle [°] and r is the pore radius [m]. Capillary pressure is dependant on various factors including the pore radius, the permeability, the fluid properties (such as density and interfacial tension) and the pore surface properties (wettability and texture) (Blunt et al., 2013; McPhee et al., 2015). For example, a formation with a small pore radius results in increased capillarity and thus a raised capillary pressure. An example $P_c - S_w$ curve is presented in Figure 2.1, which shows the typical monotonic be-

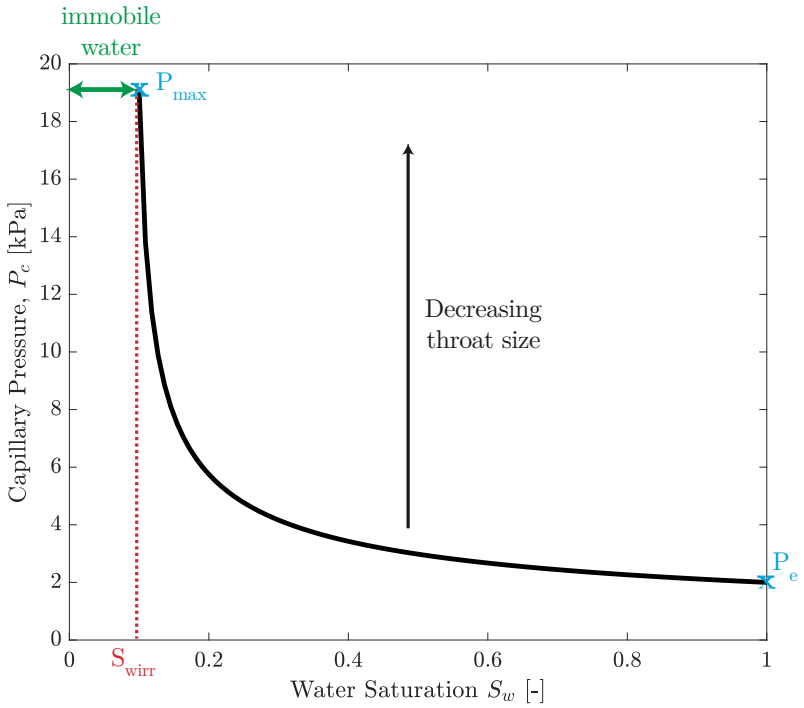


Figure 2.1: A typical drainage $P_c - S_w$ curve for a water-wet rock with a relatively uniform pore size distribution. The entry pressure, P_e, is defined as the capillary pressure, P_c, at $S_w = 1$. This is the initial capillary pressure that needs to be overcome to invade the pore system. The maximum capillary pressure, P_{max}, is defined as the capillary pressure at the irreducible water saturation, S_{wirr}. As water is drained from the porous medium, the capillary pressure gradually increases. This is indicative of water being drained from progressively smaller throat sizes. Consequently, to successfully drain the water, a higher pressure is required.

haviour. However, a recent study has found that the $P_c - S_w$ curve can exhibit non-monotonic behaviour when measured under non-equilibrium conditions caused by the presence of heterogeneity (Shokri et al., 2022).

A variety of experimental methods exist to measure capillary pressure on core samples including the porous plate, centrifuge and mercury intrusion porosimetry (MICP) tests (McPhee et al., 2015). However, the core samples used to obtain the measurements are usually very small, ranging between 1-4 cm in diameter. As such, the capillary pressure measurements obtained from these tests may only represent a small portion of the geological formation or reservoir (Ganat, 2020). This is especially true for rock types characterised by strong heterogeneities with small correlation lengths. To overcome this limitation, the Leverett J-function, $J(S_w)$, can be applied to the laboratory data:

$$J(S_w) = \frac{P_c}{\sigma cos\theta}\sqrt{\frac{K}{\phi}} \quad , \tag{2.4}$$

where σ is the interfacial tension [N·m^{-1}], θ is the contact angle [°], K is the permeability [m^2] and ϕ is the porosity [-]. Equation 2.4 can be applied to extrapolate the capillary pressure data obtained from one specific core sample to another, where both samples have been classified as the same rock type, but with varying porosity, permeability and wetting characteristics (Ganat, 2020). As such, capillary pressure curves obtained from many core samples of the same rock type should collapse onto a single curve, the Leverett J-function.

2.1.2 Relative Permeability

The relative permeability is defined as the ratio between the effective permeability of a phase to the absolute permeability of the porous medium:

$$k_{rp}(S_p) = \frac{k_{eff,p}}{K} \quad , \tag{2.5}$$

where k_{rp} is the relative permeability of phase p, K is the absolute permeability [m^2] and $k_{eff,p}$ is the effective permeability [m^2] (also termed phase permeability). The effective permeability represents the amount by which the flow of phase p is restricted due to the presence of other phases in the pore space (Blunt, 2017). The absolute permeability is defined as the permeability of the porous medium to a phase at 100% phase saturation (McPhee et al., 2015). Thus, to obtain the relative permeability, the phase permeability is normalised to the absolute permeability, and therefore ranges between 0 and 1. The key features of a relative permeability curve are presented in Figure 2.2.

Relative permeability is included in the multi-phase Darcy law as a multiplier for the absolute permeability (Muccino et al., 1998), thus accounting for all sub-Darcy scale physics (Armstrong et al., 2016). This model of the physics incorporates fluid-specific effects arising from the specific phase arrangement such as the impact of wettability on the total flow: in a two-phase system, the presence of the non-wetting phase (which has less affinity for the pore walls than the wetting phase), will impose a resistance to flow (Caruana and Dawe, 1996). Thus, the conductivity of each phase depends on both the absolute permeability of the porous medium and the relative

amount of each phase present (Esmaeili et al., 2019). "The two-phase flow coefficients such as capillary pressure or relative permeability, bridge the gap between the microscopic flow dynamics and the macroscopic behaviour at the porous medium scale" (Tsakiroglou et al., 2007). Therefore, to understand and model multiphase flow through porous media, it is key to obtain accurate estimates for these parameters.

The relative permeability can be measured in a coreflood experiment, where phases are injected into a rock sample and the resultant pressure drop and saturation are measured. Combined with a-priori knowledge of the absolute permeability and phase viscosity, the relative permeability can be calculated from Equation 2.1.

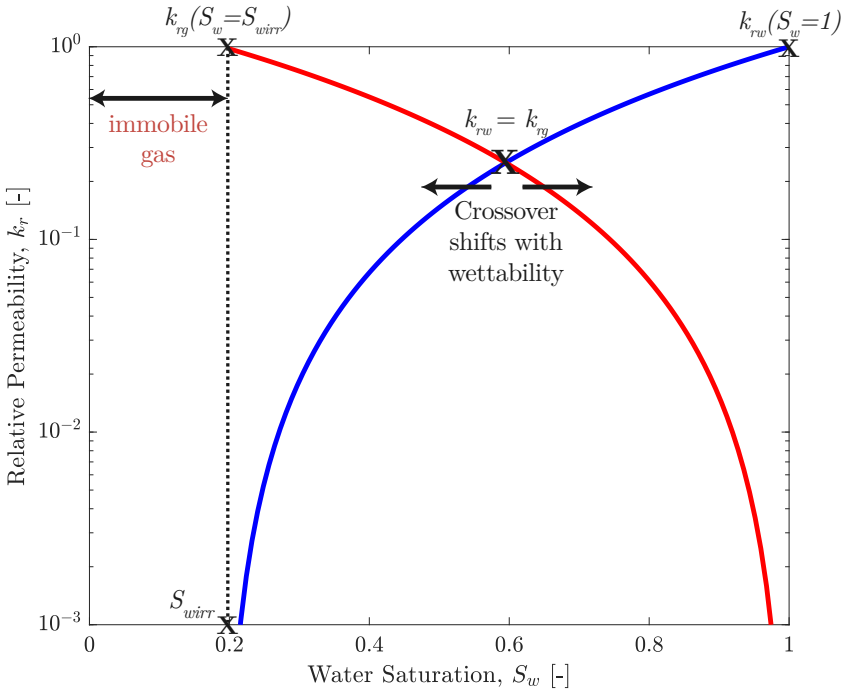


Figure 2.2: Typical drainage relative permeability curves for a gas-water system. As water is drained from the porous medium, k_{rg} gradually increases whereas k_{rw} decreases. The crossover of the two relative permeability curves is indicative of the wettability of the rock and will shift depending on the wettability of the system.

2.1.3 Phase Mobility and Fractional Flow Theory

For a gas-water system, assuming flow is unidirectional and linear, involving incompressible phases and with negligible gravity and capillary forces, Equation 2.1 can be simplified to the following for water and gas respectively:

$$q_w = -\frac{Kk_{rw}}{\mu_w}(\frac{dP}{dx}) \quad , \tag{2.6}$$

$$q_g = -\frac{Kk_{rg}}{\mu_g}(\frac{dP}{dx}) \quad , \tag{2.7}$$

where q is the Darcy velocity [m·s^{-1}], defined as the volumetric flow rate per unit area per unit time, subscript w refers to water and subscript g refers to gas. The total volumetric flow rate is defined as: $q_t = q_w + q_g$. From this, the fractional flow of water, which represents the fraction of the flowing stream comprising water (Buckley and Leverett, 1942), can be derived:

$$f_w = \frac{q_w}{q_t} = \frac{q_w}{q_g + q_w} \quad , \tag{2.8}$$

Substituting equations 2.6 and 2.7 into 2.8 and simplifying gives the following:

$$f_w = \frac{\frac{k_{rw}}{\mu_w}}{\frac{k_{rg}}{\mu_g} + \frac{k_{rw}}{\mu_w}} = \frac{1}{1 + \frac{k_{rg}\mu_w}{k_{rw}\mu_g}}, \tag{2.9}$$

The shock front saturation and average saturation behind the shock front can be determined graphically following Welge's construction (Welge, 1952) (Figure 2.3). Fractional flow theory can provide useful insights into the expected flow behaviour. For instance, Ghanbarnezhad Moghanloo et al. (2015) use the approach to estimate CO_2 storage efficiency from capillary trapping and dissolution.

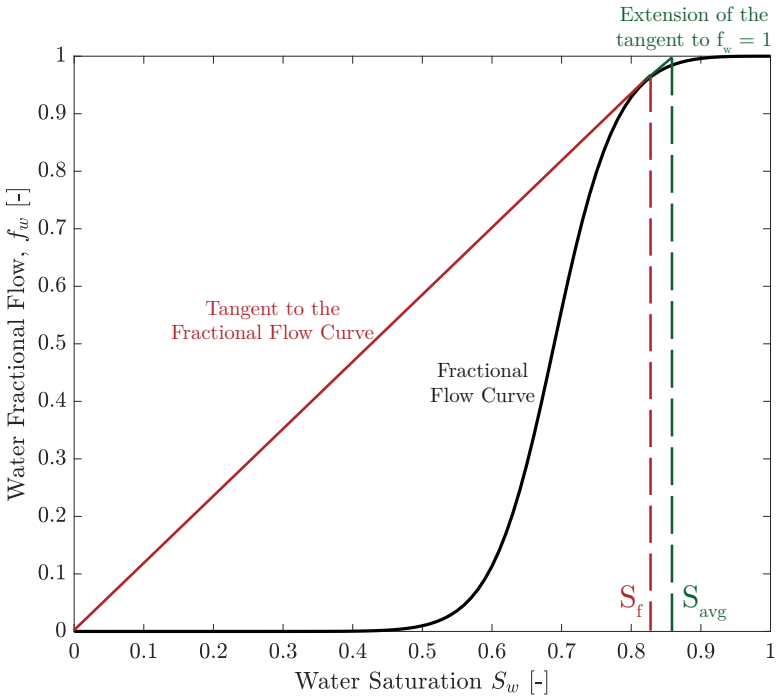


Figure 2.3: Application of Welge's analysis to estimate the shock front saturation from the fractional flow curve.

2.2 Rock Heterogeneity

2.2.1 Definition

Variations in the geographical, chemical, physical and biological conditions lead to a range of geological processes including diagenesis, deposition and deformation. These processes ultimately control the sedimentary structures that form as a result, which can be exhibited as heterogeneity in the rock's physical properties. Rock heterogeneity can be described using common petrophysical properties such as porosity, permeability or wettability and their distribution is in turn controlled by the variation in underlying rock properties including the pore size or the sedimentary fabric (Koltermann and Gorelick, 1996; Fitch et al., 2015).

Rock heterogeneity is exhibited at a range of scales from micrometres to hundreds of metres. As such, a range of technologies with variable resolution can be selected to collect petrophysical data and characterise the heterogeneity (Figure 2.4). Subsequently, this data is often applied to hierarchies of heterogeneity, which categorise the heterogeneity originating from a large domain into different groups of scales (Jung and Aigner, 2012; Fitch et al., 2015). The groups of scales presented in Figure 2.4 are discussed individually in the following sections.

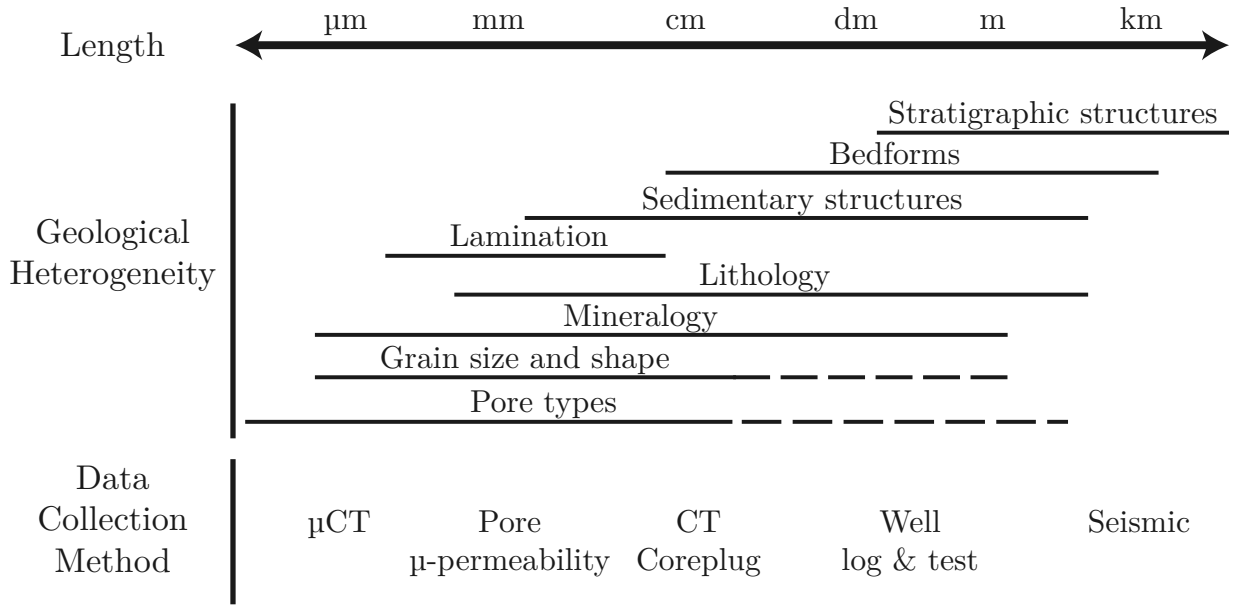


Figure 2.4: The different length scales of depositional geological heterogeneities and the most common data collection methods. Adapted from Fitch et al. (2015).

2.2.2 Micrometres

Rocks may exhibit petrophysical heterogeneity on the micrometre scale such as variations in pore structure, topology, mineralogy, grain size, grain shape, curvature and pore connectivity. Carbonates are often characterised by this type of heterogeneity. Clasts such as shell fragments can be found suspended in the rock's matrix or sparry cement due to the shallow marine depositional environment that they were deposited in. Cementation, dissolution and fracturing of the rock matrix can occur after deposition (Tavakoli, 2020). This can lead to the formation of vugs and microporosity (Cantrell and Hagerty, 1999).

High-resolution X-ray tomography (micro-CT) creates images based on the variation of X-ray attenuation within the scanned rock, which enables the visualisation of rocks at the pore-scale in a non-destructive manner. Following image processing, key petrophysical properties can be extracted such as pore and throat sizes, connectivity, grain shape and fluid curvature. For instance, the porosity field from micro-CT images was used in a simulation study to investigate the impact of heterogeneity on dissolution rates (Pereira Nunes et al., 2016). The results confirmed the impact heterogeneity can have on flow: the average dissolution rate strongly depends on the degree of heterogeneity, where the most heterogeneous sample displayed a decrease in rate of up to 2 magnitudes (Pereira Nunes et al., 2016). In the work by Andrew et al. (2014), 300 contact angles were extracted from micro-CT images of a rock sample. The measurements exhibited a large spread, attributed to hysteresis and surface heterogeneity.

Similarly, mercury intrusion porosimetry (MICP) can be utilised to infer the pore throat and size distribution of a rock sample. Here, mercury is forced to invade the pore space due to an externally applied pressure, which is incrementally increased. The pressure and volume of intruded mercury is recorded throughout, from which the pore entry distribution and capillary pressure saturation curves can be inferred. However, this technique is destructive, meaning that the sample cannot be used for further analysis. The pore size distribution can be indicative of porosity heterogeneity and microporosity. Furthermore, comparing the results from various samples of the same formation can provide information on metre-scale heterogeneity.

In Nuclear Magnetic Resonance (NMR) applications, the transverse relaxation time is used to determine petrophysical properties such as porosity or wettability (Hosseini et al., 2018). Baban et al. (2021) applied NMR to a sandstone sample and determined it to be water-wet, having imaged preferential gas occupancy by larger pores identified from pore size distribution. Similarly, Lai et al. (2016) utilised NMR technology to gain an insight into the pore structure of tight reservoir samples and identified microfractures and microporosity, based on T2 peaks and pore size distributions. Interestingly, short effective encoding periods from the first domain of signal acquisition can also be applied to NMR data to deduce the degree of heterogeneity within a rock plug, as presented by Liu et al. (2018).

2.2.3 Millimetres to Centimetres

On these length scales, micro permeameters or hand-held permeameters can be used to quantify spatial variations in permeability of core plugs (Manrique, 1994). These devices either inject or extract phases into/from a rock sample and measure the resultant pressure drop. Using the pressure drop and flow rate, the permeability can be determined using analytical expressions (Rogiers et al., 2014). This method represents a cost-effective and time-effective option to obtain petrophysical measurements of numerous samples.

Medical-CT scanners are an alternative technology to image heterogeneity on samples that are typically larger than those imaged by micro-CT scanners. As the resolution of medical CT scanners is only 0.01-1 mm, the images cannot directly image individual pores or grains. However, porosity can be inferred from the distribution of voxel grayscale values and can highlight mm-cm scale heterogeneity structures. Some work suggests that high-resolution dental CT-scanners may be superior to the traditional medical-CT scanners for porosity determination (Farokhian et al., 2019). Nevertheless, CT scanners have been used in countless studies to image fluid flow and characterise rock samples. For example the work by Huang et al. (1996) discovered, using CT imagery, a “heterogeneously-wet system” in one of their samples, which exhibited spatial variations in wettability.

Interestingly, images from medical CT can be combined with higher-resolution data to not only verify the segmentation of the high-resolution images, but to also provide further insight into the heterogeneity and its scales. Pini and Madonna (2016) applied this approach to a Berea sandstone, combining medical CT with synchrotron images, to analyse porosity heterogeneity with characteristic length scales over 8 orders of magnitude. The results provide an indication of the REV size of the sample, which was surprisingly small.

2.2.4 Metres to Kilometres

On this mesoscopic scale, wells can be drilled to sample core plugs, conduct well logging and perform well tests. Well tests, or pressure transient tests, are used to determine reservoir properties, such as permeability, averaged over 10s metres by recording the well flow rate and pressure drop. Core plugs can be analysed visually in a core store (100s metres of core). Coring is particularly important for providing information on vertical heterogeneity in a reservoir, such as unconformities or facies boundaries. The core diameter ranging between 4.5–13.5 cm (Schön, 2015) is limited by the diameter of the borehole, thus they provide limited information of the lateral extent of heterogeneity. Hence, seismic surveys are often conducted that can covers 100s km^2 areas. Seismic surveys can image large stratigraphic structures such as channels, but can also indicate the presence of faults, which can act as leakage pathways particularly important for CCS operations.

Sedimentary structures and the importance of characterising these in geomodels only became a focus in literature in the second half of the twentieth century, primarily driven by the hydrocarbon industry (Collinson, 2019). In the context of this thesis, the most important sedimentary structures are cross laminations and bedding (Figure 2.5). Cross laminations are common features of sand-grade sediments and form when sands are deposited by ripple migration in low energy environments such as deep marine (Collinson, 2019). The principal direction of laminations and their pattern are controlled by the wind/flow direction and the flow velocity (Harms, 1979) and as such can vary significantly within a reservoir. The structures are typically clustered together and can therefore have a resultant impact on fluid flow.

Many environments exhibit thick beds including river channels and tidal estuaries (Harms, 1979). The large beds usually consist of smaller sedimentary features mentioned previously. Cross bedding is a result of the migration of large-scale bedforms and is typically found at larger scales and involves coarser sands and conglomerates (Collinson, 2019). Bedding results in sharp boundaries between distinct rock types and becomes an important measure for reservoir connectivity and layer communication.

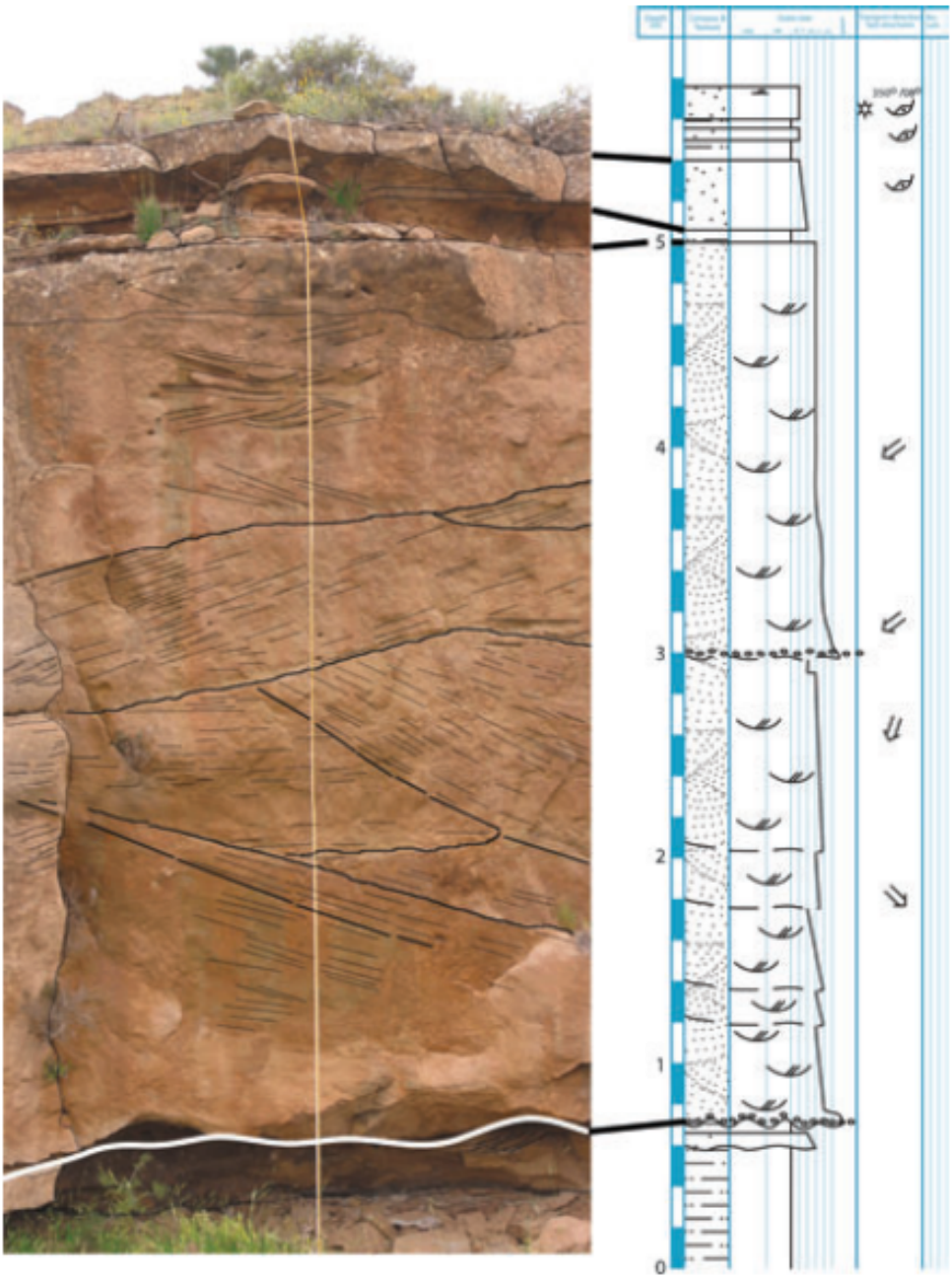


Figure 2.5: Outcrop photograph and sedimentological log of a coarse-grained meandering river sandstone with cross-bedding. From Donselaar and Schmidt (2005).

2.3 The Impact of Rock Heterogeneity on Multiphase Flow Properties

2.3.1 Rate Dependence of Relative Permeability

Relative permeability is one of the key parameters controlling fluid behaviour (Equation 2.1) and as such its role has been a focus of numerous studies over decades. Historically, relative permeability calculations assumed that the rock core, on which experiments were performed, was homogeneous (Welge, 1952; Johnson et al., 1959). Hence, the majority of research during this time focused on the impact of reservoir conditions including overburden pressure, temperature and fluid viscosity on the relative permeability (Wyckoff and Botset, 1936; Leverett, 1939; Wilson, 1956).

However, the work by Corey and Rathjens (1956) showed that rock heterogeneity significantly influences relative permeability: there was a large range of calculated permeabilities depending on the orientation of the rock's bedding plane angles to the imposed flow direction. The interplay of the heterogeneities with the fluids meant that fluid behaviour could vary on a mm by mm basis, thus the relative permeability curve averaged over the entire core would fail to describe or predict the detailed flow patterns within the core. Interestingly, the authors showed, by means of a coreflood experiment, that the gas relative permeability reduces as a result of flow directed perpendicular to the bedding. Corey and Rathjens (1956) concluded that it is necessary to incorporate these rock heterogeneities in calculations in order to improve fluid flow predictions.

Works immediately following this discovery primarily explored wettability variations and their impact on multiphase flow properties. Notable is the research by Fatt and Klikoff (1959); Fatt (1961) who showed through experimental and numerical methods that capillary pressure and relative permeability are functions of wettability and vary with the degree of trapping observed.

Only later, did the focus shift towards exploring the impact of porosity-permeability heterogeneity on multiphase flow (Huppler, 1970; Kortekaas, 1985; Hove et al., 1990; Van Duijn et al., 1995). It was shown that cores with a moderately high degree of heterogeneity could in fact behave in a homogeneous way, given their heterogeneities are well distributed. On the contrary, in the presence of large vuggy regions the obtained waterflood data showed significant rate dependency. Interestingly, it also emerged that a small heterogeneity in an overall homogeneous system can still significantly alter the fluid behaviour leading to, for example, a change in the amount of fluid trapped after displacement has taken place. Lastly, the studies exemplified the dependence of fluid flow on the orientation of the sedimentary structures present in the core. For example, Kortekaas (1985) focused their work on Festoon crossbedding, which is typically found in sandstone reservoirs. Their simulations investigated whether fluid flow was influenced by the orientation of the laminae to the principal flow direction. They found the displacement, on reservoir scales, to be more favourable when flow is directed perpendicular to these sedimentary structures. Additionally, the analysis showed significant improvement in recovery after adding a surfactant or polymer to the drive water. Overall, it became clear that rock heterogeneity plays a key role in fluid behaviour, however that it was still challenging to predict this.

2.3.2 Capillary Pressure Heterogeneity

With increasing investigations on the impact of heterogeneity on relative permeability, it emerged that rock heterogeneity can also result in capillary pressure anisotropy and effective capillary pressure variations. The former describes the phenomenon, where regions within a single rock core are characterised by individual capillary pressure characteristics and the latter describes the variation in the core-average, effective capillary pressure characteristic controlled by changes in the heterogeneity. Dawe et al. (1992) presented an extensive experimental study and found that the presence of capillary pressure variations leads to the development of irregular displacement fronts, which were visible on X-ray CT imagery, a phenomenon also reported in Cuthiell et al. (1993). The authors concluded that no single $P_c - S_w$ curve could characterise

the core.

Ferrand and Celia (1992) applied pore network modelling to simulate variations in the effective $P_c - S_w$ curves due to changes in the heterogeneity structure and noted that averaging local measurements, which was the standard method to obtain the effective capillary pressure, would not sufficiently predict saturation profiles. It became evident that it was not only important to characterise porosity-permeability variations within a rock, but also derive a relationship of these with capillary pressure. This phenomenon of capillary pressure variations within a single rock was later termed capillary heterogeneity by Chang and Yortsos (1992) and subsequent studies repeatedly confirmed the importance of incorporating capillary pressure variations in flow simulations and characterisation efforts as this enabled accurate representation of fluid flow (Bradford et al., 1998; Ho and Webb, 1998; Mannseth et al., 1998; Nordtvedt et al., 1999; Dekker and Abriola, 2000).

"Two-phase flow is a competition of nonlinear processes involving capillary, gravity, and viscous forces" (Eilertsen et al., 1997) and this force interplay is largely affected by heterogeneity. As the name suggests, capillary heterogeneity becomes increasingly important with a reduction in flow rate and an increase in capillary relative to viscous forces. The resultant shift towards capillary-limited flow emphasizes the presence of capillary heterogeneities within a rock core, which will in turn affect fluid behaviour (Ringrose et al., 1993; Graue, 1994). For example, at high flow rate Ringrose et al. (1993) observed no visible difference in oil recovery between models with perpendicular and parallel orientated heterogeneous layers. As such, it is crucial to specify the flow regime, in which multiphase flow measurements were taken. Interestingly, it used to be common practice to perform coreflood experiments at very high flow rates resulting in large core average pressure drops. With respect to typical flow rates observed in the subsurface, they fall into the capillary-controlled flow regime. Thus, rates representative of the reservoir should be used consistently in experimental and simulation studies, as emphasized by Batycky et al. (1981); Huang et al. (1995).

Herein, we use a continuum scale capillary number, N_c to describe the ratio between capillary and viscous forces (Virnovsky et al., 2004):

$$N_c = \frac{H}{L}\frac{\Delta P}{\Delta P_c} \quad , \tag{2.10}$$

where H [m] is a length scale associated with the heterogeneity, e.g. a layer thickness, L [m] is a length scale in the direction of flow, ΔP [Pa] is the pressure differential across L, and ΔP_c [Pa] is a contrast in capillary pressure imposed by the heterogeneities. The ratio of viscous to capillary forces over length scales of centimetres to metres controls the importance of capillary heterogeneity. At high flow rates i.e. high capillary numbers, viscous forces dominate the fluid flow and the impact of capillary heterogeneities diminishes. As the rate is reduced and the capillary number decreases, capillary heterogeneity becomes increasingly important. In the subsurface, flow is prevalently characterised by the capillary-controlled flow regime (Chang and Yortsos, 1992; Ringrose et al., 1993; Stubos et al., 1993; Yortsos et al., 1993; Chaouche et al., 1994; Honarpour and Saad, 1994; Huang et al., 1995; Mori et al., 2015).

Recent literature, applying a range of analytical, numerical and experimental tools, indicates that capillary heterogeneity is one of the leading causes of anisotropy and flow rate dependency in observed relative permeability (Tsakiroglou et al., 2007; Krishnamurthy et al., 2017; Jackson et al., 2018; Krishnamurthy et al., 2019; Bakhshian et al., 2020a; Boon and Benson, 2021; Ershadnia et al., 2021). At high capillary numbers the role of capillary pressure heterogeneities diminishes and a single relative permeability characteristic controls the flow in a domain. This is known as the viscous-limit or effective relative permeability, and is independent of heterogeneity (Renard and de Marsily, 1997). As the capillary number is reduced, multi-phase flow heterogeneities, specifically capillary pressure, become more important. At intermediate capillary numbers, where both viscous and capillary effects influence flow, the relative permeability is both flow rate dependent and anisotropic. Equivalent relative permeability curves should then be used to model flow, which are rate dependent and unique to a particular region of the rock that exhibits similar multiphase properties (Renard and de Marsily, 1997). At very low capillary numbers, the relative permeabilities are different from the viscous curves but are again insensitive to flow rate.

2.4 Flow Processes Resulting from Capillary Heterogeneity

As capillary heterogeneity is a major control on the resultant relative permeability, it can lead to interesting flow patterns observed during experiments and derived analytically. Interestingly, early work found the non-wetting phase to be more directional compared with the wetting phase (Smith, 1991). The authors attribute this to a significantly higher variance in non-wetting phase permeability. More recently, other factors including the phase physical properties, such as viscosity and density, as well as the host rock properties for instance wettability, have been identified as additional causes leading to the non-wetting phase being more severely affected by the presence of heterogeneity (Zhang et al., 2011; Akhlaghi Amiri and Hamouda, 2014; Debbabi et al., 2017). In the following sections, we review the leading impacts of capillary heterogeneity on upscaled flow.

2.4.1 Capillary Crossflow

If we imagine a simple, two layer rock core with distinct capillary pressure characteristics in each layer as shown in Figure 2.6. The layers are orientated parallel to the axis of flow and a wetting and non-wetting phase are co-injected into the rock core across the entire cross-sectional area. At low capillary numbers, when the importance of capillary heterogeneity increases, viscous forces drive the portion of the non-wetting phase residing in the low entry pressure layer towards the outlet. Consequently, capillary forces act on the non-wetting phase in the high-entry pressure region and force it into the low entry pressure region (Ringrose et al., 1993). This flow behaviour, enabled by the "positive force interplay" (Ringrose et al., 1993), is termed crossflow and allows for the non-wetting phase to move through the pore space more easily as it has to overcome a smaller entry pressure in layer 1. This results in raised effective phase relative permeabilities in the flow direction as it enables the phases to migrate more optimally throughout the pore space (Corey and Rathjens, 1956).

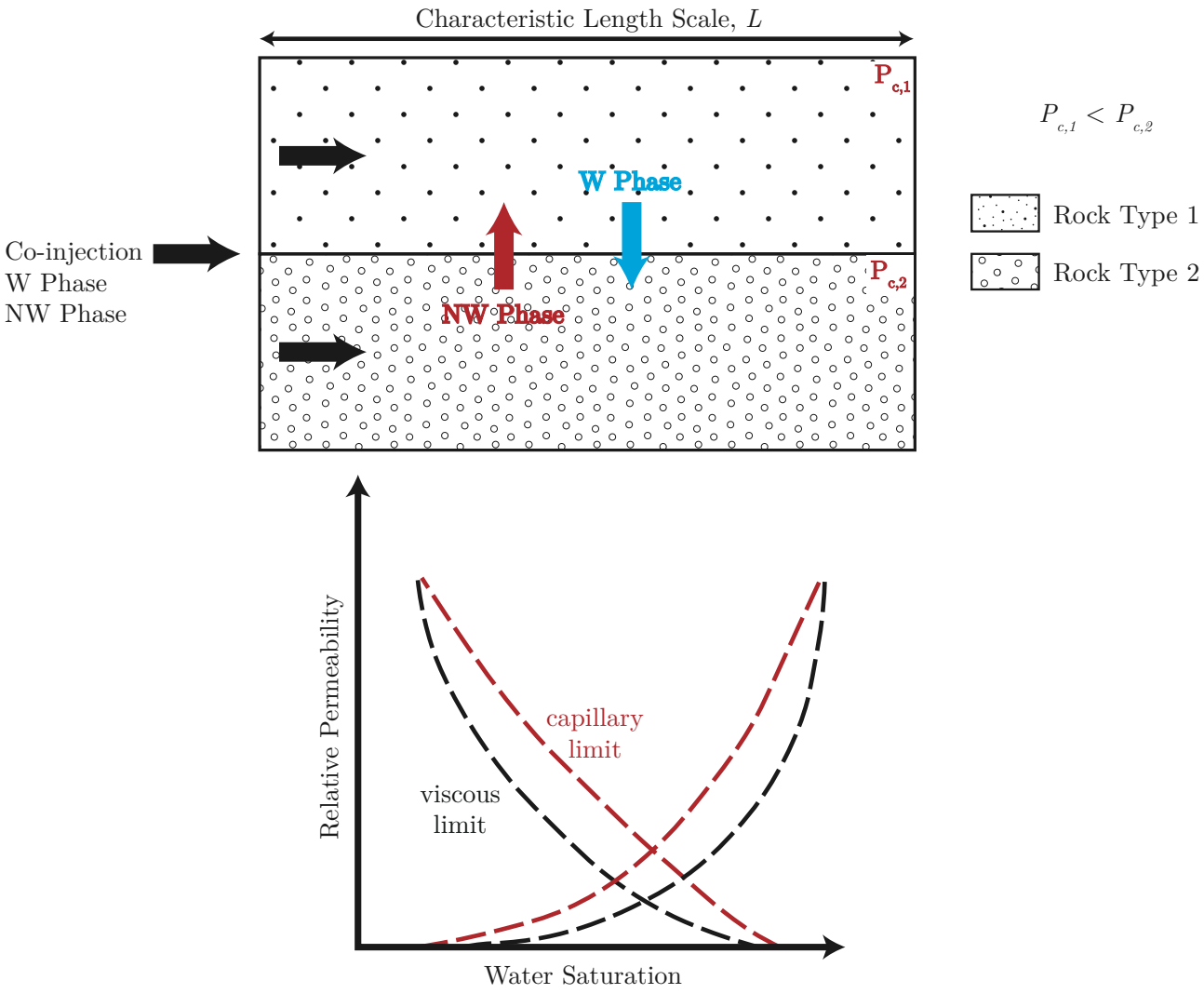


Figure 2.6: The impact of layers orientated parallel to the principal axis of flow on the relative permeabilities. Flow is directed parallel to layers. Capillary crossflow occurs and the non-wetting phase flows into the low entry pressure layer, resulting in raised phase relative permeabilities.

The amount of crossflow occurring in a medium is a function of the wettability, mobility ratio, capillary number and storage ratio and has been extensively studied (Baker, 1993; Ringrose et al., 1993; Wright and Dawe, 1983; Graue, 1994; Debbabi et al., 2017; Salmo et al., 2017; Li et al., 2017; Shiri and Shiri, 2021), Baker (1993) provides a comprehensive literature review. Interestingly, in single-phase injection of the non-wetting phase, the non-wetting phase may also crossflow into the low-permeability layer, while the wetting phase may flow across into the high-permeability layer. This is counter intuitive and according to Debbabi et al. (2017) attributed to the necessity to dampen transverse gradients in capillary pressure, caused by the rapid build up of non-wetting phase saturation in the high-permeability layer. Predominantly, the non-wetting phase is confined to the low entry pressure layer, which allows for it to move

more easily through the medium, resulting in a relative increase in the non-wetting phase permeability (Smith, 1991; Ringrose et al., 1993; Zhang et al., 2011; Reynolds and Krevor, 2015; Jackson et al., 2018). Experimental observations of crossflow involving more than two parallel layers have also been reported, see for example Zhang et al. (2014).

2.4.2 Cross-Layer Flow and Capillary Trapping

In contrast, when flow is directed perpendicular to bedding characterised by distinct capillary pressure characteristics, the high entry pressure layers act as capillary barriers. Both phases migrate through the low and high permeability regions. As noted by Ringrose et al. (1993), this scenario results in negative force interplay, where the capillary barriers hinder the viscous drive of non-wetting phase out of low entry pressure regions and migration from the high to low entry pressure layer. As a result, the non-wetting phase is trapped in the low entry pressure layers upstream of the capillary barriers and saturation discontinuities between layer boundaries form, Figure 2.7 (Ringrose et al., 1993; Krevor et al., 2011; Debbabi et al., 2017; Harris et al., 2021). The trapping ultimately leads to a reduction in non-wetting phase relative permeability (Tanzil et al., 2002; Rabinovich et al., 2016). Work has also been undertaken to investigate the fluid behaviour in domains with tilted layers, which highlighted the interplay of gravity, viscous and capillary forces as well as challenges modelling these (Børresen and Graue, 1997).

2.4.3 Connected Pathway Flow, Fingering and Channeling

Some rock types exhibit heterogeneity that cannot be grouped into distinct layers, which is particularly common for conglomerates or carbonates. For these types, flow instabilities may arise (Tsakiroglou et al., 2007) leading to the formation of connected pathway flow, capillary/viscous fingering or channeling (Perrin and Benson, 2010; Akhlaghi Amiri and Hamouda, 2014; Kim et al., 2018; Spurin et al., 2019, 2021). For instance, Kim et al. (2018) presents an extensive experimental and simulation study on a heterogeneous conglomerate reservoir core. The coreflood simulations, with input from X-ray images, revealed the formation of well-connected

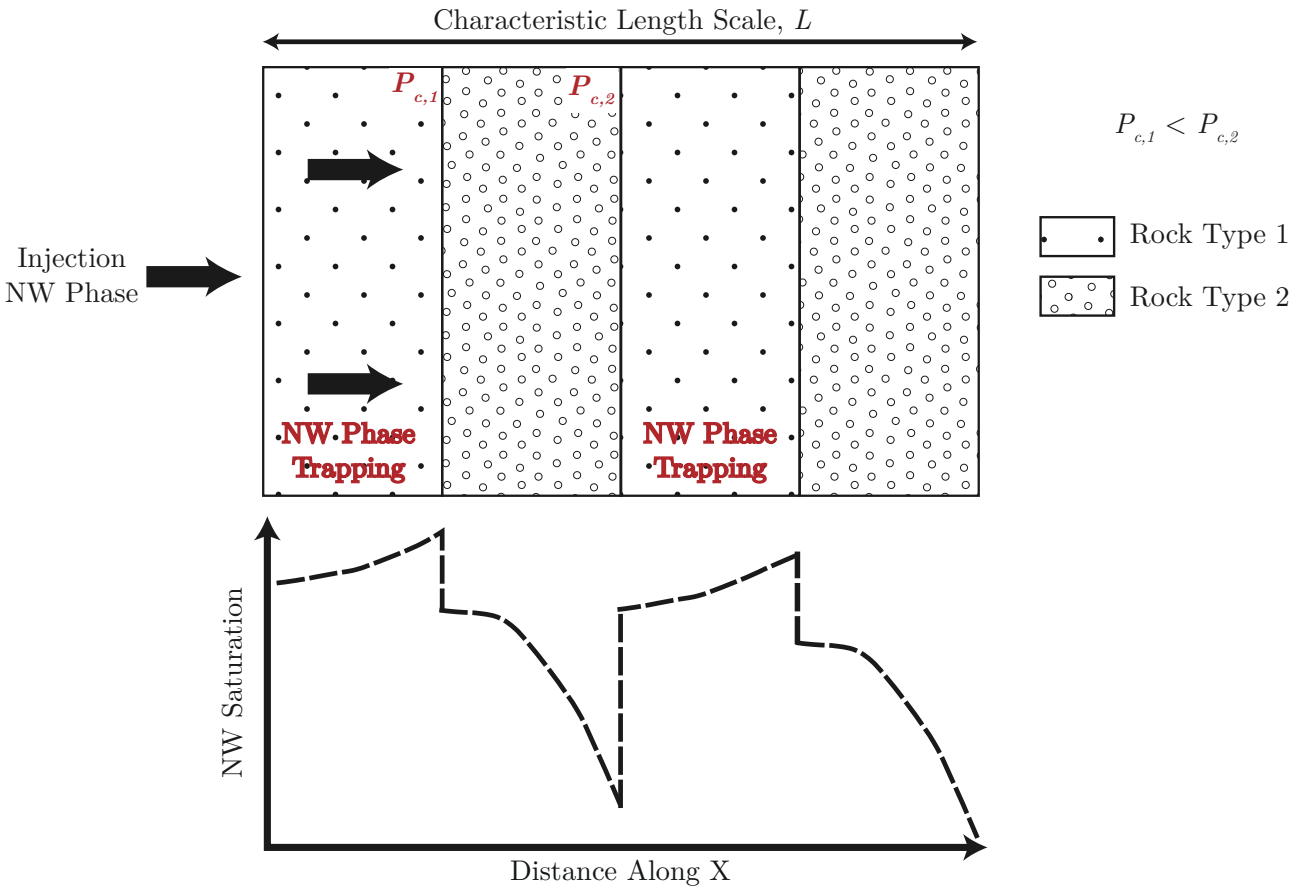


Figure 2.7: The impact of layers orientated perpendicular to the principal axis of the saturation distribution. The non-wetting phase is trapped in the low entry pressure layers upstream of the capillary barriers.

non-wetting phase pathways, owing to the dense discontinuity networks within the clasts (Figure 2.8). In contrast to the parallel/perpendicular layer cases, there is no universal trend between the phase relative permeabilities and capillary number and the two-phase behaviour can become complicated for these complex structures (Virnovsky et al., 2004; Wei et al., 2022).

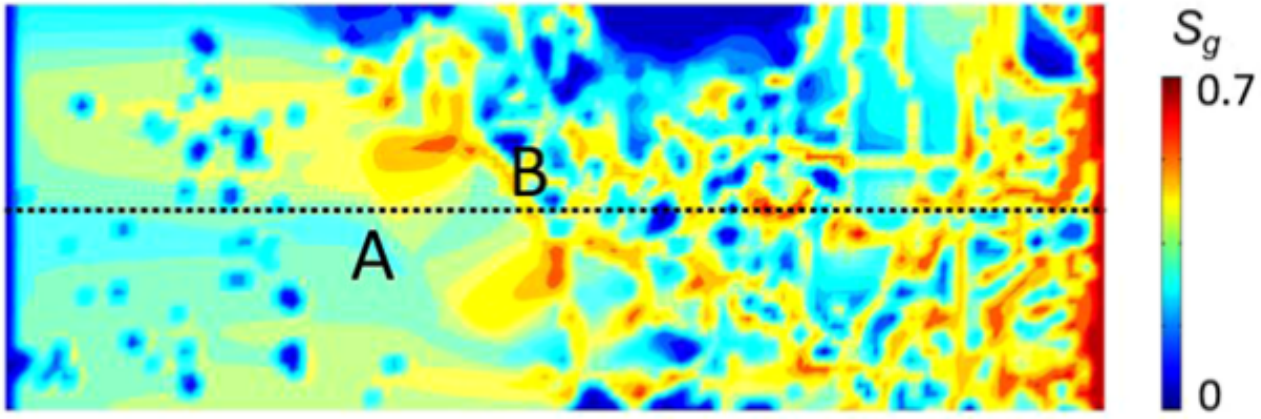


Figure 2.8: Non-wetting phase saturation through a digital model of a conglomerate rock sample, exhibiting the formation of channels. From Kim et al. (2018).

2.5 Characterising and Modelling the Impact of Capillary Heterogeneity

2.5.1 Elementary Volumes

In the following sections we review different approaches to characterising and modelling the impact of capillary heterogeneity. As discussed in Section 2.2, heterogeneity can be observed on all scales, therefore average properties have to be developed to capture the unresolved scales. To do this, it is crucial to determine the sample's representative elementary volume (REV).

Traditionally, the REV is defined as the volume at which an average property can be taken to be representative of the entire rock sample. Consequently, the lower limit, V_{min}, depends on the pore structure and size, whereas the upper limit, V_{max} is controlled by morphological changes within the rock sample, as presented in Figure 2.9 (Bear, 1988; Brown et al., 2000). As long as the chosen sampling size lies within these limits, the petrophysical property will not vary between volumes of the same size originating from different regions of the porous medium. Therefore, it is an effective property (Renard and de Marsily, 1997).

It is possible for a porous medium to be defined by multiple REVs, depending on the characteristic length scales of the heterogeneities and the flow processes that are the focus of a study. For example, a core plug may exhibit heterogeneities on a mm-scale caused by wettability variations, whilst also exhibiting cm-scale structural heterogeneities such as bedding.

When performing coreflood experiments to measure multiphase flow properties such as relative permeability, the resultant measurement only describes the impact of heterogeneities that have an REV smaller than the core plug on which the experiment was performed (Reynolds, 2016). It follows that should the porous medium under consideration be smaller than a hypothetical REV, effective medium theory (EMT) cannot be applied to describe the aggregate fluid flow behaviour (Guéguen et al., 2006). In these cases, discrete models of the porous medium are built by performing upscaling, and flow simulations are subsequently run to model the flow behaviour

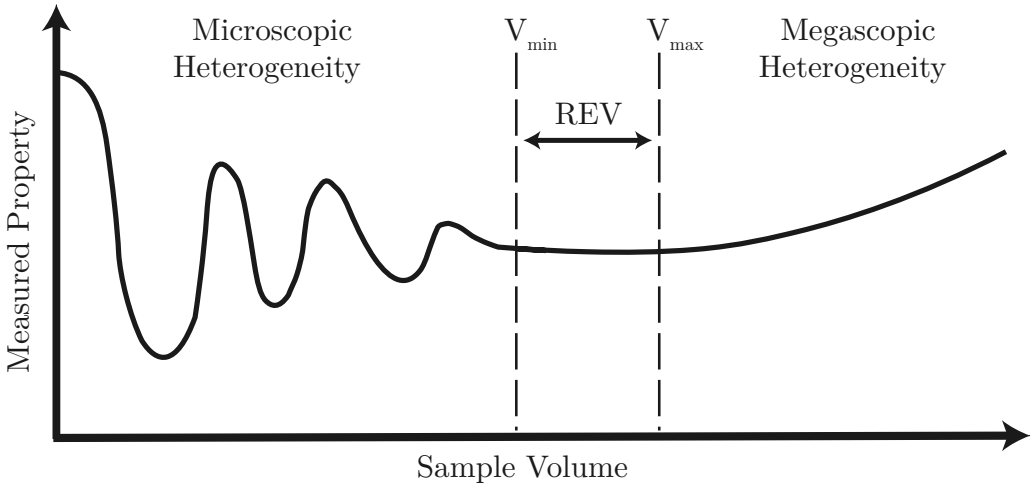


Figure 2.9: Concept of REV. Adapted from Brown et al. (2000); Nordahl and Ringrose (2008).

on that scale. An example of this is a full field reservoir model, which is characterised by strong heterogeneity with large correlation lengths.

With respect to the concept of REV, the focus of this thesis is to evaluate the impacts of heterogeneity. Thus we are not identifying a length scale at which an average property, such as porosity, can be taken to be representative of the entire core. The relevant issue for this work is to verify that the voxel scale/grid block size is large enough such that a continuum property has meaning. This can be estimated by comparing the pore structure of each rock type to the voxel size.

We note the importance of additionally considering the REV of the capillary pressure characteristic as this might be different from the REV of the porosity. However, quantifying this poses a challenge. Previous work using micrometre resolution X-ray imaging and pore network models has identified that correlation length scales of capillary pressure characteristics and porosity are of a similar order of magnitude (Jackson et al., 2020; Zahasky et al., 2020). We assume, based on the above estimates, that as long as the voxel scale allows for the porosity to be considered a valid continuum property that this also applies to the capillary pressure characteristic. Throughout the remainder of this thesis, we will use the term elementary volumes instead of REV.

2.5.2 Pore-Scale Capillary Heterogeneity

With advances in imaging technologies such as micro-CT scanners, methodologies to characterise capillary heterogeneity on the pore scale have increasingly been developed. Comprehensive reviews on pore scale modelling are widely available, see for example Celia et al. (1995); Blunt (2001); Blunt et al. (2002); Golparvar et al. (2018). As such, we only provide a brief review.

Pore-scale fluid modelling methods can be categorized into bundle of capillary tubes modelling (BCTM), direct pore scale modelling (DPSM) and pore network modelling (PNM).

In BCTM, the simplest of the three methods, a bundle of capillary tubes is chosen to represent the pore space. This method was the first to be used for pore-scale fluid modelling, but has since seen significant advancements. For instance, CT images can now be used to extract capillary tubes with irregular cross sections (Virnovsky et al., 2009; Kim and Lindquist, 2012; Zhou et al., 2014). However, these simplified models do not capture the connectivity between the pore space and therefore cannot accurately describe various pore-scale fluid phenomena such as trapping or ganglia mobilisation (Celia et al., 1995; Golparvar et al., 2018).

An alternative approach is DPSM, whereby CT images are used to build a grid-based pore space model, on which the fluid flow is subsequently simulated by solving the Navier-Stokes equation using numerical methods such as Lattize-Boltzmann (Armstrong et al., 2016; Bakhshian et al., 2020b; Zahasky et al., 2020). For example, DPSM was used to investigate the impact of surface roughness on relative permeability in Yi et al. (2019). The results indicate that an increase in surface roughness leads to a decrease in wetting and non-wetting phase relative permeabilities. Interestingly, the simulations also found that roughness can form an unsteady flow state at low wetting phase saturation, displayed as a big kink in the non-wetting phase relative permeability.

Finally, in PNM the pores and throats are represented as balls and tubes, respectively. Navier-Stokes continuum approximations are used to simulate the fluid flow, which results in reduced computational time and opens up the possibility to analyse centimetre-sized samples (Golparvar et al., 2018; Zahasky et al., 2020). Most relevant to this thesis is the work by Zahasky et al.

(2020) in which the predictive ability of PNM was assessed using coreflood experimental data. The authors applied PNM to build a Darcy-scale digital core model from a dry CT scan, with which they successfully matched the experimental saturations (Figure 2.10) and predicted the core-average relative permeability. The results show that the most time-consuming part of a core characterisation workflow, the coreflood experiment, is not needed to accurately characterise the core and its heterogeneities. However, it is important to note that this workflow was only applied to two Bentheimer sandstone cores, which are known to be well-behaved and associated with relatively simple flow behaviour. Workflow applicability limitations, with respect to more complex reservoir samples, has not yet been studied in detail.

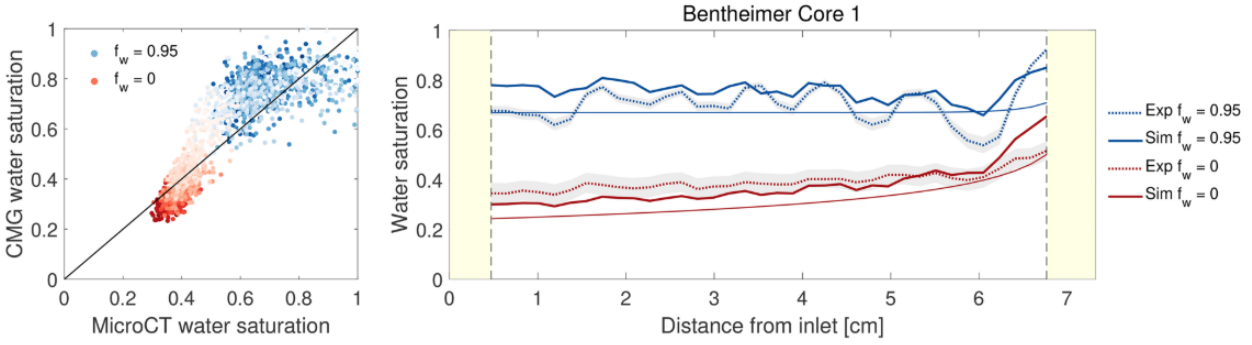


Figure 2.10: Saturation match between the digital core model and the experimental observations on a Bentheimer sandstone. Left: voxel saturation correlation between the experiment and the simulation, where darker points correspond to voxels located close to the inlet and faded points indicate locations near the outlet. Right: Slice-average saturations from the experiment (dashed) and the simulation (solid). The thick solid lines indicate results from a model using heterogeneous capillary pressure and relative permeability, whereas the thinner sold lines present results from a model, which used homogeneous properties. From Zahasky et al. (2020).

2.5.3 Core-Scale Capillary Heterogeneity

Core-scale capillary heterogeneity characterisation efforts increasingly became a focus of literature marked by the discovery of capillary heterogeneity in the 1990s. The modelling approach typically involves two steps: 1) flow experimental data of specific rock samples is collected, for instance a coreflood experiment is conducted and the saturation distribution is recorded using imaging technology, 2) the data is used to infer the capillary heterogeneity and this information is incorporated into a digital model of the core, 3) the success of the characterisation workflow is evaluated by simulating the laboratory experiment using the digital model as input, and comparing the resultant flow with laboratory observations. We review the most relevant capillary heterogeneity characterisation approaches developed since the 1990s.

One of the early methods to characterise capillary heterogeneity was developed by Huang et al. (1995), who used a combination of core flood experiments and ECLIPSE simulations to model capillary trapping mechanisms in water-wet laminated rocks. Experimentally-derived porosity and permeability data was used to obtain the localised capillary pressure through J-function scaling (Leverett, 1941), with which a 2D core model was built. The method resulted in a better agreement between experiment and simulation saturations compared with previous modelling attempts, primarily because the heterogeneity was better accounted for. Yet, the simulation was unable to replicate the saturation distribution along the whole length of the sample. This discrepancy indicates an insufficient or incomplete representation of capillary heterogeneity. Nevertheless, the model revealed that capillary heterogeneity can lead to an increase in non-wetting phase trapping in high-permeability laminae caused by the relative importance of capillary to viscous forces. This exemplifies the value of building digital core models, which strengthen our understanding of capillary heterogeneity and its control on fluid behaviour.

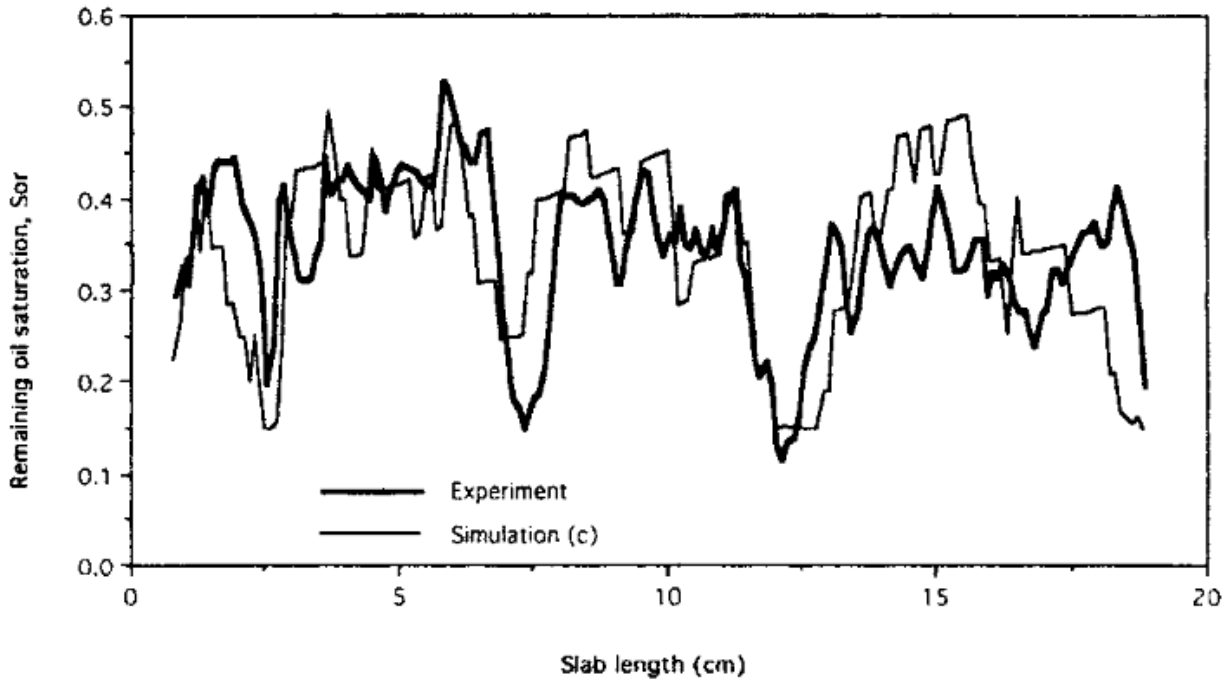


Figure 2.11: Comparison of experimental (thick line) and simulation (thin line) residual oil saturation along the length of the sample. The results display an improved match compared with previous models. Yet, there still is a significant discrepancy between the two data sets and the simulation under and over predicts the residual oil saturation in portions of the sample. From Huang et al. (1995).

The literature has also reported simpler approaches to modelling capillary heterogeneity, whereby an upper limit of the number of $P_c - S_w$ curves within a sample is introduced, three in Saad et al. (1995) and two in Fincham and Gouth (2000) and Berg et al. (2013). For instance, Saad et al. (1995) identified three separate regions or rock types within one sample, by grouping the spatial porosity-permeability data. Consequently, only three relative permeability and capillary pressure curves were assigned, which enabled the authors to successfully replicate the experimental saturation distribution. In contrast, others reported challenges matching core-flood observations using this simplified method (Børresen and Graue, 1997; Eilertsen et al., 1997). The grouping-type approach is only suitable for rock cores with simple heterogeneity. For strong capillary heterogeneity with short correlation lengths, a few $P_c - S_w$ curves will not suffice in representing the flow. Additionally, some authors derived the $P_c - S_w$ curves of one region from experimental data originating from the other region (Børresen and Graue, 1997). This assumption clearly breaks down when the core is characterised by two or more rock types.

An alternative approach exists where the local experimental saturation fluctuations, identified to be more prone to small-scale heterogeneity compared with pressure profiles, are used to infer the capillary heterogeneity (Egermann and Lenormand, 2005; Egermann et al., 2005), by means of reservoir upscaling techniques. By performing a multi-rate coreflood experiment and measuring the pressure drop across the sample upon stabilisation (no flow), the local capillary pressure can be inferred. The approach was successfully applied to a composite carbonate core by Egermann and Lenormand (2005), one of the first key works to study rocks beyond sandstones, from which 100 independent $P_c - S_w$ data points were obtained. However, the application of this method is limited to multi-rate coreflood experiments as it is centred around the derivative of saturation and pressure versus flow rate. Therefore, the literature primarily focused on improving the J-function scaling approach initially developed by Huang et al. (1995), particularly addressing limitations associated with the permeability measurements.

The main drawback associated with porosity-based permeability methods is that these are typically verified using coarse measuring devices, a probe permeameter (resolution of ≈1 cm in the testing by Huang et al. (1995)). The resolution means they are not appropriate to infer physical properties such as permeability on a sub-core scale (Krause, 2009; Kuo et al., 2010; Krause et al., 2011). Therefore, an alternative method was proposed, based on work by Nelson (1994), anchored in the argument that is it not the pores, but the pore throats that control fluid movement, and in turn the relative permeability. Hence, combining capillary pressure (which incorporates the pore throat distribution within a core sample) with the local saturation and porosity is a more appropriate way to obtain 3D permeability maps (Krause, 2009). Simultaneously, this allows for the local capillary pressure to be determined using Leverett-J function scaling (Equation 2.4) (Shi et al., 2011; Krause, 2012):

$$P_{c,i} = \sigma \cos(\theta) \sqrt{\frac{\phi_i}{k_i}} J(S_w) \tag{2.11}$$

where $P_{c,i}$ is the capillary pressure of grid block i, σ is the interfacial tension, θ is the contact angle, $J(S_w)$ is the J-function, ϕ_i is the porosity of grid block i and k_i is the permeability of grid block i.

It is important to note that the method assumes sub-core capillary equilibrium, which may break down in the presence of strong heterogeneities or at higher flow rates (Krause et al., 2011). This development not only strengthens the characterisation of heterogeneity within a sample, but it also allows for the impact of heterogeneity on multiphase flow properties to be analysed in detail. The 3D digital core model can be used to infer the effective relative permeability from the equivalent curve in an optimisation routine and flow simulations can be run to simulate the rate dependency of relative permeability. Results from Krause (2012) are presented in Figure 2.12, which highlight the added value of the full 3D model. As the flow rate in the simulation is increased the relative permeabilities at each fractional flow move closer to the effective curves, as expected. However, the points display parabolic behaviour, where the greatest deviation from the input curve is not exhibited at the lowest rate. The authors argue this nonlinear behaviour is caused by the complicated nature of the rock core, which exhibits both, parallel and perpendicular, layers orientated relative to the principal flow direction. These results highlight the importance of characterising rock cores in 3D, which allows for the rate dependency behaviour to be closely examined.

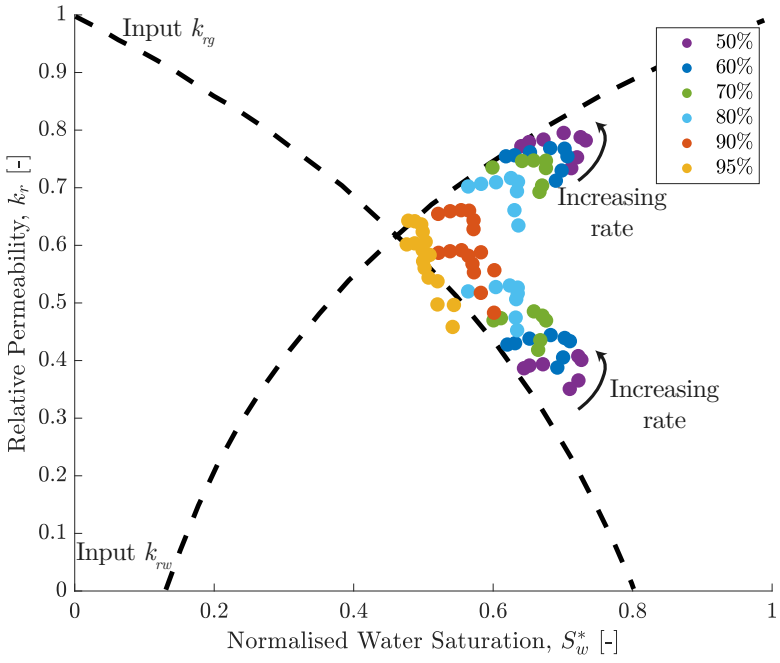


Figure 2.12: Rate dependency of relative permeability simulated on a Waare C sandstone digital model. Input effective relative permeability is plotted as dashed black lines. The percentages in the figure refer to the fractional flow of CO_2, f_{CO2}.Replotted from Krause et al. (2011).

Subsequent studies applied digital models to history match relative permeability (Krause et al., 2013; Pini et al., 2013; Pini and Benson, 2013a; Kong et al., 2015; Krause and Benson, 2015; Trevisan et al., 2015; Reynolds et al., 2018; Ni et al., 2019). They demonstrated capillary heterogeneity to be one of the dominant fluid distribution mechanisms on a sub-core scale for both brine-oil and brine-gas systems. Furthermore, they verified and strengthened the approach from Krause (2012). A scaling factor was introduced into the workflow, that describes, in a more simplified manner, the spatial variability of the capillary heterogeneity (Pini and Benson, 2013a, 2017). Furthermore, the goal of heterogeneity characterisation gradually shifted (Jackson et al., 2018). Initially, studies focused on deriving the effective relative permeability from the equivalent relative permeability, for instance Krause and Benson (2015). However, the effective relative permeability, which captures fluid flow at the viscous limit where the impact of capillary heterogeneity diminishes, is not an accurate representation of the flow regime encountered in the majority of subsurface fluid applications (Chang and Yortsos, 1992; Ringrose et al., 1993; Stubos et al., 1993; Yortsos et al., 1993; Chaouche et al., 1994; Honarpour and Saad, 1994; Huang et al., 1995). Consequently, optimisation procedures began to be applied to infer the equivalent relative permeability. Equipped with this data, the digital models were used to investigate the impact of structural orientation on the equivalent relative permeability whilst minimising experimental constraints such as boundary effects, injection limits or time constraints (Jackson et al., 2018).

Simultaneously, the literature began to focus on a greater variety of rock types such as carbonates, which often exhibit dual-porosity. An alternative workflow, developed by Hosseinzadeh Hejazi et al. (2019) and Kurotori and Pini (2021), characterises capillary heterogeneity in carbonates using multi-rate coreflood experiments, through which a large range of capillary pressures can be covered and Darcy's multiphase law can be simplified at steady-state. The authors introduced spatially varying voxel scale capillary pressure and irreducible oil saturation. The variable irreducible saturation accounts for microporosity typically encountered in carbonate rocks.

Notwithstanding these developments, uncertainty still remains in characterising more complex rocks typical of subsurface reservoirs across multiple fractional flows and flow rates, e.g. across the full range of flow conditions that would typically be encountered. The majority of research thus far has focused primarily on well-behaved sandstones, see Table 2.1. The few studies that did characterise heterogeneity on more complex systems such as carbonates focused their efforts solely on characterising the heterogeneity. However, the digital core models are valuable as they can be used to further investigate the flow behaviour resulting from heterogeneity. Furthermore, it would also be beneficial to explore workflow applicability on a wider range of rock types with varying degrees and structures of heterogeneity, which would help identify potential limitations.

Table 2.1: Summary of the most relevant studies focused on characterising capillary heterogeneity from experimental data in chronological order.

Reference	**Rock Type**
Huang et al. (1995)	Eolian outcrop sandstone from Lochabriggs quarry
Saad et al. (1995)	Composite rectangular outcrop core (unspecified rock type)
Børresen and Graue (1997)	Composite cross-bedded sandstone
Eilertsen et al. (1997)	2 sandstones: Vosges and Aerloith
Fincham and Gouth (2000)	Unconsolidated sandstone from a deep water reservoir
Egermann and Lenormand (2005)	2 carbonates: Composite rock and core
Kuo et al. (2010)l	Berea sandstone
Krause et al. (2011)	Berea sandstone
Krause (2012)	2 sandstones: Berea, Waare C
Krause et al. (2013)	2 sandstones: Berea, Waare C
Berg et al. (2013)	Berea sandstone
Pini et al. (2013)	Berea sanstone
Pini and Benson (2013b)	Berea sandstone
Pini and Benson (2013a)	Berea sandstone
Kong et al. (2015)	Berea sandstone (from Krause et al. (2011))
Krause and Benson (2015)	2 sandstones: Berea, Waare C
Pini and Benson (2017)	Berea sandstone
Reynolds et al. (2018)	3 sandstones: Bunter, Ormskirk, Captain
Jackson et al. (2018)	2 sandstones: Bentheimer, Bunter
Hosseinzadeh Hejazi et al. (2019)	3 carbonates: Ketton, Edwards, Indiana
Ni et al. (2019)	5 sandstones: Massillon, Bentheimer, Fontainebleau, Shezaf, Berea
Kurotori and Pini (2021)	Indiana limestone

2.6 Upscaling the Impact of Rock Heterogeneity to the Field Scale

Upscaling is a numerical homogenization procedure used to decrease the number of cells in a reservoir model by upscaling the properties of fine-scale cells to averaged or effective properties at a coarser scale, Figure 2.13. The typical length scales of rock heterogeneity that gives rise to capillary heterogeneity is on the order of 10s of metre to sub-metre scale depending on the rock type. Therefore, building a field-scale model, which resolves heterogeneities at these scales, would require billions of grid blocks, which is unfeasible. Even with the currently available advanced computational resources conventional flow simulators would take months to years to simulate fluid flow on such a big grid.

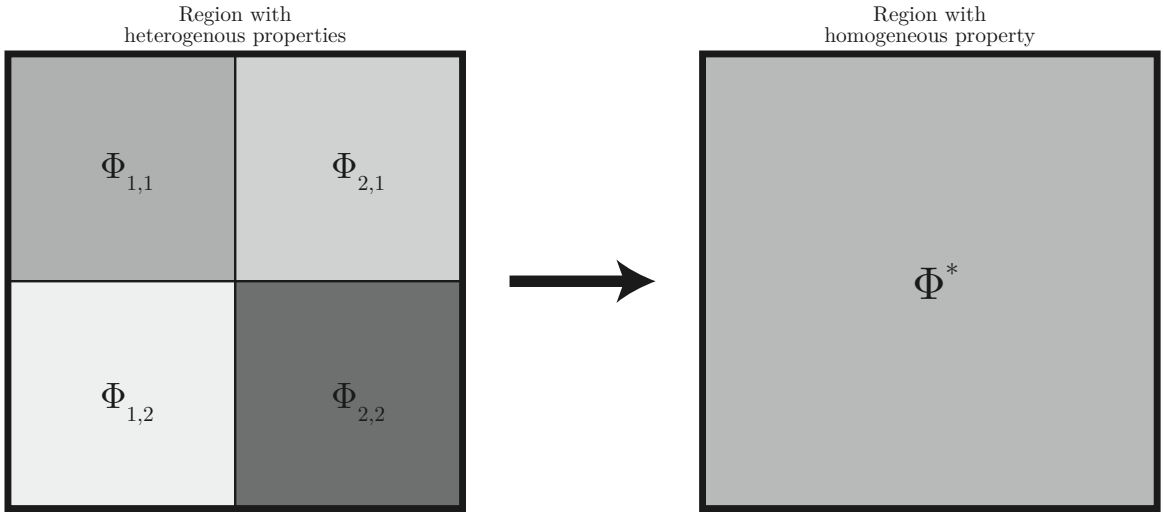


Figure 2.13: Concept of upscaling presented using the porosity property. A region defined by heterogeneous porosity is substituted with homogeneous porosity.

The following sections provide a brief overview of numerical upscaling procedure most relevant to this thesis. Herein, we categorize the numerical schemes into single-phase and two-phase upscaling. The difference between single and two-phase upscaling are that only porosity and absolute permeability are upscaled in single-phase upscaling, whereas relative permeability and capillary pressure are additionally upscaled in two-phase upscaling. For a comprehensive synopsis, the reader is referred to detailed review papers including Christie (1996); Wen and

Gómez-Hernández (1996); Renard and de Marsily (1997); Farmer (2002); Gerritsen and Durlofsky (2005) for single phase upscaling and Li (1995); Barker and Thibeau (1997); Christie (2001); Darman et al. (2002); Nicot and Duncan (2012); Zhang et al. (2021) for two phase upscaling.

For each category, the approaches can be differentiated between local, local-global and global approaches (Figure 2.14). Local methods derive the upscaled quantities based only on the local fine-scale grid within each target coarse block. Extended-local methods incorporate neighbouring grid blocks surrounding each coarse block into the numerical routine to reduce the impact of artificial boundary conditions on the target coarse block (Holstein, 2007). Lastly, global methods describe approaches where the global flow patterns are accounted for by solving the flow problem on the entire fine-scale domain, which can be computationally intensive but removes the impact of artificial boundary conditions (Holstein, 2007; Rabinovich et al., 2015).

We review the definitions of equivalent and effective properties. An equivalent property represents a heterogeneous medium and is dependent on the macroscopic boundary conditions (Renard and de Marsily, 1997). An effective property is an intrinsic physical magnitude independent of the macroscopic boundary conditions and represents a statistically homogeneous medium (Renard and de Marsily, 1997).

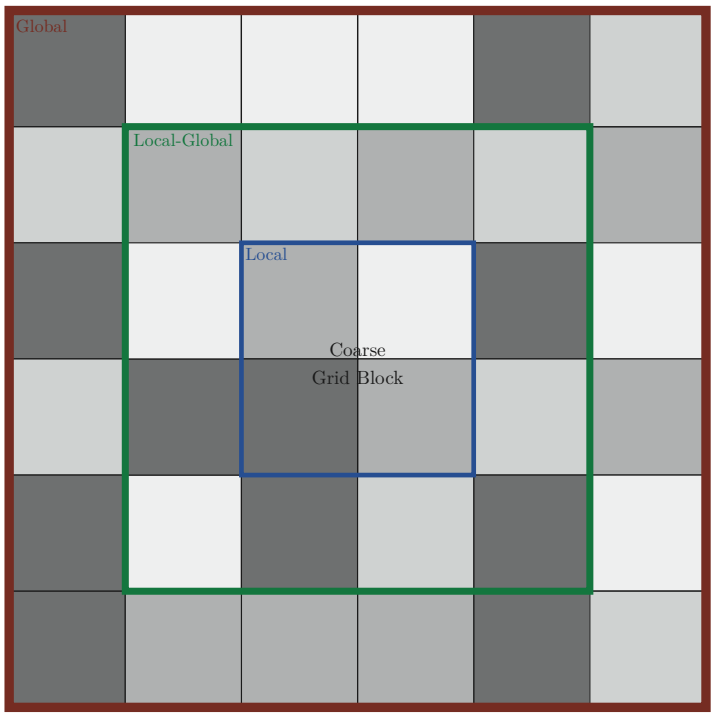


Figure 2.14: Comparison between local, local-global and global upscaling methods.

2.6.1 Single Phase Upscaling

2.6.1.1 Porosity

Additive properties such as porosity, fluid saturation or weight percentages can be upscaled using simple volume averaging, where (for 1D):

$$\phi^* = \frac{1}{V_t} \sum_{i=1}^{n} \phi_i V_i \quad , \tag{2.12}$$

where ϕ^* is the effective porosity, V_t is the volume of the coarse grid block consisting of n fine blocks, V_i and ϕ_i is the volume and porosity of fine-scale block i.

2.6.1.2 Absolute Permeability

In contrast, the upscaling of permeability, relative permeability and capillary pressure is more complex as these properties are non-additive (Qi and Hesketh, 2005).

For simple heterogeneities, analytical solutions can be applied to determine the equivalent permeability. From Begg et al. (1989), it follows that the arithmetic average, K_{arith}, can be used to estimate the equivalent permeability when flow is orientated parallel to layers (Equation 2.13), whereas the geometric average, K_{geom} can be used for flow orientated perpendicular to layers (Equation 2.14):

$$K_{arith} = \frac{1}{n} \sum_{i=1}^{n} K_i \quad , \tag{2.13}$$

$$K_{geom} = (\prod_{i=1}^{n} K_i)^{\frac{1}{n}} \quad , \tag{2.14}$$

where K_i is the absolute permeability of fine-scale block i. When the heterogeneous permeability field is uncertain, the upper and lower bounds of the equivalent permeability can be estimated

by the arithmetic, K_{arith}, and harmonic, K_{harm}, (Equation 2.15) depth averages of core-sample permeabilities, respectively (Cardwell and Parsons, 1945):

$$K_{harm} = n(\sum_{i=1}^{n} \frac{1}{K_i})^{-1} \quad , \tag{2.15}$$

Overall, the power law averaging approach is limited to domains with simple, layered heterogeneities (Figure 2.15) and breaks down when the boundary conditions are not met (i.e. when flow is not perfectly aligned with the layers), whilst it also relies on prior knowledge of the prevailing flow direction (Lie, 2019).

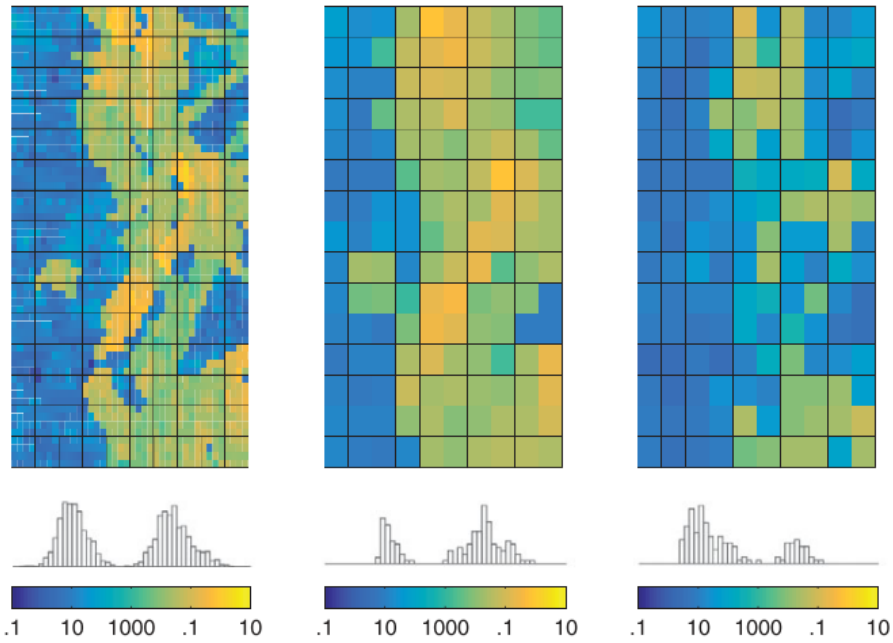


Figure 2.15: Upscaled absolute permeability of the fine-scale field (left) estimated from the arithmetic power-law average (middle) and the harmonic power-law average (right). Adapted from Lie (2019).

A more advanced approach is renormalisation whereby the numerical problem is split into more manageable parts after which a stepwise averaging procedure is followed (King et al., 1995; Qi and Hesketh, 2005). The global fine-scale grid is split into local regions, usually containing four fine-scale grid blocks for simplicity (King, 1989), and the equivalent permeability for this 'coarse' block is calculated. The resultant coarse blocks with upscaled permeabilities can then again be grouped into four and the upscaled permeability can be calculated from those. This process can be repeated until the desired coarse block size is reached. The approach is computationally efficient and allows for the impact of small-scale heterogeneities to be captured as the grid

block size is iteratively increased (Wen and Gómez-Hernández, 1996). However, it can lead to significant systematic errors, especially in the presence of high-contrast heterogeneities (King et al., 1995; Wen and Gómez-Hernández, 1996).

In the pressure solver method, flow is imposed on each coarse grid block in each dimension, after which the effective permeability is calculated from the average pressure drop using Darcy's law (Equation 2.1). This essentially replicates a coreflood experiment and is anchored in the idea that the heterogeneous domain with effective permeability and its homogeneous counterpart with effective permeability should result in the same flux for the same boundary conditions (Warren and Price, 1961). Numerical errors can arise when the pressure drop is small relative to the grid block size and it can also be computationally intensive (King, 1996). Various studies have explored the boundary conditions to be imposed in the flow problem. Periodic and no-flow boundary conditions result in a full-tensor and diagonal permeability, respectively, the latter of which cannot directly be entered into a commercial reservoir simulator (Christie, 1996). This method is slower than renormalisation, but can provide more accurate results if boundary conditions are appropriately accounted for (Christie, 1996; Peaceman, 1997). The reader is referred to Pickup and Sorbie (1994) and Lie (2019) for comprehensive reviews.

2.6.2 Two Phase Upscaling

For two phase upscaling, we focus on flow-based upscaling methods, namely dynamic pseudoisation and steady-state, as these are considered to be most reliable (Nooruddin and Blunt, 2018). We acknowledge that various other two-phase upscaling methods exist, for instance the vertical equilibrium approach (Coats et al., 1971), but these are less relevant to the objectives of this thesis.

2.6.2.1 Dynamic Pseudoisation Upscaling Methods

In this method, pseudofunctions are generated that can describe the upscaled relative permeability, mobility, fractional flow and capillary pressure. Pseudo curves can be obtained analytically for simple structures only (Gasda and Celia, 2005). Alternatively, flow simulations are run on the fine grid to determine the effective relative permeability for the coarse scale, hence termed 'dynamic' (Muggeridge et al., 1991). This approach successfully addresses the issue with numerical dispersion, encountered in alternative upscaling methods (Kyte and Berry, 1975). It is anchored in the idea that the total flow rate of a coarse grid block equals the sum of all fine-scale grid block flow rates (Gasda and Celia, 2005):

$$q_{p,t} = \sum_{i=1}^{n} q_{p,i} \quad , \tag{2.16}$$

where $q_{p,t}$ is the total flow rate over the fine-scale domain of phase p, i represents the grid block number ranging from 1 to n and $q_{p,i}$ is the flow rate of phase p of block number i. The total flow rate can also be written in terms of Darcy's law:

$$q_{p,t} = -\frac{T_x^* k_{rp}^*}{\mu_p^*}(\nabla P_p^* - \rho_p g z) \quad , \tag{2.17}$$

where T_x^* is the vertically-averaged transmissibility, k_{rp}^* is the effective relative permeability of phase p, μ_p^* is the average viscosity, ∇P_p^* is the average pressure gradient in the x direction, ρ

is the density, g is gravity and z is height. Combining Equations 2.16 and 2.17 gives:

$$\sum_{i=1}^{i=n} q_{p,i} = -\frac{T_x^* k_{rp}^*}{\mu_p^*}(\nabla P_p^* - \rho_p g z) \quad , \tag{2.18}$$

The various dynamic pseudoisation methods can be distinguished by how they solve for the average potential gradient, $(\nabla P_p^* - \rho_p g z)$, such as weighting factors incorporating local relative permeability, permeability and thickness (Kyte and Berry, 1975) or pore-volume weighted averages (Barker and Fayers, 1994). Other methods eliminate the need for calculating the average pressure gradient, for instance Stone (1991), and thereby eliminate numerical challenges associated with the Kyte and Berry (1975) method (non-monotonic, negative or infinite relative permeabilities) (Barker and Dupouy, 1999). However, this approach ignores the effect of gravity or capillary pressure on the coarse grid. Barker and Dupouy (1999) provide a comprehensive review of various other methods.

Generally, pseudoisation approaches rely on simulating flow on the fine scale or alternatively choosing a representative fine-scale subsection of the entire domain (Christie, 2001), which can become difficult for heterogeneous models. Thus, errors can arise when applying these methods to highly heterogeneous reservoirs (Barker and Dupouy, 1999; Darman et al., 2002). Furthermore, their applicability is limited to the grid, flow and boundary conditions used in their derivation (Nooruddin and Blunt, 2018).

A more advanced method is multi-step pseudoisation, which can account for several scales of rock heterogeneity and numerical dispersion. It follows a similar approach to renormalisation, whereby pseudofunctions are generated in a stepwise manner by gradually increasing the grid block size until the desired block size is reached (Suzuki and Hewett, 2002).

2.6.2.2 Steady-State Upscaling Methods

As the name suggests, steady state upscaling techniques assume that the flow in the domain has reached steady state. According to Smith (1991), this assumption holds for the majority of flow problems. They argue that capillary equilibrium will always be reached at small scales. Similarly, in viscous dominated flow regimes once the front has passed, the domain will also reach capillary equilibrium. However, in problems where this condition is violated, it can lead to erroneous results (Jonoud and Jackson, 2008). Some suggest that numerical dispersion may affect upscaling results generated with this approach more significantly than in pseudoisation. Yet, Pickup and Stephen (2000) have shown this to be insignificant. Generally, the grid block sizes are small enough for gravity to also be neglected (Nooruddin and Blunt, 2018). The assumption of steady-state turns a two phase problem into a single phase problem, thus significantly reducing its computational complexity (Pickup and Stephen, 2000). Steady-state methods are more robust and simpler as they do not depend on the grid whilst also being less sensitive to boundary conditions compared with dynamic pseudoisation (Jonoud and Jackson, 2008; Nooruddin and Blunt, 2018). Jonoud and Jackson (2008) also found this approach to be computationally cheaper.

For capillary equilibrium (CL) steady-state upscaling, the effective relative permeability is found by first estimating the saturation distribution from the fine-scale capillary pressure, after which single-phase flow simulations are run to determine the relative permeability for each phase (Nooruddin and Blunt, 2018). Traditionally, in the calculation of saturation distribution, it is assumed that all grid blocks are accessible (Pickup and Stephen, 2000). However, for a grid block to reach a certain fluid saturation, it needs to be connected to the inlet (Nooruddin and Blunt, 2018). To account for this, macroscopic invasion percolation can be applied, which follows the pore-scale percolation invasion methodology. Here, percolation is controlled by the fine-scale entry pressure distribution: a constant pressure is applied to the inlet and a grid block is invaded if it meets two conditions 1) its entry pressure is smaller than the imposed pressure, 2) its connected to the outlet. Following this, the fine-scale saturation distribution can be determined, having accounted for phase connectivity (Wolff et al., 2013).

In viscous-limit (VL) steady-state upscaling, capillary and gravity forces are assumed to be negligible. Thus, for a given fractional flow, which is constant over the inlet, the fine-scale saturation distribution can be inverted from Equation 2.9 (Pickup and Stephen, 2000).

With both, CL and VL, upscaling, it emerges that the assumption of flow regime plays a key role. As discussed by Jonoud and Jackson (2008): "It is not clear under what circumstances the assumptions used in the two methods are applicable." The authors suggest three dimensionless numbers, the end-point mobility ratio and two versions of the Peclet number, to determine which upscaling scheme is appropriate for domains with simple structures.

2.6.3 Issues and Considerations

Simulating subsurface fluid flow on a field scale requires upscaling. The previous sections have introduced some of the most widely used methods and discussed key limitations associated with each. Generally, upscaling techniques only provide an approximation of the true, equivalent fine-scale grid properties. Therefore, it is important to acknowledge some of the uncertainties and assumptions made in this procedure.

Upscaling fails at modelling extreme fields (Cuthiell et al., 1991; Li, 1995; Lie, 2019). The methods either average-out the extremes or they show bias towards one extreme. The resultant upscaled properties are also sensitive to the geometry of the extremes. Therefore, it is crucial to assess the coarse grid block size relative to the correlation length of the heterogeneity (Muggeridge et al., 1991). However, there is also a practical limit imposed on the fine-scale grid block size versus the amount of coarsening: upscaling schemes can be computationally intensive for fine-gridded or large domains. This introduces a trade-off between minimising numerical uncertainties and ensuring practicality.

All upscaling methods are also based on assumptions, for instance the dominant fluid distribution forces or the principal flow direction relative to the heterogeneity structure. These assumptions simplify the two-phase flow problem and allow it to be solved numerically. However, it can lead to oversimplification. The upscaling results are also affected by the boundary

conditions, which are chosen based on model complexity and the level of accuracy needed to be achieved (Holstein, 2007).

Lastly, numerical dispersion and diffusion, which cause smearing of the front as a result of truncation errors (Lantz, 1971), can be significant. It depends on the size and shape of the coarse grid relative to the fine-scale, the simulated timesteps as well as the flow regime (Pickup and Serbie, 1996; Pickup and Stephen, 2000). Some techniques which incorporate pseudofunctions, successfully reduce the impact of dispersion, but may be associated with other drawbacks. Care needs to be taken to choose appropriate gridding in order to minimise the impacts of numerical dispersion (Doughty and Pruess, 2004; Teletzke and Lu, 2013).

It follows that several factors should be considered when selecting an upscaling scheme (Holstein, 2007; Ezekwe, 2011):

- The complexity of the fine-scale model
- The degree of upscaling required
- Time constraints
- The intended use of the upscaled model

Chapter 3

Experimental Methods

This section summarises the experimental procedure and flow rig used to obtain these datasets. In Chapter 4 we use previously acquired coreflood experimental data to apply a novel core characterisation workflow. In Chapter 5, we conduct a steady-state relative permeability coreflood experiment on a reservoir sample from a proposed CCS storage site.

3.1 Centimetre-Scale Corefloods with Medical CT X-Ray Imaging

3.1.1 Sample Preparation

Cylindrical rock samples are plugged with variable lengths of 6-20 cm and radii of 0.6-1.9 cm. The samples from Chapter 4 have a 1.9 cm radius and a length of 15-20 cm, whereas the sample referred to as a meso-scale sample in Chapter 5 is smaller, with a 0.6 cm radius and a 6 cm length. The plugs are treated with a hot solvent soxhlet reflux to clean them and remove any resident fluids. Subsequently, they are dried in a vacuum oven. Samples frequently fracture during the plugging process. Therefore, care needs to be taken to select intact samples for the steady-state relative permeability coreflood experiment that follows.

3.1.2 Flow-Rig and Experimental Design

A flow rig, originally designed by Reynolds and Krevor (2015), is used to perform steady-state drainage coreflood experiments at constant temperature and pressure. A general schematic of the closed flow loop is shown in Figure 3.1. The rig is modified depending on the chosen pressure-temperature conditions, fluids and coreholder size. The following section describes the generalised flow rig design and experimental procedure.

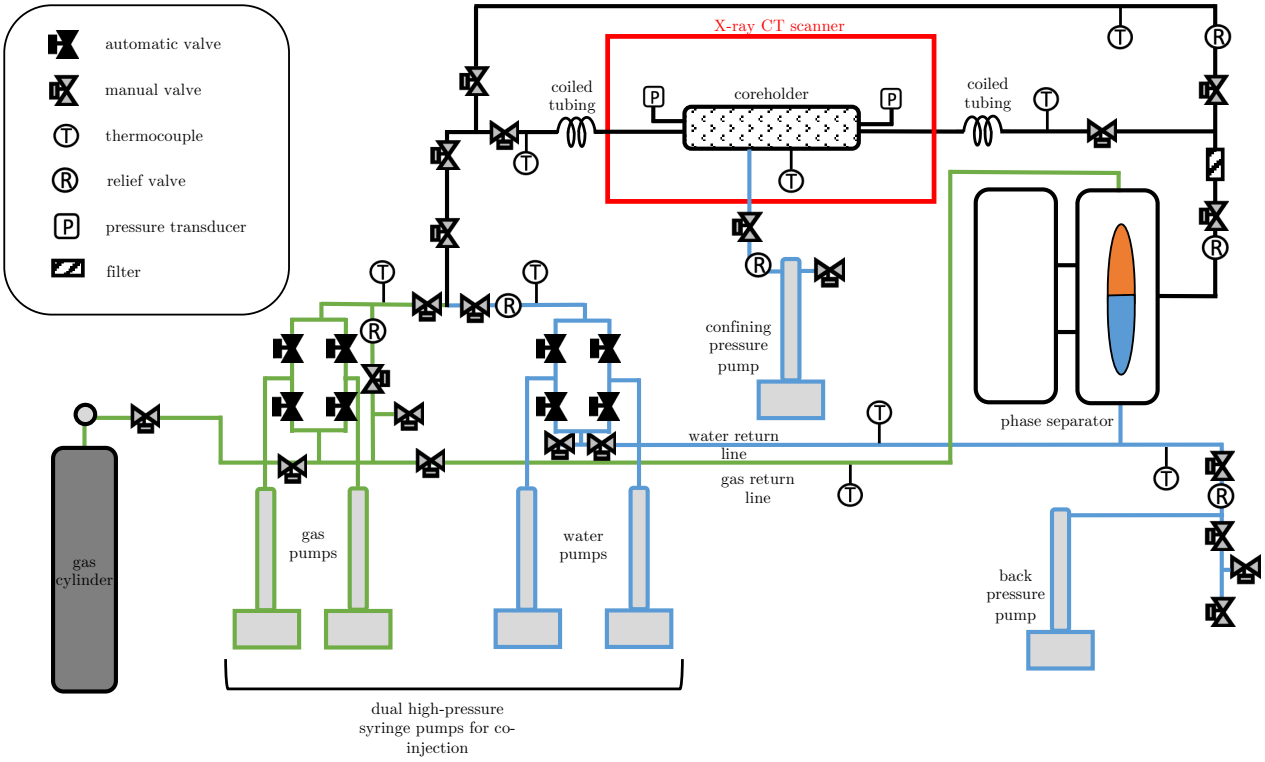


Figure 3.1: Flow loop of the steady-state drainage coreflood experiment.

The rock core is placed inside a coreholder. The difference in plug sizes means that different coreholders are utilised during the experiments. For the larger cores presented in Chapter 4, an aluminium coreholder (ICL-HA3) was built by Phoenix Instruments, with a maximum permitted sample size of 1.9 cm diameter and 25.5 cm length. For the meso sample in Chapter 5, a new coreholder made from Polyether ether ketone (PEEK) was designed by rs systems. Although the coreholders have different designs, the experimental procedure is largely the same.

The core is wrapped in heat shrink wrap and is then placed inside a rubber sleeve. The sleeve sits tightly around the core and ensures that the confining fluid does not invade the sample

during the experiment. The wrapped sample is then placed inside the coreholder. Flow lines are connected to the coreholder, which inject the fluids into the sample. End pieces, which entail groovings, are placed on the inlet and outlet sides of the core, which distribute the fluids across the whole injection face. A schematic of the meso coreholder is presented in Figure 3.2.

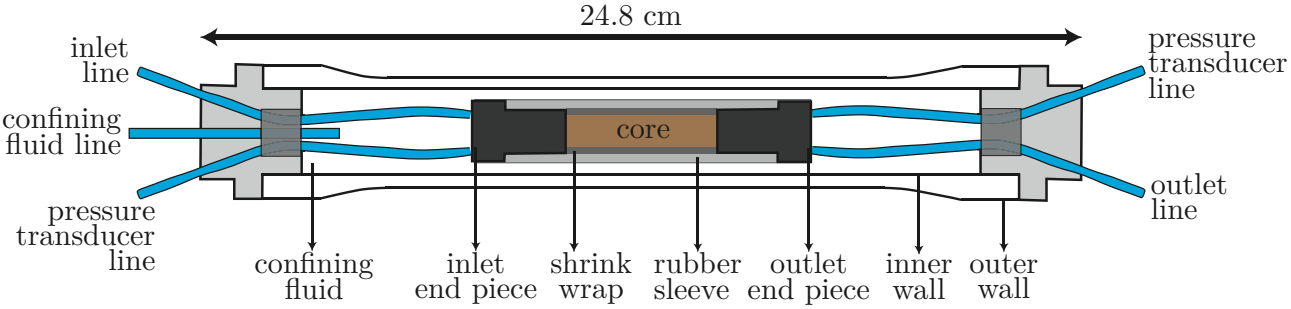


Figure 3.2: Schematic of the meso coreholder designed by rs systems.

Dual high pressure syringe pumps (Teledyne Isco, model 500D) are deployed to co-inject the wetting and non-wetting phase. Automatic valves are attached to the pumps to ensure the experimental pressure is maintained whilst periodically injecting from and refilling the pumps.

A high pressure syringe pump (Teledyne Isco, model 500D) imposes a confining pressure, above the experimental pressure, using DI water. The fluid is pumped into the coreholder, residing in the region between the rubber sleeve and the inner wall of the coreholder, until the target pressure is reached. The syringe pump runs at constant pressure throughout the entire steady-state relative permeability coreflood experiment to ensure the confining pressure is maintained.

Pore pressure is maintained on the outlet side of the coreholder using a back pressure syringe pump (Teledyne Isco, model 500D). A separator is connected to the flow loop downstream of the coreholder and separates the two phases before they return to the pumps for refilling.

Pressure transducers (Keller 33X), with a relative measurement accuracy of 0.05%, are connected to the inlet and outlet sides of the coreholder to record the core-average pressure drop throughout the experiment. The flow lines connected to the transducers are separately filled with the experimental wetting fluid, which reduces measurement fluctuations caused by trapped air bubbles.

For experiments involving CO_2, the bypass line is used to ensure the brine is fully saturated

with CO_2 prior to the experiment. For experiments with nitrogen (N_2), the bypass line is used to establish a constant fractional flow throughout the system before the flow lines are opened to the coreholder. The experiment performed on the Bunter sandstone sample presented in Chapter 4 involved CO_2 as the non-wetting phase, all remaining experiments discussed in this thesis utilised N_2.

3.1.3 Measuring Absolute Permeability

After the rock sample is placed in the coreholder and connected to the flow rig, a single phase flow experiment can be performed to measure the absolute permeability of the sample. The experimental pressure and temperature are applied to the core sample. Typically, the wetting phase is injected at a range of flow rates and the resultant core-average pressure drop is recorded. Using a simplified version of Darcy's Law (Darcy, 1856) in which gravity is negligible and the fluid density is constant, the absolute permeability can be calculated:

$$K = \frac{Q\mu L}{A\Delta P} \quad , \tag{3.1}$$

where Q is the volumetric flow rate [m^3s^{-1}], K is the permeability [m^2], μ is the viscosity [Pa·s], ΔP is the pressure drop [Pa], A is the cross-sectional area [m^2] and L is the core length [m]. The absolute permeability is determined by averaging the measurements across all flow rates.

3.1.4 Measuring Porosity and Saturation

The porosity and in-situ saturation of the rock sample are measured using an X-ray CT (medical CT) scanner, which represents a widely-used and non-invasive technique to measure these properties (Siddiqui and Sarker, 2010). The principals of the technology are briefly summarised below. For a thorough review, the reader is referred to Wellington and Vinegar (1987).

Dense materials such as the rock matrix significantly attenuate X-ray radiation, whereas softer or less-dense materials such as rock pores, are characterised by smaller attenuation coefficients

(Gharieb, 2022). The amount of radiation that passes through an object is recorded by an array of electrical detectors in the CT-scanner (Gharieb, 2022). After each complete rotation, the scanner constructs a 2D image slice. The thickness of each slice varies between 0.5-10 mm depending on the scanner (National Institute of Biomedical Imaging and Bioengineering, 2022). The process is repeated until a full 3D scan has been constructed by stacking the 2D slices. The resultant DICOM image contains a distribution of CT numbers, measured in Hounsfield units [H]. 1 H represents a 0.1% change in density relative to the calibration density scale (Reynolds, 2016).

For the sandstone experiments in Chapter 4, the Universal Systems HD-350 medical CT scanner was utilised with a voltage of 120 kV and current of 225 mA. For the carbonate experiments in Chapter 4 and the sandstone experiment in Chapter 5, the TOSHIBA Aquilion medical CT scanner was used with a voltage of 120 kV and a current of 200 mA. As shown in Figure 3.3, the coreholder is placed on the sliding table. Test scans are taken to minimise the drift of the coreholder. Once a suitable position has been found, the coreholder and flow lines are secured in place using industrial tape, which ensures the sample location within the scanned image is fixed during the entire experiment. At each stage, 3-5 repeat scans are taken to improve voxel precision and reduce image noise.

Example DICOM images and the corresponding CT profiles are displayed in Figure 3.4. As shown, the resultant CT profile varies depending on the coreholder utilised in the experiment. The aluminium coreholder designed for the larger rock samples causes a significant spike in the CT number, which is visible on the profile. The interfaces between the confining fluid sleeve, the core sample and the coreholder are easily distinguishable. In comparison to this, the coreholder utilised for meso-scale samples is made from PEEK, which results in a more subtle CT contrast with the confining fluid.

To derive the porosity and saturation distribution, four types of scans are required. The first is a dry scan of the vacuum-dried core sample placed inside the coreholder with the experimental confining pressure applied. The second is a gas scan, where the sample is fully saturated with the non-wetting experimental fluid. The third is a water scan, where the sample is saturated

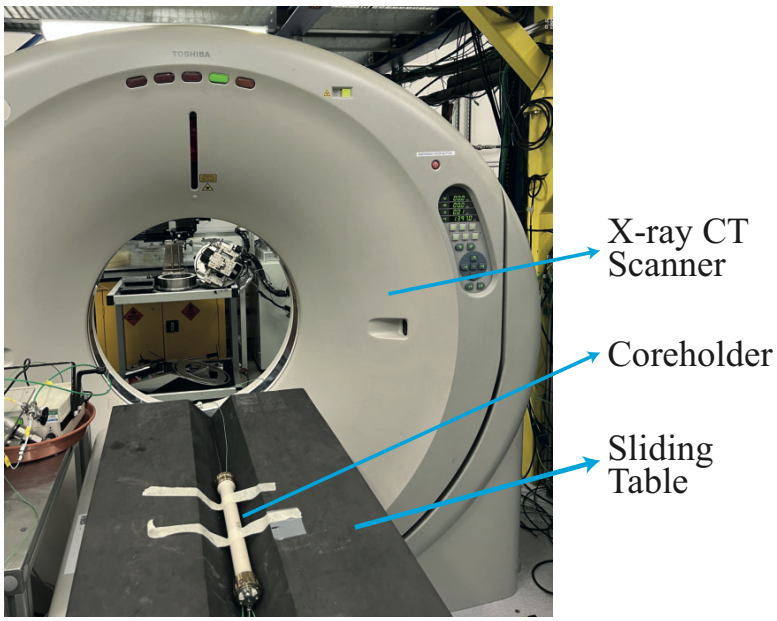


Figure 3.3: Photograph of the coreholder placed on the sliding table of the X-ray CT scanner.

with the wetting fluid. Lastly, scans are taken throughout the steady-state relative permeability coreflood experiment, where the rock sample is partially saturated with one fluid.

Porosity in each voxel can be calculated using each voxel's CT number following the standard method by Withjack (1988).:

$$\phi_{ijk} = \frac{CT_{wtr,ijk} - CT_{dry,ijk}}{I_{wtr} - I_{air}} \quad , \tag{3.2}$$

where $CT_{wtr,ijk}$ and $CT_{dry,ijk}$ are the voxel's CT values from the water and dry scans, respectively. I_{wtr} and I_{air} are the CT values of water and air. These can be determined directly from the CT images (using the CT value from the confining fluid and from outside the coreholder).

The in-situ voxel-scale gas saturation can be determined using:

$$S_{g,ijk} = \frac{CT_{exp,ijk} - CT_{wtr,ijk}}{CT_{gas,ijk} - CT_{wtr,ijk}} \quad , \tag{3.3}$$

where $CT_{exp,ijk}$ is the voxel-scale CT number measuring during the steady-state relative permeability coreflood experiment, $CT_{gas,ijk}$ is the voxel-scale CT number measured from the gas scan and $CT_{wtr,ijk}$ is the voxel-scale CT number measured from the water scan.

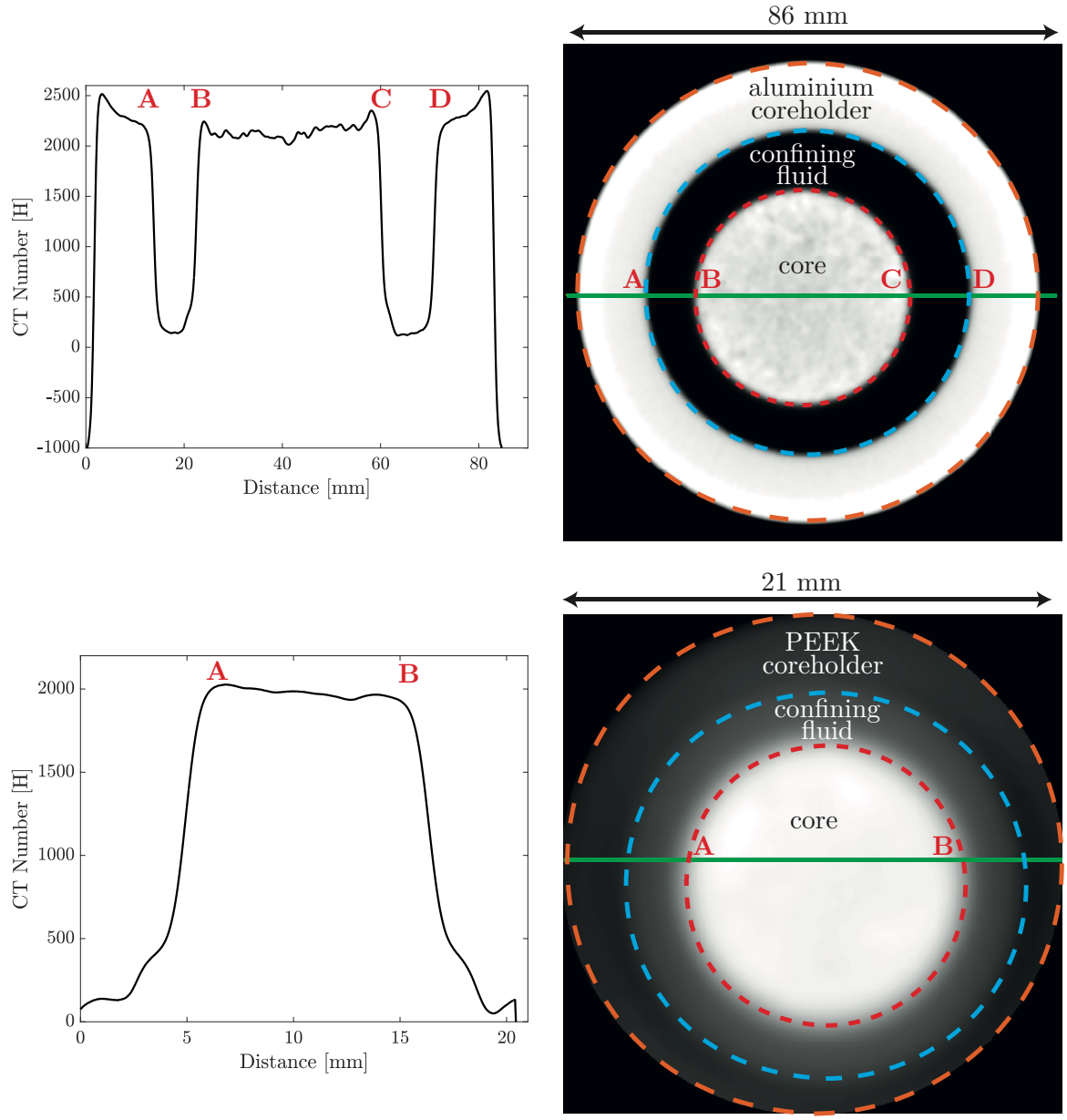


Figure 3.4: DICOM images of the Indiana sandstone from Chapter 4 shown at the top and of the Endurance reservoir sample from Chapter 5 shown at the bottom. The graphs on the left display the corresponding CT numbers along the green line plotted in the DICOM images. The dashed red and blue circles show the approximate location of the core-sleeve and sleeve-coreholder boundaries, respectively. The dashed orange circle shows the edge of the circular CT image. Note: in the bottom scan the outer regions of the coreholder are cropped and have not been captured in the image.

3.1.5 Measuring Steady-State Drainage Relative Permeability

The relative permeability of a core sample can be obtained during the steady-state relative permeability coreflood experiment. The two experimental fluids are co-injected into a water saturated core at a specific fractional flow, with the fractional flow of water defined as:

$$f_w = \frac{q_w}{q_t} = \frac{q_w}{q_g + q_w} \quad , \tag{3.4}$$

where the total volumetric flow rate is the sum of the water flow rate, q_w, and the gas flow rate, q_g, $q_t = q_w + q_g$ and f_w is the water fractional flow.

The core-average pressure drop is recorded. Once the pressure drop and core saturation are stable, we assume steady-state has been reached. CT scans of the core are then taken and the core-average pressure drop is noted. Using the multiphase Darcy Law, we can then calculate the relative permeability to a phase (Muskat and Meres, 1936; Muskat et al., 1937):

$$q_p = -\frac{K k_{rp}(S_p)}{\mu_p}\left(\frac{dP}{dx} - \rho_p g\right) \quad , \tag{3.5}$$

where q is the Darcy velocity [m·s^{-1}], K is the permeability [m^2], μ is the viscosity [Pa·s], $\frac{dP}{dx}$ is the pressure gradient in the direction of flow [Pa·m^{-1}], ρ is the density [kg·m^{-3}] and g is gravity [m·s^{-2}]. k_{rp} is the relative permeability of phase p at saturation S_p. We assume the flow in the sample can be approximated as 1D in the primary axis of flow and the fluid phases are immiscible and incompressible. To obtain relative permeability measurements at a range of saturations, the fractional flow of gas is gradually increased until $f_g = 1$. At each fractional flow, the steps outlined above are repeated. This is done until a sufficiently large saturation range has been covered.

In the presence of strong rock heterogeneity and capillary end effects, Equation 3.5 alone is insufficient to interpret the data obtained during the steady-state coreflood experiment. Instead, a computer-based history match of the experimental observations (pressure drop and

saturation) is required. A 1D history match, of the core-average pressure drop and the saturation profiles, is standard special core analysis (SCAL) practice and can be conducted using available software such as SENDRA. In Chapter 5 we present an extended 3D history match process using MATLAB, which accounts for both, capillary end effects and rock heterogeneity.

3.1.6 Experimental Procedure

The steps taken during the entire steady-state relative permeability coreflood experiment are summarised below.

1. All flow lines are cleaned using compressed N_2/CO_2 to ensure any ambient air is removed from the system.
2. All pumps are emptied to ensure the pressure readings are reset.
3. Pumps are filled with the experimental fluids and are run at constant pressure for half a day-one day to test for leakage.
4. If no leakage has occurred inside the pumps, fill the separator and return line with wetting fluid. Pressurise the system to the experimental pressure using the back pressure pump. Pressurise the injection pumps. For the gas pump, use the gas cylinder to pressurise.
5. Place the coreholder inside the medical CT and apply the confining pressure. Leave the confining pressure pump running for a few hours to ensure no leakage occurs inside the coreholder.
6. Conduct test scans to find the optimal location of the coreholder. After it has been found, secure it to the table.
7. Take a dry scan of the core.
8. Attach the inlet and outlet lines to the coreholder and pressurise the system using N_2/CO_2 in a stepwise manner using the injection pumps. Ensure any ambient air has been removed from the lines connected to the pressure transducer using a syringe.

9. Switch all pumps off and leave the system overnight. This ensure no leakage has occurred and system pressure is maintained

10. Take a 'gas' scan (core fully saturated with gas)

11. If using N_2 as a non-wetting fluid, disconnect the flow lines from the coreholder and flush it with CO_2 to remove all N_2 from the system for 1 hour. Subsequently, flush the core with wetting fluid to displace any resident gas. This may take 20 hours depending on the core sample.

12. After all gas has been flushed from the core, connect the flowlines to the coreholder and pressurise it again in a stepwise manner with the wetting phase.

13. Once the target experimental pressure is reached, take a 'water' scan (core fully saturated with water). To ensure the core is fully saturated with water, inject a minimum of 7 pore volumes.

14. Measure the absolute permeability of the core (Section 3.1.3).

15. Set the pumps to the experimental flow conditions of the first fractional flow and begin injecting the fluids.

16. Once the core-average pressure drop has stabilised, steady-state has been reached and a scan can be taken. This can take several days depending on the sample and experimental conditions.

17. The fractional flow is increased and step 16 is repeated. This is done until all fractional flows have been completed.

3.2 Micro-CT Dry Scans

In Chapter 5, we also present micro-CT scans of a vacuum-dried reservoir sample from a proposed CCS site. This section summarises the relevant technical background and experimental procedure.

3.2.1 Image Acquisition

We utilise the Zeiss Versa XRM-510 micro-CT scanner to acquire high-resolution images of the pore structure in the rock sample. Similar to the medical-CT scanner, the micro-CT scanner utilises X-rays to image the internal structure of the rock. The attenuated X-rays are detected by a flat panel detector. However, rather than a sliding table, the sample is placed on a rotating table, meaning that the sample is imaged from different directions during each scan. A computer algorithm later reconstructs these images to produce a 3D scan of the sample (Carl Zeiss X-ray Microscopy, 2016).

The image resolution is determined by the distance of the detector from the sample. With decreasing distance, the image resolution improves. However, this also results in a smaller field of view. Thus, a trade-off between image resolution and sample size exists. We scan the entire sample at 5.8 µm resolution. A subvolume of the sample is additionally scanned at a higher resolution of 2 µm.

We do not employ a flow loop for this work as we are interested in acquiring dry scans of the samples. Therefore, placing the sample in a coreholder is unnecessary and instead we tape it to a small platform, as shown in Figure 3.5.

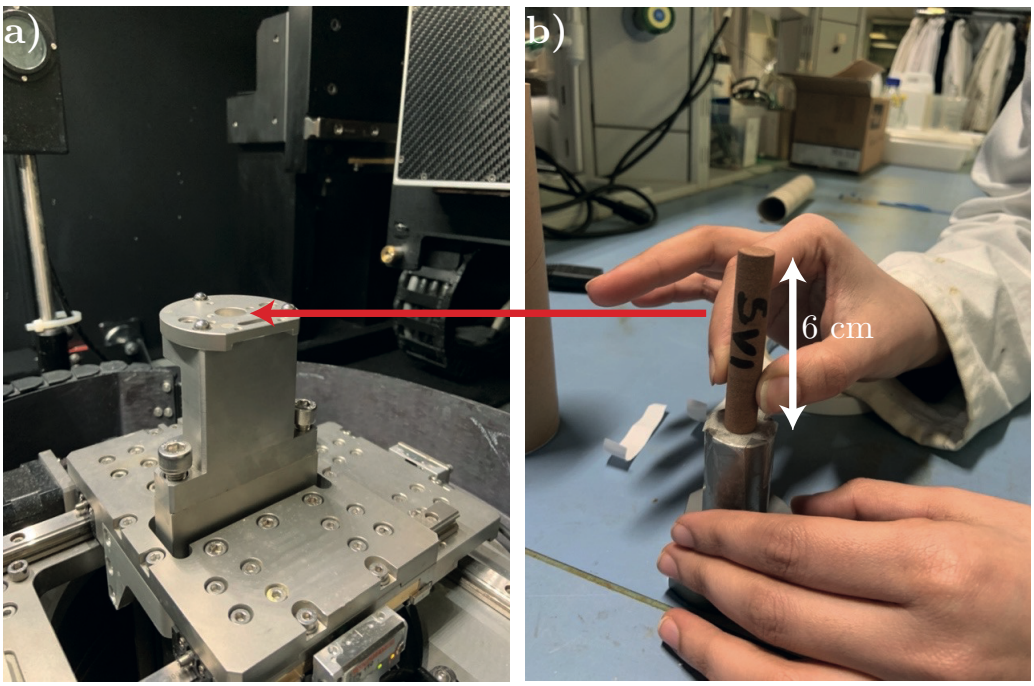


Figure 3.5: a) Photograph of the Zeiss Versa scanner, b) Photograph of a sample fixed onto a small platform. The red arrow points to the location on the rotating table where the platform with the sample is attached to.

3.2.2 Image Processing

Image processing is conducted using the Avizo 2019 Software by Thermofisher. To reduce the signal-to-noise ratio, the images are filtered. There are various filters available for micro-CT images. Recently, application of the non-local means filter has grown, notably applied by Spurin et al. (2019); Yang et al. (2019b); Alhosani et al. (2020); Su et al. (2022). We compare the resultant images from the Gaussian, median and non-local means filters in Figure 3.6. The Gaussian filter smoothes the image using a kernel based on a Gaussian distribution (Thermofisher, 2019). The median filter is a lowpass filter, which reduces the contrast and softens the edges of objects within an image (Thermofisher, 2019). It is the preferred filter to reduce salt and pepper noise or to remove very small artefacts (Sarker et al., 2012). The non-local means filter is the preferred method to denoise scalar volume data and is most effective for white noise (Sarker et al., 2012). We find that the non-local means filter sufficiently reduces the signal-to-noise ratio, whilst enhancing the grain-pore boundary contrast. We opt for a similarity value, which represents the weighting factor assigned to each voxel inside a search window, of 0.2. We choose a search window radius of 10 pixels. This combination of parameters

ensures the image is not over-smoothed, whilst increasing the signal-to-noise ratio.

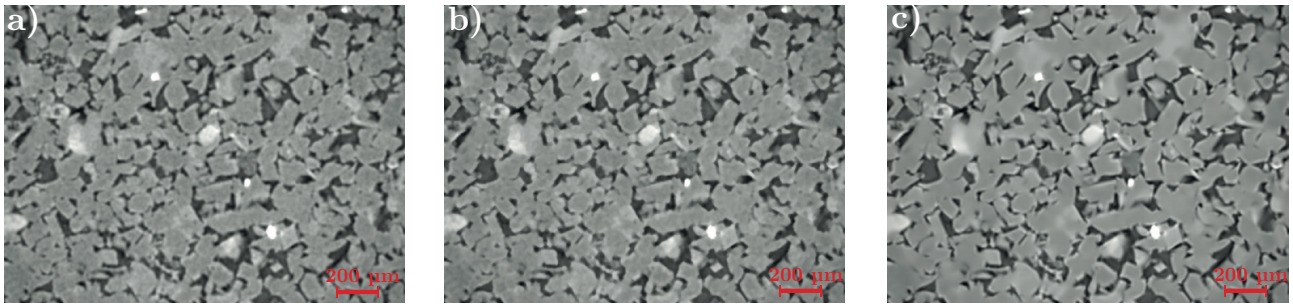


Figure 3.6: Comparison of filtering techniques using a 2 micron scan (from Chapter 5). a) Gaussian filter, b) Median filter and c) non-local means filter.

To segment the pores and grains, we follow a global thresholding approach, whereby a range of grayscale values is selected to represent a specific material. This technique has been applied in previous works including Van Geet et al. (2000); Tuller et al. (2013), with a recent review by Rezaei et al. (2019). With other methods, including watershed segmentation, we find that the algorithm generally assigns clay-rich regions with intermediate grayscale values as pores, which is erroneous. We verify the accuracy of segmentation by comparing the resultant average porosity to the independent measurement from the medical-CT scanner. For the 2 micron scan, we estimate the total porosity of the subvolume to be 0.2069, which is in agreement with the average porosity determined in the steady-state relative permeability coreflood experiment of 0.2088. Figure 3.7 summarises the image processing workflow.

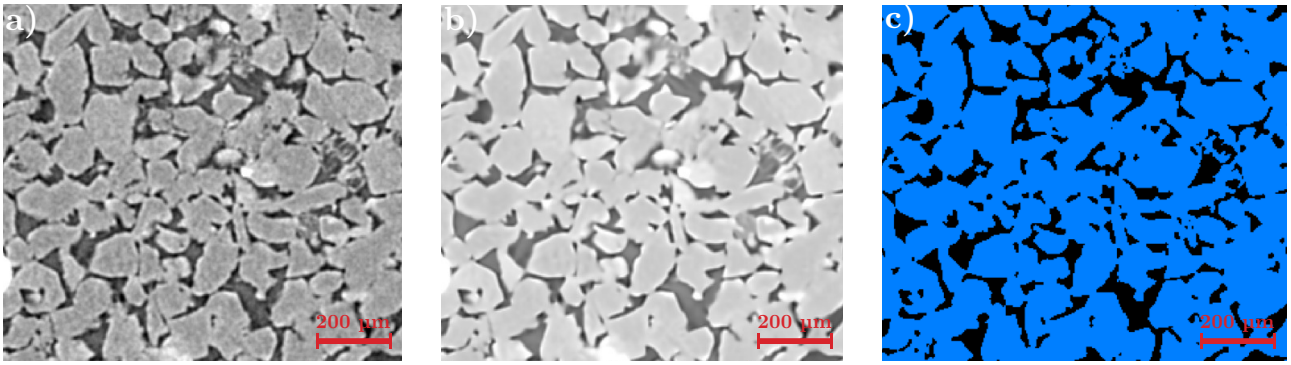


Figure 3.7: Summary of the image processing workflow presented with a 2 micron image. a) raw image, b) filtered image using the non-local means filter and c) segmented image following a global thresholding approach.

Chapter 4

Characterising and Simulating Corefloods in Heterogeneous Rocks

The majority of this material has been published in Wenck et al. (2021).

4.1 Objectives

In this chapter we evaluate the approach described by Jackson et al. (2018) to characterise heterogeneity across five rock samples selected for their range of heterogeneity types and length scales comprising two sandstones and three carbonates. The approach combines experimental and numerical methods to characterise capillary heterogeneity within rock cores, and originates in the work by Krause et al. (2011, 2013). The workflow was developed and demonstrated on simple sandstones and its performance on more complex rock structures, including rocks with sub-resolution heterogeneity or with correlation lengths larger than the rock cores themselves, is largely uncertain. The sandstones exhibit distinctly-orientated planar bedding, whereas the carbonates are characterised by isotropic cementation of varying length scale. The range of rock types allows us to systematically evaluate the inversion approach against a systematic variation in rock structures. Using the validated models, we investigate the impact of heterogeneity on the rate dependency of relative permeability and draw conclusions on the varying flow behaviour.

4.2 Materials and Methods

4.2.1 Heterogeneous Rock Types

Previously acquired experimental datasets of five rock cores are studied, with experimental methods and data reported in Reynolds and Krevor (2015); Reynolds et al. (2018); Manoorkar et al. (2021). These datasets comprise observations from corefloods performed on two sandstones, a Bentheimer and a Bunter, and three carbonates, Indiana, Estaillades and Edwards Brown. The rock samples are analysed to gain an understanding for characterising more complex rocks typical of subsurface reservoirs.

Reservoir sandstones can be significantly affected by diagenetic and compactional processes, which lead to substantial porosity and permeability variations (Worden et al., 2018; Heidsiek et al., 2020). These often cluster into complex sedimentary structures such as cross-bedding or flute casts. Carbonate rocks are also characterised by heterogeneity, though on a larger range of scales. On a core to field scale, they exhibit facies and diagenetic distribution patterns, often at sub-seismic resolution (Petrovic et al., 2018). At the pore-scale, variations in pore network topology and wettability add further complexity to spatial porosity and permeability distributions, the latter manifesting as isotropic heterogeneity at larger scales (Rebelle et al., 2009; Ji et al., 2012; Lin et al., 2016). These complex rock types comprise a major reservoir resource and techniques for rock characterisation capturing the impact of these heterogeneities is important for field studies (Al-Kharusi and Blunt, 2008; Sayers, 2008).

The Bentheimer sandstone is a shallow-marine deposit widely used for experimental studies due to its homogeneity (Peksa et al., 2015). The Bunter sandstone is a geological unit from a previously proposed CCS site in the Southern North Sea. It was deposited in a predominantly alluvial environment and exhibits characteristics of early diagenetic processes such as grain dissolution and cementation (Brook et al., 2003). The three carbonate samples display a range of heterogeneity types and lengthscales due to the depositional environments. The Indiana limestone, quarried from the Salem Formation in Indiana (USA) is formed of mainly

calcite cemented grain stone (El-Maghraby, 2012). The Estaillades, a calcite-rich limestone, originates from a quarry in Southeast France and is characterised by intergranular macropores and intragranular micropores (Lai et al., 2015; Al-Menhali et al., 2016). The Edwards Brown dolomite was sampled from the Upper Cretaceous formation in Texas (USA) (Manoorkar et al., 2021).

4.2.2 Experimental Conditions and Fluids

Coreflood experiments were performed at two flow rates on the five rock samples following the experimental procedure outlined in Chapter 3. The conditions imposed during the experiments are summarised in Table 4.1. For further details on the experimental procedures, please see Reynolds and Krevor (2015); Reynolds et al. (2018); Manoorkar et al. (2021).

Table 4.1: Summary of the experimental parameters for the five samples.

Parameters	**Bentheimer**	**Bunter**	**Indiana**	**Estaillades**	**Edwards Brown**
Nonwetting phase, nw	N_2	CO_2	N_2	N_2	N_2
Wetting phase, w	DI Water	Brine	DI Water	DI Water	DI Water
Q_{tot} high/low [ml·min^{-1}]	40/7	20/0.2	5/0.5	20/0.5	5/0.5
Number of fractional flows high/low	10/6	8/6	13/13	13/10	10/16
Pressure, P [MPa]	15.5	13.1	10	10	10
Temperature, T [°C]	50	53	20	20	20
nw density, ρ_{nw} [kg m^{-3}]	115	604	115	115	115
w density, ρ_w [kg m^{-3}]	997	1022	998	998	998
nw viscosity, μ_{nw} [μPa s]	22.1	45.9	19.7	19.7	19.7
w viscosity, μ_w [μPa s]	550	582	1070	1070	1070
IFT, γ [mN·m^{-1}]	62	34.7	62	62	62
Experimental core length, L [m]	0.198	0.151	0.148	0.148	0.148
Experimental core radius, r [m]	0.019	0.019	0.019	0.019	0.019
Raw voxel Δx, Δy [m]	0.00023	0.00023	0.00017	0.00017	0.00017
Raw voxel Δz [m]	0.005	0.003	0.001	0.001	0.001

4.2.3 Capillary Number

Throughout this work, the definition of capillary number by Virnovsky et al. (2004) is used, Equation 2.10.

For the Bentheimer sandstone with a 2-layer system orientated parallel to the axis of flow, H is estimated to be half of the core diameter. For the Bunter sandstone, the average spacing between the perpendicular layers is used for H. For both cores, ΔP_c is determined by comparing the variation in entry pressure between layers obtained from the digital, calibrated models. L is set to the core length and ΔP as the pressure drop across the sample at $f_g = 0.5$. At $f_g = 0.5$ the competition between both fluids through the pore space is highest, which typically results in the largest pressure drop during a coreflood experiment.

For the carbonates, the average size of the vugs is used for H. To estimate ΔP_c, a different approach is followed for each sample as discussed in Manoorkar et al. (2021). For the Indiana limestone, ΔP_c is assumed to be the pressure differential across the core at which low permeability layers are invaded. We acknowledge that this estimates the upper limit for ΔP_c, thus the resultant capillary number is a conservative estimate. For the Estaillades limestone, the method from Reynolds et al. (2018) is followed: ΔP_c is obtained from the saturation distribution in a given slice. For the Edwards dolomite, the maximum pressure differential across the core is used for ΔP_c. This is chosen because the gas did not invade parts of the impermeable structure towards the outlet of the core. For further information, please see Manoorkar et al. (2021). Similarly to the sandstones, L is set to the core length and ΔP as the pressure drop across the sample at $f_g = 0.5$.

4.2.4 Image Coarsening

Prior to building digital core models and performing flow simulations, we coarsen the CT images to speed up the simulations and improve experimental saturation precision. The coarsened grid size for the digital models is guided by the elementary volume (EV) of the rock structure, the experimental saturation precision and the run time of the simulations. The EV can be estimated by comparing the pore structure of each rock type to the voxel size.

For the Estaillades limestone, a pore reaches a maximum pore volume of $9 \times 10^3 \mu\text{m}^3$, using the maximum pore radius from MIP data presented in Lai et al. (2015). From the voxel dimensions the coarsened voxel size of the CT images is $1.21 \times 10^{10} \mu\text{m}^3$. An estimated $2.9 \times 10^9 \mu\text{m}^3$ of pores is present within each voxel. This translates to approximately 3.2×10^5 pores. Following the same workflow, the number of pores within each voxel is estimated as 5.6×10^2 and 1.2×10^5 for the Indiana limestone and Edwards Brown dolomite, respectively.

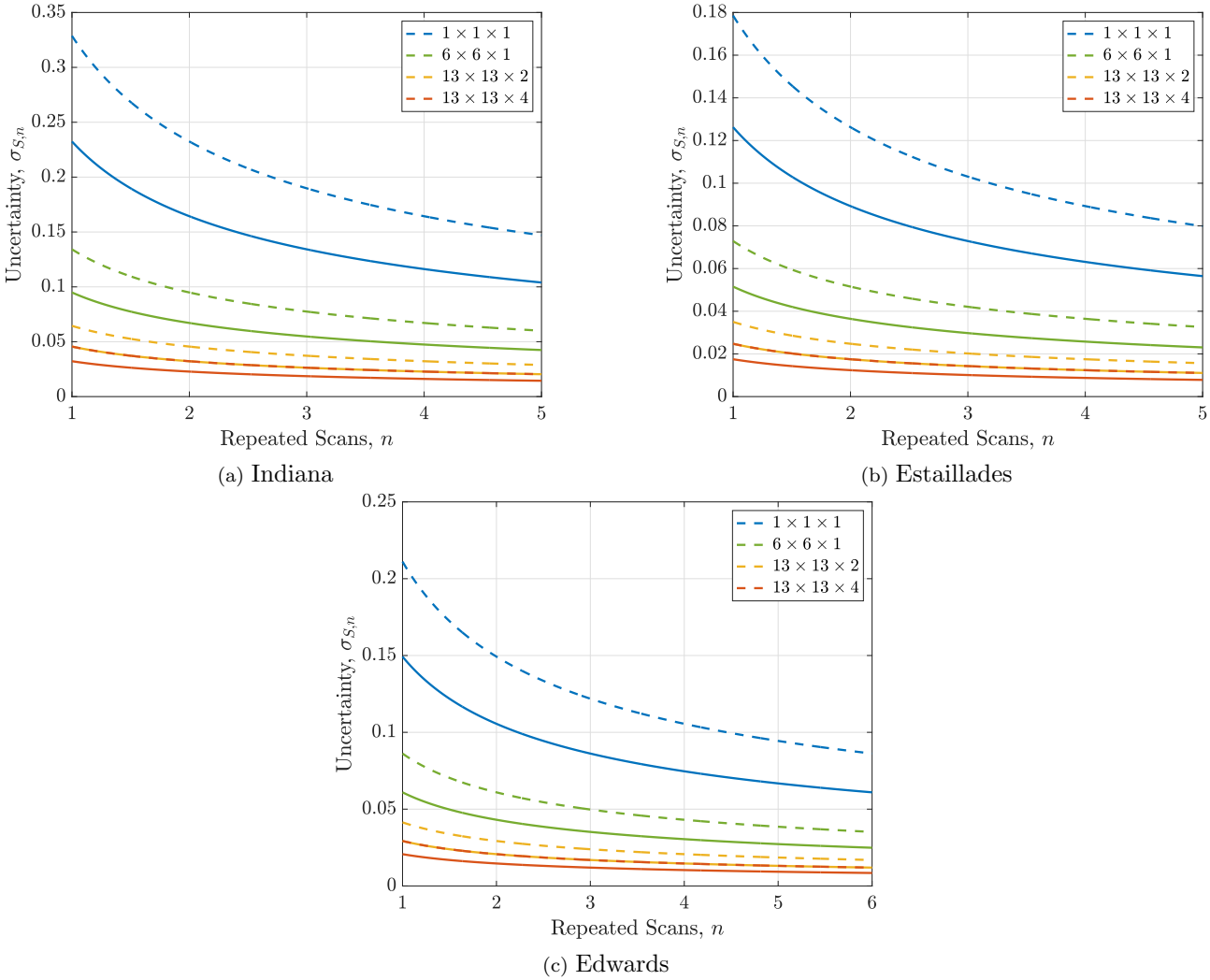
To estimate the amount of pores required within each voxel such that a continuum property has meaning, we refer to the work by Jackson et al. (2020). The authors conducted a detailed EV analysis on two Bentheimer sandstone samples. They estimated the EV for porosity and capillary pressure to be 20 mm^3 for two Bentheimer sandstone samples. Using a maximum pore throat radius of 0.16 mm (Peksa et al., 2015), this translates to approximately 116 pores present within an EV in the Bentheimer samples. The grid size chosen for all carbonate samples allows for > 500 pores to be present. Thus, a continuum property has meaning on the voxel scale used in our work.

We note the importance of additionally considering the EV of the capillary pressure characteristic as this might be different from the EV of the porosity. However, quantifying this poses a challenge. Previous work using micrometre resolution X-ray imaging and pore network models has identified that correlation length scales of capillary pressure characteristics and porosity are of a similar order of magnitude (Jackson et al., 2020; Zahasky et al., 2020). We assume, based on the above estimates, that the voxel scale allows for the capillary pressure characteristic to also be considered a valid continuum property.

The uncertainty in the experimental saturation data is also considered in the numerical modelling approach. We estimate the uncertainty in the saturation values measured during the experiments following the method by Pini et al. (2012). X-ray CT images at centimetre scale resolution are significantly affected by random noise. Averaging data over repeat scans taken during the experiment and processing the images through coarsening can reduce the image noise. Figure 4.1 assesses the impact of repeat scans and image coarsening on the resultant experimental saturation uncertainty in the saturations for the carbonate samples. As shown, the voxel scale uncertainties are significantly reduced from image coarsening and averaging over repeated scans. Table 4.2 summarises the final saturation uncertainties associated with the coarsening schemes used in this work. The voxel saturation uncertainties for all samples fall below 0.05. We use a grid size of 9×9×74 (13×13×2 coarsening) in the workflow described in Section 4.2.6.1. Coarsening of 13×13×4 is applied to speed up the simulations in the extended approach outlined in Section 4.2.6.2 resulting in a grid size of 9×9×37.

Table 4.2: Uncertainty in the saturations for the five rock samples after specific coarsening schemes were applied to the raw CT images. For the carbonates, 9×9×74 and 9×9×37 are the digital core dimensions used in the capillary heterogeneity characterisation workflow and history match, respectively.

Rock Sample	**Grid size**	$\sigma_{\mathbf{S=0,vox}}$	$\sigma_{\mathbf{S=1,vox}}$
Bentheimer	11×11×41	0.027	0.038
Bunter	11×11×52	0.036	0.051
Indiana Digital	9×9×74	0.011	0.016
Indiana HM	9×9×37	0.08	0.011
Estaillades Digital	9×9×74	0.012	0.001
Estaillades HM	9×9×37	0.017	0.012
Edwards Digital	9×9×74	0.020	0.029
Edwards HM	9×9×37	0.014	0.020



(a) Indiana

(b) Estaillades

(c) Edwards

Figure 4.1: Uncertainty in the saturations as a function of the number of repeat scans for the three carbonate samples. Six repeat scans were available for the Edwards Brown dataset and five for the other two samples. The colours represent the uncertainty for specific coarsening schemes as indicated. The solid and dashed lines refer to the uncertainty at $S_w = 0.0$ and $S_w = 1.0$, respectively.

4.2.5 Building Digital Core Models

To build digital models of the rock cores, we collate experimental observations. The parameters used in the workflow are summarised in Table 4.3. We provide further detail in the subsequent subsections.

Table 4.3: Summary of the core characterisation parameters for the five samples. * indicates modelling parameters used from Jackson et al. (2018).

Parameters	**Bentheimer**	**Bunter**	**Indiana**	**Estaillades**	**Edwards Brown**
Digital core dimensions [x,y,z]	11x11x41	11x11x52	9x9x74	9x9x74	9x9x74
Upscaled voxel Δx, Δy [m]	0.0032	0.00277	0.00246	0.00246	0.00246
Upscaled voxel Δz [m]	0.005	0.003	0.002	0.002	0.002
Digital core length, L [m]	0.195	0.150	0.144	0.144	0.144
Digital core radius, r [m]	0.018	0.015	0.011	0.011	0.011
Entry pressure, P_e [kPa]	3.51*	1.62*	2.96	9.30	9.18
Pore distribution, λ [-]	2.3*	1.43*	0.86	1.45	0.48
Porosity, ϕ [-]	0.21	0.25	0.14	0.24	0.23
Permeability, K_{abs} [D]	1.86	2.20	0.024	0.14	0.046
Chierici k_{rw}, A/L [-]	3/0.75*	3/0.9*	4.37/1.01	5.26/0.8	15.7/1.06
Chierici k_{rg}, B/M [-]	5/0.65*	3.75/0.4*	3.30/0.83	1.21/1.22	2.66/0.54
$k_{rg}(S_{wirr}$/ $k_{rw}(S_{gc}$ [-]	1/1*	1/1*	1/1	1/1	1/1
S_{wirr}, S_{gc} [-]	0.08/0.0*	0.08/0.0*	0.0/0.0	0.07/0.0	0.0/0.0
Capillary Number, N_c [-] high/low	14.4/1.72	20.5/0.85	3.66/0.10	2.00/0.04	0.76/0.04

4.2.5.1 Permeability

The 3D porosity and saturation distributions are obtained by processing the medical CT images following the method detailed in Chapter 3.

The permeability is assumed to be constant throughout the samples and is set to the absolute permeability measured in a single phase flow experiment.

For the sandstones, this assumption is tested by performing the characterisation effort twice: once with a homogeneous and once with a heterogeneous permeability distribution. Leverett-J function scaling is applied to obtain the permeability structure within the sample (Jackson et al., 2018). The analysis demonstrates that it is the capillary heterogeneity, and not the permeability variation, that is the major control on the fluid distribution in the sandstones analysed herein. However, we note that this may not apply to more heterogeneous sandstone

samples. For instance, Boon et al. (2022) attribute the flow-rate dependent drainage behaviour observed in sandstone samples from the Otway site to the permeability variation arising from core-scale laminae.

For rock samples with large permeability variations, such as carbonates, the permeability structure could significantly impact the resultant fluid behaviour, particularly at flow rates between the viscous and capillary limits. In cases like this, it may be key to match both, the absolute permeability and capillary pressure characteristics, for an accurate model. We test the application of Leverett-J function scaling to the carbonates by following an iterative approach similar to Hosseinzadeh Hejazi et al. (2019), and find that it fails to converge on a suitable match. As discussed in Sarwaruddin et al. (2001), the Leverett-J function is dependant on additional factors including the pore size distribution and the irreducible water saturation. Thus, scaling of the capillary pressure following this method should be limited to rock types displaying a homogeneous pore structure (Sarwaruddin et al., 2001). These parameters are likely non-uniform in a carbonate core sample, which demonstrates that this scaling method is unsuitable for the carbonate samples. This is additionally confirmed by the lack of correlation between voxel-scale P_e and $\frac{1}{\sqrt{\phi}}$ in the carbonate models. Based on these findings, we model the rock cores with a uniform permeability field.

4.2.5.2 Relative Permeability

At high capillary numbers the role of capillary pressure heterogeneities diminishes and a single relative permeability characteristic controls the flow in a domain. This is known as the viscous-limit or effective relative permeability, and is independent of heterogeneity (Renard and de Marsily, 1997). The viscous-limit relative permeability curves are obtained with the high flow rate experiments. All viscous-limit relative permeabilities are assumed to be uniform throughout the rock domain and are modelled using the Chierici functional form, which is found to be the most suitable functional fit to the experimental data (Chierici, 1984):

$$k_{rg} = k_{rg}(S_{wirr})e^{-BR_w^m}, \qquad k_{rw} = k_{rw}(S_{gc})e^{-AR_w^{-L}}, \qquad R_w = \frac{S_w - S_{wirr}}{1 - S_{gc} - S_w}, \tag{4.1}$$

where k_{rg} and k_{rw} are the gas and water relative permeabilities, respectively. S_w, S_{wirr} and S_{gc} refer to the water saturation, irreducible water saturation and critical gas saturation, respectively. A, B, M and L are empirical parameters that control the shape of the curves.

For the sandstones, the Chierici parameters from Jackson et al. (2018) are used. For the Estaillades, the fitting parameters are obtained by history matching the high flow-rate experiment using the 1D simulator SENDRA. For the Indiana limestone and the Edwards Brown dolomite, Matlab's *fmincon* function is applied to the experimentally measured high-rate relative permeabilities to obtain the parameters. The data points from the first fractional flows are associated with the largest uncertainties as the gas saturation is very small. Thus, greater weighting is given to the remaining data points when fitting the relative permeability data.

4.2.5.3 Intrinsic Capillary Pressure

An average, or intrinsic, capillary pressure characteristic is obtained from observations made during mercury intrusion porosimetry (MICP). The data is fit with the Brooks-Corey model (Brooks and Corey, 1964):

$$P_c(S_w) = P_e(\frac{1 - S_{wirr}}{S_w - S_{wirr}})^{\frac{1}{\lambda}} \quad , \tag{4.2}$$

where P_c [Pa] is the capillary pressure as a function of water saturation, S_w [-], P_e [Pa] is the entry pressure, S_{wirr} [-] is the irreducible water saturation and λ [-] is the pore size distribution factor.

The values of P_e, S_{wirr} and λ from Jackson et al. (2018) are used in the sandstone workflow. For the carbonates, the MICP data is cropped prior to fitting due to the large pressures (>1000kPa) reached during mercury injection. Thereafter, the capillary pressure at $S_w = 1.0$ is taken as P_e, and S_{wirr} and λ are obtained by minimising the misfit between the MICP data and Equation 4.2.

One of the main assumptions in this characterisation workflow is that λ is uniform throughout the rock core. For the sandstones analysed in this work, this assumption can be tested by studying the MICP data from different regions within a single sample or across different samples from the same rock type. We refer to the works by Olafuyi et al. (2006); Reynolds and Krevor (2015); Shikhov and Arns (2015); Jackson and Krevor (2020); Zahasky et al. (2020), which show that λ is uniform between different sandstone samples. Furthermore, Jackson et al. (2018) found that the match between the experiment and the simulation did not improve with a variation in λ for both sandstone samples. For carbonates, typically characterised by facies, λ could vary between regions in a sample. However, the works by Hosseinzadeh Hejazi et al. (2019) and Kurotori and Pini (2021) show that m in the van Genuchten relation (the equivalent to λ in the Brooks Corey model) is constant between small plugs sampled from the same carbonate core. Hence we opt to characterise the capillary heterogeneity through variation of P_e only.

4.2.5.4 Boundary Conditions

For the coreflood simulations, fictitious inlet and outlet slices are used to mimic the experimental conditions. The following parameters are assigned to these end slices:

1. Linearly varying relative permeabilities: $k_{rw} = S_w$, $k_{rg} = -S_w + 1$
2. Zero capillary pressure: $P_c = 0$
3. A large permeability: $K_{endslice} \approx 7 \times K_{abs}$
4. A constant porosity: $\phi_{endslice} = \phi_{core,avg}$

Injection 'wells' are defined in the centre of the inlet slice — two injected gas and two injected water. Two fluid sink locations – modelled as production wells – are placed in the centre of the outlet slice. The supplementary material of Jackson et al. (2018) provides a more detailed discussion on the choice of these boundary conditions.

4.2.6 History Match of the Numerical Models

The approach of Jackson et al. (2018) is applied to history match the numerical core models for all of the rock samples. With two of the carbonate rocks, the Indiana and Estaillades limestone, the approach is either unsuccessful or only partially successful. In these cases an extended approach is used. We summarise the approach of Jackson et al. (2018) and the extended approach below.

4.2.6.1 Approach of Jackson et al. (2018)

The 3D saturation maps of the rock cores obtained during the corefloods at all fractional flows are used to infer the heterogeneity in capillary pressure characteristics. An initial guess is made based on an inversion of the saturation maps, followed by an iterative process whereby capillary pressure characteristics is updated based on the comparison between simulated 3D saturation maps and the observations. The workflow is briefly described below.

For the initial guess, capillary pressure in each slice is assumed to be constant, i.e. at equilibrium. The average saturation in that slice is assumed to map to the Brooks-Corey fit of the capillary pressure characteristic curve measured during routine core analysis (Equation 4.2). Voxel scale variation in the saturation within the slice is assumed to be caused by the capillary heterogeneity within the slice. From this a scaling factor κ is assigned to each voxel, adjusting the local capillary pressure characteristic curve, to minimise the mismatch between the slice-average and voxel-specific values:

$$P_{c,ijk}(S_{ijk}) = \kappa_{ijk} \cdot P_{c,avg}(S_{ijk}) \quad , \tag{4.3}$$

$$\Theta = \sum_{i}^{N_v} \sum_{j}^{N_f} \sqrt{(\kappa_{ijk} P_{c,avg}(S_{ijk}^{exp}) - P_{c,ijk}(S_{ijk}^{exp}))^2} \sqrt{(S(\kappa_{ijk} P_{c,avg}) - S_{ijk}^{exp})^2} \quad , \tag{4.4}$$

where $P_{c,ijk}$ is the individual voxel capillary pressure, $P_{c,avg}$ is the average capillary pressure

curve, S_{ijk}^{exp} is the experimental voxel saturation, κ_{ijk} is the individual voxel scaling parameter, N_v is the total number of voxels, N_f is the total number of fractional flows and $S(\kappa_{ijk}P_{c,avg})$ represents the saturation of the average capillary pressure curve after it has been scaled (using the slice-average capillary pressure). Through this, a 3D map of the initial scaling factor is built. The scaling is then used to populate the capillary pressure characteristics of numerical simulations of corefloods. Flow simulations are performed with CMG ™IMEX, a fully-implicit, isothermal black oil fluid simulator, which uses the finite difference method to solve the governing equations, conservation of mass and Darcy's law. The capillary heterogeneity is introduced alongside the porosity heterogeneity, the core-average characteristic capillary pressure behaviour and the viscous-limit relative permeability.

The iterative calibration of the capillary pressure characteristics follows from this. After the first simulation, 3D saturation and capillary pressure maps are extracted and compared to the experimental values. A deviation from the experimental observations (both P_c and S_w) is assumed to stem from an incorrect scaling parameter assigned to the voxel. κ is then updated, minimising the mismatch between the experiment and simulation. The objective function becomes the following, where the slice-average P_c values have been replaced by the simulation values:

$$\Theta = \sum_{i}^{N_v}\sum_{j}^{N_f}\sqrt{(\kappa_{ijk}P_{c,avg}(S_{ijk}^{exp}) - P_{c,ijk}(S_{ijk}^{sim}))^2}\sqrt{(S(\kappa_{ijk}P_{c,avg}) - S_{ijk}^{exp})^2} \quad , \tag{4.5}$$

where S_{ijk}^{exp} has been replaced with the simulation voxel saturation, S_{ijk}^{sim}. Now, $S(\kappa_{ijk}P_{c,avg})$ represents the saturation of the average capillary pressure curve after it has been scaled using the individual simulated voxel capillary pressure rather than the experimental slice-average capillary pressure.

The iterative optimisation scheme is summarised graphically in Figure 4.2.

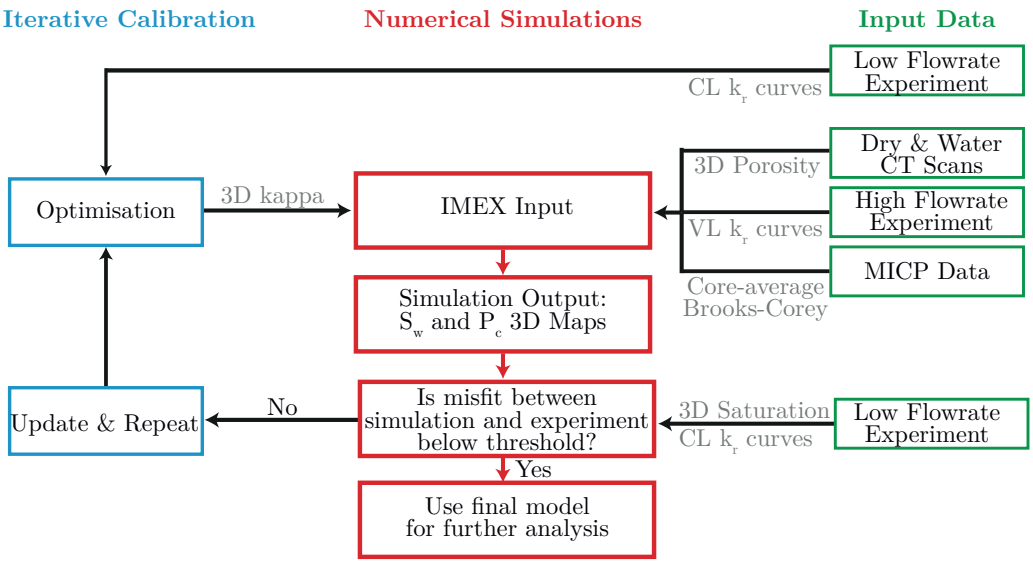


Figure 4.2: Flowchart summarising the workflow and iterative calibration scheme followed to characterise the capillary heterogeneity in a core.

4.2.6.2 Extended Approaches Using Relative Permeability as a Fitting Parameter

The viscous-limit relative permeability curves used as input to the simulation are a major control on the results and ideally are measured with very little uncertainty in the observation. However, coreflood experiments are challenging and the measurements can be affected by sources of error (Krause and Benson, 2015; Berg et al., 2021). As such, it may be necessary to implement an alternative numerical-based approach to obtain a viscous-limit relative permeability. In this work the observations from the carbonate rocks are difficult to match following the conventional workflow. Hence we explore improvement in the history-matched simulation by additionally using the core-averaged input viscous-limit relative permeability as a fitting parameter, with the observed relative permeability at the low flow rate as an additional matching target. The steps followed are described in the following:

1. Explore a large range of Chierici parameters, A and B, initially, which are centred around the Chierici values obtained from the high rate experimental dataset.

2. Model the viscous-limit input curve with the new Chierici parameters from step 1) and conduct the iterative optimisation procedure. The limit for the number of iterations in the calibration scheme is set to 4.

3. Use the digital model to simulate the low flow rate experiment and calculate the root mean square errors for the relative permeabilities, core-average saturations and voxel saturations.

4. Use the errors from step 3) to constrain the parameter space of the Chierici parameters. Repeat the history match with the constrained range of A and B values.

5. Repeat the above steps until the error in the simulated and experimental observations at the low flow rate is minimised.

The above workflow, which uses the experimental low flow rate relative permeability as an additional matching target, results in an unsatisfactory prediction of the voxel saturations and relative permeabilities at high rate. Therefore, we extend the history match to incorporate the high rate experimental data. The procedure uses the errors in both, the low and high rate relative permeabilities and voxel saturations, to guide the history match. The updated workflow follows these steps:

1. Explore a large range of Chierici parameters, A and B, initially, which are centred around the Chierici values obtained from the high rate experimental dataset.

2. Model the viscous-limit input curve with the new Chierici parameters from step 1) and conduct the iterative optimisation procedure. The limit for the number of iterations in the calibration scheme is set to 4.

3. Use the digital model to simulate the low and high flow rate experiments and calculate the root mean square errors for the relative permeabilities, core-average saturations and voxel saturations at both flow rates.

4. Use the errors from step 3) to constrain the parameter space of the Chierici parameters. Repeat the history match with the constrained range of A and B values.

5. Repeat the above steps until the errors in the simulated and experimental observations at the low and high flow rates are minimised.

4.3 Results and Discussion

4.3.1 Heterogeneous Porosity Distribution

Using the images obtained with the medical CT scanner, we obtain the 3D porosity distribution in the five samples. The 1D and 2D porosity distribution are presented in Figure 4.3 and Figure 4.4, respectively. As shown, the five rock samples cover a range of depositional facies and exhibit distinct heterogeneity types and length scales.

The Bentheimer sandstone exhibits a simple porosity heterogeneity orientated as a single layer parallel to the flow direction. The Bunter sandstone exhibits characteristics of early diagenetic processes (Brook et al., 2003). As such, our sample features noticeable heterogeneity in porosity, which can be grouped into layers perpendicular to the axis of flow.

The three carbonate samples, Indiana limestone, Estaillades limestone, and Edwards Brown dolomite, exhibit varying degrees of cementation resulting in distinct length scales of isotropic heterogeneity resolved by the CT scanner. The Indiana limestone has the smallest scale porosity heterogeneity ($\approx$1 mm). The Estaillades has an order of magnitude larger scale porosity heterogeneity ($\approx$1 cm). The Edwards Brown dolomite has a multi centimetre length low-porosity region towards the outlet of the core.

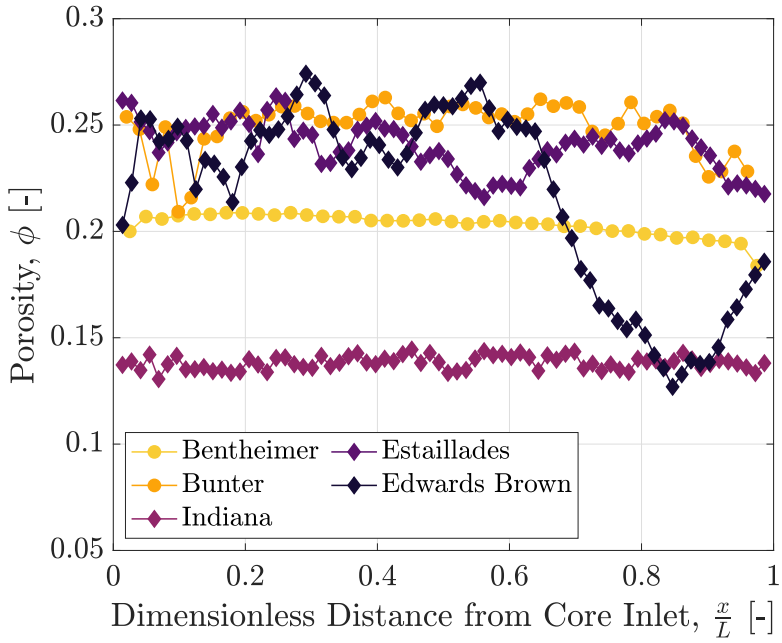


Figure 4.3: Porosity profiles for the five cores displaying the range of heterogeneity types and length scales. Sandstones and carbonates are plotted as circle and diamond markers, respectively.

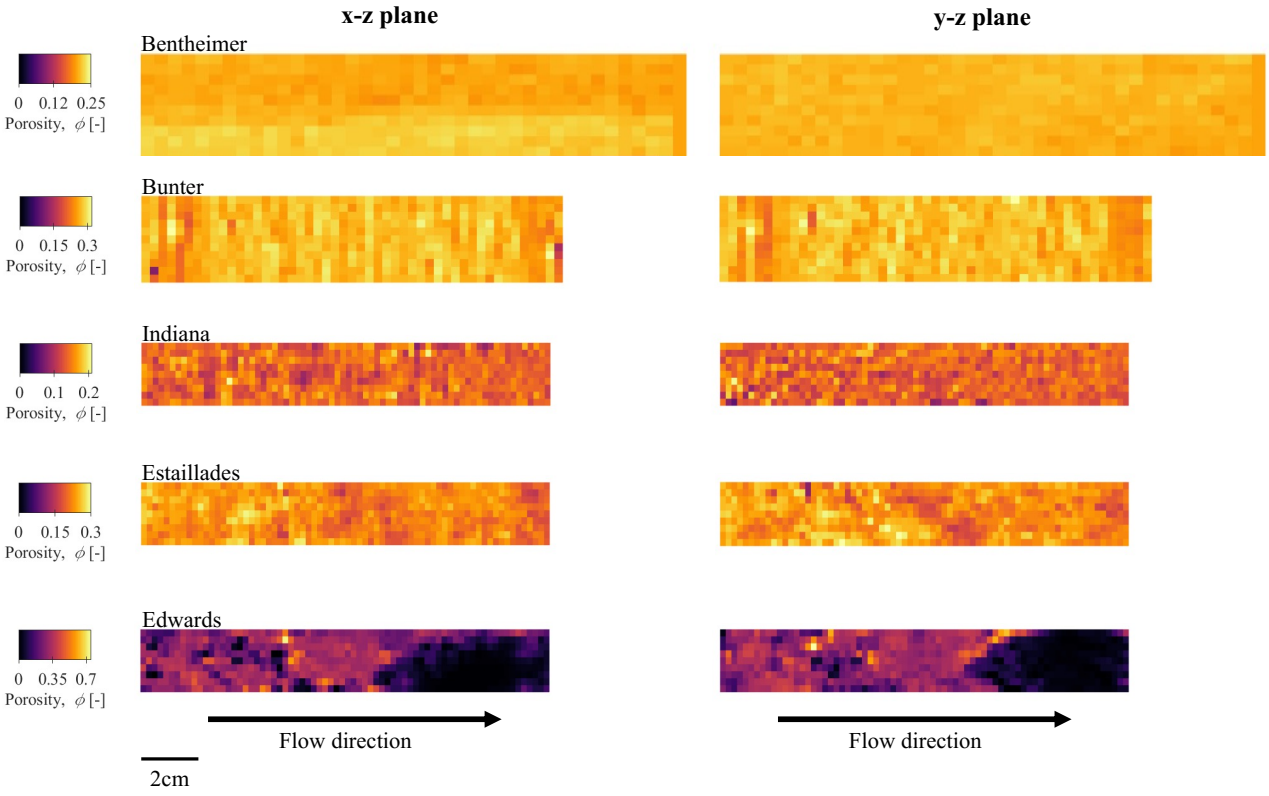


Figure 4.4: Porosity maps through the centre planes of each sample showing the 2D porosity heterogeneity. Note: the image sizes are slightly smaller than the physical cores as outer voxels impacted by imaging artefacts have been removed.

4.3.2 Measures to Evaluate the Workflow Success

The iterative calibration scheme is said to have converged when the error between the experiment and simulation voxel saturations is stable i.e. when the relative change in R^2 between iterations falls below 2%. This limit was pragmatically chosen based on the typical changes in R^2 observed between iterations, whereby 2% envelopes the variance in R^2. As shown in Figure 4.5, the sandstones generally exhibit an earlier convergence compared with the carbonates. The R^2 stabilises after three iterations. The error in the voxel saturations reaches a plateau after four iterations for the Estaillades and Edwards Brown. The results for the Indiana sample indicate that the calibration scheme is likely affected by convergence issues. During the calibration scheme, the κ values assigned to the Indiana core are changed significantly to minimise the error in the voxel saturations. With each iteration, the range of κ values increases. Beyond five iterations, the κ values reach physically unrealistic values ($\kappa > 700$). Thus, we opt to terminate the optimisation scheme after five iterations as displayed in Figure 4.5.

The R^2 for the voxel saturations is only one indication of the success of the workflow. It is also guided by the errors in the core-average pressure drop and the voxel entry pressures. Terminating the calibration after 5 iterations for the Indiana sample ensures that there still is physical meaning to the digital rock model. Further iterations could lead to convergence in R^2, whilst we could also lose physical meaning in the entry pressure distribution. The trade-off between minimising the saturation and pressure drop fitting errors has previously been presented by Hosseinzadeh Hejazi et al. (2019). The error in the saturation and pressure drop, which guide the optimisation, are related through a reciprocal function, a "pareto front" (Hosseinzadeh Hejazi et al., 2019): minimising the error in one variable, leads to a large error in the other variable. The R^2 associated with the final calibrated models are summarised in Table 4.4.

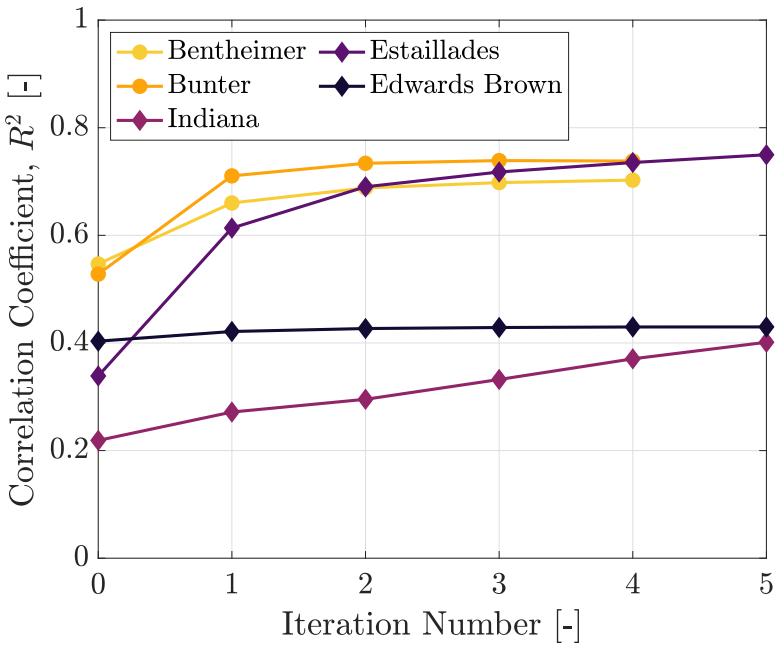


Figure 4.5: R^2 values for the experiment and simulation voxel saturations for the five rock samples plotted against the number of simulation runs. Sandstones and carbonates are plotted as yellow-orange circle and purple diamond markers, respectively.

Table 4.4: R^2 values associated with the final calibrated models for each rock type.

Rock Sample	**Number of Iterations**	**R^2**
Bentheimer	4	0.701
Bunter	4	0.738
Indiana	5	0.401
Estaillades	5	0.750
Edwards Brown	5	0.430

To evaluate the matching procedure, the voxel-scale fluid saturations are compared between the experiments and the simulations. In the initial approach, the high flow rate, viscous-limit relative permeability is input into the simulations. The evaluation of the predictive capability is based on the predicted observations at the low flow rate, which reflect the impact of the heterogeneities inverted from the experimental saturation data. The success of the workflow from Jackson et al. (2018) is discussed for the sandstones and carbonates in the following sections.

4.3.3 Characterisation of Heterogeneous Sandstones

The digital models for the two sandstones created by the iterative calibration scheme are presented in Figure 4.6. To evaluate the applicability of the workflow, experimental and simulation voxel-scale fluid saturations and relative permeabilities are compared in Figure 4.7. The relative permeabilities from the coreflood simulations align well with the experimental data for both sandstone samples, although the Bentheimer generally exhibits a closer match. These results demonstrate the replicability of the digital models: using identical modelling parameters in the unaltered iterative calibration workflow allows us to replicate the findings presented in Jackson et al. (2018).

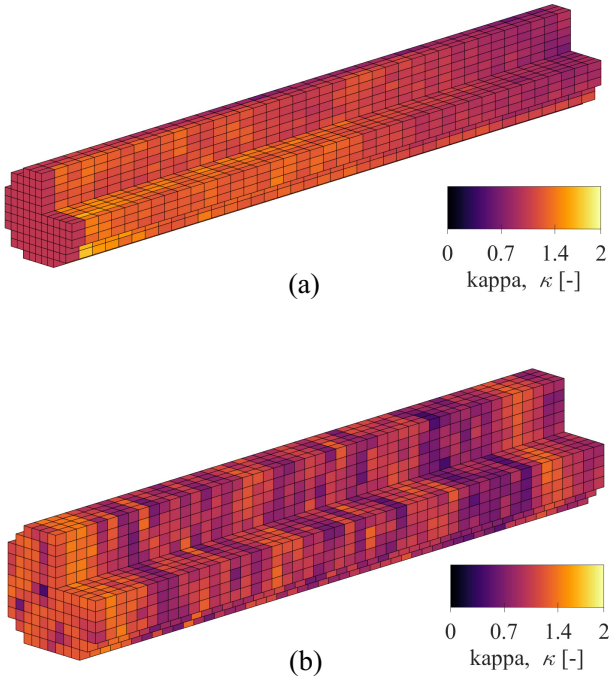


Figure 4.6: 3D digital model displaying the kappa values obtained after 4 iterations for a) Bentheimer sandstone and b) Bunter sandstone. The Bentheimer sandstone exhibits layers parallel to the axis of flow, whereas the Bunter sandstone is characterised by heterogeneities aligned perpendicular to the axis of flow. Digital core dimensions for the Bentheimer and Bunter sandstones respectively: $L = 0.195$m, $r = 0.018$m and $L = 0.150$m, $r = 0.015$m.

As shown in Figure 4.7, the gas relative permeability is raised relative to the viscous-limit curve, whereas the water relative permeability is lowered in the Bentheimer sample. This is as expected: the parallel layering allows for the two phases to arrange themselves optimally,

discussed in previous work such as Krause and Benson (2015) and Rabinovich et al. (2016). In comparison to this, both relative permeabilities are lowered relative to the viscous-limit curves in the Bunter sandstone. This indicates that the perpendicular layering restricts the flow of the phases.

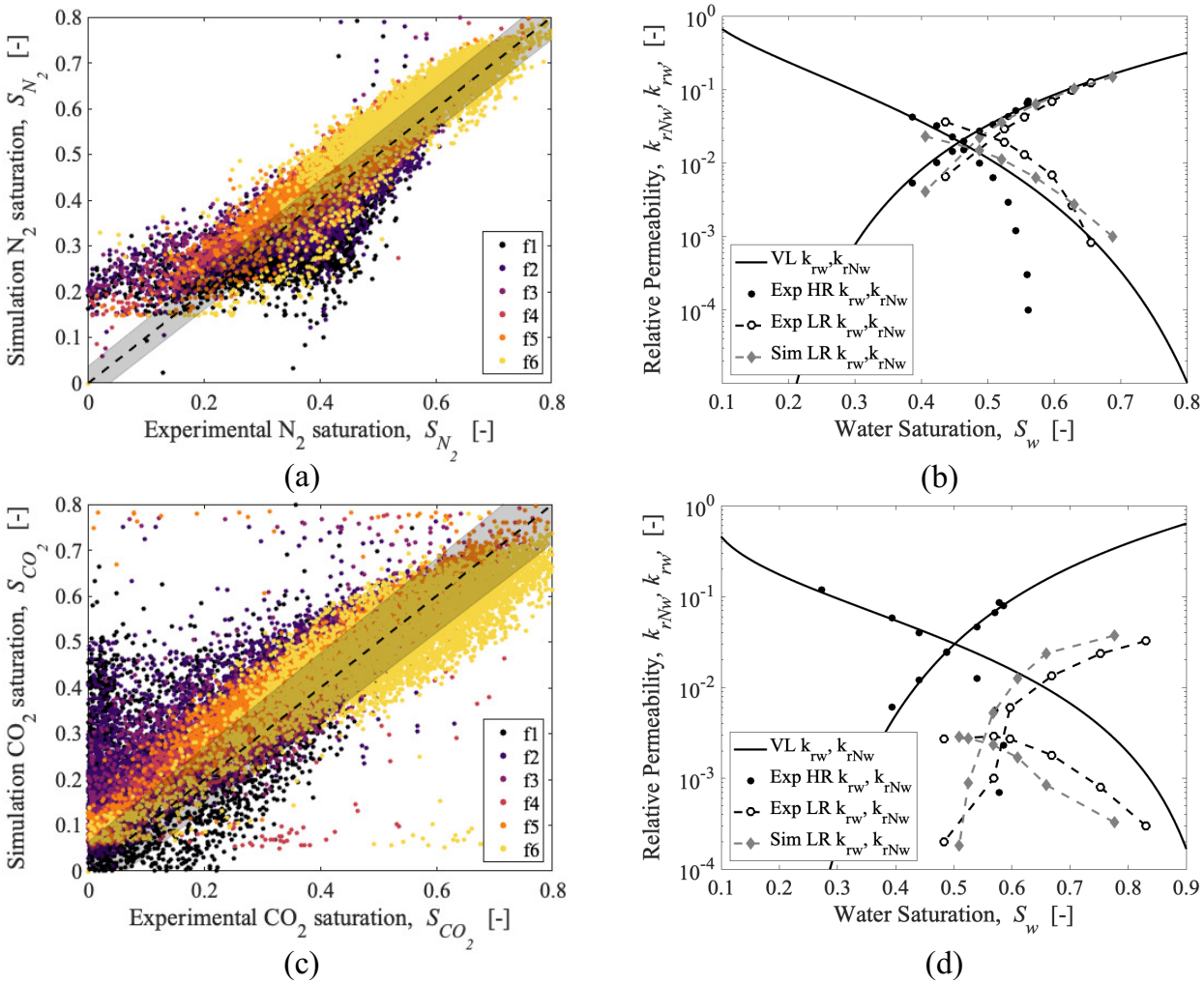


Figure 4.7: Computed relative permeabilities for a) the Bentheimer and b) Bunter sandstone samples obtained from numerical simulations using the iteratively calibrated digital models as input. As shown, the relative permeabilities from the simulations align well with the experimental data for both samples. VL stands for the viscous-limit relative permeabilities used as input to the simulations. Exp LR and HR refer to the low and high rate relative permeabilities respectively, obtained from the coreflood experiment. Sim LR refers to the relative permeabilities obtained from the simulation of the low rate experiment.

To quantitatively assess the success of the optimisation scheme, we calculate the percentage errors associated with the core-average saturation and pressure drop at all fractional flows from the experiment and the simulation. The percentage error for the majority of fractional flows falls below 20% for both cores, which is below the experimental uncertainty. Furthermore, given the significant contrast in pressure drop and saturation between the low and high rate

experiments, a 20% error still allows us to model the variation in flow behaviour between those regimes. Thus, we conclude that the agreement between the experimental observations and numerical simulations is good. The errors for all fractional flows are provided in tabular format in Appendix B.

4.3.4 Characterisation of Heterogeneous Carbonates

Numerical core models incorporating capillary heterogeneity are created for the carbonates following the conventional approach from Jackson et al. (2018), see Figure 4.8. The matching procedure and predictive capability are assessed in Figure 4.9. The results for each rock sample are discussed separately in the subsequent sections.

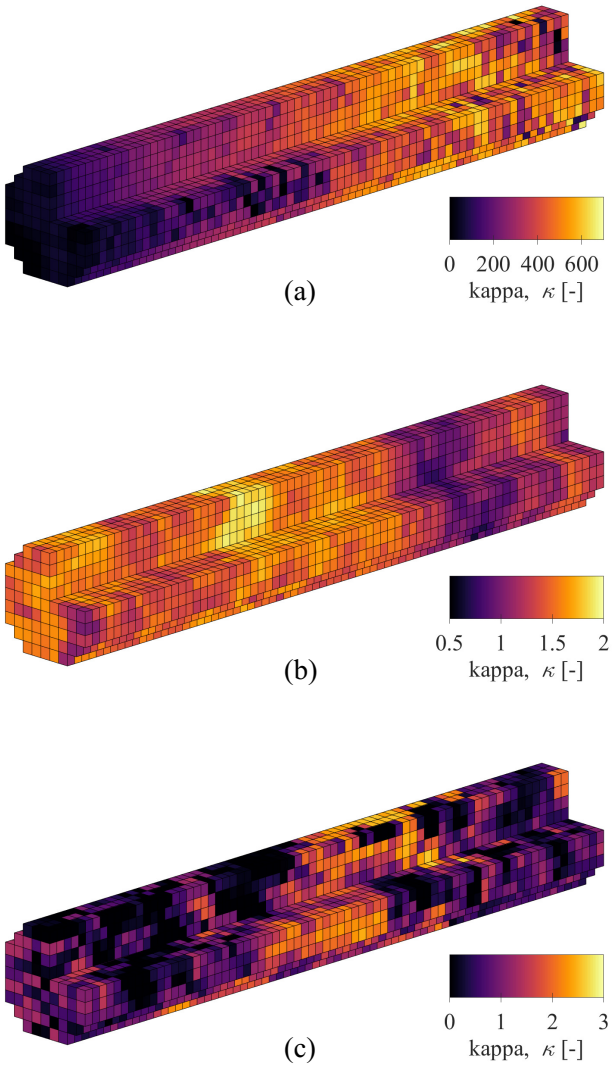


Figure 4.8: 3D digital model displaying the values of κ obtained after 5 iterations for (a) Indiana limestone, (b) Estaillades limestone and (c) Edwards Brown dolomite. Digital core dimensions: $L = 0.144$m, $r = 0.011$m.

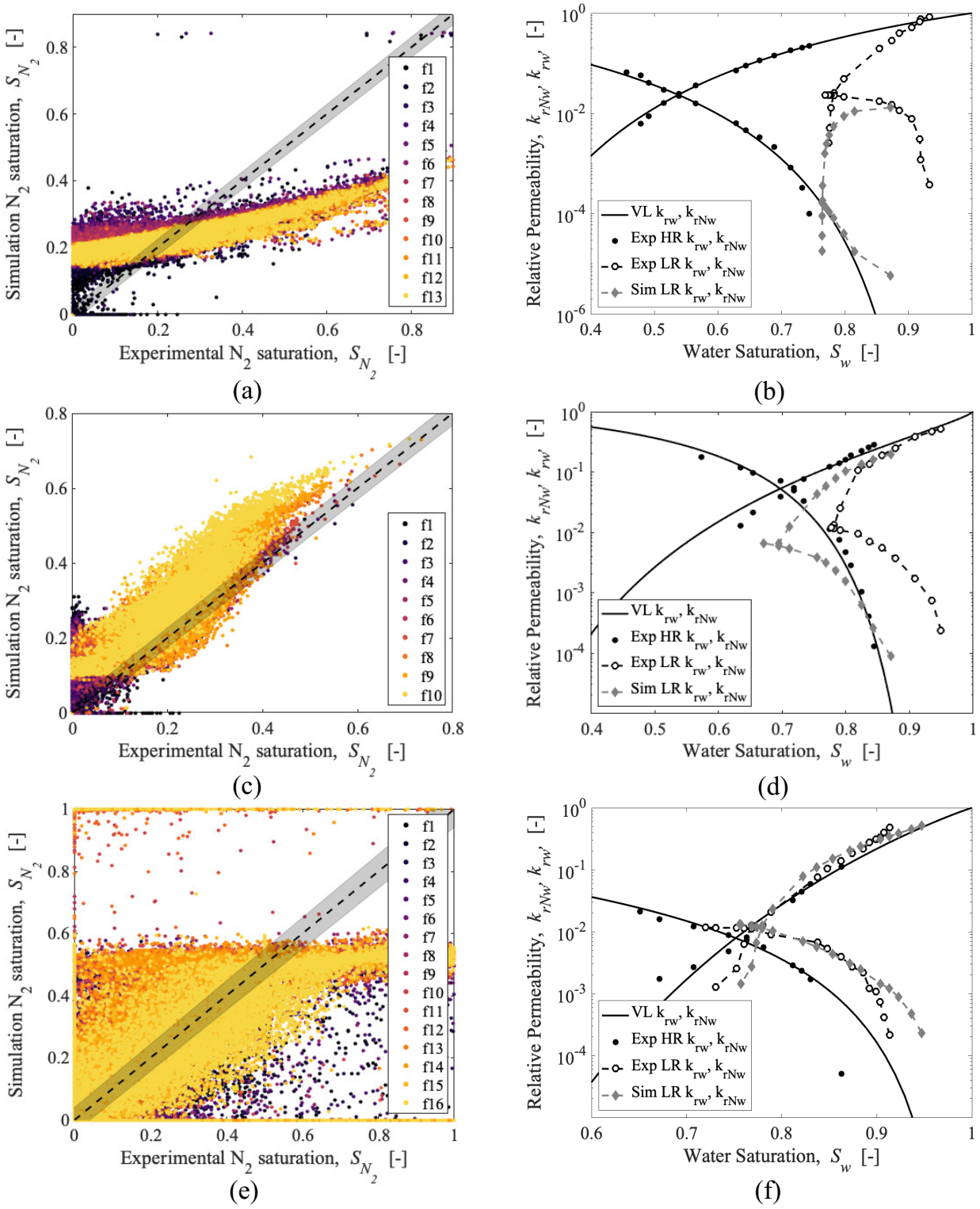


Figure 4.9: An evaluation of the history match and predictive ability of models of carbonate rocks generated with the high flow rate relative permeability curve as input after 5 iterations. Left: voxel saturation correlation plot comparing the experiment and the simulation. The colours correspond to the individual fractional flows. Right: Computed relative permeabilities obtained from numerical simulations using the iteratively calibrated digital models as input. Top: Indiana, Middle: Estaillades, Bottom: Edwards Brown. VL stands for the viscous-limit relative permeabilities used as input to the simulations. Exp LR and HR refer to the low and high rate relative permeabilities respectively, obtained from the coreflood experiment. Sim LR refers to the relative permeabilities obtained from the simulation of the low rate experiment.

4.3.4.1 Indiana Limestone

As shown in Figure 4.8, the Indiana limestone displays the finest-scaled and largest range of variations in κ ($0 < \kappa < 700$). The sample has the smallest scale of heterogeneity resolved by the CT scanner ($\approx$ 1mm) and it displays the poorest match in the voxel saturations (Figure 4.9a). The simulation results in a homogeneous saturation distribution and fails to reproduce the experimental observations.

This is also supported by the 3D saturation maps presented in Figure 4.10. As shown, the simulation results in a homogeneous saturation distribution and the majority of voxels have gas saturations $S_{N_2} < 0.4$. In the experiment, the core exhibits a heterogeneous saturation distribution where small regions are associated with anomalously high gas saturations. These are not reproduced in the simulation.

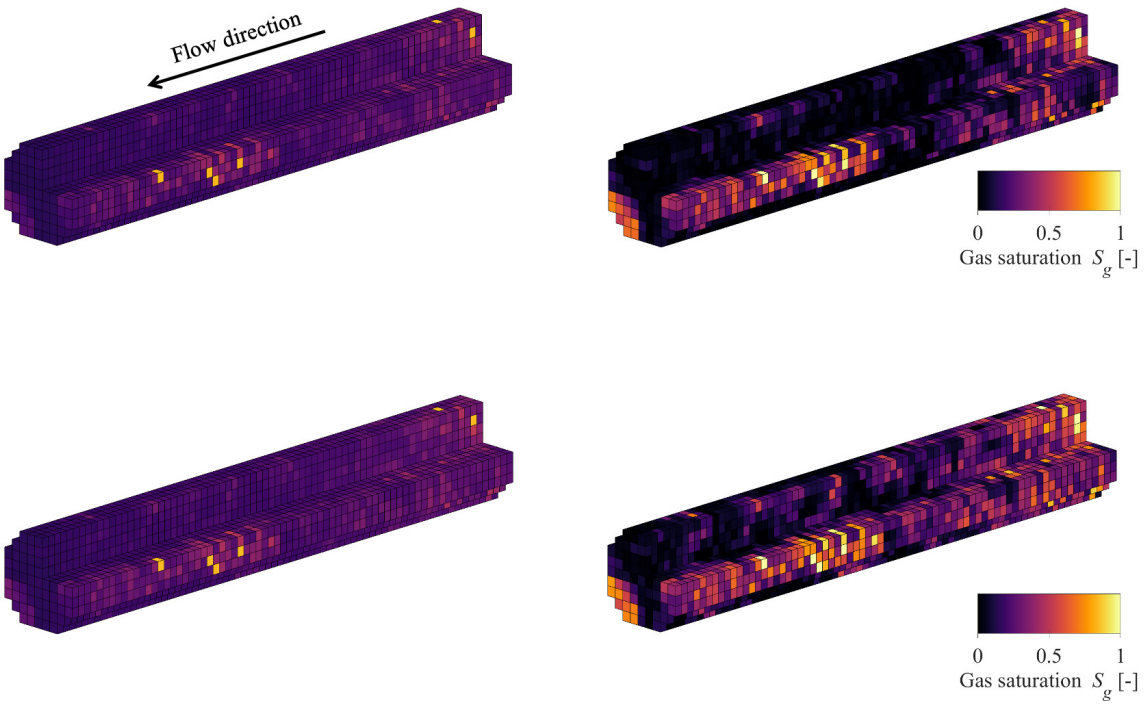


Figure 4.10: 3D saturation maps of the Indiana limestone for the simulation (left) and experiment (right) at two different fractional flows: $fN_2 = 0.612$ (top) and $fN_2 = 1.0$ (bottom). Digital core dimensions: $L = 0.144$m, $r = 0.011$m. The simulation displays a severe mismatch of the experimental voxel saturations.

This mismatch results in a poor prediction of the relative permeability (Figure 4.9b). Both, k_{rg} and k_{rw} are underpredicted. The experimental k_{rw} curve has almost 100 times larger

relative permeability compared with the simulation. The simulated k_{rg} curve plots closely to the viscous-limit. This suggests we do not capture the key features of the heterogeneity in the digital model, which is responsible for the shift in the relative permeability observed experimentally.

A large core-average pressure drop results in the low k_{rg} in the simulation. This could be caused by poor connectivity of the heterogeneity. If some areas of the core are assigned a high P_e, they inhibit the flow and cause a large pressure drop. The κ distribution supports this hypothesis: the optimisation has resulted in a large range of κ values, with some reaching 700 (i.e. P_e is 700 times the 2.96 kPa core-average), which would significantly hinder fluid invasion into these parts of the core. Comparing different iterations shows that the range of κ values significantly increases with each iteration: from 0 - 8 to 0 - 280 between iteration 1 and iteration 4. The large change in κ barely impacts the trend produced by the saturation correlation plot and it remains horizontal. Hence, the iterative optimisation fails to match the experimental observations. These findings imply that there may be other factors beyond capillary heterogeneity, which control the fluid distribution.

4.3.4.2 Estaillades Limestone

The length scale of heterogeneity for the Estaillades ($\approx$ 1cm) is between that of the Indiana and the Edwards Brown. It is associated with the least variation in entry pressures with a range $0.5 < \kappa < 2$, Figure 4.8b. It exhibits a gradual distribution of κ clustered into relatively large regions within the core.

The voxel saturation plot displays a linear correlation between the experiment and the simulation ($R^2 = 0.75$) (Figure 4.9c). The iterative calibration partially matches the saturation distribution captured in the CT scans. This is also supported by the 3D saturation maps presented in Figure 4.11. The saturation distribution pattern observed in the experiment is well-reproduced using the digital model. Both 3D maps exhibit a high-saturated region close to the inlet and a low gas saturation two-thirds into the core. However, the gas saturation is systematically overestimated in the simulation.

The digital model fails to predict the experimental low rate relative permeability (Figure 4.9d): k_{rg} is significantly underpredicted. The prediction of water relative permeability fits the experimental data better, but the curve is shifted to lower water saturations. This is consistent with the voxel saturation correlations. The experimental data displays a raised k_{rg} relative to the viscous-limit k_{rg}, suggesting that the heterogeneity enhances gas flow. This is not reproduced in the simulation. The offset in k_{rg} is not caused by some areas of the core being assigned very high P_e, the range of κ values is small.

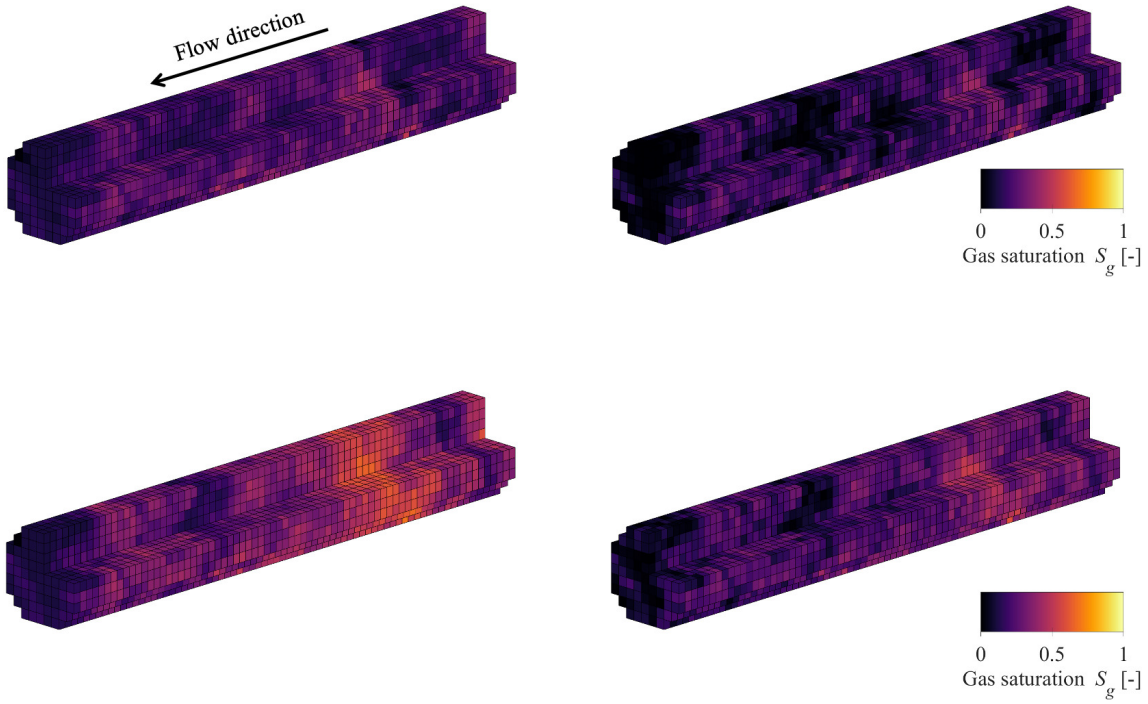


Figure 4.11: 3D saturation maps of the Estaillades limestone for the simulation (left) and experiment (right) at two different fractional flows: $fN_2 = 0.612$ (top) and $fN_2 = 1.0$ (bottom). Digital core dimensions: $L =$ 0.144m, $r=$ 0.011m. The Estaillades exhibits the closest match of the voxel saturations compared to the other two carbonates.

4.3.4.3 Edwards Brown Dolomite

The initial matching procedure results in a large spread of voxel saturations for the Edwards core, which implies that the workflow is unable to match individual voxel saturations well (Figure 4.9e). However, the spatial distribution is reproduced - a high number of voxels plot closely to the 1:1 trendline. This is also observed in the 3D saturation maps, see Figure 4.12. The numerical model accurately predicts the capillary-limit relative permeabilities (Figure

4.9f), significantly better than the other two carbonate samples. Overall, this suggests that the model captures the controlling heterogeneity within the Edwards Brown dolomite. The low rate experiment exhibits a raised k_{rg} compared with the viscous-limit curve, which is reproduced in the simulation.

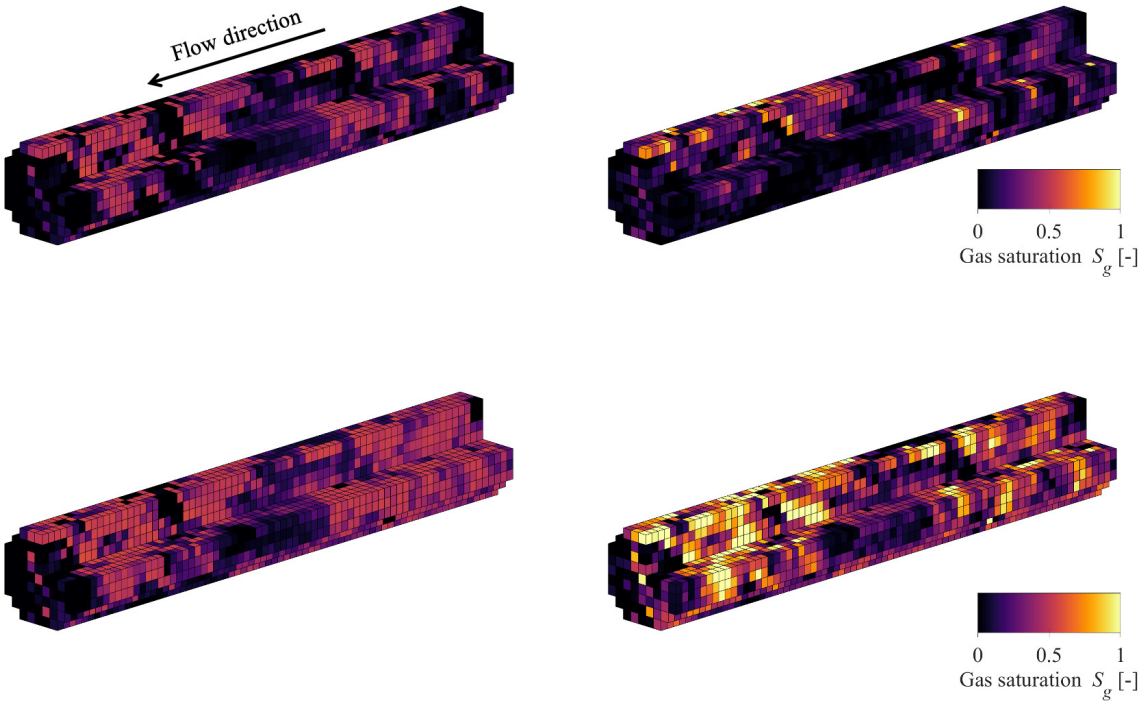


Figure 4.12: 3D saturation maps of the Edwards Brown dolomite for the simulation (left) and experiment (right) at two different fractional flows: $fN_2 = 0.612$ (top) and $fN_2 = 1.0$ (bottom). Digital core dimensions: $L =$ 0.144m, $r=$ 0.011m. The general saturation distribution trend is well reproduced, but individual voxels display a significant mismatch.

4.3.4.4 Sensitivity to the End-Effect

An end-effect may be introduced to the simulated coreflood due to the imposed boundary conditions. As presented in Jackson et al. (2018), once the end-effect is reduced in the digital core model, the severity of rate dependency in the Bentheimer sandstone significantly reduces. These findings demonstrate that it is not just the capillary heterogeneity but also the end-effect that is causing the apparent rate dependence of relative permeability measured during the coreflood.

Using the digital carbonate core models, we explore the sensitivity of the rate dependency of relative permeability to the boundary conditions to these rock samples. The authors in Jackson et al. (2018) remove the end-effect by shortening the digital cores of the sandstones. However, for the carbonate samples, shortening the digital cores would remove key heterogeneities located near the outlet, particularly for the Edwards Brown. Thus, we set P_c to a finite, but constant value in the end slice instead, which also acts to reduce the end-effect. Interestingly, the resultant relative permeabilities are unchanged relative to the original results, which indicates that the simulations are not strongly impacted by end-effects.

This can be explained with reference to the size and orientation of the heterogeneities compared with those in the sandstones. The Bunter sandstone exhibits a minimal change in rate dependency after the core is shortened. The perpendicular layers act to compartmentalise the core, meaning that the impact of boundary effects on the core are localised to the few end slices. In comparison to this, the impact of the end-effect prevails all the way through the core in the Bentheimer sandstone with a parallel heterogeneity. Therefore, digitally reducing the end-effect significantly alters the relative permeability curves in the Bentheimer. In the carbonates, the vug-matrix systems could act as to compartmentalise the core similar to the Bunter sandstone, which reduces the impact of the end-effect.

4.3.5 Evaluation of the Extended Approach

In the extended numerical approach, with the carbonate rocks, the input relative permeability is used as a tuning parameter for matching the experimental data. Thus, rather than predicting the low rate relative permeabilities, they are used as an additional matching target. The voxel saturation correlation and relative permeabilities obtained from the extended approach are presented in Figure 4.13. Table 4.5 compares the viscous-limit relative permeability Chierici parameters obtained from the high-rate experiment to the parameters obtained from the extended history-match workflow. The results for each sample are discussed individually in the subsequent sections.

Table 4.5: Comparison of the viscous-limit relative permeability Chierici parameters, A and B, as obtained from the high rate experiment compared to the results from the extended history match approach.

Name	**Source of Chierici Parameters**	**Chierici A**	**Chierici B**
Indiana	High Rate Experiment	4.37	3.30
Indiana	Extended Approach	1.00	0.45
Estaillades	High Rate Experiment	5.26	1.21
Estaillades	Extended Approach	4.75	0.70
Edwards	High Rate Experiment	15.7	2.66
Edwards	Extended Approach	14.00	2.00

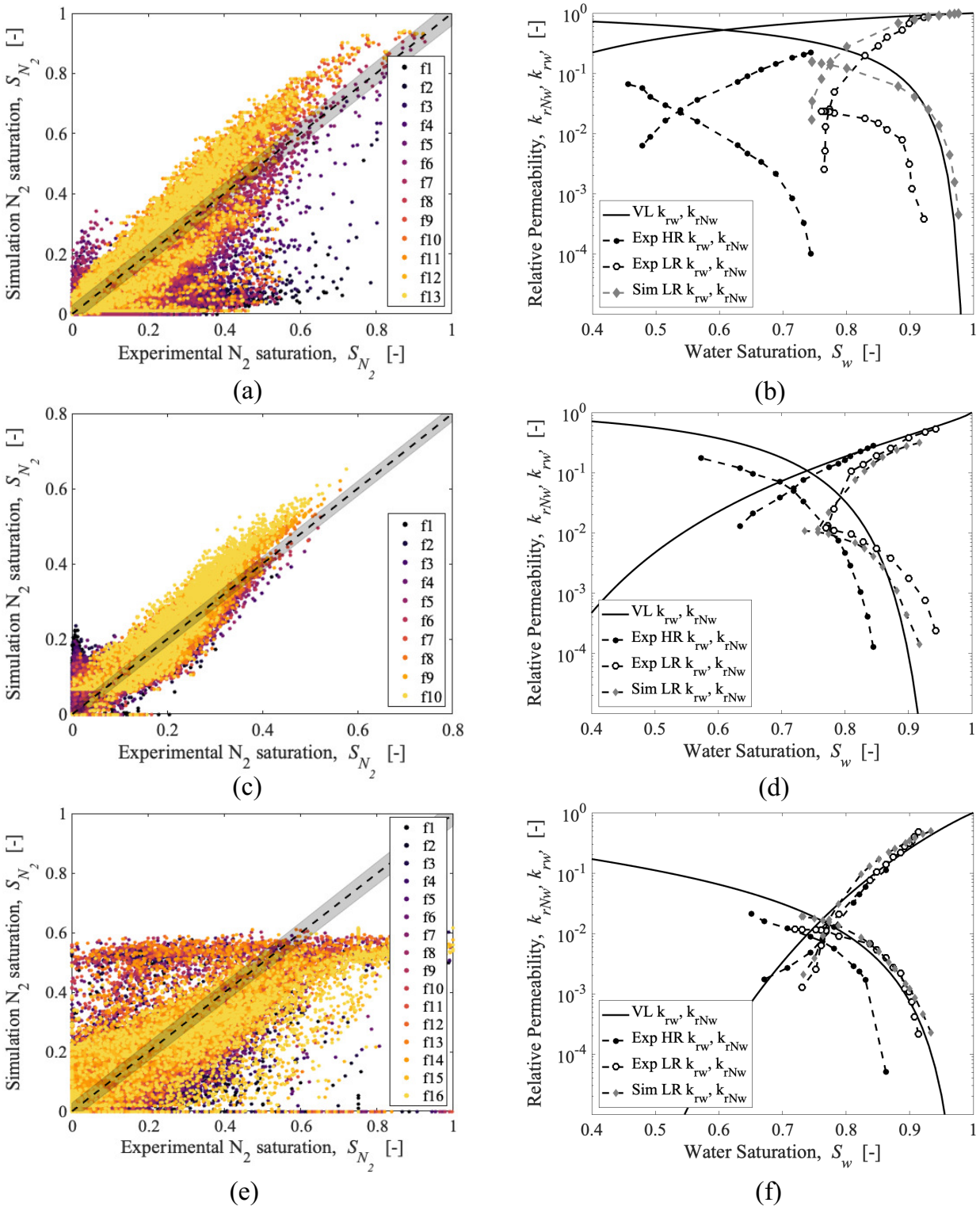


Figure 4.13: History match results for the carbonates when the viscous-limit relative permeability was used as a fitting parameter and the observed relative permeability at low flow rate was an additional matching target after 4 iterations. Left: voxel saturation correlation plot comparing the experiment and the simulation. The colours correspond to the individual fractional flows. Right: Computed relative permeabilities obtained from numerical simulations using the iteratively calibrated digital models as input and compared to the experimental measurements. Top: Indiana, Middle: Estaillades, Bottom: Edwards Brown. VL stands for the viscous-limit relative permeabilities used as input to the simulations. Exp LR and HR refer to the low and high rate relative permeabilities respectively, obtained from the coreflood experiment. Sim LR refers to the relative permeabilities obtained from the simulation of the low rate experiment.

4.3.5.1 Indiana

Conducting the history match using the viscous-limit relative permeabilities as fitting parameters results in a significant improvement in the match of the low flow rate saturation data, Figure 4.13a. The capillary-limit relative permeabilities plot notably closer to the experimental data, Figure 4.13b. Furthermore, the voxel saturation correlation follows a linear trend, which suggests the iterative matching is successful using the updated viscous-limit curves.

However, the updated models are now unable to predict the saturations or relative permeabilities measured during the high rate experiment. Additionally, the history match produces a model associated with close to no rate dependency, where the updated viscous-limit curves (solid black lines) plot very near the simulated low rate relative permeabilities (dashed grey lines). Thus, the shift observed in the experiment with changing flow rate is not reproduced in the history matched simulation. It is thus possible that, unlike the sandstone rock samples, features of the Indiana limestone that are controlling the multiphase flow properties are not resolved in the imagery and/or not properly accounted for in the digital model. Therefore, while we can obtain a satisfactory match in the fluid saturation distribution, this inversion does not result in a physically representative model of the rock core.

Motivated by the unsatisfactory prediction of the high rate relative permeabilities, the history match is repeated, with the error of the low and high rate datasets guiding the match. With this updated workflow, we are unable to obtain a combination of Chierici parameters that minimises the errors in both, the low and high rate observations. For instance, the smallest error in k_{rw} is achieved at low B values for the low rate experiment and at high B values for the high rate experiment. A figure illustrating this behaviour is provided in Appendix C. This issue is also encountered for the other two carbonate samples.

4.3.5.2 Estaillades

The history match using the input relative permeability as a fitting parameter is applied to the Estaillades dataset. As shown in Figure 4.13c and 4.13d this results in a significant improvement in the match of the saturation distribution and relative permeability at low flow rate. However, similarly to the Indiana limestone, the predictive capability of the model is lost and it fails to reproduce the observations at high flow rate. When using both high and low flow rate experimental datasets in the workflow, the history match fails to find a suitable combination of Chierici parameters that minimises the errors in both datasets, similarly to the Indiana limestone. This suggests that the optimisation procedure successfully calibrates to the saturation map and relative permeability at a given flow rate, but fails to result in a physical representation of the rock sample that can replicate the rate dependency of the relative permeability observed in the laboratory.

4.3.5.3 Edwards Brown

To improve the voxel saturation correlation, we apply the history match workflow to this dataset (Figure 4.13e and 4.13f). Similarly to the Indiana and Estaillades limestones, whilst the match in the voxel saturations significantly improves, the predictive capability of the high rate experiment is lost. Additionally, the shift in the capillary-limit relative permeabilities from the viscous-limit curves observed experimentally, also diminishes. The low rate relative permeabilities now plot near the viscous-limit input curves. Once incorporating both datasets into the numerical approach, the workflow fails to minimise the errors in both datasets, as was observed for the other two carbonate cores. With the Indiana and Estaillades, the use of the viscous-limit relative permeability does not improve the predictive ability of the numerical model. A notable finding with the Edwards is that using the simulation relative permeability as a tuning parameter can lead directly to the loss of predictive capability in the simulation.

4.3.6 Discussion of the Workflow Applicability

Carbonates are associated with complex, often bimodal, pore systems, which affect the flow behaviour (Cantrell and Hagerty, 1999; Prodanović et al., 2015). The Estaillades limestone in particular exhibits significant microporosity, which is not explicitly characterised in the digital core models. To test whether this causes the deviation between the experiment and the simulation, we refit the MICP data using more suitable functional forms that model a bimodal pore size distribution. We repeat the optimisation and observe no visible improvement in the results. A more extensive approach to model microporosity is to include variations in S_{wirr} within the sample (Kurotori and Pini, 2021), which is suggested as future work. Microporosity may also be characterised by a different set of relative permeabilities. However, more detailed data collection is required to explore this, such as performing coreflood experiments on separate small plugs corresponding to distinct facies within the larger core sample.

The complex pore structure, as exhibited in the carbonate samples, also likely causes variations in the permeability, which will impact the observed fluid behaviour and is not accounted for in the digital models presented herein. However, to infer the 3D permeability distribution, either pore-based modelling (e.g. pore-network modelling (Zahasky and Benson, 2018) or positron emission tomography (Zahasky et al., 2020)) or an empirical correlation is required. Based on these constraints, we opt for a uniform permeability distribution. Future work could explore the impact of permeability variations on the fitting success. Lastly, the carbonate pore structure likely enables combined drainage and imbibition to occur during the coreflood experiments. In that case, basing the modelling effort solely on drainage behaviour would not suffice. To explore this further, pore scale coreflood observations are required. Overall this suggests that the workflow likely does not entail enough degrees of freedom to infer the full physics of the fluid behaviour exhibited in the core. This ultimately results in a poor characterisation of the samples, whereby the saturation in the simulation is more diffuse than the capillary heterogeneity maps, derived from the experimental saturations, would seem to indicate.

Non-uniqueness is a well-known issue in history matching (Berg et al., 2021). By using multiple datasets (low and high flow rate) and $S_w - P_c$ observations from all fractional flows (max. 16 for the Edwards Brown), the simulations are better constrained, further reducing the potential impact of non-uniqueness. The high volume of data guiding the workflow also differentiates it from previous studies (Krause et al., 2011; Hosseinzadeh Hejazi et al., 2019; Ni et al., 2019) and ensures the physical properties of the sample are replicated. Testing the fully empirical approach (Section 4.2.6.2) emphasizes this. It leads to the loss of predictive capability achieved with the initial iterative approach on the Edwards Brown. This underscores the importance of incorporating the physical mechanisms controlling the fluid behaviour by integrating a large number of datasets. To evaluate the impact of grid convergence issues, a locally-refined grid is implemented in the simulation of one of the carbonates. The resultant voxel saturation correlation displays no improvement, hence it is eliminated as a major control on the results.

The success of the workflow correlates with the characteristic length scale of the heterogeneity in each sample. The Edwards Brown dolomite is the only carbonate sample with a successful model - its porosity heterogeneity was clearly resolved by the imagery. Thus, a factor likely responsible for the breakdown of the calibration is the extent to which the controlling features are resolved by the medical CT scanner. The Indiana and Estaillades limestone samples are known for their pore-scale heterogeneities (Ji et al., 2012; Nejad Ebrahimi et al., 2013; Lin et al., 2016; Muljadi et al., 2016; Pereira Nunes et al., 2016). Hence, the CT images fail to provide sufficient detail to infer the capillary heterogeneity in these two samples, which ultimately results in a poor characterisation. Out of three samples with successful characterisation - the Bentheimer, Bunter and Edwards Brown - the Bunter sandstone has the smallest heterogeneity. The perpendicular layers have dimensions of approximately 30 mm × 30 mm × 3mm in the x, y and z directions, respectively. Thus, the ratio of raw voxel to feature size is 13:1 in the x and y dimension and 1:1 in the z dimension. Similar ratios have been observed as necessary in the accurate analysis of other X-ray imagery (Lin et al., 2018; Jackson et al., 2020).

4.3.7 Rate-Dependant Behaviour of Relative Permeability

Using the successful models for the Bentheimer sandstone, Bunter sandstone and Edwards Brown dolomite, coreflood simulations are run at varying flow rates to investigate the rate dependency of relative permeability, Figure 4.14. The trend varies strongly between the sandstones and the carbonate. The perpendicular layering in the Bunter sandstone generally reduces the permeabilities of both phases, and as the total rate is increased, the relative permeabilities also increase. Comparatively, the Bentheimer sandstone, with parallel layering, allows for the phases to distribute more optimally, leading to a raised gas relative permeability relative to the viscous-limit curve.

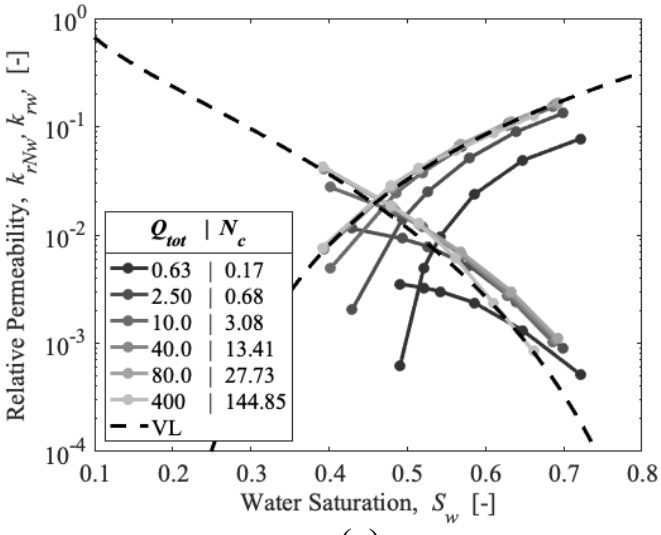
The carbonate sample displays a different trend. Of key interest is that, distinct from the sandstones, the variation in relative permeability is non-monotonic with varying flow rate. From the lowest flow rate, the relative permeability initially increases in the wetting and non-wetting fluid phases before decreasing again towards the viscous-limit curve. This is related to the isotropic nature of the heterogeneity. This non-monotonic behaviour was hypothesised in Virnovsky et al. (2004). Additionally, the rate dependency is weaker than in the sandstones. This is because of the large size of the heterogeneity in the Edwards Brown. Ultimately, this controls the fluid behaviour even in the high rate experiment. At varying rates, the shift in relative permeabilities is stronger for k_{rw} than k_{rg}. This suggests that the relative strength of capillary forces has a stronger impact on the water flow compared with the gas.

To investigate, in more detail, the varying flow dynamics caused by capillary heterogeneity within each sample, we extract 3D saturation maps at distinct flow rates. From Figure 4.15 it can be seen that the parallel layering in the Bentheimer sample results in capillary cross-flow in the low rate simulation, which enhances gas flow. After invading the sample, the gas preferentially flows laterally first into the low entry pressure region, and only then migrates towards the outlet. This results in a raised gas relative permeability at high water saturations ($S_w > 0.6$) compared to the viscous-limit curve as the flow rate is lowered, whereas the water relative permeability is reduced (Figure 4.14a). At lower water saturations, the end-effect is

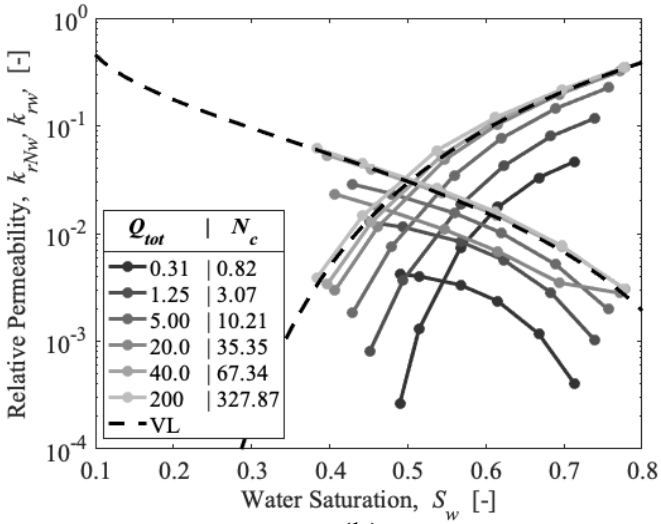
artificially lowering the relative permeability. The high-rate simulation results in a homogeneous saturation distribution and thus a lower gas relative permeability.

The Edwards Brown, characterised by isotropic heterogeneity, displays a different flow behaviour. Referring to the 3D saturation maps from the low and high rate simulations shown in Figure 4.12, it emerges that the isotropic heterogeneity leads to the formation of connected pathway flow, where the gas forms a channel through the low entry pressure regions in the sample. This results in an increased gas permeability, which is visible in Figure 4.14c. In contrast to this, the high-rate core flood results in a very uniform saturation map, which translates to a lower permeability.

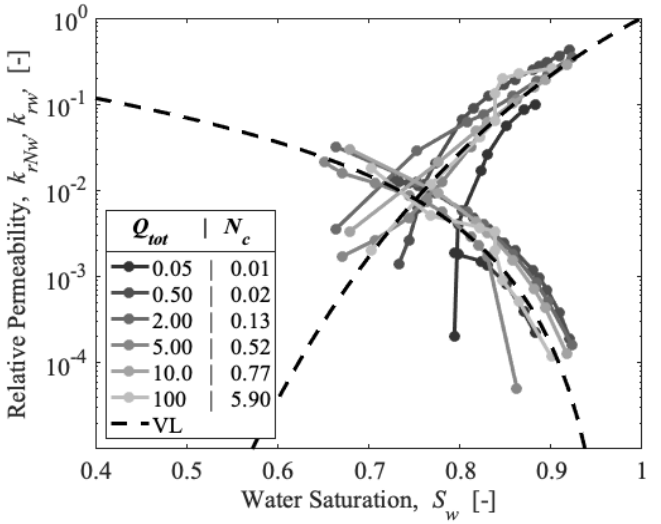
These findings further illustrate the value added to our understanding of flow dynamics in heterogeneous rocks by building digital core models. They also emphasize the importance of incorporating the impact of capillary heterogeneity into flow simulations.



(a)



(b)



(c)

Figure 4.14: Equivalent relative permeabilities for the a) Bentheimer, b) Bunter and c) Edwards Brown at varying flow rates. VL stands for the viscous-limit relative permeability. The relative permeabilities obtained from these simulations are provided in tabular format in Appendix D.

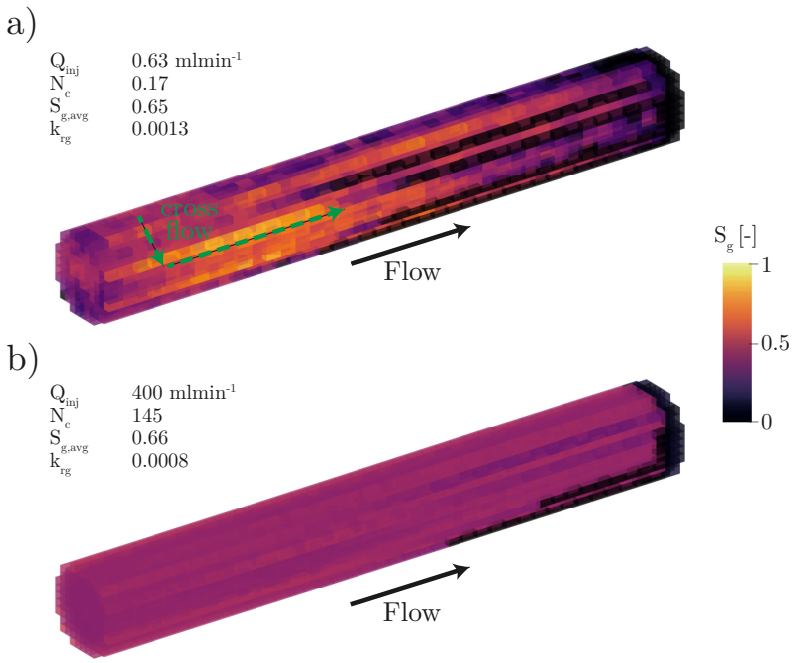


Figure 4.15: 3D saturation maps at f2 ($f_g = 0.4$) of the Bentheimer sandstone at a) low and b) high simulated flow rates. Key measures are provided for each subfigure. Q_{tot} is the total injection rate, N_c is the capillary number, $S_{g,avg}$ is the average gas saturation and k_{rg} is the gas relative permeability. Green arrows indicate the flow pattern, which forms as a result of capillary heterogeneity.

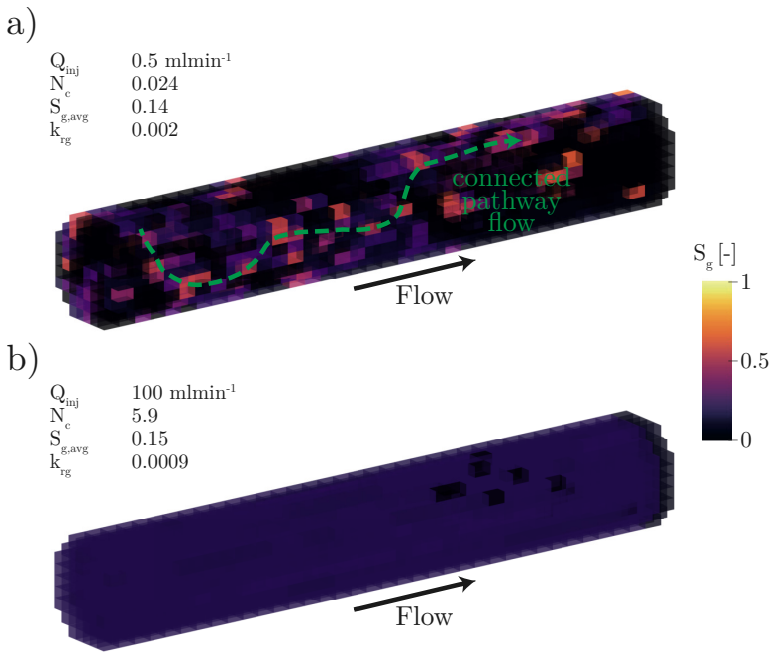


Figure 4.16: 3D saturation maps at f6 ($f_g = 0.995$) of the Edwards Brown dolomite at a) low and b) high simulated flow rates. Key measures are provided for each subfigure. Q_{tot} is the total injection rate, N_c is the capillary number, $S_{g,avg}$ is the average gas saturation and k_{rg} is the gas relative permeability. Green arrow indicates the flow pattern, which forms as a result of capillary heterogeneity.

4.4 Conclusions

We have applied the capillary heterogeneity characterisation workflow presented in Jackson et al. (2018) to five samples with varying degrees of heterogeneity. This allowed us to systematically evaluate the inversion approach against a systematic variation in rock structures, from relatively homogeneous sandstones to complex carbonates with sub-resolution porosity.

The workflow successfully characterised the heterogeneity in the two sandstones, where a good match in the experiment and simulation measurements was observed. In contrast to this, the successful application of the workflow to the carbonates was found to correlate with the size of the controlling heterogeneous features resolved by the scanner. The Indiana and Estaillades limestone with sub-resolution porosity led to unsuccessful models. Comparatively, the Edwards Brown with a large cemented region clearly resolved in the imagery exhibited a good agreement between the experiment and the simulation. This supports the hypothesis that the iterative calibration is dependent on the amount of controlling rock structure that can be resolved with the medical CT scanner.

To improve the predictions, we tested a fully empirical approach whereby the input viscous-limit relative permeabilities were used as fitting parameters. This approach failed to result in predictive capability for the impact of flow rate on saturation distribution or relative permeability in all three carbonates. Notably, it led to the loss of predictive capability achieved with the initial iterative approach on the Edwards Brown. This finding emphasizes the importance of considering the physical mechanisms controlling the fluid behaviour in the creation of a numerical model of the rock cores. The purely numerical approach to matching the experiments led to a complete loss of the predictive capabilities of the models.

For the Bentheimer, Bunter and Edwards Brown samples with successful models, we investigated the flow rate dependency of the upscaled relative permeability. We found that the isotropic heterogeneity in the Edwards Brown resulted in non-monotonic behaviour; initially relative permeability was increased, and subsequently decreased with increasing flow rate.

The work both underscores the importance of capturing small-scale heterogeneities in characterising subsurface fluid flows, as well as the challenges in doing so. Where imagery can sufficiently resolve heterogeneous features and where the model contains sufficient degrees of freedom to infer the full physics, the 3D history match procedure can be performed entirely within the realm of Darcy based reservoir simulators. For rocks where smaller scale features evidently place controls on the upscaled flow or where the heterogeneity is more complex, further advancements are likely required.

This work has since served as the underpinning of new developments in the approach, whereby a multi-parameter capillary pressure fitting and a grid block-based permeability fitting has been incorporated into the algorithm (An et al., 2023). This increased the degrees of freedom in the models and led to a significant improvement in the match between the experimental observations and the simulations for all carbonate rock cores presented in this Chapter.

Chapter 5

Advanced Experimental Study for Reservoir Characterisation

5.1 Objectives

This chapter presents an experimental and characterisation study conducted on reservoir samples from the proposed Endurance CCS site in the UK. We acquired a limited number of reservoir samples and took the opportunity to collect independent experimental data, which provides a useful insight into the potential impact of capillary heterogeneity on CO_2 flow at this site. We conduct mercury intrusion porosimetry experiments on six samples to successfully derive the presence of capillary heterogeneity across a 70 m depth interval. In subsequent chapters, this information, alongside well log data and field-scale geological interpretations, is used to construct a reservoir model of the Endurance site. We also present findings from a steady-state relative permeability coreflood experiment performed on one reservoir sample. The experiment was only partially successful, however it provides information implemented in the upscaling workflow presented in Chapter 7. Using the experimental observations, we apply a modified version of the core characterisation workflow from Chapter 4 to further evaluate its applicability to complex reservoir samples. Lastly, we investigate the dominant length scales of heterogeneity at the Endurance site using pore and core scale observations.

5.2 The Endurance Proposed CCS Site

5.2.1 White Rose Project

The Endurance site is a proposed CCS site located offshore in the North Sea, 60 miles from the East coast of the UK (BEIS, 2021a). A CO_2 storage license was awarded to National Grid Carbon Ltd in 2011, when Endurance was first proposed as a CCS site, as part of the White Rose CCS project (White Rose, 2016a).

The project aim was to capture CO_2 from a coal-fired power plant, located in Selby, using oxy-fuel technology and transport this offshore where it would be injected into the Endurance formation (White Rose, 2016a). The project was led by Capture Power Limited in partnership with National Grid. Numerous characterisation and modelling studies were conducted. However, the project ultimately failed due to a lack of funding.

5.2.2 Net Zero Teesside Project

The storage license for the Endurance site has since been transferred to BP, one of the partners in the Net Zero Teesside project. The Net Zero Teesside project, in association with the Northern Endurance Partnership, is a collaborative effort to decarbonise two industrial clusters in the UK: Humber and Teesside (BEIS, 2021c), as shown in Figure 5.1. The Northern Endurance Partnership provides the means to capture, transport and store the CO_2 emissions from the industrial cluster, and was recognised as a priority cluster in phase-1 of the UK Government's Carbon Capture, Usage and Storage (CCUS) cluster sequencing process (OGCI, 2017). Commencement of CO_2 injection is planned for 2026. Phase 1 of the project aims to develop infrastructure to sequester 4 MTPAa (million tonnes per annum average) of CO_2.

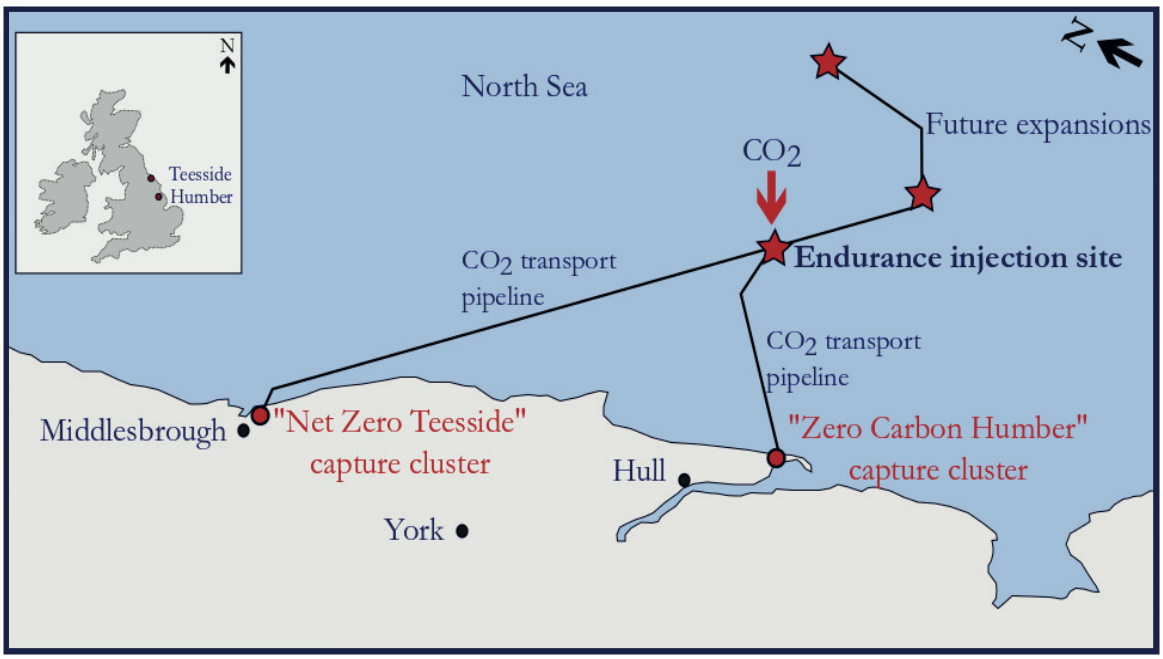


Figure 5.1: Map of the Endurance proposed storage site relative to the two industrial clusters, Humber and Teesside, from which CO_2 is planned to be captured, transported and stored. Modified from BEIS (2021b).

5.2.3 Geological Setting

Endurance lies 144 km from Teesside and 83 km from Humberside within the United Kingdom Continental Shelf in the Southern North Sea (BEIS, 2021e). The structure is a saline aquifer, characterised by a distinct NW-SE orientated four way dip closure, which formed as a result of the underlying Zechstein halite diapir (White Rose, 2016a). The anticline is approximately 25 km long and 8 km wide. The region experienced complex tectonic evolution consisting of multiple episodes of uplift and erosion. These resulted in a complex stratigraphic system and structural configuration, with Figure 5.2 summarising the key formations.

5.2.4 Storage Complex

The Bunter sandstone formation, 150-250 m thick, is the interval of interest for CO_2 injection. White Rose (2016a) and BEIS (2021e) provide thorough sedimentalogical analysis of the depositional environment. In the following two paragraphs, we summarise the most relevant findings from these two studies and refer the reader to White Rose (2016a) and BEIS (2021e) for further detail.

The Bunter sandstone was deposited in a broad, land-locked, semi-arid environment. A mix of sands and mudstones was deposited, resulting from rivers and streams draining into the basin. During periods of uplift resulting in a drier climate, aeolian processes eroded the sands and desiccated the mudstones. During wetter periods and playa lake expansions, shales were deposited. Due to the changing depositional environment, the Bunter is characterised by numerous, large-scale fining upwards units, with coarse-grained sandstones transitioning into siltstones and claystones. It follows that the reservoir entails a mix of low and high permeability facies, with average permeabilities measured at 100 mD to 800 mD depending on the location in the reservoir. Reservoir quality is postulated to be controlled by diagenetic processes, cementation and dissolution involving hydrated minerals such as anydrite.

The Bunter sandstone is overlain by the Rot Clay, which is on average 10 m thick and acts as the primary seal. Above this lies a thick, 800 m sequence of shales and evaporites, referred to as the Rot Halite unit, which covers the wider basin. It displays marginally changing thickness across the region and represents the main sealing unit. Although some diffusion of CO_2 into the Rot clay is expected over >10,000 year timescales, the overlying secondary seal should prevent any leakage. Well log interpretations alongside seismic data of the storage complex are shown in Figure 5.3.

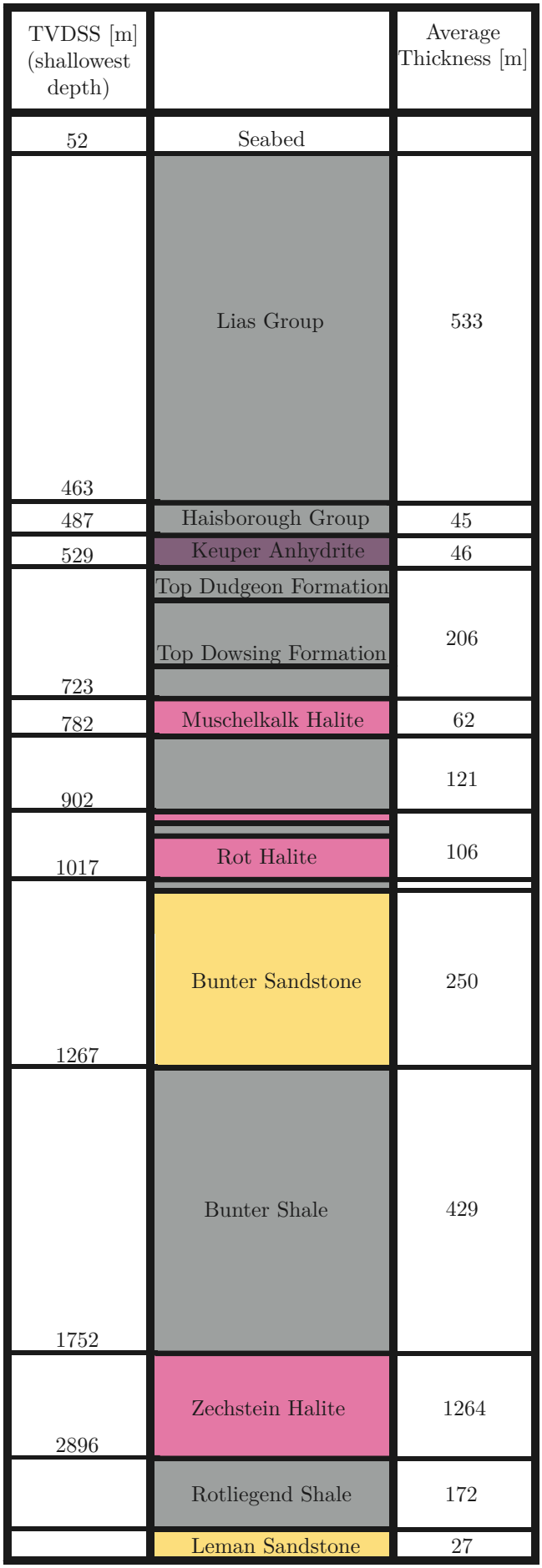


Figure 5.2: Lithostratigraphic column of the Endurance structure. Modified from White Rose (2016a).

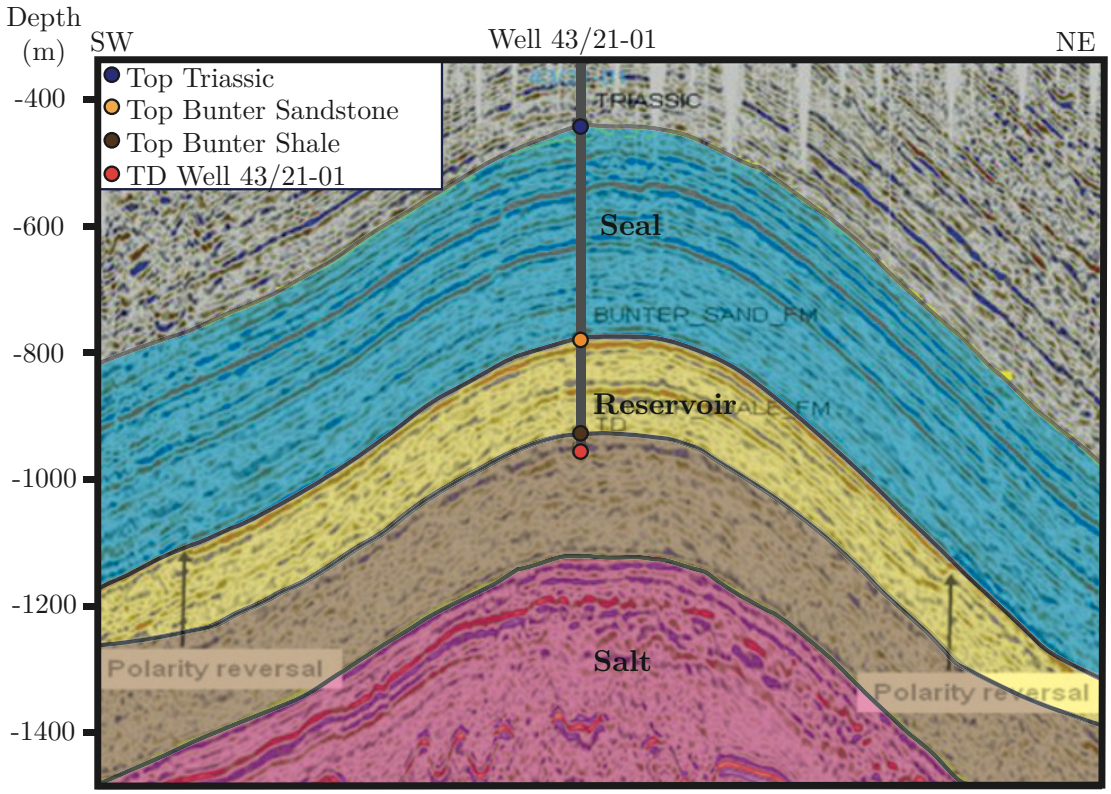


Figure 5.3: Seismic data overlain by interpretation and formation tops obtained from well 42/25-1. Modified from: White Rose (2016a).

5.2.5 Wells

3 wells have been drilled at this site. A map of the well locations is presented in Figure 5.4. The first, well 43/21-1, was drilled for hydrocarbon exploration purposes by Mobil in 1970, which led to the discovery of the Endurance formation (BEIS, 2021e). The well log found hypersaline brine and was later abandoned (BEIS, 2021e).

This was followed by well 42/25-1 drilled by BP. It targeted a deeper section of the reservoir, which was also found to be water-bearing (BEIS, 2021e).

The final well, 42/25d-3, was drilled as part of the appraisal stage of the White Rose CCS project in 2013. It produced 190 m of core, on which an extensive experimental and characterisation study was conducted. The study discovered low permeable regions consisting of cement and heterolithics, which were identified as potential barriers to CO_2 flow (White Rose, 2016a).

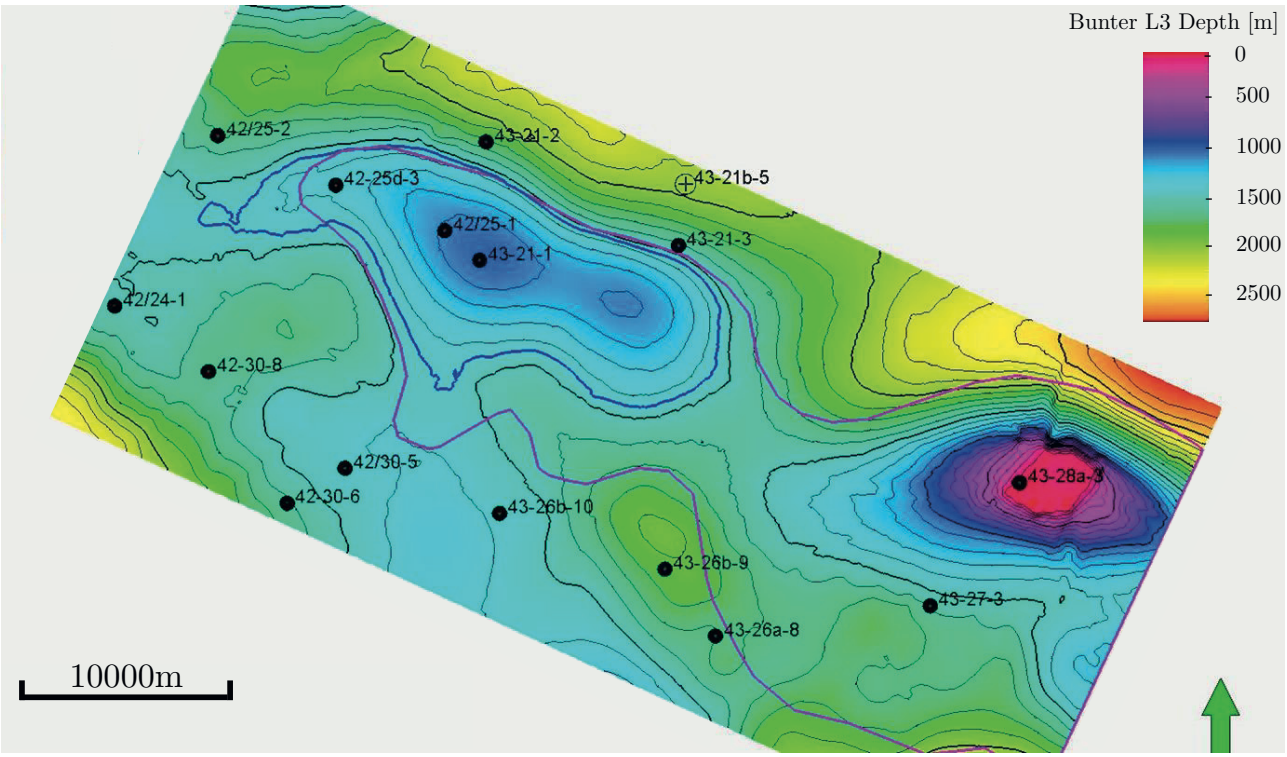


Figure 5.4: Contour map of the Bunter sandstone depth overlain with all legacy wells drilled in the region. The spill point is highlighted as a blue line (Modified from: BEIS (2021a)

5.3 Results

We obtained 23 samples from the cored section of well 42/25d-3, 8 of which were vertical plugs with a diameter of approximately 12 mm and the remaining were horizontal plugs with a diameter of approximately 10 mm. The sample depths were chosen to cover a large depth interval.

The plugs were cut from the consolidated core and trimmed. Thereafter, the samples were treated with standard hot solvent Soxhlet reflux cleaning and subsequently oven dried. A list of samples and properties are provided in table 5.1.

Table 5.1: List of plug samples obtained from well 42/25d-3.

Number	**Name**	**Depth [m]**	**Orientation**	**Diameter [mm]**
1	1V1	1399.85	Vertical	12
2	1V2	1399.85	Vertical	12
3	1H1	1400.05	Horizontal	10
4	1H2	1400.08	Horizontal	10
5	1H3	1400.10	Horizontal	10
6	1H4	1400.13	Horizontal	10
7	1H5	1400.14	Horizontal	10
8	2H1	1444.69	Horizontal	10
9	2H2	1444.80	Horizontal	10
10	2H3	1444.83	Horizontal	10
11	2H4	1444.89	Horizontal	10
12	2H5	1444.95	Horizontal	10
13	4V1	1462.67	Vertical	12
14	4V2	1462.67	Vertical	12
15	5V1	1464.52	Vertical	12
16	5V2	1464.52	Vertical	12
17	3V1	1465.81	Vertical	12
18	3H1	1465.87	Horizontal	10
19	3H2	1465.89	Horizontal	10
20	3V2	1465.89	Vertical	12
21	3H3	1465.92	Horizontal	10
22	3H4	1465.94	Horizontal	10
23	3H5	1465.97	Horizontal	10

5.3.1 MICP to Characterise Reservoir Heterogeneity

We perform mercury intrusion porosimetry (MICP) on six samples to obtain $P_c - S_w$ characteristics at a range of depths. This provides information on the presence of rock type variations within the injection interval and an indication of the strength of capillary heterogeneity at 100s metre length scales. We choose samples from a range of depths to cover a sufficiently large interval whilst selecting plugs that displayed no visible brittleness/fracturing. MICP was performed using the AutoPore IV 9500 V1.09 device. The samples are listed in Table 5.2 alongside the porosity and permeability measured during the experiment. The $P_c - S_w$ data is presented in Figure 5.5.

Table 5.2: List of plug samples analysed in MICP alongside the porosity and permeability measured during the experiment.

Sample	**Depth [m]**	**Porosity [-]**	**Permeability [mD]**
1V1	1399.85	0.10	31.64
1H3	1400.1	0.10	1.93
2H4	1444.89	0.20	32.21
4V1	1462.67	0.24	61.37
3V1	1465.81	0.24	30.95
3H5	1465.97	0.27	106.80

As shown in Figure 5.5, the MICP data exhibits different characteristics between samples 1H3 and 1V1 and the remaining four samples. This is as expected as these samples originate from the Rot Clay unit, the seal lying above the Bunter sandstone. The clay is an entirely different rock type and results in a completely different $P_c - S_w$ characteristic.

Petrographical analysis shows that the Rot Clay is characterised by detrital grains, with illite-rich clay, silt-grade quartz, feldspar and carbonate identified as the key components (White Rose, 2016a; BEIS, 2021e). Data from NMR logging indicates a bimodal pore throat size distribution, which is most likely a result of cementation (White Rose, 2016a; BEIS, 2021e). The porosity and permeability is generally small, which makes the Rot Clay unit a suitable primary seal. Ultimately, this results in a steep capillary pressure curve, which is displayed in Figure 5.5. The kink in the curves between $S_w = 0.4 - 0.6$ suggests that these two samples are characterised by a bimodal pore size distribution, which confirms observations from previous

petrographical studies (White Rose, 2016a; BEIS, 2021e).

In comparison to this, the four remaining samples, originating from the Bunter sandstone formation, can be clearly distinguished from the clay plugs. The $P_c - S_w$ curves are smooth and exponential, which indicates that the pore throat distributions exhibit one large peak. However, the entry pressure ($P_c(S_w = 1)$) between the four samples varies between 5-12 kPa, which demonstrates that the target interval is characterised by capillary heterogeneity. The mineral composition of numerous samples along the whole injection interval was extensively tested in White Rose (2016a). The primary minerals are quartz, feldspar and plagioclase, but the exact composition varies with depth. This will likely give rise to capillary pressure variations.

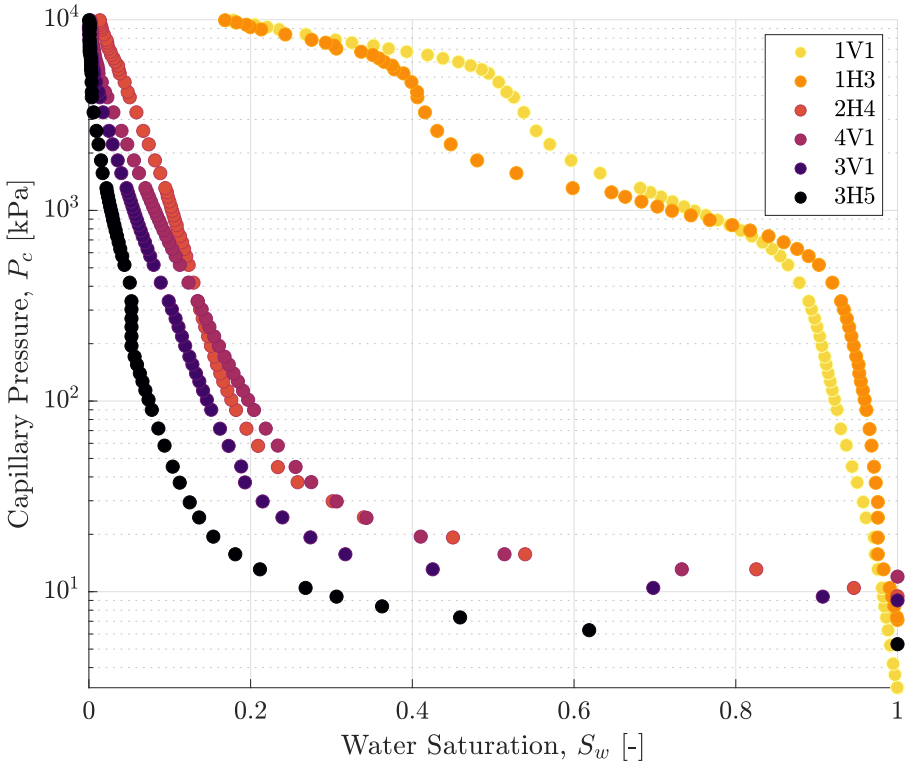
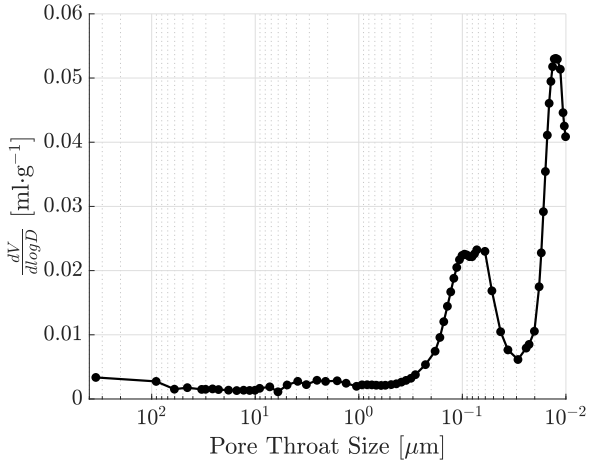


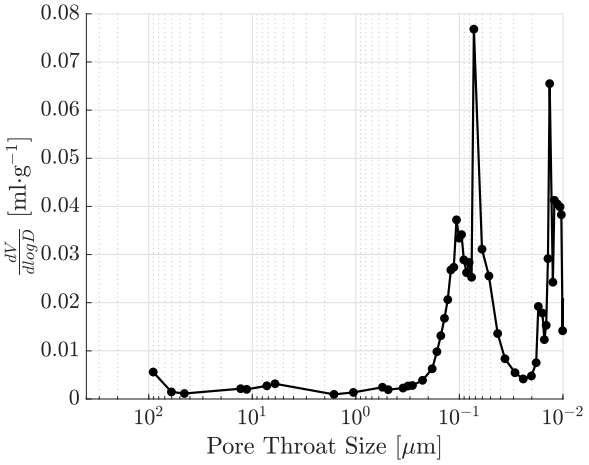
Figure 5.5: Results from the MICP experiments performed on six samples from the Endurance site. The points are colour coded based on their depths. A correction for interfacial tension was applied to the raw measurements to convert from mercury-air to carbon dioxide-brine.

To visualise the pore size distribution, we extract the incremental intrusion volume against the pore diameter, Figure 5.6. The two samples from the Rot Clay unit, 1V1 and 1H3, are characterised by a bimodal pore size distribution. Overall, they exhibit a much smaller average pore throat size with a peak at 0.1 and 0.01 μm for 1V1 and 1H3, respectively. This corresponds

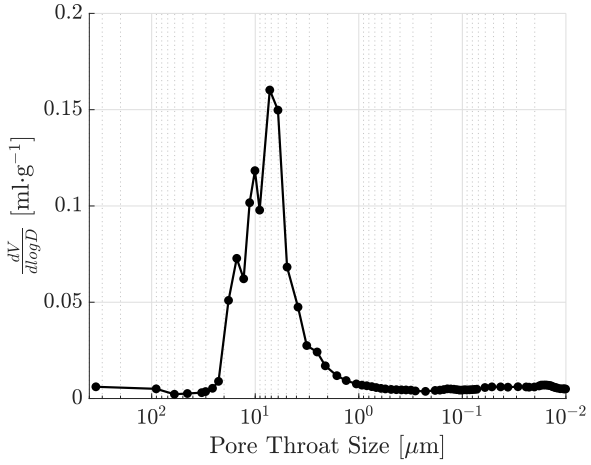
to the low porosity of 0.1 measured during the MICP experiments (Table 5.2). In comparison to this, all four sandstone samples display a single peak. However, the distributions are not smooth, especially for samples 2H4 and 4V1. This demonstrates that the pore structure may be characterised by stronger variability. For all samples, there is a significant amount of pores with sizes below 10 μm, which demonstrates that the reservoir rock is relatively tight.



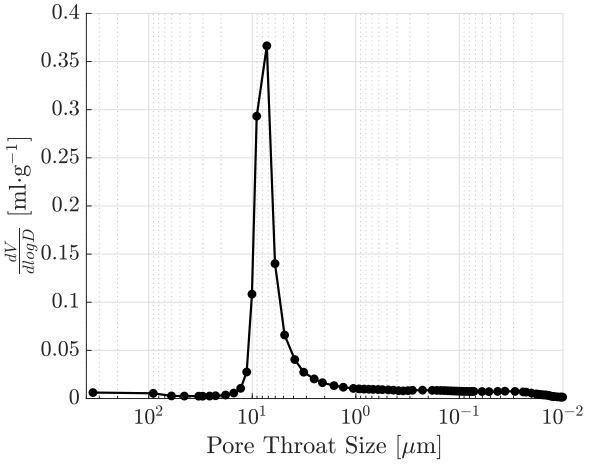
(a) 1V1



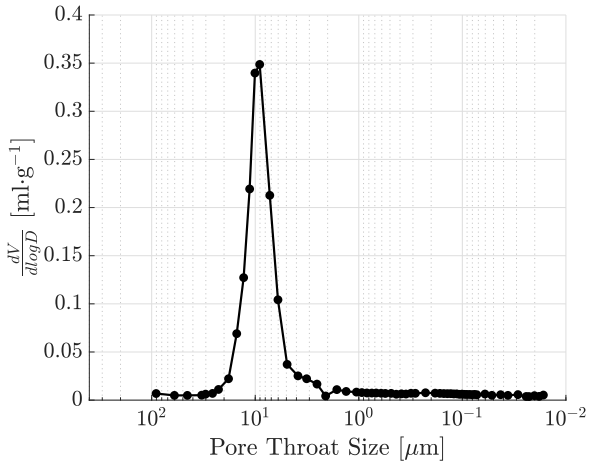
(b) 1H3



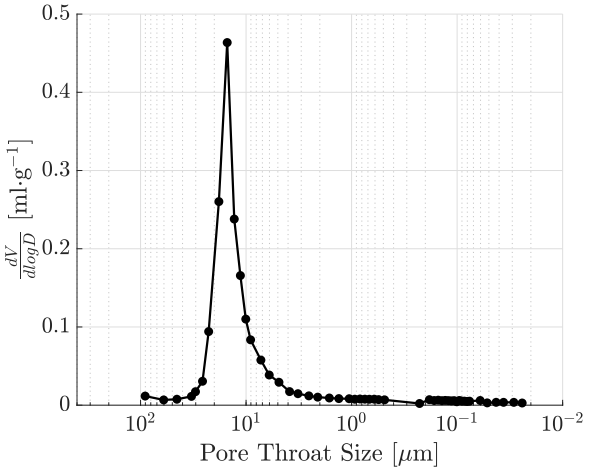
(c) 2H4



(d) 4V1



(e) 3V1



(f) 3H5

Figure 5.6: Pore size distribution for the six reservoir samples from MICP experiments.

5.3.2 Steady-State Coreflood Experiment to Obtain the Relative Permeability

5.3.2.1 Experimental Conditions

A steady-state relative permeability coreflood experiment was conducted on the reservoir sample 5V1. The plug exhibits various thin dark streaks, which could be indicative of laminations. The sample is 6 cm long with an 1.18 cm diameter, see Figure 5.7 for a photo.

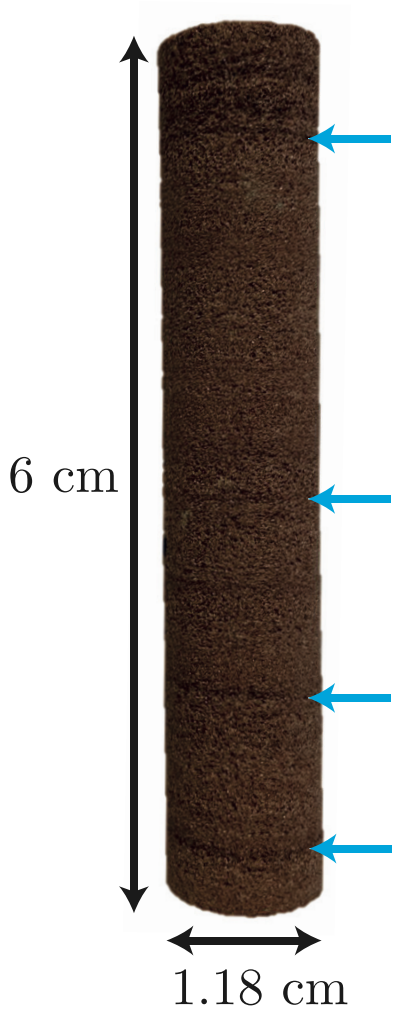


Figure 5.7: Photograph of sample 5V1. Blue arrows indicate regions of the sample that exhibit darker streaks.

We perform a steady-state drainage experiment with nitrogen and DI water at ambient temperature and 70 bar pressure. Nitrogen is chosen to be a suitable analogue for CO_2 (Al-Menhali et al., 2015; Niu et al., 2015; Reynolds and Krevor, 2015). The sample is initially saturated

with DI water, after which the two fluids are co-injected at 0.1 ml·min^{-1}. After steady-state is reached, the core-average pressure drop is measured and a CT scanner is used to image the saturation distribution in the sample. The experimental conditions are summarised in Table 5.3 and the fractional flows in Table 5.4. The detailed steady-state relative permeability coreflood experimental procedure is described in Chapter 3.

Table 5.3: Experimental conditions imposed in the steady-state relative permeability coreflood experiment.

Parameters	**Sample 5V1**
Nonwetting phase, nw	N_2
Wetting phase, w	DI Water
Flow rate, Q_{tot} [ml·min^{-1}]	0.1
Number of fractional flows	6
Pressure, P [bar]	70
Temperature, T [°C]	20
nw density, ρ_{nw} [kg m^{-3}]	115
w density, ρ_w [kg m^{-3}]	998
nw viscosity, μ_{nw} [μPa s]	19.7
w viscosity, μ_w [μPa s]	1070
IFT, γ [mN·m^{-1}]	62
Experimental core length, L [mm]	60
Experimental core radius, r [mm]	11.8
Raw voxel Δx, Δy [mm]	0.04
Raw voxel Δz [mm]	0.5

Table 5.4: Fractional flows imposed in the steady-state relative permeability coreflood experiment.

Fractional Flow Number	f_w [-]	f_g [-]
f1	0.85	0.15
f2	0.65	0.35
f3	0.25	0.75
f4	0.05	0.95
f5	0.02	0.98
f6	0	1

5.3.2.2 Coarsening and Elementary Volumes

The CT images are cropped and coarsened to reduce the uncertainty in the voxel-scale experimental saturation and speed up the numerical simulations presented in subsequent sections. The amount of coarsening applied to the images is also governed by the elementary volume (EV). It is important to choose a voxel size under which a continuum property has meaning. We verify the EV for porosity by estimating the number of pores present within each voxel using the maximum pore radius obtained from the MICP experiment conducted on a sister sample, 3V1. The resolution of the raw image (x,y,z) is 0.04 mm, 0.04 mm and 0.5 mm. We upscale the voxels by a factor of 8 in the x and y dimension and a factor of 2 in the z. Thus the upscaled voxels have dimensions of (x,y,z) 0.32 mm, 0.32 mm and 1 mm.

To verify that our grid block size is sufficient such that a continuum property has meaning, we follow the same approach as detailed in Chapter 4 Section 4.2.4. For the Bunter sandstone, a pore reaches a maximum pore volume of $382 \times 10^3 \mu m^3$ (using the maximum pore radius of 45 μm from the MICP data of sample 3V1). Using the upscaled voxel dimensions the volume of a coarsened voxel is $1.02 \times 10^8 \mu m^3$. Thus, a minimum of 268 pores is present within each upscaled voxel, which demonstrates that a continuum property has meaning (Peksa et al., 2015).

Figure 5.8 assesses the impact of repeat scans and image coarsening on the resultant experimental saturation uncertainty in the saturations, following the workflow from Pini et al. (2012). As shown, the voxel scale uncertainties are significantly reduced from image coarsening and averaging over repeated scans. For our coarsening scheme of $8 \times 8 \times 2$ the standard deviation of the saturation is reduced to under 1%.

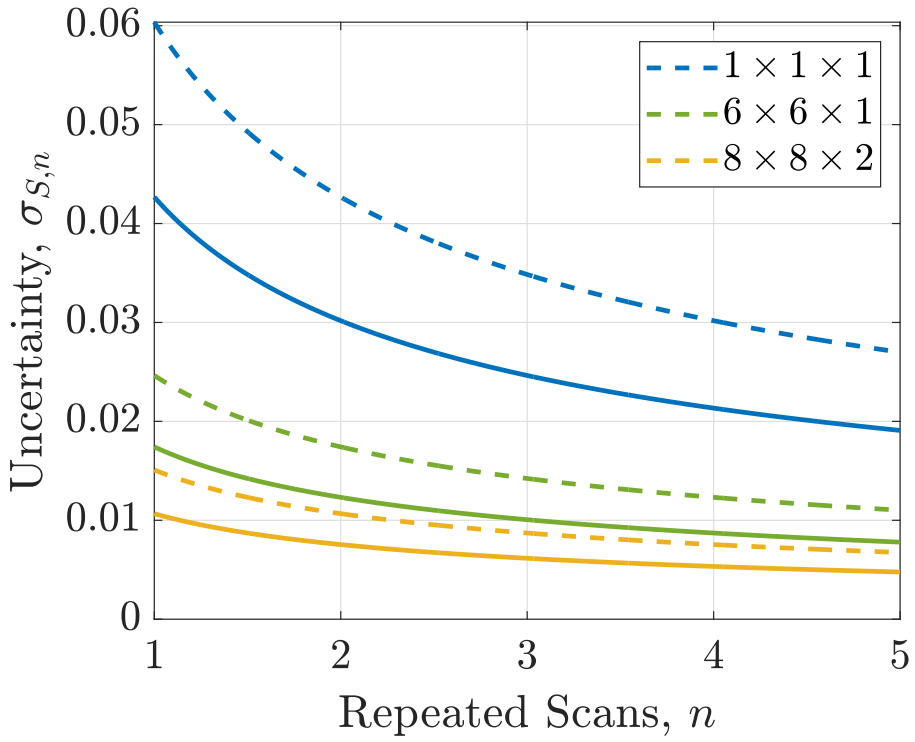


Figure 5.8: Uncertainty in the saturations as a function of the number of repeat scans. Five repeat scans were performed. The colours represent the uncertainty for specific coarsening schemes as indicated. The solid and dashed lines refer to the uncertainty at $S_w = 0.0$ and $S_w = 1.0$, respectively.

5.3.2.3 Absolute Permeability

The absolute permeability of the sample is measured prior to the drainage experiment following the method detailed in Chapter 3. The results, presented in Figure 5.9, show that the sample follows the expected linear trend according to Darcy's Law. We also do not observe the need for a pressure correction as the trendline intercepts the origin. We calculate the absolute permeability at each flow rate and find the average to be 31 mD.

5.3.2.4 Porosity Distribution

To obtain the 3D porosity distribution in the rock core, the CT images are processed using the method described in Chapter 3.

Figure 5.10 presents the resultant porosity profile along the length of the core. As shown, the sample appears relatively homogeneous with a maximum porosity variation of 0.03. However, on this scale we observe some subtle variations in the slice-average porosity. This confirms

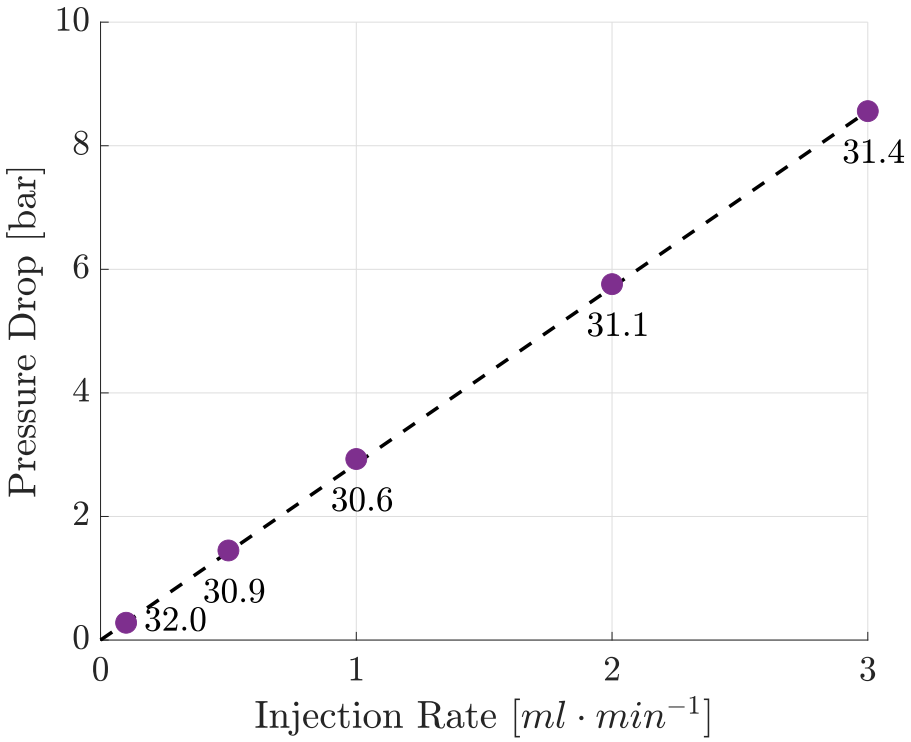


Figure 5.9: Single-phase flow experimental measurements to determine the absolute permeability of the sample. The annotation at each data point is the absolute permeability [mD] calculated from the corresponding pressure drop and flow rate.

the observations from the visual inspection of the core sample, where we found laminations orientated perpendicular to the length of the core. From the inlet of the core until ≈30 mm, we observe a gentle increase in porosity of 0.02. This is followed by a more abruptly decreasing and variable slice-average porosity, with the lowest porosity found at 45 mm.

Figure 5.11 presents the porosity distribution in 3D, which provides further insight into the heterogeneity exhibited in the sample. We observe some low-porosity layering perpendicular to the axis of flow, which becomes more frequent as we move towards the outlet of the core. We also observe higher porosities towards the top of the sample, which indicates that there may also be some layering parallel to the axis of flow. The low-porosity slice discovered in the porosity profile can clearly be distinguished in 3D as well. It appears that the central part of that slice is characterised by a circular region with a low porosity of $\phi < 0.1$. Others parts of the sample display a similar shaped low-porosity region. The variation in heterogeneity is in agreement with the core analysis presented in BEIS (2021e), where different types of geological structures were identified including laminations, ripples, drapes, disturbed laminae, cross-bedding and interbedded silt layers.

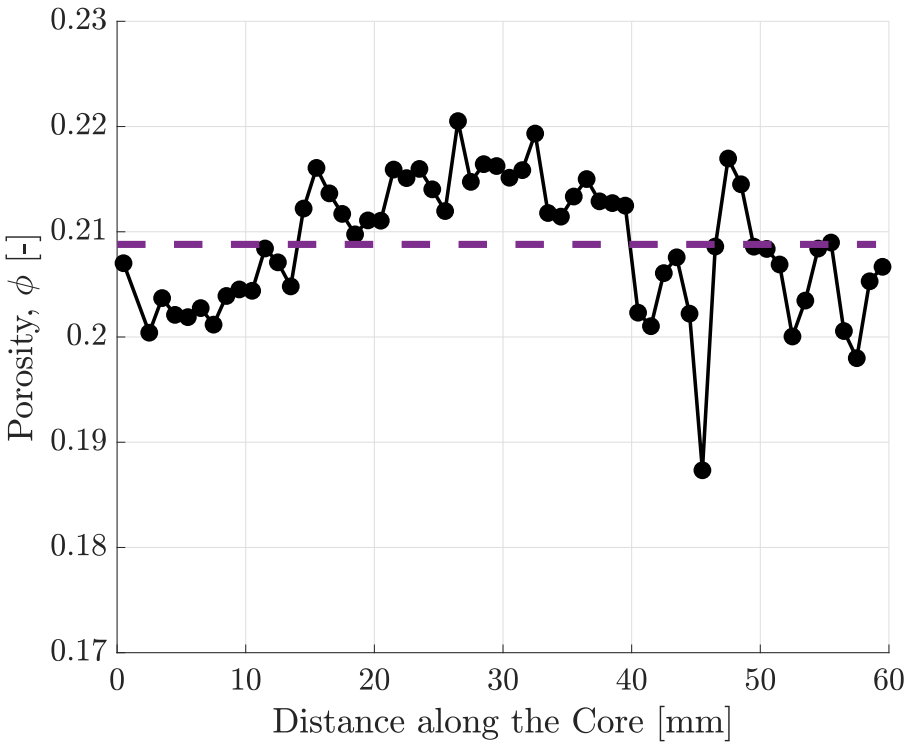


Figure 5.10: Porosity profile along the length of the core. The average porosity of the sample is 0.2088 and is plotted as a purple dashed line.

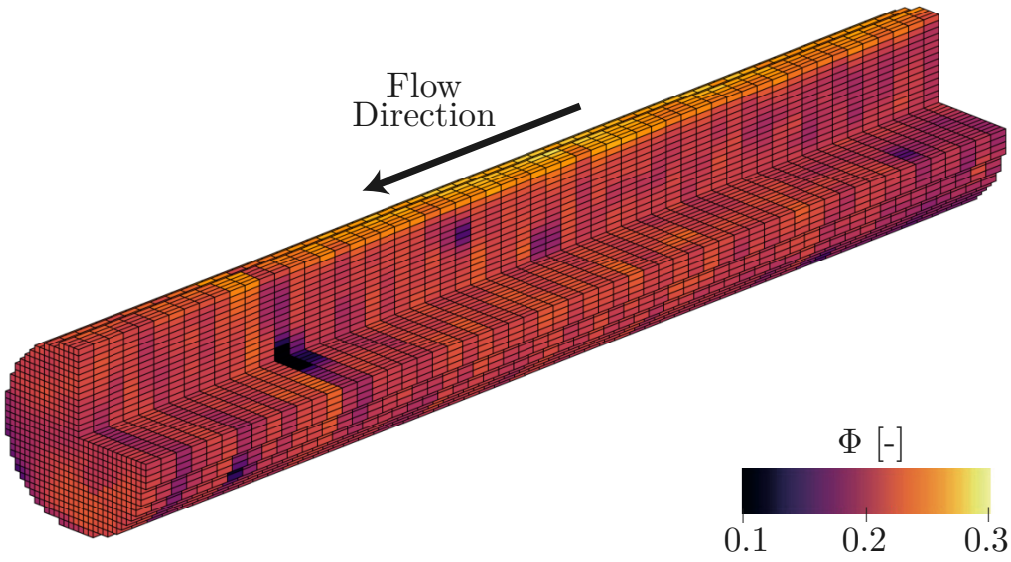


Figure 5.11: 3D porosity distribution.

5.3.2.5 Saturation Distribution

The saturation profiles from the six fractional flows are plotted in Figure 5.12. As shown, the profiles are largely homogeneous, although the core is characterised by some subtle saturation variability, which is likely attributed to porosity heterogeneity. For instance, the higher porosity slice between 15-16 mm corresponds to a raised nitrogen saturation at all fractional flows. We also observe a steeply rising nitrogen saturation towards the outlet of the sample, from approximately 45 mm to 60 mm, which is most prominent in the first three fractional flows. We postulate this is caused by an outlet end effect. Typically, an end effect is characterised by a rise in the wetting phase saturation towards the outlet. It is caused by the discontinuity of capillary pressure at the boundary between the core sample and the outlet, where the capillary pressure abruptly changes from a finite value to zero. This makes it more difficult for the wetting phase to leave the system and leads to a build-up of wetting phase saturation upstream of this discontinuity (Hadley and Handy, 1956).

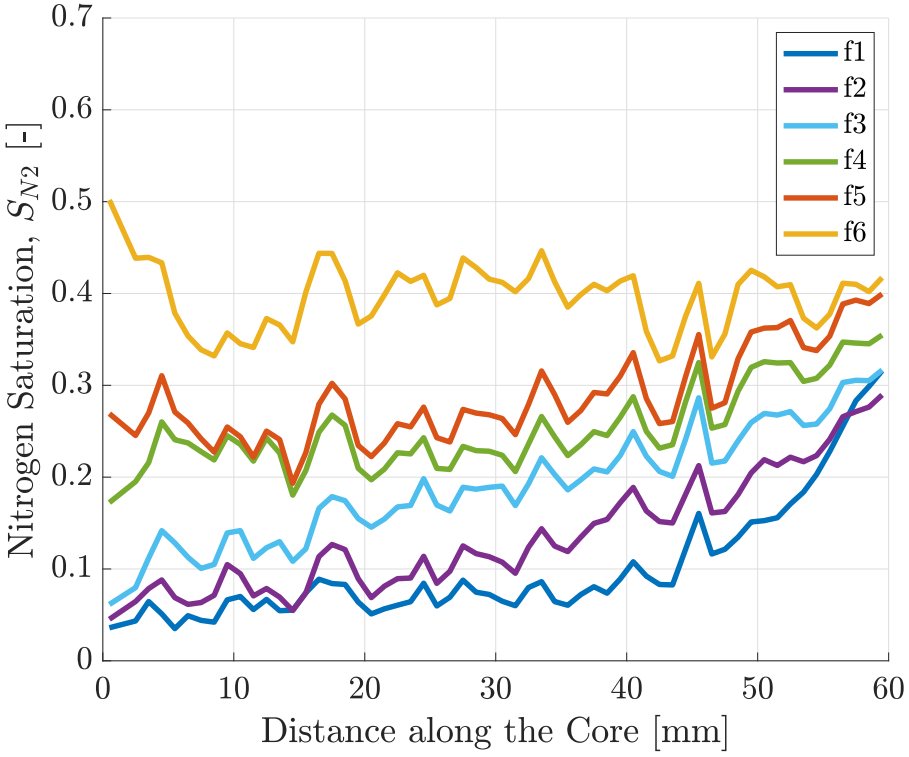


Figure 5.12: Saturation profiles along the length of the core for the six fractional flows.

In our experiment, we observe the opposite effect, whereby the assumed non-wetting fluid (nitrogen) accumulates in the outlet region of the sample. The inlet and outlet tubing has a $\frac{1}{16}$ inch diameter, which may be sufficiently small to result in an entry pressure in those lines. Furthermore, the end piece, which connects the outlet flow lines to the coreholder, may be intermediate or oil-wet. These two effects could result in nitrogen not being able to flow out of the system and would lead to an upstream accumulation of nitrogen. This would also explain why this effect diminishes at higher fractional flows: at a higher fractional flow, the nitrogen phase pressure is also higher, meaning it is easier to displace the water and also overcome the entry pressure in the outlet flow line.

Figure 5.13 presents the corresponding 3D saturation distributions. At all fractional flows, we observe some variability within each slice, which is in agreement with the porosity heterogeneity identified in the previous section. The perpendicular layering can also be recognised. Most prominent is the anomalously high saturation at 45-46 mm, which corresponds to the low-porosity circular heterogeneity discussed previously. Based on the saturation response, we infer this to be an imaging artefact, possibly some clay minerals, which interfered with the X-rays.

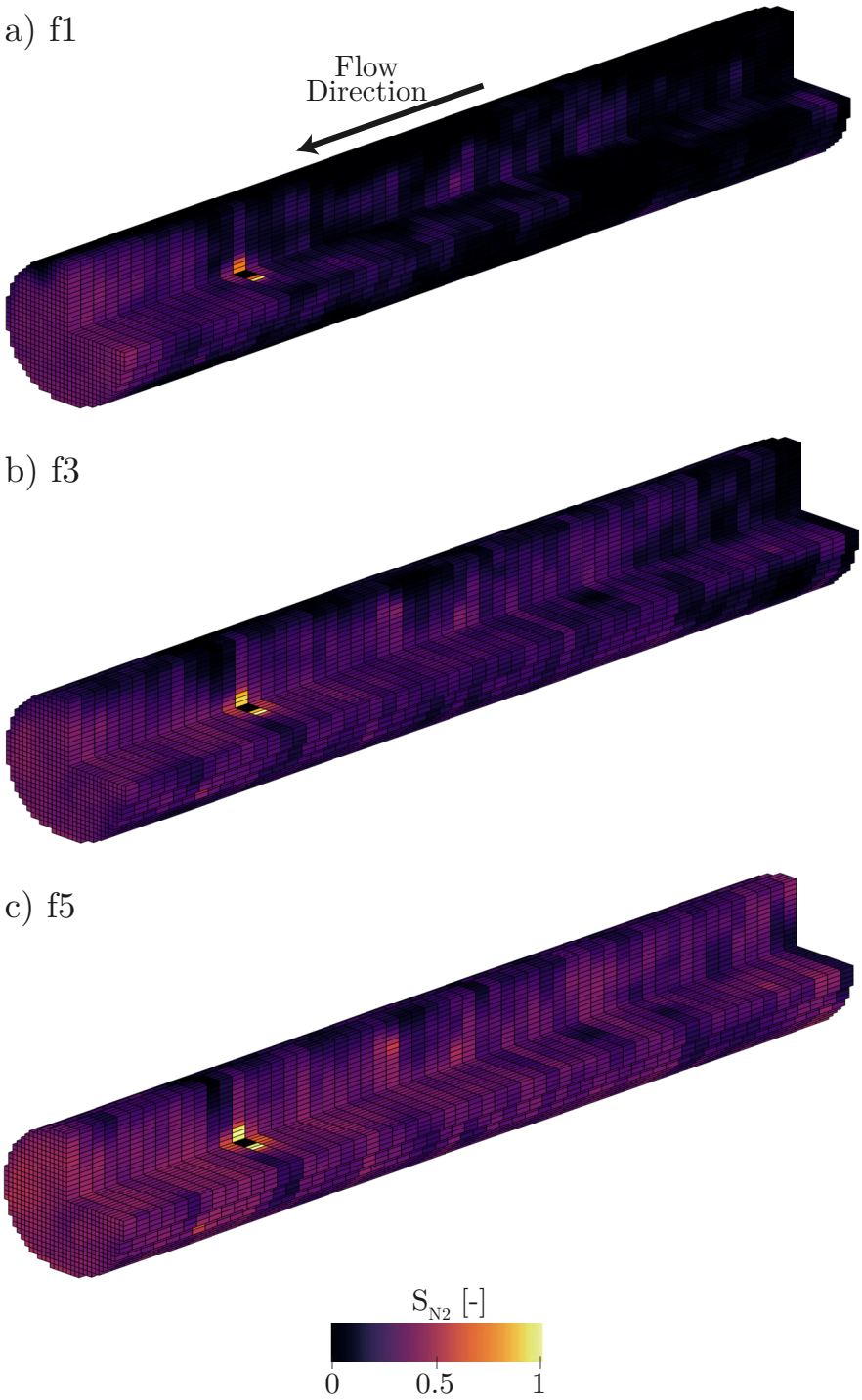


Figure 5.13: 3D Nitrogen saturation distribution at three fractional flows, f1, f3 and f5.

5.3.2.6 Relative Permeability

At each fractional flow, we measure the core-average pressure drop using pressure transducers connected to the coreholder. After steady-state is reached, indicated by a stable pressure drop, the pressure drop is recorded, which can later be used to determine the relative permeability at that fractional flow. The core-average pressure drop at steady-state at each fractional flow is listed in Table 5.5. The pressure drop recorded during the entire experiment is also presented in Appendix E.

Table 5.5: Core average pressure drop measured at steady-state at each fractional flow.

Fractional Flow	**Pressure Drop [kPa]**
f1	68.58
f2	265.96
f3	159.67
f4	96.34
f5	42.27
f6	32.34

5.3.2.7 Clay Mobilisation

After the first coreflood conducted at $Q = 0.1$ ml·min^{-1}, we repeat the single-phase coreflood to determine the absolute permeability in the core. This ensures the sample has not undergone any physical or chemical changes prior to conducting the high flow rate co-injection experiment.

We observe a significant variation in pressure drop at each injection rate, which progressively worsens at higher flow rates, see Figure 5.14. Overall, the absolute permeabilities are significantly smaller compared with the initial absolute permeability of 31 mD measured prior to the first co-injection cycle. The variation in permeability and the overall permeability reduction is indicative of clay swelling/mobilisation and fines migration (Al-Sarihi et al., 2018; Sazali et al., 2018; Russell et al., 2018; Yang et al., 2019a) and clay swelling (Zhou et al., 1996; Tariq et al., 2021).

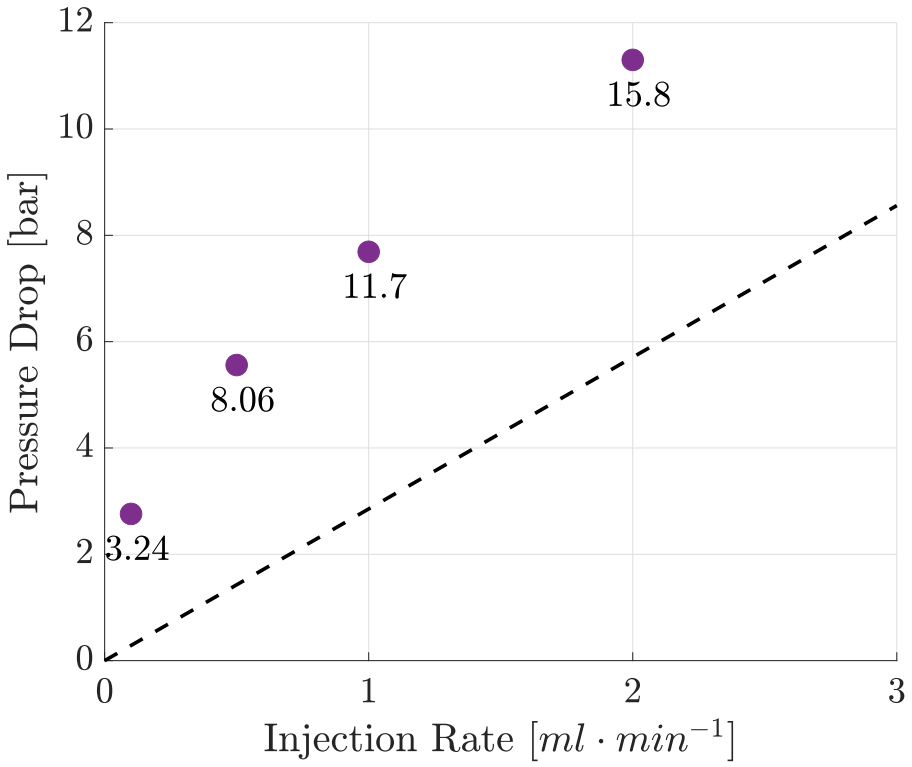


Figure 5.14: Single-phase flow experimental measurements to determine the absolute permeability of the sample after the low rate drainage experiment. The annotation at each data point is the absolute permeability calculated from the corresponding pressure drop and flow rate. The linear trend from Figure 5.9 is also plotted to demonstrate the changes in permeability.

Laboratory testing was conducted on a range of Bunter sandstone cores from well 42/25d-3 by White Rose (2016a). One test involved the continuous injection of supercritical CO_2 into brine-saturated cores (using synthetic brine matching the composition of the formation brine) to determine the impact of CO_2 exposure on the core permeability. The tests displayed an average permeability reduction of 19.2%. The authors postulate that this permeability reduction can be attributed to 1) salt precipitation, 2) clay mobilisation and 3) mobilised amorphous/microcrystalline iron carbonate (White Rose, 2016a). The fines migration was confirmed by Scanning Electron Microscopy (SEM) images. These findings are in agreement with observations from our steady-state relative permeability coreflood experiment and suggest that the Bunter sandstone will likely undergo geochemical reactions that will alter its flow properties. This has important implications for CCS operations as this will have to be considered during storage estimates and field development planning.

The Endurance formation fluid is hyper-saline and the flow rig is not designed for hyper-saline brines. Using a hyper-saline fluid would introduce significant complexities to the experiment, for instance rusting and corrosion of the stainless steel equipment. Rather than using a different, low-salinity synthetic brine, which could result in uncertainties regarding chemical effects, we opted to use a well-characterised, widely-used water, namely DI water, in our steady-state relative permeability coreflood experiment. This may have led to an enhancement of clay swelling/mobilisation and a subsequent permeability reduction (Russell et al., 2018). However, the coreflood experiments performed on composite Bunter sandstone reservoir samples by White Rose (2016a) also displayed a permeability reduction even though a synthetic brine matching the reservoir fluid composition was used as the wetting fluid. The authors attributed this phenomenon to clay swelling, as well. Thus, whilst DI water may have enhanced clay swelling, we would have likely observed a similar effect in a CO_2-brine steady-state relative permeability coreflood experiment. This highlights the added complexity of performing experiments on heterogeneous reservoir samples.

The reduction in permeability hinders any further experiments to be conducted on this rock sample. Its flow properties have been severely altered, thus comparisons in the flow behaviour observed in the low and high rate experiments could not be drawn. We acknowledge that this limits the analysis that can be conducted on the impact of capillary heterogeneity on the relative permeability at varying flow rates in this sample. However, the primary objective of this chapter is to sufficiently characterise the rock sample and obtain petrophysical measurements that can be used to build a field-scale model of the Endurance site. The data collected herein is sufficient to do this.

5.3.2.8 End Effect and History Match

To estimate the viscous-limit, intrinsic relative permeability of the core sample, we perform a 1D history match. The end effect, identified from the saturation measurements, will impact the core-average pressure drop and saturation distribution, which in turn will introduce artefacts into the relative permeability calculations. Therefore, we additionally remove the impact of the end effect during the history match procedure.

The history match is performed using CMG IMEX by building a simplified model of the core sample. We impose a 1D porosity variation along the length of the model using data from Figure 5.10. We vary the core-average permeability, measured during the single-phase coreflood experiment, and the capillary pressure curve, obtained from MICP on sample 3V1, to replicate clay swelling/mobilisation and/or fines migration. MICP was not performed on sample 5V1 as it is destructive. We also vary the flow properties (entry pressure, capillary pressure curve, absolute permeability) of the end slice to replicate the end effect. We match the slice-average saturation distribution and the core average pressure drop.

We obtain the best match by reducing the core-average absolute permeability from 31 mD to 3 mD, which is in agreement with the reduction of permeability measured after the 0.1 ml·min^{-1} experiment. We scale the $P_c - S_w$ characteristic curve in the entire core by a factor of 10.7, which also replicates a reduction in permeability caused by clay swelling/mobilisation and/or fines migration. To model the end effect, we set the entry pressure in the end slice to 215 kPa and the permeability to 100 D. The resultant match in the saturation profiles and pressure drops are displayed in Figure 5.15 and the history match parameters are summarised in Table 5.6.

We successfully match the pressure drop and saturation profiles from the experiment. Note we do not aim to match the experimental relative permeability. The rationale of this history match is to estimate the viscous-limit, intrinsic relative permeability of the core sample and remove experimental artefacts. Based on the successful match of the pressure drop and saturation profiles, we conclude that the resultant relative permeability (Figure 5.15c) is a suitable estimate

for the viscous-limit relative permeability. We acknowledge that the history match overpredicts the pressure drop at f1 (Figure 5.15a). We postulate that the majority of fines migration and clay swelling occurred after f1, which would explain the 200 kPa increase in the pressure drop from f1 to f2. This is also confirmed by the trend in the pressure drop recorded during the entire coreflood experiment (Appendix E). The remaining fractional flows display a good match.

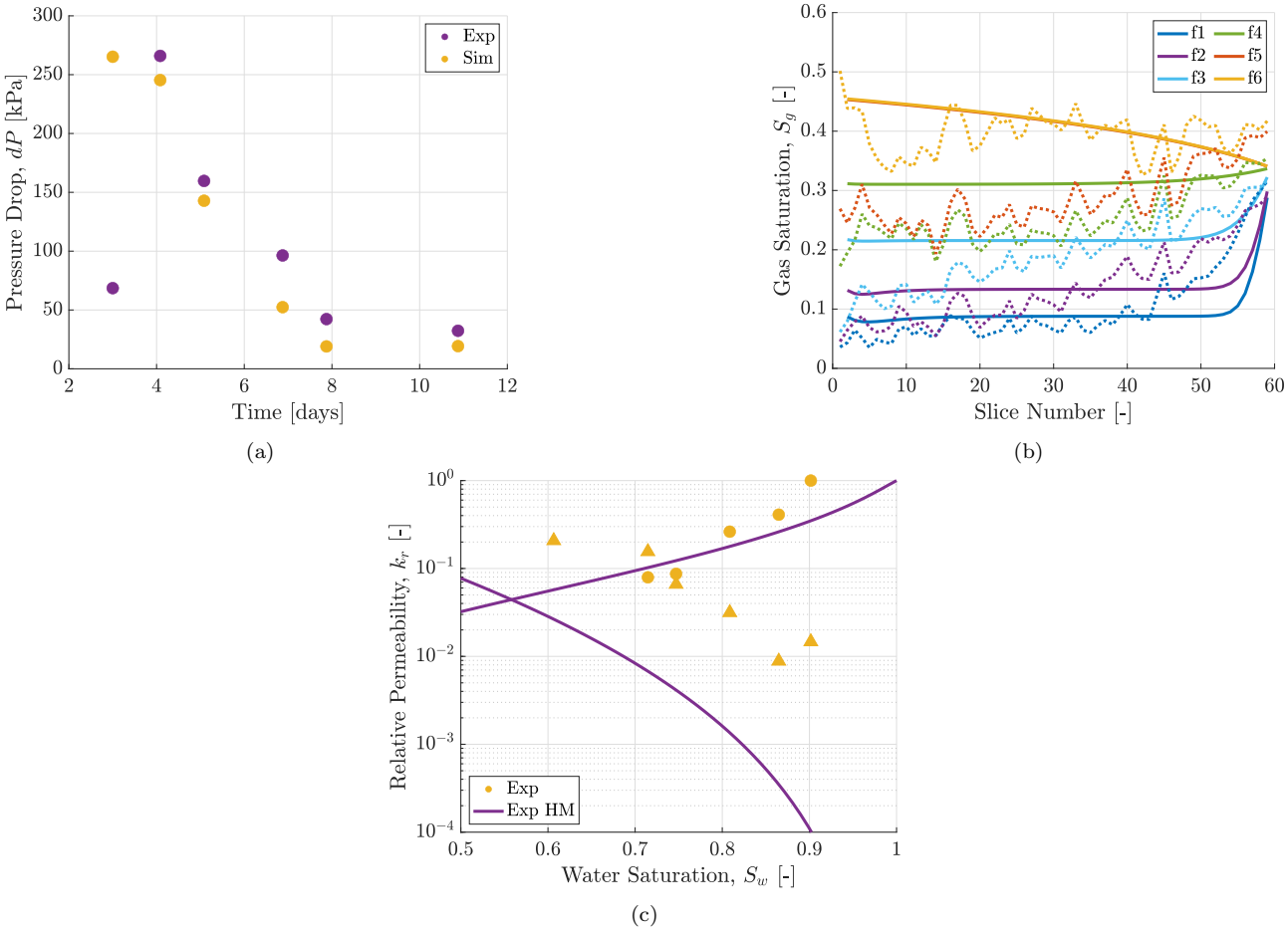


Figure 5.15: History match results to correct for the end effect observed in the experiment. a) Pressure drops at all fractional flows from the experiment and the history match, b) Saturation profiles at all fractional flows from the experiment and history match, c) Relative permeabilities from the steady-state relative permeability coreflood experiment (yellow points) compared with those obtained from the history match (purple lines). For the experimental data points, water and gas relative permeabilities are plotted as circles and triangles, respectively.

Table 5.6: Parameters obtained from the history match.

Parameter	**Value/Scaling**
Core $P_c - S_w$	3V1 curve scaled by 10.7
Core K_{abs}	3 mD
k_{rw} (L,E,T)	(1.5, 18, 6)
k_{rg} (L,E,T)	(3.67, 2.99, 1.09)
Endslice P_c	215 kPa
Endslice K_{abs}	100 D

5.3.2.9 Capillary Heterogeneity Workflow Development (An et al., 2023)

Following the findings from Chapter 4, which highlight the challenges associated with characterising more complex rock samples including carbonates, the characterisation workflow was further developed in An et al. (2023). We introduced a multi-parameter capillary pressure fitting and a grid block-based permeability fitting to the workflow. Using this advanced method, the match between the experimental observations and the simulations for all carbonates significantly improved. Figure 5.16 demonstrates the improvement in the voxel saturation correlation and the relative permeability prediction for the Estaillades limestone sample analysed in Chapter 4.

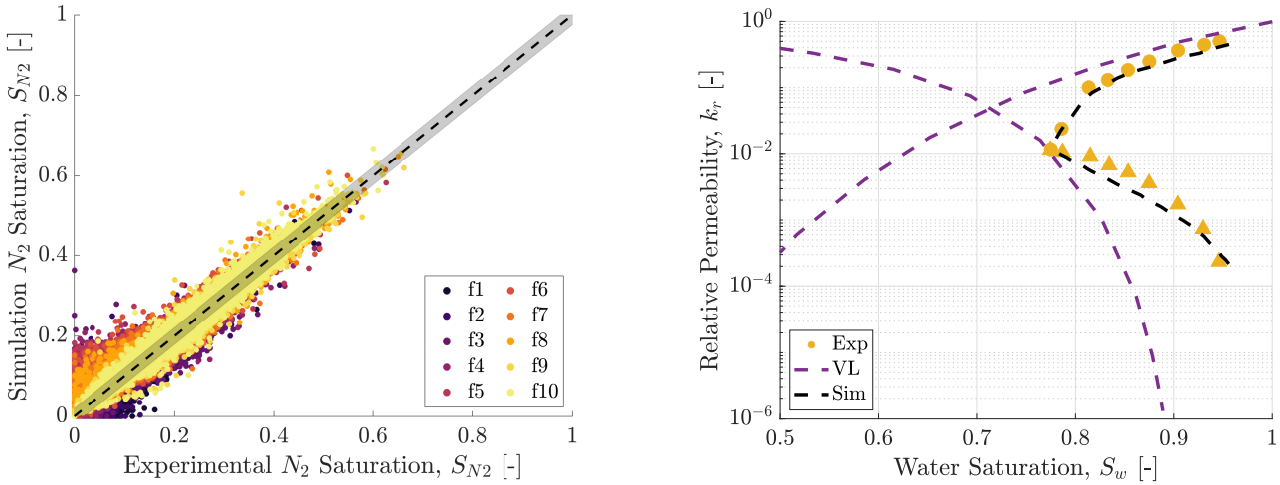


Figure 5.16: a) Voxel saturation correlation plot comparing the experiment and the simulation for the Estaillades limestone obtained from the updated workflow by An et al. (2023). The colours correspond to the individual fractional flows. b) Computed relative permeabilities obtained from numerical simulations using the iteratively calibrated digital model as input (dashed black lines) and compared to the experimental measurements (yellow symbols) and the viscous-limit relative permeability (dashed purple lines). For the symbols, water and gas relative permeabilities are plotted as circles and triangles, respectively. Both figures are from An et al. (2023).

Considering that the Endurance reservoir sample presented in this chapter likely exhibits complex heterogeneity, we opt to apply this updated workflow to characterise the capillary heterogeneity within our sample. We will briefly describe the workflow below. For a full discussion of the rationale, please see Chapter 4. For verification of the updated method, please see An et al. (2023).

Similar to the workflow from Chapter 4, the method is a numerical history match of a steady-state relative permeability coreflood experiment with the 3D saturation distribution as a matching target and the capillary pressure characteristics as a fitting parameter. An initial guess is made based on an inversion of the saturation maps, followed by an iterative process whereby the capillary pressure characteristics are updated based on the comparison between simulated 3D saturation maps and the observations.

For the initial guess, the capillary pressure in each slice is assumed to be constant, i.e. at equilibrium. The average saturation in that slice is assumed to map to the Brooks-Corey fit of the capillary pressure characteristic curve measured during routine core analysis (Equation 4.2). Voxel scale variation in the saturation within the slice is assumed to be caused by the capillary heterogeneity within the slice. From this a scaling factor κ is assigned to each voxel, adjusting the local capillary pressure characteristic curve, to minimise the mismatch between the slice-average and voxel-specific values:

$$P_{c,ijk}(S_{ijk}) = \kappa_{ijk} \cdot P_{c,avg}(S_{ijk}) \quad , \tag{5.1}$$

$$\Theta = \sum_{i}^{N_v} \sum_{j}^{N_f} \sqrt{(\kappa_{ijk} P_{c,avg}(S_{ijk}^{exp}) - P_{c,ijk}(S_{ijk}^{exp}))^2} \sqrt{(S(\kappa_{ijk} P_{c,avg}) - S_{ijk}^{exp})^2} \quad , \tag{5.2}$$

where $P_{c,ijk}$ is the individual voxel capillary pressure, $P_{c,avg}$ is the average capillary pressure curve, S_{ijk}^{exp} is the experimental voxel saturation, κ_{ijk} is the individual voxel scaling parameter, N_v is the total number of voxels, N_f is the total number of fractional flows and $S(\kappa_{ijk} P_{c,avg})$ represents the saturation of the average capillary pressure curve after it has been scaled (using the slice-average capillary pressure). Through this, a 3D map of the initial scaling factor is built. The scaling is then used to populate the capillary pressure characteristics of numerical simulations of corefloods using the CMG ™IMEX fluid simulator. The capillary heterogeneity is introduced alongside the porosity heterogeneity, the core-average characteristic capillary pressure behaviour and the viscous-limit relative permeability.

The iterative calibration of the capillary pressure characteristics follows from this. We now adopt a multi-parameter capillary pressure function, which originates in the work by Li (2004). The model is based on the Brooks-Corey relationship (Brooks and Corey, 1964) and introduces additional degrees of freedom to match the experimental observations:

$$P_c = P_{\max}\left(1-\left(1-\alpha^{-\lambda}\right)S^*\right)^{-\frac{1}{\lambda}} \quad , \tag{5.3}$$

where $\alpha = P_e/P_{\max}$ is the ratio of entry pressure, P_e, to the maximum capillary pressure, $P_{\max}$. λ is a parameter related to the pore throat size distribution, and the wetting phase saturation normalised to an irreducible saturation, S_{wirr}, is $S^* = (S_w - S_{wirr})/(1 - S_{wirr}) \in [0, 1]$. In the first fitting loop, P_e, $P_{\max}$ and λ are used in a sequential fitting, which mitigates non-uniqueness arising from the simultaneous coupling of multiple parameters. A range for each parameter is also implemented to avoid non-uniqueness. Thereafter, a second fitting loop is implemented by An et al. (2023), which additionally varies the absolute permeability in each grid block using a porosity-capillary pressure correlation originating in the work by Li et al. (2021):

$$k = a_1\phi^{a_2}\left(1-S_{wi}\right)^{a_3}\frac{1}{P_{max}^{a_4}}\left(\frac{\lambda}{\lambda+2}\frac{1-\alpha^{-(\lambda+2)}}{1-\alpha^{-\lambda}}\right)^{a_5}. \tag{5.4}$$

We adopt the coefficients $a_{2\ldots5}$ from Li et al. (2021). a_1 for all grid blocks is adjusted such that the core-average absolute permeability matches the experimentally measured value. The digital model is iteratively updated following the fitting loops described above until the error between the experimental and simulation saturation is satisfactory. The parameters used in the modelling workflow are summarised in Table 5.7.

We conduct the iterative calibration scheme for 20 iterations and present the resultant correlation coefficient, R^2, for the voxel-scale experimental and simulation saturation in Figure 5.17. In the first 10 iterations R^2 increases up to a maximum of 0.92, which indicates that the error in the simulated voxel saturation progressively reduces. After iteration 10, R^2 marginally decreases again. Thus we will use the results from iteration 10 for subsequent analyses.

Table 5.7: Parameters used in the core characterisation workflow.

Parameters	**Endurance**
Digital core dimensions [x,y,z]	29×29×59
Upscaled voxel Δx, Δy [m]	0.0032
Upscaled voxel Δz [m]	0.001
Digital core length, L [m]	0.059
Digital core radius, r [m]	0.009
Entry pressure, P_e [kPa]	270
Pore distribution, λ [-]	1.75
Porosity, ϕ [-]	0.21
Permeability, K_{abs} [D]	0.003
k_{rw} (L,E,T)	(1.5, 18, 6)
k_{rg} (L,E,T)	(3.67, 2.99, 1.09)
$k_{rg}(S_{wirr}$/ $k_{rw}(S_{gc}$ [-]	1/1
S_{wirr}, S_{gc} [-]	0.001/0.0

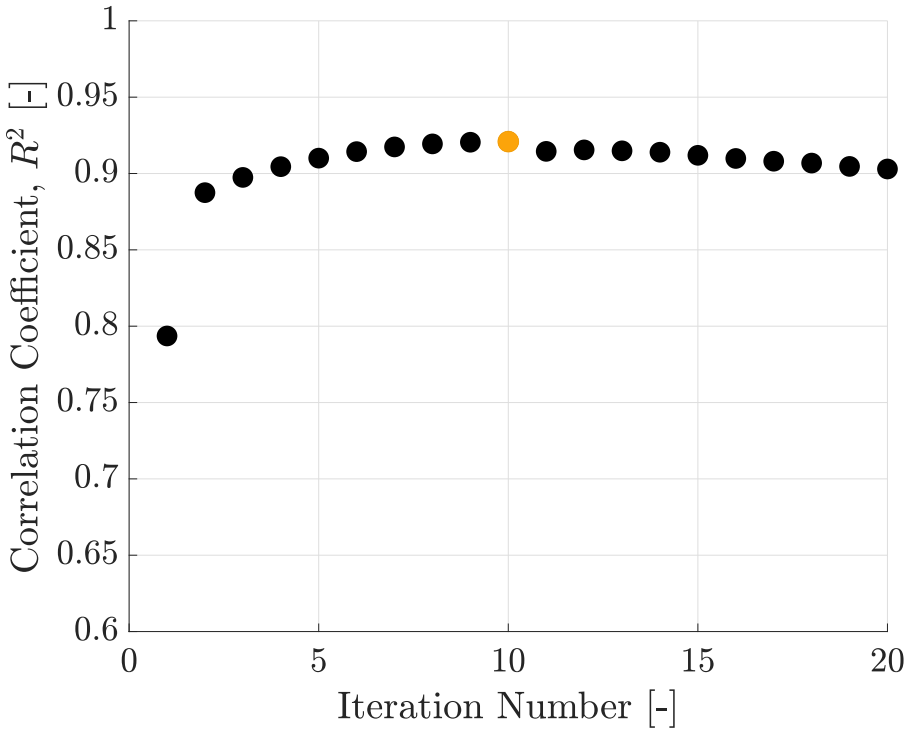
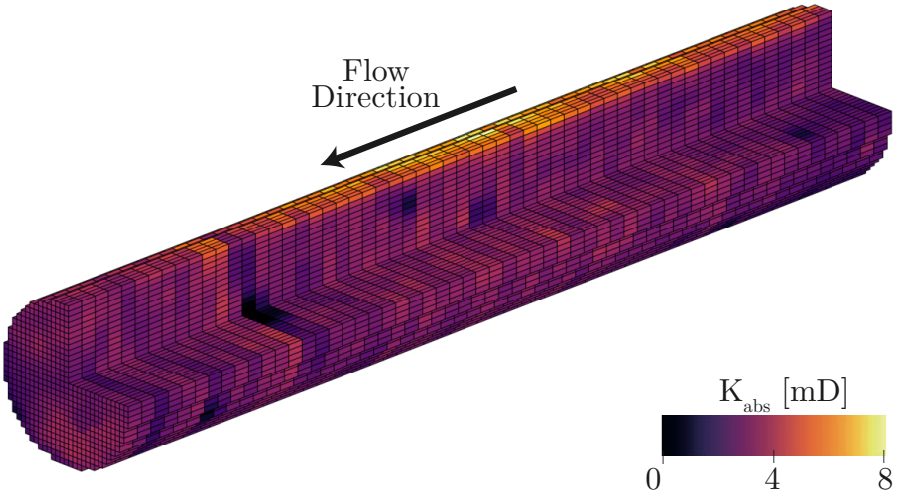


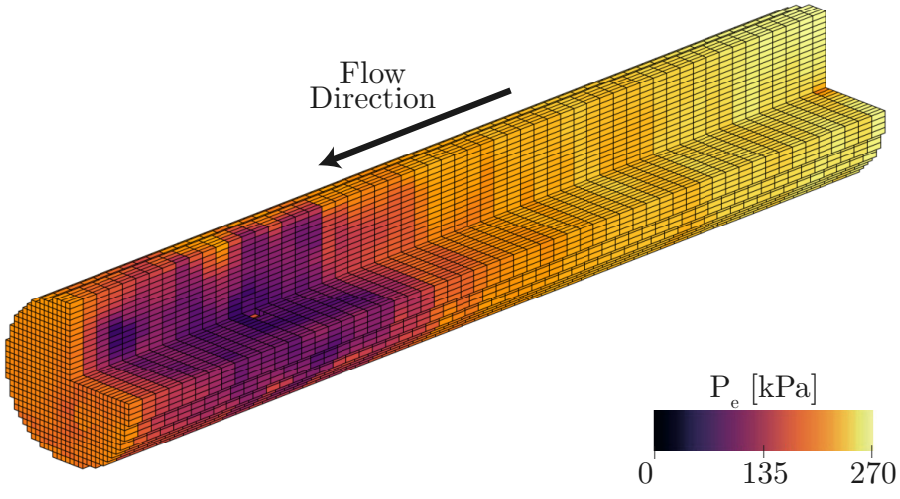
Figure 5.17: Correlation length coefficient, R^2 for each iteration in the calibration scheme. Iteration 10 corresponds to the largest R^2 (R^2=0.921) and is plotted in yellow.

The digital core model resulting from iteration 10 is displayed in Figure 5.18. As shown, the absolute permeability distribution matches the 3D porosity variation, with subtle layering orientated perpendicular to the axis of flow. We also observe a high permeability layer towards the top of the sample, which is orientated parallel to the axis of flow.

The first two thirds of the entry pressure distribution are in agreement with these observations, and the core is characterised by subtle layering with variable entry pressures. However, towards the outlet of the sample a region of approximately 20 mm in length has been assigned very low entry pressures. This does not seem to correspond to the expected geological features observed in the porosity distribution. Therefore, we postulate that the results are partly affected by the end effect and the calibration scheme is attempting to reproduce the rise in gas saturation towards the outlet. This is achieved by decreasing the entry pressure in the outlet region. Therefore, we conclude that this region of the digital model likely does not represent the geological heterogeneity within the sample but rather an experimental artefact.



(a)



(b)

Figure 5.18: a) 3D absolute permeability distribution from iteration 10, b) 3D entry pressure distribution from iteration 10.

The corresponding 1D saturation profiles are presented in Figure 5.19a and display a good match. This demonstrates that the digital core model successfully replicates the experimental saturation trend in 1D. The simulation also reproduces the steep rise in gas saturation towards the outlet at all fractional flows. This corroborates that the region in the digital model with anomalously low entry pressure is an end-effect artefact.

The corresponding 3D voxel saturation correlation is shown in Figure 5.19b. Overall, the digital model reproduces the voxel-scale saturations well, particularly at higher gas saturations. We also observe an improvement in the match between the simulation and experiment saturations with fractional flow. The voxel saturations for f6 plot close to the 1:1 trendline. This is in agreement with observations from the previous chapter and reflects the decrease of uncertainty in the gas saturation at higher gas fractional flows.

We simulate the steady-state relative permeability coreflood experiment using the digital model to assess its predictive ability of the relative permeability. The results are shown in Figure 5.19c. Overall, we observe a satisfactory match between the simulation and the experiment. The simulation successfully replicates the raised gas relative permeability from the input, viscous-limit curve. This implies that the capillary heterogeneity imposed in the model enhances gas migration. In comparison to this, the water relative permeability from the simulation plots closer to the viscous-limit curve, which suggests that the water is largely unaffected by the heterogeneity in the model. We observe the best agreement in relative permeability for f4 and f5, which corresponds to the closely matched saturation profiles presented in Figure 5.19a.

Using the digital model, we estimate the capillary number of the steady-state relative permeability coreflood experiment. We follow the same procedure as Chapter 4 Section 4.2.3. The reader is referred to this section for a detailed discussion. From inspecting the digital model and disregarding the region likely affected by end-effect artefacts, we find $H = 5$ mm, $L = 60$ mm, $\Delta P = 265$ kPa (f2) and $\Delta P_c = 8$ kPa. With these parameters, we estimate $N_c = 398$, which indicates that viscous forces were likely the dominant fluid distribution mechanism during the steady-state relative permeability coreflood experiment. This finding further justifies the use of the history-matched relative permeability as the viscous-limit input curve.

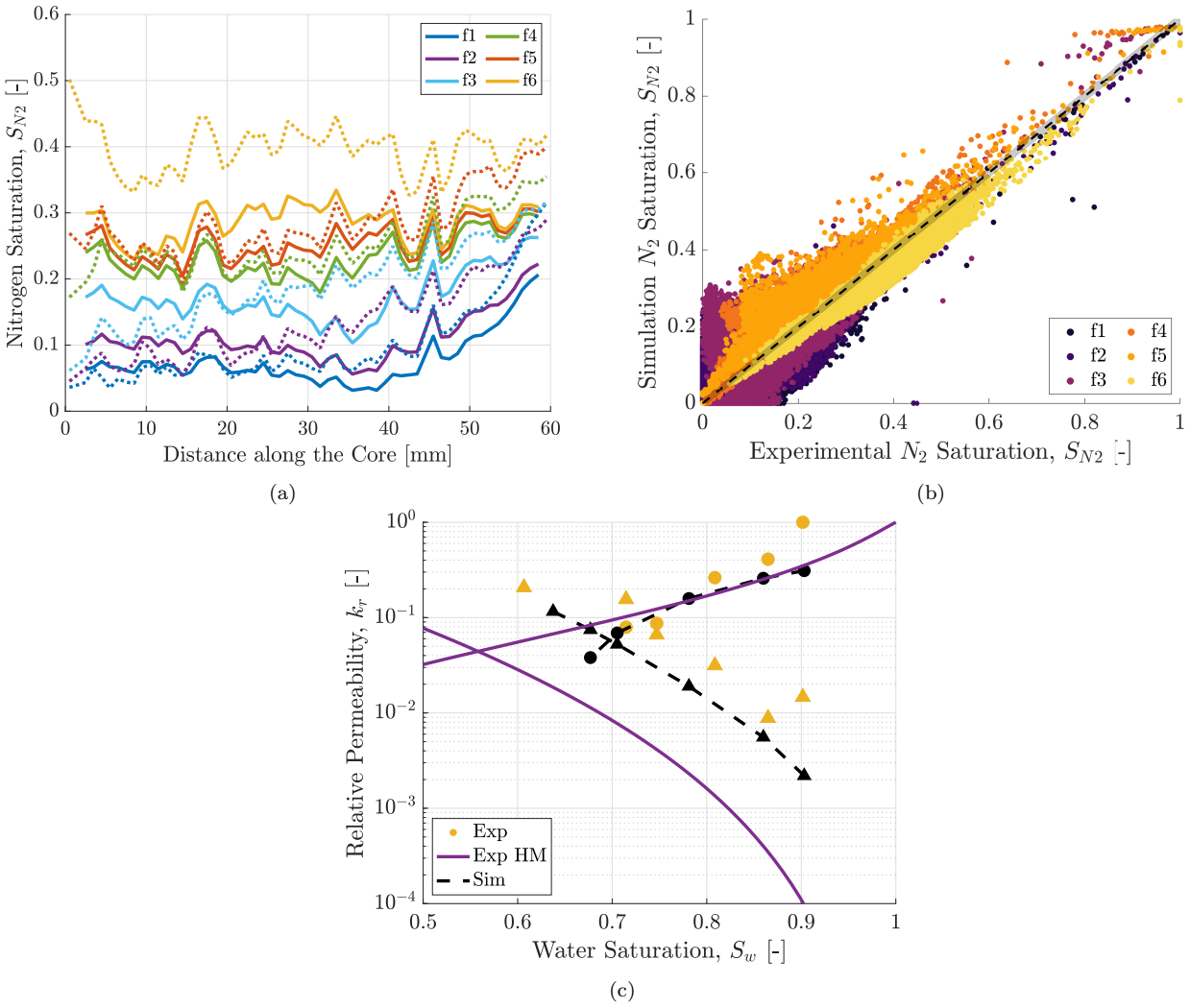


Figure 5.19: a) Saturation profiles comparing the experiment (dotted lines) with the simulation at for iteration 10. b) Voxel saturation correlation plot comparing the experiment and the simulation for iteration 10. The colours correspond to the individual fractional flows. c) Computed relative permeabilities obtained from numerical simulations using the iteratively calibrated digital model from iteration 10 as input (plotted as dashed black lines with black symbols) and compared to the experimental measurements (plotted as yellow symbols) and the history matched relative permeability (purple lines). For the symbols, water and gas relative permeabilities are plotted as circles and triangles, respectively.

Although the capillary number is very high, we still observe a shift in the gas relative permeability once capillary heterogeneity is incorporated in the model (Figure 5.19c). This suggests that even at high flow rates, the large, low-entry pressure region near the outlet affects the flow behaviour. This has important implications for experimental procedures. It may be challenging to achieve near-viscous flow conditions in rock samples with large heterogeneities, such as vuggy carbonates. The resultant relative permeabilities will likely still be affected by heterogeneities and this may introduce erroneous assumptions in modelling workflows.

5.3.2.10 Implications

Our findings demonstrate the challenges associated with performing corefloods on complex reservoir samples, where the sample's flow properties are largely uncertain prior to the experiment. Compared with relatively homogeneous sandstones such as Bentheimer sandstones, the Bunter sandstone sample from the Endurance reservoir is characterised by relatively low connectivity and a significant amount of clay, which was only identified during and after the steady-state relative permeability coreflood experiment. It was difficult to estimate likely flow properties using the MICP data as the data displayed noticeable differences between the samples. Clay swelling/mobilisation and fines migration likely had a more pronounced impact on the absolute permeability of the sample as the plug already had a low permeability at the start of the experiment. Although these challenges were encountered, they do not pose a major concern for the field-scale model developed in subsequent chapters as we successfully obtained sufficient data required for this workflow.

To alleviate the uncertainties introduced by the experimental design, it would be necessary to perform another set of steady-state relative permeability coreflood experiments on a fresh sample, which we recommend as future work. We would suggest using formation brine rather than DI water as the wetting fluid as this may reduce the severity of clay swelling. However, as highlighted in preceding sections, White Rose (2016a) also reported clay effects in coreflood experiments using synthetic brine matching the composition of the formation brine. Thus, it is uncertain whether switching from DI water to synthetic brine would truly reduce the impact of clays. If successful, we also recommend performing a coreflood at a low and high rate to obtain experimental observations near the capillary and viscous limits. This would provide experimental constraints that can be incorporated into the capillary characterisation workflow to reduce non-uniqueness. In general, for any experimental analysis focused on reservoir samples, we highly recommend performing extensive preliminary studies to understand the petrographical composition and flow properties.

Although a history match was performed to remove experimental artefacts, we find that the subsequent core characterisation workflow is still impacted by these uncertainties. Therefore, it will also be important to re-assess the laboratory design to identify any potential equipment responsible for the end-effect. Other factors may also have led to a build-up of gas towards the outlet such as wettability variations in the sample. Performing another set of experiments could help identify and understand the root cause.

Albeit these uncertainties and challenges, we find that the advanced core characterisation workflow developed by An et al. (2023) successfully replicates the voxel-scale saturation distribution and predicts the relative permeability. Even though the model likely compensates for the end-effect and does not represent the true geological heterogeneity within the sample, it is still able to reproduce the complex experimental observations. This demonstrates that the optimisation algorithm does not break down when applied to complex datasets. However, it also highlights the importance of considering non-uniqueness of the model. By implementing a breadth of experimental observations, we would be able to guide the calibration scheme based on the physical mechanisms observed in the experiment and thereby better constrain the digital model. Therefore, we highly recommend conducting further experimental analyses on reservoir samples from the Endurance site.

A Bunter sandstone core was also characterised in Chapter 4. Whilst both samples exhibit similar layering orientated primarily perpendicular to the axis of flow, we find that the rate dependency of relative permeability differs between the two. In the sample from Chapter 4, both, the water and gas, relative permeabilities decrease with a decrease in flow rate. In comparison to this, the sample analysed in this Chapter exhibits an increase in the gas relative permeability with a decreasing flow rate and a negligible change in the water relative permeability. A plausible explanation for this contrasting behaviour is that the samples originate from different wells, one from an onshore geothermal borehole (Chapter 4) and one from an offshore appraisal well (Chapter 5). Whilst both samples stem from the same rock formation, the likely contrast in the reservoir and borehole environments could impact the flow properties. To investigate this further, we recommend performing additional coreflood experiments on multiple Bunter sandstone reservoir samples with similar heterogeneity structures.

5.3.3 Digital Rock Analysis of Micro X-Ray CT Imagery from a Bunter Sandstone

Prior to the steady-state relative permeability coreflood experiment presented in the previous section, we scan the dry rock sample with a micro-CT scanner to resolve the pore structure and heterogeneity on a μm scale. The principles of a micro-CT scanner and the image processing workflow we apply to the scans are detailed in Chapter 3.

We scan the entire rock sample at a resolution of 6 μm. We additionally scan a subvolume of size 2 mm $\times$ 2 mm $\times$ 2 mm at 2 μm resolution. We only scan a subvolume of the sample at a higher resolution due to time and computational constraints. The subvolume took over 12 hours to scan and has a size of 2GB. Scanning the entire sample at this resolution would thus take approximately 130 days and result in images with a total size of approximately 522 GB, which is unfeasible to process on computers available to us.

From visual analysis, we observe bright spots scattered across the 2 micron scan as shown in Figure 5.20. These represent regions of dense materials which enhance light attenuation such as metallic minerals (Andrews, 2022). In the work of Peksa et al. (2015), bright spots in the micro-CT images of a Bentheimer sandstone sample were attributed to feldspars. Based on the mineral composition of Bunter sandstone samples presented in White Rose (2016a), these bright spots could thus indicate the presence of feldspar or plagioclase. We also observe an abundance of clay in the 2 micron scan (Figure 5.20). This confirms the hypothesis discussed in the preceding section, where the decrease in permeability during the steady-state relative permeability coreflood experiment was attributed to clay swelling and migration.

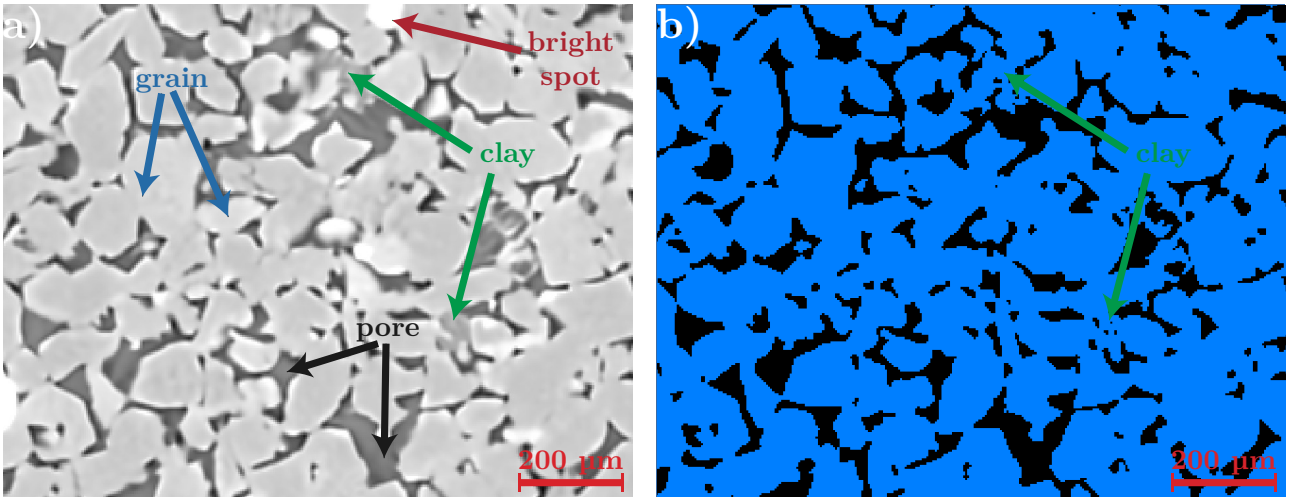


Figure 5.20: a) Filtered slice from the 2 micron scan. Green arrows point to clay-rich regions, blue arrows point to grains and black arrows point to pores. b) corresponding segmented slice from the 2 micron scan with blue representing the rock matrix and black representing the pores. Green arrows point to the clay-rich regions identified in subfigure a).

5.3.3.1 High Resolution Pore Network Extraction

The scans can be used to analyse the pore size distribution, which provides an insight into the heterogeneity of the sample. To do this, we apply the pore network extraction algorithm, *pnextract*, developed by Raeini et al. (2017). The authors successfully address issues of oversimplification of the pore space, which is common in more conventional network extraction tools. They achieve this by discretising the pore space in a CT image into pores, half-throats and corners. It has been validated using synthetic and experimental data sets (Raeini et al., 2017) and has since been widely applied to analyse the pore structure in rock samples (AlRatrout et al., 2018; Scanziani et al., 2018; Gao et al., 2019).

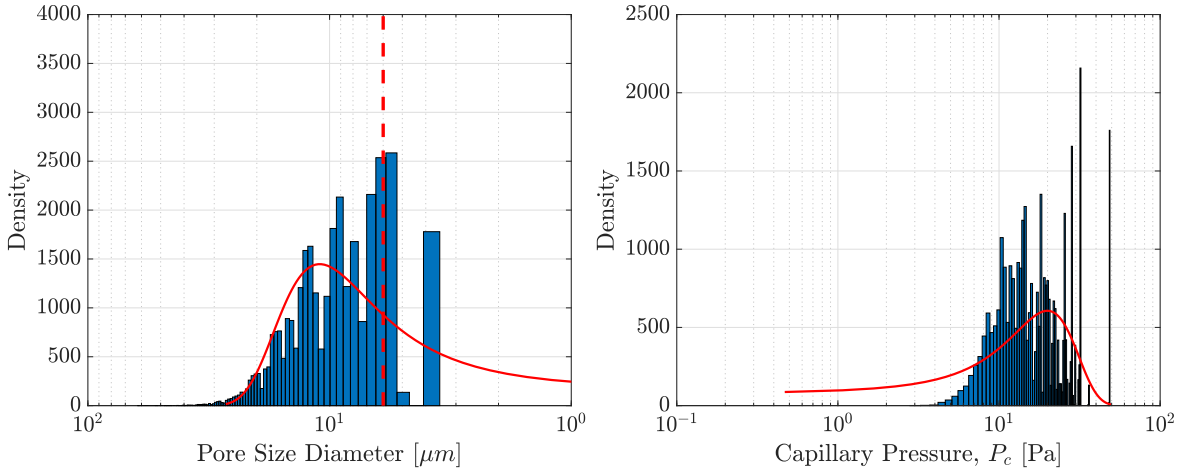
We apply *pnextract* to the segmented 2 micron scan and plot the resultant pore size distribution in Figure 5.21a. We find that the sample is characterised by a heterogeneous pore size distribution with a range in pore diameter from 3.6 to 62 μm. The peak of the histogram is located at 5.5 μm, which indicates that a large portion of pores have diameters of 5.5 μm. However this is closely followed by peaks at 6.1, 6.7 and 9.1 μm, which shows the variability in pore structure within the sample. We also observe a large number of pores with a 3.8 μm diameter, which has important implications for the analysis of the whole-core 6 μm scan, which is discussed in subsequent sections.

To estimate the distribution of capillary pressure as a result of the pore throat diameter, we apply the Young-Laplace equation to the data presented in Figure 5.21a:

$$P_c = \frac{2\sigma cos(\theta)}{r} \quad , \tag{5.5}$$

where P_c is the capillary pressure, σ is the interfacial tension (estimated as 62 mN·m^{-1} for the N_2-DI Water system), θ is the contact angle estimated at 45° and r is the pore radius. The results are shown in Figure 5.21b.

Similarly to the pore size distribution, we observe a highly variable capillary pressure. The peak is located at 32 kPa, which is relatively high for a sandstone sample. The secondary and tertiary peaks are also characterised by high capillary pressures of 48 kPa and 28 kPa, respectively. This indicates that the sample is relatively tight, with a large number of pores with small radii that correspond to high capillary pressures. These findings are in agreement with observations from the steady-state relative permeability coreflood experiment, where we measured an absolute permeability of 31 mD prior to the two-phase coreflood. The pore-size distribution is compared to the experimental MICP data in the subsequent section.



(a) (b)

Figure 5.21: a) Pore size distribution extracted from the 2 micron scan using *pnextract*. The red dashed line represents a diameter of 6 μm, which corresponds to the image resolution of the whole-core scan. The normal distribution fit to the histogram is plotted as a red solid line with $\mu = 11$ kPa and $\sigma = 5.3$. b) Estimated pore-scale capillary pressure distribution using the Young-Laplace equation. The normal distribution fit to the histogram is plotted as a red solid line with $\mu = 20$ kPa and $\sigma = 9.9$.

5.3.3.2 High Resolution Pore Network Flow Simulation

Using the pore network model generated from the 2 micron scan, we simulate drainage in a Nitrogen-DI Water system using the *pnflow* algorithm from Raeini et al. (2018), verified by Bultreys et al. (2018) and Raeini et al. (2019). The authors developed a generalised network model, which simulates single phase flow through the "corners" of the pore space obtained from *pnextract*.

The algorithm estimates the total porosity of the subvolume to be 0.2069, which is in agreement with the average porosity determined in the steady-state relative permeability coreflood experiment of 0.2088. However, the absolute permeability from *pnflow* is significantly larger than that obtained from the single-phase flow experiment, namely 137 mD to 31 mD.

The 2 micron scan is a 2 mm sized cube. The average porosity of the micro-CT scan aligns well with that obtained during the steady-state relative permeability coreflood experiment, which suggests that the cube represents an elementary volume (EV) for porosity. However, the deviation in permeability obtained from the two independent analyses suggests that the EV assumption may not hold for permeability. It is plausible that the region that was imaged by the micro CT scanner is particularly permeable. To investigate the assumption of EV in more detail, it is necessary to image other regions of the rock sample at this resolution and compare the resultant network models.

Resolution limitations also likely had a measurable impact on the deviation in the permeability. Whilst the porosity from the micro-CT scan matches the medical-CT measurement, the 2 micron resolution likely does not capture the smallest throats, which would alter the permeability extracted from the images. Jackson et al. (2020) found that micro-CT scans with a resolution of 3.5 μm were unable to resolve all connectivity in Bentheimer sandstones samples with permeabilities of 700-1700 mD. Based on this, we would expect to require a much higher resolution to resolve the connectivity in the tight Bunter sandstone sample analysed herein.

Another possibility is that clay swelling/mobilisation and fines migration occurred at the start of the single phase flow experiment from which we determine the absolute permeability on a core scale. DI water is injected in the single-phase experiment, which can hydrate the exchangeable cations in the clay, subsequently causing swelling and break-off (Civan, 2007). This phenomenon would lower the permeability and could be responsible for a decrease from 137 mD to 31 mD. Considering that the porosity from the two datasets aligns well, it is likely that fines migration primarily affected narrow throats. Whilst these throats do not significantly contribute to the average porosity measurement, they may act as the main control on flow. Once blocked by clay particles, the permeability of the sample could reduce significantly. Therefore, the deviation in permeability between the two datasets can be attributed to clay effects.

A third possibility is that the deviation between the two absolute permeability measurements is caused by uncertainties in the digital rock workflow. Although the pore network extraction and modelling algorithms have been extensively verified and used, digital rock techniques are error-prone, especially when applied to complex rock systems (Saxena et al., 2017). Furthermore, uncertainties introduced by the user's processing choices can severely impact the multiphase flow properties extracted from a micro-CT X-ray imagery, particularly the permeability, as demonstrated by Garfi et al. (2020).

We also obtain a drainage $P_c - S_w$ curve from the pore network model simulation. We apply an interfacial tension correction to the data to convert from a N_2-DI Water to CO_2-Brine system, and plot the result alongside the converted MICP measurements, see Figure 5.22. The entry pressure estimated from the simulation is 10.1 kPa, which falls between the MICP samples 3V1 and 2H4. This aligns well with the depths of the samples, as these three samples originate from a similar depth interval. The 5V1 curve exhibits a gentler slope compared to the MICP samples, with the capillary pressure rising gradually until $S_w = 0.15$. This behaviour is not observed in the MICP data and is indicative of resolution limitations in the micro-CT scan. Pores with a diameter smaller than 2 μm, corresponding to a capillary pressure of >88 kPa, remain unresolved. Thus the pore network model would not capture fluid invasion into these regions of the pore space, which reduces the capillary pressure at low water saturations.

The relative permeability obtained from the pore network flow simulation is compared to the experimental history-match curves in Figure 5.23. As shown, the water and gas relative permeabilities from the pore network are larger relative to the results from the history match. This is consistent with previous observations. If clay swelling and mobilisation occurred during the steady-state relative permeability coreflood experiment, not only would we expect a decrease in the absolute permeability of the sample but we would also expect to observe a decrease in the phase relative permeabilities. The clogging up of pore throats by clay minerals will impose a resistance to flow and this will affect the multiphase flow properties. However, similar to the preceding discussion, the 2 micron scan may not represent an EV, which would also cause a deviation in the relative permeability from the measurement obtained at the core scale.

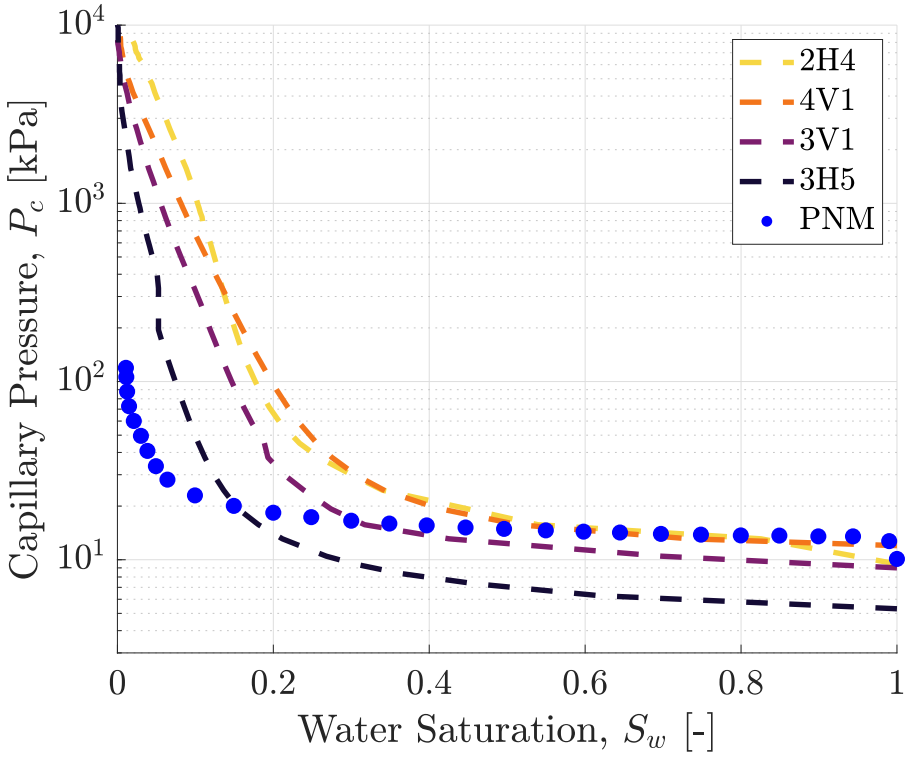


Figure 5.22: Results from the MICP experiments performed on four Bunter sandstone samples from the Endurance site plotted as dashed lines. The lines are colour coded based on their depths. Blue points represent the result obtained from the pore network simulation. A correction for interfacial tension was applied to the MICP measurements to convert from mercury-air to carbon dioxide-brine. We also apply an interfacial tension correction to the pore network data to convert from nitrogen-DI water to carbon dioxide-brine.

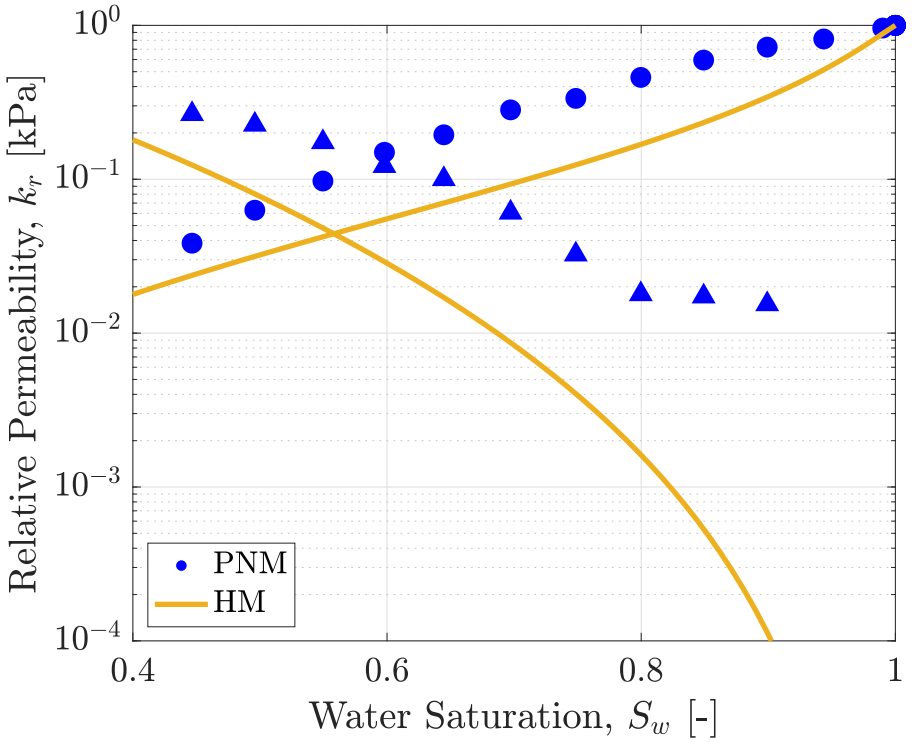


Figure 5.23: Drainage relative permeability obtained from the pore network simulation (blue points) compared with the history-matched relative permeability from the steady-state relative permeability coreflood experiment (yellow lines). Gas and water relative permeabilities are plotted as triangles and circles, respectively.

5.3.3.3 Resolution Limitations

We design a pore network model simulation scheme, in which we utilise the full-core micro-CT scan, with a resolution of 6 μm, to simulate the steady-state relative permeability coreflood experiment we performed in the laboratory. The motivation behind this work is to assess the predictive capabilities of pore network models for darcy-scale multiphase flow on a complex reservoir sample. Zahasky et al. (2020) previously successfully demonstrated the ability for pore network models to predict the relative permeability by validating the results against experimental observations. However, the authors focused on two Bentheimer sandstone samples due to their "stability and large pore size" (Zahasky et al., 2020). As such, it would be interesting to explore the applicability of pore network models to more complex rocks.

To do this, we first process the 6 micron scan following the workflow detailed in Chapter 3. Following this and prior to the darcy scale simulation work, it is important to verify the images against the high resolution scan. This ensures that we resolve the pores controlling the connectivity of the sample at 6 micron resolution. We extract the subvolume corresponding

to the 2 micron domain from the 6 micron scan. We then apply the *pnextract* and *pnflow* algorithms to the coarser subvolume and compare the results with findings from the preceding sections. A good match between the 2 and 6 micron datasets indicates that the coarser scan sufficiently resolves the pores controlling the fluid distribution.

The capillary pressure and relative permeability obtained from the pore network simulation are displayed in Figure 5.24 alongside the results from the 2 micron scan. As shown, the multiphase flow properties are noticeably different. The entry pressures from both scans align well at 10.1 kPa, which indicates that the segmentation of the largest pores in both scans is successful (Figure 5.24a). However, the capillary pressure curve from the 6 micron dataset rises steeply near $S_w = 1$, whereas the 2 micron scan exhibits a gently rising capillary pressure. This implies that it is more difficult to invade the subvolume from the coarser scan and we only drain up to $S_w = 0.55$ at the end of the cycle. We also observe an increase in the gas relative permeability and a decrease in the water relative permeability in the 6 micron results (Figure 5.24b).

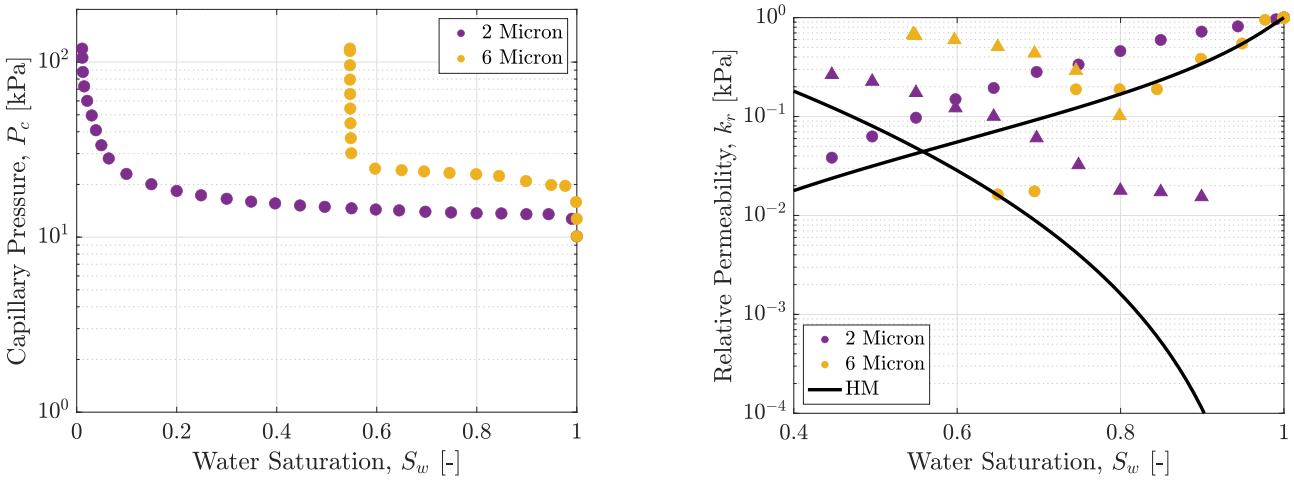


Figure 5.24: a) $P_c - S_w$ curves from *pnflow* for the 2 micron scan (purple points) and 6 micron scan (yellow points). Note: the yellow and purple points overlay each other at S_w=1. b) Relative permeability curves from *pnflow* for the 2 micron scan (yellow symbols) and 6 micron scan (purple symbols) plotted alongside the history-matched experimental relative permeability (black lines). Gas and water relative permeabilities are plotted as triangles and circles, respectively.

This can be explained with respect to the pore size distribution extracted from the scans shown in Figure 5.25. The smallest pores that are resolved in the coarser scan have diameters of 11 μm (Figure 5.25b). However, Figure 5.25a indicates that there is a significant amount of pores characterised by diameters smaller than 11 μm present in the sample and we observe a large

peak between 3 and 4 μm. These are not resolved in the coarser scan, which results in a large deviation in the pore structures obtained by the two scans. Figure 5.26 further demonstrates this resolution limitation. Compared with the 2 micron images (Figure 5.20), the images from the 6 micron scan display a significantly worsened resolution and appear blurry. This increases the complexity associated with segmentation as pore-grain boundaries are smeared.

As a result, *pnflow* estimates the permeability and porosity of the sample to be only 2.1 mD and 0.11, respectively. Thus the segmented 6 micron scan underestimates the porosity and connectivity of the core. Ultimately this results in an increase in the capillary pressure and a decrease in the water relative permeability (assuming the sample is water-wet). This demonstrates that smaller pores control the fluid flow in our sample and require a higher resolution scan to resolve them. Jackson et al. (2022b) explored the impact of scan resolution on multi-scale modelling with a Bentheimer sandstone sample. They found that the relative permeability obtained from a pore network was largely insensitive to resolution and was sufficiently characterised with a 6 micron scan. This is because the connectivity of this Bentheimer sample was controlled by fairly large non-wetting phase pathways, which were well-resolved in the coarser scan. In comparison to this, we find that fluid flow in the Bunter sandstone sample is controlled by smaller pore sizes.

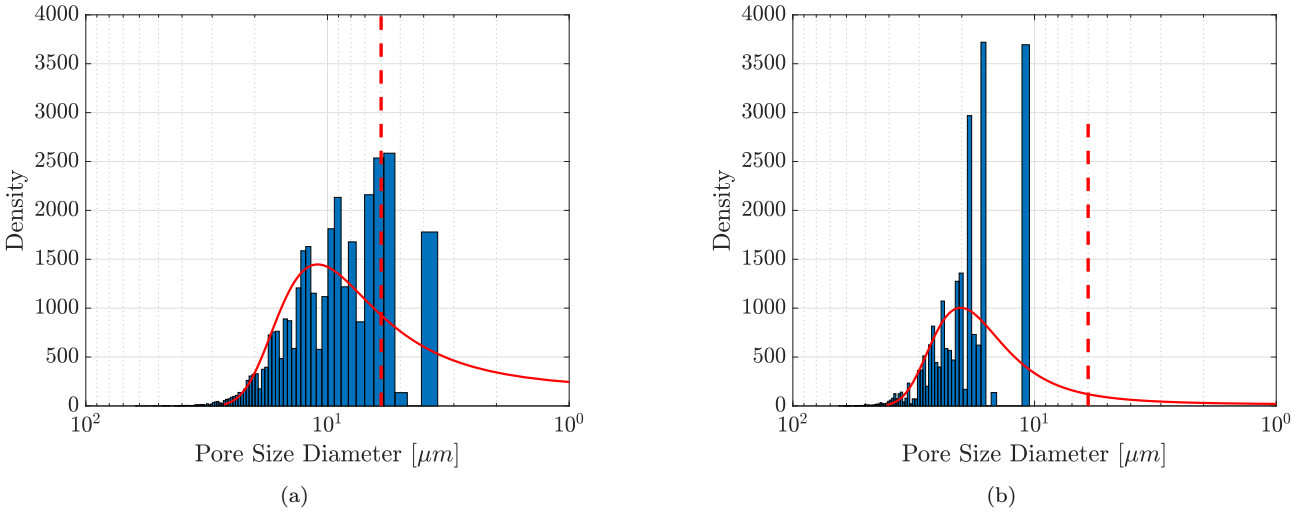


Figure 5.25: a) Pore size distribution extracted from the 2 micron scan using *pnextract*. The red dashed line represents a diameter of 6 μm, which corresponds to the image resolution of the whole-core scan. The normal distribution fit to the histogram is plotted as a red solid line with $\mu = 11$ kPa and $\sigma = 5.3$. b) Pore size distribution extracted from the 6 micron scan using *pnextract*. The red dashed line represents a diameter of 6 μm, which corresponds to the image resolution of the whole-core scan. The normal distribution fit to the histogram is plotted as a red solid line with $\mu = 20$ kPa and $\sigma = 6.9$.

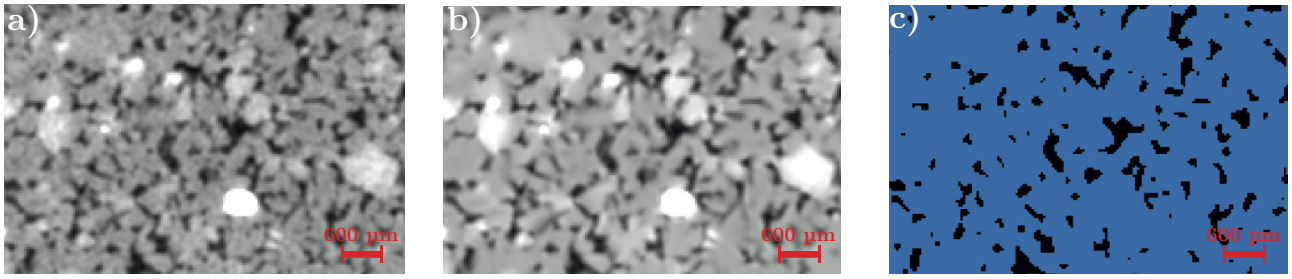


Figure 5.26: a) Slice from the raw 6 micron scan, b) filtered slice, c) segmented slice.

To quantitatively assess the impact of image resolution on the results, we calculate the ratio of feature size to voxel size R_f, following the method by Jackson et al. (2022b):

$$R_f = \frac{r}{V_x} = \frac{2\sigma}{P_c V_x} \quad , \tag{5.6}$$

where r is the feature size, V_x is the voxel size, σ is the interfacial tension and P_c is the capillary pressure. This provides an indication of the accuracy of the curvature estimates obtained from CT images (Jackson et al., 2022b). Although we do not conduct any wettability analysis on our scans, a high accuracy of curvature estimates will also likely result in accurate multiphase flow property estimates. Thus we can use this measure in our work. Jackson et al. (2022b) collated various studies and found that for geological media, R_f needs to be larger than 5 for estimates to be accurate. For our scans, with $V_x = 2$ μm, $\sigma = 62$ mN·m, $P_c = 10$ kPa, we estimate $R_f = 2$. This indicates that even a scan at 2 μm resolution may not be sufficient to characterise our sample, which could have led to the deviation in relative permeability between the 2 micron scan and the coreflood history match.

5.3.3.4 Implications and Future Work

These findings have important implications for future work focused on reservoir samples. It is crucial to conduct preliminary analysis on the specific sample to determine the most suitable voxel size for a micro-CT scan. From our reservoir samples, we observe a large variation in flow properties even along a small depth interval. Thus, the preliminary analysis has to be conducted on a suitable sister sample. Important considerations are the permeability and pore size distributions, which could be estimated from MICP. This will ensure a successful experimental suite.

The results also provide useful insights into the microscopic flow behaviour of a Bunter sandstone sample. The data has demonstrated that connectivity is controlled by rather small pores that may be significantly affected by phenomena such as fines migration. For CCS operations at the Endurance site, it will be important to minimise these effects to maintain well injectivity throughout the field development phase. For instance, it may be of value to conduct preliminary tests assessing the potential for pore blockage by salt precipitation. These impacts also ought to be incorporated in uncertainty estimates.

To analyse the predictive capabilities of pore network models of complex reservoir samples we propose the following workflow (see next page). By conducting an MICP experiment before the scanning procedure, a suitable voxel size can be chosen to alleviate resolution issues. The MICP data can also be used to infer any changes in the sample's properties during the coreflood and to verify the pore network modelling results. By approaching the capillary heterogeneity characterisation from a pore and core scale, we also bridge the gap between the two scales. We propose for this workflow to be applied in future work.

1. Obtain multiple reservoir samples from the same depth interval and rock type.
2. Conduct an MICP experiment on a small sample (maximum 1 cm length) to estimate the flow properties.
3. Use the results from 2) to determine a suitable voxel size for the micro-CT scans.
4. Scan a dry rock sample (minimum 5 cm length) with the micro-CT scanner at the chosen resolution from 3).
5. Use the same sample to perform a steady-state relative permeability coreflood experiment at two flow rates with the medical-CT scanner.
6. Cut a small plug from the large sample and perform MICP on this. Compare the results to 2), which provides information on changes in the sample's flow properties during the coreflood (e.g. from clay).
7. The porosity from the medical-CT scanner can be used to verify the segmentation of the micro-CT scans.
8. Extract a pore network model from the micro-CT images and conduct a network simulation. Build a darcy-scale flow model of the core and simulate the steady-state relative permeability coreflood experiment.
9. Verify the results from the simulation against the independent relative permeability measurements from the steady-state coreflood experiment.
10. Verify the capillary pressure results from the simulation against the MICP data collected in 2) and 6).
11. Conduct a core-scale capillary heterogeneity characterisation and compare the digital core model to the one obtained from the pore network workflow.

We note that this workflow relies on the micro-CT image being able to resolve the pore space. For samples with a large EV, such as the Bunter sandstone sample analysed herein, it is likely unfeasible to scan an EV-sized subvolume at the required resolution due to hardware limitations and time constraints. In these cases, an alternative method to image the pore space is required.

Deep learning represents a potential alternative solution and has recently been applied to low-resolution micro-CT images, tackling the issues of field-of-view and resolution trade-offs (Jackson et al., 2022b). The authors utilised deep learning to create super-resolution images from low-resolution micro-CT images of a Bentheimer sandstone sample. They subsequently used these images to create a multi-scale digital rock model of the sample and successfully verified it against independent observations including multiphase flow experiments. Albeit the successful results, Jackson et al. (2022b) focused their work on Bentheimer sandstone samples, which are known to exhibit relatively simple pore structures and heterogeneity. It would be interesting to test the applicability of this method to more complex reservoir samples with multi-scale heterogeneity, which we recommend for future work.

An alternative, novel approach to reduce field-of-view and resolution trade-offs was also recently developed by Blykers et al. (2021), who combined X-ray CT imaging and dark field tomography to quantify sub-resolution feature sizes. Dark field tomography utilises X-ray scattering to infer information of unresolved micro-structure down to nanometre length scales (Blykers et al., 2021). The authors successfully quantified the pore sizes of alumina particles ranging between 50-150 nm. This method has yet to be applied to core samples, but it represents a potential solution to resolution limitations of traditional micro-CT imaging.

Thus, for samples where hardware limitations or time constraints pose challenges to capture the heterogeneity with traditional micro-CT imaging technology, the above mentioned methods could be incorporated into the experimental workflow described previously.

5.4 Conclusions

In this chapter, we presented an advanced experimental and characterisation study conducted on reservoir samples from a proposed CCS site in the UK, the Endurance site. Analysing these reservoir samples provided a useful insight into the potential impact of capillary heterogeneity on CO_2 flow at this site. We will use this information in subsequent chapters to model CO_2 plume migration at larger scales.

The MICP experiments displayed a variability of entry pressure with depth in the injection interval. This suggests that the Endurance site is characterised by strong capillary heterogeneity. This is a novel finding as capillary heterogeneity has previously been disregarded in Endurance characterisation studies. It is an important aspect to incorporate in reservoir simulations as it may impact the flow of CO_2, which is a focus of subsequent chapters.

We conducted a steady-state relative permeability coreflood experiment on one of the reservoir samples and identified an abundance of clay minerals, which alongside fines migration, likely reduced the absolute permeability of the sample by a factor of 10. This has important implications for CCS operations at the Endurance site as clay/fines effects may impact well injectivity and the CO_2 flow pattern. From the experiment, we obtained a core-average relative permeability, which we will use alongside the capillary pressure curves to perform large-scale simulation studies.

The micro-CT scans of the coreflood sample confirmed the presence of clay minerals and also identified small throats as the main controls on connectivity. This is an important finding as small throats can easily be blocked by salt precipitation or fines, both of which may significantly reduce the permeability of the reservoir during CO_2 injection.

Based on the challenges encountered during this experimental suite, we highlighted key considerations for future work, which will provide additional validity of core-scale experimental observations.

Chapter 6

Impact of Capillary Heterogeneity on CO_2 Flow at the Metre Scale

6.1 Objectives

This chapter uses data from Chapter 5 to investigate the impact of capillary heterogeneity on CO_2 flow at the metre scale. We explore the variations in migration speed, plume footprint area and volumetric sweep with flow rate, correlation length and tilt. As discussed in Chapter 2, conventional reservoir simulations fail to account for the impact of small scale rock heterogeneity on the multiphase flow properties, the relative permeability and the capillary pressure. It is possible that this is one of the leading causes for the deviation in CO_2 flow behaviour obtained from field observations and flow simulations. Chapter 4 and 5 explore the impact of rock heterogeneity on fluid flow at the millimetre to centimetre scale and demonstrate the importance of incorporating capillary heterogeneity in characterisation workflows. Motivated by this, we now investigate the impact of capillary heterogeneity on CO_2 flow behaviour at the metre scale. These fine-scale studies allow us to evaluate the impact of capillary heterogeneity in models in which we resolve all of the heterogeneity down to the centimetre scale. Thus, we ensure the physics is fully represented in our models. The fine-scale simulations are also used to validate our upscaling approach, although those results are presented in a separate chapter.

6.2 Methods

Our focus is the proposed Endurance CCS site in the UK, where CO_2 will be injected into the Bunter sandstone formation. Using publicly available well data (White Rose, 2016a,b; BEIS, 2021e) in combination with laboratory measurements from Chapter 5, we build fine-scale, high resolution 3D flow models. The domain dimensions are (x,y,z) 10 m, 10 m and 5 m, with 0.1 m grid block sizes in all dimensions. These models allow us to investigate the impact of capillary heterogeneity at the metre scale with sub-metre resolution, informed by the petrophysical characteristics of the Endurance site.

We follow a geostatistical approach, based on the work by Jackson and Krevor (2020), to generate 19 models varying the correlation length of the heterogeneity in all three dimensions. Thus, the models are specific realisations of each heterogeneity structure. Through this, we fully control the correlation lengths imposed in the models and cover a large parameter space. Rather than performing flow simulations on a model with a single combination of correlation lengths, we systematically vary the length scales of heterogeneity. The changes in the observed flow patterns provide key insights into the dominating heterogeneity, interactions between heterogeneities from different dimensions and the resultant impact on CO_2 flow. The correlation lengths imposed in each model are summarised in Table 6.1. Model 1 represents the base case, characterised by correlation lengths equal to the grid block size ($\frac{r_y}{r_z}$=1, $\frac{r_y}{r_x}$=1, $\frac{r_y}{L}$=0.01). This provides a means for comparing the flow behaviour observed in a specific case to a model without any structured heterogeneity. To investigate the relationship between the correlation lengths in the three dimensions and the resultant flow pattern, we present all results in terms of the correlation length ratios, which are also summarised in Table 6.1.

The combination of correlation lengths represent a range of plausible variations in lithology that may be encountered in a heterogeneous reservoir at the 10s of metre length scale. Bedding and layering can exhibit a range of correlation lengths depending on the depositional environment under which it formed. For example, thin extensive beds would be characterised by large r_x and r_y and a smaller r_z (Bao et al., 2019). Layers may deposit that are constrained laterally

in one dimension, thus they would either have a large r_x or r_y and a variable r_z. Channels are expected to have a large r_z compared with r_x and r_y (Campion et al., 2000). With respect to the proposed Endurance CCS site, baffles, thin interbedded mudstone layers and crossbeds have been identified in the cored interval (BEIS, 2021e), which would be characterised by variable correlation lengths.

Table 6.1: Summary of the correlation lengths (r_x, r_y and r_z) and corresponding correlation length ratios ($\frac{r_y}{r_x}$, $\frac{r_x}{r_z}$ and $\frac{r_y}{r_z}$) for each model. L and W are the total system length and width, respectively. It follows that $\frac{r_y}{L}$ and $\frac{r_x}{W}$ represent the ratio of correlation length to system size in the y and x dimensions, respectively.

Model Number	r_x [m]	r_y [m]	r_z [m]	$\frac{r_y}{r_z}$	$\frac{r_x}{r_z}$	$\frac{r_y}{r_x}$	$\frac{r_y}{L}$	$\frac{r_x}{W}$
1	0.1	0.1	0.1	1	1	1	0.01	0.01
2	2	10	1	10	2	5	1	0.2
3	2	10	5	2	0.4	5	1	0.2
4	2	10	10	1	0.2	5	1	0.2
5	2	20	1	20	2	10	2	0.2
6	2	20	5	4	0.4	10	2	0.2
7	2	20	10	2	0.2	10	2	0.2
8	10	2	1	2	10	0.2	0.2	1
9	10	2	5	0.4	2	0.2	0.2	1
10	10	2	10	0.2	1	0.2	0.2	1
11	10	20	1	20	10	2	2	1
12	10	20	5	4	2	2	2	1
13	10	20	10	2	1	2	2	1
14	20	2	1	2	20	0.1	0.2	2
15	20	2	5	0.4	4	0.1	0.2	2
16	20	2	10	0.2	2	0.1	0.2	2
17	20	10	1	10	20	0.5	1	2
18	20	10	5	2	4	0.5	1	2
19	20	10	10	1	2	0.5	1	2

6.2.1 Geostatistical Approach to Create Heterogeneous Domains

A random porosity field is generated using the standard deviation obtained from fitting an extreme value distribution to the porosity data of well 42/25d-3 (Figure 6.1b). The extreme value functional form is chosen to be the most suitable fit for the porosity data as it captures the peak at low porosity, which is underpredicted with a log-normal or normal functional form. Following this, the correlated porosity field is produced with anisotropic correlation lengths using ellipsoidal averaging, originating in the work by Durlofsky et al. (1997) and applied to 2D models in Jackson and Krevor (2020).

The correlated field is re-scaled to match the mean and standard deviation from the extreme value model of the porosity well data, and the depth transform from Figure 6.1a is applied. This results in a correlated field that matches the statistical information obtained from characterisation and data collection studies conducted as part of the Northern Endurance Partnership project development. The reader is referred to Jackson and Krevor (2020) Section S3 in the supplementary information for a detailed verification of the geostatistical approach.

The fine-scale grid block permeability is calculated using the porosity-permeability relation from BEIS (2021e):

$$K = 10^{4.19log(\phi)+5.17} \quad , \tag{6.1}$$

where K is the permeability and ϕ is the porosity. The relation is also displayed in graphical form in Figure 6.1. We calculate the fine-scale entry pressure distribution using J-function scaling (Equation 2.11), where the J-function was determined from MICP data collected on samples from the Endurance site (Chapter 5). The relative permeability in the domain is set to the history-matched relative permeability from Chapter 5. Thus, we assume that the viscous-limit relative permeability at the grid block and core scale are comparable. The core sample and grid block have similar length scales. Based on this and the dominant heterogeneity correlation lengths reported in BEIS (2021e), we conclude this to be a valid assumption.

For each model, we generate two cases: one with heterogeneous and one with homogeneous capillary pressure. Note, both cases are characterised by a heterogeneous porosity and permeability field. This allows us to separate the impact of capillary heterogeneity from other petrophysical heterogeneity.

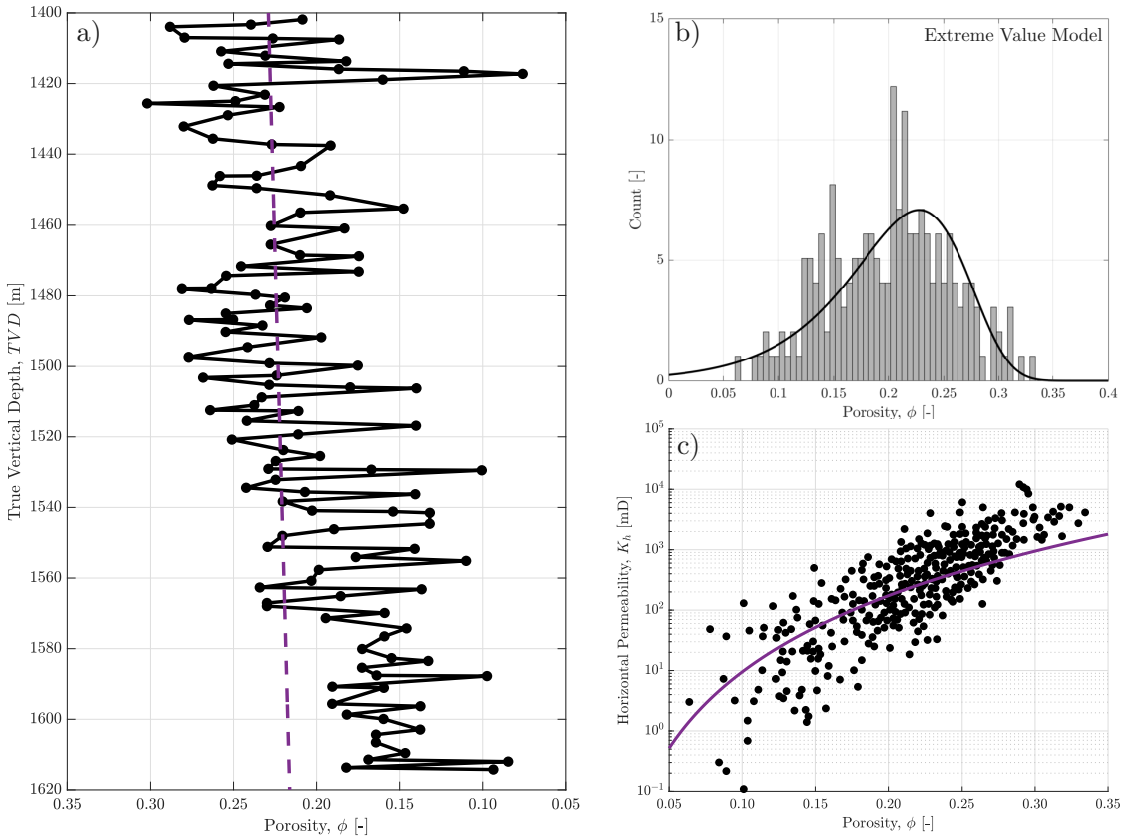


Figure 6.1: a) Porosity data from well 42/25d-3 alongside the porosity-depth trend plotted as a purple line and obtained from White Rose (2016a): $\phi = \frac{TVDSS-5331.5}{-171.68}$. "The porosity-depth trend was estimated from good quality Bunter Sandstones from 7 wells in the Endurance area" (White Rose, 2016a). b) Histogram of the porosity data alongside the extreme value distribution fit with $\mu = 0.23$ and $\sigma = 0.049$. c) Porosity-permeability correlation from well log data. The purple line represents the trendline $K = 10^{4.19log(\phi)+5.17}$ from BEIS (2021e).

6.2.2 Simulator

The fully implicit, isothermal, multiphase fluid simulator CMG IMEX® is used to simulate CO_2 injection. The models are fully saturated with water. No flow boundaries are imposed on the x=1 and x=100 faces, see Figure 6.2. CO_2 is injected at constant rate along the whole face of the x-z plane (y=102) to simulate linear flow. Producers are completed along the whole face of the x-z plane (y=1). Thus flow is directed along the y-axis.

The porosity and permeability are set to high, constant values and the capillary pressure to zero in the inlet and outlet faces to reduce well convergence issues and ensure consistent boundary conditions are implemented across all simulations. To ensure solver stability and acceptable run times, we set grid blocks with $\phi < 6 \times 10^{-3}$ to inactive cells. Under these flow conditions, grid blocks with a porosity below this threshold are unlikely to be invaded by CO_2, thus the impact on the flow pattern caused by setting them to inactive cells is negligible.

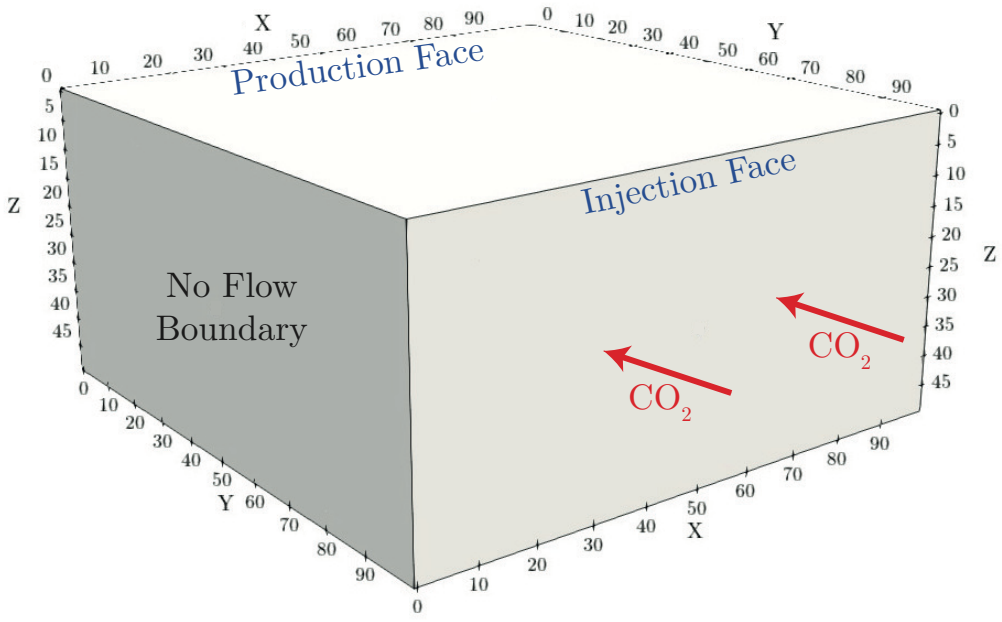


Figure 6.2: Simulation model set-up showing the location of the injection and production faces.

6.3 Results and Discussion

6.3.1 Impact of Capillary Heterogeneity at Typical Reservoir Flow Rates

We will first compare the homogeneous to the heterogeneous cases of the 19 models, where CO_2 is injected at a rate of 2 m^3d^{-1}. Observations from CCS sites and CO_2 injection simulation studies demonstrate that CO_2 plume advance rates vary depending on the geological setting. For instance, the plume at Sleipner advanced at 1 $m{\cdot}d^{-1}$ between 2001 and 2004 (Chadwick et al., 2009), whereas simulations of the Goldeneye field experiment displayed an average advance rate of 0.375 $m{\cdot}d^{-1}$ (Saleem et al., 2021). Both of these reservoirs exhibit a dip. The work by Han and Kim (2018) demonstrates that CO_2 frontal advance rates vary significantly depending on the tilt of the domain. The authors find that the frontal advance rate increases from 0.15 $m{\cdot}d^{-1}$ to 0.49 $m{\cdot}d^{-1}$ when the tilt is increased from 2° to 10°. In hydrocarbon reservoir engineering, an advance rate of 0.3 $m{\cdot}d^{-1}$ is taken as a rule of thumb for typical frontal advance rates. An injection rate of 2 m^3d^{-1} results in a frontal advance rate of 0.2 $m{\cdot}d^{-1}$ in our domain, which falls in the range of typical average flow rates encountered during CCS reservoir operations in an untilted domain. Thus, this section investigates the importance of capillary heterogeneity at typical reservoir flow rates.

We measure the breakthrough time of the plume, which provides an indication of the plume migration speed. We define breakthrough time as the time at which S_{CO2} in any cell at the outlet is larger than 10^{-4}. We also calculate the plume swept volume and the plume footprint area at multiple time steps. Plume footprint area is defined as the area of the CO_2 plume when it is projected onto a horizontal plane and plume swept volume is the volume of all grid blocks invaded by CO_2 ($S_{CO2,block} > 10^{-4}$). Herein, we refer to time in the dimensionless unit of pore volumes injected, PV_{inj}.

These three measures provide useful information on the plume flow behaviour and the field scale phenomena that result from this. The breakthrough time describes the lateral plume migration speed, which controls the time it takes for the CO_2 to reach the spill point in a reservoir. Footprint area is a control on dissolution and residual trapping rates within the plume. The more the plume spreads, the more trapping and dissolution may occur (Sundal et al., 2015). The swept volume provides an indication of the efficiency of pore space use, which is directly linked to the storage efficiency of a formation.

6.3.1.1 The Impact of Heterogeneity on CO_2 Migration Speed

To analyse the impact of heterogeneity on CO_2 migration, we calculate the relative migration speed, V_r, which we define as the inverse of relative breakthrough time (Jackson and Krevor, 2020):

$$V_r = \frac{t_0}{t_i} \quad , \tag{6.2}$$

where t_0 is the breakthrough time of the uncorrelated base case (model 1, unstructured heterogeneities with $\frac{r_y}{r_z}$=1, $\frac{r_y}{r_x}$=1, $\frac{r_y}{L}$=0.01) and t_i is the breakthrough time of the specific model. Note: t_0 is adjusted based on whether the model imposes homogeneous or heterogeneous capillary pressure. For instance, to calculate the relative migration speed of the homogeneous models, we use model 1 with homogeneous capillary pressure as t_0. This is done as there are inherent differences in the t_0 between the homogeneous and heterogeneous cases. Breakthrough time is measured as the time at which S_{CO2} in any block at the outlet is a larger than 10^{-4}. If V_r is smaller than 1, it means that the plume in the model travels slower than the uncorrelated case, whereas if it is larger than 1, the plume is travelling faster. Relative migration speed provides an indication of the lateral migration speed of a CO_2 plume. At a CCS site, this an important measure for predicting the time at which the plume reaches a certain point in the formation such as the spill point.

The results for the homogeneous and heterogeneous runs are displayed in Figure 6.3 against the two correlation length ratios $\frac{r_y}{r_x}$ and $\frac{r_y}{r_z}$. These two ratios are all that is needed to describe the results in terms of the correlation lengths. Performing a Buckingham π analysis (Buckingham, 1914), we find that our problem has 3 variables (r_x, r_y and r_z), $m = 3$, and one dimension, $n = 1$, corresponding to the length scale. Applying $p = m - n$, we find that two correlation length ratios are sufficient to describe the results. We also plot the results against $\frac{r_y}{L}$ to investigate the impact of correlation to system length on the flow behaviour. We show the results for one realisation for each combination of correlation lengths. We acknowledge that plume speed will likely vary between different realisations. However, the overall physics and the trends of the problem can be highlighted and discussed with the current set of models. The reader is referred to Section 6.3.5 for a more detailed discussion on the modelling assumptions.

Generating these plots allows us to understand how the migration speed varies with correlation length by distinguishing the heterogeneity structure in each dimension. The difference in the results between the heterogeneous and homogeneous models is a direct reflection of the impact of capillary heterogeneity as both models incorporate an identical, heterogeneous porosity and permeability distribution.

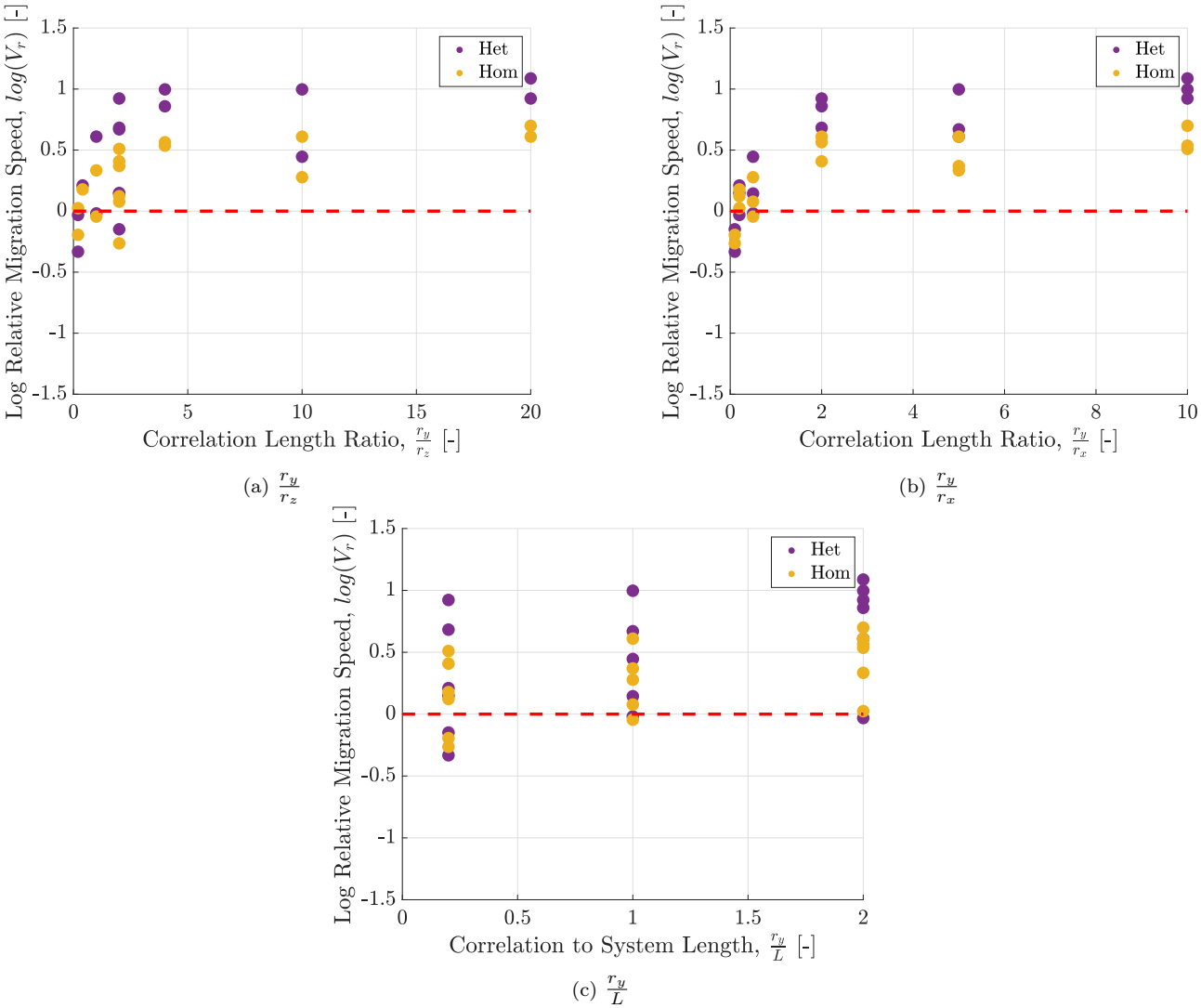
The plume in the homogeneous runs generally travels slower ($V_{r,max} = 5$) than that in the heterogeneous models ($V_{r,max} = 12$), which indicates that capillary heterogeneity enhances the CO_2 flow speed. Thus, omitting capillary heterogeneity from characterisation studies may result in a significant underestimation of migration speeds. We also find that increasing correlation length anisotropy increases the migration speed for both, the homogeneous and heterogeneous cases.

The results also indicate that rock heterogeneity may slow down the plume if layers are predominantly orientated perpendicular to the flow axis, corresponding to a small $\frac{r_y}{r_x}$. The layers act as barriers to the CO_2 and the gas accumulates upstream of these structures. Ultimately, this slows the plume down, which corresponds to relative migration speeds below 1. This is observed for both, the homogeneous and heterogeneous cases. Thus, porosity and permeability heterogeneity alone can both, speed up and slow down, the plume. However, this effect is

further enhanced by incorporating capillary pressure variations.

We also observe a slight increase in the relative migration speed at larger $\frac{r_y}{L}$ (Figure 6.3c). The formation of laterally extensive channels is enhanced and these control the CO_2 flow speed. In comparison to this, at small $\frac{r_y}{L}$, we discover a slightly larger spread in migration speed, which is a result of the variable correlation length ratios in this parameter space.

Figure 6.4 presents the migration speeds against both correlation length ratios in one scatter plot to emphasize the interaction between the correlation lengths in the three dimensions. Focusing on the heterogeneous runs, the highest speeds are a result of large $\frac{r_y}{r_x}$ and large $\frac{r_y}{r_z}$. In these cases, the layers are primarily orientated parallel to the axis of flow. This geometry leads to the development of channels along which the plume can migrate more efficiently. In this parameter space, the difference between homogeneous and heterogeneous migration speeds is also the biggest. Therefore, omitting capillary pressure variations from reservoir models may lead to the biggest uncertainties when layers are predominantly orientated parallel to the axis of flow. In these cases, 'homogeneous' flow models will not sufficiently capture the CO_2 channeling, which may result in inaccurate migration speed estimates.



(a) $\frac{r_y}{r_z}$ (b) $\frac{r_y}{r_x}$

(c) $\frac{r_y}{L}$

Figure 6.3: Relative migration speed versus a) $\frac{r_y}{r_z}$, b) $\frac{r_y}{r_x}$ and c) $\frac{r_y}{L}$ at injection rate of 2 m^3d^{-1}. Note: the log of the relative migration speed is plotted to emphasize which models exhibit a migration speed slower than the base case (below zero) and which models exhibit a migration speed faster than the base case (above zero). The dashed red line plotted at y=0 indicates the region where the migration speed in the model is unchanged from the base i.e. heterogeneity has no impact on the migration speed of that model relative to the uncorrelated base case.

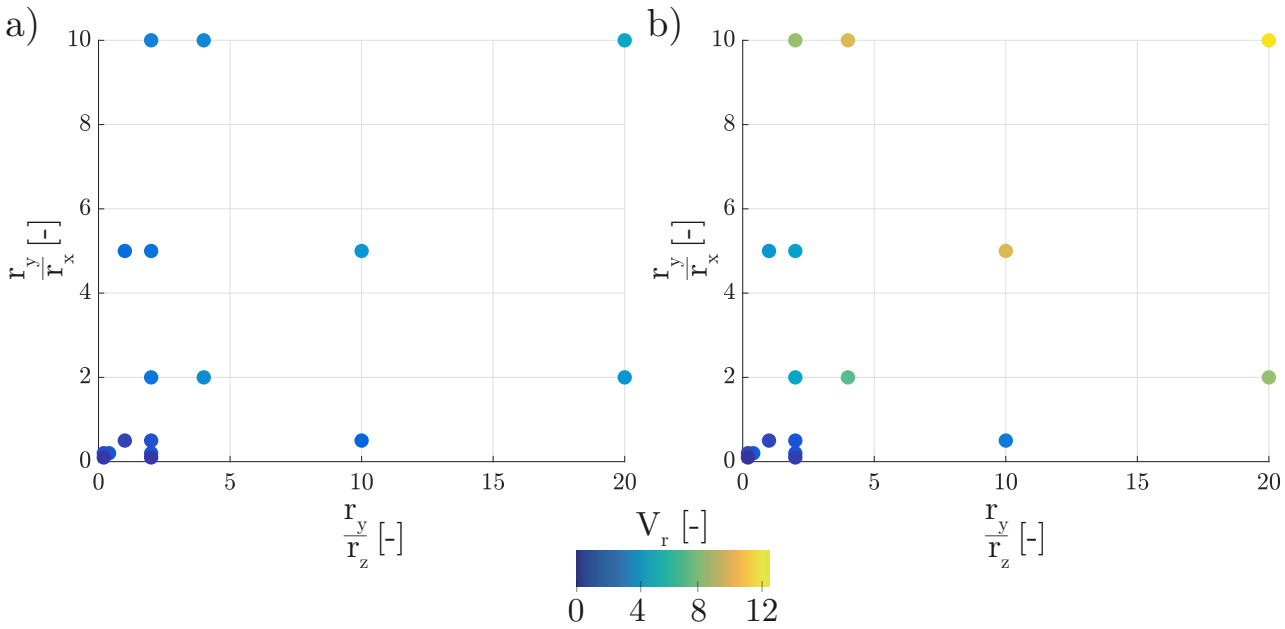
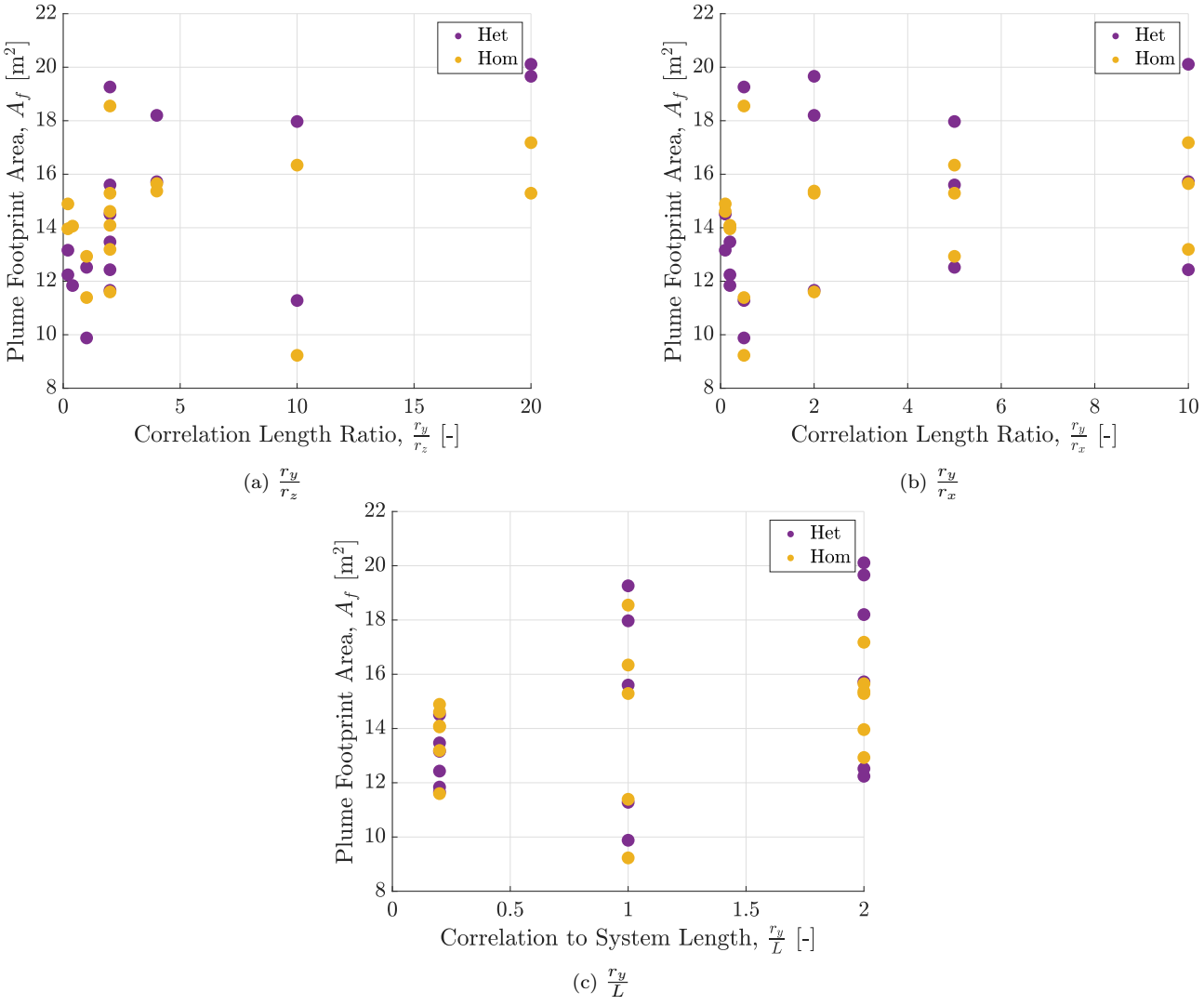


Figure 6.4: Relative migration speed of the a) homogeneous and b) heterogeneous runs plotted against their respective correlation length ratios at injection rate of 2 m^3d^{-1}.

6.3.1.2 The Impact of Heterogeneity on Plume Footprint Area

Footprint area is defined as the area of the plume when it is projected onto a horizontal plane. It is a control on the amount of CO_2 that is immobilised due to dissolution and capillary trapping. The wider the plume spreads, the more trapping and dissolution may occur. Figure 6.5 presents the footprint area of the 19 models measured at $PV_{inj} = 0.005$ plotted against the two correlation length ratios, $\frac{r_y}{r_x}$ and $\frac{r_y}{r_z}$, and against $\frac{r_y}{L}$.



(a) $\frac{r_y}{r_z}$ (b) $\frac{r_y}{r_x}$ (c) $\frac{r_y}{L}$

Figure 6.5: Plume footprint area versus a) $\frac{r_y}{r_z}$, b) $\frac{r_y}{r_x}$ and c) $\frac{r_y}{L}$ at injection rate of $2m^3d^{-1}$ at $PV_{inj} = 0.005$.

The results emphasize that the orientation of heterogeneity is a main control on the resultant flow pattern in these models. If layers are predominantly orientated perpendicular to the principal axis of flow, corresponding to a small $\frac{r_y}{r_x}$, they can act as barriers to the CO_2 and reduce the spread of the plume, corresponding to a smaller footprint area. In a reservoir

setting, a reduction in CO_2 plume spreading will lead to a smaller amount of immobilised CO_2. This in turn has important implications for CCS operations and storage integrity. Mobile gas may escape through leakage pathways such as faults. Thus, maximising CO_2 immobilisation processes reduces this risk.

As $\frac{r_y}{L}$ increases, we observe an increase in the range of footprint areas (Figure 6.5c), from 11.6-15 at $\frac{r_y}{L}$=0.2 to 9.2-19.2 at $\frac{r_y}{L}$=1. Within this parameter space, the models with a corresponding small $\frac{r_y}{r_z}$ and $\frac{r_y}{r_x}$ exhibit the smallest footprint areas.

Results for one such model are displayed in Figure 6.6. The model is characterised by $\frac{r_y}{r_z}$=0.2, meaning that it has a short correlation length in the axis of flow (y-axis) compared with the correlation length in depth (z-axis). It is also described by $\frac{r_y}{r_x}$=0.2, meaning that the heterogeneity is more continuous in the x-axis. The heterogeneity orientated parallel to the x-axis and z-axis acts as a barrier to CO_2 and hinders the plume from migrating towards the outlet. Thus, CO_2 accumulates upstream of these layers. This behaviour is observed for the homogeneous and heterogeneous runs.

This suggests that all three petrophysical heterogeneities (porosity, permeability, capillary pressure) influence the resultant CO_2 flow behaviour. However, capillary heterogeneity additionally hinders the lateral CO_2 migration (see blue arrow in Figure 6.7), resulting in a heterogeneous frontal saturation distribution and a smaller footprint area. This can be attributed to the small $\frac{r_y}{r_z}$ and $\frac{r_y}{r_x}$ imposed in the model. This finding demonstrates that in extreme cases capillary heterogeneity can slow the plume down relative to the uncorrelated base model, for instance by a factor of two for this heterogeneous run.

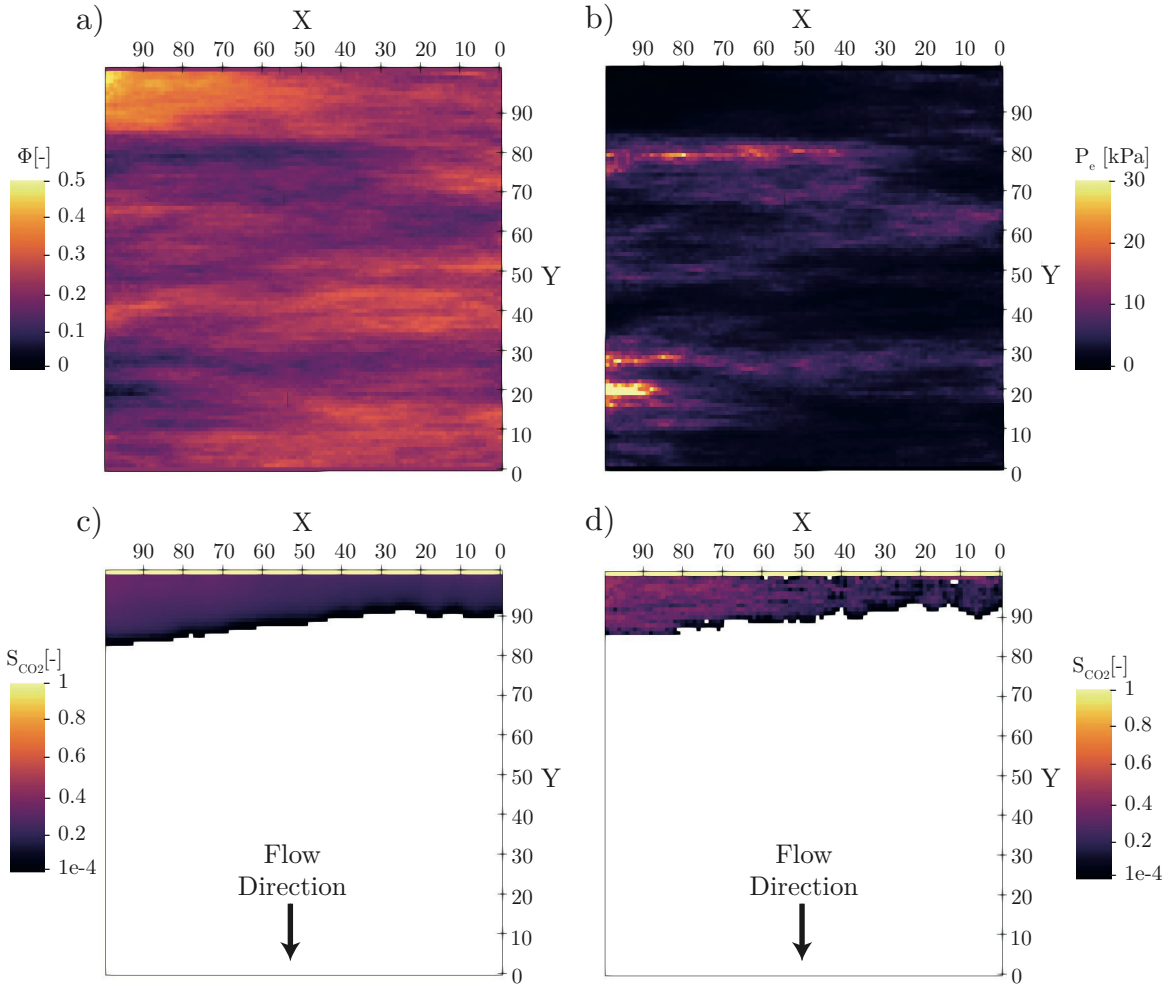


Figure 6.6: Model input parameters and resulting CO_2 saturations for model 10 ($\frac{r_y}{r_z}$=0.2, $\frac{r_y}{r_x}$=0.2, $\frac{r_y}{L}$=0.2). a) porosity distribution and b) entry pressure distribution. CO_2 saturation at PV_{inj}=0.005 for the c) homogeneous case and d) heterogeneous case. Note: the homogeneous model incorporates heterogeneous porosity and permeability and homogeneous entry pressure. The heterogeneous model incorporates heterogeneous porosity, permeability and entry pressure.

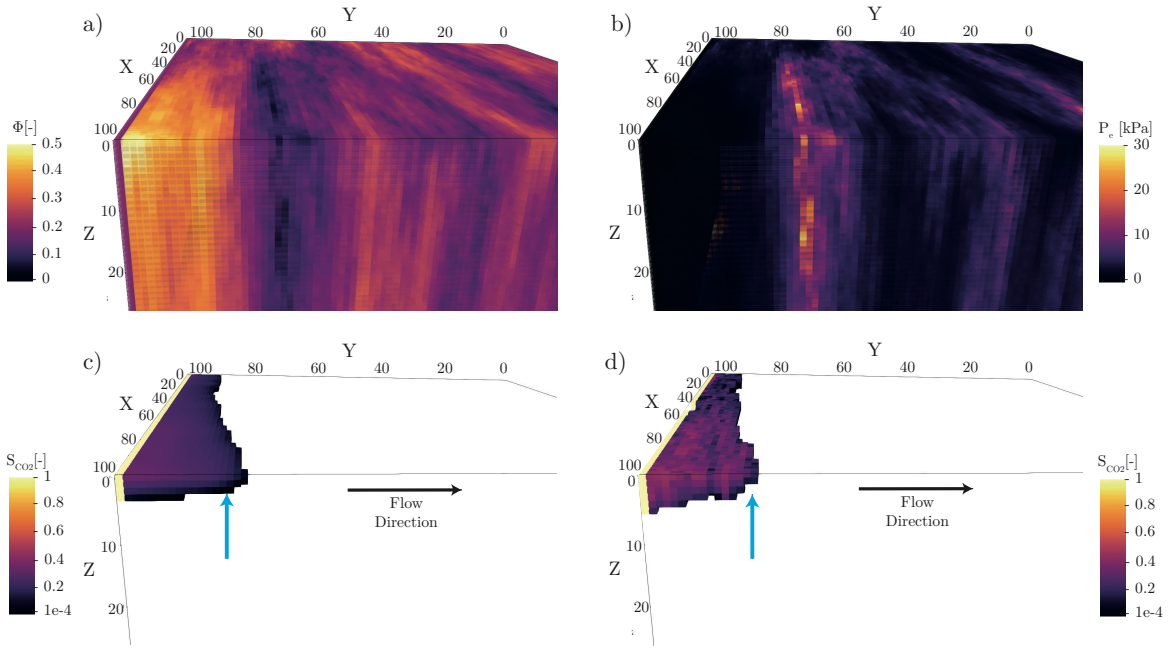


Figure 6.7: Side view of the model input parameters and resulting CO_2 saturations for model 10 ($\frac{r_y}{r_z}$=0.2, $\frac{r_y}{r_x}$=0.2, $\frac{r_y}{L}$=0.2). Note: the figures show a subsection of the entire domain. a) porosity distribution and b) entry pressure distribution. CO_2 saturation at PV_{inj}=0.005 for the c) homogeneous case and d) heterogeneous case. Note: the homogeneous model incorporates heterogeneous porosity and permeability and homogeneous entry pressure. The heterogeneous model incorporates heterogeneous porosity, permeability and entry pressure. The blue arrow points to a location, where the capillary heterogeneity orientated parallel to the x-axis and z-axis additionally slows down the lateral plume migration.

If heterogeneity is orientated parallel to the principal axis of flow corresponding to a large $\frac{r_y}{r_z}$ and $\frac{r_y}{r_x}$, the heterogeneity allows the CO_2 to migrate through preferred flow pathways. The plume spreads over a wider area and migrates more quickly. As shown in Figure 6.5a, models with a large $\frac{r_y}{r_z}$ are characterised by a large footprint area. Generally, the heterogeneous runs reach higher footprint areas compared with the homogeneous runs. This demonstrates the importance of characterising capillary pressure variations in reservoir models, through which the spreading of the plume can be more closely captured.

To examine the effect of layering on CO_2 flow, we analyse the saturation distribution maps of model 11 ($\frac{r_y}{r_z}$=20, $\frac{r_y}{r_x}$=2, $\frac{r_y}{L}$=2) in Figure 6.8. This combination of correlation length ratios produces a two-layer system as shown in Figure 6.8a and 6.8b. As injection commences, CO_2 preferentially flows along the high porosity, low entry pressure layer (right layer). Both, the homogeneous and heterogeneous runs, exhibit a distinct elongated plume shape. This emphasizes that all three petrophysical properties as well as $\frac{r_y}{L}$ affect flow at this injection rate. However, it can be seen that the heterogeneous model results in a worse flood front conformance and a larger spread of CO_2. At $PV_{inj} = 0.005$, the plume has migrated an additional ≈2 m into the domain in the heterogeneous run. This corresponds to a larger migration speed, which was observed in the previous section. Therefore, omitting capillary pressure variations in flow models may result in an underprediction of migration speed and plume spreading when layers are orientated parallel to the axis of flow.

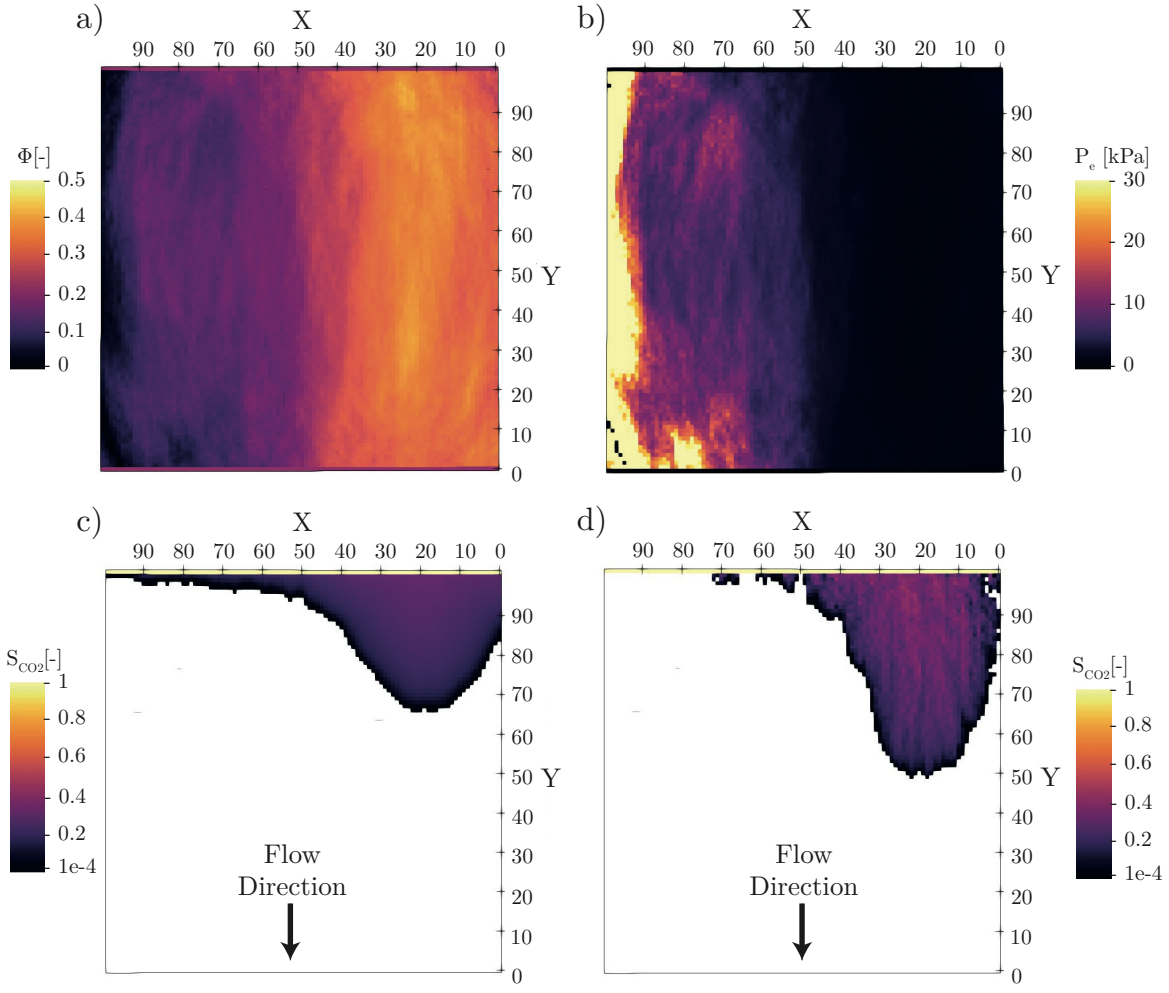


Figure 6.8: Model input parameters and resulting CO_2 saturations for model 11 ($\frac{r_y}{r_z}$=20, $\frac{r_y}{r_x}$=2, $\frac{r_y}{L}$=2): a) porosity distribution and b) entry pressure distribution. The CO_2 saturation distribution at PV_{inj}=0.005 is shown for c) the homogeneous case and d) the heterogeneous case. Note: the homogeneous model incorporates heterogeneous porosity and permeability and homogeneous entry pressure. The heterogeneous model incorporates heterogeneous porosity, permeability and entry pressure.

Comparison of the saturation distribution from model 10 ($\frac{r_y}{r_z}$=0.2, $\frac{r_y}{r_x}$=0.2, $\frac{r_y}{L}$=0.2) and model 11 ($\frac{r_y}{r_z}$=20, $\frac{r_y}{r_x}$=2, $\frac{r_y}{L}$=2) emphasizes the contrast in plume shape that results from the structure of heterogeneity imposed in the models. Model 11, with continuous layers orientated parallel to the y-axis (Figure 6.8) exhibits an elongated plume, with the saturation focused on a thin region 20 blocks (2 m) wide at the tip of the plume. In comparison to this, model 10 with continuous layers parallel to the x-axis and z-axis, results in a continuous saturation distribution along the x-axis (Figure 6.6). In the same time, the plume migrated an additional ≈3.5 m into the domain for the heterogeneous run of model 11, characterised by a favourable heterogeneity structure, with layers orientated parallel to the axis of flow that have correlation lengths larger than the system length.

This behaviour is also captured in Figure 6.5b. At large $\frac{r_y}{r_x}$, the resultant footprint areas spread over a large range, depending on the corresponding $\frac{r_y}{r_z}$ and $\frac{r_y}{L}$ imposed in each model. When the layers are favourably orientated with a large $\frac{r_y}{r_z}$ and a large $\frac{r_y}{L}$, such as model 11, the CO_2 plume covers a larger area in the heterogeneous compared with the homogeneous run, due to an increase in migration speed. On the other hand, if $\frac{r_y}{r_x}$ and $\frac{r_y}{L}$ are small, the CO_2 accumulates upstream of these layers, resulting in a smaller footprint area.

Overall, it can be seen that extensive lateral layers perpendicular to the axis of flow inhibit CO_2 migration, whereas layers orientated parallel to the axis of flow enhance CO_2 migration. The Endurance site is characterised by strong heterogeneity that can be predominantly grouped into laterally extensive layers. Therefore, the orientation of the primary CO_2 flow axis to the layers will play a key role in determining the resultant plume shape and migration speed.

Changing Impact of Heterogeneity with PV_{inj}

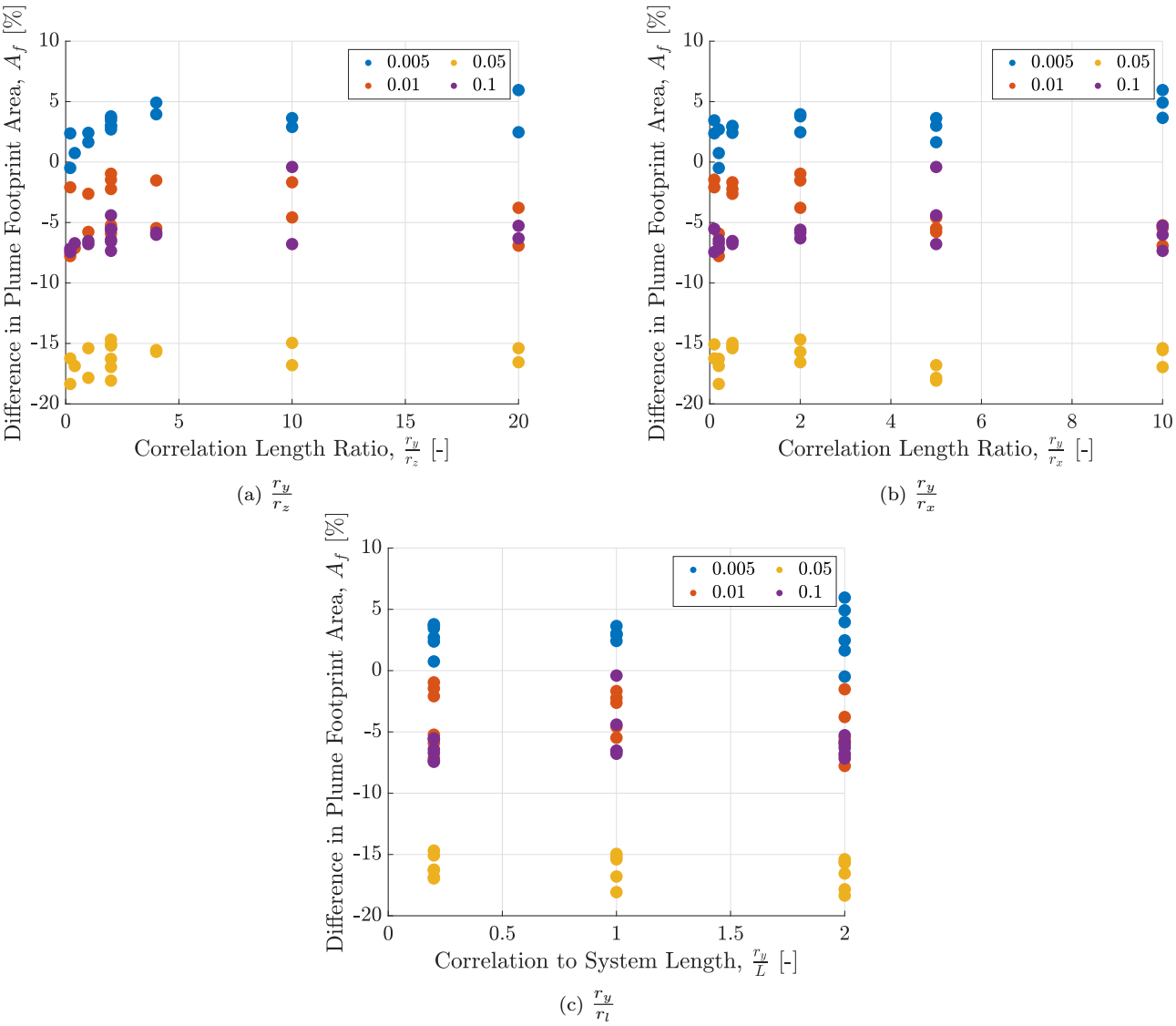
To examine the temporal variation of plume spreading between homogeneous and heterogeneous cases, we calculate the percentage relative difference in footprint area between the homogeneous and heterogeneous runs for all models at different PV_{inj}, Figure 6.9.

Near the start of injection (PV_{inj}=0.005), capillary heterogeneity enhances the plume spread in all models and it is easier for the CO_2 to invade the domain. The heterogeneous cases have larger footprint areas compared with the homogeneous runs, reaching a 6% difference. The plumes in the homogeneous models rise buoyantly upwards and CO_2 flow is confined to few shallow grid blocks. In comparison to this, the thresholding effect introduced by capillary heterogeneity results in an uneven vertical gas saturation distribution in the heterogeneous runs. The CO_2 invades the domain across a larger number of layers located near the top of the model, which results in a larger footprint area.

At later time (PV_{inj}=0.1), this effect diminishes and plume spread is now hindered by capillary heterogeneity. The homogeneous cases are now characterised by larger footprint areas, resulting in a negative percentage difference. As capillary pressure variations are omitted from the homogeneous runs, the resultant plume is more homogeneous and spreads out laterally in these simulations. The majority of CO_2 flow is restricted to the uppermost blocks.

In the heterogeneous runs, the CO_2 flows through preferential flow pathways with low entry pressures and forms fingers. The CO_2 is confined to these regions, even after breakthrough has occurred. Therefore, the heterogeneous runs are characterised by a reduced plume spread. In a reservoir setting, these results imply that CO_2 immobilisation in the presence of capillary heterogeneity may retard.

Interestingly, the absolute difference in footprint area between the homogeneous and heterogeneous runs decreases from PV_{inj}=0.05 to PV_{inj}=0.1. This is indicative of the thresholding effect introduced by capillary heterogeneity. If CO_2 reaches a region with higher entry pressure, it accumulates upstream of this. Once it has reached a sufficient phase pressure, it invades that entire region in a short amount of time. Thus, plume migration is highly dynamic.



(a) $\frac{r_y}{r_z}$ (b) $\frac{r_y}{r_x}$ (c) $\frac{r_y}{r_l}$

Figure 6.9: Relative difference in plume footprint area between the homogeneous and heterogeneous cases for all models at different PV_{inj} (corresponding to the colours) plotted against the correlation length ratios. Injection rate is $2m^3d^{-1}$.

To investigate this phenomenon in more detail, we present the results from model 3 ($\frac{r_y}{r_z}$=2, $\frac{r_y}{r_x}$=5, $\frac{r_y}{L}$=1) in Figure 6.10 and Figure 6.11. In the homogeneous case, the CO_2 sweeps a large portion of the domain between PV_{inj}=0.01 and PV_{inj}=0.05, which results in a noticeable increase in the footprint area (Figure 6.11a and 6.11c). In comparison to this, the CO_2 in the heterogeneous case has swept less of the pore space in the same time due to the thresholding effect introduced by the capillary pressure variations. This leads to a large, negative relative difference in the footprint areas between the two runs, as presented in Figure 6.9.

From PV_{inj}=0.05 to PV_{inj}=0.1, the plume in the heterogeneous run now catches up with that in the homogeneous simulation, as it has overcome the entry pressures required to invade certain regions in the domain. This decreases the absolute difference in footprint area between the two cases. It is interesting that this shift in the difference of footprint area is observed for all models independent of the correlation lengths.

These results show that the differences in plume migration between homogeneous and heterogeneous cases changes over time, which is most likely caused by the thresholding effect introduced from the entry pressure spatial variation. This dynamic behaviour indicates that regions of a CO_2 plume may migrate at unsteady-state, which would have important implications for upscaling techniques.

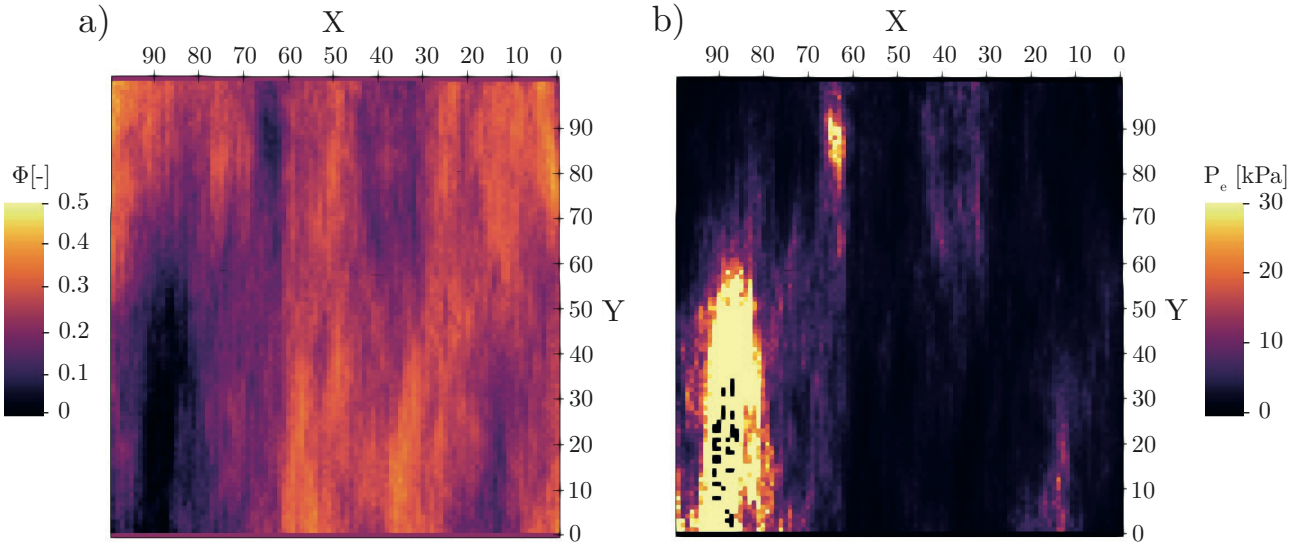


Figure 6.10: Input parameters for model 3 ($\frac{r_y}{r_z}$=2, $\frac{r_y}{r_x}$=5, $\frac{r_y}{L}$=1). a) porosity distribution implemented in the homogeneous and heterogeneous runs, b) entry pressure distribution implemented in the heterogeneous run only.

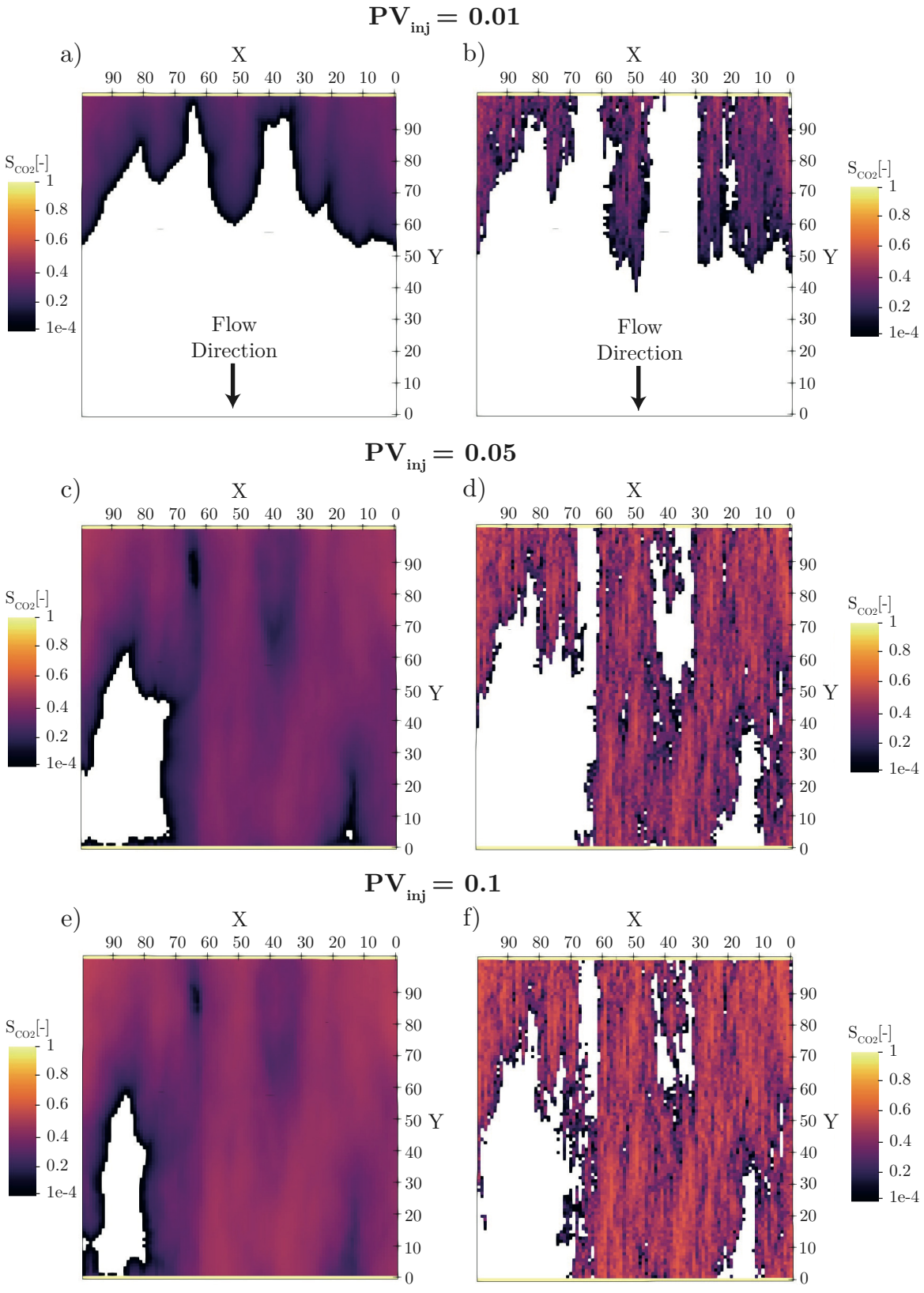


Figure 6.11: CO_2 saturation distribution for model 3 ($\frac{r_y}{r_z}$=2, $\frac{r_y}{r_x}$=5, $\frac{r_y}{L}$=1) at different PV_{inj}. Left: homogeneous model, Right: heterogeneous model. The homogeneous run imposes heterogeneous porosity and permeability and homogeneous entry pressure. The heterogeneous run imposes heterogeneous porosity, permeability and entry pressure.

6.3.1.3 The Impact of Heterogeneity on Plume Volume

The plume swept volume for all models at different PV_{inj} is presented in Figure 6.12. We define the plume swept volume as the volume of the total number of grid blocks invaded by CO_2 ($S_{CO2} > 10^{-4}$). The larger the volume, the more efficient the use of pore space is, which corresponds to an increased CO_2 storage efficiency.

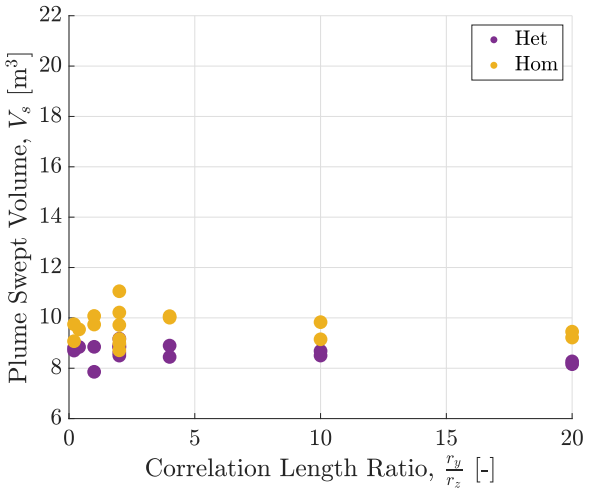
At early times (Figure 6.12 left column), sweep efficiency reduces in the presence of capillary heterogeneity. The thresholding effect due to capillary pressure variations results in a heterogeneous saturation front. The CO_2 is confined to preferential flow pathways and migrates along thin channels. Ultimately, this reduces the efficiency of the reservoir sweep. Plume swept volume is on average 13% higher in the homogeneous runs. These findings demonstrate that storage efficiency of a reservoir may decrease due to capillary pressure variations. The average difference in swept volume between the homogeneous and heterogeneous models increases from 13% at PV_{inj}=0.005 to 24% at PV_{inj}=0.01 (Figure 6.12 right column). This demonstrates that storage efficiency as a result of capillary heterogeneity reduces further at later times. We also observe a slight decrease in plume swept volume with increasing $\frac{r_y}{L}$ at both PV_{inj}. At large $\frac{r_y}{L}$, CO_2 flow is confined to channels, which corresponds to a reduced swept volume.

The swept volume generally decreases with an increase in $\frac{r_y}{r_z}$ and a decrease in $\frac{r_y}{r_x}$. To examine this trend more closely, we plot the footprint area and swept volume against both correlation length ratios in Figure 6.13. For the homogeneous and heterogeneous scenarios, a model with small $\frac{r_y}{r_x}$ and relatively small $\frac{r_y}{r_z}$ results in small footprint areas and volumes. Here, the heterogeneities act as barriers to the flow because they are orientated perpendicular to the principal flow axis. Thus, gas accumulates upstream of these layers, resulting in fewer number of grid blocks saturated with gas, but with higher total CO_2 saturation in each.

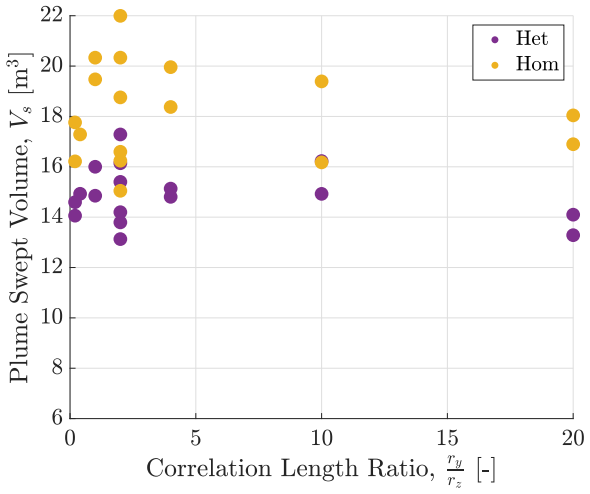
As we move to larger $\frac{r_y}{r_x}$, the volumes and areas increase for both cases, with the homogeneous runs generally having a higher plume volume but similar footprint area. This demonstrates the impact of capillary heterogeneity orientated perpendicular to the z-axis corresponding to a small $\frac{r_y}{r_z}$: these layers acts as barriers to the CO_2 whilst it is migrating towards the outlet,

leading to a heterogeneous saturation distribution. Ultimately, this results in a smaller volume for the heterogeneous cases.

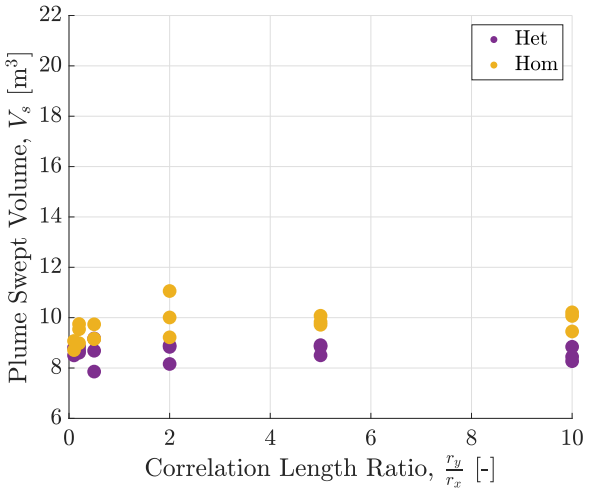
If we also increase $\frac{r_y}{r_z}$, the cases are characterised by large footprint areas and small plume volumes. With such continuous layers orientated parallel to the y-axis, the CO_2 forms distinct channels and restricts its flow to those, allowing it to migrate quickly whilst invading only a relatively small amount of the pore space. This corresponds to a large footprint area, but a small swept volume. Interestingly, the difference in results between the two models with highest $\frac{r_y}{r_z}$ is negligible, although the respective $\frac{r_y}{r_x}$ in each model differs. This implies that, in extreme cases where the correlation length in one dimension is significantly larger than that of the other dimensions, the flow behaviour is solely controlled by this one correlation length. In these two models it is r_y and the corresponding $\frac{r_y}{L}$ that control the flow of CO_2.



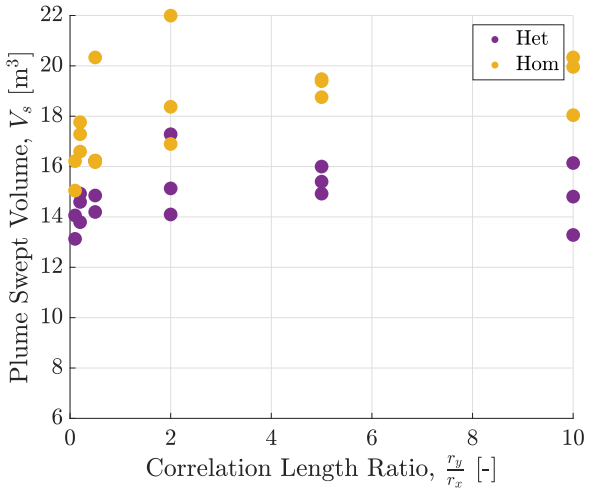
(a) PV = 0.005



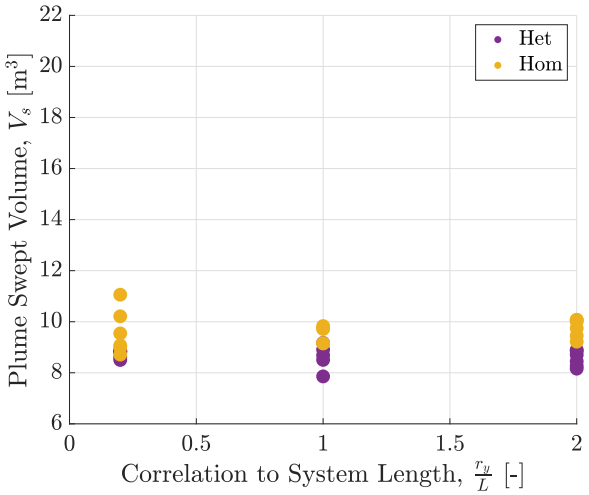
(b) PV = 0.01



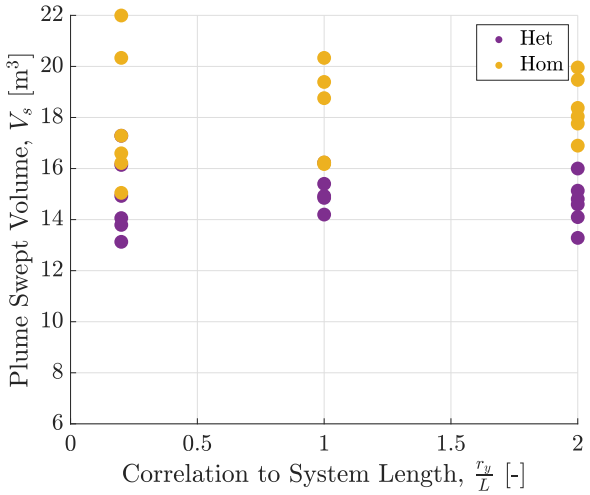
(c) PV = 0.005



(d) PV = 0.01



(e) PV = 0.005



(f) PV = 0.01

Figure 6.12: Plume swept volume plotted against a) and b) $\frac{r_y}{r_z}$, c) and d) $\frac{r_y}{r_x}$, e) and f) $\frac{r_y}{L}$ at 2 m^{3}d^{-1} injection rate. Left column: $PV_{inj} = 0.005$, Right column: $PV_{inj} = 0.01$.

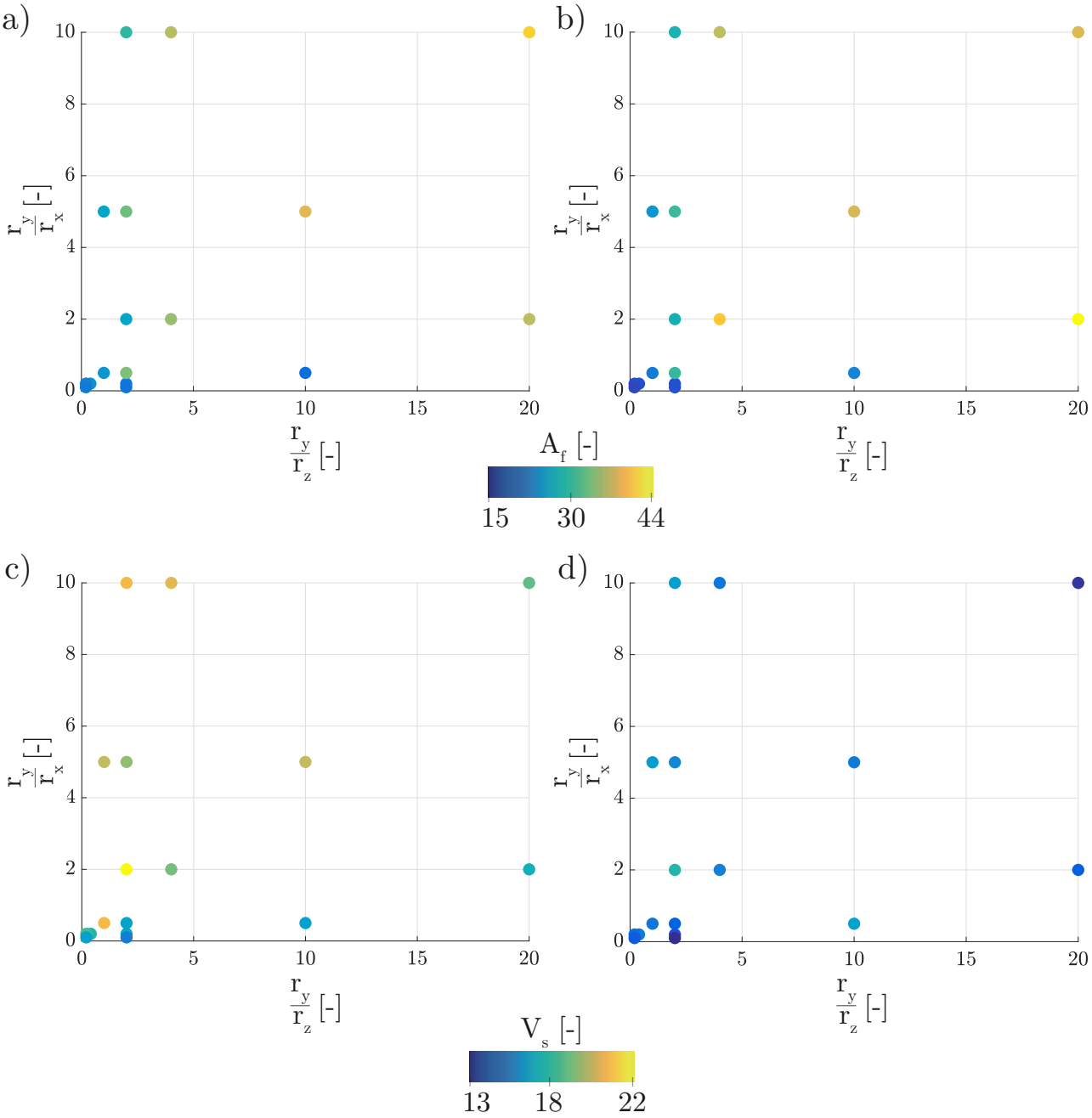


Figure 6.13: Plume footprint area and swept volume for all models plotted against their respective correlation length ratios at PV_{inj}=0.01. a) and b) are the footprint areas and c) and d) are the swept volumes. Left column: homogeneous runs, Right column: heterogeneous runs.

6.3.2 The Importance of Representing Flow in 3D

To analyse what, if any, differences there are between representing the domain in 2D to 3D, we extract five 2D slices from the 3D models with heterogeneous capillary pressure. We simulate CO_2 injection into each of these 2D slices. We choose an injection rate that results in a frontal advance rate of 0.2 m·d^{-1}, consistent with the medium injection rate scenarios presented in 3D. We calculate the migration speed at each correlation length, averaged over the five slices, and plot them alongside the 3D results, see Figure 6.14a and 6.14b.

As shown, the 2D models exhibit a dampening of the migration speed enhancement attributed to structured heterogeneity. For instance, the relative migration speed in Model 7 ($\frac{r_y}{r_z}$=2, $\frac{r_y}{r_x}$=10, $\frac{r_y}{L}$=2) decreases from 8.4 in 3D to 2.8 in 2D. In comparison to this, the majority of 3D models that exhibit a diminution of migration speed due to heterogeneity ($log(V_r) < 0$), are characterised by larger relative migration speeds in 2D. For instance, Model 14 ($\frac{r_y}{r_z}$=2, $\frac{r_y}{r_x}$=0.1, $\frac{r_y}{L}$=0.2) results in a relative migration speed of 0.7 in 3D, which increases to 1.2 in 2D. By examining Figure 6.14b, we also find that the difference in migration speed between the 2D and 3D models is not attributed to $\frac{r_y}{L}$. Overall, these results imply that the impact of capillary heterogeneity is dampened when reducing the domain dimensions from 3D to 2D.

We also assess these results against the 2D results presented in Jackson and Krevor (2020). The authors studied the impact of capillary heterogeneity on CO_2 flow at the Goldeneye field in the UK. They simulated CO_2 injection in fine-scale, high resolution domains with dimensions (y,z) 50 m and 5 m, varying the correlation length ratio, at a frontal advance rate of 0.2 m·d^{-1}. Thus, this analysis provides a direct comparison between the CO_2 flow behaviour at the Goldeneye and Endurance sites.

We plot the relative migration speeds from our medium rate 2D simulations alongside those from Jackson and Krevor (2020) in Figure 6.14c. There is a significant contrast in the relative migration speeds obtained from both studies. Generally, our simulations are characterised by a much larger spread in relative migration speeds. Whilst Jackson and Krevor (2020) found a maximum relative migration speed of 1.4 in this parameter space, our simulations reach a

relative migration speed of 12. This suggests that the impact of heterogeneity is more significant in models implementing data from the Endurance site.

This can be attributed to the parameters used in the statistical approach. The Goldeneye field is characterised by a smaller variation in porosity, a standard deviation of 0.0243 was imposed to generate the correlated models (Jackson and Krevor, 2020). In comparison to this, the Endurance site exhibits a stronger variation in the porosity well data with a standard deviation of 0.049. Therefore, the strength in capillary heterogeneity between the two studies varies, which will ultimately impact the trends we observe. This demonstrates that the pronounced impact of capillary heterogeneity will likely vary between geological settings. These findings also highlight the importance of accurately interpreting and characterising the well log information as this can otherwise lead to erroneous results.

Reduced-dimensionality models are commonly used to conduct uncertainty analysis, screening studies and risk assessments for CCS projects (Bianchi et al., 2016). This is primarily driven by the reduced computational cost of 2D models. However, our findings demonstrate that there is a significant deviation in the impact of capillary heterogeneity on multiphase flow between 2D and 3D, where the 2D models exhibit a dampened impact. Thus, whilst 2D models may provide an indication of the overall trends expected at a specific site, it is crucial to represent the flow field in full 3D to make informed decisions and predictions.

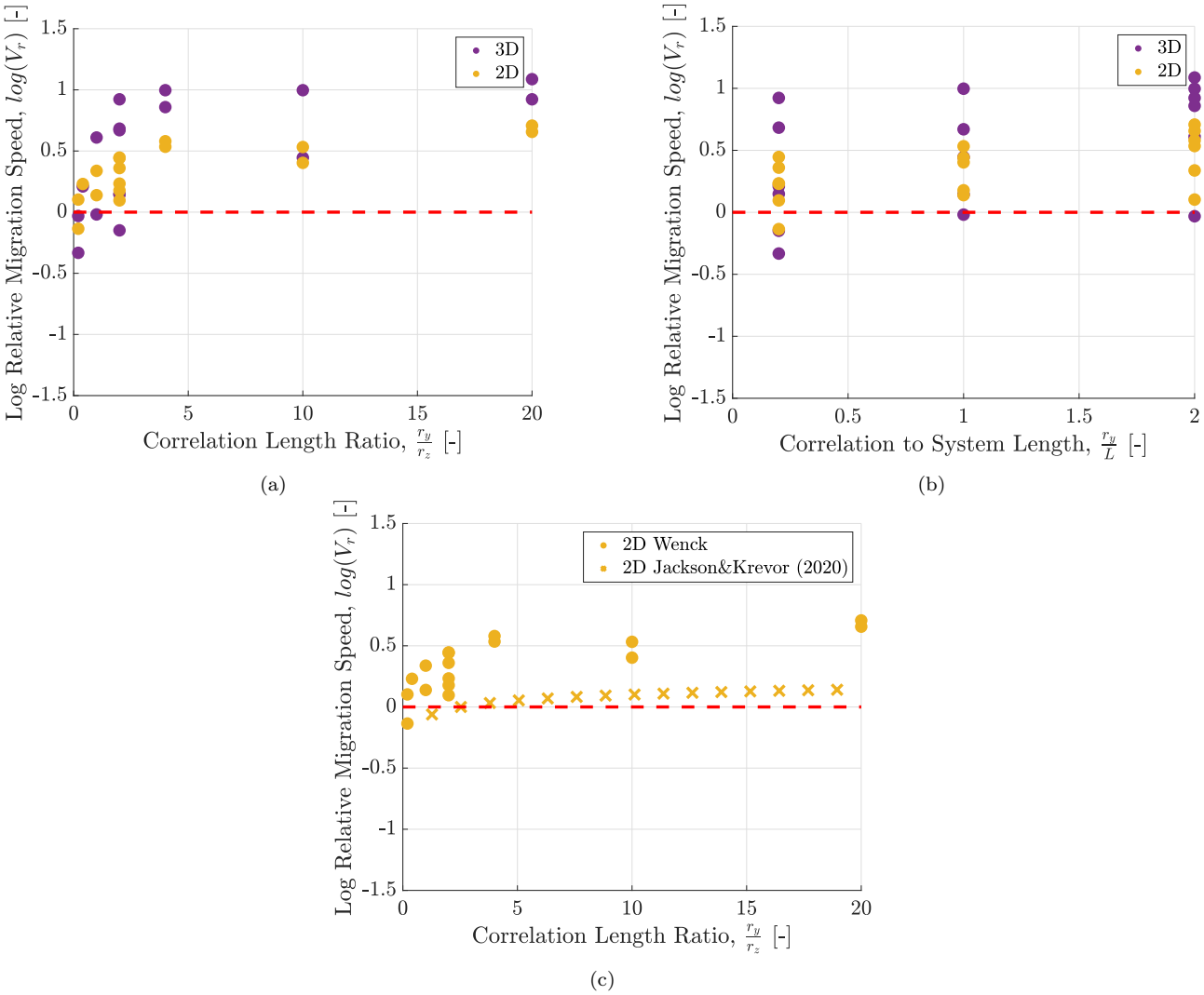


Figure 6.14: a) Relative migration speed versus a) $\frac{r_y}{r_z}$ and b) $\frac{r_y}{L}$ at a frontal advance rate of 0.2 m·d^{-1}. Purple and yellow points are the results from the 3D and 2D simulations, respectively. c) Relative migration speed versus $\frac{r_y}{r_z}$ at frontal advance rate of 0.2 m·d^{-1}. Yellow points are the results from the 2D simulations presented in this thesis and yellow crosses are results from 2D simulations conducted as part of the work by Jackson and Krevor (2020). Note: the log of the relative migration speed is plotted to emphasize which models exhibit a migration speed slower than the base case (below zero) and which models exhibit a migration speed faster than the base case (above zero). The dashed red line plotted at y=0 indicates the region where the migration speed in the model is unchanged from the base i.e. heterogeneity has no impact on the migration speed of that model relative to the uncorrelated base case.

6.3.3 Impact of Capillary Heterogeneity at Varying Flow Rate

In the previous section, we show how the orientation and length scales of heterogeneity affects CO_2 plume migration at a typical reservoir-average rate. However, during CO_2 storage operations, the flow rate within a plume varies. In the vicinity of the injection well, viscous forces dominate and flow rates are high. Further into the reservoir, flow rates decrease and capillary forces dominate. Therefore, it is crucial to understand how the impact of capillary heterogeneity varies with flow rate. We simulate CO_2 injection at three flow rates (0.02, 2 and 200 m^3d^{-1}) on the 19 models to cover a range of plausible flow regimes. As we presented the results from Q = 2 m^3d^{-1} in the previous sections, we now focus on comparing the low (0.02 m^3d^{-1}) and high (200 m^3d^{-1}) rate cases only.

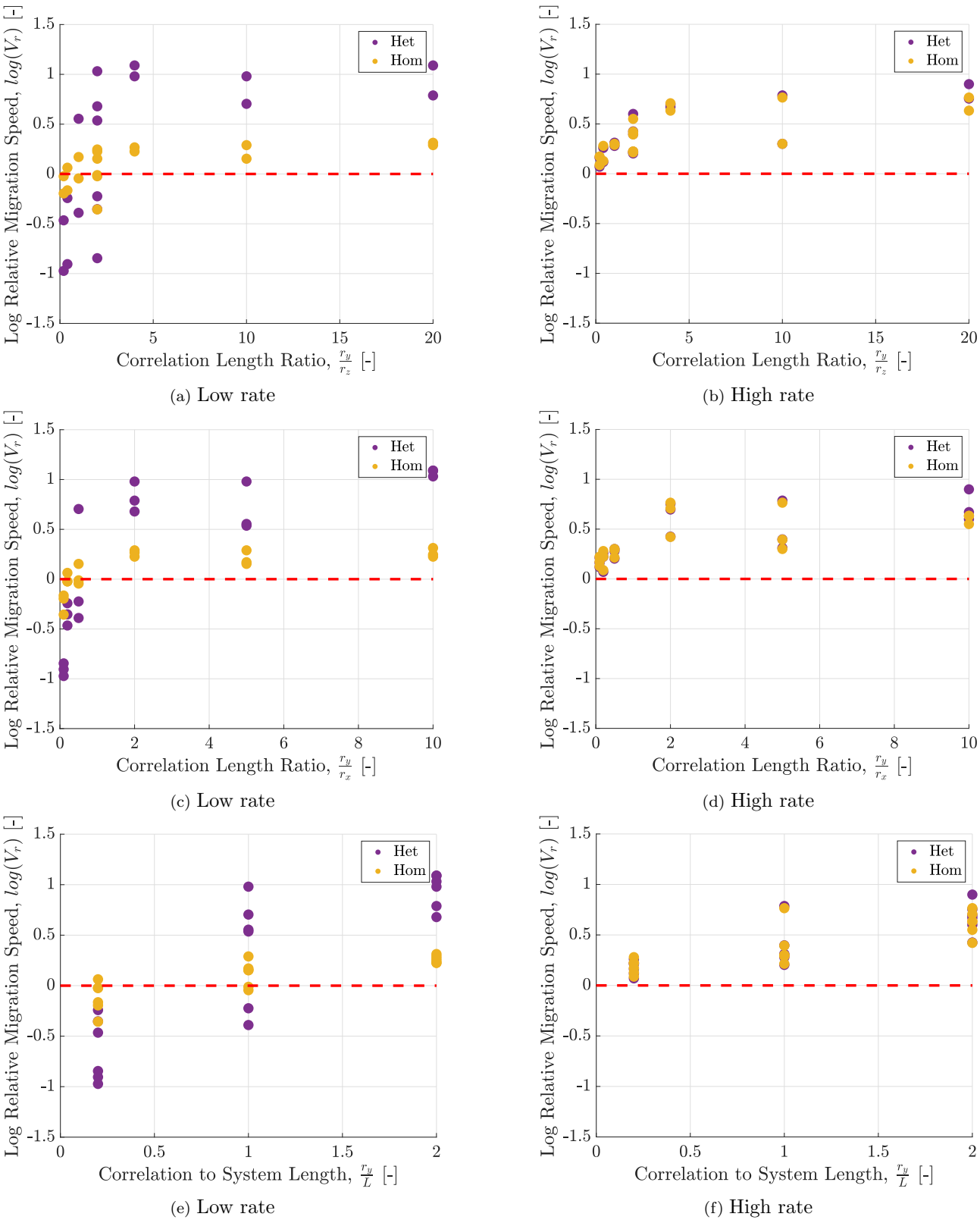
Figures 6.15 and 6.16 present the relative migration speeds for the low and high rate simulations. Capillary heterogeneity has a more prevalent impact on CO_2 migration at lower rates where capillary forces dominate. CO_2 migrates along preferential flow pathways characterised by low entry pressures, which allows the CO_2 to migrate more quickly. In the high flow rate simulations, viscous forces force the CO_2 into the domain. The low entry pressure pathways are no longer significant and instead the absolute permeability controls the regions the gas invades.

In the low rate simulations, we observe an increased contrast in the relative migration speeds between the homogeneous (0.4-2 migration speeds) and heterogeneous runs (0.1-12 migration speeds). This indicates the enhanced impact of capillary heterogeneity at lower flow rate. The relation between speed and correlation length ratios observed in the medium rate simulations is preserved in these low rate runs. Migration speeds lower than 1 are encountered in models with small $\frac{r_y}{r_x}$, where the CO_2 cannot easily migrate towards the outlet. This can ultimately slow down the plume by a factor of 10. As $\frac{r_y}{r_x}$ and $\frac{r_y}{r_z}$ increase, the CO_2 flows along the laterally extensive layers, resulting in accelerated migration by a maximum factor of 12. This emphasizes the impact that capillary heterogeneity can have on plume migration. We also observe an enhanced impact of $\frac{r_y}{L}$ on the migration speed at lower injection rates, where the relative migration speed increases significantly with an increase in $\frac{r_y}{L}$ (Figure 6.15e).

As demonstrated in Figure 6.15, the impact of capillary heterogeneity diminishes at high injection rate. The heterogeneous and homogeneous runs exhibit similar migration speeds for the majority of models. Only model 5 with $\frac{r_y}{r_x}$=10, $\frac{r_y}{r_z}$=20 and $\frac{r_y}{L}$=2 is characterised by a noticeable higher migration speed in the heterogeneous run. Interestingly, none of the relative migration speeds for the homogeneous or heterogeneous runs fall below 1 for the high injection rate. This reveals that heterogeneity only has a positive impact on flow speed, even for models with small $\frac{r_y}{r_x}$ where layers are orientated perpendicular to the principal flow axis. The viscous forces are strong enough to force the CO_2 across these layers and we do not observe a diminution of migration speed.

Based on these results, it follows that the region near the wellbore, subject to strong viscous forces due to high CO_2 flow rates, will likely experience a dampened effect of capillary heterogeneity. However, it is important to recognise that in an environment with strong heterogeneity dominant in one dimension, capillary heterogeneity may still impact CO_2 flow. As the distance to the injector is increased and CO_2 flow rates reduce, capillary heterogeneity is the dominant fluid distribution mechanism and can both, slow down and speed up, plume migration depending on the heterogeneity structure.

Figure 6.17 displays the 3D saturation distribution for model 6 ($\frac{r_y}{r_z}$=4, $\frac{r_y}{r_x}$=10, $\frac{r_y}{L}$=2) at low and high flow rate. As shown, CO_2 breaks through after only PV_{inj}=0.004 in the low rate simulation (Figure 6.17a) as a result of thin, laterally continuous channels corresponding to a high footprint area and small swept volume. Rather than buoyantly rising upwards and migrating along the uppermost layers, CO_2 flows along deeper layers in the high rate simulation as viscous forces dominate over buoyancy, leading to a large swept volume and small footprint area (Figure 6.17b). As more CO_2 is injected, more channels appear near the top of the domain at low injection rate (Figure 6.17c and 6.17e) and CO_2 flow is confined to these channels. This also reveals the increased importance of gravity forces at low injection rate. In comparison to this, the CO_2 migrates along the whole height of the domain in the high rate scenario. The plume is also uneven (Figure 6.17d and 6.17f), which is a result of the strong porosity and permeability heterogeneity imposed in the model. Overall, the gas breaks through after PV_{inj}=0.034 in the high rate scenario (Figure 6.17f), thus requiring 8.5 times more volume of CO_2.



(a) Low rate (b) High rate

(c) Low rate (d) High rate

(e) Low rate (f) High rate

Figure 6.15: Plume relative migration speed versus a) and b) $\frac{r_y}{r_z}$, c) and d) $\frac{r_y}{r_x}$, e) and f) $\frac{r_y}{L}$ for the heterogeneous and homogeneous runs at the two injection rates. Left column: 0.02 m^3d^{-1} injection rate. Right column: 200 m^3d^{-1} injection rate. Note: the log of the relative migration speed is plotted to emphasize which models exhibit a migration speed slower than the base case (below zero) and which models exhibit a migration speed faster than the base case (above zero). The dashed red line plotted at y=0 indicates the region where the migration speed in the model is unchanged from the base i.e. heterogeneity has no impact on the migration speed of that model relative to the uncorrelated base case.

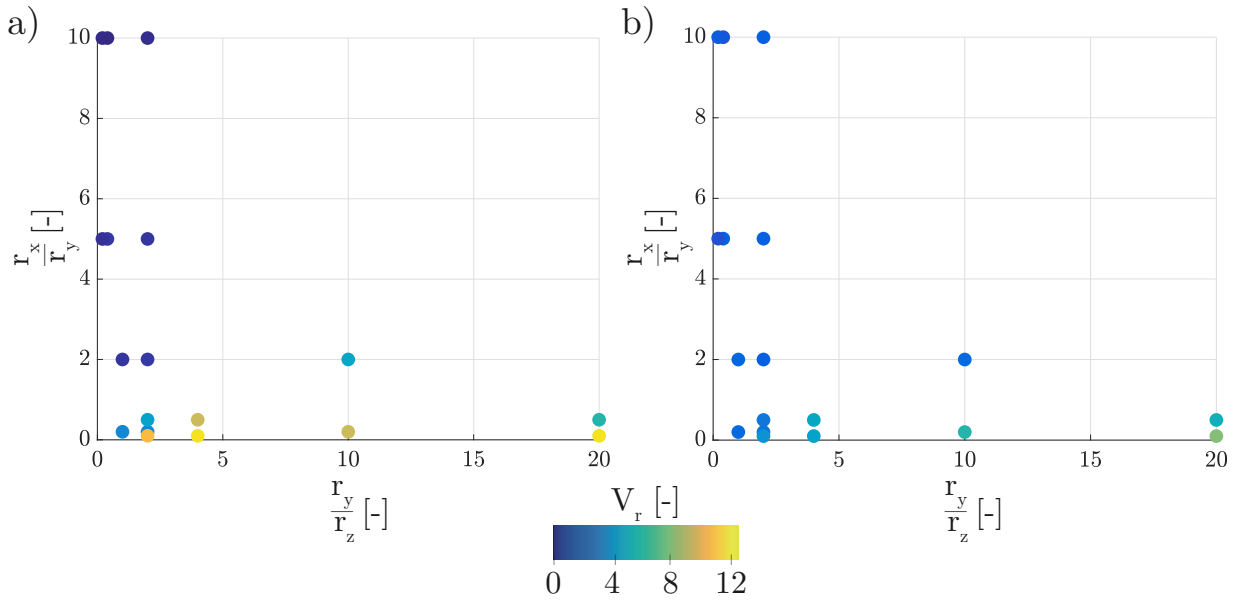


Figure 6.16: Relative migration speed of the heterogeneous runs for a) 0.02 m^3d^{-1} and b) 200 m^3d^{-1} injection rate simulations plotted against their respective correlation length ratios.

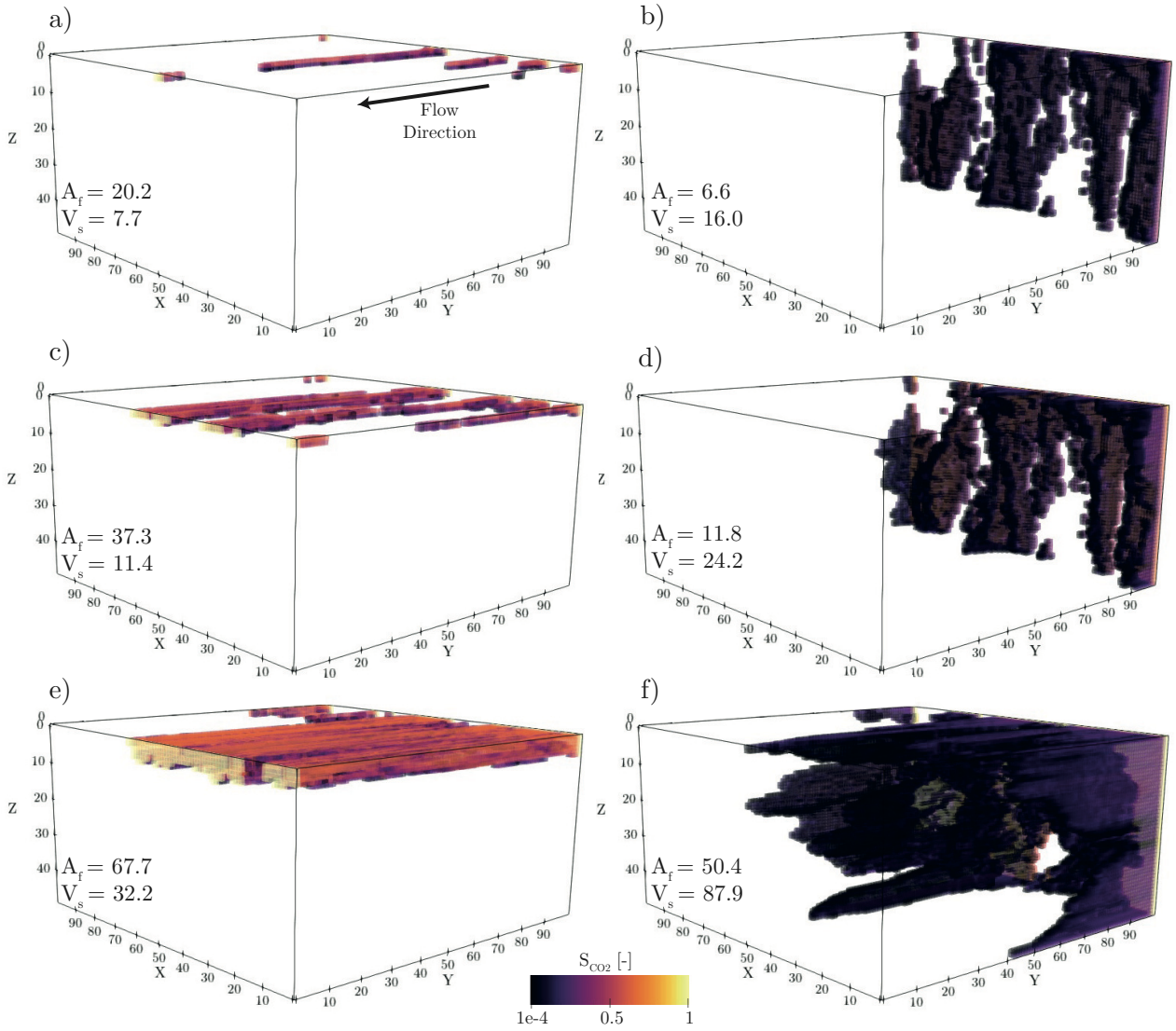


Figure 6.17: CO_2 saturation distribution from model 6 ($\frac{r_y}{r_z}$=4, $\frac{r_y}{r_x}$=10, $\frac{r_y}{L}$=2) at different PV_{inj}. Left: 0.02 m^3d^{-1} injection rate. Right: 200 m^3d^{-1} injection rate. a) and b) PV_{inj} = 0.004, c) and d) PV_{inj} = 0.008, e) and f) PV_{inj} = 0.035. Annotations in the figure correspond to the footprint area (A_f) and swept volume (V_s) of the plume in m^2 and m^3, respectively.

6.3.4 Tilted Domain

The Endurance four-way dip closure, like many other CCS sites, is characterised by a tilt. Tilted layers will likely impact the CO_2 flow behaviour observed. To investigate this, we tilt the domain by 5° in the y-axis, which matches the average dipping angle at Endurance (White Rose, 2016a), and place the CO_2 injector downdip. The porosity, permeability and entry pressure distributions imposed in the models are kept constant.

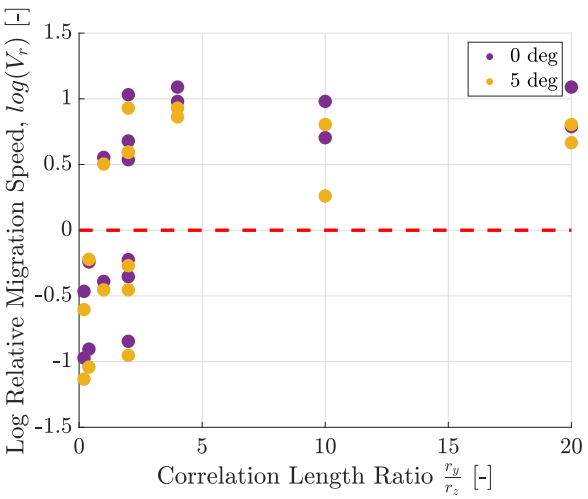
Figure 6.18 presents the resultant relative migration speeds. In these models, we find that the enhancement of plume migration speed attributed to capillary heterogeneity is dampened in a tilted domain. The buoyant force acts on the CO_2, which reduces the relative strength of capillary to buoyant forces. This is exhibited as a reduction in the relative migration speed for models with $log(V_r) > 0$ at all injection rates.

This reduction in relative migration speed enhancement becomes more severe with increasing $\frac{r_y}{r_z}$ due to the orientation of the tilt: the buoyant force acts on the CO_2 and forces it towards the outlet. This occurs in all models, even the base case with uncorrelated heterogeneity. Therefore, the relative difference in CO_2 migration speed between the base case and cases with structured heterogeneity reduces, even in models with strong heterogeneity. The high rate simulations generally exhibit a smaller percentage decrease in relative migration speed compared with the low rate cases, for instance 30% relative to 50% for a run with $\frac{r_y}{r_z}$=20. The impact of $\frac{r_y}{L}$ on migration speed also decreases in a tilted domain at all flow rates, which is attributed to the increase in buoyancy.

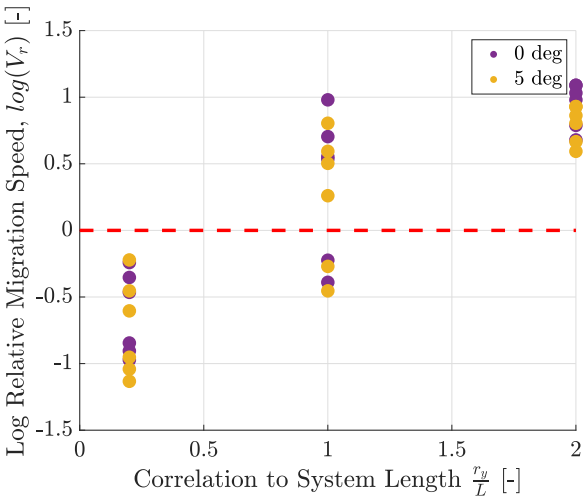
Interestingly, the diminution in relative migration speed due to the presence of capillary heterogeneity is enhanced in the tilted domains. For example, the plume relative migration speed in model 16 ($\frac{r_y}{r_z}$=0.2, $\frac{r_y}{r_x}$=0.1, $\frac{r_y}{L}$=0.2) decreases by 30% from 0.1 in the untilted model to 0.07 in the tilted model at low injection rate. Thus, whilst the enhancement of migration speed due to heterogeneity is dampened, the diminution of migration speed becomes more significant in a tilted domain.

Figure 6.20 presents the saturation distribution for model 16 ($\frac{r_y}{r_z}$=0.2, $\frac{r_y}{r_x}$=0.1, $\frac{r_y}{L}$=0.2) to explain this behaviour. The model is characterised by strong vertical and horizontal heterogeneity aligned primarily with the x-axis (Figure 6.19). As CO_2 is injected, these layers act as barriers to flow, requiring large pressures to invade them. CO_2 accumulates downdip of these layers (Figure 6.20b) until a sufficiently high phase pressure is reached (Figure 6.20d). This behaviour is observed in the untilted models, but it is enhanced here as the buoyant force drives the CO_2 updip, making it more difficult for the gas to find a preferred flow pathway. Ultimately this results in a decrease in relative migration speed compared with the untilted runs.

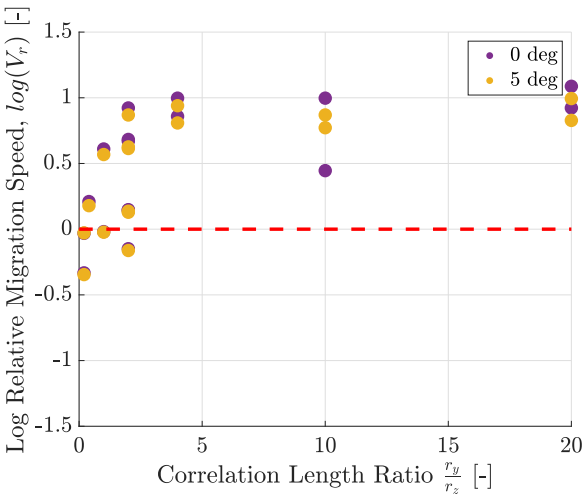
These simulations provide a novel insight into the importance of capillary heterogeneity in a tilted domain. The diminution of migration speed due to capillary heterogeneity, exhibited in models with small $\frac{r_y}{r_x}$ and $\frac{r_y}{r_z}$, reduces in a tilted domain. Whilst the enhancement of migration speed due to capillary heterogeneity also dampens with an increased reservoir dip, the impact of capillary forces is still noticeable. Similar to observations from the untilted runs, models with large $\frac{r_y}{r_z}$, $\frac{r_y}{r_x}$ and $\frac{r_y}{L}$ correspond to increased migration speeds. Thus, in a reservoir with a 5° dip or less, we would still expect to observe a noticeable effect of capillary heterogeneity. Both, Sleipner and Otway, are characterised by gently dipping slopes with laterally extensive layering. Based on our results the plumes at these sites are likely impacted by capillary heterogeneity and it is thus crucial to properly account for heterogeneity in flow simulations.



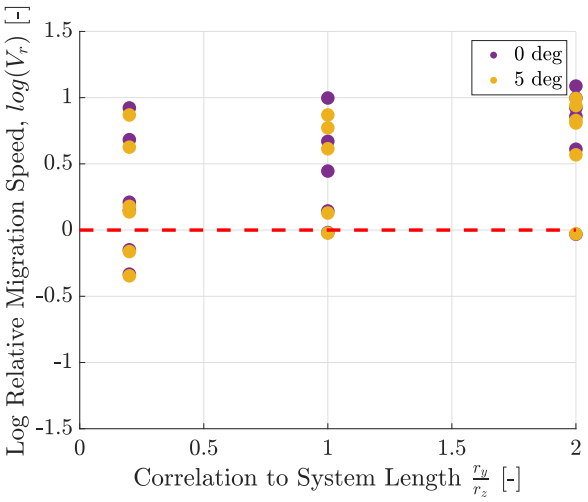
(a) Low Rate



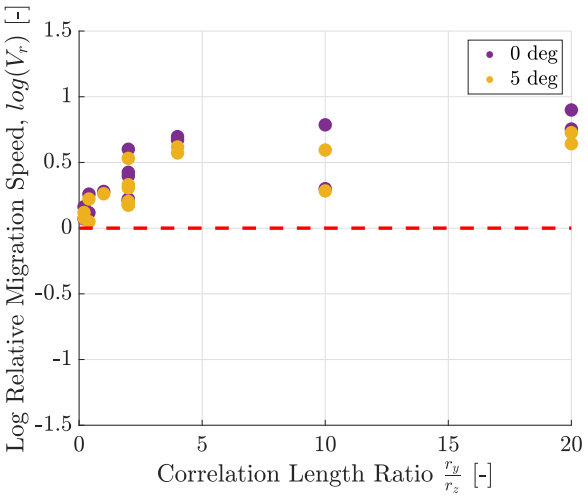
(b) Low Rate



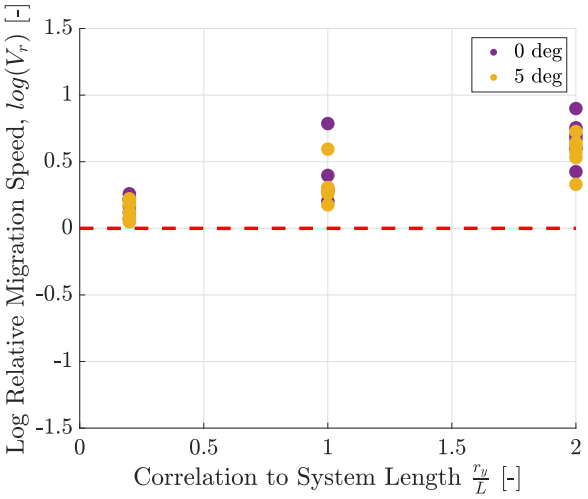
(c) Medium Rate



(d) Medium Rate



(e) High Rate



(f) High Rate

Figure 6.18: Relative migration speed for the 19 models plotted against the $\frac{r_y}{r_z}$ correlation length ratio for the untilted and tilted heterogeneous runs at the three different injection rates. Note: the log of the relative migration speed is plotted to emphasize which models exhibit a migration speed slower than the base case (below zero) and which models exhibit a migration speed faster than the base case (above zero). The dashed red line plotted at y=0 indicates the region where the migration speed in the model is unchanged from the base i.e. heterogeneity has no impact on the migration speed of that model relative to the uncorrelated base case.

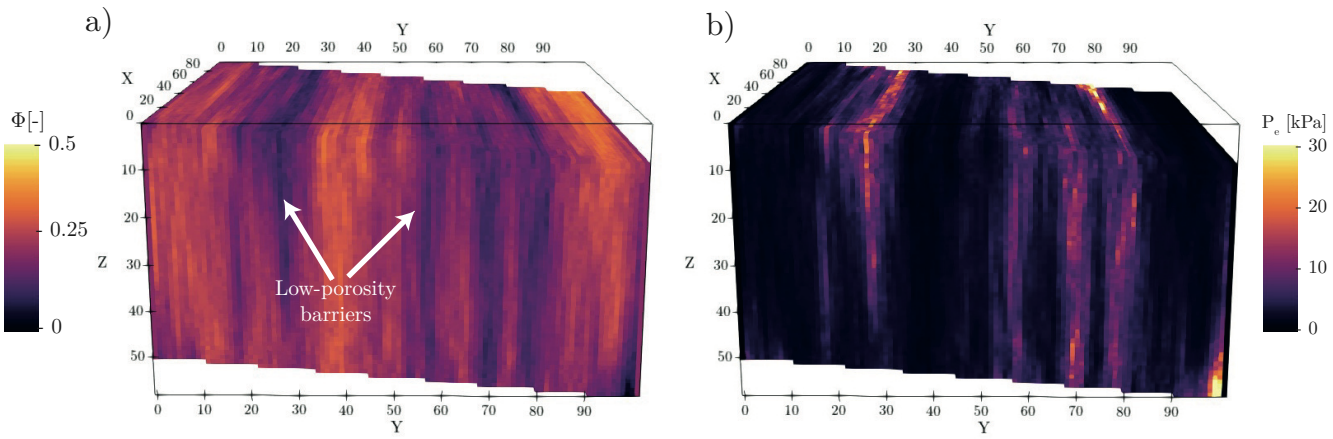


Figure 6.19: a) Porosity and b) entry pressure distribution for model 16 ($\frac{r_y}{r_z}$=0.2, $\frac{r_y}{r_x}$=0.1, $\frac{r_y}{L}$=0.2) in a tilted domain.

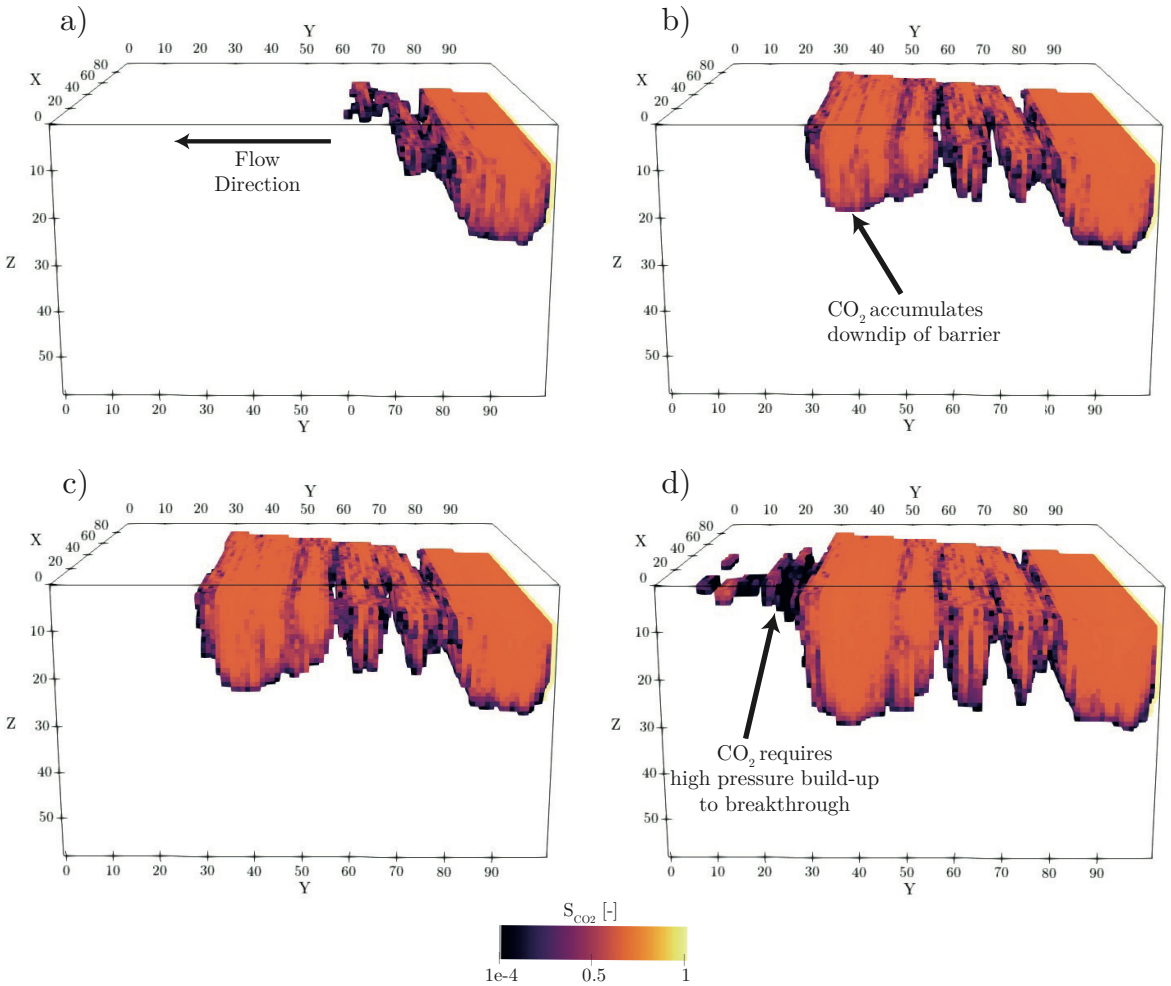


Figure 6.20: CO_2 saturation maps for model 16 ($\frac{r_y}{r_z}$=0.2, $\frac{r_y}{r_x}$=0.1, $\frac{r_y}{L}$=0.2) in a tilted domain at low injection rate at different PV_{inj}. a) PV_{inj}=0.04, b) PV_{inj}=0.08, c) PV_{inj}=0.1 and d) PV_{inj}=0.13.

6.3.5 Modelling Assumptions

We impose no-flow boundary conditions on two faces, whilst injecting and producing at constant rate from the remaining two faces. This set-up results in linear flow orientated primarily along one axis. In a reservoir, radial flow is expected near the wellbore, whereas flow becomes increasingly linear with distance from the injector. Therefore the boundary conditions imposed in the models are deemed suitable for the aim of this study: understand the impact of capillary heterogeneity on linear flow. It would be interesting to explore the impact of capillary heterogeneity on radial flow, however this is beyond the scope of this thesis. We opt for a constant flow rather than constant pressure boundary condition at the producing face, because it enables us to closely monitor the flow rates and regulate the mass of CO_2 in the domain across all runs. This allows us to directly compare the various scenarios that were simulated.

As CO_2 is injected across the whole x-z plane, the gas distribution at the inlet varies between different flow rates due to changes in the gravity to viscous ratio. This impacts the resultant plume shape. For instance, at low injection rate, the CO_2 rises buoyantly in the first few x-z slices, whereas the CO_2 is forced into the domain across the entire face at high injection rate. The aim of this study is to understand the impact of heterogeneity on linear CO_2 flow, thus the relationship between buoyant, capillary and viscous forces is key. The well set-up allows us to observe how the CO_2 first migrates into the domain under varying conditions and how buoyancy affects its flow pattern.

This study covers 19 different depositional settings and their impact on CO_2 migration in 3D, which provides an insight into the leading controls on the resultant flow and their relative importance with varying flow conditions. We build the heterogeneity as linear layers, which are the most common geological structure in sedimentary rocks, as described in Chapter 2. Furthermore, these are the heterogeneities characteristic of the Endurance CCS site, a central focus of this thesis. However, we acknowledge that the impact of less-well structured heterogeneity, such as vugs typical for carbonates (Chapter 4), may be different to the behaviour we have presented herein. Future work could explore this in more detail.

The parameter space covers three different correlation lengths in three dimensions with $\frac{r_y}{L}$=0.2, $\frac{r_y}{L}$=1 and $\frac{r_y}{L}$=2. These were chosen to cover a range of heterogeneity extremes that may occur in the subsurface on metre length scales. With correlation lengths approaching or reaching above the respective system size, system representativeness may be unattainable (Jackson and Krevor, 2020). To overcome the issue of system representativeness, a model at least 20 times the size of the correlation length in that dimension is required (An et al., 2020). In these models, keeping the same grid block resolution, this would result in a grid with dimensions 4000x4000x200, totalling over 3 billion active cells, which is completely unfeasible to run with available computing resources. However, future work could explore the model parameters and the implications on system representativeness in more detail by generating additional realisations for each model and comparing the resultant flow behaviour.

Each model takes multiple days to weeks to run, even on a high performance computing (HPC) cluster which is utilised for this study. The long run times are primarily attributed to the finely-gridded domain. Running such a large number of simulations with a commercial simulation package also requires a large number of commercial licenses that can be activated in parallel. Thus, we opt for generating one realisation for each combination of correlation lengths. We acknowledge that more realisations for each model may be needed to draw statistically meaningful conclusions. However, the overall physics and the trends of the problem can be highlighted and discussed with the current set of models.

6.4 Conclusions

Using fine-scale simulations, we investigated the impact of rock heterogeneity on CO_2 plume migration at the metre scale with varying flow rate, heterogeneity structure and tilt. The results demonstrate the prevalent impact that rock heterogeneity has on the observed CO_2 flow pattern, CO_2 plume shape and CO_2 migration speed. The simulations show that, porosity and permeability heterogeneity, the parameters typically defined in conventional reservoir simulations, have a strong impact on flow.

However, this study emphasizes the importance of characterising and incorporating capillary heterogeneity in the flow models. It can lead to a noticeable increase in relative migration speed, reaching a maximum increase of 12. This occurs when the heterogeneity is aligned parallel with the primary axis of flow, which enables the gas to invade the pore space through channels.

On the contrary, capillary pressure variations can also reduce relative migration speed, which arises when the heterogeneity is aligned perpendicular to the primary axis of flow (small $\frac{r_y}{r_x}$) or where the model is characterised by strong vertical layering (small $\frac{r_y}{r_z}$). In that case, heterogeneity can act as a barrier to CO_2, slowing it down and resulting in the accumulation of CO_2 upstream of the heterogeneity. The effects of capillary heterogeneity decrease in a 2D model, which suggests that reduced-dimensionality models may under-predict the importance of capillary heterogeneity.

By simulating CO_2 injection at a range of flow rates, we have found that the impact of capillary heterogeneity on fluid flow is emphasized at lower injection rates. This can be attributed to the relative increase in capillary to viscous forces.

In a tilted domain the relative importance of capillary forces reduces. In models with capillary heterogeneity aligned parallel to the flow axis, this results in a dampened increase in the relative migration speed. However, the results have also shown that a tilt enhances the impact of unfavourable heterogeneities aligned perpendicular to the flow axis (small $\frac{r_y}{r_x}$).

These novel findings have important implications for geological carbon storage. In the subsurface, flow is prevalently characterised by the capillary-controlled flow regime (Chang and Yortsos, 1992; Ringrose et al., 1993; Stubos et al., 1993; Yortsos et al., 1993; Chaouche et al., 1994; Honarpour and Saad, 1994; Huang et al., 1995; Mori et al., 2015). Thus, capillary heterogeneity will strongly influence CO_2 flow and it is crucial to characterise the dominant correlation lengths of heterogeneity in order to predict the flow behaviour. The models show that capillary heterogeneity affects fluid flow on a metre length scale. Therefore, to build reservoir models and simulate field-scale flow, it is crucial to upscale the impact of capillary heterogeneity from fine-scale grid blocks, which is the focus of Chapter 7.

Chapter 7

The Impact of Capillary Heterogeneity on CO_2 Flow at the Field Scale

7.1 Objectives

The previous chapter investigated the impact of capillary heterogeneity on CO_2 plume migration at the metre scale using data from the proposed Endurance CCS site. The results revealed the variations in CO_2 flow patterns that arise from capillary heterogeneity. However, the study resolved flow only on metre length scales and the impact of capillary heterogeneity on CO_2 plume migration in 3D at the field scale is largely uncertain. This chapter focuses on upscaling the impact of capillary heterogeneity on the multiphase flow properties, the capillary pressure and the relative permeability, to model kilometre scale CO_2 plume migration under the influence of capillary heterogeneity. For this purpose, we focus our investigation on the proposed Endurance CCS site, which is characterised by strong lateral and vertical rock heterogeneity. Furthermore, the site is a four-way dip closure with distinct topography, which enables us to investigate the interplay between buoyancy and heterogeneity in more detail, following results from Section 6.3.4 of the previous chapter. We also explore the impact of well location on the resultant plume migration.

7.2 Methods

7.2.1 Building a Fine-Scale Reservoir Model

We build a fine-scale reservoir model, informed by well log data, coreflood measurements and geological constraints following a geostatistical approach based on the work by Jackson and Krevor (2020). We opt for a geostatistical approach for two principal reasons. Firstly, a simplified statistical representation compared with a real geologic system allows us to clearly identify the role of salient features including correlation lengths and degree of heterogeneity on plume migration. Secondly, the geostatistical information is obtained directly from data collected as part of characterisation studies performed on the Endurance site. Therefore using geostatistics we can control the field properties including the dominating correlation lengths and ensure they align with available data from the Endurance site. The additional creation of a model with geologically representative sedimentary structures, such as cross-beds, forms a natural next step for which the analyses presented herein will provide important insights.

White Rose (2016a) also state: "Based on the distribution of facies porosity from well 42/35d-3 core, reservoir quality was found to be largely independent of depositional facies [...] The formation as a whole can be approximated to a single "tank", with occasional laterally impersistent barriers to vertical permeability associated with thin mudstone horizons, and more widespread baffles associated either with concentrations of such mudstones (e.g. within playa margin facies), or cemented horizons". This further justifies the use of the geostatistical approach. Additionally, the objective of this work is not to predict the flow behaviour at the Endurance site, but rather identify the potential degree of impact of incorporating small-scale heterogeneity. The study will provide key insights into the main drivers of CO_2 plume migration in 3D under the influence of gravity using the geological setting of a real, proposed CCS site. Thus, our results can provide generalised conclusions.

Our model, with dimensions (x,y,z) 6000 m, 4000 m and 250 m, encloses the central portion of the Endurance anticline, as shown in Figure 7.1. This was driven by computational constraints and data availability. Nonetheless, the extent of the model was chosen to enclose the location of four out of five CO_2 injectors planned for phase 1 of the Northern Endurance Partnership project (Figure 7.1). Thus, we can simulate the flow behaviour in the central portion of the reservoir with reference to the development plan. The model is characterised by fine-scale grid block sizes of (x,y,z) 10 m, 10 m and 1 m. The grid block size was chosen to be suitable to represent the smallest discretisations of the geological setting based on information provided in BEIS (2021e).

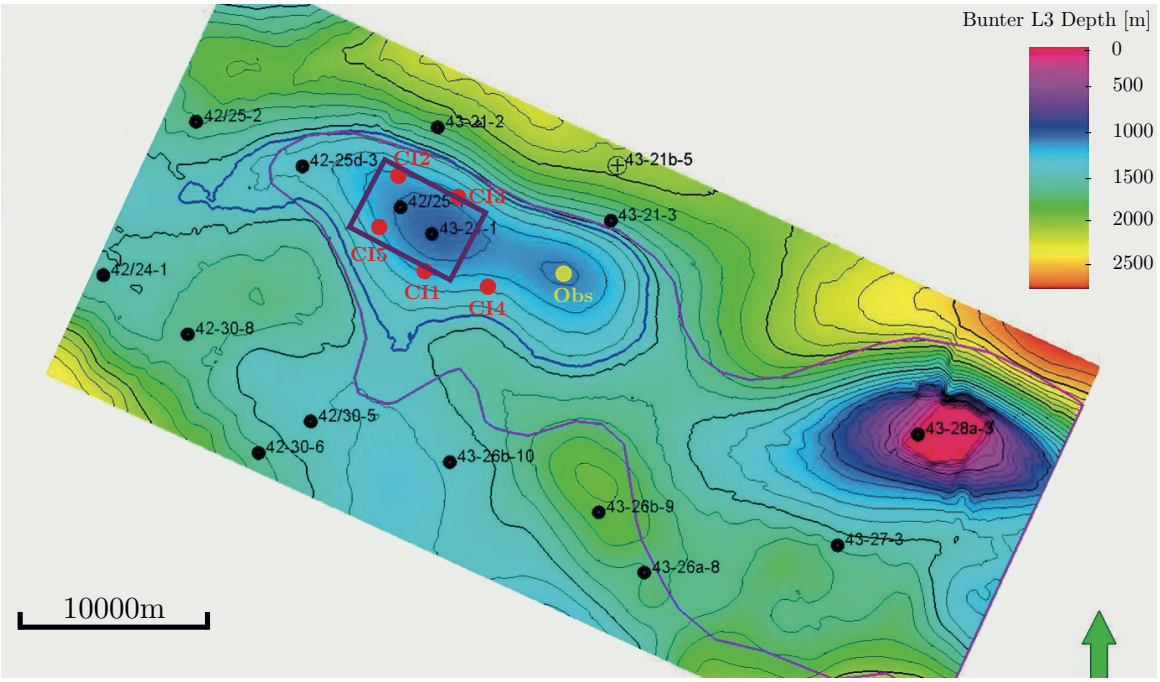


Figure 7.1: Endurance field development plan displaying the location of five CO_2 injectors and one observation well. The purple box represents the approximate outline of our model domain. Adapted from BEIS (2021b).

We follow the same geostatistical approach as presented in Chapter 6. A random porosity field is generated on the fine-scale grid using the standard deviation obtained from fitting an extreme value distribution to the porosity data of well 42/25d-3 (Figure 7.2c). The extreme value functional form was chosen to be the most suitable fit for the porosity data as it captures the peak at low porosity, which was underpredicted with a log-normal or normal functional form.

The anisotropic, correlated porosity field is produced with ellipsoidal averaging, originating in

the work by Durlofsky et al. (1997) and applied to a 2D model in Jackson and Krevor (2020). The correlation lengths in our model are set to (r_x,r_y,r_z) 1000 m, 760 m, 4 m. r_x and r_y are based on a geological study provided in BEIS (2021e). r_z was obtained by generating a semi-variogram using the porosity data from well 42/25d-3, as shown in Figure 7.2b. The initial sill distance of 4 m, plotted as a purple line in Figure 7.2b, indicates the correlation length of the vertical heterogeneity. The variogram is also characterised by periodicity at larger lag distances, which is indicative of depositional periodicity (Gringarten and Deutsch, 2001; Jackson and Krevor, 2020).

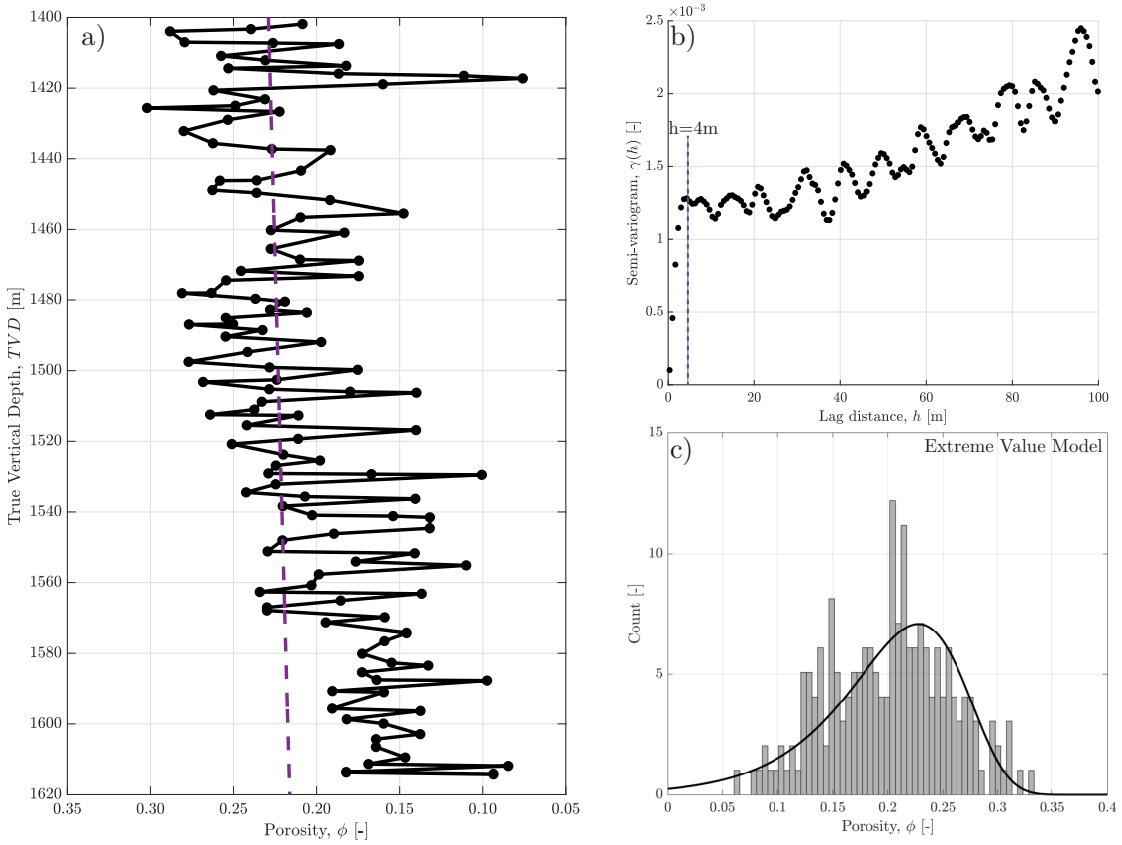


Figure 7.2: a) Porosity data from well 42/25d-3 alongside the porosity-depth trend plotted as a purple line and obtained from White Rose (2016a): $\phi = \frac{TVDSS-5331.5}{-171.68}$. "The porosity-depth trend was estimated from good quality Bunter Sandstones from 7 wells in the Endurance area" (White Rose, 2016a). b) Semi-variogram of the porosity data. The purple line indicates the initial sill distance at 4 m. c) Histogram of the porosity data alongside the extreme value distribution fit with $\mu = 0.23$ and $\sigma = 0.049$.

The correlated field is re-scaled to match the mean and standard deviation from the extreme value model of the porosity well data, and the depth transform from Figure 7.2a is applied. This results in a correlated field that matches the statistical information obtained from characterisation and data collection studies conducted as part of the Northern Endurance Partnership

project. The reader is referred to Jackson and Krevor (2020) Section S3 in the supplementary information for a detailed verification of the geostatistical approach. After the correlated field is generated, the four-way dip closure, characteristic of the Endurance site, is applied to the data with a depth transform. The depth transform follows the topography of the top Bunter sandstone presented on contour maps in White Rose (2016a). The resultant top structure of our model is presented on a topography contour map in Figure 7.3.

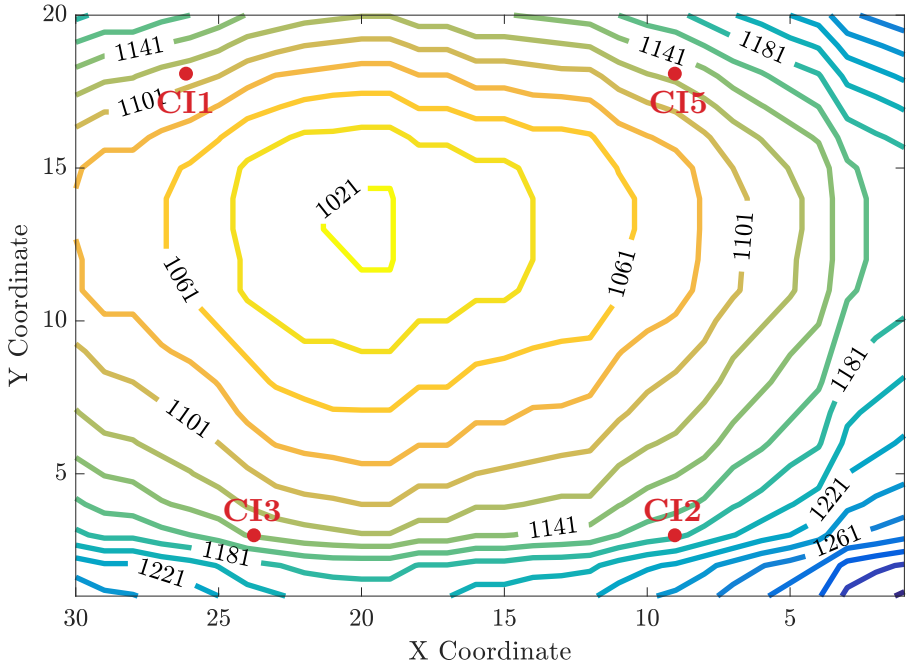


Figure 7.3: Contour depth map of the top structure in metres plotted against the grid coordinates of the model domain. The shallowest point is located at (x,y) coordinates: (19,12). The location of the four injectors (CI1,CI2,CI3,CI5) from the field development plan (Figure 7.1) enclosed in our model domain are also plotted. The coordinates are (x,y): CI1 (26, 17), CI2 (9,3), CI3 (24,3), CI5 (9,17).

The fine-scale grid block permeability is calculated using the porosity-permeability trend from BEIS (2021e):

$$K = 10^{4.19log(\phi)+5.17} \quad , \tag{7.1}$$

where K is the permeability and ϕ is the porosity. We calculate the fine-scale entry pressure distribution using J-function scaling (Equation 2.11), where the J-function is determined from MICP data collected on samples from the Endurance site, see Chapter 5.

7.2.2 A 3D Capillary-Limit Upscaling Workflow

The fine-scale model has 60 million grid blocks, which is unfeasible to use in a fluid flow simulator, even with state-of-the-art computational resources available to us. Therefore, the fine-scale grid properties need to be upscaled, which will reduce the number of grid blocks in the model. As discussed in Chapter 2, two-phase, flow-based upscaling schemes can be categorised into pseudoisation and steady-state methods, following local, local-global or global approaches. Pseudoisation methods are less suitable for heterogeneous domains and are also more sensitive to boundary conditions (Christie, 2001). Thus, we focus on steady-state upscaling schemes.

The fine-scale model is characterised by strong heterogeneity, which is expected to be the dominant fluid distribution mechanism, even at a relatively large scale. Thus, to incorporate the impact of capillary heterogeneity on the multiphase flow properties, a capillary-limit upscaling approach is more suitable. A simple calculation can be performed to estimate whether capillary-limit flow conditions are likely to hold in an upscaled grid block with dimensions (x,y,z) 200 m, 200 m and 3 m. The Endurance field development plan states a proposed average well injection rate of 3130 m^3d^{-1} (BEIS, 2021b). This corresponds to a flow rate on the order of 10^{-8} m^3s^{-1} at a radial distance of 100 m from the injector. Using a CO_2 viscosity of $\mu = 4.74 \cdot 10^{-5}$ Pa·s, an average permeability of 1 D, we estimate a pressure drop of 2 Pa across a coarse grid block with a 200 m length. We estimate ΔP_c, the contrast in capillary pressure imposed by the heterogeneities, as $P_c(S_{wirr}) - P_c(S_w = 1)$, taken from the MICP data corrected for CO_2-brine. It follows that $\Delta P_c = 40$ kPa. We estimate the corresponding capillary number, N_c, from $N_c = \frac{H}{L}\frac{\Delta P}{\Delta P_c}$ (Virnovsky et al., 2004), with $H = L = 200$ m and find $N_c \approx 10^{-5}$.

This demonstrates that capillary forces likely dominate at a distance of 100 m from a well. Our upscaled grid block sizes have dimensions of 200 m in the x and y. Thus, the block where the injector is completed is likely to be the only block where viscous forces dominate. This signifies that capillary-limit upscaling is suitable to be applied in this work. To further verify that the capillary-limit assumption holds, we perform an extensive verification study presented in Section 7.2.2.4, which confirms that the upscaling approach is appropriate to use.

We base our approach on the work by Jackson and Krevor (2020), who developed a steady-state, capillary-limit upscaling scheme using macroscopic invasion percolation for 2D domains. Their method is grounded in theoretical developments of macroscopic invasion percolation and steady-state upscaling (Pickup and Stephen, 2000; Virnovsky et al., 2004; Braun et al., 2005; Wolff et al., 2013; Yang et al., 2013; Odsæter et al., 2015; Hilden and Berg, 2016; Rabinovich et al., 2016). Rather than using an adaptive mesh approach (Wolff et al., 2013), Jackson and Krevor (2020) implemented a fixed, uniform Cartesian mesh, which simplifies the method and ensures the algorithm is parallelisable. Through this, the method becomes more easily applicable to full 3D problems, which is the focus of this thesis.

Chapter 6 examined the interplay between heterogeneities extending in all three dimensions and their significance on the resultant CO_2 flow pattern. The results emphasized the importance of representing the CO_2-brine system as a full 3D problem, which allows for the presence of 3D heterogeneity to be characterised and its impact on flow behaviour to be modelled. Motivated by this, we extend the workflow from Jackson and Krevor (2020) to the third dimension and apply it to the fine-scale reservoir model of the Endurance site. The site is characterised by strong heterogeneity in all three dimensions indicated by the correlation lengths implemented in the geological model. Endurance also has a distinct, four-way dip closure, which will likely interact with the CO_2 as it migrates through the pore space. Therefore, extending this upscaling scheme to 3D allows us to understand the leading controls on the CO_2 flow behaviour. The approach is outlined in the subsequent sections.

7.2.2.1 Porosity Upscaling

The global domain consists of $N_I \times N_J \times N_K$ coarse grid blocks. Each coarse grid block consists of $n_i \times n_j \times n_k$ fine-scale cells with assigned petrophysical parameters ϕ_{ijk}, K_{ijk} and $P_{c,ijk}$. The upscaled porosity of each coarse grid block is calculated using volume averaging:

$$\phi^* = \frac{1}{V_t} \sum_{i=1}^{n_i} \sum_{j=1}^{n_j} \sum_{k=1}^{n_k} \phi_{ijk} V_{ijk} \quad , \tag{7.2}$$

where ϕ^* is the effective porosity, V_t is the volume of the coarse grid block, V_{ijk} and ϕ_{ijk} is the volume and porosity of fine-scale block ijk.

7.2.2.2 Permeability Upscaling

As the permeability field in each coarse grid block may not be clustered into simple structures, analytical solutions cannot be used to calculate the upscaled permeability. Instead, a pressure solver method is applied, whereby flow is imposed separately in each dimension for each coarse grid block. The effective permeability in each dimension is calculated using the average pressure drop across the domain using Darcy's law:

$$K_x^* = \frac{Q_x \mu L_x}{\Delta P_x A_{yz}} \quad , \tag{7.3}$$

$$K_y^* = \frac{Q_y \mu L_y}{\Delta P_y A_{xz}} \quad , \tag{7.4}$$

$$K_z^* = \frac{Q_z \mu L_z}{\Delta P_z A_{xy}} \quad , \tag{7.5}$$

where x, y and z refer to each dimension, L is the length, A is the cross-sectional area, Q is the specified volume flux, μ is the viscosity and ΔP is the average pressure drop.

7.2.2.3 Capillary Pressure and Relative Permeability Upscaling

To account for fluid connectivity, we adopt a macroscopic invasion percolation approach to obtain upscaled, drainage capillary pressures and relative permeabilities for each coarse grid block. The saturation range, from $S_w = S_{wirr}$ to $S_w = 1$, is split into 40 equal increments, which results in a saturation resolution of approximately 0.025. The increments represent the desired water saturations, S_w^*, at which the upscaled macroscopic flow functions will be calculated. The domain is fully saturated with wetting phase. The initial, macroscopic boundary pressure, P_b^* is set to the average capillary pressure, P_c , at S_w^*. The local system is invaded with non-wetting phase starting from the boundary at which the macroscopic pressure is applied. A fine cell is invaded if it meets two criteria: 1) is is connected to the outlet or to a fine cell that is connected to the outlet, 2) the P_b^* exceeds the local entry pressure $P_{e,ijk}$. Away from the block boundaries, two additional potential flow pathways are introduced into the percolation approach when considering a 3D, rather than 2D, domain. These are incorporated into the percolation algorithm. Once all accessible and available cells are invaded, the fine-scale saturation distribution, $S_{w,ijk}$, can be inverted from the fine-scale capillary pressure, $P_{c,ijk}$, using the fine-scale P_c-S_w functional form:

$$S_{w,ijk} = S_w(P_{c,ijk} = P_b^*) \quad , \tag{7.6}$$

The upscaled saturation in each coarse grid block is calculated using volume averaging:

$$S_w^* = \frac{1}{\phi^* V_t} \sum_{i=1}^{n_i} \sum_{j=1}^{n_j} \sum_{k=1}^{n_k} S_{w,ijk} \phi_{ijk} V_{ijk} \quad , \tag{7.7}$$

If the difference between the obtained upscaled S_w^* and the desired S_w^* is greater than 0.001, the boundary pressure P_b^* is updated using a Newton-Raphson iteration:

$$P_{b,new}^* = P_{b,old}^* + \Delta S_w^* \frac{\delta P_b}{\delta S_w^*} \quad , \tag{7.8}$$

where the gradient $\frac{\delta P_b}{\delta S_w^*}$ is either determined from past iterations or from the P_c-S_w functional form. After $P_{b,new}^*$ has been determined, the macroscopic invasion percolation procedure is repeated, until the difference between the obtained upscaled S_w^* and the desired S_w^* is below the error threshold. Once achieved, the upscaled capillary pressure can be calculated using the intrinsic phase averages:

$$P_c^* = \frac{1}{\phi^* V_t S_{nw}^*} \sum_{i=1}^{n_i} \sum_{j=1}^{n_j} \sum_{k=1}^{n_k} P_{c,ijk} S_{nw,ijk} \phi_{ijk} V_{ijk} \quad , \tag{7.9}$$

where $S_{nw}^* = 1 - S_w^*$.

For each coarse grid block, the fine-scale phase relative permeability distribution, $k_{rw,ijk}$ and $k_{rnw,ijk}$, is inverted from the fine-scale saturation and permeability distribution:

$$k_{rw,ijk} = k_{rw}(S_{w,ijk}) \times K_{ijk} \quad , \tag{7.10}$$

$$k_{rnw,ijk} = k_{rnw}(S_{w,ijk}) \times K_{ijk} \quad , \tag{7.11}$$

where w and nw stands for the wetting and non-wetting phase, respectively. A single phase flow simulation is performed to determine the upscaled anisotropic relative permeabilities. The flow simulation is performed individually in each dimension to obtain directional relative permeabilities. Thus, extending the upscaling approach from 2D to 3D domains requires an additional set of single-phase flow simulations for the new dimension. The fine-scale phase relative permeability distribution is used as the underlying permeability distribution, which changes for the wetting and non-wetting phase. Using the imposed flow rate and average pressure drop in Darcy's law, the macroscopic relative permeability is calculated:

$$k_{r,x}^* = \frac{Q_x \mu L_x}{\Delta P_x A_{yz} K_x^*} \quad , \tag{7.12}$$

$$k^*_{r,y} = \frac{Q_y \mu L_y}{\Delta P_y A_{xz} K^*_y} \quad , \tag{7.13}$$

$$k^*_{r,z} = \frac{Q_z \mu L_z}{\Delta P_z A_{xy} K^*_z} \quad , \tag{7.14}$$

The above steps are repeated until all 40 increments of the saturation range have been covered. Thereafter, the $k_r(S_w)$ and $P_c - S_w$ points are fitted with the LET and Brooks-Corey functional forms, respectively, to ensure the upscaled curves are smooth and monotonic.

The procedure is repeated for all coarse grid blocks until upscaled properties have been obtained for the entire domain.

7.2.2.4 Verification of the Upscaling Workflow

The upscaling scheme was extensively tested for 2D domains in Jackson and Krevor (2020), with the results presented in Section S5.1 of the supplementary information of Jackson and Krevor (2020). It was shown that the upscaled model accurately replicates the 2D CO_2 distribution at low capillary numbers. As expected, the match between the fine-scale and upscaled saturation worsens as capillary numbers are progressively increased. The scheme is based on the capillary-limit flow assumption, which does not hold at high flow rates in viscous flow conditions. The method was also successfully applied to various models with varying correlation lengths. Based on these successful results, the focus of this section is to ensure the applicability of the approach to 3D models.

We initially verify the approach using simple heterogeneity structures, where we compare the upscaled block relative permeabilities to analytical solutions. We test numerous combinations of homogeneous, layered and isotropic systems, where we derive the analytical solutions using the works by Corey and Rathjens (1956); Rabinovich et al. (2016). The results successfully match the analytical solutions, with percentage relative errors of $< 0.005\%$ or smaller.

Next, we apply the geostatistical and upscaling approaches outlined above to a model with

dimensions (x,y,z) 60 m, 60 m and 20 m. We choose this model size to reduce computational expense, whilst testing a sufficiently large domain with an adequate level of upscaling. We impose correlation lengths of (x,y,z) 30 m, 10 m, 10 m. The fine-scale and upscaled grid blocks have lengths of 1 m and 10 m, respectively, in all dimensions. Thus, we upscale by a factor of 10.

To verify the upscaling scheme, we simulate CO_2 injection on the fine-scale and upscaled models and subsequently compare the saturation distribution and pressure response. This indicates whether the upscaled model adequately characterises the flow properties and replicates the fine-scale flow pattern.

The E100 simulator, part of the ECLIPSE® simulator suite, is utilised to model CO_2 injection. E100 is a fully-implicit, three phase, three dimensional, general purpose black oil simulator (Schlumberger, 2017), which is widely used in industry. In contrast to CMG IMEX, E100 implements anisotropic relative permeabilities, which are one of the outputs from the upscaling scheme. Thus, E100 is more suited for this work. We inject CO_2 at a range of flow rates, corresponding to capillary dominated flow, for which the upscaling scheme is applicable to. The CO_2 injector is located at x=1 and y=30 (fine grid coordinates) and the producer is completed on the opposite side of the model at x=60 y=30 (fine grid coordinates). We implement no-flow boundary conditions on the remaining two sides of the model. The set up is shown in Figure 7.4.

Extensive testing reveals that grid refinement and boundary conditions significantly impact the simulation results by interfering with wells, causing pressure anomalies and convergence issues. Ultimately, this may lead to false conclusions regarding the accuracy of the upscaling scheme. Particularly with a model of this size, testing shows that the impact of wells can propagate far into the model domain. These challenges demonstrate the added complexity of simulating flow on heterogeneous models with strong capillary heterogeneity. Care needs to be taken to choose appropriate conditions suitable for a model and ensure the boundary conditions allow for comparability between the fine-scale and upscaled models.

The design shown in Figure 7.4 is found to minimise numerical issues and reduce the impact

of boundary conditions on the flow pattern. We perform local grid refinement on the region in proximity to the injector in the upscaled model ('region 1'). We assign fine-sale heterogeneous properties to these refined blocks. This allows us to implement consistent boundary conditions between both models. We also test a solution where we implement a synthetic inlet with high porosity/permeability and low entry pressure. However, this causes a severe end effect in the region between the inlet and model domain, which propagates through the entire model and leads to significant discrepancies between the fine and upscaled simulations. On the side of the producer, we set the properties of the slice to homogeneous, high porosity and permeability and constant entry pressure (set to the fine-scale average entry pressure) in the fine and upscaled models ('region 3'). This minimises the unrealistic rise in bottom hole pressure at the producer caused by strong, small-scale heterogeneity in the fine-scale model. The central region of the domain is refined to the fine-scale grid block size in the upscaled model, but with upscaled, homogeneous properties assigned ('region 2'). This reduces numerical dispersion and allows us to capture the gravity segregation.

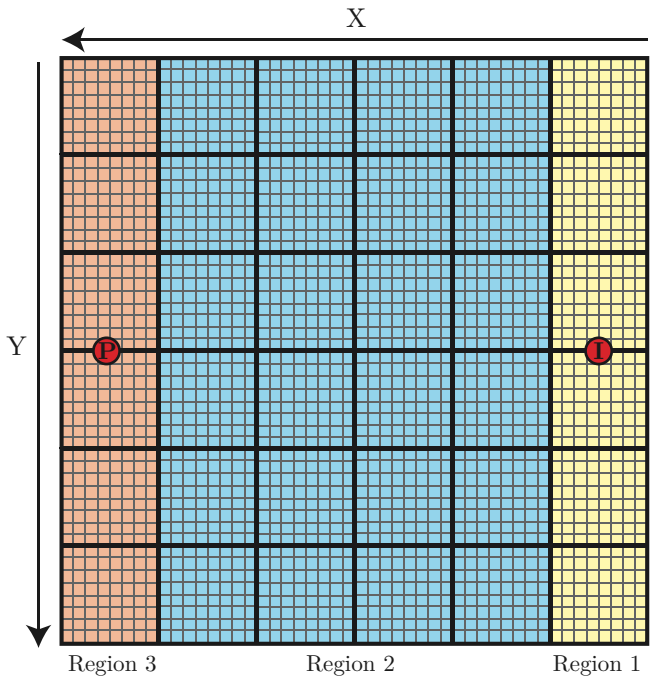


Figure 7.4: Boundary conditions and regions used to define grid refinement during the upscaling verification. The grid refers to the upscaled model dimensions and the image shows a plan view of the model. Thick lines represent the coarse cells and thin lines represent the local grid refinement. 'I' and 'P' stand for injector and producer, respectively. In region 1, local grid refinement is performed, with heterogeneous, fine-scale properties (porosity, permeability, entry pressure) assigned. Region 2 represents the central part of the domain and is refined to the fine-scale level. However, the parent cell (upscaled) properties are assigned, so they exhibit homogeneity. In region 3, a high porosity (0.3) and permeability (2000 mD) are assigned and a constant capillary pressure set to the average entry pressure.

The saturation profiles and pressure drops for the fine and upscaled models are presented in Figure 7.5, for a CO_2 injection rate of 30 m^3d^{-1}. This injection rate results in a frontal advance rate of 0.125 $m{\cdot}d^{-1}$ in our domain, which falls in the range of typical average flow rates encountered during CCS reservoir operations in an untilted domain (see Chapter 6 Section 6.3.1 for a detailed discussion). The saturation distributions closely match. The upscaled model reproduces the plume extent in both, the x and y dimensions, at all time steps. The local fluctuations of saturation in the y-axis corresponds to variations in the heterogeneity. These are captured very well in the upscaled model. The error in the pressure drop across the domain is relatively constant through time and averages to 17% over the injection period, which is an acceptable range. The error is primarily attributed to the boundary conditions imposed in the models.

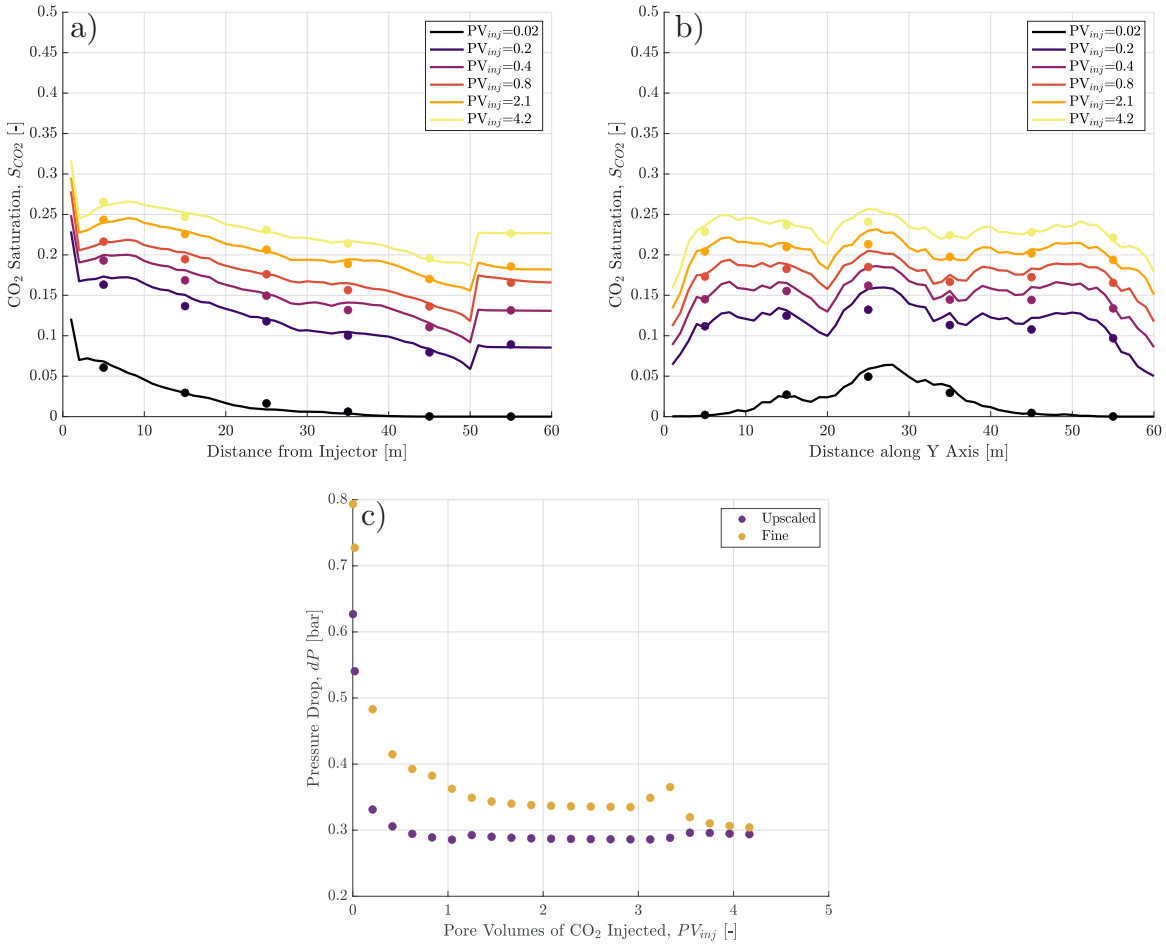


Figure 7.5: Saturation profiles along the a) x-axis and b) y-axis for the fine-scale (lines) and upscaled (points) models at a range of PV_{inj} corresponding to the color. c) Pressure drop measured from the injector and producer bottom hole pressure for the fine-scale (yellow) and upscaled (purple) simulations.

The corresponding 3D saturation distributions at different time steps are presented in Figure 7.6 and display a high correlation in block saturations between the two runs. Local saturation variations caused by heterogeneity are reproduced in the upscaled model. The cone-shaped CO_2 plume near the CO_2 injector, characterised by a lower gas saturation, is indicative of the strong, gravity-dominated flow.

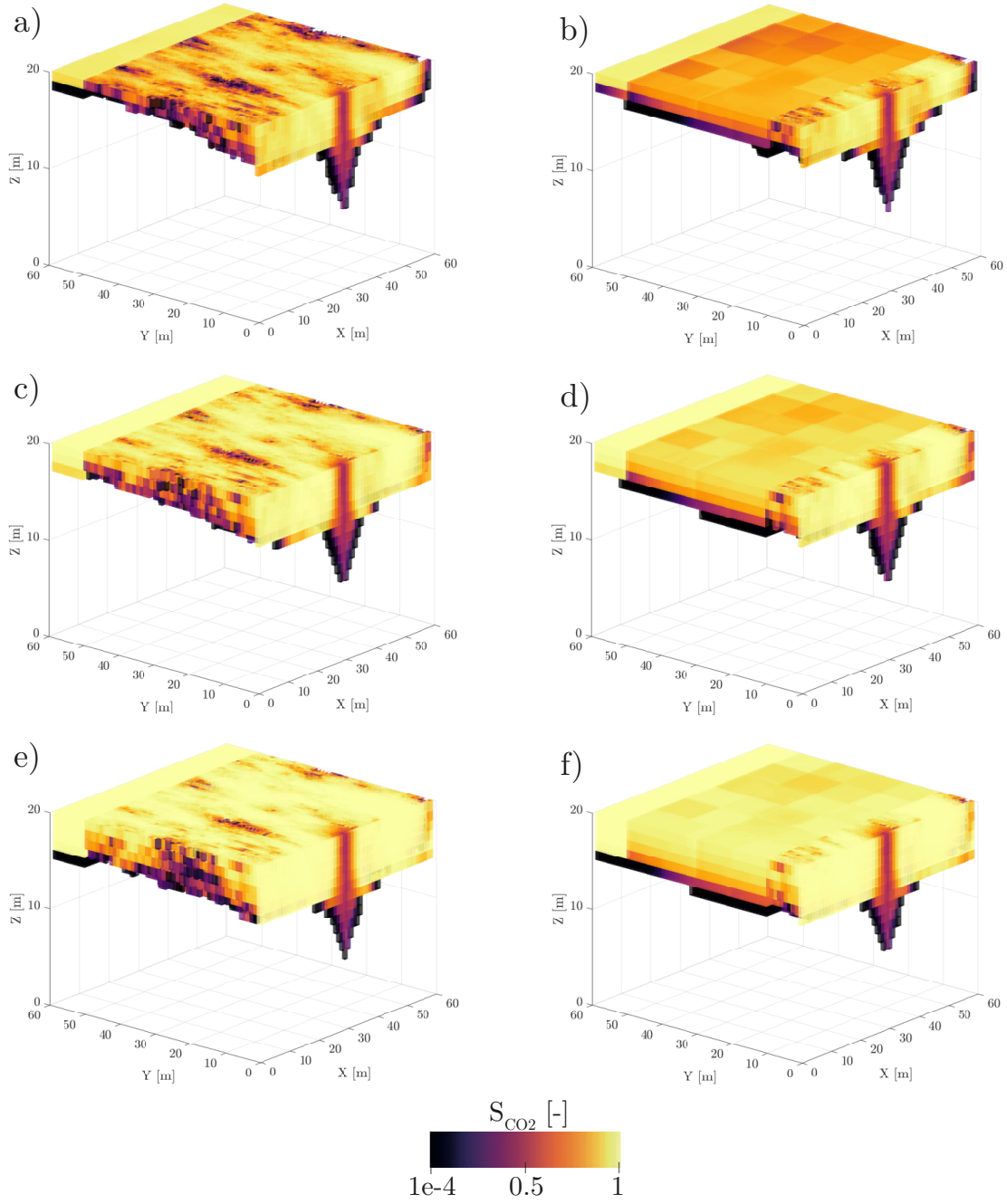


Figure 7.6: 3D saturation distribution for the fine-scale (left) and upscaled (right) models at different time steps. a) and b): $PV_{inj} = 0.2$, c) and d): $PV_{inj} = 0.8$, e) and f): $PV_{inj} = 4.2$.

7.2.2.5 Field-Scale Simulation

We use the E100 simulator to simulate CO_2 injection in our upscaled reservoir model. We simulate isothermal CO_2 injection as the focus of this study is to investigate the impact of capillary heterogeneity on flow behaviour. We acknowledge that temperature variations may additionally impact CO_2 migration as shown by Al-Khdheeawi et al. (2018) and Abdoulghafour et al. (2020). However, this is beyond the scope of this thesis. We propose a future study to separately investigate the additional impact of phase-mixing on flow behaviour. The reservoir temperature is set to 56°C (White Rose, 2016a) and the reservoir pressure is determined assuming hydrostatic equilibrium, with the depth of the top of the anticline set to 1020 m, and averages to 146.4 bar. Under these conditions the viscosity of CO_2 and brine (with average salinity of 250,000 ppm (BEIS, 2021e)) are approximately 4.74×10^{-5} Pa·s and 9.99×10^{-4} Pa·s, respectively (BEIS, 2021d). The density of CO_2 and brine are estimated to be 700 kg·m^{-3} and 1190 kg·m^{-3}, respectively (White Rose, 2016b; BEIS, 2021d). The CO_2-brine interfacial tension is approximated at 36 mN·m^{-1} (Li et al., 2012). Based on the mineral composition measured on Bunter sandstone plugs from well 42/25d-3 combined with the measurements by Haeri et al. (2020), we estimate a contact angle of 37°.

We do not incorporate dissolution effects into the simulation as the focus of this work is to understand the isolated impact of small-scale heterogeneity. Based on recent studies including Lindeberg and Begmo (2003); Ampomah et al. (2016); Gilmore et al. (2020); Yuan et al. (2020) we recognise that dissolution will likely be an important mechanism to consider in reservoir models simulating CO_2 injection, particularly in the presence of heterogeneity. However, this also significantly increases the complexity of the simulations and the flow and transport processes observed. Thus, we suggest for these effects to be incorporated in future work for which the analyses presented herein will provide important information in the interpretation.

In the vicinity of the wells, the assumption of linear flow breaks down. Thus the steady-state upscaling method described in the previous section is not appropriate to represent the radial flow encountered in this region of the model. Generally, near wellbore upscaling methods rely on a numerical flow simulation on the fine-scale grid surrounding the well (Ding et al., 1998).

For our model, this adds significant computational expense and complexity. Furthermore, the work by Muggeridge et al. (2002) demonstrates that the accuracy of near wellbore upscaling reduces in 3D models. Therefore, we choose not to apply a near wellbore upscaling scheme.

We initially implemented local grid refinement in proximity to the wells and assigned the heterogeneous, fine-scale properties to these regions. However, extensive testing of this approach discovered that the heterogeneous fine-scale grid interfered with the wells, leading to numerical errors, convergence issues and a significant, unrealistic pressure build-up in the domain. We concluded that this approach is not suitable to implement. Rather than introducing numerical errors, which could severely affect the flow pattern on the entire grid, we apply the steady-state upscaling to the entire domain including the region in proximity to the wells. We acknowledge that this may not accurately capture the radial flow near the wells. However, this solution will minimise numerical errors that would otherwise propagate further in the domain.

To limit numerical dispersion and capture the strong buoyancy effects, we refine the coarse grid blocks near the injector, but assign the upscaled properties to these cells rather than the fine-scale, heterogeneous properties. The y-z plane containing the injector is refined by a factor of 20, which generates the fine-scale grid block sizes. The y-z plane on either side of this slice is refined by a factor of 8 and the slice adjacent to this is refined by a factor of 4. Simulator testing has shown that local grid refinement can lead to severe numerical errors resulting in anomalous pressure distributions (Section 7.2.2.4). Therefore, we opt for limited local grid refinement implemented only in regions in close proximity to injectors to capture the gravity segregation.

In the analysis of the simulation results, we set a CO_2 saturation threshold of 5×10^{-3} to remove noise and numerical uncertainties from the results. A cutoff of 5×10^{-3} is able to detect 95% of the CO_2 plume at early injection times (days-weeks), which increases to 98% for later times (months-years).

7.2.2.6 2D Simulation Design

Building a full 3D model is complex, computationally expensive and time-consuming. In Chapter 6 we have demonstrated the complex flow behaviour that arises as a result of 3D heterogeneity on a metre scale. However, the value added from representing CO_2 flow in 3D at the kilometre scale with realistic well patterns has not yet been quantified and is explored in this chapter. We simulate CO_2 injection on a 2D slice extracted from our 3D upscaled model of the Endurance reservoir, see Figure 7.7. The 2D grid has 1, 20 and 192 cells in the x, y and z dimension, respectively. Each block has dimensions of (x,y,z) 200 m, 200 m and 3 m. We simulate CO_2 injection from grid location y=3, which corresponds to the location of the CI2 well in the Endurance field development plan, across a 100 m perforated interval, which also matches the field development plan. We impose constant pressure boundary conditions on the y=1 and y=20 faces. Local grid refinement is applied to the region in the vicinity of the injector to reduce numerical dispersion, following the same pattern as implemented in the 3D models. CO_2 is injected at constant rate for 25 years. We scale the target injection rate for the 3D case using the ratio of pore volumes in the 2D to 3D model. This ensures the flow regime is consistent in the 2D and 3D simulations.

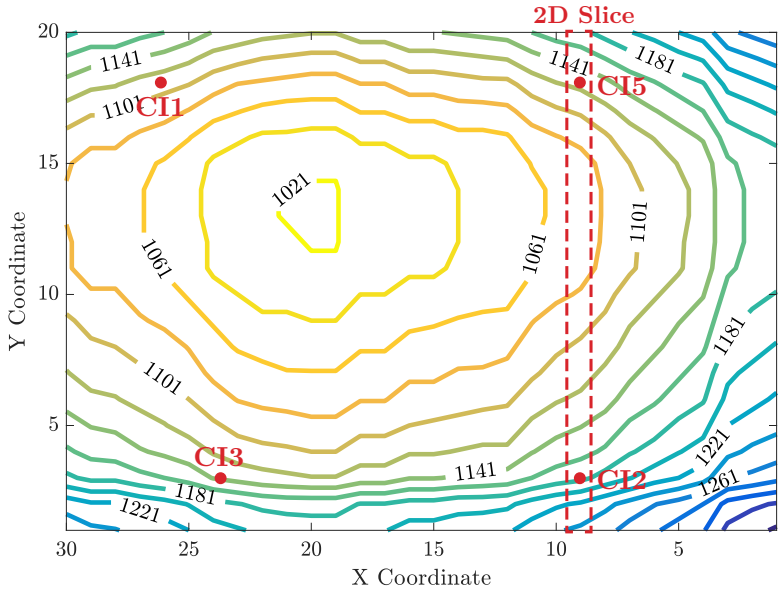


Figure 7.7: Contour depth map of the top structure in metres plotted against the grid coordinates of the model domain. The shallowest point is located at (x,y): (19,12). The location of the four injectors (CI1, CI2, CI3, CI5) from the field development plan (Figure 7.1) enclosed in our model domain are also plotted. The coordinates are (x,y): CI1 (26, 17), CI2 (9,3), CI3 (24,3), CI5 (9,17). The red dashed box represents the location of the 2D slice, which is extracted from the upscaled 3D model.

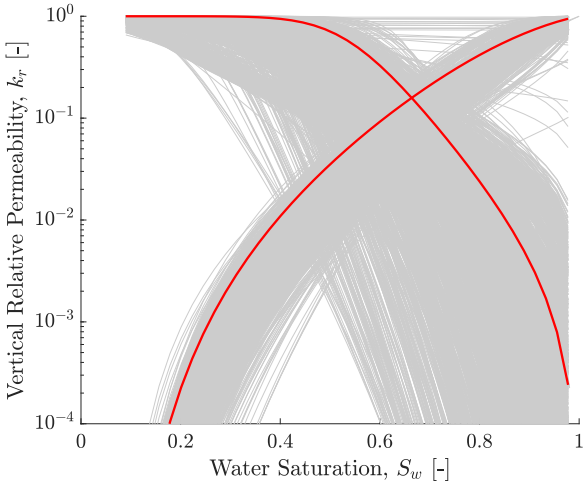
7.3 Results and Discussion

7.3.1 The Impact of Capillary Heterogeneity in 2D

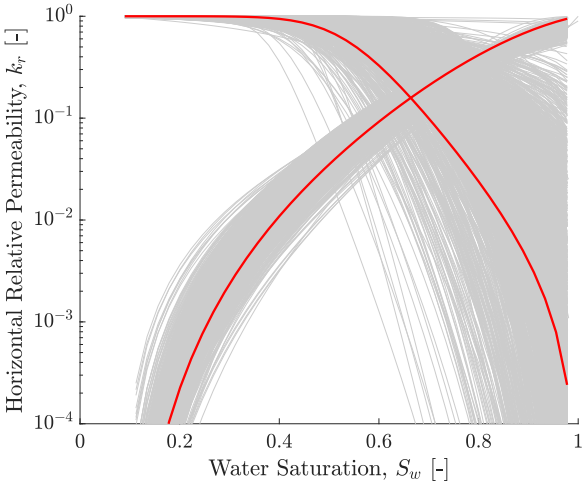
We simulate three scenarios on the 2D model to systematically evaluate the flow behaviour due to capillary heterogeneity. The first implements a constant relative permeability set to the fine-scale viscous-limit curve and zero capillary pressure, referred to as 'VL Zero' simulation in the remainder of this chapter. The second scenario imposes the heterogeneous, upscaled relative permeability and zero capillary pressure, which is referred to as 'CL Zero'. The final scenario implements the heterogeneous, upscaled relative permeability and the heterogeneous, upscaled capillary pressure, which will be termed 'CL Pc'. All models incorporate the upscaled, heterogeneous porosity and permeability field. The block relative permeabilities and capillary pressures implemented in the 2D models are displayed in Figure 7.8.

The three scenarios allow us to differentiate the impact of capillary pressure from relative permeability anisotropy. Comparing the VL Zero and CL Zero cases will provide information on the impact of relative permeability anisotropy on CO_2 fluid flow. The difference in CO_2 flow behaviour between the CL Zero and CL Pc cases provides an insight into the impact of capillary pressure variations on fluid flow. Lastly, comparing the VL Zero and CL Pc scenarios demonstrates the impact of completely omitting the impact of capillary heterogeneity on multiphase flow (VL Zero simulation) versus fully accounting for it (CL Pc simulation).

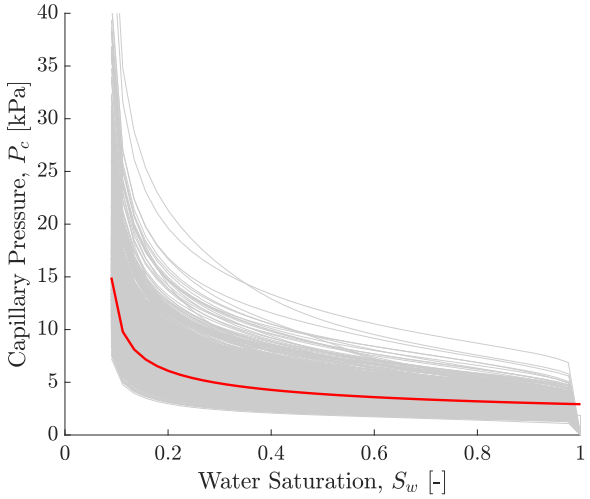
We will use the vertical and horizontal distance travelled by the plume as measures to compare the three scenarios. Vertical distance travelled is defined as the distance between the top of the CO_2 plume and the caprock at the injector location. A vertical distance of zero indicates that the plume has reached the caprock. The horizontal distance is defined as the distance along the y-axis measured from the furthest CO_2-saturated block to the injector location. Thus these measures provide an indication of 1) how far the plume has spread and 2) the migration speed (the steeper the gradient, the faster the plume is travelling).



(a) Upscaled relative permeability in z.



(b) Upscaled relative permeability in y.



(c) Upscaled capillary pressure.

Figure 7.8: Relative permeabilities and capillary pressures used as input to the 2D simulations. The red lines represent the fine-scale, intrinsic curves. The grey lines are the curves for each upscaled grid block.

7.3.1.1 The Impact of Heterogeneity on Vertical CO_2 Flow in 2D

The horizontal and vertical distance travelled by the plume in the three simulations are displayed in Figure 7.9. We find that the relative permeability is the dominant control on vertical plume migration speed as it significantly slows the vertical rise of the plume.

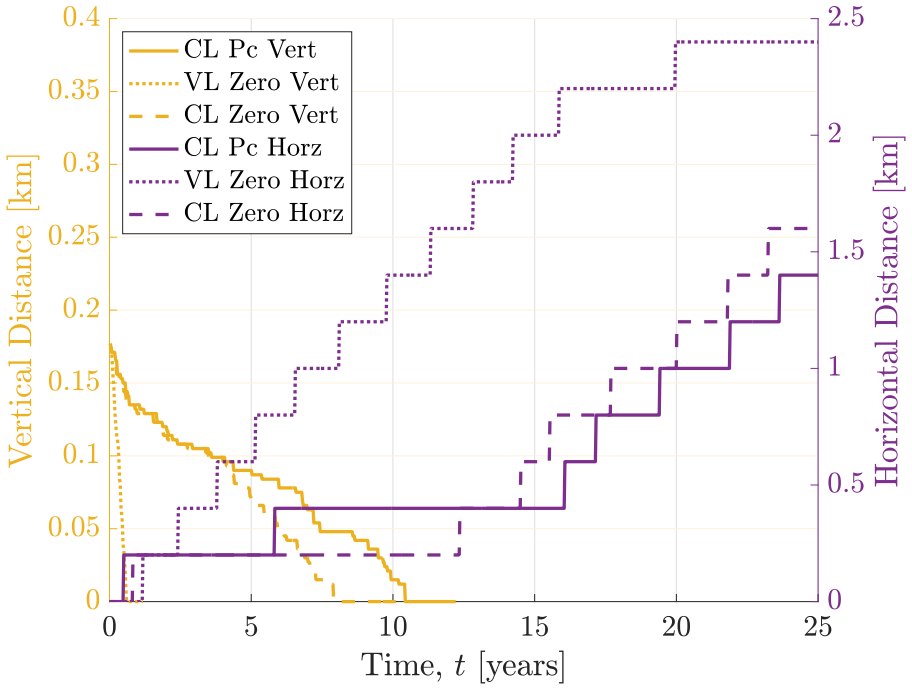


Figure 7.9: Vertical and horizontal travelled distance of the plume for the three 2D models. Vertical distance refers to the distance between the CO_2 plume and the caprock in the inlet slice. Horizontal distance is the distance in the y-axis between the plume and the inlet slice. VL Zero implements a constant relative permeability set to the fine-scale viscous limit curve and zero capillary pressure. CL Zero implements heterogeneous, upscaled relative permeability and zero capillary pressure. CL Pc imposes heterogeneous, upscaled relative permeability and capillary pressure.

The VL Zero simulation is characterised by a steep gradient in vertical distance travelled and reaches the caprock after 0.5 years following the onset of injection. The gradient also shows little variation, which implies that the vertical migration speed is relatively constant during the buoyant rise. In comparison to this, the CL Zero and CL Pc curves exhibit a much shallower, but highly variable gradient. This demonstrates that the plume travels much slower in the models that implement the heterogeneous, upscaled relative permeabilities. The variation in the gradient also suggests that the migration is dynamic.

In the first 4 years, the CL Pc and CL Zero simulations follow the same trend, which illustrates that the capillary pressure variations implemented in the CL Pc model have no noticeable

impact on the resultant plume migration speed. After approximately 4 years, the curves diverge with the CL Pc model characterised by a slower vertical migration speed. This results in the plume reaching the caprock after 8 years and 10.5 years in the CL Zero and CL Pc scenarios, respectively. Thus, at later times, capillary pressure variations additionally act on the plume and slow it down. These results demonstrate that disregarding capillary pressure upscaling may lead to an overestimation of vertical migration speed. We also find that the impact of relative permeability exceeds that introduced by capillary pressure variations.

As shown in Figure 7.8, the majority of grid blocks are characterised by an upscaled vertical gas relative permeability that is smaller than the viscous-limit input curve. This results in a slower vertical migration in the CL models. Additionally, the heterogeneous capillary entry pressure and the low viscous pressure gradient in the vertical direction slows the plume down. The CO_2 plume can only migrate upwards once the hydrostatic head exceeds the entry pressure of the block overlaying the plume, which corresponds to a critical plume thickness: $h_{critical} = \frac{P_e}{\Delta\rho \times g}$. For example, an approximately 2 m thick column of CO_2 would be required to vertically migrate into a cell with an entry pressure of 10 kPa.

7.3.1.2 The Impact of Heterogeneity on Horizontal CO_2 Flow in 2D

The horizontal migration speed displays significant differences between the three simulated scenarios. The results indicate that the relative permeability is also the leading control on lateral plume migration and predominantly slows it down.

In the first few months, the CL models exhibit a slightly larger lateral migration distance compared with the VL case. Whilst the vertical relative permeabilities are lower than the intrinsic curves, the horizontal curves are generally higher due to the correlation lengths imposed in the model. Thus, it is easier for the CO_2 to migrate laterally than vertically. This results in a slightly faster lateral migration at early times.

After 1 year, the VL Zero case is characterised by the fastest migration speed, with a steep gradient in the horizontal distance travelled that is constant for the majority of the injection period. In this simulation, all the CO_2 has risen to the top, resulting in a high gas saturation and an increased gas mobility. This ultimately increases the lateral plume migration speed, which is also further enhanced by the impact of dip and buoyancy. In contrast to this, both the CL Pc and the CL Zero simulations exhibit a much slower lateral migration speed, which varies in time. Until approximately 15 years, the plume in the CL Pc model travels a factor of 5 slower than that in the VL Zero simulation. After this point, the gradient in the CL Pc simulation increases significantly beyond the VL Zero run. However, the plume only extends 1.4 km into the domain, compared with 2.4 km in the VL Zero run, after 25 years of injection. Over the first 15 years, the CL Pc plume travels faster than the CL Zero run.

7.3.1.3 Channel Formation due to Heterogeneity in 2D

To evaluate the variation in flow behaviour between the three models in more detail, we extract the CO_2 saturation maps at varying time steps over the 25 year injection period. See Figures 7.10, 7.11 and 7.12 for the VL Zero, CL Zero and CL Pc results, respectively.

At early times, the plume in the VL Zero model is exclusively rising buoyantly and is confined to the y location of the injector (Figure 7.10a). In contrast to this, the plumes in CL Pc and CL Zero models are more heterogeneous and primarily spread laterally rather than vertically (Figure 7.11a and Figure 7.12a). The CO_2 invades the neighbouring columns of grid blocks through thin channels that are 10s metres thick. The CL Pc simulation exhibits a higher number of channels. The plume in the VL Zero simulation reaches the caprock after merely 0.6 years at which point the plumes in the remaining two runs are 135 m away from it. Overall this flow pattern is in agreement with the observations made in the previous sections whereby the VL Zero case exhibits a larger vertical, but smaller horizontal migration speed.

These trends can be explained with respect to the impact of capillary heterogeneity. Near the injector, the capillary heterogeneity orientated perpendicular to the z-axis acts as barriers to the CO_2 and it rises much more slowly. The barriers also force the CO_2 to migrate laterally in channels, which can be clearly observed in the saturation distribution maps. This allows the CO_2 to spread further into the model and corresponds to a larger horizontal migration speed. Some of the CO_2 also leaves the system through thin channels at y=1. In comparison to this, the plume in the VL Zero case rises buoyantly exclusively.

As more CO_2 is injected (t=7.9 years), the homogeneous plume in the VL Zero simulation migrates laterally. In comparison to this, the plume in the CL Zero run has just reached the caprock, whereas the tip of the plume in the CL Pc model is 50 m away from the caprock. This is due to the slow vertical migration caused by the heterogeneity. In the first 7 years, the lateral channels in both CL models have noticeably grown in the both directions along the y-axis. The CL Pc simulation exhibits more pronounced channels compared with the CL Zero model. This is due to the thresholding effect introduced by capillary pressure variations.

It takes the plume in the CL Pc run an additional two years to reach the caprock, at which point the plume in the VL Zero model has travelled 1 km laterally. Thus, the restrained vertical flow also has a prolonged effect on the horizontal migration distance as it delays the time at which the CO_2 collects underneath the caprock and begins to travel laterally in the uppermost layers.

Overall, the saturation maps show that reservoir sweep is enhanced near the injector due to capillary heterogeneity by means of channel formation. This is in agreement with the observations made in Chapter 6. Furthermore, it has been shown that capillary heterogeneity can result in slower lateral migration.

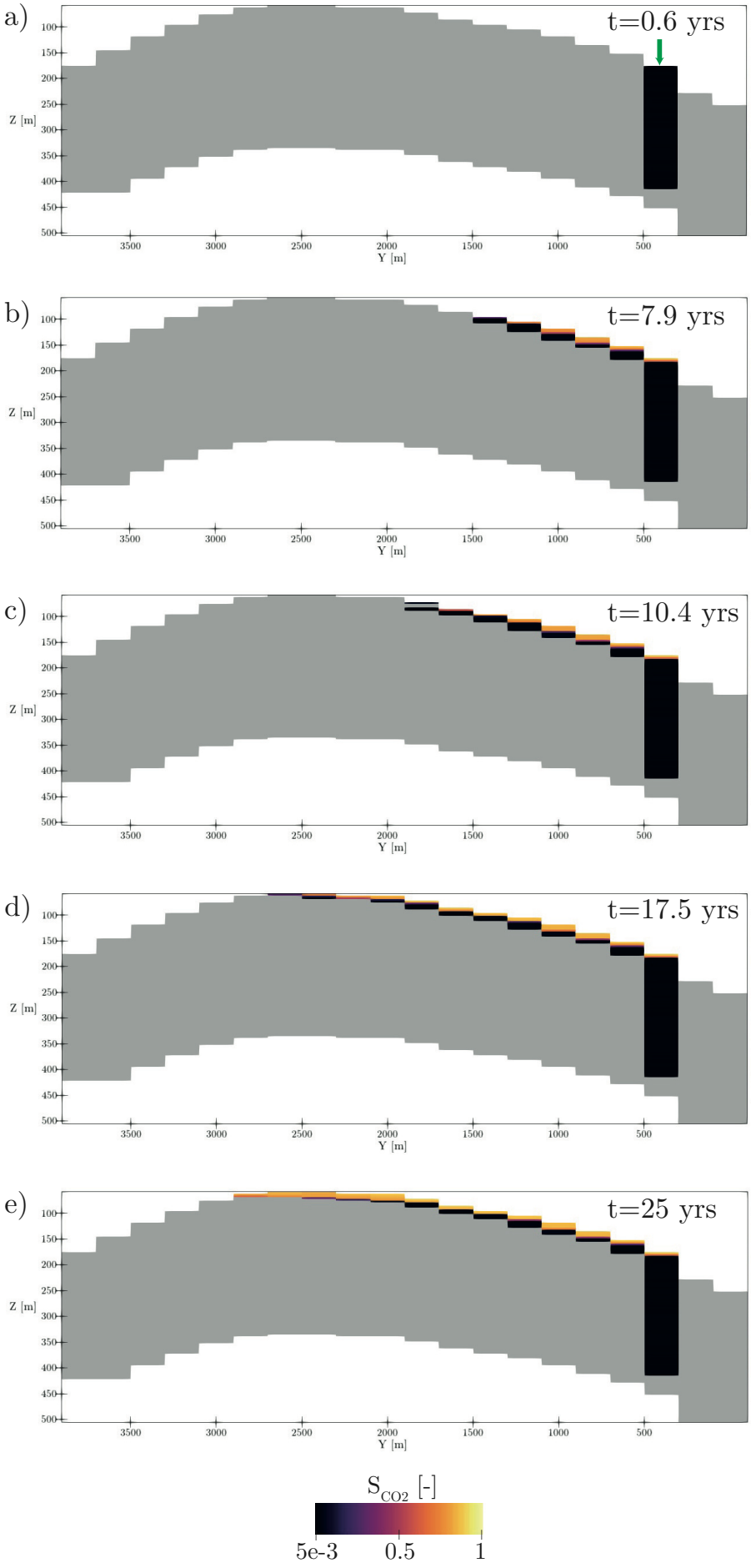


Figure 7.10: CO_2 saturation distribution at different time steps for the VL Zero simulation, where a constant relative permeability and zero capillary pressure is implemented. Note: grid blocks with $S_{CO2} < 5 \times 10^{-3}$ are coloured in grey. The green arrow in the first panel indicates the injector location.

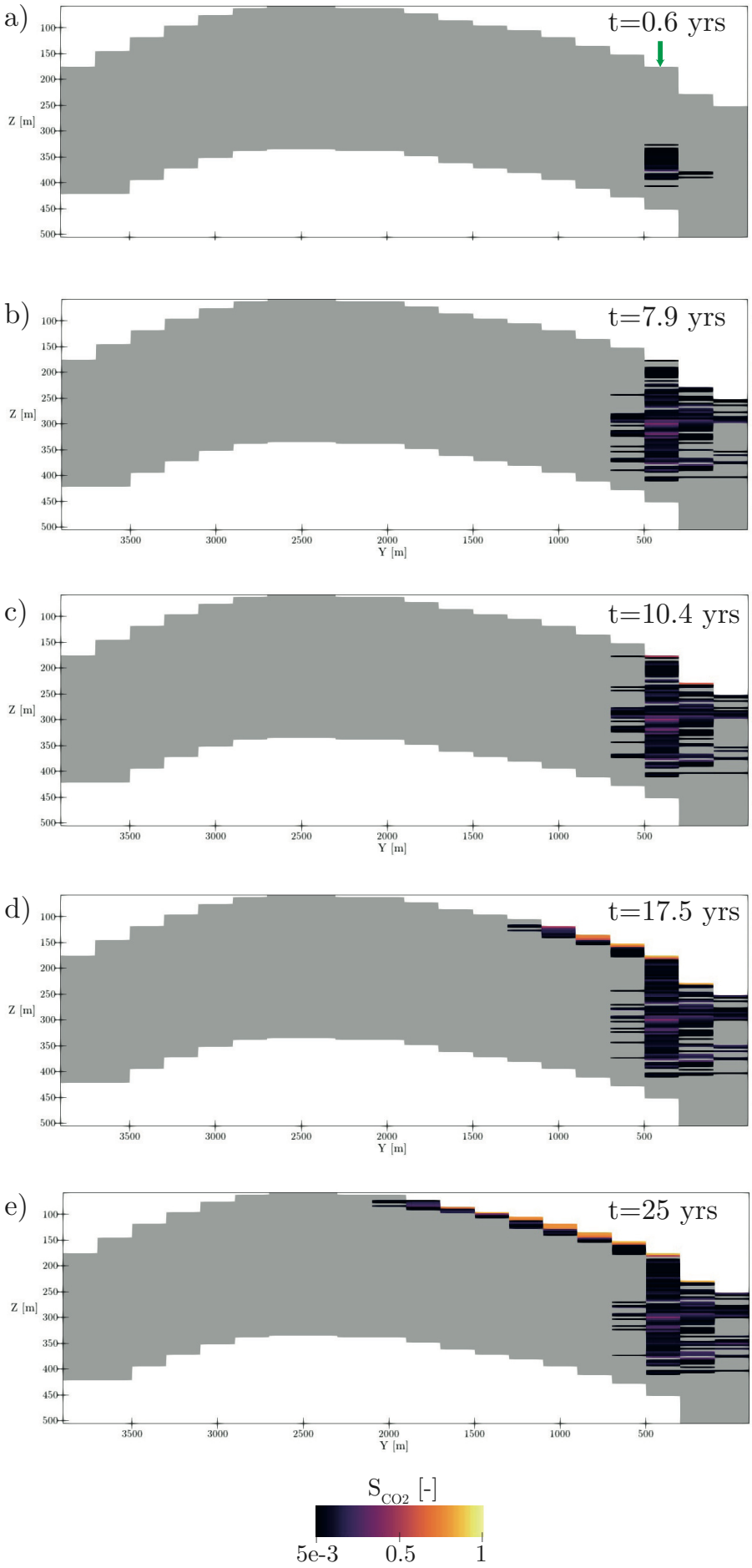


Figure 7.11: CO_2 saturation distribution at different time steps for the CL Zero simulation, where the heterogeneous, upscaled relative permeability and zero capillary pressure is implemented. Note: grid blocks with $S_{CO2} < 5 \times 10^{-3}$ are coloured in grey. The green arrow in the first panel indicates the injector location.

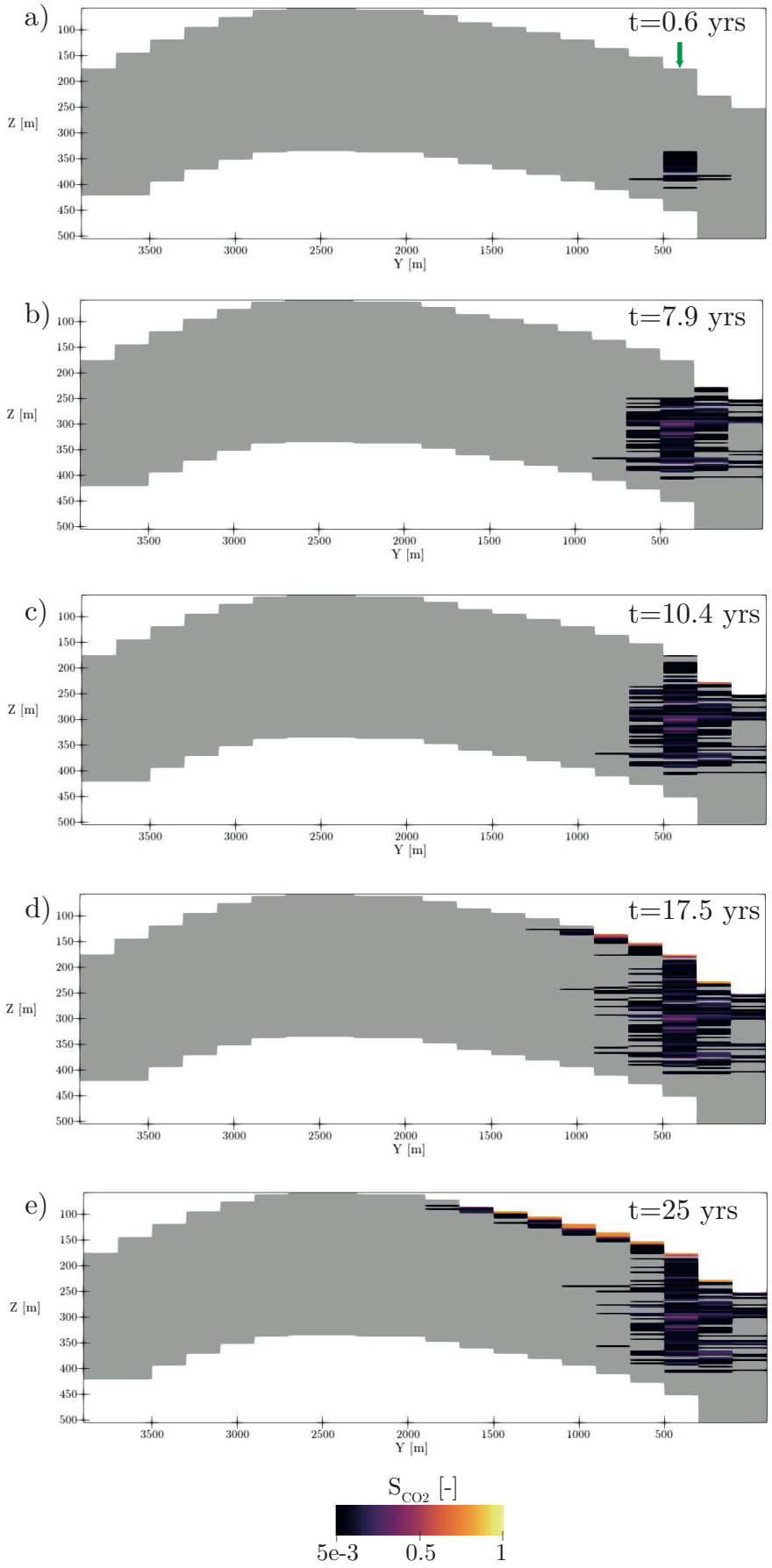


Figure 7.12: CO_2 saturation distribution at different time steps (indicated in figure) for the VL Zero simulation, where the heterogeneous, upscaled relative permeability and heterogeneous, upscaled capillary pressure is implemented. Note: grid blocks with $S_{CO2} < 5 \times 10^{-3}$ are coloured in grey. The green arrow in the first panel indicates the injector location.

7.3.2 Simulating the Impact of Capillary Heterogeneity in 3D

In this Section, we simulate CO_2 injection in the full 3D model at a constant rate of 3131 m^3d^{-1} from well CI2 shown in the field development plan (Figure 7.1). Rather than injecting from all four planned wells, we initially opt for a single well to remove the complexities of multi-plume interactions. We increase the well complexity in Section 7.3.5. Constant pressure boundary conditions, which are widely implemented in CO_2 injection simulation studies (Doughty, 2010; Zhou and Birkholzer, 2011; Shao et al., 2022), are implemented on all four sides of the domain. This allows fluids to leave the system, which is a suitable choice considering our model domain is smaller than the entire Endurance structure. Thus, we would expect to observe fluids flowing out of the region that we have characterised in our model.

We generate six models using a combination of data from the Endurance site to differentiate the impact of capillary pressure variations and relative permeability anisotropy on CO_2 flow behaviour. The six models can be categorised into two groups: one that incorporates the upscaled, heterogeneous relative permeabilities (referred to as 'CL') and one that assumes constant relative permeability set to the fine-scale viscous-limit relative permeability (referred to as 'VL'). For each category, we generate three models: one with the heterogeneous, upscaled capillary pressure ('Pc'), one with constant capillary pressure set to the entry pressure of the fine-scale $P_c - S_w$ curve ('Pe') and a third with capillary pressure set to zero ('Zero'). Thus the six cases from most to least heterogeneous are:

- CL Pc: heterogeneous, upscaled relative permeability and capillary pressure
- CL Pe: heterogeneous, upscaled relative permeability and constant capillary pressure
- CL Zero: heterogeneous, upscaled relative permeability and zero capillary pressure
- VL Pc: homogeneous relative permeability and heterogeneous, upscaled capillary pressure
- VL Pe: homogeneous relative permeability and constant capillary pressure
- VL Zero: homogeneous relative permeability and zero capillary pressure

Note, all six cases incorporate the upscaled, heterogeneous porosity and permeability distributions obtained from the upscaling scheme. The upscaled, heterogeneous porosity, permeability and entry pressure are displayed in Figure 7.13. As shown, the model is characterised by laterally extensive heterogeneity, which corresponds to the $r_x = 1000$ m implemented.

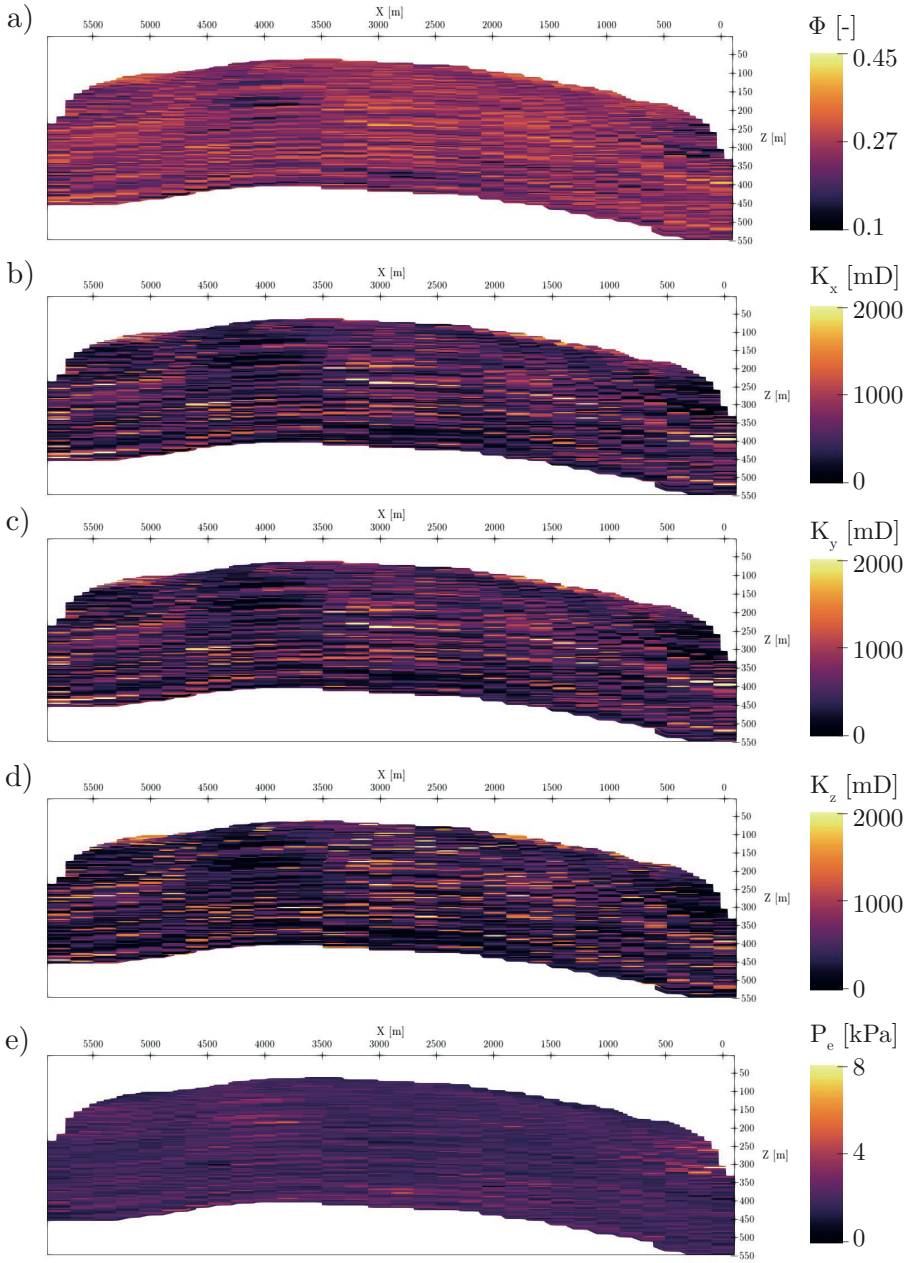
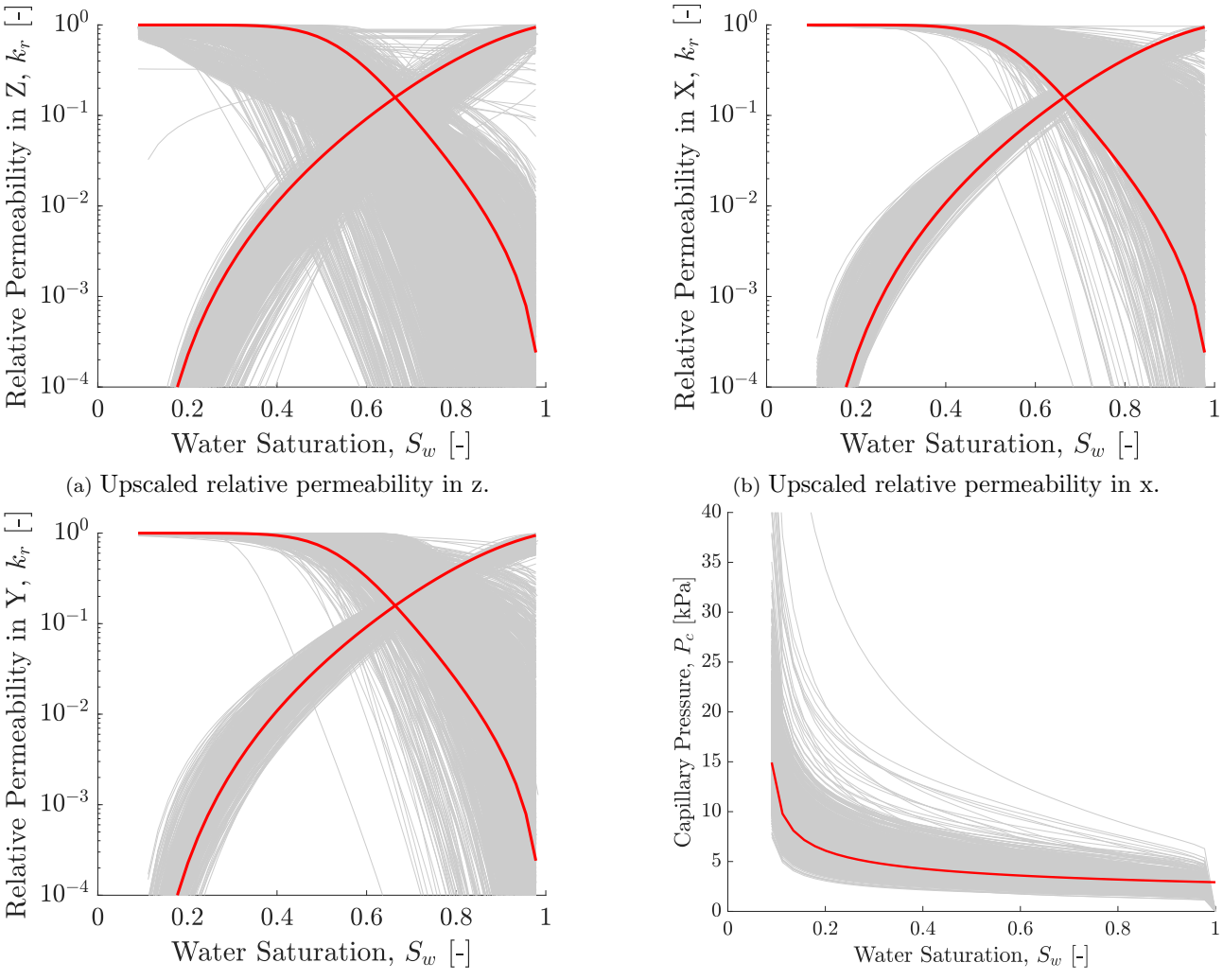


Figure 7.13: Upscaled petrophysical properties displayed in cross-sectional view: a) porosity, b) permeability in x, c) permeability in y, d) permeability in z and e) entry pressure.

Figure 7.14 displays a selection of upscaled block relative permeabilities and capillary pressures, which originate from a y-z plane at x=20 in the 3D model. We observe an increase in the x and y gas relative permeabilities compared with the intrinsic curves (Figure 7.14b and 7.14c),

which is a result of the large correlation lengths imposed in the x and y dimensions. This may enhance gas flow in these dimensions. In comparison to this, the majority of blocks exhibit a decrease in the vertical gas relative permeability (Figure 7.14a), which can also be attributed to the heterogeneity structure imposed in the model. For all dimensions, the gas relative permeabilities are characterised by a larger variation, which is a result of the lower viscosity and density compared with the brine as well as the water-wet nature of the system. We also observe a higher trapped gas saturation for z than x or y, which is likely a result of the heterogeneity structure.



(a) Upscaled relative permeability in z.

(b) Upscaled relative permeability in x.

(c) Upscaled relative permeability in y.

(d) Upscaled capillary pressure.

Figure 7.14: Upscaled relative permeabilities and capillary pressures used as input to the 3D simulations. The red lines represent the fine-scale, intrinsic curves. The grey lines are the curves for each grid block along the x=20 plane. Note, none of the relative permeabilities exhibit non-monotonic behaviour, these corresponds to very high gas or water relative permeabilities.

7.3.2.1 Migration Speed

To analyse the variation in plume migration speed between the six simulations, we extract the maximum spread of CO_2 in the x, y and z dimensions, presented in Figure 7.15. This is defined as the difference between the maximum and minimum coordinates in a single dimension invaded by CO_2 ($S_{CO2} > 5 \times 10^{-3}$). The steeper the gradient, the faster the plume is travelling in that dimension.

From the onset of injection, the plume migration speed in the x-axis is higher for the models implementing the heterogeneous, upscaled relative permeabilities (plotted as purple lines in Figure 7.15a). The difference in x lateral migration between the CL and VL models increases with time and the plume has spread an additional 600 m after 25 years of injection, which represents 10% of the total domain size in the x dimension. Thus, capillary heterogeneity enhances plume spreading in the x-axis.

In comparison to this, the trend in the migration speed in the y-axis is slightly different (Figure 7.15b). Initially, the CL models are characterised by larger speeds. However, the plumes in the VL runs soon overtake and migrate faster between 1.7-6.8 years. This is followed by a region where the plumes in the CL models spread further. After 25 years, the CL models have spread an additional 200 m in the y-axis. By comparing the observations from Figure 7.15a and Figure 7.15b, it emerges that all plumes generally spread further along the x-axis than the y-axis. This is partly influenced by the topography implemented in the model. The topographic high is located at x=19, y=12. Thus, the buoyant force will cause the plume to migrate towards this region, which corresponds to a larger distance in x than y. Secondly, the heterogeneity imposed in the model will impact the resultant plume shape. In our model, r_x is 30% larger than r_y. Therefore, the layers are more continuous in the x-axis, which may result in the plume migration trending in that direction.

Until 5.4 years, the VL models are associated with significantly larger vertical spread, reaching a maximum difference of 80 m. The VL curves are also characterised by significantly steeper gradients, which means that the plume is rising more quickly. Ultimately, the fast vertical

migration means the plume reaches the caprock after merely 74 days in the VL cases, whereas it takes nearly 400 days longer for the plume in the CL runs to do so. This is in agreement with observations from the 2D simulations discussed in the preceding section. However, after 5.7 years the behaviour changes and the CL models are now characterised by a larger spread in the z-axis. This suggests that the plume in regions beyond the injection point spreads over a larger vertical distance in the CL models. Reasons for this are investigated in subsequent sections.

Interestingly, the impact of capillary pressure variations on migration speed in any dimension is negligible for both the CL and VL runs. This demonstrates that relative permeability anisotropy is the main control on migration speed. Whilst the relative permeability was also identified as the main control on flow behaviour in the 2D simulations, the 2D results also demonstrated that capillary pressure variations had a measurable impact (Section 7.3.1). This diminishes in 3D. This underpins a major qualitative difference between the 2D and 3D simulations, which is discussed in more detail in Section 7.3.3.

The breakthrough time at the top structure is 8.5 years for the VL Zero simulation, while the plume in the CL Pc model breaks through roughly 2.5 years later. Therefore, the slower vertical migration exhibited in the CL simulations at early times has a prolonged effect on the lateral distance travelled by the plume. These results imply that capillary heterogeneity has a stronger upscaled impact on plume migration speed compared with topography.

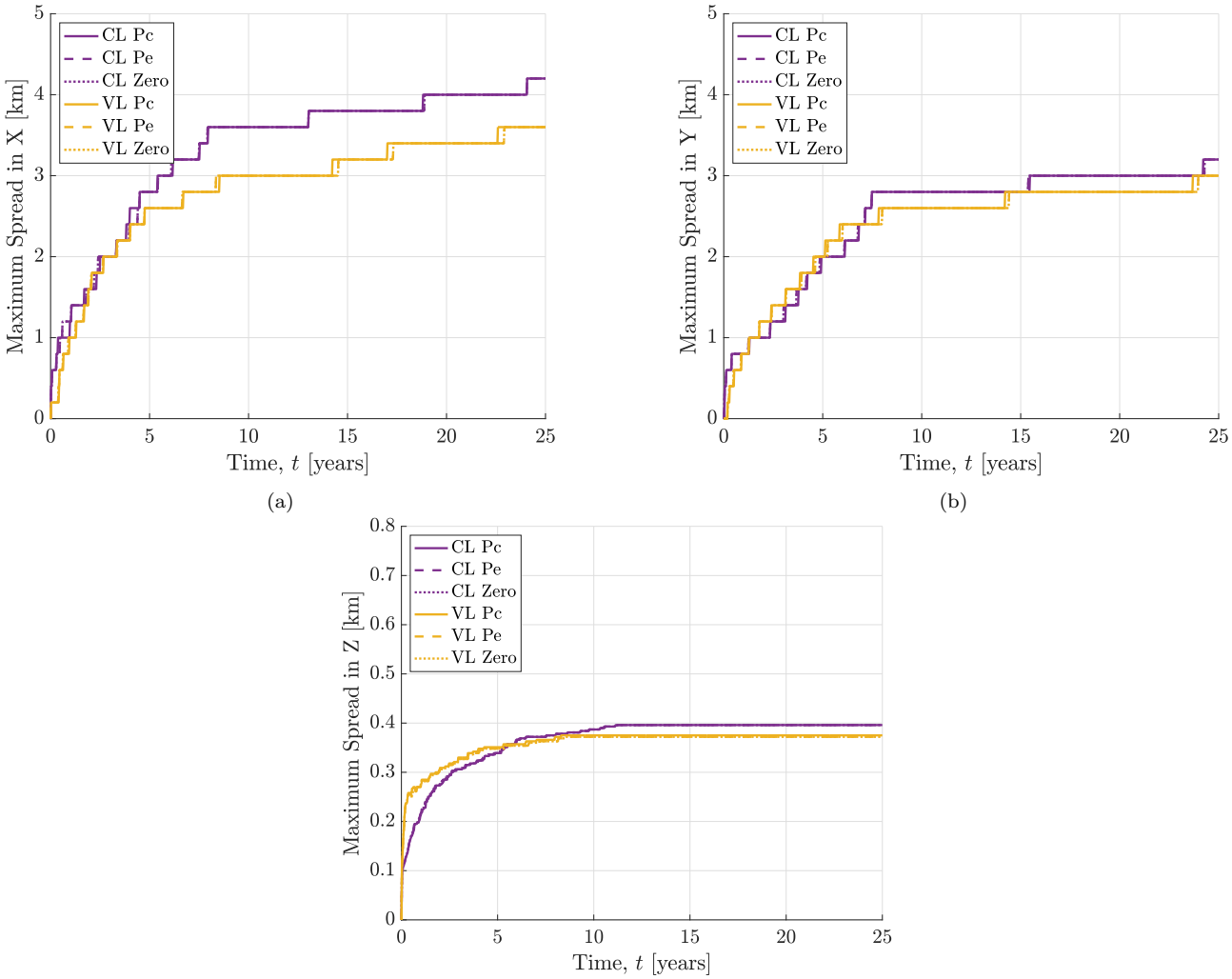


Figure 7.15: Plume spread along the three dimensions for the six simulations in the CI2 injector scenario. Note the three capillary pressure cases for the CL simulations overlie each other. We observe the same behaviour for the VL simulations.

7.3.2.2 Footprint Area

We define plume footprint area as the area of the CO_2 plume when it is projected onto a horizontal plane and entails plume spreading in any vertical layer of the reservoir. This is also positively correlated with the amount of CO_2 that is immobilised due to dissolution and capillary trapping, if it were modelled (Sundal et al., 2015). The plume footprint area over the 25 year injection period is plotted in Figure 7.16 for the six simulations. The relation between the VL and CL runs can be categorised into four distinct regions, which are annotated accordingly. We will discuss each of these regions separately in the following.

At early times (region A in Figure 7.16), the CL cases all have a higher footprint area compared with the VL cases. The initial large footprint area in the CL model matches the behaviour observed in the 2D simulation from the previous section and the findings presented in Chapter 6. The heterogeneity orientated perpendicular to the z-axis hinders the CO_2 from rising buoyantly, which causes the CO_2 to invade the domain laterally along a range of depths near the perforation interval. This corresponds to a large footprint area. Ultimately, this results in a slow vertical migration in the CL runs, which is also observed in Figure 7.15c. The invasion of CO_2 along deep layers near the well perforation interval in the CL runs can clearly be seen on saturation maps, as shown in Figure 7.18. Whilst the CO_2 in the VL run primarily rises upwards and accumulates under the caprock (Figure 7.17), the plume in the CL case is more heterogeneous and spreads out through channels. Figure 7.18c highlights a noticeable amount of CO_2, which has accumulated at $z \approx 400$ m, which does not occur in the VL simulation.

The relative percentage difference in footprint area between the CL and VL runs decreases from 400% to 20% within the first year, until the curves crossover at 1.7 years. The VL cases now have a larger footprint area, which is a result of the plume having risen rapidly due to the lack of capillary heterogeneity orientated perpendicular to the z-axis. The CO_2 in the VL runs reaches the caprock 400 days earlier and thus begins migrating laterally underneath the caprock confined to the uppermost layers. The larger footprint area in the VL models during this time period is attributed to a larger plume spread in the y-axis, as shown in Figure 7.19.

At 4.4 years, the footprint areas converge for all six cases, as indicated by annotation C in Figure 7.16. The results displayed in Figure 7.19 and Figure 7.20 show that both plumes are spreading out laterally in this period. Interestingly, the plume in the VL simulation is more circular, extending a similar distance in x and y, whereas the plume in the CL run trends towards the x-axis. This is in agreement with the results displayed in Figure 7.15.

Beyond roughly 6.9 years, the CL models are now characterised by a larger footprint area, which can be particularly attributed to the spread in the x-axis. The plume spreads out laterally more quickly and results in a heterogeneous frontal saturation distribution, see for instance Figure 7.20e. The impact of capillary heterogeneity enhances the lateral spread of CO_2. In this time period, we also observe a slight deviation in footprint areas between the three capillary pressure cases, which suggests that capillary pressure variations become more important at later stages. This is in agreement with findings from the 2D simulations discussed in the previous section.

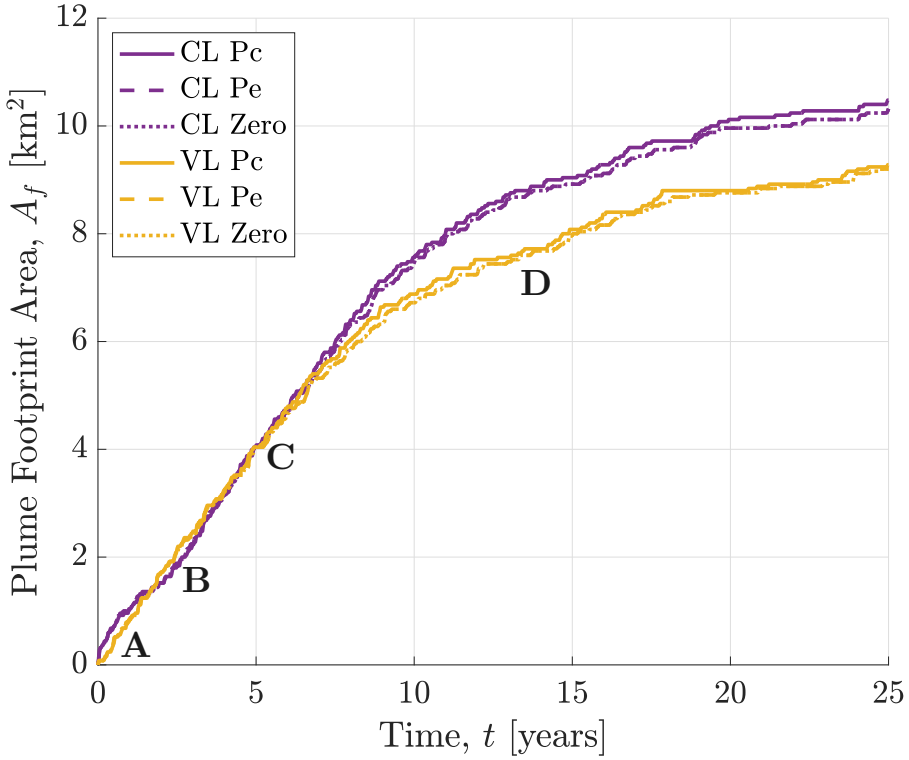


Figure 7.16: Plume footprint area for the six simulations in the CI2 injector scenario.

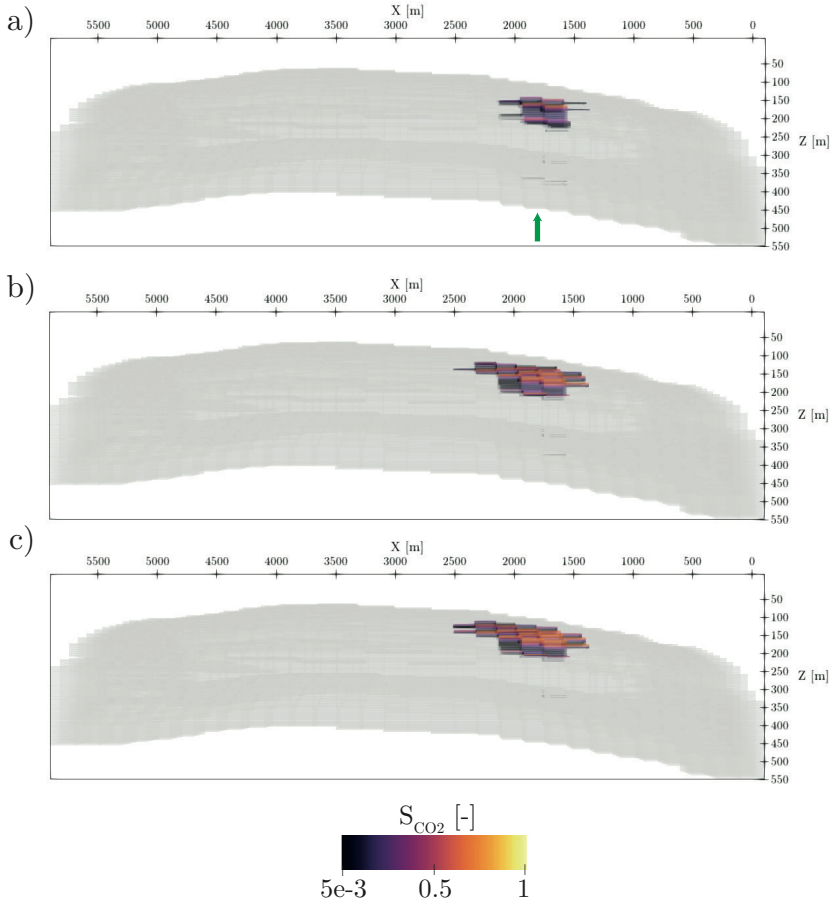


Figure 7.17: Cross sectional view of the CO_2 saturation distribution in the VL Zero simulation in the CI2 injector scenario at different timesteps: a) 0.5 years, b) 1 year and c) 1.25 years. Note: grid blocks with $S_{CO2} < 5 \times 10^{-3}$ are coloured in grey. Colours are moderately opaque so that the plume extent is visible. The green arrow in the first panel indicates the x coordinate of the injector.

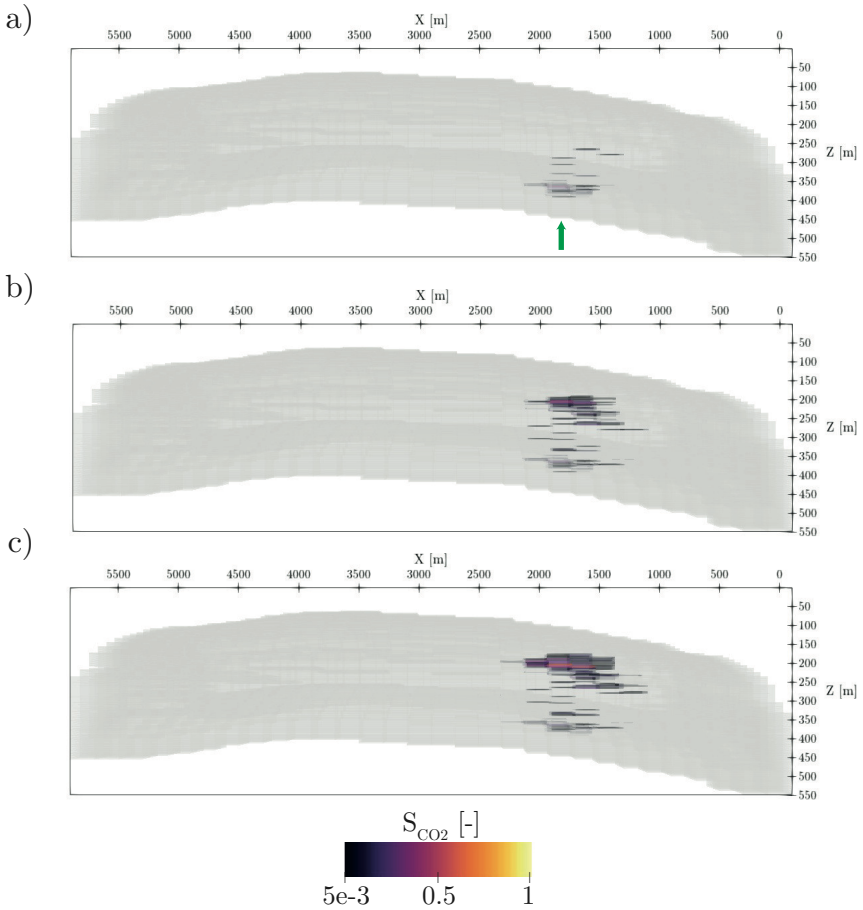


Figure 7.18: Cross sectional view of the CO_2 saturation distribution in the CL Pc simulation in the CI2 injector scenario at different timesteps: a) 0.5 years, b) 1 year and c) 1.25 years. Note: grid blocks with $S_{CO2} < 5 \times 10^{-3}$ are coloured in grey. Colours are moderately opaque so that the plume extent is visible. The green arrow in the first panel indicates the x coordinate of the injector.

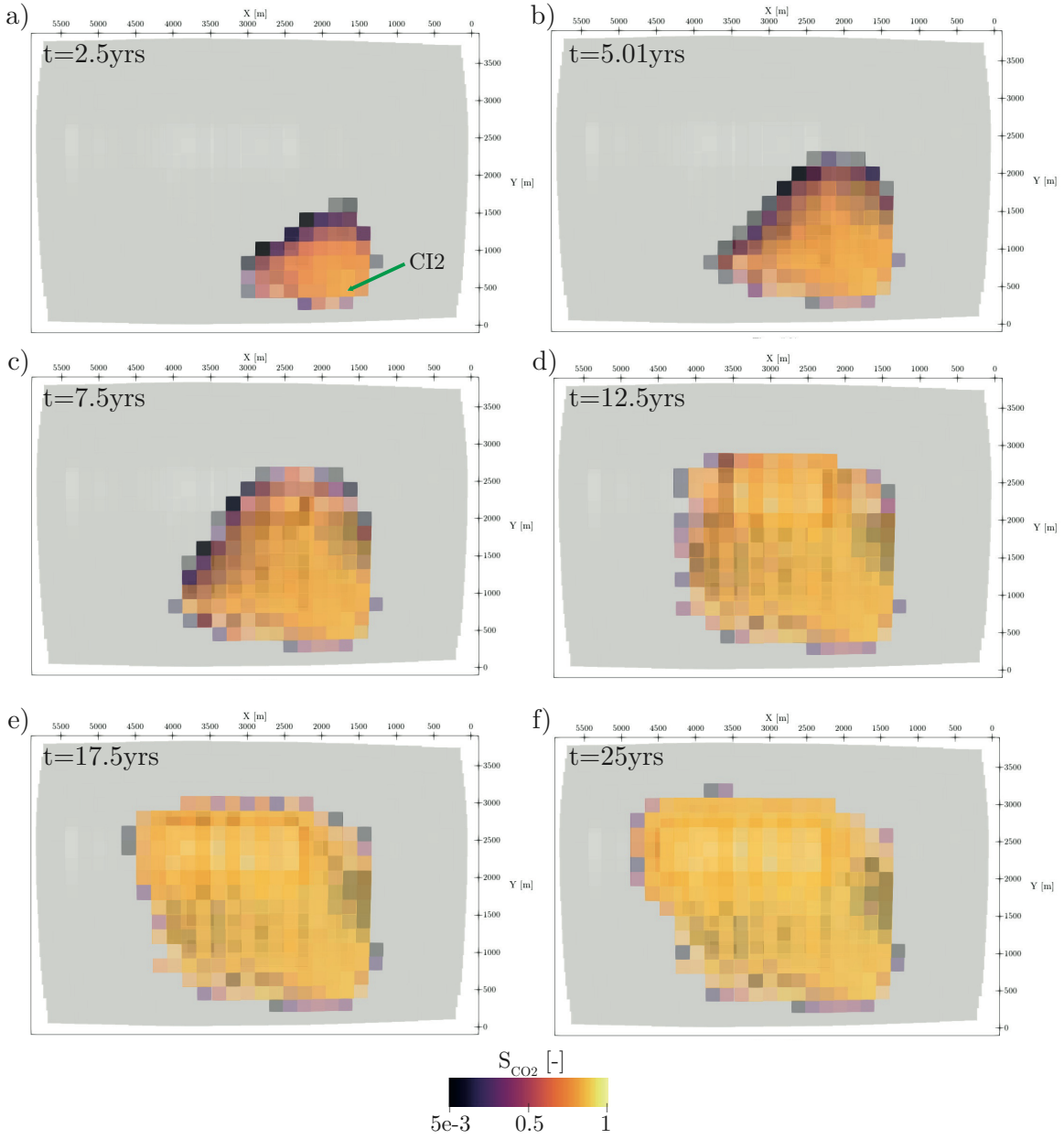


Figure 7.19: Plan view of the CO_2 saturation distribution in the VL Zero simulation in the CI2 injector scenario at different timesteps as annotated. Note: grid blocks with $S_{CO2} < 5 \times 10^{-3}$ are coloured in grey. Colours are moderately opaque so that the plume extent is visible. The green arrow in the first panel indicates the (x,y) location of the injector.

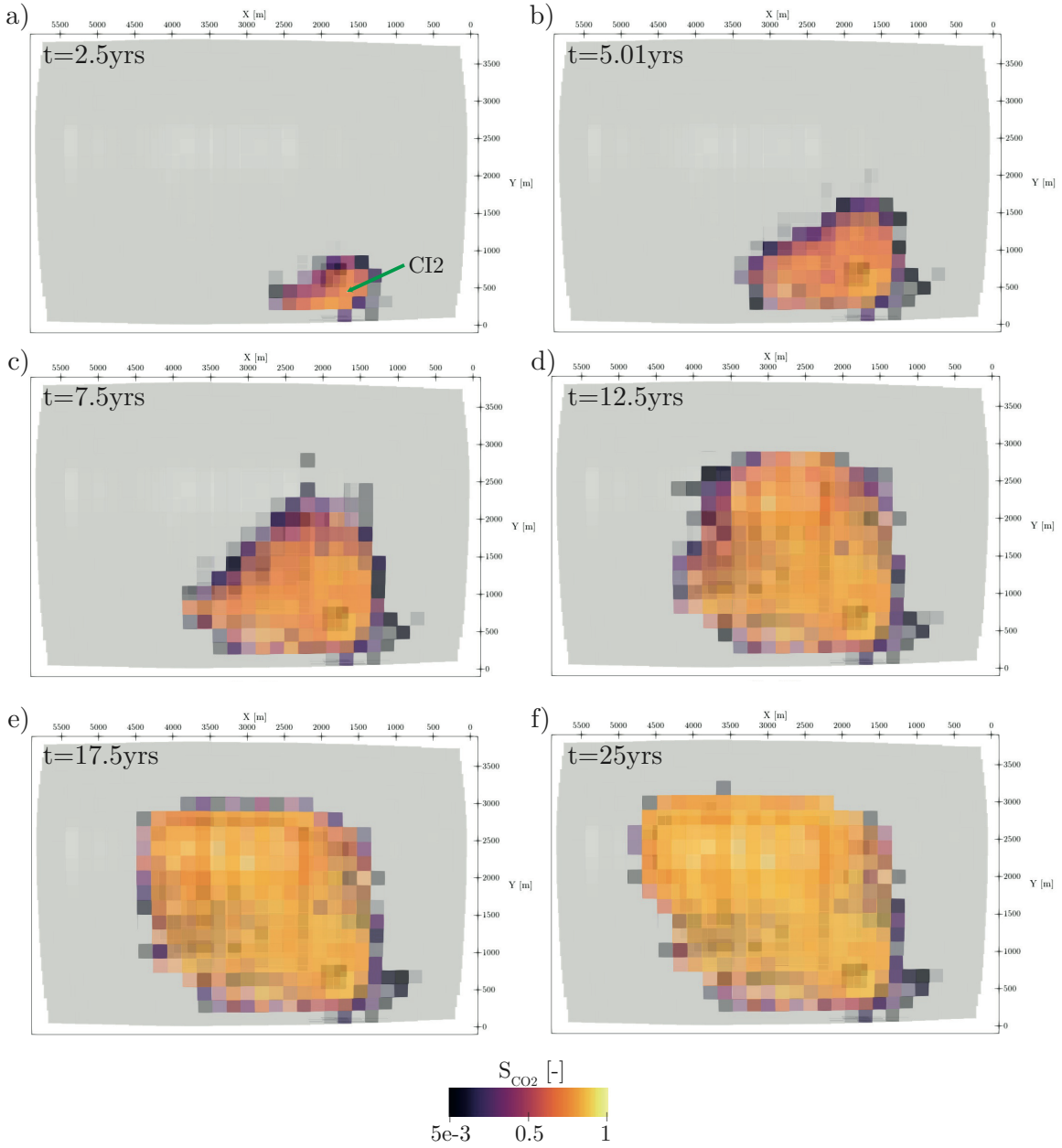


Figure 7.20: Plan view of the CO_2 saturation distribution in the CL Pc simulation in the CI2 injector scenario at different timesteps as annotated. Note: grid blocks with $S_{CO2} < 5 \times 10^{-3}$ are coloured in grey. Colours are moderately opaque so that the plume extent is visible. The green arrow in the first panel indicates the (x,y) location of the injector.

7.3.2.3 Plume Swept Volume

The plume swept volume is defined as the volume of all grid blocks invaded by CO_2 ($S_{CO2,block} > 5 \times 10^{-3}$). The swept volume provides an indication of the efficiency of pore space use, which is directly linked to the CO_2 storage efficiency of a reservoir. It is also able to provide further insight into more subtle differences in the plume shapes, particularly the formation of thin channels that may not be distinguished by the footprint area.

The plume swept volume for the six simulations is shown in Figure 7.21. From the onset of injection, all three CL models are characterised by a larger swept volume, which increases significantly with time. The maximum difference in swept volume between the CL and VL models occurs at 1.6 years with a 130% relative difference. These results demonstrate that the reservoir sweep is significantly enhanced in the presence of capillary heterogeneity. After approximately 2 years, we also observe a deviation between the three capillary pressure cases (Pc, Pe and Zero) of the CL runs, which enhances with time. Thus, similar to the conclusions drawn in the previous sections, the impact of capillary pressure variations plays an increased role at later stages of the injection scenario. However, compared with the footprint area, the impact of capillary thresholding is more pronounced in the swept volume, as this measure is indicative of channel formation.

To investigate the impact of capillary pressure variations in more detail, we extract the CO_2 saturation maps for the CL Pe and CL Pc simulations, see Figure 7.22. The saturation distribution for the CL Zero run is not shown as this displays the same characteristics as the CL Pe model. As indicated by the plume swept volume, a higher number of channels form in the model with heterogeneous capillary pressure, particularly in proximity to the injector. Based on the observation that the CL Pe and CL Zero models exhibit the same flow behaviour, it emerges that it is not the absolute capillary pressure but the variations in capillary pressure with saturation that affect the CO_2 flow pattern. The thresholding effect introduced by capillary pressure enhances the formation of channels. This behaviour is most prominent near the injector, where CO_2 is introduced into the reservoir across a 100 m perforated interval.

The cross-sectional saturation maps also highlight the formation of a laterally extensive channel that is orientated in the x-axis and present in the CL Pc and CL Pe simulations (see annotation in Figure 7.22). This channel does not form in the VL simulations, which suggests that it is attributed to the relative permeability anisotropy. We extract the x relative permeabilities of blocks in proximity to this channel, Figure 7.23. As shown, the majority of blocks are characterised by a raised gas relative permeability compared with the intrinsic curve, which is attributed to the impact of capillary heterogeneity. Thus, these cells are favourable flow pathways for the CO_2, which leads to the formation of the channel. Channelling is further enhanced by the adverse mobility ratio between the CO_2 and brine. These findings are in agreement with previous works including Chang et al. (1999), Chasset et al. (2011), Hesse et al. (2006) and Shao et al. (2022). However, our work demonstrates that it is both the anisotropic relative permeability and the capillary pressure variations that cause the CO_2 channelling to begin with.

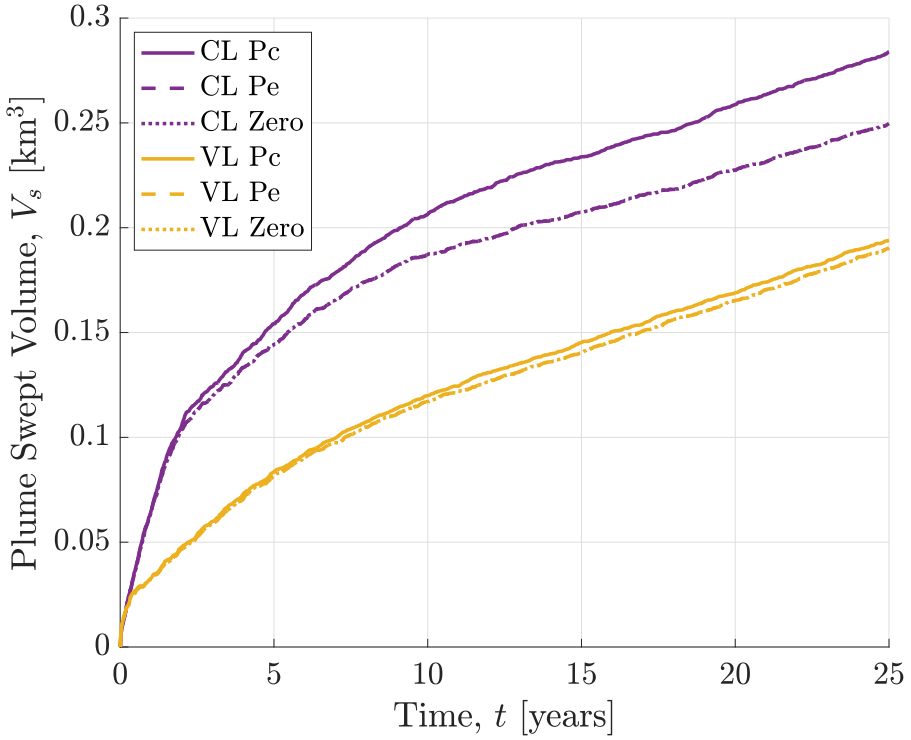


Figure 7.21: Plume swept volume for the six simulations in the CI2 injector scenario. Note: the CL Pe and CL Zero simulations overlie each other. The VL Pe and VL Zero simulations also overlie each other.

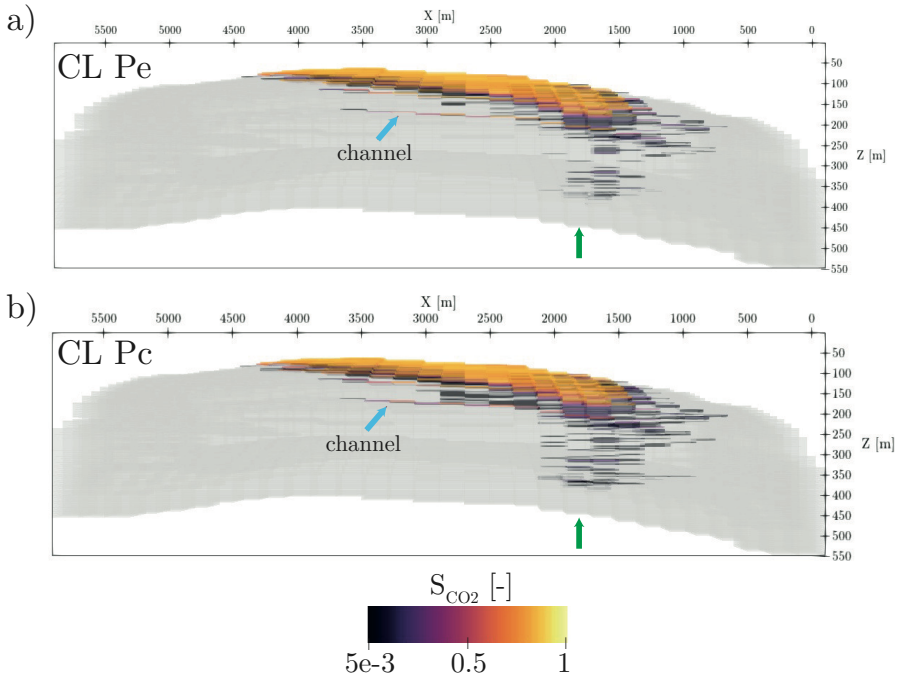


Figure 7.22: Cross-sectional view of the CO_2 saturation distribution after 25 years injection for the a) CL Pe and b) CL Pc simulations in the CI2 injector scenario. The green arrow points to the x location of the injector. The blue arrow points to a laterally extensive channel that is discussed in the main text. Note: the saturation distribution for the CL Zero run is not shown as this displays the same characteristics as the CL Pe simulation.

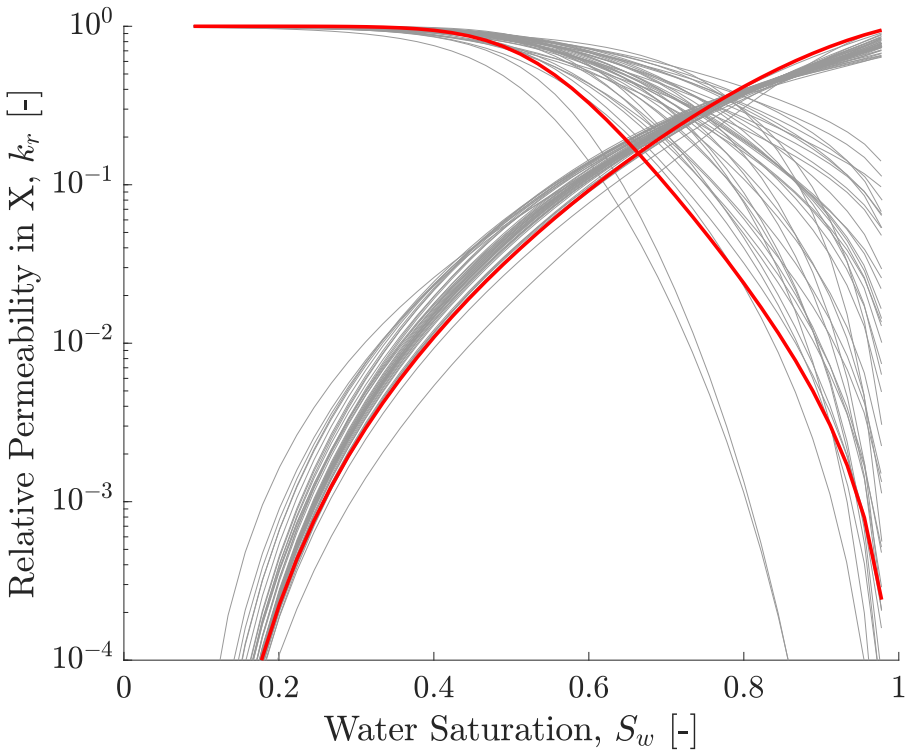


Figure 7.23: Upscaled relative permeabilities in the x dimension from blocks surrounding the channel that is annotated in Figure 7.22. The red curves represent the intrinsic, viscous-limit relative permeabilities.

7.3.2.4 Increased Sweep Efficiency Near Injector

To visualise how channel formation affects the thickness of the plume, we calculate the difference in plume thickness between the two end-member simulations, CL Pc and VL Zero, over time, see Figure 7.24.

At early times (Figure 7.24a) we observe the largest absolute difference in plume thickness between the two simulations. Near the injector the plume is thicker in the CL Pc simulation, indicated by the density of the red-shaded grid blocks. The column of CO_2 is a maximum of 150 m thicker in this region, which is significant. This is a result of the channels that form at a range of depths, which lead to a multi-layer plume exhibiting a large sweep and spread. This is particularly evident in the cross-sectional saturation distribution maps, such as Figure 7.22b. As we move away from the injector and further into the reservoir, the difference in plume thickness abruptly decreases. The VL Zero simulation exhibits a maximum 30 m thicker column of CO_2 in this region, which reflects the higher lateral migration speed observed in the VL Zero run at early times.

As more CO_2 is injected, the contrast between the two simulations becomes less severe, yet a clear trend is observed. Near the injector, the CL Pc simulation is still characterised by a significantly thicker plume. In the central portion of the plume, the region closer to the injector is primarily characterised by light-red shading. This indicates that even in the central portion of the plume, the CL Pc simulation is characterised by a thicker column of CO_2. Whilst the CO_2 in the VL Zero simulation solely migrates along the uppermost layers with a homogeneous saturation front, the gas in the CL Pc simulation exhibits a heterogeneous saturation front and invades the reservoir through multiple stacked channels. This leads to a thicker column of gas. As we move even further away from the injector, the majority of regions now exhibit larger plume thicknesses in the VL Zero simulation. This indicates that the gravity tongue thins as a result of capillary heterogeneity, which is attributed to the enhanced spread and sweep encountered by the plume.

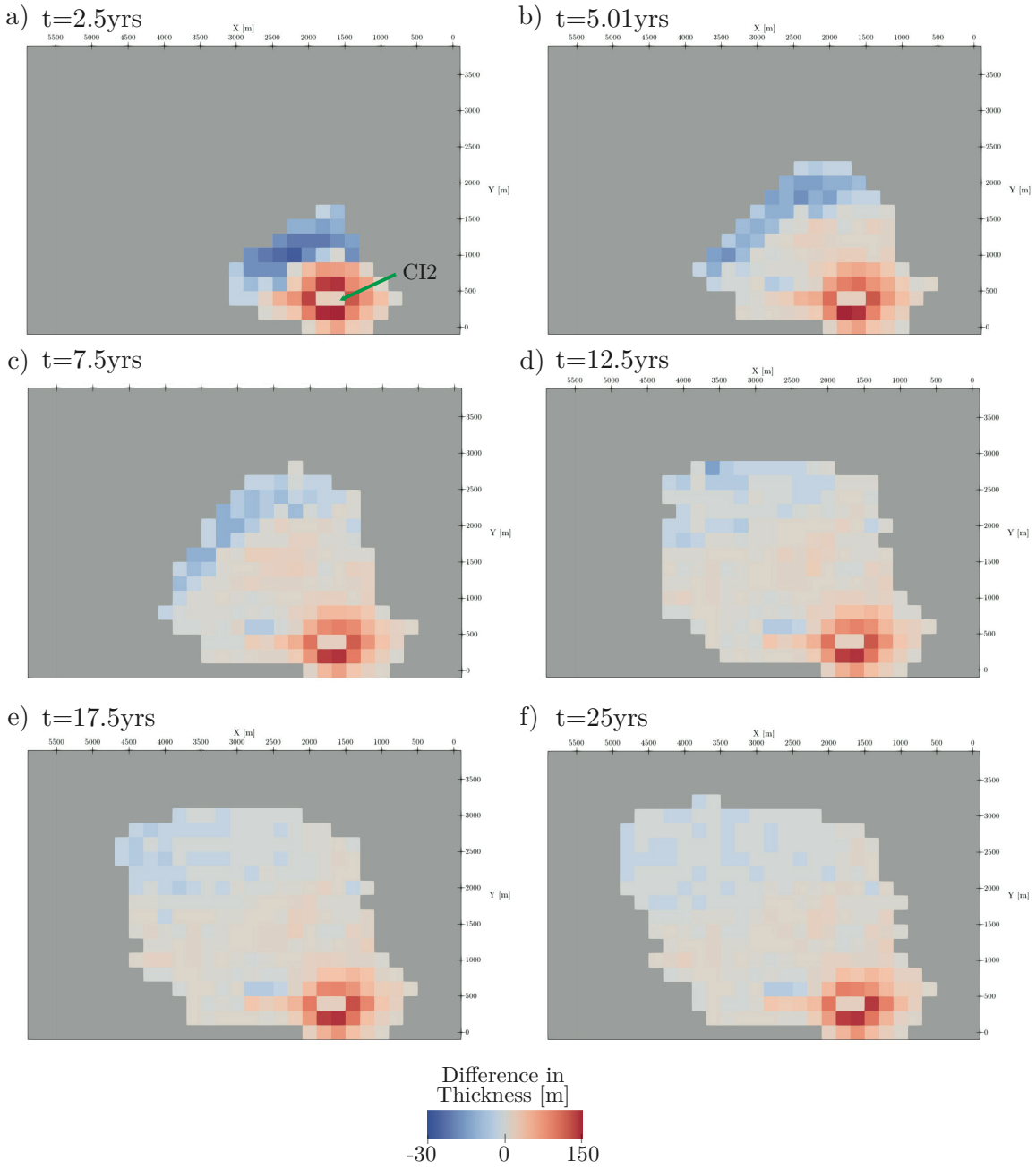


Figure 7.24: Topdown view of the difference in plume thickness between the VL Zero and CL Pc simulations at 25 years in the CI2 injector scenario. Red grid blocks refers to regions where the CL Pc simulation is characterised by a thicker plume and blue grid blocks represent regions where the VL Zero plume is thicker. The green arrow points to the (x,y) location of the injector.

7.3.2.5 Leading Edges of Plume under Seismic Detection

Seismic surveys are one of the key technologies utilised to monitor CO_2 plume migration in ongoing CCS projects (Daley and Korneev, 2006; Verdon et al., 2010; Diao et al., 2020). As such, it is important to examine the plume thickness in our simulation against the seismic detection limit. The resolution of seismic surveys largely depends on the reservoir (rock types, layer thicknesses, depth to the plume, onshore vs offshore, fluid density ratios etc) and the available equipment. Gasperikova et al. (2022) estimates the seismic detection limit for CCS operations to be 30 m, the work by Pevzner et al. (2015) suggest CO_2 plumes thicker than 7 m can be resolved on seismic images, whereas Lüth et al. (2015) provide a detection limit of 6.5 m. Based on these findings, we set the seismic detection limit for this investigation to 9 m. We plot the thickness of the plume in the VL Zero and CL Pc simulations at varying timesteps, highlighting the regions that correspond to plume thicknesses of 9 m or below. These regions represent locations where the plume likely will not be detected by seismic techniques. See Figure 7.25 and Figure 7.26. We also plot the total number of (x,y) locations with plume thicknesses of 9 m or below for both simulations over the 25 year injection period in Figure 7.27. This provides a direct comparison between the two runs.

At early times (Figure 7.25a, 7.26a and 7.27a), the leading edges of the plume on the left and right sides are thinner in the CL Pc simulation compared with the VL Zero run, and fall below the seismic detection limit. These regions correspond to the location of the initial, thin CO_2 channels that form due to capillary heterogeneity. They will likely remain unidentified on seismic images.

As more CO_2 is injected in the domain (Figure 7.25b-c and Figure 7.26b-c), the number of channels increases and the thickness of the CO_2 column progressively increases. However, in both, the CL Pc and VL Zero, simulations we observe the leading edges of the plume fall below the seismic detection limit. Across the 25 year injection period, the CL Pc simulation exhibits a larger number of locations undetected by seismics than the VL Zero run for a total of 8 years (Figure 7.27). Thus, for the majority of time, capillary heterogeneity in fact reduces the number of regions at risk of being undetected. This is because, rather than confined to the uppermost

layers, the plume forms channels at a range of depths that eventually are thick enough to be detected.

At 25 years, the central portion of the plume, regions in proximity to the injector and the leading edges of the plume in the maximum y direction fall above the detection limit in the CL Pc simulation (Figure 7.26d). However, the results also demonstrate that the leading edges on the remaining sides of the plume will likely fall below the seismic detection, even after 25 years of continuous CO_2 injection. The figure highlights a region of approximately 1400 m length extending along the x axis at 25 years, which is characterised by a plume thickness smaller than 9 m (see blue arrow on Figure). This region partly overlaps with the location of the thin channel that was discussed in the previous section. This channel has not formed in the same location in the VL Zero simulation.

Particularly thin channels and the leading edges of the plume are important for estimating the plume extent and migration speed, ultimately to determine any containment risks. The results suggest that a significant amount of the plume (reaching 1400m length) may be undetected. However, compared with the VL Zero simulation, we observe a decrease in the total number of locations exhibiting thin CO_2 columns. This indicates that capillary heterogeneity may reduce the challenges associated with seismic detection limitations.

These findings have important implications for CCS operations. On one hand, thin channels in parts of the reservoir may stay undetected, which can lead to erroneous estimates of plume extent and migration speed. On the other hand, capillary heterogeneity may increase the CO_2 column thickness in other parts of the reservoir, which would ensure detection. This highlights the importance of incorporating the impact of capillary heterogeneity on the multiphase flow properties in reservoir models, which may improve the prediction of channel formation and flow behaviour.

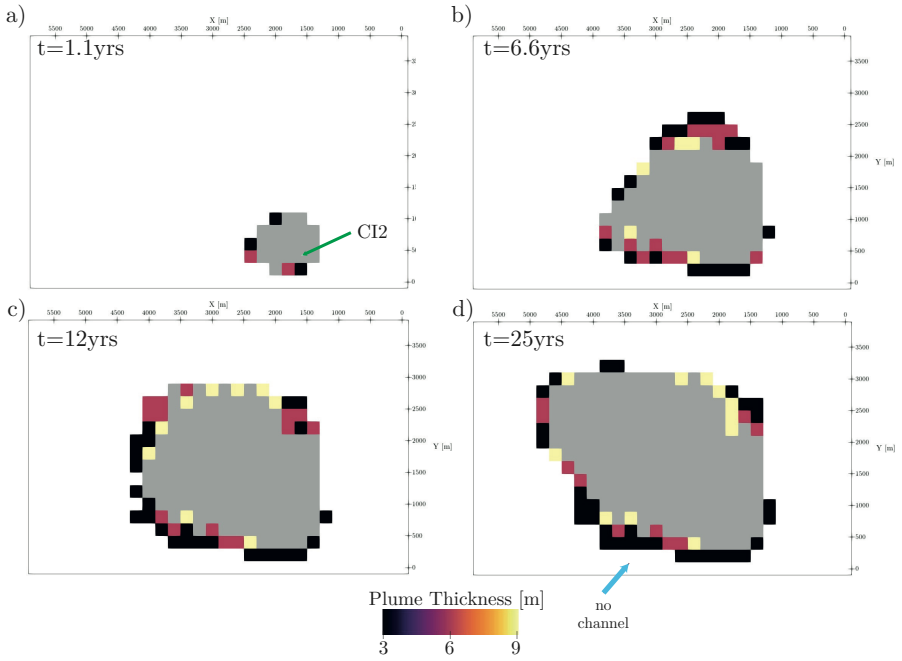


Figure 7.25: Topdown view of the plume thickness in the VL Zero simulation at different timesteps in the CI2 injector scenario. Grid blocks with a plume thickness above 9 m are coloured in grey. Grid blocks with a plume thickness between 3 m and 9 m are colored accordingly. Green arrow points to the (x,y) location of the injector. Blue arrow points to a region that is discussed in the main text.

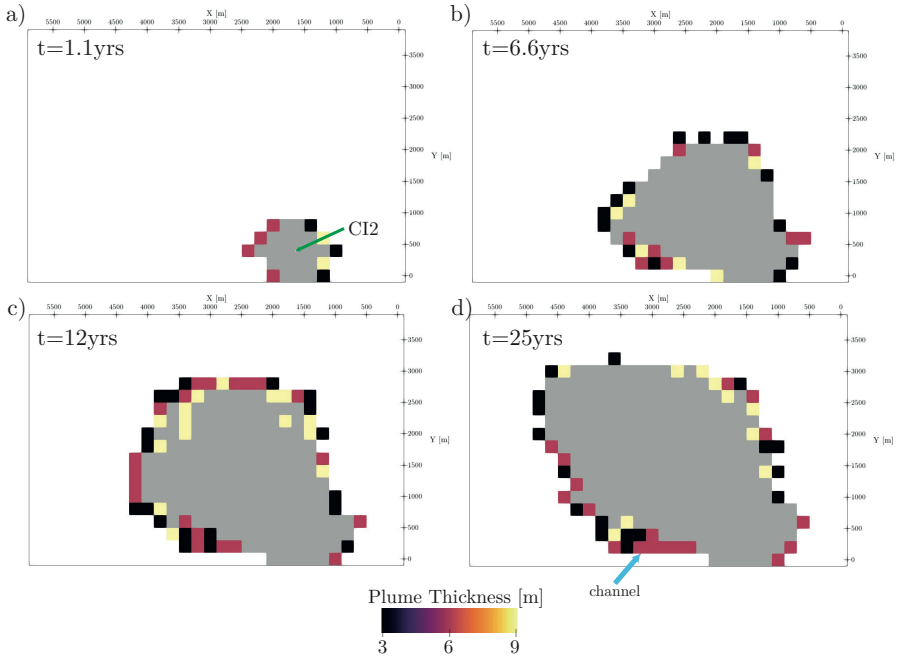


Figure 7.26: Topdown view of the plume thickness in the CL Pc simulation at different timesteps in the CI2 injector scenario. Grid blocks with a plume thickness above 9 m are coloured in grey. Grid blocks with a plume thickness between 3 m and 9 m are colored accordingly. Green arrow points to the (x,y) location of the injector. Blue arrow points to a region that is discussed in the main text.

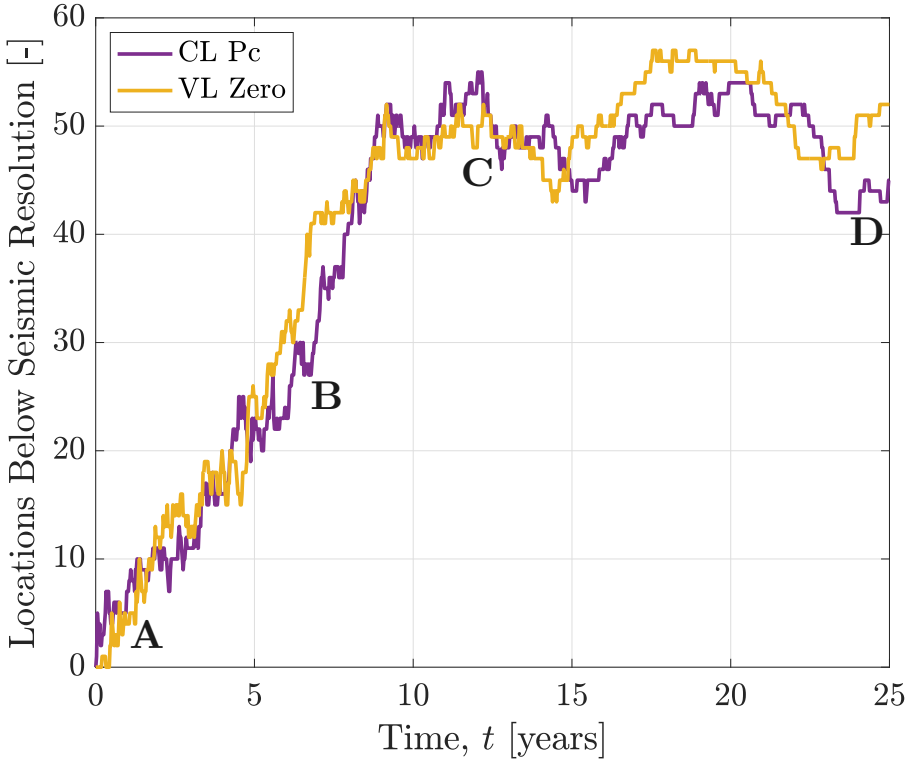


Figure 7.27: Number of (x,y) locations in the domain with a CO_2 column characterised by a thickness of 9 m or below (below seismic resolution). Purple and yellow lines are results from the CL Pc and VL Zero simulations, respectively. The annotations refer to regions discussed in the main text.

7.3.3 The Importance of Building a 3D Reservoir Model

The comparison of the results from Section 7.3.1 and Section 7.3.2 provides an insight into flow behaviour variations between a 2D and 3D model. Thus, the analysis provides a means to estimate whether a simplified 2D flow model can represent the impact of capillary heterogeneity expected in a 3D domain. In both the 2D and 3D simulations, the models which implement the intrinsic, viscous-limit relative permeability generally exhibit a faster vertical plume migration speed. This agreement is expected as the 2D models cover the full vertical section of the 3D model. We observe the formation of channels near the injector as a result of capillary heterogeneity in 2D and 3D.

Both sets of models also exhibit an increase in the lateral migration speed over time in the CL scenarios. However, the difference in the lateral distance travelled by the plume between the VL and CL scenarios differs. Whilst the plume spreads out further in the x and y dimension in the CL models in 3D, this is not observed in 2D. Instead, the plume in the VL models travels

nearly 1 km further. These results imply that the enhancement of the lateral migrated distance and lateral migration speed due to capillary heterogeneity is qualitatively distinct in the 2D models.

One reason for this may be the difference in the heterogeneity structure imposed in the 2D versus 3D domains. In 3D, the third dimension opens the possibility for many alternative flow pathways, which can help the plume avoid capillary barriers. In 2D this effect is lost and the plume may be held up behind capillary barriers (low k_r/high P_e barriers in the CL Pc simulation, low k_r barriers in the CL Zero simulation), which results in a less efficient migration. This shows a major qualitative difference to the 3D models.

The diminution in lateral migration distance due to capillary heterogeneity was not observed in the 2D simulations of Jackson and Krevor (2020) and is likely a result of a variation in the strength of heterogeneity imposed in the two studies. The Goldeneye field, the focus of Jackson and Krevor (2020), is characterised by a smaller variation in porosity, a standard deviation of 0.0243 was imposed to generate the reservoir model. In comparison to this, the Endurance site exhibits a stronger variation in the porosity well data with a standard deviation of 0.049. A higher standard deviation increases the likelihood for capillary barriers in the model, which will ultimately impact the trends we observe.

As we have scaled the CO_2 injection rate to the pore volume, we ensure the capillary number is consistent between the 2D and 3D scenarios. However, the models exhibit a variation in tilt, which may influence the flow pattern. We measure the dip from the base of the injector to the top of the structure in the 2D and 3D models. We find that the dip is 1° larger in the 2D models, which would not drastically decrease the capillary to gravity ratio. Therefore, we expect this to be a negligible influence on the variation in flow behaviour observed.

We also consider the impact of grid block orientation on the plume shape as this differs between the 2D and 3D models. Whilst CO_2 flow is directed perpendicular to the cells in 2D, it is orientated diagonally across the cells in 3D due to the location of the well and the imposed topography. This may affect the migration of the plume and future work could explore this by implementing specialised gridding procedures (Durlofsky, 2005) such as unstructured/irregular

grids (Heinemann et al., 1989; Prévost et al., 2005) or Voronoi grids (Aziz, 1993).

The comparison presented herein reveals that vertical 2D slices are unable to represent the flow that is observed in a full 3D model. We opt for vertical 2D slices as we are interested in investigating variations in the flow behaviour in a capillary-buoyancy dominated flow regime. Thus, capturing the vertical flow of CO_2 is crucial. However, it is important to acknowledge that the differences between 2D and 3D models highlighted in this section may vary when considering horizontal, rather than vertical, 2D slices. To investigate this in more detail, we propose future work that performs vertical equilibrium upscaling to generate horizontal slices, following the work by Gasda et al. (2012, 2013).

Overall, the results emphasize the importance of representing flow in 3D, which enables the flow pattern to be more closely replicated. Whilst key trends such as channelling near the wellbore, are retained in 2D, the influence of heterogeneity in the third dimension is a key control on the plume shape, flow pattern and speed. Variations between 2D and 3D flow processes have previously been examined. Whilst some studies concluded the difference to be negligible (Fu et al., 2013), others highlighted the contrast in results obtained from 2D and 3D models (Tchelepi and Orr, 1994). Following these contradictory findings, the importance of representing flow in 3D, specifically for CO_2 injection studies, remained unclear. Reduced-dimensionality models are commonly used to conduct uncertainty analysis, screening studies and risk assessments (Bianchi et al., 2016), which is primarily driven by the reduced computational cost. Our novel findings show that 2D models will likely oversimplify the impact of heterogeneity on plume migration, in agreement with observations from Chapter 6. Thus, it is crucial to represent the flow field in full 3D to make informed decisions and predictions.

7.3.4 Changes in Behaviour with Well Placement

We explore the impact of well placement by moving the point of injection from CI2 to CI5 in Figure 7.3. Rather than simulating all six cases, we now focus only on the two end-members: CL Pc and VL Zero. The injection rate and boundary conditions remain the same.

The resultant plume footprint area and plume swept volume are shown in Figure 7.28. The new well location has resulted in an absolute decrease in both measures for both simulations, see Table 7.1. This is expected as we are injecting into another region of the reservoir, which is characterised by a different tilt, a different heterogeneity distribution and the injector is located nearer to the top of the structure. As a result, the plume elongation in the x-axis is enhanced in the CL and VL simulations, see Figure 7.29 and 7.30.

To investigate potential variations in the influence of gravity on plume migration between the two injector scenarios, we calculate the maximum tilt, which we define as the dip from the base of the injector to the top structure. We find that the CI5 scenario exhibits a maximum tilt that is approximately 2° higher than the CI2 scenario (an increase from 8° to 10°). This demonstrates that the influence of gravity is likely stronger in the CI5 case, which may decrease the capillary-to-gravity ratio and dampen the impact of capillary heterogeneity on plume migration. Whilst the relative importance of capillary-to-gravity may decrease, a stronger tilt may also enhance the presence of heterogeneities as buoyancy may force CO_2 into layers that would otherwise be avoided by the gas. This behaviour was previously discussed in Chapter 6.

The results provided in Table 7.1 suggest that the impact of capillary heterogeneity on plume shape is comparable in the two injector scenarios, with a maximum deviation of 5%. Furthermore, the key temporal trends in footprint area and swept volume, that were previously identified in the CI2 scenario, persist with the new well configuration (Figure 7.28).

Initially, the CL simulation is characterised by a larger plume footprint, attributed to channel formation near the injector. This is followed by a period where the plume in the VL simulation spreads out laterally more quickly primarily due to the initial fast vertical migration. Whilst the CI2 injection scenario is characterised by an approximately 4-year long period where the CL

and VL footprint areas converge, this is not observed for the CI5 injection simulations. Instead, the plume footprint area in the CL simulation surpasses the VL simulation sooner. Thus, the enhancement of plume spreading due to capillary heterogeneity occurs sooner in the new well configuration. However, the absolute impact of capillary heterogeneity on plume footprint area remains unchanged.

The difference in the plume swept volume between the CL and VL simulations are consistent in the CI2 and CI5 configurations. The CL Pc simulation is characterised by a larger swept volume than the VL Zero simulation from the onset of CO_2 injection, and this contrast increases with time.

These results demonstrate that the impact of capillary heterogeneity on plume migration persists, even in a more strongly dipping domain. Thus, the importance of capillary heterogeneity is largely independent of the reservoir tilt, for models that have a tilt smaller than 10°. This is in agreement with observations from Chapter 6, where we observed the strong influence of capillary heterogeneity in a 5° tilted domain. These results also align with the findings from Shao et al. (2022), where both, gravity and heterogeneity, were identified to control plume migration in a 2-5° dipping model. Based on these findings, the transition from a capillary to gravity dominated flow likely occurs in domains with a tilt higher than 10°. However, other factors including the level of heterogeneity may also influence this.

Table 7.1: Plume footprint area and swept volume for the two injection scenarios (CI2 and CI5) for the VL Zero and CL Pc simulations after 25 years injection. The percentage relative change is calculated as: $(\frac{CI5-CI2}{CI2})\times 100$, where CI2 and CI5 are the corresponding measures for each scenario.

	CI2		**CI5**		**% Relative Change**	
Measures	A_f [km^2]	V_s [km^3]	A_f [km^2]	V_s [km^3]	A_f [%]	V_s [%]
VL Zero	9.02	0.19	6.60	0.16	28	16
CL Pc	10.44	0.28	8.00	0.24	23	14

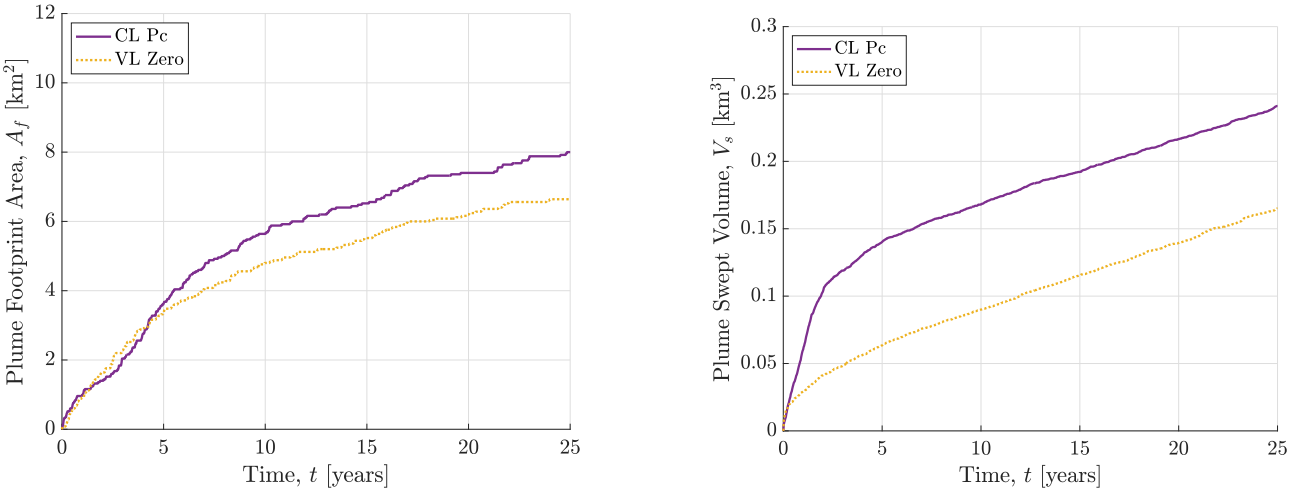


Figure 7.28: a) plume footprint area and b) plume swept volume over the 25 year injection period for the CI5 injector scenarios.

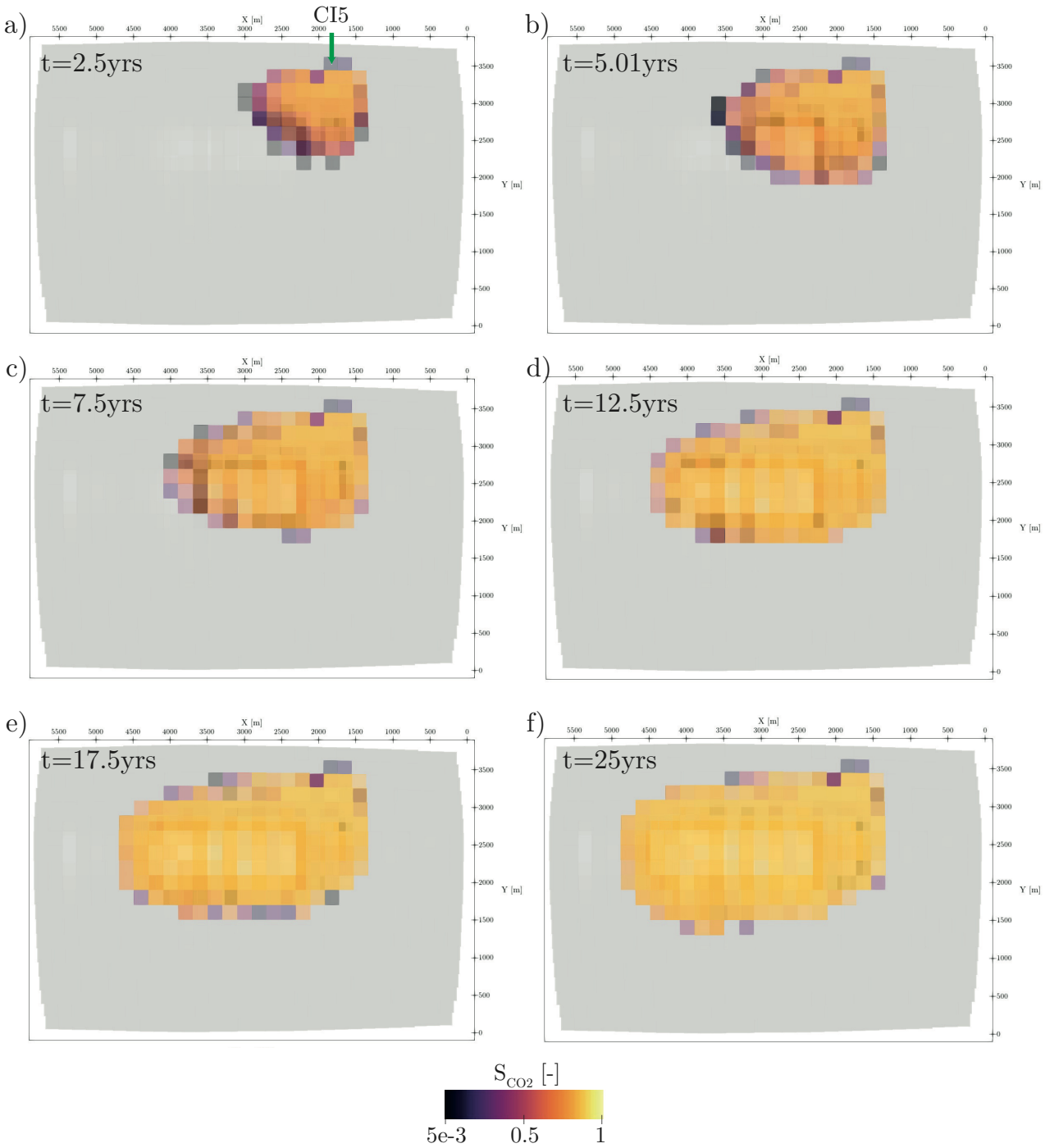


Figure 7.29: Plan view of the CO_2 saturation distribution in the VL Zero simulation at different timesteps, as annotated, for the CI5 injector scenario. Note: grid blocks with $S_{CO2} < 5 \times 10^{-3}$ are coloured in grey. Colours are moderately opaque so that the plume extent is visible. The green arrow in the first panel indicates the (x,y) injector location.

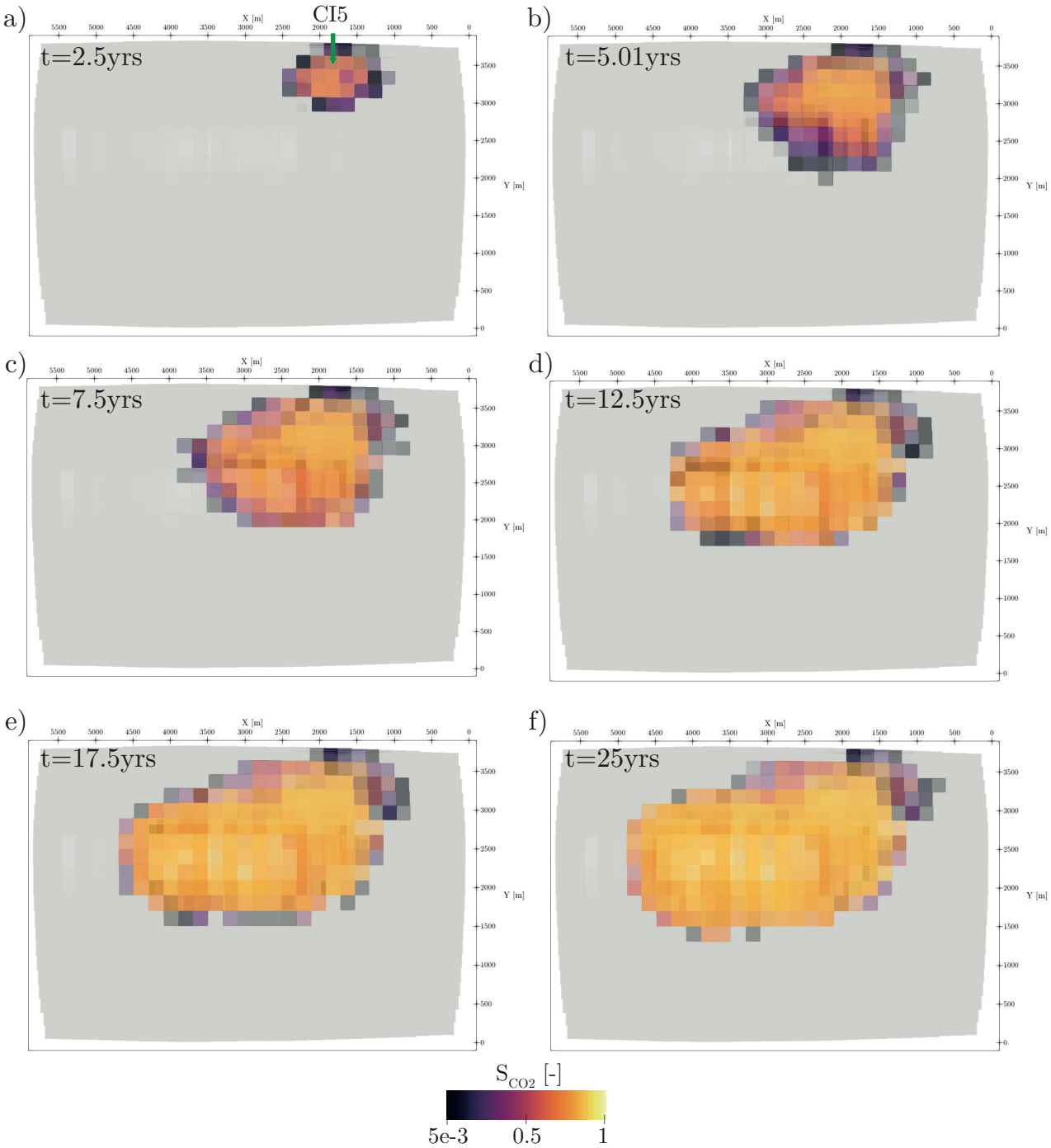


Figure 7.30: Plan view of the CO_2 saturation distribution in the CL Pc simulation at different timesteps, as annotated, for the CI5 injector scenario. Note: grid blocks with $S_{CO2} < 5 \times 10^{-3}$ are coloured in grey. Colours are moderately opaque so that the plume extent is visible. The green arrow in the first panel indicates the (x,y) injector location.

7.3.5 The Impact of Multi-Point Injection

7.3.5.1 Footprint and Volume

We now increase the level of complexity of the well configuration to replicate the Endurance field development plan. Rather than injecting from one well, we now inject from all four wells that are enclosed in our model domain. The reader is referred to Figure 7.3 for a schematic of the well locations. The well injection rate is kept constant at 3131 m^3d^{-1} for all four wells, which also matches the field development plan. We focus our analysis on the two end-member models: CL Pc and VL Zero.

We present the plume footprint area for the two simulations over time in Figure 7.31a. The temporal trend, which was observed for the CI2 and CI5 injector scenarios, is replicated. Initially, the CL Pc simulation is associated with a larger footprint area due to enhanced channelling near the wellbore. As we inject more CO_2, the plume in the VL Zero simulation spreads laterally more quickly under the caprock, which results in a larger footprint. This lasts for approximately 5 years, after which the plume in the CL Pc model spreads across a much larger area. At these later stages, the difference between the VL Zero and CL Pc footprint areas is on average 7% larger in the four-injector scenario compared with the single injector models. Thus, the impact of capillary heterogeneity on lateral plume spreading is enhanced with four injectors.

Similarly, the plume swept volume over time displays the same trends as were observed in the single injector scenarios, see Figure 7.31b. From the onset of injection, the CL Pc model is characterised by a sharply increasing volume, which is significantly larger than that from the VL Zero simulation. After 25 years of injection, the relative difference between the CL Pc and VL Zero model is 38%, which is approximately 10% smaller than the difference exhibited in the single injector scenarios. This is attributed to the increase in total CO_2 volume injected in the domain. Although channel formation remains enhanced in the CL model with four injectors, these begin to merge over time as we introduce more gas and fill the reservoir. Ultimately, as progressively more of the reservoir is filled, the difference in the swept volume between the two simulations begins to decrease.

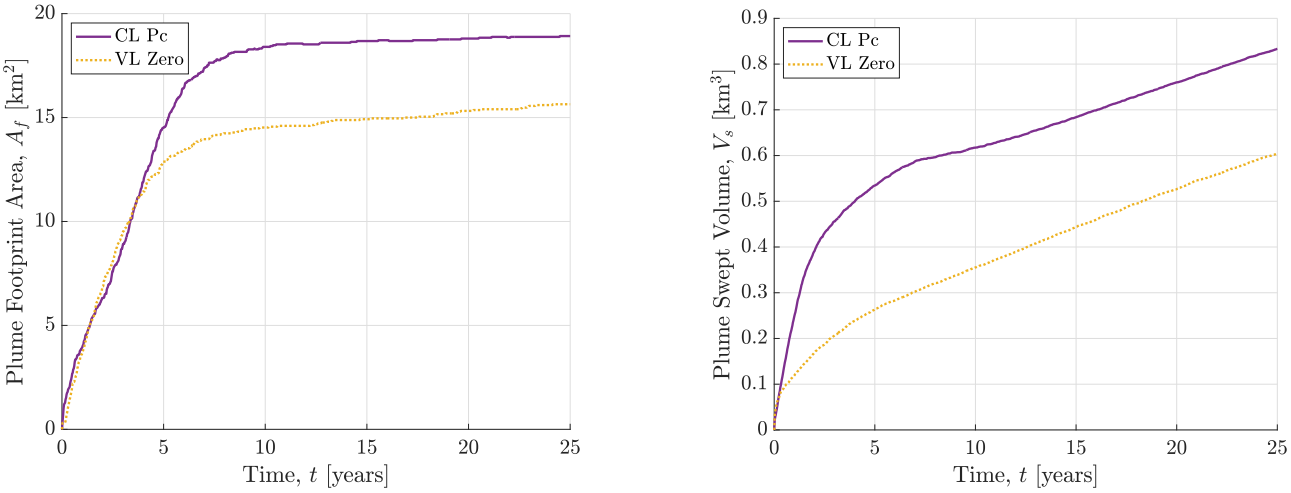


Figure 7.31: a) Plume footprint area and b) Plume swept volume over the 25 year injection period for the VL Zero and CL Pc simulations implementing the four injector configuration.

To analyse the flow behaviour in more detail, we plot saturation distribution maps, see Figure 7.32 to Figure 7.35. Figure 7.32a and Figure 7.33a demonstrate the change in plume shape that occurs as a result of variations in topography. The plume at CI1 spreads out the most, whereas the plumes at CI5 and CI2 spread out the least. As more CO_2 is injected, the four plumes begin to merge. The time at which the merge occurs is dependent on the initial vertical plume migration speed. The plumes in the VL Zero models begin to migrate laterally sooner, which ultimately results in the merge to occur sooner compared with the CL Pc simulations (Figure 7.32b and Figure 7.33b).

Interestingly, the central portion of the uppermost layers is swept last (Figure 7.32c-d and Figure 7.33c-d). This may be a result of the grid block orientation relative to the topography, which is discussed in more detail in Section 7.3.6. After 12.5 years, the leading edges of the plume in the CL Pc model exhibit a more variable saturation distribution compared with the VL Zero run. We also notice that the increase in footprint area relative to the VL Zero model can be primarily attributed to regions in the vicinity of the injectors. Channels form in all directions from the injectors, which result in an enhanced plume spread.

The channel formation can be more closely examined in Figure 7.34 and Figure 7.35. Whilst the CO_2 primarily migrates upwards following the topography in the VL Zero model, lateral channels form at all injector locations in the CL Pc model. These observations support the findings from the single-injector scenarios discussed in preceding sections. It also underpins

that this near-injector channelling behaviour is independent of injector location.

Figure 7.35c to Figure 7.35e also demonstrate how the CO_2 channels may improve storage efficiency. As indicated by the green arrow in Figure 7.35c, separate lateral channels form orientated parallel to the x-axis along which CO_2 invades the domain. Eventually, these channels merge (Figure 7.35d) and CO_2 has completely invaded these layers. There are grid blocks in proximity to this region that have not been invaded by CO_2 due to the low gas relative permeability. After the channels have merged, these regions progressively get filled with gas and they are completely swept by CO_2 after 25 years (Figure 7.35e, arrow). In comparison to this, the plume has not swept this part of the domain in the VL Zero simulation. Therefore, capillary heterogeneity has improved the storage efficiency in these runs.

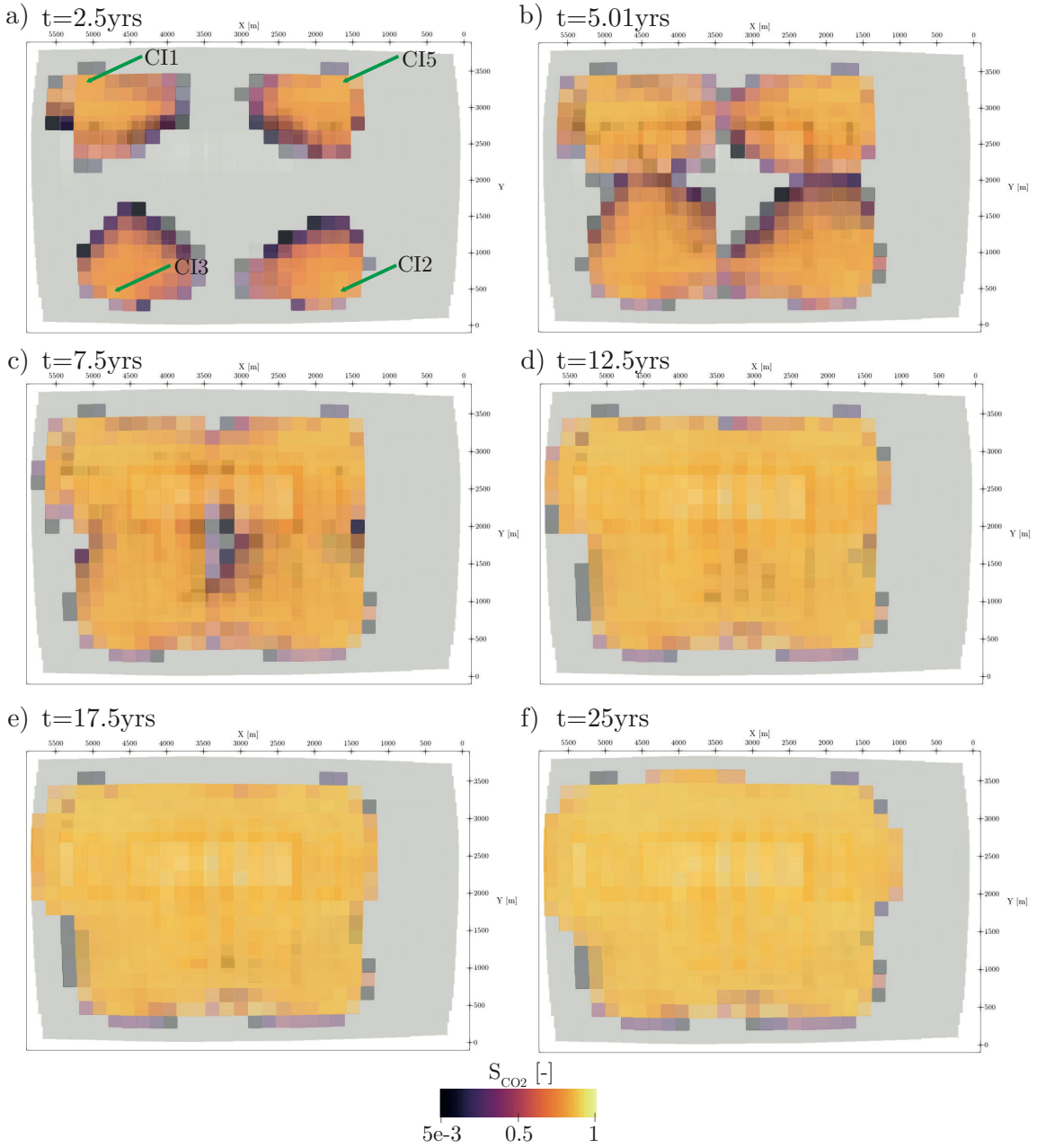


Figure 7.32: Plan view of the CO_2 saturation distribution in the VL Zero simulation at different timesteps, as annotated, for the four-injector scenario. Note: grid blocks with $S_{CO2} < 5 \times 10^{-3}$ are coloured in grey. Colours are moderately opaque so that the plume extent is visible. The green arrows in the first panel indicate the (x,y) injector locations.

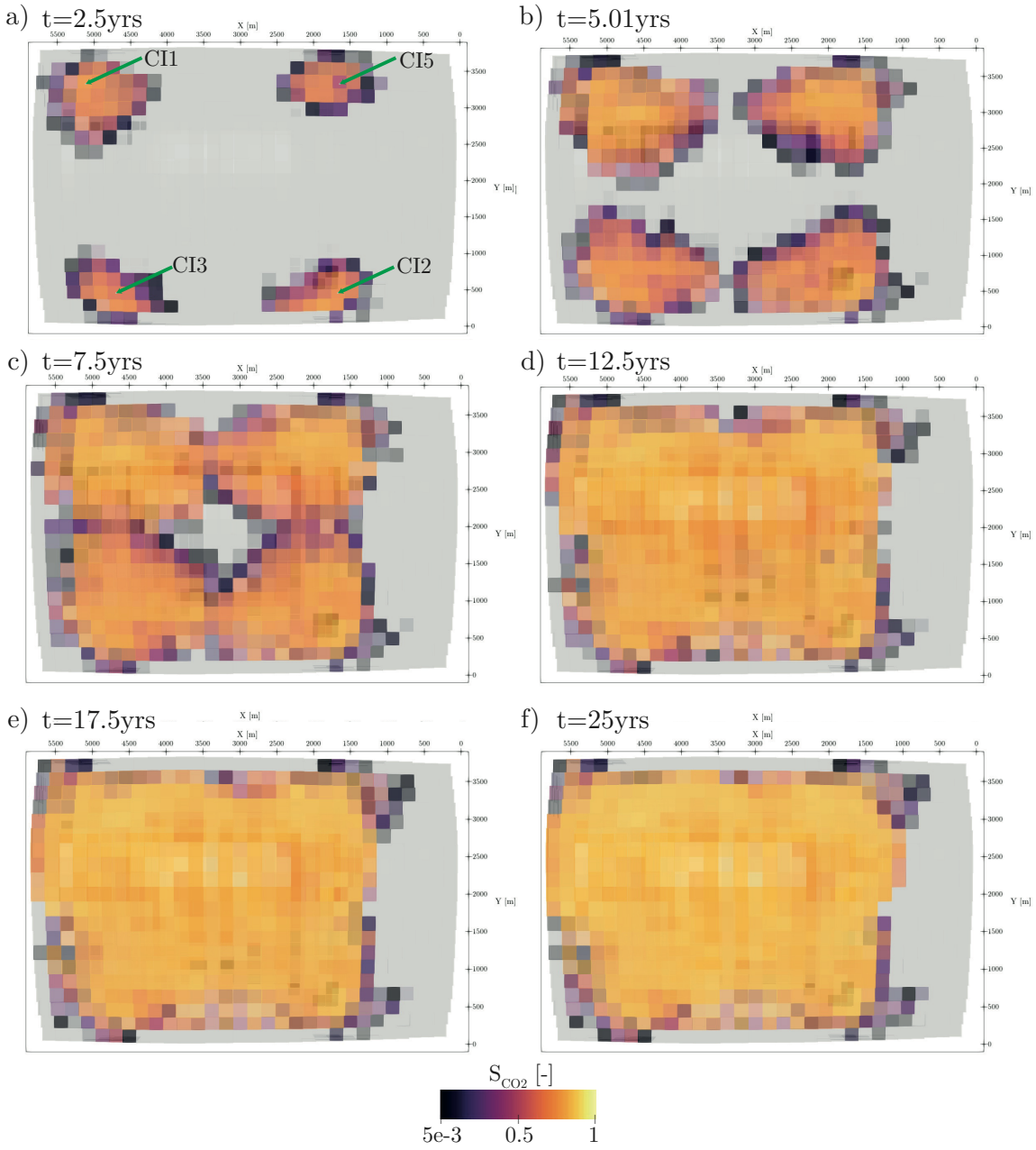


Figure 7.33: Plan view of the CO_2 saturation distribution in the CL Pc simulation at different timesteps, as annotated, for the four-injector scenario. Note: grid blocks with $S_{CO2} < 5 \times 10^{-3}$ are coloured in grey. Colours are moderately opaque so that the plume extent is visible. The green arrows in the first panel indicate the (x,y) injector locations.

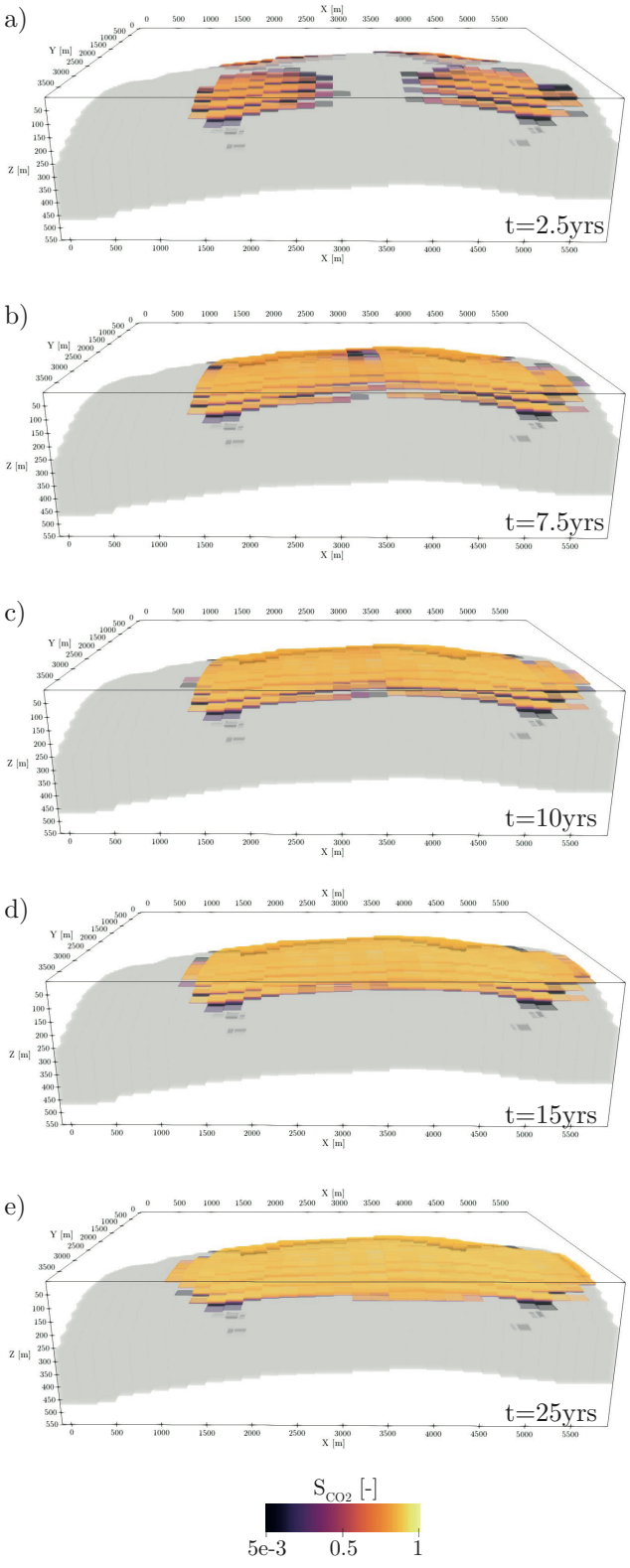


Figure 7.34: Side view of the CO_2 saturation distribution in the VL Zero simulation at different timesteps, as annotated, for the four-injector scenario. Note: grid blocks with $S_{CO2} < 5 \times 10^{-3}$ are coloured in grey. Colours are moderately opaque so that the plume extent is visible.

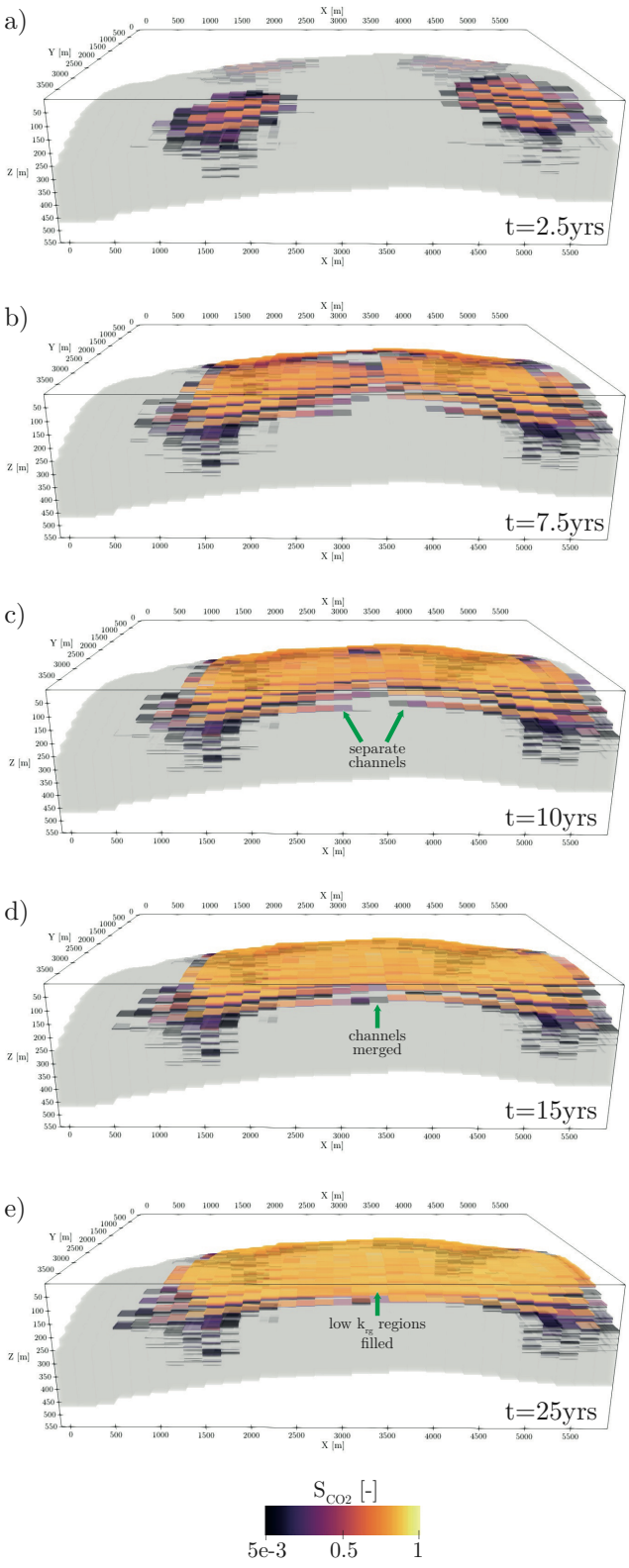


Figure 7.35: Side view of the CO_2 saturation distribution in the CL Pc simulation at different timesteps, as annotated, for the four-injector scenario. Note: grid blocks with $S_{CO2} < 5 \times 10^{-3}$ are coloured in grey. Colours are moderately opaque so that the plume extent is visible.

7.3.5.2 Plume Thickness

To further analyse the variation in saturation distribution between the two simulations, we calculate the difference in plume thickness at each (x,y) location, where red blocks represent locations where the CL Pc simulation exhibits a thicker plume and blue blocks represent locations where the VL Zero simulation is characterised by a thicker column. The results at varying timesteps are presented in Figure 7.36.

As shown, the trend between the two end-member simulations persists when increasing the number of injectors from one to four. The regions in the vicinity of the injectors display a much thicker plume in the CL Pc simulation, with a maximum difference of 160 m. The difference in thickness is attributed to the enhancement of channel formation due to capillary heterogeneity, as shown in the cross-sectional saturation distribution maps from the previous section.

At early times (Figure 7.36a), we can identify the faster lateral spreading plume exhibited in the VL Zero simulation, which is caused by a faster initial vertical migration. The cells further away from the injector are characterised by a large negative difference in plume thickness, which corresponds to the blue colour. As more CO_2 is injected, the difference in plume thickness in the main region of the reservoir varies. Nearer the injectors, the regions generally exhibit a thicker CL Pc plume, whereas the central part displays a thicker VL Zero plume. The absolute difference in plume thickness decreases at later stages as shown in Figure 7.36e and Figure 7.36f. This reflects the progressive filling of the reservoir.

Overall, the results demonstrate that there is a noticeable difference in plume thickness between the VL Zero and CL Pc simulations. Therefore, disregarding the upscaled impact of capillary heterogeneity will likely result in erroneous saturation distribution predictions, with a significant underprediction in plume thickness near the injectors.

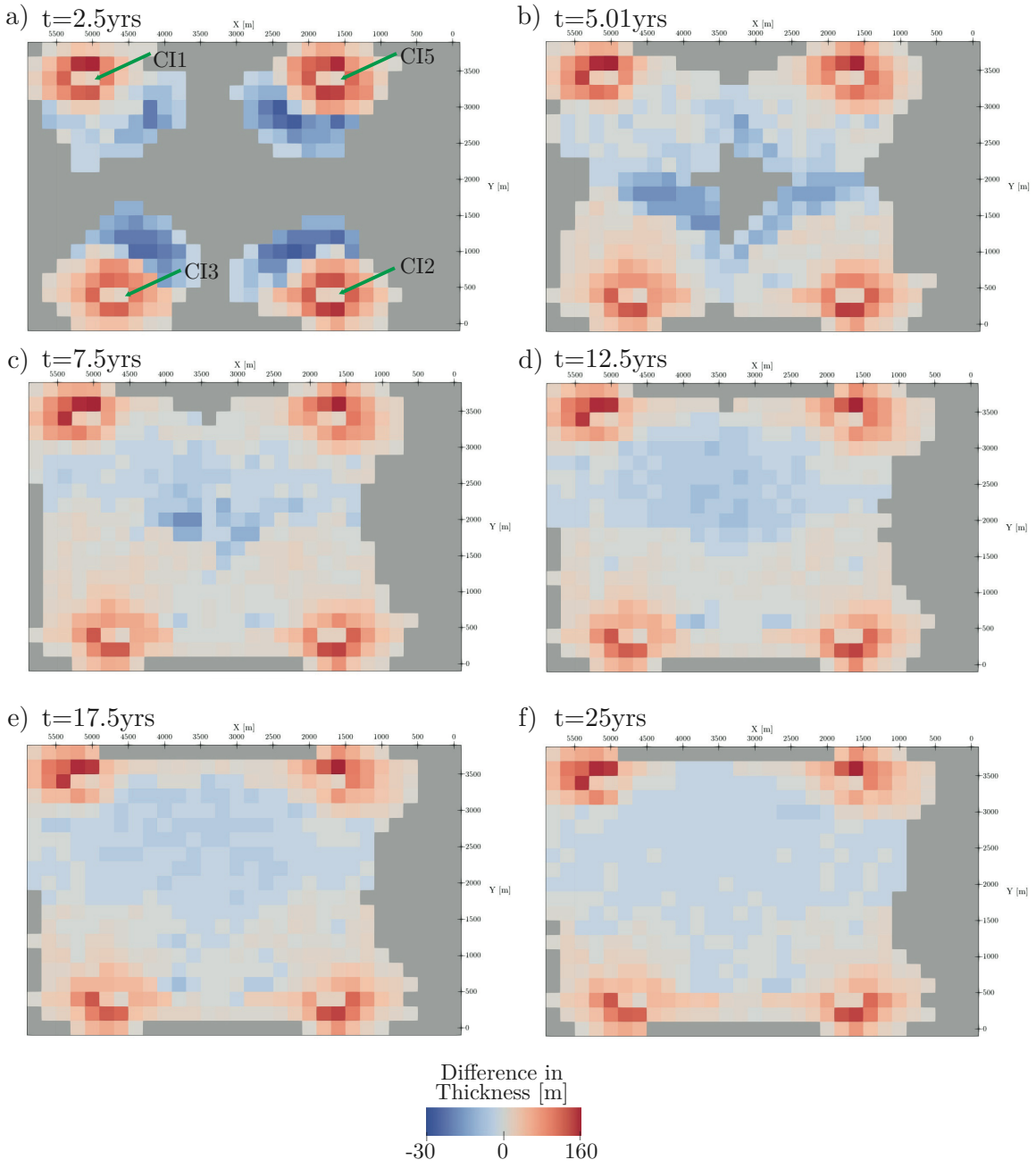


Figure 7.36: Topdown view of the difference in plume thickness between the VL Zero and CL Pc simulations at different timesteps as indicated for the four-injector scenario. Red grid blocks refers to regions where the CL Pc simulation is characterised by a thicker plume and blue grid blocks represent regions where the VL Zero plume is thicker. Green arrows point to the injector locations.

7.3.5.3 Seismic Detection

In this section, we examine the plume thickness in the CL Pc simulation against the seismic detection limit. We plot the thickness of the plume at varying timesteps in Figure 7.37, highlighting the regions that correspond to plume thicknesses of 9 m or below. These regions represent locations where the plume likely will not be detected by seismic techniques.

The key trends observed in the CI2 injection scenario can also be identified here. At early times, Figure 7.37a, the leading edges of all four plumes fall below the seismic detection limit, which corresponds to the thinned gravity tongue observed in the simulations. Once the individual plumes have merged into one large plume, Figure 7.37c, the regions exhibiting plume thicknesses under 9 m are located on the edges of this bigger plume, which again corresponds to the thinned gravity tongue. After 25 years, there are a smaller number of blocks with thicknesses less than 9 m compared with the CI2 simulation. This is expected, because we have introduced four times as much volume of CO_2 into the model, which is filling the reservoir and flowing out of the system along the edges of the domain.

The blue arrow in Figure 7.37c points to the region where the channels originating from the CI3 and CI2 wells merge. The increase in thickness from 15 years to 25 years (Figure 7.37c to Figure 7.37d) in this region demonstrates the improved sweep efficiency due to channelling. These cells are not invaded by CO_2 in the VL Zero simulation.

To compare these trends with the VL Zero simulation, we extract the total number of locations with plume thickness smaller or equal to 9 m for both runs in Figure 7.38. The general trend observed for the CI2 injector scenario is preserved herein, where capillary heterogeneity reduces the risk of the leading edges of the plume remaining undetected in seismic surveys after 25 years of injection. However, the total number of years where the CL Pc simulation is characterised by a greater number of thin-plume locations increased from 8 years in the CI2 scenario to 12 years in the four-well scenario. Thus, the presence of capillary heterogeneity becomes less favourable with respect to seismic detection with an increase in the number of injectors.

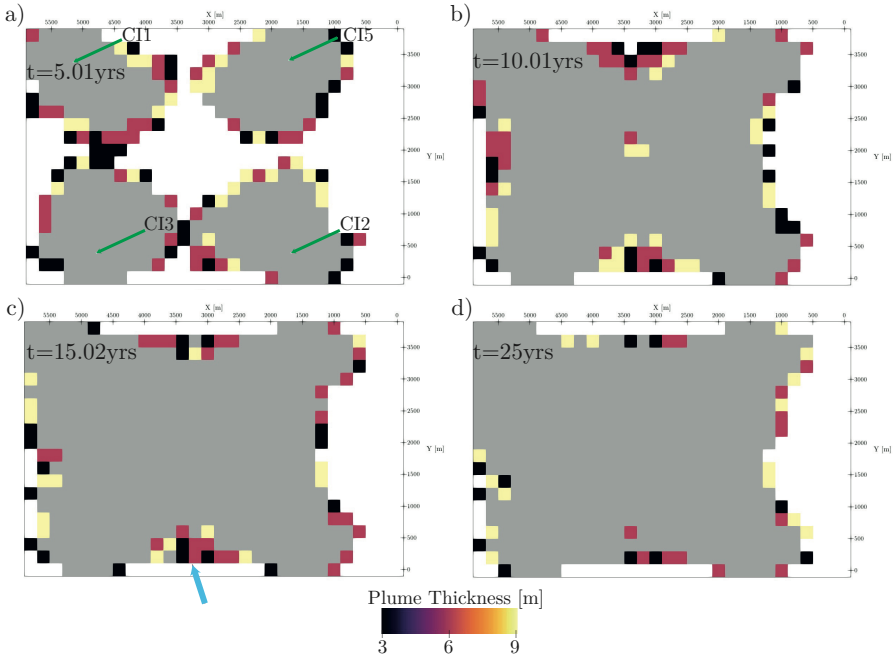


Figure 7.37: Topdown view of the plume thickness in the CL Pc simulation at different timesteps in the four-injector scenario. Grid blocks with a plume thickness above 9 m are coloured in grey. Grid blocks with a plume thickness between 3 and 9 m are colored accordingly. The green arrows in the first panel indicate the (x,y) injector locations. Blue arrow points to a region that is discussed in the main text.

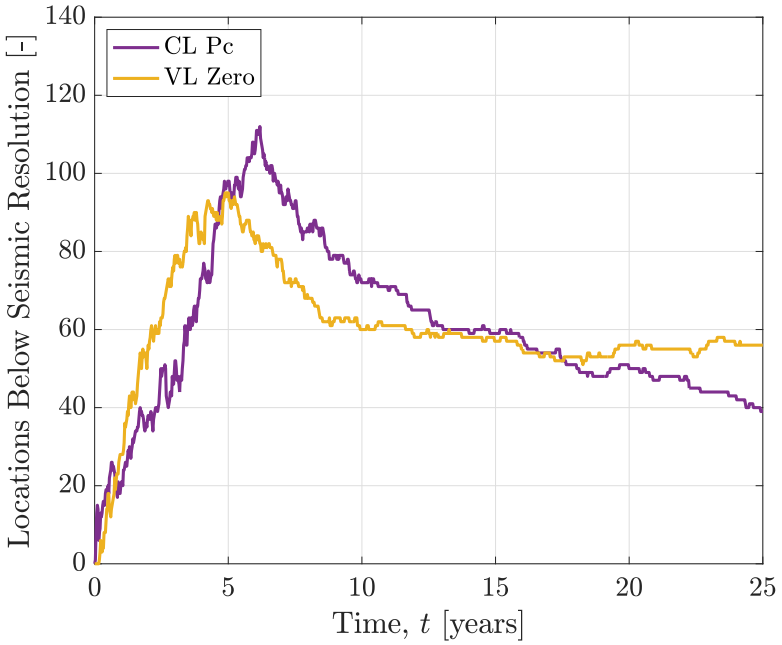


Figure 7.38: Number of (x,y) locations in the domain with a CO_2 column characterised by a thickness of 9 m or below (below seismic resolution). Purple and yellow lines are results from the CL Pc and VL Zero simulations, respectively.

7.3.6 Modelling Assumptions

The model we have built to represent the Endurance site encloses the central portion of the Endurance anticline. The entire structure is estimated to extend over 22 km and 8 km in the x and y dimension, respectively (BEIS, 2021a). We acknowledge that our model would likely be more representative of the Endurance site if we had generated a model covering the entire structure. However, this is computationally unfeasible and also not essential to meet our objectives. The main aim of this study was to develop an upscaling scheme to assess the impact of capillary heterogeneity on CO_2 plume migration using available petrophysical data from the Endurance site. Our model enabled us to analyse the relative importance of heterogeneity and tilt with a sufficiently fine grid resolution to resolve the plume structure. Building a larger model would likely require further grid coarsening, with which key features such as thin channels may not have been resolved.

Due to computational constraints, we focused our analysis on one realisation, which was generated from a geostatistical approach. Generating additional realisations would enable uncertainty investigation, for instance variability in the correlation lengths or system representativeness. However, this is beyond the scope of this thesis, but is suggested to be a focus of future work.

Our work is anchored in the steady-state assumption. This chapter and Chapter 6 have shown that the plume movement is dynamic as a result of heterogeneity. This may result in unsteady-state flow behaviour, in which case the assumption of steady-state would break down. However, our results also indicate that the unsteady-state behaviour likely occurs only in the leading edges of the plume, whereas the central portion of the plume will be at steady-state. Thus, numerical uncertainties in the upscaled CO_2 saturation may be constrained to the leading edges of the plume. Nevertheless, the verification of the upscaling method presented in this chapter demonstrates that the steady-state upscaling scheme successfully reproduces the fine-scale saturation distribution. Thus, the impact of the dynamic behaviour on the steady-state assumption is likely negligible.

Similarly, our work assumes a capillary-limit flow regime and we use a single set of upscaled relative permeabilities in each dimension in each coarse cell. However, CO_2 migration speed likely varies within the plume. On a kilometre scale, faster rates are expected near the injectors, which decrease with increasing distance from the injector. Within each channel, we also expect to see some variation in flow rate, with the tip of the gravity tongue flowing faster than the base. Thus, there may be regions within the plume that do not confine to the capillary-limit assumption. Shao et al. (2022) implemented rate-dependent, anistropic relative permeabilities in each grid block to model the impact of heterogeneity at the Otway site. The authors showed that there was a negligible difference in the plume shape and flow pattern between models that implemented one set of capillary-limit relative permeabilities versus models that incorporated rate-dependent relative permeabilities. The paper suggests that the velocity variation within the plume is insufficient to cause a significant change in the block relative permeability, which results in a similar flow behaviour between the models (Shao et al., 2022). Whilst the implementation of rate-dependent relative permeabilities would take into account any variations in flow regime, it would also significantly increase the computational resource requirements and overhead costs. Based on this and the observations from Shao et al. (2022), we find our current approach to be most suitable as it is scaleable.

The upscaling is performed on a fine grid with cell dimensions (x,y,z) 10 m, 10 m and 1 m and results in coarsened grid blocks with dimensions (x,y,z) 200 m, 200 m and 3 m. Inherent to the upscaling scheme is the separation of scales concept and the assumption that the coarsened grid blocks represent elementary volumes with homogeneous properties, the 'homogenisation assumption' (Chapter 2 Section 2.6). In our model, the correlation lengths are larger than the cell lengths in all dimensions. Thus, strictly speaking the homogenisation assumption may not hold, which may enhance the impact of grid block boundary conditions in the upscaling scheme. To address this, alternative upscaling schemes could be implemented such as facies-type modelling (Mikes et al., 2006; Sundal et al., 2015) or global upscaling methods (Holstein, 2007; Rabinovich et al., 2015). However, these may additionally increase the computational resource requirements, which already posed challenges in the current workflow. Therefore, we propose for this to be investigated in more detail in future work.

We impose constant temperature in the simulations as the focus of this study is the isolated impact of capillary heterogeneity on CO_2 flow behaviour. Temperature variations with the Endurance structure are mostly uncertain. However, modular dynamic tester long duration temperature measurements were made in the 42/25d-3 appraisal well. The measurements display a variation of 7°C across a 200 m interval (White Rose, 2016a). Thus, temperature variations may affect the fluid densities and alter the flow pattern. We conducted some uncertainty analysis to understand the impact of fluid property variations on flow behaviour, by reducing the mobility ratio by 5 (from 21 to 16). Some variations in the resultant saturation distribution were observed, mostly a reduction in the length of the CO_2 channels. However, these variations were small and the key trends persisted. Thus, the main conclusions drawn in this chapter are likely unaffected by uncertainties in reservoir fluid properties. Based on the work by Al-Khdheeawi et al. (2018); Abdoulghafour et al. (2020); Nazarian and Furre (2022), it would interesting to explore geochemical and compositional effects on CO_2 plume migration at the Endurance site in more detail. This is suggested for future work.

Our simulations do not explicitly model dissolution effects as the focus of our work was to understand the isolated impact of the small-scale heterogeneity prior to modelling the complex, fully coupled flow and transport processes. We recognise, based on work by Lindeberg and Begmo (2003); Ampomah et al. (2016); Gilmore et al. (2020); Yuan et al. (2020), that dissolution will likely be an important mechanism to incorporate in CO_2 injection simulations, particularly in the presence of heterogeneities. With respect to CCS, dissolution will improve CO_2 storage security as it immobilises the gas. Thus, the simulations presented herein represent the end member cases which are characterised by a reduced storage security due to the lack of geochemical effects. We suggest for dissolution effects to be incorporated in future work for which the analyses presented herein will provide important information in the interpretation.

7.3.7 Implications for Endurance Operations

Our findings provide novel insights into the leading controls on plume migration using available data from the proposed Endurance CCS site. Our simulations have demonstrated flow phenomena that occur as a result of capillary heterogeneity and will likely be observed at the Endurance CCS site once CO_2 injection has commenced.

In our simulations, which implemented the proposed well injection rates, the flow is largely capillary-dominated. This signifies that capillary heterogeneity will likely have leading order impacts on the flow of CO_2 at the Endurance site. Therefore, it is crucial to incorporate the upscaled impact of capillary heterogeneity on the multiphase flow properties. Thus far, the flow simulations published as part of the publicly available Northern Endurance Partnership reports disregard this (BEIS, 2021d), which may cause erroneous plume migration predictions.

The results also indicate that the leading edges of the plume and the thin channels that form at early times due to capillary heterogeneity will likely fall under the seismic detection limit. However these features are important for estimating the plume extent and migration speed, ultimately to determine any containment risks. The results suggest that a significant amount of the plume (reaching 1400m length for the single-injector scenario) may be undetected. Therefore, it will be important to utilise a range of monitoring techniques to track the plume in time.

Whilst a change in injector location results in variations in the total plume footprint area and swept volume, the overarching impact of capillary heterogeneity remains. We also observe a similar impact of capillary heterogeneity after increasing the number of injectors from one to four. The five-well field development plan was designed partially to provide "better mitigation against any unforeseen field heterogeneities" (BEIS, 2021b). However, our results show that the impact of capillary heterogeneity does not diminish in this well configuration. Instead, a larger number of channels form and the individual plumes interact, which increases the complexity of the plume shape.

7.3.8 Implications for CCS Operations

This study has demonstrated the prevalent impact that capillary heterogeneity has on CO_2 plume migration. By generating multiple models with different levels of heterogeneity accounted for, we were able to identify the main drivers behind variations in flow behaviour. Our results show the significant difference in plume shape and speed that arises from disregarding the upscaled impact of capillary heterogeneity on the multiphase flow functions. To understand and accurately model CO_2 migration, it is crucial to properly account for capillary heterogeneity and its impact of multiphase flow in a full 3D reservoir model.

Near the injector, enhanced CO_2 channelling increases the plume swept volume and improves sweep efficiency. This may result in enhanced capillary trapping and dissolution due to the increase in plume spread. This has important implications for CCS operations as injection could be designed to maximise channel formation and thereby improve storage efficiency. The multi-layer plume formation has been observed at other CCS sites around the world, which indicates that this is not an Endurance-specific phenomenon. For example, the plume at the Sleipner site in Norway can be described as having a "Christmas Tree" shape (Chadwick and Noy, 2010) consisting of 9 separate layers characterised by high CO_2 saturations.

As we move away from the injector, the lateral plume speed mostly increases due to the presence of capillary heterogeneity. The plume also spreads out over a significantly larger area and exhibits a thinned gravity tongue. These observations are important to consider in forecasting and leakage prevention studies. Disregarding the upscaled impact of capillary heterogeneity will likely underpredict migration speeds and spreading. Unexpected fast migration speeds have been observed at CCS sites worldwide. In Salah is one example, where the plume was characterised by 3 times faster migration rates than had been predicted previously with flow simulations (Ringrose et al., 2009). This demonstrates that our conclusions are applicable to other CCS sites.

We also find that the leading edges of the plume will likely fall below the seismic detection limit. This is especially applicable for the thin, laterally extensive channels that form as a

result of capillary heterogeneity. This is an important finding, because it implies that seismic surveys will likely underpredict plume migration speed and produce erroneous CO_2 location estimations. In the vicinity of leaky wells, faults or spill points, this may have detrimental consequences. Thus, it is crucial to properly characterise the target reservoir prior to injection and use a variety of monitoring techniques to track the plume. However, we also discovered that capillary heterogeneity reduces the total number of locations which exhibit plume thicknesses smaller than the seismic detection limit after 25 years of injection. Thus, the formation of a multi-layered plume, attributed to the presence of capillary heterogeneity, may in fact reduce the challenges associated with plume detection.

These insights are summarised in a schematic in Figure 7.39. The dark red plume shape represents the conventional view of CO_2 migration away from an injector, where the plume gradually thins towards the gravity tongue (Krevor et al., 2015). Our results indicate that CO_2 plume migration is more complex under the influence of capillary heterogeneity. Near the injector, channel formation is enhanced, which improves sweep efficiency and increases capillary trapping. As we move away from the injector, the gravity tongue thins and we observe faster migration speeds.

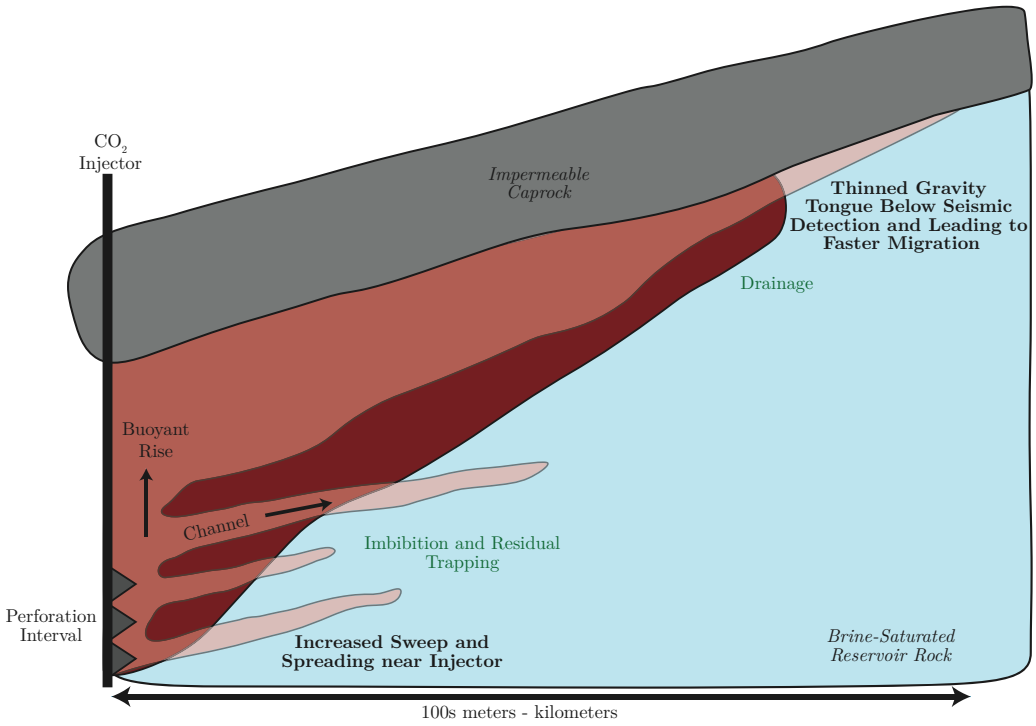


Figure 7.39: Sketch summarising some of the novel insights from the Endurance field simulation work.

7.4 Conclusions

In this Chapter, we have extended a 2D capillary-limit, steady-state upscaling scheme to model the 3D upscaled impact of capillary heterogeneity on the multiphase flow properties, capillary pressure and relative permeability. Using the workflow, we have investigated the impact of capillary heterogeneity on plume migration at the proposed Endurance storage site.

By means of an extensive core characterisation study, we characterised the injection interval at the Endurance site, which allowed us to replicate likely flow behaviour encountered in the reservoir. We investigated variations in flow behaviour with changes in well location and topography by replicating the proposed field development plan. Thus, the focus of our study was the impact of heterogeneity at an industrial scale geological carbon storage site using realistic injection rates and multi-point CO_2 injection. This sets our work apart from previous publications such as Shao et al. (2022).

We find that the impact of capillary heterogeneity on plume migration differs between 2D and 3D models, primarily because the interactions of heterogeneities in all three dimensions affect the CO_2 flow pattern. This is particularly evident for the lateral migration speed, which is slowed down in 2D. These are novel insights that have previously been overlooked and clearly demonstrate the value of building a full 3D reservoir model.

Our work has shown that capillary heterogeneity has a prevalent impact on plume migration. Near the injector, it enhances the formation of CO_2 channels, which significantly improves sweep efficiency and may result in an increase in capillary trapping and dissolution, if it were modelled. At distances far from the injectors, the gravity tongue is thinner and the plume travels faster as a result of capillary heterogeneity. These are novel insights and have important implications for CCS operations. On one hand, we can take advantage of capillary heterogeneity to improve storage efficiency. On the other hand, it can lead to large variations in plume migration speed and needs to be properly accounted for in reservoir models.

Chapter 8

Conclusions and Future Work

8.1 Summary of Thesis Achievements

The central topic of this thesis was to investigate the impact of capillary heterogeneity on fluid flow, in complex rock systems, in three dimensions, and at scales ranging from the laboratory to the field. The topics identified were primarily focused on applications for CCS. However, the issues tackled also have relevance for other scientific and engineering processes where multiphase fluid flow in porous media is central. In Chapter 4, we systematically evaluated a state-of-the-art workflow that characterises capillary heterogeneity on the core-scale using coreflood experimental data. Using the successful results, we investigated the impact of heterogeneity on multiphase flow properties in these heterogeneous rocks. In Chapter 5, we presented the results from an experimental study conducted on reservoir samples from the proposed Endurance CCS site in the UK. The experimental observations were subsequently used in Chapters 6 and 7. Chapter 6 explored the impact of capillary heterogeneity in 3D at the metre scale with numerical simulations that evaluated sensitivity to varying flow rate, dip and heterogeneity. In Chapter 7, an extension of a 2D capillary-limit, steady-state upscaling scheme was presented, which models the 3D upscaled impact of capillary heterogeneity on the multiphase flow properties. We built a reservoir model representative of the Endurance site and simulated CO_2 injection to study the flow behaviour arising from capillary heterogeneity.

8.2 Conclusions

The above work has resulted in novel findings on the impact of capillary heterogeneity on subsurface CO_2 storage, which are summarised below.

1. Capturing small-scale heterogeneities for characterising subsurface fluid flow is important, but challenging.

- Strongly-heterogeneous rocks such as carbonates or reservoir samples introduce complexities that warrant further advancements in core characterisation approaches.
- It is crucial to consider the physical mechanisms controlling the fluid behaviour in the creation of a numerical model of a rock core.
- Isotropic core-scale capillary heterogeneity results in a non-monotonic behaviour of the rate dependency of relative permeability.

2. The proposed Endurance CCS site exhibits strong capillary heterogeneity and the reservoir sample is characterised by restricted connectivity.

- MICP experiments demonstrated that the reservoir is characterised by strong capillary heterogeneity along a 70 m depth interval.
- Pore-network modelling indicates that connectivity in a reservoir sample from the Endurance site is controlled by small throats.

3. Capillary heterogeneity has a significant impact on the observed CO_2 flow pattern, CO_2 plume shape and CO_2 migration speed at the metre scale.

- Capillary heterogeneity can significantly speed up or slow down the CO_2 plume migration speed depending on the orientation of the heterogeneity relative to the flow direction.
- A tilted domain may dampen or enhance the presence of capillary heterogeneity depending on the underlying structure of heterogeneity.

4. Upscaling the impact of capillary heterogeneity on the multiphase flow properties is crucial to represent subsurface fluid flow.

- Capillary heterogeneity significantly enhances channel formation, increases reservoir sweep and reduces vertical migration speed near CO_2 injectors.
- Capillary heterogeneity thins gravity tongues and enhances lateral plume migration.
- Relative permeability, rather than capillary pressure, anisotropy is the main control on CO_2 flow behaviour.

5. Reduced-dimensionality models cannot represent the impact of capillary heterogeneity on subsurface fluid flow.

- There are major qualitative differences in the impact of capillary heterogeneity on CO_2 flow observed in 2D vertical and 3D models.
- On a metre length scale the effects of capillary heterogeneity are dampened in 2D.
- Field-scale reduced-dimensionality models exhibit lowered migration speeds compared with 3D models.

8.3 Recommendations for Future Research

Whilst this work has provided novel insights into the impact of capillary heterogeneity on subsurface fluid flow, it also highlighted the need for additional future work.

8.3.1 Geochemical and Phase Mixing Effects

The simulations presented herein focused on understanding the isolated impact of small-scale heterogeneity, which has provided novel insights into the leading order mechanisms of subsurface fluid flow. However, literature has shown that the CO_2-brine flow in the subsurface is influenced by complex geochemical, compositional and phase behaviour effects (Lindeberg and Begmo, 2003; Ampomah et al., 2016; Gilmore et al., 2020; Yuan et al., 2020). These are likely also influenced by temperature variations (Al-Khdheeawi et al., 2018; Abdoulghafour et al., 2020; Nazarian and Furre, 2022). Thus we propose future work that models the fully-coupled flow and transport processes between CO_2 and brine in the presence of heterogeneity. We would also recommend the investigation of the impact of the injected CO_2 purity on the flow behaviour as well as the interactions of CO_2 with any resident hydrocarbons, which is important for CCS operations targeting depleted hydrocarbon reservoirs.

8.3.2 Geologically-Based Reservoir Modelling Approach

The reservoir modelling and upscaling workflow presented in Chapter 7 is based on a geostatistical approach. This allowed us to identify the role of salient features including correlation lengths and degree of heterogeneity on plume migration and align the reservoir model properties with available data from the case study site. We suggest future research that explores a more geological-driven approach to building a reservoir model, which could be incorporated into the current workflow. It would be of interest to model the impact of geologically representative sedimentary structures such as cross-beds on the CO_2 flow pattern.

Furthermore, a geologically-driven approach may also reduce the computational resource requirements associated with building a reservoir model. Due to the computational constraints, we focused our investigation on a subsection of the case study site. Thus, reducing these requirements would open the possibility of building larger models at higher resolution or generate multiple realisations for uncertainty analyses. Facies-type modelling could represent a suitable approach (Mikes et al., 2006; Sundal et al., 2015).

8.3.3 Unsteady-State Versus Steady-State Behaviour

There remain outstanding questions regarding the difference between unsteady-state and steady-state experimental relative permeabilities and associated flow behaviour. Whilst some literature found the difference between steady-state and unsteady-state relative permeability coreflood experiments to be unimportant at low capillary numbers (Aleman et al., 1989), others have highlighted the differences between the two methods (Tsakiroglou et al., 2007; Yaslam, 2012). Moreover, the implications for field-scale modelling of CO_2 injection in heterogeneous systems remains unclear. Thus, we propose for future research to investigate this in more detail. It would be of interest to revisit the difference in measured relative permeabilities obtained from steady-state and unsteady-state coreflood experiments by performing an experimental study in the laboratory. This would provide novel insights into the variations in flow behaviour at that scale and also indicate the implications and assumptions associated with using a particular relative permeability in further modelling. We suggest for these observations to also be combined with pore-scale observations, whereby the role of pore-scale intermittency could be further investigated (Spurin et al., 2019, 2021).

Secondly, the dynamic nature of plume migration, which was highlighted in our work, could be analysed using these experimental relative permeabilities. Regions within a CO_2 plume that are hypothesised to undergo unsteady-state behaviour (for instance the leading edges of the plume), could be assigned the unsteady-state experimental relative permeability in a numerical simulation. The results could then be compared to a simulation implementing steady-state relative permeabilities.

8.3.4 Representative Relative Permeability Measurements

Our work has highlighted the challenges associated with performing laboratory experiments on complex reservoir samples. We suggest an extensive experimental suite to investigate the most appropriate experimental procedures to obtain representative relative permeabilities of a reservoir core sample. The study could focus on the following outstanding questions using larger scale corefloods and undertaking systematic testing at different flow rates: 1) Are samples representative of the reservoir after they have been plugged from a formation i.e. drilling damage? 2) What are the impacts of drilling mud composition on the wettability of the sample? 3) What fluids should be used to perform relative permeability coreflood experiments on reservoir samples, especially when the reservoir fluids are difficult to handle in a laboratory setting? 4) How can we minimise the impacts of the laboratory design and equipment on the resultant relative permeability measurements? 5) What are the most suitable treatments and cleaning procedures to be applied to core samples? 6) What is the repeatability of coreflood tests?

8.3.5 Application to Operational CCS Site

The upscaling and reservoir modelling workflow was applied to a proposed Endurance storage site, where we demonstrated the measurable impact of capillary heterogeneity on subsurface fluid flow. Following these discoveries, it would be of interest to apply the workflow to an operational CCS site. Results from the simulations could be directly compared to observations from the site such as seismic surveys. Through this, other areas of uncertainty within the workflow could be tested, for instance the impact of boundary conditions imposed in the upscaling workflow.

8.3.6 Impact of Geological Uncertainty

Chapter 6 demonstrated the variability in flow behaviour that emerges from changes in the underlying heterogeneity. Future research could explore these effects in more detail and at a range of scales. On a metre length scale, it would be interesting to investigate the variations in flow behaviour with different realisations and also using a greater range of heterogeneity types and length scales. This would also help identify the implications for upscaling procedures. On a field-scale, generating numerous realisations would provide key insights into the ranges of flow behaviour that can be expected at a specific site and any associated risks. These realisations could then be incorporated in an uncertainty framework to assess risks, containment concerns and mitigation scenarios, which is particularly important for CCS operations.

8.3.7 Reservoir Pressure

The Snøhvit case study, discussed in Chapter 1, highlighted the challenges that can be encountered when injecting CO_2 into a heterogeneous formation. The pressure gauges on the well head indicated a significant buildup of reservoir pressure thought to be caused by reservoir compartmentalisation and salt precipitation (Birkholzer et al., 2015). Beyond injectivity reductions, variations in reservoir pressure are "one of the best indicators of CO_2 movement" (Kelemen et al., 2019) and are also significantly impacted by heterogeneity (Gasda et al., 2021). As such, it would be interesting to perform a detailed analysis of the pressure in the field-scale simulations presented in Chapter 7 and understand how it is affected by capillary heterogeneities and whether it can provide useful information on the plume movement.

8.3.8 Near Wellbore Upscaling

Whilst capillary effects diminish near the wellbore, it would be of value to develop a near-wellbore upscaling scheme, which takes into account the presence of rock heterogeneities. This could be incorporated into the upscaling workflow and would enable the radial flow pattern near the wellbore to be explored in more detail. This would particularly be of interest for studies focused on modelling salt precipitation at CCS sites. Furthermore, a simulation study could be performed to assess which injection strategies maximise the formation of channeling observed near the injectors, which we discovered in our simulations.

8.3.9 Improvement of Numerical Methods

Throughout this work, we have come across significant challenges associated with numerical simulator performance. Incorporating capillary heterogeneity into numerical models resulted in significant convergence issues and slow run times, which increased overhead costs and computational requirements. These issues were observed for all numerical simulations, which modelled flow behaviour at a range of scales from millimetres to kilometres. Based on this, we propose future research that focuses on advancing numerical methods required to simulate fluid flow in heterogeneous systems.

8.3.10 Bridging the Gap Between Pore-Scale Observations and Field-Scale Modelling

To upscale the impact of small-scale rock heterogeneities, the separation of scales concept is central and it is important to assess the dominant length scales of heterogeneities at a particular site. To fully account for the range of heterogeneity length scales, it would be highly beneficial to develop an upscaling workflow that upscales observations from the pore to the field scale. We propose for this to be an area of active future research.

Bibliography

Abdoulghafour, H., Sarmadivaleh, M., Hauge, L. P., Fernø, M., and Iglauer, S. (2020). Capillary pressure characteristics of CO_2-brine-sandstone systems. *International Journal of Greenhouse Gas Control*, 94(July 2019):102876.

Akai, T., Kuriyama, T., Kato, S., and Okabe, H. (2021). Numerical modelling of long-term CO_2 storage mechanisms in saline aquifers using the Sleipner benchmark dataset. *International Journal of Greenhouse Gas Control*, 110:103405.

Akhlaghi Amiri, H. A. and Hamouda, A. A. (2014). Pore-scale modeling of non-isothermal two phase flow in 2D porous media: Influences of viscosity, capillarity, wettability and heterogeneity. *International Journal of Multiphase Flow*, 61:14–27.

Al-Kharusi, A. S. and Blunt, M. J. (2008). Multiphase flow predictions from carbonate pore space images using extracted network models. *Water Resources Research*, 44(6):1–14.

Al-Khdheeawi, E. A., Vialle, S., Barifcani, A., Sarmadivaleh, M., and Iglauer, S. (2017). Impact of reservoir wettability and heterogeneity on CO_2-plume migration and trapping capacity. *International Journal of Greenhouse Gas Control*, 58:142–158.

Al-Khdheeawi, E. A., Vialle, S., Barifcani, A., Sarmadivaleh, M., and Iglauer, S. (2018). Effect of wettability heterogeneity and reservoir temperature on CO_2 storage efficiency in deep saline aquifers. *International Journal of Greenhouse Gas Control*, 68(May 2017):216–229.

Al-Menhali, A., Niu, B., and Krevor, S. (2015). Capillarity and wetting of carbon dioxide and brine during drainage in Berea sandstone at reservoir conditions. *Journal of the American Water Resources Association*, 51(10):7895–7914.

Al-Menhali, A. S., Menke, H. P., Blunt, M. J., and Krevor, S. C. (2016). Pore Scale Observations of Trapped CO_2 in Mixed-Wet Carbonate Rock: Applications to Storage in Oil Fields. *Environmental Science and Technology*, 50(18):10282–10290.

Al-Sarihi, A., Zeinijahromi, A., Genolet, L., Behr, A., Kowollik, P., and Bedrikovetsky, P. (2018). Effects of Fines Migration on Residual Oil during Low-Salinity Waterflooding. *Energy and Fuels*, 32(8):8296–8309.

Aleman, M. A., Ramamohan, T. R., and Slattery, J. C. (1989). The Difference Between Steady-State and Unsteady-State Relative Permeabilities. *Transport in Porous Media*, 4(i):449–493.

Alhosani, A., Scanziani, A., Lin, Q., Raeini, A. Q., Bijeljic, B., and Blunt, M. J. (2020). Pore-scale mechanisms of CO_2 storage in oilfields. *Scientific Reports*, 10(1):1–9.

Alnes, H., Eiken, O., Nooner, S., Sasagawa, G., Stenvold, T., and Zumberge, M. (2011). Results from Sleipner gravity monitoring: Updated density and temperature distribution of the CO_2 plume. *Energy Procedia*, 4:5504–5511.

AlRatrout, A., Blunt, M. J., and Bijeljic, B. (2018). Wettability in complex porous materials, the mixed-wet state, and its relationship to surface roughness. *Proceedings of the National Academy of Sciences of the United States of America*, 115(36):8901–8906.

Ambrose, W. A., Lakshminarasimhan, S., Holtz, M. H., Núñez-López, V., Hovorka, S. D., and Duncan, I. (2008). Geologic factors controlling CO_2 storage capacity and permanence: Case studies based on experience with heterogeneity in oil and gas reservoirs applied to CO_2 storage. *Environmental Geology*, 54(8):1619–1633.

Aminu, M. D., Nabavi, S. A., Rochelle, C. A., and Manovic, V. (2017). A review of developments in carbon dioxide storage. *Applied Energy*, 208(August):1389–1419.

Ampomah, W., Balch, R., Cather, M., Rose-Coss, D., Dai, Z., Heath, J., Dewers, T., and Mozley, P. (2016). Evaluation of CO_2 Storage Mechanisms in CO_2 Enhanced Oil Recovery Sites: Application to Morrow Sandstone Reservoir. *Energy and Fuels*, 30(10):8545–8555.

An, S., Hasan, S., Erfani, H., Babaei, M., and Niasar, V. (2020). Unravelling Effects of the Pore-Size Correlation Length on the Two-Phase Flow and Solute Transport Properties: GPU-based Pore-Network Modeling. *Water Resources Research*, 56(8).

An, S., Wenck, N., Manoorkar, S., Berg, S., Taberner, C., Pini, R., and Krevor, S. (2023). Inverse modelling of core flood experiments for predictive models of sandstone and carbonate rocks. *Authorea*, (May).

Andrew, M., Bijeljic, B., and Blunt, M. J. (2014). Pore-scale contact angle measurements at reservoir conditions using X-ray microtomography. *Advances in Water Resources*, 68:24–31.

Andrews, E. (2022). *Pore scale insights into the impacts of wetting state, pore structure and sandstone mineralogy on low salinity water flooding*. PhD thesis.

Armstrong, R. T., McClure, J. E., Berrill, M. A., Rücker, M., Schlüter, S., and Berg, S. (2016). Beyond Darcy's law: The role of phase topology and ganglion dynamics for two-fluid flow. *Physical Review E*, 94(4):1–10.

Arts, R., Eiken, O., Chadwick, A., Zweigel, P., van der Meer, L., and Zinszner, B. (2004). Monitoring of CO_2 injected at Sleipner using time-lapse seismic data. *Energy*, 29(9-10):1383–1392.

Aziz, K. (1993). Reservoir simulation grids:opportunities and problems. *Journal of Petroleum Technology*, 45(7):658–663.

Baban, A., Al-Yaseri, A., Keshavarz, A., Amin, R., and Iglauer, S. (2021). CO_2 – brine – sandstone wettability evaluation at reservoir conditions via Nuclear Magnetic Resonance measurements. *International Journal of Greenhouse Gas Control*, 111:103435.

Baker, R. O. (1993). *Effect of reservoir heterogeneities and flow mechanisms on numerical simulation requirements*. PhD thesis.

Bakhshian, S., Hosseini, S. A., and Lake, L. W. (2020a). CO_2-brine relative permeability and capillary pressure of Tuscaloosa sandstone: Effect of anisotropy. *Advances in Water Resources*, 135:103464.

Bakhshian, S., Rabbani, H. S., Hosseini, S. A., and Shokri, N. (2020b). New Insights Into Complex Interactions Between Heterogeneity and Wettability Influencing Two-Phase Flow in Porous Media. *Geophysical Research Letters*, 47(14):1–10.

Bao, H., Zhai, Y., Lan, H., Zhang, K., Qi, Q., and Yan, C. (2019). Distribution characteristics and controlling factors of vertical joint spacing in sand-mud interbedded strata. *Journal of Structural Geology*, 128(August):103886.

Barker, J. and Fayers, F. (1994). Transport coefficients for compositional simulation with coarse grids in heterogeneous media. *SPE Advanced Technology Series*, 2(02):103–112.

Barker, J. W. and Dupouy, P. (1999). An analysis of dynamic pseudo-relative permeability methods for oil-water flows. *Petroleum Geoscience*, 5(4):385–394.

Barker, J. W. and Thibeau, S. (1997). A Critical Review of the Use of Pseudorelative Permeabilities for Upscaling. *SPE Reservoir Engineering*, 12(2):138–143.

Batycky, J. P., McCaffery, F. G., Hodgins, P. K., and Fisher, D. B. (1981). Interpreting relative permeability and wettability from unsteady-state displacement measurements. *Society of Petroleum Engineers of AIME*, 21(3):296–308.

Bauer, R. A., Will, R., E. Greenberg, S., and Whittaker, S. G. (2019). *Illinois Basin–Decatur Project*, page 339–370. Cambridge University Press.

Bear, J. (1988). *Dynamics of fluids in porous media*. Elsevier Science.

Begg, S. H., Carter, R. R., and Dranfield, P. (1989). Assigning effective values to simulator gridblock parameters for heterogeneous reservoirs. *SPE Reservoir Engineering*, 4(4):455–463.

BEIS (2021a). *Endurance Storage Development Plan Key Knowledge Document*. `https://assets.publishing.service.gov.uk/government/uploads/system/uploads/attachment_data/file/1079825/NS051-SS-REP-000-00010-Storage_Development_Plan.pdf`.

BEIS (2021b). *Multi-Store Development Philosophy*. `https://assets.publishing.service.gov.uk/government/uploads/system/uploads/attachment_data/file/1079820/NS051-SS-PHI-000-00010-Store_Development_Philosophy.pdf`.

BEIS (2021c). *Net Zero Teesside & Northern Endurance Partnership Technology Plan.* https://assets.publishing.service.gov.uk/government/uploads/system/uploads/attachment_data/file/1079819/NS051-EN-PLN-000-00007-Technology_Plan.pdf.

BEIS (2021d). *Primary Store Dynamic Model and Report.* https://assets.publishing.service.gov.uk/government/uploads/system/uploads/attachment_data/file/1079814/NS051-SS-REP-000-00015-Dynamic_Model___Report.pdf.

BEIS (2021e). *Primary Store Geological Model And Report.* https://assets.publishing.service.gov.uk/government/uploads/system/uploads/attachment_data/file/1079813/NS051-SS-REP-000-00014-Geological_Model___Report.pdf.

Berg, S., Oedai, S., and Ott, H. (2013). Displacement and mass transfer between saturated and unsaturated CO_2-brine systems in sandstone. *International Journal of Greenhouse Gas Control*, 12:478–492.

Berg, S., Unsal, E., and Dijk, H. (2021). Non-uniqueness and uncertainty quantification of relative permeability measurements by inverse modelling. *Computers and Geotechnics*, 132:1–18.

Bianchi, M., Zheng, L., and Birkholzer, J. T. (2016). Combining multiple lower-fidelity models for emulating complex model responses for CCS environmental risk assessment. *International Journal of Greenhouse Gas Control*, 46:248–258.

Birkholzer, J. T., Oldenburg, C. M., and Zhou, Q. (2015). CO_2 migration and pressure evolution in deep saline aquifers. *International Journal of Greenhouse Gas Control*, 40:203–220.

Blunt, M. J. (2001). Flow in porous media — pore-network models and multiphase flow. *Current Opinion in Colloid & Interface Science*, 6(3):197–207.

Blunt, M. J. (2017). *Multiphase flow in permeable media- a pore-scale perspective.* Cambridge University Press, 1 edition.

Blunt, M. J., Bijeljic, B., Dong, H., Gharbi, O., Iglauer, S., Mostaghimi, P., Paluszny, A.,

and Pentland, C. (2013). Pore-scale imaging and modelling. *Advances in Water Resources*, 51:197–216.

Blunt, M. J., Jackson, M. D., Piri, M., and Valvatne, P. H. (2002). Detailed physics, predictive capabilities and upscaling for pore-scale models of multiphase flow. *Advances in Water Resources*, 25:1069–1089.

Blykers, B. K., Organista, C., Boone, M. N., Kagias, M., Marone, F., Stampanoni, M., Bultreys, T., Cnudde, V., and Aelterman, J. (2021). Tunable X-ray dark-field imaging for sub-resolution feature size quantification in porous media. *Scientific Reports*, 11(1):1–14.

Boon, M. and Benson, S. M. (2021). A physics-based model to predict the impact of horizontal lamination on CO_2 plume migration. *Advances in Water Resources*, 150(October 2020):103881.

Boon, M., Matthäi, S. K., Shao, Q., Youssef, A. A. A., Mishra, A., and Benson, S. M. (2022). Anisotropic rate-dependent saturation functions for compositional simulation of sandstone composites. *Journal of Petroleum Science and Engineering*, 209(September 2021).

Børresen, K. A. and Graue, A. (1997). Fluid Flow Across Capillary Heterogeneities, Experiments and Simulations. *Transport in Porous Media*, 29(2):141–158.

Bradford, S. A., Abriola, L. M., and Rathfelder, K. M. (1998). Flow and entrapment of dense nonaqueous phase liquids in physically and chemically heterogeneous aquifer formations. *Advances in Water Resources*, 22(2):117–132.

Braun, C., Helmig, R., and Manthey, S. (2005). Macro-scale effective constitutive relationships for two-phase flow processes in heterogeneous porous media with emphasis on the relative permeability-saturation relationship. *Journal of Contaminant Hydrology*, 76(1-2):47–85.

Brook, M., Shaw, K., Vincent, C., and Holloway, S. (2003). Gestco case study 2a-1: Storage Potential of the Bunter Sandstone in the UK sector of the Southern North Sea and the adjacent onshore area of Eastern England. page 37.

Brooks, R. H. and Corey, A. T. (1964). Hydraulic Properties of Porous Media. *Colorado State University: Hydrology Papers*, 3(1):1–23.

Brown, G. O., Hsieh, H. T., and Lucero, D. A. (2000). Evaluation of laboratory dolomite core sample size using representative elementary volume concepts. *Water Resources Research*, 36(5):1199–1207.

Buckingham, E. (1914). Illustrations of the use of dimentional equations. *On physically similar systems*, 6.

Buckley, S. and Leverett, M. (1942). Mechanism of Fluid Displacement in Sands. *Transactions of the AIME*, 146(01):107–116.

Bultreys, T., Lin, Q., Gao, Y., Raeini, A. Q., Alratrout, A., Bijeljic, B., and Blunt, M. J. (2018). Validation of model predictions of pore-scale fluid distributions during two-phase flow. *Physical Review E*, 97(5).

Buscheck, T. A., White, J. A., Carroll, S. A., Bielicki, J. M., and Aines, R. D. (2016). Managing geologic CO_2 storage with pre-injection brine production: A strategy evaluated with a model of CO_2 injection at Snøhvit. *Energy and Environmental Science*, 9(4):1504–1512.

Campion, K. M., Sprague, A. R., Mohrig, D., Lovell, R. W., Drzewiecki, P. A., Sullivan, M. D., Ardill, J. A., Jensen, G. N., and Sickafoose, D. K. (2000). *Deep-Water Reservoirs of the World*, volume 20. Society for Sedimentary Geology.

Cantrell, D. L. and Hagerty, R. M. (1999). Microporosity in Arab Formation Carbonates, Saudi Arabia. *GeoArabia*, 4(2):129–154.

Cardwell, W. and Parsons, R. (1945). Average Permeabilities of Heterogeneous Oil Sands. *Transactions of the AIME*, 160(01):34–42.

Carl Zeiss X-ray Microscopy (2016). ZEISS Xradia Versa User's Guide.

Caruana, A. and Dawe, R. A. (1996). Flow behaviour in the presence of wettability heterogeneities. *Transport in Porous Media*, 25(2):217–233.

Cavanagh, A. and Nazarian, B. (2014). A new and extended Sleipner Benchmark model for CO_2 storage simulations in the Utsira Formation. *Energy Procedia*, 63:2831–2835.

Celia, M. A., Reeves, P. C., and Ferrand, L. A. (1995). Recent advances in pore scale models for multiphase flow in porous media. *Reviews of Geophysics*, 33(2 S):1049–1057.

Chadwick, R. A., Noy, D., Arts, R., and Eiken, O. (2009). Latest time-lapse seismic data from Sleipner yield new insights into CO_2 plume development. *Energy Procedia*, 1(1):2103–2110.

Chadwick, R. A. and Noy, D. J. (2010). History-matching flow simulations and time-lapse seismic data from the Sleipner CO_2 plume. *Geological Society, London, Petroleum Geology Conference Series*, 7(1):1171–1182.

Chang, J. and Yortsos, Y. (1992). Effect of capillary heterogeneity on Buckley-Leverett displacement. *SPE Reservoir Engineering*, 7:285 – 293.

Chang, Y. B., Lim, M. T., Pope, G. A., and Sepehrnoori, K. (1999). CO_2 flow patterns under multiphase flow: Heterogeneous field-scale conditions. *SPE Reprint Series*, (51):145–153.

Chaouche, M., Rakotomalala, N., Salin, D., Xu, B., and Yortsos, Y. C. (1994). Capillary effects in drainage in heterogeneous porous media: continuum modelling, experiments and pore network simulations. *Chemical Engineering Science*, 49(15):2447–2466.

Chasset, C., Jarsjö, J., Erlström, M., Cvetkovic, V., and Destouni, G. (2011). Scenario simulations of CO_2 injection feasibility, plume migration and storage in a saline aquifer, Scania, Sweden. *International Journal of Greenhouse Gas Control*, 5(5):1303–1318.

Chierici, G. L. (1984). Novel relations for drainage and imbibition relative permeabilities. *SPE Journal*, 24:275–276.

Christie, M. (1996). Upscaling for reservoir simulation. *SPE Journal*.

Christie, M. A. (2001). Flow in porous media - Scale up of multiphase flow. *Current Opinion in Colloid and Interface Science*, 6(3):236–241.

Civan, F. (2007). *Chapter 2 - Mineralogy and Mineral Sensitivity of Petroleum-Bearing Formations*, pages 13–77. Gulf Professional Publishing, Burlington, second edition edition.

CO2CRC (2022). Storage Research. *Oil and Gas Science and Technology*. https://co2crc.com.au/research/storage-research/.

Coats, K. H., Dempsey, J. R., and Henderson, J. H. (1971). Simulation of Three-Dimensional Reservoir Performance. *SPE Journal*, 11(1):63–71.

Collinson, J. (2019). *Sedimentary structures*. Dunedin Academic Press Ltd.

Corey, A. and Rathjens, C. (1956). Effect of Stratification on Relative Permeability. *Journal of Petroleum Technology*, 8:69 – 71.

Couëslan, M. L., Butsch, R., Will, R., and Locke, R. A. (2014). Integrated reservoir monitoring at the Illinois Basin - Decatur Project. *Energy Procedia*, 63:2836–2847.

Cuthiell, D., Bachu, S., Kramers, J., and LP, Y. (1991). Characterizing shale clast heterogeneities and their effect on fluid flow. *Reservoir characterization II*, pages 226–250.

Cuthiell, D., Sedgwick, G., Kissel, G., and Woolley, J. (1993). Steam Corefloods With Concurrent X-Ray Ct Imaging. *Journal of Canadian Petroleum Technology*, 32(03).

Daley, T. M. and Korneev, V. A. (2006). In-situ borehole seismic monitoring of injected co2 at the friosite. Technical report, Lawrence Berkeley National Lab.(LBNL), Berkeley, CA (United States).

Dance, T. (2013). Assessment and geological characterisation of the CO_2CRC Otway Project CO_2 storage demonstration site: From prefeasibility to injection. *Marine and Petroleum Geology*, 46:251–269.

Dance, T., LaForce, T., Glubokovskikh, S., Ennis-King, J., and Pevzner, R. (2019). Illuminating the geology: Post-injection reservoir characterisation of the CO_2CRC Otway site. *International Journal of Greenhouse Gas Control*, 86(May):146–157.

Dando, B. D., Goertz-Allmann, B. P., Kühn, D., Langet, N., Dichiarante, A. M., and Oye, V. (2021). Relocating microseismicity from downhole monitoring of the Decatur CCS site using a modified double-difference algorithm. *Geophysical Journal International*, 227(2):1094–1122.

Darcy, H. (1856). *Les fontaines publiques de la ville de Dijon. Exposition et application des principes à suivre et des formules à employer dans les questions de distribution d'eau: ouvrage terminé par un appendice relatif aux fournitures d'eau de plusieurs villes au filtrage des eaux et à la fabrication des tuyaux de fonte, de plomb, de tole et de bitume.* Dalmont.

Darman, N. H., Pickup, G. E., and Sorbie, K. S. (2002). A comparison of two-phase dynamic upscaling methods based on fluid potentials. *Computational Geosciences*, 6(1):5–27.

Dawe, R. A., Wheat, M. R., and Bidner, M. S. (1992). Experimental investigation of capillary pressure effects on immiscible displacement in lensed and layered porous media. *Transport in Porous Media*, 7:83 – 101.

Debbabi, Y., Jackson, M. D., Hampson, G. J., and Salinas, P. (2017). Capillary Heterogeneity Trapping and Crossflow in Layered Porous Media. *Transport in Porous Media*, 120(1):183–206.

Deflandre, J. P., Estublier, A., Baroni, A., Fornel, A., Clochard, V., and Delépine, N. (2013). Assessing field pressure and plume migration in CO_2 storages: Application of case-specific workflows at in Salah and Sleipner. *Energy Procedia*, 37:3554–3564.

Dekker, T. J. and Abriola, L. M. (2000). The influence of field-scale heterogeneity on the infiltration and entrapment of dense nonaqueous phase liquids in saturated formations. *Journal of Contaminant Hydrology*, 42(2-4):187–218.

Diao, Y., Zhu, G., Li, X., Bai, B., Li, J., Wang, Y., Zhao, X., and Zhang, B. (2020). Characterizing CO_2 plume migration in multi-layer reservoirs with strong heterogeneity and low permeability using time-lapse 2D VSP technology and numerical simulation. *International Journal of Greenhouse Gas Control*, 92(February 2019):102880.

Ding, Y., Renard, G., and Weill, L. (1998). Representation of Wells in Numerical Reservoir Simulation. *SPE Reservoir Engineering (Society of Petroleum Engineers)*, 1(1):18–23.

Donselaar, M. E. and Schmidt, J. M. (2005). Integration of outcrop and borehole image logs for high-resolution facies interpretation: Example from a fluvial fan in the Ebro Basin, Spain. *Sedimentology*, 52(5):1021–1042.

Doughty, C. (2010). Investigation of CO_2 Plume Behavior for a Large-Scale Formation. *Transport in Porous Media*, 82:49–76.

Doughty, C. and Pruess, K. (2004). Modeling supercritical carbon dioxide injection in heterogeneous porous media. *Vadose Zone Journal*, 3(3):837–847.

Durlofsky, L., Jones, R. C., and Milliken, W. J. (1997). A nonuniform coarsening approach for the scale-up of displacement processes in heterogeneous porous media. *Advances in Water Resources*, 20(5-6):335–347.

Durlofsky, L. J. (2005). Upscaling and gridding of fine scale geological models for flow simulation. *8th International Forum on Reservoir Simulation*, pages 1–59.

Egermann, P. and Lenormand, R. (2005). A new methodology to evaluate the impact of localized heterogeneity on petrophysical parameters (k_r,P_c) applied to carbonate rocks. *Petrophysics*, 46(5):335–345.

Egermann, P., Lombard, J. M., Fichen, C., Rosenberg, E., Tachet, E., and Lenormand, R. (2005). A new experimental method to determine interval of confidence for capillary pressure and relative-permeability curves. *Proceedings - SPE Annual Technical Conference and Exhibition*, pages 3561–3569.

Eiken, O., Ringrose, P., Hermanrud, C., Nazarian, B., Torp, T. A., and Høier, L. (2011). Lessons Learned from 14 years of CCS Operations: Sleipner, In Salah and Snøhvit. *Energy Procedia*, 4:5541–5548.

Eilertsen, T., Børresen, K. A., Bertin, H., and Graue, A. (1997). Experiments and numerical simulations of fluid flow in a cross layered reservoir model. *Journal of Petroleum Science and Engineering*, 18(1-2):49–60.

El-Maghraby, R. M. (2012). *Measurements of CO_2 Trapping in Carbonate and Sandstone Rocks - Dissertation*. PhD thesis.

Elenius, M. T., Tchelepi, H. A., and Johannsen, K. (2010). CO_2 Trapping in Sloping Aquifers: High Resolution Numerical Simulations. pages 1–8.

Ershadnia, R., Hajirezaie, S., Amooie, A., Wallace, C. D., Gershenzon, N. I., Hosseini, S. A., Sturmer, D. M., Ritzi, R. W., and Soltanian, M. R. (2021). CO_2 geological sequestration in multiscale heterogeneous aquifers: Effects of heterogeneity, connectivity, impurity, and hysteresis. *Advances in Water Resources*, 151(March):103895.

Esmaeili, S., Sarma, H., Harding, T., and Maini, B. (2019). Review of the effect of temperature on oil-water relative permeability in porous rocks of oil reservoirs. *Fuel*, 237:91–116.

Ezekwe, N. (2011). *Petroleum reservoir engineering practice*. Pearson Education.

Farmer, C. L. (2002). Upscaling: a review. 78(1-2):63–78.

Farokhian, D., Azin, R., and Ranjbar, A. (2019). Application of medical and dental CT-Scan technologies for determining porosity distribution of the Persian Gulf coastal zone and Zagros basin core samples. *Journal of African Earth Sciences*, 150:96–106.

Fatt, I. (1961). Influence of Dead-End Pores on Relative Permeability of Porous Media. *Science*, 134(3492):1750–1751.

Fatt, I. and Klikoff, W. A. (1959). Effect of Fractional Wettability on Multiphase Flow Through Porous Media. *Journal of Petroleum Technology*, 11(10):71–76.

Feitz, A., Tertyshnikov, K., Pevzner, R., Ricard, L., Harris, B., Schaa, R., Schacht, U., Kalinowski, A., Vialle, S., Glubokovskikh, S., Lebedev, M., Tenthorey, E., Pan, Z., Ennis-King, J., Wang, L., Hossein, S., Ransley, T., Radke, B., Urosevic, M., and Singh, R. (2018). The CO_2CRC Otway shallow CO_2 controlled release experiment: Preparation for Phase 2. *Energy Procedia*, 154:145–150.

Ferrand, L. A. and Celia, M. A. (1992). The Effect of Heterogeneity on the Drainage Capillary Pressure-Saturation Relation. *Water Resources Research*, 28(3):859–870.

Fincham, A. and Gouth, F. (2000). Improvements of Coreflood Design and Interpretation Using a New Software. *SCA Annual Symposium, Proceedings: Society of Core Analysts*, SCA 2000-19.

Finley, R. J., Frailey, S. M., Leetaru, H. E., Senel, O., Couëslan, M. L., and Marsteller, S. (2013). Early operational experience at a one-million tonne CCS demonstration project, Decatur, Illinois, USA. *Energy Procedia*, 37:6149–6155.

Fitch, P. J., Lovell, M. A., Davies, S. J., Pritchard, T., and Harvey, P. K. (2015). An integrated and quantitative approach to petrophysical heterogeneity. *Marine and Petroleum Geology*, 63:82–96.

Flett, M., Gurton, R., and Weir, G. (2007). Heterogeneous saline formations for carbon dioxide disposal : Impact of varying heterogeneity on containment and trapping. 57:106–118.

Frailey, S. M. and Leetaru, H. (2009). Energy Procedia Geological Factors Affecting CO_2 Plume Distribution. *Energy Procedia*, 1(1):3107–3112.

Fu, X., Cueto-Felgueroso, L., and Juanes, R. (2013). Pattern formation and coarsening dynamics in three-dimensional convective mixing in porous media. *Philosophical Transactions of the Royal Society A: Mathematical, Physical and Engineering Sciences*, 371(2004).

Furre, A. K., Eiken, O., Alnes, H., Vevatne, J. N., and Kiær, A. F. (2017). 20 Years of Monitoring CO_2-injection at Sleipner. *Energy Procedia*, 114:3916–3926. 13th International Conference on Greenhouse Gas Control Technologies, GHGT-13, 14-18 November 2016, Lausanne, Switzerland.

Furre, A. K., Meneguolo, R., Ringrose, P., and Kassold, S. (2019). Building confidence in CCS: From sleipner to the northern Lights project. *First Break*, 37(7):81–87.

Ganat, T. A.-A. O. (2020). *Fundamentals of reservoir rock properties*. Springer.

Gao, Y., Qaseminejad Raeini, A., Blunt, M. J., and Bijeljic, B. (2019). Pore occupancy, relative permeability and flow intermittency measurements using X-ray micro-tomography in a complex carbonate. *Advances in Water Resources*, 129(April):56–69.

Garfi, G., John, C. M., Berg, S., and Krevor, S. (2020). The Sensitivity of Estimates of Multiphase Fluid and Solid Properties of Porous Rocks to Image Processing. *Transport in Porous Media*, 131(3):985–1005.

Gasda, S., Tveit, S., and Pettersson, P. (2021). Dynamic Assessment of Basin-scale Pressure Dissipation and Impact on Storage Capacity Using Accelerated Methodology. *SSRN Electronic Journal*, (March).

Gasda, S. E. and Celia, M. A. (2005). Upscaling relative permeabilities in a structured porous medium. *Advances in Water Resources*, 28:493–506.

Gasda, S. E., Nilsen, H. M., and Dahle, H. K. (2013). Impact of structural heterogeneity on upscaled models for large-scale CO2 migration and trapping in saline aquifers. *Advances in Water Resources*, 62:520–532.

Gasda, S. E., Nilsen, H. M., Dahle, H. K., and Gray, W. G. (2012). Effective models for CO2 migration in geological systems with varying topography. *Water Resources Research*, 48(10):1–17.

Gasperikova, E., Appriou, D., Bonneville, A., Feng, Z., Huang, L., Gao, K., Yang, X., and Daley, T. (2022). Sensitivity of geophysical techniques for monitoring secondary CO_2 storage plumes. *International Journal of Greenhouse Gas Control*, 114:103585.

Gerritsen, M. G. and Durlofsky, L. J. (2005). Modeling fluid flow in oil reservoirs. *Annual Review of Fluid Mechanics*, 37:211–238.

Gershenzon, N. I., Ritzi, R. W., Dominic, D. F., Mehnert, E., and Okwen, R. T. (2016). Advances in Water Resources Comparison of CO_2 trapping in highly heterogeneous reservoirs with Brooks-Corey and van Genuchten type capillary pressure curves. 96:225–236.

Gershenzon, N. I., Ritzi, R. W., Dominic, D. F., Mehnert, E., and Okwen, R. T. (2017). Capillary trapping of CO_2 in heterogeneous reservoirs during the injection period. *International Journal of Greenhouse Gas Control*, 59:13–23.

Gershenzon, N. I., Soltanian, M., Jr, R. W. R., and Dominic, D. F. (2014). Influence of small scale heterogeneity on CO_2 trapping processes in deep saline aquifers. *Energy Procedia*, 59:166–173.

Ghanbarnezhad Moghanloo, R., Dadmohammadi, Y., Bin, Y., and Salahshoor, S. (2015). Applying fractional flow theory to evaluate CO_2 storage capacity of an aquifer. *Journal of Petroleum Science and Engineering*, 125:154–161.

Gharieb, R. R. (2022). X-Rays and Computed Tomography Scan Imaging: Instrumentation and Medical Applications. In Gharieb, R. R., editor, *Computed-Tomography (CT) Scan*, chapter 1. IntechOpen, Rijeka.

Gilmore, K. A., Neufeld, J. A., and Bickle, M. J. (2020). CO_2 Dissolution Trapping Rates in Heterogeneous Porous Media. *Geophysical Research Letters*, 47(12).

Gollakota, S. and McDonald, S. (2014). Commercial-scale CCS project in Decatur, Illinois - Construction status and operational plans for demonstration. *Energy Procedia*, 63:5986–5993.

Golparvar, A., Zhou, Y., Wu, K., Ma, J., and Yu, Z. (2018). A comprehensive review of pore scale modeling methodologies for multiphase flow in porous media. *Advances in Geo-Energy Research*, 2(4):418–440.

Graue, A. (1994). Imaging the Effects of Capillary Heterogeneities on Local Saturation Development in Long Corefloods. *SPE Drilling & Completion*, 9(01):57–64.

Green, C. P. and Ennis-King, J. (2010). Effect of vertical heterogeneity on long-term migration of CO_2 in saline formations. *Transport in Porous Media*, 82(1):31–47.

Gringarten, E. and Deutsch, C. V. (2001). Variogram interpretation and modeling. *Mathematical Geology*, 33(4):507–534.

Guéguen, Y., Le Ravalec, M., and Ricard, L. (2006). Upscaling: Effective medium theory, numerical methods and the fractal dream. *Pure and Applied Geophysics*, 163(5-6):1175–1192.

Guo, B., Zheng, Z., Bandilla, K. W., Celia, M. A., and Stone, H. A. (2016). Flow regime analysis for geologic CO_2 sequestration and other subsurface fluid injections. *International Journal of Greenhouse Gas Control*, 53:284–291.

Hadley, G. F. and Handy, L. L. (1956). A theoretical and experimental study of the steady state capillary end effect. *Society of Petroleum Engineers - Fall Meeting of the Petroleum Branch of AIME, FM 1956*.

Haeri, F., Tapriyal, D., Sanguinito, S., Shi, F., Fuchs, S. J., Dalton, L. E., Baltrus, J., Howard, B., Crandall, D., Matranga, C., and Goodman, A. (2020). CO_2-Brine Contact Angle Measurements on Navajo, Nugget, Bentheimer, Bandera Brown, Berea, and Mt. Simon Sandstones. *Energy and Fuels*, 34(5):6085–6100.

Han, W. S. and Kim, K. Y. (2018). Evaluation of CO_2 plume migration and storage under dip and sinusoidal structures in geologic formation. *Journal of Petroleum Science and Engineering*, 169(March):760–771.

Han, W. S., Lee, S. Y., Lu, C., and Mcpherson, B. J. (2010). Effects of permeability on CO_2 trapping mechanisms and buoyancy - driven CO_2 migration in saline formations. 46:1–20.

Hansen, O., Gilding, D., Nazarian, B., Osdal, B., Ringrose, P., Kristoffersen, J. B., Eiken, O., and Hansen, H. (2013). Snøhvit: The history of injecting and storing 1 Mt CO_2 in the fluvial Tubåen Fm. *Energy Procedia*, 37:3565–3573.

Harms, J. C. (1979). Primary sedimentary structures. *Annual review of earth and planetary science*, 7(1):227–248.

Harris, C., Jackson, S. J., Benham, G. P., Krevor, S., and Muggeridge, A. H. (2021). The impact of heterogeneity on the capillary trapping of CO_2 in the Captain Sandstone. *International Journal of Greenhouse Gas Control*, 112:103511.

Heidsiek, M., Butscher, C., Blum, P., and Fischer, C. (2020). Small-scale diagenetic facies heterogeneity controls porosity and permeability pattern in reservoir sandstones. *Environmental Earth Sciences*, 79(425):1–14.

Heinemann, Z. E., Brand, C., Munka, M., and Chen, Y. M. (1989). Modeling reservoir geometry with irregular grids. *Society of Petroleum Engineers Journal*, pages 37–54.

Hesse, M., Riaz, A., and Tchelepi, H. A. (2006). Resolving Density Fingering During CO_2 Sequestration: A Challenge for Reservoir Simulation. In *International Symposium on Site Characterization for CO_2 Geological Storage*, pages 33–35.

Hilden, S. T. and Berg, C. F. (2016). An Analysis of Unsteady Flooding Processes: Varying Force Balance and the Applicability of Steady-State Upscaling. *Transport in Porous Media*, 115(1):125–152.

Ho, C. K. and Webb, S. W. (1998). Capillary barrier performance in heterogeneous porous media. *Water Resources Research*, 34(4):603–609.

Holstein, E. D. (2007). *Reservoir Engineering and Petrophysics*. Society of Petroleum Engineers.

Honarpour, M. M. and Saad, N. (1994). Influence of Small-Scale Rock Laminations on Core Plug Oil/Water Relative Permeability and Capillary Pressure. page 11.

Hosseini, M., Tavakoli, V., and Nazemi, M. (2018). The effect of heterogeneity on NMR derived capillary pressure curves, case study of Dariyan tight carbonate reservoir in the central Persian Gulf. *Journal of Petroleum Science and Engineering*, 171:1113–1122.

Hosseinzadeh Hejazi, S. A., Shah, S., and Pini, R. (2019). Dynamic measurements of drainage capillary pressure curves in carbonate rocks. *Chemical Engineering Science*, 200:268–284.

Hove, A. O., Nilsen, V., and Jorgen, L. (1990). Visualization of Xanthan flood behavior in core samples by means of X-ray tomography. *SPE Reservoir Engineering*, 5:475 – 480.

Hovorka, S. D., Doughty, C., Benson, S. M., Pruess, K., and Knox, P. R. (2004). The impact of geological heterogeneity on CO_2 storage in brine formations : a case study from the Texas Gulf Coast. *Geological Society of London, Special Publications*, 233:147–163.

Huang, Y., Ringrose, P. S., and Sorbie, K. S. (1995). Capillary trapping mechanisms in water-wet laminated rocks. *SPE Reservoir Engineering*, 10(4):287–292.

Huang, Y., Ringrose, P. S., Sorbie, K. S., and Larter, S. R. (1996). The effects of heterogeneity and wettability on oil recovery from laminated sedimentary structures. *SPE Journal*, 1(4):451–460.

Huppler, J. D. (1970). Numerical investigation of the effects of core heterogeneities on waterflood relative permeabilities. *AIME Petroleum Transcations*, 10:381 – 392.

Ide, S. T., Jessen, K., and Jr, F. M. O. (2007). Storage of CO_2 in saline aquifers : Effects of gravity , viscous , and capillary forces on amount and timing of trapping. 1:481–491.

IEA (2020). *CCUS in Clean Energy Transitions*.

IEA (2022). Renewables 2022. Technical report, IEA, Paris. `https://www.iea.org/reports/renewables-2022`.

IPCC (2021). *Summary for Policymakers*, pages 3—32. Cambridge University Press, Cambridge, United Kingdom and New York, NY, USA.

IPCC (2022). Climate Change 2022: Impacts, Adaptation and Vulnerability. Contribution of Working Group II to the Sixth Assessment Report of the Intergovernmental Panel on Climate Change [H.-O. Pörtner, D.C. Roberts, M. Tignor, E.S. Poloczanska, K. Mintenbeck, A. Alegr. Technical report, IPCC, New York.

Jackson, S., Gunning, J., Dance, T., Bagheri, M., Barraclough, P., Pevzner, R., Ennis-King, J., and Jenkins, C. (2022a). Time-lapse pressure tomography of a migrating CO_2 plume at the Otway Stage 3 site. *SSRN Electronic Journal*, (October).

Jackson, S. J., Agada, S., Reynolds, C. A., and Krevor, S. (2018). Characterizing Drainage Multiphase Flow in Heterogeneous Sandstones. *Water Resources Research*, 54(4):3139–3161.

Jackson, S. J. and Krevor, S. (2020). Small-Scale Capillary Heterogeneity Linked to Rapid Plume Migration During CO_2 Storage. *Geophysical Research Letters*, 47(18).

Jackson, S. J., Lin, Q., and Krevor, S. (2020). Representative Elementary Volumes, Hysteresis, and Heterogeneity in Multiphase Flow From the Pore to Continuum Scale. *Water Resources Research*, 56(6):1–24.

Jackson, S. J., Niu, Y., Manoorkar, S., Mostaghimi, P., and Armstrong, R. T. (2022b). Deep Learning of Multiresolution X-Ray Micro-Computed-Tomography Images for Multiscale Modeling. *Physical Review Applied*, 17(5):1–22.

Jenkins, C., Ennis-King, J., Green, C., Jackson, S., Gunning, J., and Wilkins, A. (2022). Monitoring with earth tides at the CO_2CRC Otway Project. *SSRN Electronic Journal*, (October).

Ji, Y., Baud, P., Vajdova, V., and Wong, T. F. (2012). Caractérisation de la géométrie des pores dans le calcaire de l'Indiana (États-Unis) en relation avec la compaction mécanique. *Oil and Gas Science and Technology*, 67(5):753–775.

Johnson, E., Bossler, D., and Bossler, V. N. (1959). Calculation of Relative Permeability from Displacement Experiments. *Transactions of the AIME*, 216(01):370–372.

Jonoud, S. and Jackson, M. D. (2008). New criteria for the validity of steady-state upscaling. *Transport in Porous Media*, 71(1):53–73.

Jung, A. and Aigner, T. (2012). Carbonate geobodies: Hierarchical classification and database - a new workflow for 3D reservoir modelling. *Journal of Petroleum Geology*, 35(1):49–65.

Kaven, J. O., Hickman, S. H., McGarr, A. F., Walter, S., and Ellsworth, W. L. (2014). Seismic monitoring at the Decatur, IL, CO_2 sequestration demonstration site. *Energy Procedia*, 63(Il):4264–4272.

Kelemen, P., Benson, S. M., Pilorgé, H., Psarras, P., and Wilcox, J. (2019). An Overview of the Status and Challenges of CO2 Storage in Minerals and Geological Formations. *Frontiers in Climate*, 1(November):1–20.

Kim, D. and Lindquist, W. B. (2012). A semianalytic model for the computation of imbibition through polygonal cross sections. *Water Resources Research*, 48(4):1–16.

Kim, K. Y., Oh, J., Han, W. S., Park, K. G., Shinn, Y. J., and Park, E. (2018). Two-phase flow visualization under reservoir conditions for highly heterogeneous conglomerate rock: A core-scale study for geologic carbon storage. *Scientific Reports*, 8(1):1–10.

King, M. J., King, P. R., McGill, C. A., and Williams, J. K. (1995). Effective properties for flow calculations. *Transport in Porous Media*, 20(1-2):169–196.

King, P. R. (1989). The use of renormalization for calculating effective permeability. *Transport in Porous Media*, 4(1):37–58.

King, P. R. (1996). Upscaling permeability: Error analysis for renormalization. *Transport in Porous Media*, 23(3):337–354.

Koltermann, C. E. and Gorelick, S. M. (1996). Heterogeneity in sedimentary deposits: A review of structure-imitating, process-imitating, and descriptive approaches. *Water Resources Research*, 32(9):2617–2658.

Kong, X., Delshad, M., and Wheeler, M. F. (2015). History matching heterogeneous coreflood of CO_2/brine by use of compositional reservoir simulator and geostatistical approach. *SPE Journal*, 20(2):267–276.

Kortekaas, T. F. (1985). Water/Oil Displacement Characteristics in Crossbedded Reservoir Zones. *Society of Petroleum Engineers journal*, 25(6):917–926.

Krause, M. and Benson, S. M. (2015). Accurate determination of characteristic relative permeability curves. *Advances in Water Resources*, 83:376–388.

Krause, M., Krevor, S., and Benson, S. M. (2013). A Procedure for the Accurate Determination of Sub-Core Scale Permeability Distributions with Error Quantification. *Transport in Porous Media*, 98(3):565–588.

Krause, M., Perrin, J. C., and Benson, S. M. (2011). Modeling permeability distributions in a sandstone core for history matching coreflood experiments. *SPE Journal*, 16(4):768–777.

Krause, M. H. (2009). Modelling sub-core scale permeability in sandstone for use in studying multiphase flow of CO_2 and brine in core flooding experiments. page 113.

Krause, M. H. (2012). Modeling and investigation of the influence of capillary heterogeneity on relative permeability. *Proceedings SPE Annual Technical Conference and Exhibition*, 6:4770 – 4787.

Krevor, S., Blunt, M. J., Benson, S. M., Pentland, C. H., Reynolds, C., Al-Menhali, A., and Niu, B. (2015). Capillary trapping for geologic carbon dioxide storage - From pore scale physics to field scale implications. *International Journal of Greenhouse Gas Control*, 40:221–237.

Krevor, S., Blunt, M. J., Trusler, J., and De Simone, S. (2019). An introduction to subsurface CO_2 storage. In *Carbon Capture and Storage*, volume 26 of *Energy and Environment Series*, pages 238–295. Royal Society of Chemistry, Cambridge.

Krevor, S., de Coninck, H., Gasda, S. E., Ghaleigh, N. S., de Gooyert, V., Hajibeygi, H., Juanes, R., Neufeld, J., Roberts, J. J., and Swennenhuis, F. (2023). Subsurface carbon dioxide and hydrogen storage for a sustainable energy future. *Nature Reviews Earth & Environment*, 4(2):102–118.

Krevor, S. C. M., Pini, R., Li, B., and Benson, S. M. (2011). Capillary heterogeneity trapping of CO_2 in a sandstone rock at reservoir conditions. 38(August):1–5.

Krishnamurthy, P. G., Meckel, T. A., and DiCarlo, D. (2019). Mimicking Geologic Depositional Fabrics for Multiphase Flow Experiments. *Water Resources Research*, 55(11):9623–9638.

Krishnamurthy, P. G., Trevisan, L., and Meckel, T. (2017). Investigating the Influence of Geological Heterogeneity on Capillary Trapping of Buoyant CO_2 Using Transmitted-light Flow Visualization Experiments. *Energy Procedia*, 114(November 2016):4961–4966.

Kuo, C. W., Perrin, J. C., and Benson, S. M. (2010). Effect of gravity, flow rate, and small scale heterogeneity on multiphase flow of $CO_2$and Brine. *Society of Petroleum Engineers Western North American Regional Meeting 2010 - In Collaboration with the Joint Meetings of the Pacific Section AAPG and Cordilleran Section GSA*, 1:377–389.

Kurotori, T. and Pini, R. (2021). A general capillary equilibrium model to describe drainage experiments in heterogeneous laboratory rock cores. *Advances in Water Resources*, page 103938.

Kyte, J. R. and Berry, D. W. (1975). New Pseudo Functions To Control Numerical Dispersion. *Soc Pet Eng AIME J*, 15(4):269–276.

Lai, J., Wang, G., Fan, Z., Chen, J., Wang, S., Zhou, Z., and Fan, X. (2016). Insight into the pore structure of tight sandstones using NMR and HPMI measurements. *Energy and Fuels*, 30(12):10200–10214.

Lai, P., Moulton, K., and Krevor, S. (2015). Pore-scale heterogeneity in the mineral distribution and reactive surface area of porous rocks. *Chemical Geology*, 411:260–273.

Lantz, R. (1971). Quantitative evaluation of numerical diffusion (truncation error). *SPE Journal*, 11(3):315–320.

Leetaru, H. E. and Freiburg, J. T. (2014). Litho-facies and reservoir characterization of the Mt Simon Sandstone at the Illinois Basin – Decatur Project. *Greenhouse Gases: Science and Technology*, 4(5):580–595.

Leverett, M. (1941). Capillary Behavior in Porous Solids. *Transactions of the AIME*, 142(01):152–169.

Leverett, M. C. (1939). Flow of oil-water mixtures through unconsolidated sands. *Transactions of the AIME*, 132(01):149–171.

Li, B. and Benson, S. M. (2015). Advances in Water Resources Influence of small-scale heterogeneity on upward CO_2 plume migration in storage aquifers. *Advances in Water Resources*, 83:389–404.

Li, C., Dai, W., Luo, B., Pi, J., Liu, Y., and Zhang, Y. (2021). New fractal-dimension-based relation model for estimating absolute permeability through capillary pressure curves. *Journal of Petroleum Science and Engineering*, 196:107672.

Li, D. (1995). *Scaling and upscaling of fluid flow through permeable media*. PhD thesis. `http://dx.doi.org/10.1016/j.jaci.2012.05.050`.

Li, J., Jiang, H., Wang, C., Zhao, Y., Gao, Y., Pei, Y., Wang, C., and Dong, H. (2017). Pore-scale investigation of microscopic remaining oil variation characteristics in water-wet sandstone using CT scanning. *Journal of Natural Gas Science and Engineering*, 48:36 – 45.

Li, K. (2004). Generalized capillary pressure and relative permeability model inferred from fractal characterization of porous media. *SPE Annual Technical Conference and Exhibition*.

Li, X., Boek, E. S., Maitland, G. C., and Trusler, J. P. M. (2012). Interfacial Tension of (Brines + CO_2): (0.864 NaCl + 0.136 KCl) at Temperatures between (298 and 448) K, Pressures between (2 and 50) MPa, and Total Molalities of (1 to 5) molkg^{-1}. *Journal of Chemical and Engineering Data*, 57:1078–1088.

Lie, K.-A. (2019). *An Introduction to Reservoir Simulation using MATLAB/GNU Octave*. Cambridge University Press.

Lin, Q., Al-Khulaifi, Y., Blunt, M., and Bijeljic, B. (2016). Quantification of sub-resolution porosity in carbonate rocks by applying high-salinity contrast brine using x-ray microtomography differential imaging.

Lin, Q., Bijeljic, B., Pini, R., Blunt, M. J., and Krevor, S. (2018). Imaging and Measurement of Pore-Scale Interfacial Curvature to Determine Capillary Pressure Simultaneously With Relative Permeability. *Water Resources Research*, 54(9):7046–7060.

Lindeberg, E. and Begmo, P. (2003). The Long-Term Fate of CO_2 Injected into an Aquifer. *SINTEF Petroleum Research*, (7465):1–6.

Liu, H., Xiao, L., Deng, F., Chen, W., and Galvosas, P. (2018). Emerging NMR approaches for characterizing rock heterogeneity. *Microporous and Mesoporous Materials*, 269:118–121.

Lüth, S., Ivanova, A., and Kempka, T. (2015). Conformity assessment of monitoring and simulation of CO_2 storage: A case study from the Ketzin pilot site. *International Journal of Greenhouse Gas Control*, 42:329–339.

Mannseth, T., Mykkeltveit, J., Nordtvedt, J. E., and Sylte, A. (1998). Effects of Rock Heterogeneities on Capillary Pressure and Relative Permeabilities. *European Petroleum Conference*.

Manoorkar, S., Jackson, S. J., and Krevor, S. (2021). Observations of the impacts of 0.001m - 0.1m heterogeneities on relative permeability and trapping in carbonate rocks. *Water Resources Research*.

Manrique, J. F. (1994). *A detailed study of geometric factors for probe permeameter measurements on heterogeneous and anisotropic rocks*. PhD thesis, The University of Tulsa.

McPhee, C., Reed, J., and Zubizarreta, I. (2015). *Core Analysis: A Best Practice Guide*, volume 64.

Mehin, K. and Constantine, A. E. (1999). Hydrocarbon potential of the western onshore Otway Basin in Victoria: 1999 Acreage Release. *Victorian Initiative for Minerals and Petroleum Report*, 62(1).

Mikes, D., Barzandji, O. H., Bruining, J., and Geel, C. R. (2006). Upscaling of small-scale heterogeneities to flow units for reservoir modelling. *Marine and Petroleum Geology*, 23(9-10):931–942.

Mishra, A., Kurtev, K. D., and Haese, R. R. (2020). Composite rock types as part of a workflow for the integration of mm-to cm-scale lithological heterogeneity in static reservoir models. *Marine and Petroleum Geology*, 114(January):104240.

Mori, H., Trevisan, L., and Illangasekare, T. H. (2015). Evaluation of relative permeability functions as inputs to multiphase flow models simulating supercritical CO_2 behavior in deep geologic formations. *International Journal of Greenhouse Gas Control*, 41:328–335.

Muccino, J., Gray, W., and Ferrand, L. (1998). Toward Improved Understanding of Multiphase Flow in Porous Media. *Reviews of Geophysics*, 36(3):401–422.

Muggeridge, A., Lake, L., Carroll, H., and Wesson, T. (1991). Generation of effective relative permeabilities from detailed simulation of flow in heterogeneous porous media. *Reservoir characterization II*, pages 197–225.

Muggeridge, A. H., Cuypers, M., Bacquet, C., and Barker, J. W. (2002). Scale-up of well performance for reservoir flow simulation. *Petroleum Geoscience*, 8(2):133–139.

Muljadi, B. P., Blunt, M. J., Raeini, A. Q., and Bijeljic, B. (2016). The impact of porous media heterogeneity on non-darcy flow behaviour from pore-scale simulation. *Advances in water resources*, 95:329–340.

Muskat, M. and Meres, M. W. (1936). The Flow of Heterogeneous Fluids Through Porous Media. *Physics*, 7(9):346–363.

Muskat, M., Wyckoff, R. D., Botset, H. G., and Meres, M. W. (1937). Flow of Gas-liquid Mixtures through Sands. *Transactions of the AIME*, 123(01):69–96.

National Institute of Biomedical Imaging and Bioengineering (2022). `https://www.nibib.nih.gov/science-education/science-topics/computed-tomography-ct#pid-1021`.

Nazarian, B. and Furre, A. K. (2022). Simulation Study of Sleipner Plume on Entire Utsira Using A Multi-Physics Modelling Approach. In *SSRN Electronic Journal*, number Proceedings of the 16th Greenhouse Gas Control Technologies Conference (GHGT-16) 23-24 Oct 2022, pages 1–14.

Nejad Ebrahimi, A., Jamshidi, S., Iglauer, S., and Boozarjomehry, R. (2013). Genetic algorithm-based pore network extraction from micro-computed tomography images. *Chemical Engineering Science*, 92:157–166.

Nelson, P. H. (1994). Permeability-porosity relationships in sedimentary rocks. *The Log Analyst*, 35(3):38–62.

Ni, H., Boon, M., Garing, C., and Benson, S. M. (2019). Predicting CO_2 residual trapping ability based on experimental petrophysical properties for different sandstone types. *International Journal of Greenhouse Gas Control*, 86(May):158–176.

Ni, H. and Meckel, T. (2022). Effects of Flow Pulsation on CO_2 Buoyant Migration and Capillary Trapping. *SSRN Electronic Journal*, (October):1–9.

Nicot, J. P. and Duncan, I. J. (2012). Review: Common attributes of hydraulically fractured oil and gas production and CO_2 geological sequestration. *Greenhouse Gases: Science and Technology*, 2(5):352–368.

Niu, B., Al-Menhali, A., and Krevor, S. (2015). The impact of reservoir conditions on the residual trapping of carbon dioxide in Berea sandstone. *Water Resources Research*, 51:2009–2029.

Nooruddin, H. A. and Blunt, M. J. (2018). Large-scale Invasion Percolation with Trapping for Upscaling Capillary-Controlled Darcy-scale Flow. *Transport in Porous Media*, 121(2):479–506.

Nordahl, K. and Ringrose, P. S. (2008). Identifying the representative elementary volume for permeability in heterolithic deposits using numerical rock models. *Mathematical Geosciences*, 40(7):753–771.

Nordtvedt, J. E., Urkedal, Ebeltoft, Kolltveit, K., Petersen, E. B., Sylte, and Valestrand (1999). The Significance of Violated Assumptions on Core Analysis Results. In *Proceedings of the 1999 International Symposium of the SCA*, number 1, Golden.

Nutting, P. G. (1930). Physical analysis of oil sands. *AAPG Bulletin*, 14(10):1337–1349.

Odsæter, L. H., Berg, C. F., and Rustad, A. B. (2015). Rate Dependency in Steady-State Upscaling. *Transport in Porous Media*, 110(3):565–589.

OGCI (2017). *Net Zero Teesside*.

Olafuyi, A. O., Sheppard, A. P., Arns, C. H., Sok, R. M., Cinar, Y., Knackstedt, M. A., and Pinczewski, W. V. (2006). Experimental investigation of drainage capillary pressure computed from digitized tomographic images. *Proceedings - SPE Symposium on Improved Oil Recovery*, 2:876–882.

Onoja, M. U. and Shariatipour, S. M. (2019). Assessing the impact of relative permeability and capillary heterogeneity on Darcy flow modelling of CO_2 storage in Utsira Formation. *Greenhouse Gases: Science and Technology*, 9(6):1221–1246.

Pamukcu, Y., Hurter, S., Jammes, L., Vu-Hoang, D., and Pekot, L. (2011). Characterizing and predicting short term performance for the in Salah Krechba field CCS joint industry project. *Energy Procedia*, 4:3371–3378.

Park, S. S., Kim, T. H., Jeong, M. S., and Lee, K. S. (2016). Evaluating the impacts of fine-scale capillary heterogeneity and wettability on the behavior of buoyancy-driven CO_2 migration and trapping mechanisms. *Environmental Earth Sciences*, 75(7):1–12.

Pawar, R. J., Bromhal, G. S., Carey, J. W., Foxall, W., Korre, A., Ringrose, P. S., Tucker, O., Watson, M. N., and White, J. A. (2015). Recent advances in risk assessment and risk management of geologic CO2 storage. *International Journal of Greenhouse Gas Control*, 40:292–311.

Peaceman, D. W. (1997). Effective transmissibilities of a gridblock by upscaling - Comparison of direct methods with renormalization. *SPE Journal*, 2(3):338–349.

Peksa, A. E., Wolf, K. H. A., and Zitha, P. L. (2015). Bentheimer sandstone revisited for experimental purposes. *Marine and Petroleum Geology*, 67:701–719.

Pereira Nunes, J., Bijeljic, B., and Blunt, M. (2016). Pore-space structure and average dissolution rates: A simulation study.

Perrin, J. C. and Benson, S. (2010). An experimental study on the influence of sub-core scale heterogeneities on CO_2 distribution in reservoir rocks. *Transport in Porous Media*, 82(1):93–109.

Petrovic, A., Aigner, T., and Pontiggia, M. (2018). Facies Heterogeneities in a Ramp Carbonate Reservoir Analogue: a New High-Resolution Approach for 3D Facies Modelling. *Journal of Petroleum Geology*, 41(2):155–174.

Pevzner, R., Caspari, E., Gurevich, B., Dance, T., and Cinar, Y. (2015). Feasibility of CO_2 plume detection using 4D seismic: CO2CRC Otway Project case study - Part 2: Detectability analysis. *Geophysics*, 80(4):B105–B114.

Pickup, G. E. and Serbie, K. S. (1996). The scaleup of two-phase flow in porous media using phase permeability tensors. *SPE Journal*, 1(4):369–381.

Pickup, G. E. and Sorbie, K. S. (1994). Development and application of a new two-phase scaleup method based on tensor permeabilities. *Proceedings - SPE Annual Technical Conference and Exhibition*, Sigma(pt 1):217–225.

Pickup, G. E. and Stephen, K. D. (2000). An assessment of steady-state scale-up for small-scale geological models. *Petroleum Geoscience*, 6(3):203–210.

Pini, R. and Benson, S. M. (2013a). Characterization and scaling of mesoscale heterogeneities in sandstones. *Geophysical Research Letters*, 40(15):3903–3908.

Pini, R. and Benson, S. M. (2013b). Simultaneous determination of capillary pressure and relative permeability curves from core-flooding experiments with various fluid pairs. *Water Resources Research*, 49(6):3516–3530.

Pini, R. and Benson, S. M. (2017). Capillary pressure heterogeneity and hysteresis for the supercritical CO_2/water system in a sandstone. *Advances in Water Resources*, 108:277–292.

Pini, R., Krevor, S., Krause, M., and Benson, S. (2013). Capillary heterogeneity in sandstone rocks during CO_2/water core-flooding experiments. *Energy Procedia*, 37:5473–5479.

Pini, R., Krevor, S. C., and Benson, S. M. (2012). Capillary pressure and heterogeneity for the CO_2/water system in sandstone rocks at reservoir conditions. *Advances in Water Resources*, 38:48–59.

Pini, R. and Madonna, C. (2016). Moving across scales: a quantitative assessment of X-ray CT to measure the porosity of rocks. *Journal of Porous Materials*, 23(2):325–338.

Popik, S., Pevzner, R., Tertyshnikov, K., Popik, D., Urosevic, M., Shulakova, V., Glubokovskikh, S., and Gurevich, B. (2020). 4D surface seismic monitoring the evolution of a small CO_2 plume during and after injection: CO_2CRC Otway Project study. *Exploration Geophysics*, 51(5):570–580.

Prévost, M., Lepage, F., Durlofsky, L. J., and Mallet, J. L. (2005). Unstructured 3D gridding and upscaling for coarse modelling of geometrically complex reservoirs. *Petroleum Geoscience*, 11(4):339–345.

Prodanović, M., Mehmani, A., and Sheppard, A. P. (2015). Imaged-based multiscale network modelling of microporosity in carbonates. *Geological Society Special Publication*, 406(1):95–113.

Qi, D. and Hesketh, T. (2005). An analysis of upscaling techniques for reservoir simulation. *Petroleum Science and Technology*, 23(7-8):827–842.

Rabinovich, A., Itthisawatpan, K., and Durlofsky, L. J. (2015). Upscaling of CO_2 injection into brine with capillary heterogeneity effects. *Journal of Petroleum Science and Engineering*, 134:60–75.

Rabinovich, A., Li, B., and J., D. L. (2016). Analytical approximations for effective relative permeability in the capillary limit Avinoam. *Journal of the American Water Resources Association*, 5(3):2–2.

Raeini, A. Q., Bijeljic, B., and Blunt, M. J. (2017). Generalized network modeling: Network extraction as a coarse-scale discretization of the void space of porous media. *Physical Review E*, 96(1):1–17.

Raeini, A. Q., Bijeljic, B., and Blunt, M. J. (2018). Generalized network modeling of capillary-dominated two-phase flow. *Physical Review E*, 97(2).

Raeini, A. Q., Yang, J., Bondino, I., Bultreys, T., Blunt, M. J., and Bijeljic, B. (2019). Validating the Generalized Pore Network Model Using Micro-CT Images of Two-Phase Flow. *Transport in Porous Media*, 130(2):405–424.

Rebelle, M., Umbhauer, F., and Poli, E. (2009). Pore to Grid Carbonate Rock-Typing Geological Facies Petro-Geologic Groups (PGG) Petrophysical Groups (PG) Dynamic Rock-Types (DRT) Core to log. *Petrophysics*, (December):7–9.

Renard, P. and de Marsily, G. (1997). Calculating Equivalent permeability: a review. *Advances in Water Resources*, 20:253–278.

Reynolds, C. A. (2016). *Two-phase Flow Behaviour and Relative Permeability between CO_2 and Brine in Sandstones at the Pore and Core Scales*. PhD thesis.

Reynolds, C. A., Blunt, M. J., and Krevor, S. (2018). Multiphase Flow Characteristics of Heterogeneous Rocks From CO_2 Storage Reservoirs in the United Kingdom. *Water Resources Research*, 54(2):729–745.

Reynolds, C. A. and Krevor, S. (2015). Characterizing flow behavior for gas injection: Relative permeability of CO_2-brine and N_2-water in heterogeneous rocks. *Water Resources Research*.

Rezaei, F., Izadi, H., Memarian, H., and Baniassadi, M. (2019). The effectiveness of different thresholding techniques in segmenting micro CT images of porous carbonates to estimate porosity. *Journal of Petroleum Science and Engineering*, 177(December 2018):518–527.

Ringrose, P. (2020). *How to Store CO_2 Underground: Insights from early-mover CCS Projects*.

Ringrose, P., Atbi, M., Mason, D., Espinassous, M., Myhrer, ø., Iding, M., Mathieson, A., and Wright, I. (2009). Plume development around well KB-502 at the In Salah CO_2 storage site. *First Break*, 27(1):85–89.

Ringrose, P. and Sæther, Ø. (2020). CO_2 injection operations: Insights from Sleipner and Snøhvit. *SPE CCUS Conference*, (October):1–14.

Ringrose, P. S., Mathieson, A. S., Wright, I. W., Selama, F., Hansen, O., Bissell, R., Saoula, N., and Midgley, J. (2013). The in salah CO_2 storage project: Lessons learned and knowledge transfer. *Energy Procedia*, 37:6226–6236.

Ringrose, P. S., Sorbie, K. S., Corbett, P. W., and Jensen, J. L. (1993). Immiscible flow behaviour in laminated and cross-bedded sandstones. *Journal of Petroleum Science and Engineering*, 9(2):103–124.

Ritchie, H., Roser, M., and Rosado, P. (2020). Co_2 and greenhouse gas emissions. *Our World in Data*. https://ourworldindata.org/CO_2-and-greenhouse-gas-emissions.

Rogiers, B., Beerten, K., Smeekens, T., Mallants, D., Gedeon, M., Huysmans, M., Batelaan, O., and Dassargues, A. (2014). The usefulness of outcrop analogue air permeameter measurements for analyzing aquifer heterogeneity: Quantifying outcrop hydraulic conductivity and its spatial variability. *Hydrological Processes*, 28(20):5176–5188.

Rohde, R. A. and Hausfather, Z. (2020). The berkeley earth land/ocean temperature record. *Earth System Science Data*, 12(4):3469–3479.

Russell, T., Pham, D., Petho, G., Neishaboor, M. T., Badalyan, A., Behr, A., Genolet, L., Kowollik, P., Zeinijahromi, A., and Bedrikovetsky, P. (2018). Kaolinite mobilisation in unconsolidated porous media: Effect of brine salinity and salt type Na- and Ca salts. *Society*

of Petroleum Engineers - SPE Asia Pacific Oil and Gas Conference and Exhibition 2018, APOGCE 2018.

Saad, N., Cullick, A. S., and Honarpour, M. M. (1995). Immiscible displacement mechanisms and scale-up in the presence of small-scale heterogeneities. *Proceedings - SPE Annual Technical Conference and Exhibition*, Sigma:795–804.

Saadatpoor, E., Bryant, S. L., and Sepehrnoori, K. (2010). New trapping mechanism in carbon sequestration. *Transport in Porous Media*, 82(1):3–17.

Saleem, U., Dewar, M., Chaudhary, T. N., Sana, M., Lichtschlag, A., Alendal, G., and Chen, B. (2021). Numerical modelling of CO_2 migration in heterogeneous sediments and leakage scenario for STEMM-CCS field experiments. *International Journal of Greenhouse Gas Control*, 109(December 2020):103339.

Salmo, I. C., Pettersen, ø., and Skauge, A. (2017). Polymer Flooding at an Adverse Mobility Ratio: Acceleration of Oil Production by Crossflow into Water Channels. *Energy and Fuels*, 31(6):5948–5958.

Sarker, S., Chowdhury, S., Laha, S., and Dey, D. (2012). Use of non-local means filter to denoise image corrupted by salt and pepper noise. *Signal & Imaging Processing: An International Journal*, 3(2):223–235.

Sarwaruddin, M., Skauge, A., and Torsaeter, O. (2001). Modeling of Capillary Pressure for Heterogeneous Reservoirs By a Modified J-Function. (September 2014).

Saxena, N., Hofmann, R., Alpak, F. O., Berg, S., Dietderich, J., Agarwal, U., Tandon, K., Hunter, S., Freeman, J., and Wilson, O. B. (2017). References and benchmarks for pore-scale flow simulated using micro-CT images of porous media and digital rocks. *Advances in Water Resources*, 109:211–235.

Sayers, C. M. (2008). The elastic properties of carbonates. *The Leading Edge*, 27(8):1020–1024.

Sazali, Y., Gödeke, S., Sazali, W. L., Ibrahim, J. M., Graham, G. M., Kidd, S. L., and Ohen, H. A. (2018). Fines migration during CO_2 saturated brine flow in carbonate reservoirs with

some migratory clay minerals - The Malaysian formations. *Proceedings - SPE International Symposium on Formation Damage Control*, 2018-Febru.

Scanziani, A., Singh, K., Bultreys, T., Bijeljic, B., and Blunt, M. J. (2018). In situ characterization of immiscible three-phase flow at the pore scale for a water-wet carbonate rock. *Advances in Water Resources*, 121(September):446–455.

Schlumberger (2017). *Eclipse Industry-Reference Reservoir Simulator: Technical Description*. Schlumberger.

Schön, J. H. (2015). Chapter 1 - rocks—their classification and general properties. In Schön, J. H., editor, *Physical Properties of Rocks*, volume 65 of *Developments in Petroleum Science*, pages 1–19. Elsevier.

Senel, O., Will, R., and Butsch, R. J. (2014). Integrated reservoir modeling at the Illinois Basin – Decatur Project. *Greenhouse Gases: Science and Technology*, 4(5):662–684.

Seyyedi, M., Clennell, M. B., and Jackson, S. J. (2022). Time-lapse imaging of flow instability and rock heterogeneity impacts on CO_2 plume migration in meter long sandstone cores. *Advances in Water Resources*, 164:104216.

Shao, Q., Boon, M., Youssef, A. A., Kurtev, K., Benson, S. M., and Matthai, S. K. (2022). Modelling CO_2 plume spreading in highly heterogeneous rocks with anisotropic, rate-dependent saturation functions: A field-data based numeric simulation study of Otway. *International Journal of Greenhouse Gas Control*, 119(May):103699.

Shi, J.-q., Xue, Z., and Durucan, S. (2011). Supercritical CO_2 core flooding and imbibition in Tako sandstone — Influence of sub-core scale heterogeneity. *International Journal of Greenhouse Gas Control*, 5(1):75–87.

Shikhov, I. and Arns, C. H. (2015). Evaluation of Capillary Pressure Methods via Digital Rock Simulations. *Transport in Porous Media*, 107(2):623–640.

Shiri, Y. and Shiri, A. (2021). Numerical investigation of fluid flow instabilities in pore-scale

with heterogeneities in permeability and wettability. *The Mining-Geology-Petroleum Engineering Bulletin)*, 36(3):143–156.

Shokri, J., Godinez-Brizuela, O. E., Erfani, H., Chen, Y., Babaei, M., Berkowitz, B., and Niasar, V. (2022). Impact of Displacement Direction Relative to Heterogeneity on Averaged Capillary Pressure-Saturation Curves. *Water Resources Research*, 58(2):1–14.

Siddiqui, S. and Sarker, M. (2010). Trends in CT-Scanning of Reservoir Rocks: Medical CT to Micro CT. *Advances in Computed Tomography for Geomaterials: GeoX 2010*, pages 189–196.

Sidenko, E., Tertyshnikov, K., Gurevich, B., and Pevzner, R. (2022). DAS signature of reservoir pressure changes caused by a CO_2 injection: Experience from the CO_2CRC Otway Project. *International Journal of Greenhouse Gas Control*, 119(January):103735.

Singh, M., Chaudhuri, A., Soltanian, M. R., and Stauffer, P. H. (2021). Coupled multiphase flow and transport simulation to model CO_2 dissolution and local capillary trapping in permeability and capillary heterogeneous reservoir. *International Journal of Greenhouse Gas Control*, 108(March):103329.

Smith, E. (1991). The influence of small-scale heterogeneity on average relative permeability. *Reservoir Characterization II*, pages 52–76.

Spurin, C., Bultreys, T., Bijeljic, B., Blunt, M. J., and Krevor, S. (2019). Intermittent fluid connectivity during two-phase flow in a heterogeneous carbonate rock. *Physical Review E*, 100(4):1–10.

Spurin, C., Bultreys, T., Rücker, M., Garfi, G., Schlepütz, C. M., Novak, V., Berg, S., Blunt, M. J., and Krevor, S. (2021). The development of intermittent multiphase fluid flow pathways through a porous rock. *Advances in Water Resources*, 150(November 2020):103868.

Stone, H. L. (1991). Rigorous black oil pseudo functions. *Proceedings of the SPE Symposium on Reservoir Simulation*, pages 57–68.

Strandli, C. W., Mehnert, E., and Benson, S. M. (2014). CO_2 plume tracking and history

matching using multilevel pressure monitoring at the Illinois basin - Decatur project. *Energy Procedia*, 63:4473–4484.

Stubos, A. K., Satik, C., and Yortsos, Y. C. (1993). Effects of capillary heterogeneity on vapor-liquid counterflow in porous media. *International Journal of Heat and Mass Transfer*, 36(4):967–976.

Su, Y., Zha, M., Jiang, L., Ding, X., Qu, J., Jin, J., and Iglauer, S. (2022). Pore structure and fluid distribution of tight sandstone by the combined use of SEM, MICP and X-ray micro-CT. *Journal of Petroleum Science and Engineering*, 208.

Sundal, A., Miri, R., Ravn, T., and Aagaard, P. (2015). Modelling CO_2 migration in aquifers; considering 3D seismic property data and the effect of site-typical depositional heterogeneities. *International Journal of Greenhouse Gas Control*, 39:349–365.

Suzuki, K. and Hewett, T. A. (2002). Sequential upscaling method. *Transport in Porous Media*, 46(2-3):179–212.

Sweatman, R., Crookshank, S., and Edman, S. (2011). Outlook and Technologies for Offshore CO_2 EOR/CCS Projects. *Offshore Technology Conference*, May:2–5.

Tanzil, D., Hirasaki, G. J., and Miller, C. A. (2002). Mobility of foam in heterogeneous media: Flow parallel and perpendicular to stratification. *SPE Journal*, 7(2):203–212.

Tariq, Z., Kamal, M. S., Mahmoud, M., Murtaza, M., Abdulraheem, A., and Zhou, X. (2021). Dicationic Surfactants as an Additive in Fracturing Fluids to Mitigate Clay Swelling: A Petrophysical and Rock Mechanical Assessment. *ACS Omega*, 6(24):15867–15877.

Tavakoli, V. (2020). *Microscopic Heterogeneity*. Number 2010.

Tchelepi, H. A. and Orr, F. M. (1994). Interaction of viscous fingering, permeability heterogeneity, and gravity segregation in three dimensions. *SPE Reservoir Engineering (Society of Petroleum Engineers)*, 9(4):266–271.

Teletzke, G. F. and Lu, P. (2013). Guidelines for reservoir modeling of geologic CO_2 storage. *Energy Procedia*, 37:3936–3944.

Thermofisher (2019). *Avizo's User Guide 2019*.

Trevisan, L., Pini, R., Cihan, A., Birkholzer, J. T., Zhou, Q., and Illangasekare, T. H. (2015). Experimental analysis of spatial correlation effects on capillary trapping of supercritical CO_2 at the intermediate laboratory scale in heterogeneous porous media. *Water Resources Research*, 51:8791–8805.

Tsakiroglou, C. D., Avraam, D. G., and Payatakes, A. C. (2007). Transient and steady-state relative permeabilities from two-phase flow experiments in planar pore networks. *Advances in Water Resources*, 30:1981–1992.

Tuller, M., Kulkarni, R., and Fink, W. (2013). Segmentation of x-ray ct data of porous materials: A review of global and locally adaptive algorithms. *Soil-Water-Root Processes: Advances in Tomography and Imaging*, page 157 – 182.

Turan, G., Zapantis, A., Kearns, D., Tamme, E., Staib, C., Zhang, T., Burrows, J., Gillespie, A., Havercroft, I., Rassool, D., Consoli, C., and Liu, H. (2021). Global status of CCS 2021. Technical report, Global CCS Institute. `https://www.japanccs.com/wp/wp-content/uploads/2021/10/0-4-GCCSI_Jarad-Daniels.pdf`.

Van Duijn, C. J., Molenaar, J., and De Neef, M. J. (1995). The effect of capillary forces on immiscible two-phase flow in heterogeneous porous media. *Transport in Porous Media*, 21(1):71–93.

Van Geet, M., Swennen, R., and Wevers, M. (2000). Quantitative analysis of reservoir rocks by microfocus X-ray computerised tomography. *Sedimentary Geology*, 132(1-2):25–36.

Verdon, J. P., Kendall, J., White, D. J., Angus, D. A., Fishes, Q. J., and Urbancic, T. (2010). Passive seismic monitoring of carbon dioxide storage at Weyburn. *The Leading Edge*, 29(2):200–206.

Virnovsky, G. A., Friis, H. A., and Lohne, A. (2004). A Steady-State Upscaling Approach for Immiscible Two-Phase Flow. *Transport in Porous Media*, 54(2):167–192.

Virnovsky, G. A., Lohne, A., and Frette, O. I. (2009). Modeling capillary pressure using capillary bundles with arbitrary cross-sections obtained from photomicrographs. *Journal of Petroleum Science and Engineering*, 69(1-2):117–128.

Warren, J. and Price, H. (1961). Flow in Heterogeneous Porous Media. *Society of Petroleum Engineers Journal*, 1(03):153–169.

Wei, H., Zhu, X., Liu, X., Yang, H., Tao, W. Q., and Chen, L. (2022). Pore-scale study of drainage processes in porous media with various structural heterogeneity. *International Communications in Heat and Mass Transfer*, 132:105914.

Welge, H. J. (1952). A Simplified Method for Computing Oil Recovery by Gas or Water Drive. *Journal of Petroleum Technology*, 4:370 – 372.

Wellington, S. L. and Vinegar, H. J. (1987). X-Ray Computerized Tomography. *Journal of Petroleum Technology*, 39(8):885–898.

Wen, G. and Benson, S. M. (2019). CO_2 plume migration and dissolution in layered reservoirs. *International Journal of Greenhouse Gas Control*, 87(January):66–79.

Wen, X. H. and Gómez-Hernández, J. J. (1996). Upscaling hydraulic conductivities in heterogeneous media: An overview. *Journal of Hydrology*, 183(1-2).

Wenck, N., Jackson, S. J., Manoorkar, S., Muggeridge, A., and Krevor, S. (2021). Simulating Core Floods in Heterogeneous Sandstone and Carbonate Rocks. *Water Resources Research*, 57(9):1–11.

White Rose (2016a). *K40: Subsurface Geoscience and Production Chemistry Reports. Technical: Storage.* `https://assets.publishing.service.gov.uk/government/uploads/system/uploads/attachment_data/file/531045/K40_Subsurface_Geoscience_and_Production_Chemistry.pdf`.

White Rose (2016b). *K41: Reservoir Engineering Field Report. Category: Storage.* `https://assets.publishing.service.gov.uk/government/uploads/system/uploads/attachment_data/file/531046/K41_Reservoir_Engineering-Field_Report.pdf`.

Williams, G. A. and Chadwick, R. A. (2021). Influence of reservoir-scale heterogeneities on the growth, evolution and migration of a CO_2 plume at the Sleipner Field, Norwegian North Sea. *International Journal of Greenhouse Gas Control*, 106(December 2020):103260.

Wilson, J. W. (1956). Determination of relative permeability under simulated reservoir conditions. *AIChE Journal*, 2(1):94–100.

Withjack, E. M. (1988). Computed tomography for rock-property determination and fluid-flow visualization. *SPE Formation Evaluation*, 3(4):696–704.

Wolff, M., Flemisch, B., and Helmig, R. (2013). An adaptive multiscale approach for modeling two-phase flow in porous media including capillary pressure. *Water Resources Research*, 49(12):8139–8159.

Worden, R. H., Armitage, P. J., Butcher, A. R., Churchill, J. M., Csoma, A. E., Hollis, C., Lander, R. H., and Omma, J. E. (2018). Petroleum reservoir quality prediction: overview and contrasting approaches from sandstone and carbonate communities. *Geological Society, London, Special Publications*, 435(1):1–31.

Wright, R. J. and Dawe, R. A. (1983). Fluid displacement efficiency in layered porous media. mobility ratio influence. *Oil & Gas Science and Technology-revue De L Institut Francais Du Petrole*, 38:455–474.

Wyckoff, R. and Botset, H. (1936). The flow of gas-liquid mixtures through unconsolidated sands. *Physics*, 7(9):325–345.

Yamamoto, H. (2009). Numerical investigation for the impact of CO_2 geologic sequestration on regional groundwater flow. *International Journal of Greenhouse Gas Control*, pages 35–43.

Yang, S., Russell, T., Badalyan, A., Schacht, U., Woolley, M., and Bedrikovetsky, P. (2019a). Characterisation of fines migration system using laboratory pressure measurements. *Journal of Natural Gas Science and Engineering*, 65(October 2018):108–124.

Yang, Y., Li, Y., Yao, J., Zhang, K., Iglauer, S., Luquot, L., and Wang, Z. (2019b). Formation damage evaluation of a sandstone reservoir via pore-scale X-ray computed tomography analysis. *Journal of Petroleum Science and Engineering*, 183:106356.

Yang, Z., Tian, L., Niemi, A., and Fagerlund, F. (2013). Upscaling of the constitutive relationships for CO_2 migration in multimodal heterogeneous formations. *International Journal of Greenhouse Gas Control*, 19:743–755.

Yaslam, M. M. (2012). Characterization and Modeling on Unsteady State Relative Permeability. Master's thesis, The Petroleum Institute.

Yavuz, S., Isaenkov, R., Pevzner, R., Gurevich, B., Tertyshnikov, K., Yurikov, A., Correa, J., Wood, T., and Freifeld, B. (2021). Processing of multi-well offset vertical seismic profile data acquired with distributed acoustic sensors and surface orbital vibrators: Stage 3 of the CO_2CRC Otway Project case study. *Geophysical Prospecting*, 69(8-9):1664–1677.

Yi, J., Xing, H., Wang, J., Xia, Z., and Jing, Y. (2019). Pore-scale study of the effects of surface roughness on relative permeability of rock fractures using lattice Boltzmann method. *Chemical Engineering Science*, 209:115178.

Yortsos, Y. C., Satik, C., Bacri, J. C., and Salin, D. (1993). Large-scale percolation theory of drainage. *Transport in Porous Media*, 10(2):171–195.

Yuan, L., Zhang, Y., Zhao, J., Song, Y., and Chi, Y. (2020). Molecular simulation of equal density temperature in CCS under geological sequestration conditions. *Greenhouse Gases: Science and Technology*, 10(1):90–102.

Zahasky, C. and Benson, S. M. (2018). Micro-positron emission tomography for measuring sub-core scale single and multiphase transport parameters in porous media. *Advances in Water Resources*, 115:1–16.

Zahasky, C., Jackson, S. J., Lin, Q., and Krevor, S. (2020). Pore Network Model Predictions of Darcy-Scale Multiphase Flow Heterogeneity Validated by Experiments. *Water Resources Research*, 56(6):1–16.

Zhang, X., Ma, F., Yin, S., Wallace, C. D., Reza, M., Dai, Z., Ritzi, R. W., Ma, Z., Zhan, C., and Lü, X. (2021). Application of upscaling methods for fluid flow and mass transport in multi-scale heterogeneous media : A critical review. *Applied Energy*, 303:117603.

Zhang, X., Shapiro, A., and Stenby, E. H. (2011). Upscaling of Two-Phase Immiscible Flows in Communicating Stratified Reservoirs. *Transport in Porous Media*, 87(3):739–764.

Zhang, Y., Jackson, C., and Krevor, S. (2022). An Estimate of the Amount of Geological CO_2 Storage over the Period of 1996-2020. *Environmental Science and Technology Letters*, 9(8):693–698.

Zhang, Y., Nishizawa, O., Kiyama, T., Chiyonobu, S., and Xue, Z. (2014). Flow behaviour of supercritical CO_2 and brine in Berea sandstone during drainage and imbibition revealed by medical X-ray CT images. *Geophysical Journal International*, 197(3):1789–1807.

Zhou, Q. and Birkholzer, J. T. (2011). On scale and magnitude of pressure build-up induced by large-scale geologic storage of CO_2. *Greenhouse Gases: Science and Technology*, 1:11–20.

Zhou, Y., Helland, J. O., and Hatzignatiou, D. G. (2014). Pore-scale modeling of waterflooding in mixed-wet-rock images: Effects of initial saturation and wettability. *SPE Journal*, 19(1):88–100.

Zhou, Z., Gunter, W. D., Kadatz, B., and Cameron, S. (1996). Effect of clay swelling on reservoir quality. *Journal of Canadian Petroleum Technology*, 35(7):18–23.

Appendix A

Fractional Flows of Carbonates and Sandstones Experiments

The fractional flows imposed in the sandstone and carbonate coreflood experiments analysed in Chapter 4 are provided in the following Tables.

Table A.1: Fractional flows used in the optimisation scheme for the Bentheimer sandstone.

	7ml min^{-1}		**40ml min^{-1}**	
Fractional flow number	fN_2	fw	fN_2	fw
f1	0.1429	0.857	0.025	0.975
f2	0.4	0.600	0.1	0.900
f3	0.7143	0.286	0.375	0.625
f4	0.8857	0.114	0.625	0.375
f5	0.9429	0.057	0.825	0.175
f6	0.9929	0.007	0.9	0.100
f7	-	-	0.95	0.050
f8	-	-	0.975	0.025
f9	-	-	0.9875	0.013
f10	-	-	0.995	0.005

Table A.2: Fractional flows used in the optimisation scheme for the Bunter sandstone.

	0.2ml min^{-1}		**20ml min^{-1}**	
Fractional flow number	fN_2	fw	fN_2	fw
f1	0.1	0.900	0.0926	0.907
f2	0.31	0.690	0.2662	0.734
f3	0.63	0.370	0.5176	0.482
f4	0.85	0.150	0.7738	0.226
f5	0.975	0.025	0.9262	0.074
f6	0.995	0.005	0.9768	0.023
f7	-	-	0.9919	0.008
f8	-	-	0.9996	0.000

Table A.3: Fractional flows used in the optimisation scheme for the Indiana limestone.

	0.5ml min^{-1}		**5ml min^{-1}**	
Fractional flow number	fN_2	fw	fN_2	fw
f1	0.024	0.976	0.024	0.976
f2	0.080	0.920	0.080	0.920
f3	0.200	0.800	0.200	0.800
f4	0.450	0.550	0.450	0.550
f5	0.612	0.388	0.612	0.388
f6	0.740	0.260	0.740	0.260
f7	0.830	0.170	0.830	0.170
f8	0.960	0.040	0.960	0.040
f9	0.980	0.020	0.980	0.020
f10	0.990	0.010	0.990	0.010
f11	0.996	0.004	0.996	0.004
f12	0.998	0.002	0.998	0.002
f13	1	0	1.000	0.000

Table A.4: Fractional flows used in the optimisation scheme for the Estaillades limestone.

	0.5ml min^{-1}		**20ml min^{-1}**	
Fractional flow number	fN_2	fw	fN_2	fw
f1	0.024	0.976	0.024	0.976
f2	0.080	0.920	0.080	0.920
f3	0.200	0.800	0.200	0.800
f4	0.450	0.550	0.450	0.550
f5	0.612	0.388	0.612	0.388
f6	0.740	0.260	0.740	0.260
f7	0.830	0.170	0.830	0.170
f8	0.960	0.040	0.960	0.040
f9	0.980	0.020	0.980	0.020
f10	1.000	0.000	0.990	0.010
f11	-	-	0.996	0.004
f12	-	-	0.998	0.002
f13	-	—-—	1.000	0.000

Table A.5: Fractional flows used in the optimisation scheme for the Edwards Brown dolomite.

	0.5ml min^{-1}		**5ml min^{-1}**	
Fractional flow number	fN_2	fw	fN_2	fw
f1	0.024	0.976	0.024	0.976
f2	0.054	0.946	0.612	0.388
f3	0.110	0.890	0.740	0.260
f4	0.162	0.838	0.830	0.170
f5	0.200	0.800	0.960	0.040
f6	0.360	0.640	0.980	0.020
f7	0.450	0.550	0.990	0.010
f8	0.612	0.388	0.996	0.004
f9	0.740	0.260	0.998	0.002
f10	0.830	0.170	1.000	0.000
f11	0.960	0.040	-	-
f12	0.980	0.020	-	-
f13	0.990	0.010	-	-
f14	0.996	0.004	-	-
f15	0.998	0.002	-	-
f16	1.000	0.000	-	-

Appendix B

Percentage Errors of Simulated Corefloods

Percentage errors of the core-average pressure and core-average saturation between the coreflood experiment and coreflood simulation discussed in Chapter 4 Section 4.3.2, provided in tabular formation for the five rock cores.

Table B.1: Percentage errors of the core-average saturation and pressure drop recorded in the experiment and the core-flood simulation for the Bentheimer sandstone.

	Experiment		**Simulation**		**Errors**	
Fractional flow	S_w [-]	ΔP [kPa]	S_w [-]	ΔP [kPa]	Error S_w [%]	Error ΔP [%]
1	0.66	42.34	0.69	32.96	4.29	22.16
2	0.63	37.27	0.63	33.64	0.14	9.75
3	0.60	25.39	0.57	25.85	5.28	1.81
4	0.57	16.56	0.52	18.21	7.98	9.95
5	0.54	12.00	0.49	14.60	9.99	21.66
6	0.45	6.66	0.41	9.90	10.50	48.58

Table B.2: Percentage errors of the core-average saturation and pressure drop recorded in the experiment and the core-flood simulation for the Bunter sandstone.

	Experiment		**Simulation**		**Results**	
Fractional flow	S_w [-]	ΔP [kPa]	S_w [-]	ΔP [kPa]	Error S_w [%]	Error ΔP [%]
1	0.83	3.20	0.78	2.44	6.52	23.87
2	0.75	3.39	0.66	2.93	12.33	13.53
3	0.67	3.20	0.61	2.97	8.74	7.23
4	0.60	2.88	0.57	2.91	4.93	1.19
5	0.57	3.03	0.53	2.83	7.66	6.56
6	0.48	3.32	0.51	2.79	5.44	15.92

Table B.3: Percentage errors of the core-average saturation and pressure drop recorded in the experiment and the core-flood simulation for the Indiana limestone.

	Experiment		**Simulation**		**Results**	
Fractional flow	S_w [-]	ΔP [kPa]	S_w [-]	ΔP [kPa]	Error S_w [%]	Error ΔP [%]
1	0.93	58.30	0.87	3411.40	6.59	5751.71
2	0.92	61.00	0.81	3815.29	11.38	6157.67
3	0.92	59.69	0.80	4181.60	13.03	6906.04
4	0.91	53.42	0.78	4574.26	13.59	8463.48
5	0.89	48.96	0.78	4741.86	12.44	9584.95
6	0.87	45.98	0.77	4850.36	11.74	10449.38
7	0.85	43.48	0.77	4918.29	10.01	11212.73
8	0.80	41.07	0.77	5005.89	4.15	12088.54
9	0.78	39.54	0.76	5018.63	2.33	12591.35
10	0.78	39.27	0.76	5024.82	1.73	12696.12
11	0.78	39.30	0.76	5028.05	1.50	12693.10
12	0.77	39.65	0.76	5029.54	1.37	12586.13
13	0.77	39.61	0.76	5030.98	0.66	12601.43

Table B.4: Percentage errors of the core-average saturation and pressure drop recorded in the experiment and the core-flood simulation for the Estaillades limestone.

	Experiment		**Simulation**		**Results**	
Fractional flow	S_w [-]	ΔP [kPa]	S_w [-]	ΔP [kPa]	Error S_w [%]	Error ΔP [%]
1	0.95	16.15	0.87	38.53	8.34	138.55
2	0.94	17.03	0.84	44.13	9.90	159.08
3	0.91	18.25	0.82	45.42	9.25	148.94
4	0.88	19.02	0.80	42.07	8.82	121.17
5	0.86	17.76	0.78	38.08	8.42	114.47
6	0.84	16.72	0.77	34.21	8.07	104.7
7	0.82	13.96	0.75	31.14	7.88	123.10
8	0.79	13.95	0.71	25.20	10.03	80.69
9	0.78	13.23	0.69	23.61	11.11	78.48
10	0.78	13.28	0.67	21.62	13.73	62.83

Table B.5: Percentage errors of the core-average saturation and pressure drop recorded in the experiment and the core-flood simulation for the Edwards Brown dolomite.

	Experiment		**Simulation**		**Results**	
Fractional flow	S_w [-]	ΔP [kPa]	S_w [-]	ΔP [kPa]	Error S_w [%]	Error ΔP [%]
1	0.91	53.78	0.95	45.53	3.65	15.35
2	0.91	62.63	0.94	49.94	3.15	20.27
3	0.90	71.35	0.92	55.10	2.17	22.77
4	0.90	71.59	0.92	58.43	1.51	18.38
5	0.90	78.42	0.90	61.19	1.31	21.97
6	0.89	78.48	0.88	64.69	0.32	17.57
7	0.87	79.51	0.87	64.49	0.30	18.90
8	0.86	74.21	0.85	61.47	1.02	17.18
9	0.85	66.01	0.84	56.92	1.30	13.77
10	0.84	59.19	0.82	52.00	1.83	12.17
11	0.79	50.91	0.79	41.31	0.25	18.86
12	0.77	42.28	0.78	37.87	1.48	10.43
13	0.76	41.93	0.77	36.41	1.72	13.17
14	0.75	41.23	0.77	35.30	2.07	14.37
15	0.73	41.54	0.76	33.46	3.64	19.44
16	0.72	40.8	0.76	33.20	5.00	18.62

Appendix C

Error Surfaces

Figure C.1 illustrates the challenge in simultaneously minimising the error between the experiment and the simulation at both, low and high rate.

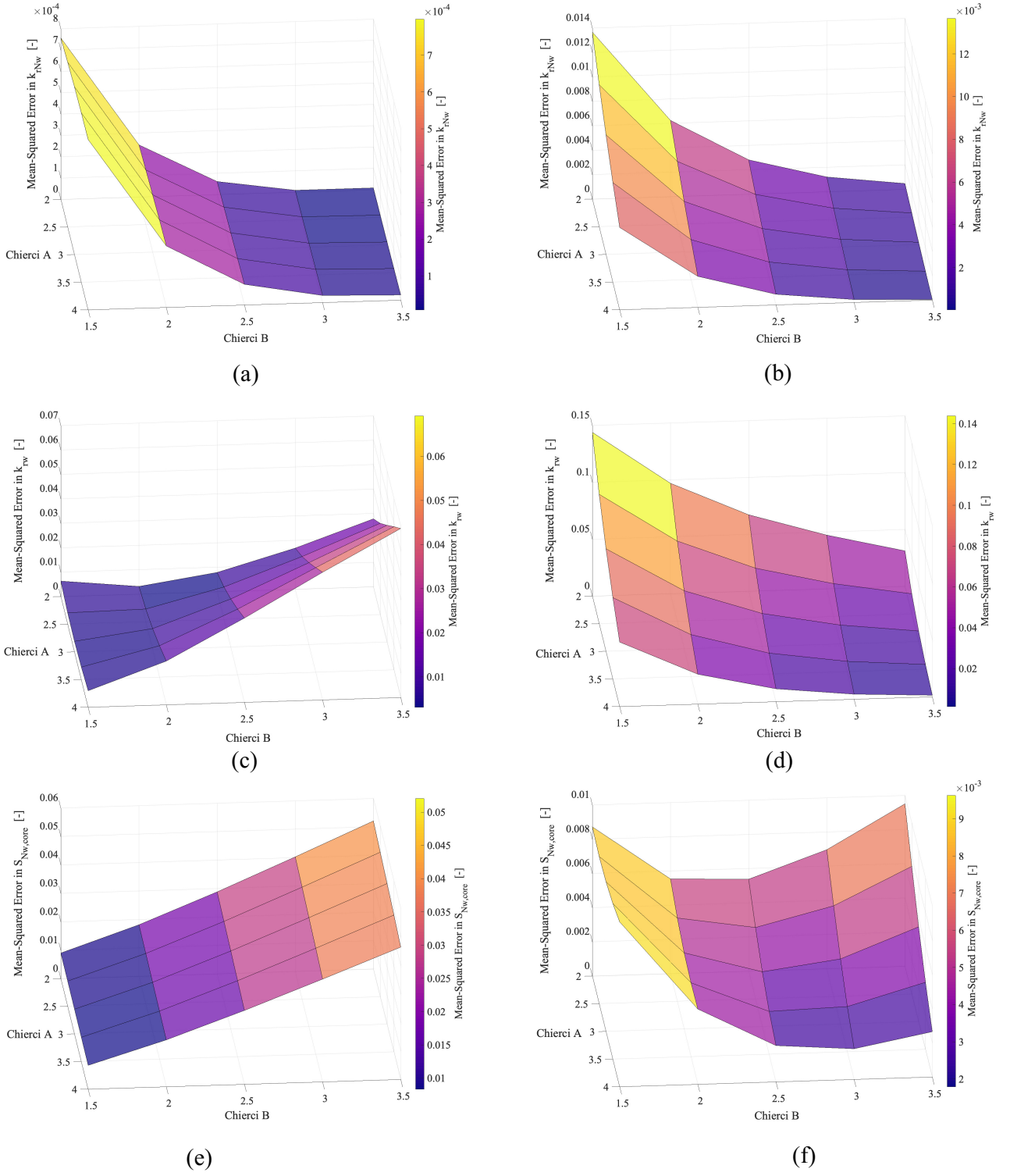


Figure C.1: Mean-squared error between the simulation and experiment relative permeabilities and voxel saturations for the Indiana limestone. The errors are calculated using a range of A and B parameters as input. Figures (a), (c) and (e) are the errors for the low rate experiment and Figures (b), (d), (f) are the errors for the high rate experiment.

Appendix D

Rate Dependency Tabular Data

Tabular data for the results presented in Figure 4.14 for the Bentheimer, Bunter and Edwards Brown samples.

Table D.1: Relative permeability for the Bentheimer sandstone at varying total flow rates. Data is displayed graphically in Figure 4 in the main paper and was obtained from numerical simulations.

N_c	**0.170**			**13.41**			**144.85**		
f_g	S_w	k_{rw}	k_{rg}	S_w	k_{rw}	k_{rg}	S_w	k_{rw}	k_{rg}
0.14	0.7210	0.0771	0.0005	0.6893	0.1620	0.0011	0.6612	0.1256	0.0008
0.4	0.6478	0.0489	0.0013	0.6294	0.1092	0.0029	0.6108	0.0867	0.0023
0.71	0.5853	0.0236	0.0024	0.5671	0.0664	0.0067	0.5621	0.0604	0.0061
0.86	0.5417	0.0097	0.0030	0.5143	0.0400	0.0125	0.5139	0.0412	0.0128
0.94	0.5208	0.0049	0.0033	0.4803	0.0273	0.0181	0.4787	0.0284	0.0189
0.99	0.4908	0.0006	0.0035	0.3934	0.0073	0.0409	0.3912	0.0076	0.0430

Table D.2: Relative permeability for the Bunter sandstone at varying total flow rates. Data is displayed graphically in Figure 4 in the main paper and was obtained from numerical simulations.

N_c	**0.130**			**13.31**			**72.24**		
f_g	S_w	k_{rw}	k_{rg}	S_w	k_{rw}	k_{rg}	S_w	k_{rw}	k_{rg}
0.1	0.7131	0.0464	0.0004	0.7781	0.3482	0.0031	0.7765	0.3487	0.0031
0.31	0.6677	0.0331	0.0012	0.6966	0.2129	0.0075	0.6970	0.2172	0.0077
0.63	0.6152	0.0176	0.0024	0.6126	0.1107	0.0149	0.6118	0.1191	0.0160
0.85	0.5677	0.0074	0.0033	0.5431	0.0527	0.0236	0.5365	0.0588	0.0263
0.98	0.5145	0.0013	0.0040	0.4539	0.0129	0.0396	0.4419	0.0145	0.0447
0.995	0.4899	0.0003	0.0042	0.3972	0.0034	0.0533	0.3836	0.0039	0.0612

Table D.3: Relative permeability for the Edwards Brown dolomite at varying total flow rates. Data is displayed graphically in Figure 4 in the main paper and was obtained from numerical simulations.

N_c	**0.007**			**0.129**			**5.904**		
f_g	S_w	k_{rw}	k_{rg}	S_w	k_{rw}	k_{rg}	S_w	k_{rw}	k_{rg}
0.024	1.0000	0.9601	0.0004	0.9232	0.3555	0.0002	0.9003	0.2609	0.0001
0.110	0.8823	0.0995	0.0002	0.8964	0.2299	0.0005	0.8652	0.2253	0.0005
0.200	0.8698	0.0856	0.0004	0.8839	0.1858	0.0009	0.8466	0.1987	0.0009
0.450	0.8505	0.0557	0.0008	0.8586	0.1239	0.0019	0.8386	0.1357	0.0020
0.740	0.8301	0.0259	0.0014	0.8260	0.0767	0.0040	0.8386	0.0642	0.0033
0.830	0.8233	0.0170	0.0015	0.8080	0.0623	0.0056	0.8219	0.0417	0.0037
0.960	0.7979	0.0041	0.0018	0.7529	0.0286	0.0126	0.7678	0.0116	0.0051
1.000	0.7940	0.0002	0.0019	0.6635	0.0035	0.0323	0.7021	0.0020	0.0183

Appendix E

Experimental Pressure Drop

Figure E.1 presents the core-average pressure drop recorded throughout the entire coreflood experiment performed on the reservoir sample from the Endurance site.

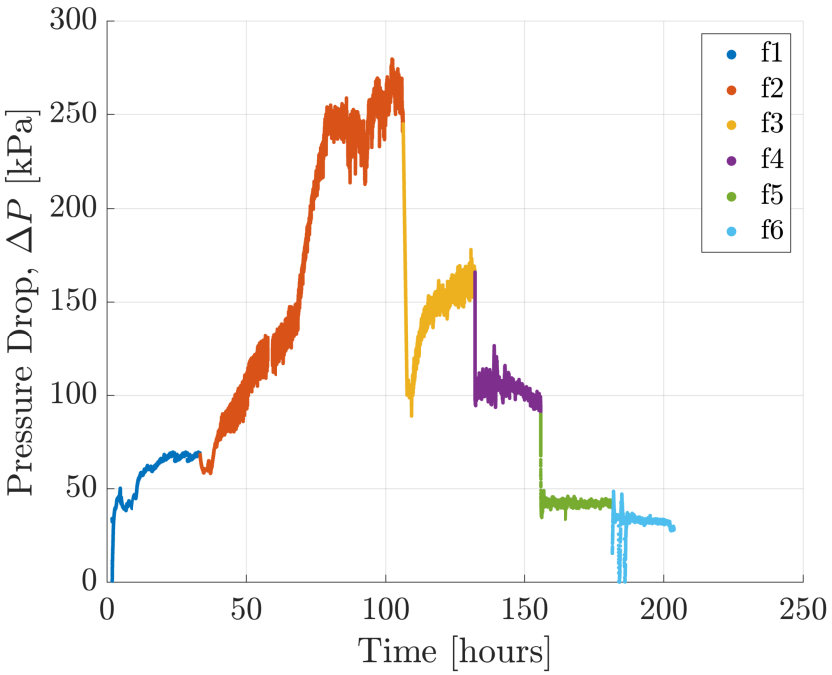


Figure E.1: Core-average pressure drop recorded during the coreflood experiment. The colours refer to the various fractional flows.

Appendix F

Permissions

PLS Clear

PARTIES:

1. **Cambridge University Press** (Licensor); and
2. **Nele Wenck** (Licensee).

Thank you for your recent permission request. Some permission requests for use of material published by the Licensor, such as this one, are now being facilitated by PLSclear.

Set out in this licence cover sheet (the **Licence Cover Sheet**) are the principal terms under which Licensor has agreed to license certain Licensed Material (as defined below) to Licensee. The terms in this Licence Cover Sheet are subject to the attached General Terms and Conditions, which together with this Licence Cover Sheet constitute the licence agreement (the **Licence**) between Licensor and Licensee as regards the Licensed Material. The terms set out in this Licence Cover Sheet take precedence over any conflicting provision in the General Terms and Conditions.

Free Of Charge Licence Terms

Licence Date:	04/08/2023
PLSclear Ref No:	85181

The Licensor

Company name:	Cambridge University Press
Address:	University Printing House Shaftesbury Road Cambridge CB2 8BS GB

The Licensee

Licensee Contact Name:	Nele Wenck
Licensee Address:	

Licensed Material

title:	Geophysics and Geosequestration
ISBN:	9781107137493
publisher:	Cambridge University Press

Are you requesting permission to reuse the cover of the publication?	No
Figure number & title	Figure 19.29 Plume simulation and forward-modeled acoustic impedance change. (Left) Aerial view of simulated 2015 monitor CO2 plume and outline of 2001–2015 surface seismic time-lapse NRM attribute (from Figure 19.17). (Right) Aerial view of forward
Page numbers	368
Are you the author of the content that you are requesting to reuse?	No
Additional Information	I would like to feature the figure in my dissertation.
Will you be changing or editing the image?	No

For Use In Licensee's Publication(s)

usage type	Book, Journal, Magazine or Academic Paper-Thesis or Dissertation
Will your dissertation be placed in an online repository?	Yes
Author	Nele Mareike Wenck
Language	English
Title of dissertation/thesis	The Impact of Capillary Heterogeneity on Subsurface Carbon Dioxide Storage
University or institution	Imperial College London
Unlimited circulation?	No

Rights Granted

Exclusivity:	Non-Exclusive
Format:	Thesis or Dissertation
Language:	English
Territory:	UK & Commonwealth
Duration:	Lifetime of Licensee's Edition
Maximum Circulation:	1

GENERAL TERMS AND CONDITIONS

1. Definitions and Interpretation

1.1 Capitalised words and expressions in these General Terms and Conditions have the meanings given to them in the Licence Cover Sheet.

1.2 In this Licence any references (express or implied) to statutes or provisions are references to those statutes or provisions as amended or re-enacted from time to time. The term including will be construed as illustrative, without limiting the sense or scope of the words preceding it. A reference to in writing or written includes faxes and email. The singular includes the plural and vice versa.

2. Grant of Rights

2.1 The Licensor grants to Licensee the non-exclusive right to use the Licensed Material as specified in the Licence Cover Sheet.

2.2 The rights licensed to Licensee under this Licence do not include the right to use any third party copyright material incorporated in the Licensed Material. Licensee should check the Licensed Material carefully and seek permission for the use of any such third party copyright material from the relevant copyright owner(s).

2.3 Unless otherwise stated in the Licence Cover Sheet, the Licensed Material may be:

2.3.1 subjected to minor editing, including for the purposes of creating alternative formats to provide access for a beneficiary person (provided that any such editing does not amount to derogatory treatment); and/or

2.3.2 used for incidental promotional use (such as online retail providers' search facilities).

2.4 Save as expressly permitted in this Licence or as otherwise permitted by law, no use or modification of the Licensed Material may be made by Licensee without Licensor's prior written permission.

3. Copyright Notice and Acknowledgement

3.1 Licensee must ensure that the following notices and acknowledgements are reproduced prominently alongside each reproduction by Licensee of the Licensed Material:

3.1.1 the title and author of the Licensed Material;

3.1.2 the copyright notice included in the Licensed Material; and

3.1.3 the statement "Reproduced with permission of The Licensor through PLSclear."

4. Reversion of Rights

4.1 The rights licensed to Licensee under this Licence will terminate immediately and automatically upon the earliest of the following events to occur:

4.1.1 the Licensed Material not being used by Licensee within 18 months of the Licence Date;

4.1.2 expiry of the Licence Duration; or

4.1.3 the Maximum Circulation being reached.

5. Miscellaneous

5.1 By using the Licensed Material, Licensee will be deemed to have accepted all the terms and conditions contained in this Licence.

5.2 This Licence contains the entire understanding and agreement of the parties relating to its subject matter and supersedes in all respects any previous or other existing arrangements, agreements or understandings between the parties whether oral or written in relation to its subject matter.

5.3 Licensee may not assign this Licence or any of its rights or obligations hereunder to any third party without Licensor's prior written consent.

5.4 This Licence is governed by and shall be construed in accordance with the laws of England and Wales and the parties hereby irrevocably submit to the non-exclusive jurisdiction of the Courts of England and Wales as regards any claim, dispute or matter arising under or in relation to this Licence.

PLS Clear

PARTIES:

1. **Cambridge University Press** (Licensor); and
2. **Nele Wenck** (Licensee).

Thank you for your recent permission request. Some permission requests for use of material published by the Licensor, such as this one, are now being facilitated by PLSclear.

Set out in this licence cover sheet (the **Licence Cover Sheet**) are the principal terms under which Licensor has agreed to license certain Licensed Material (as defined below) to Licensee. The terms in this Licence Cover Sheet are subject to the attached General Terms and Conditions, which together with this Licence Cover Sheet constitute the licence agreement (the **Licence**) between Licensor and Licensee as regards the Licensed Material. The terms set out in this Licence Cover Sheet take precedence over any conflicting provision in the General Terms and Conditions.

Free Of Charge Licence Terms

Licence Date:	04/08/2023
PLSclear Ref No:	85182

The Licensor

Company name:	Cambridge University Press
Address:	University Printing House Shaftesbury Road Cambridge CB2 8BS GB

The Licensee

Licensee Contact Name:	Nele Wenck
Licensee Address:	United Kingdom

Licensed Material

title:	An Introduction to Reservoir Simulation Using MATLAB/GNU Octave User Guide for the MATLAB Reservoir Simulation Toolbox (MRST)

ISBN:	9781108492430
publisher:	Cambridge University Press
Are you requesting permission to reuse the cover of the publication?	No
Figure number & title	Figure 15.4 Arithmetic, harmonic, and harmonic-arithmetic averaging applied to a 40 × 60 subset of Layer 46 from the SPE 10 data set.
Page numbers	568
Are you the author of the content that you are requesting to reuse?	No
Will you be changing or editing the image?	Yes
Will it be cropped?	Yes
Full details of how it will be altered	I would like to crop the right panel ('Harmonic-arithmetic'), thus would like to show the remaining 3 panels.

For Use In Licensee's Publication(s)

usage type	Book, Journal, Magazine or Academic Paper-Thesis or Dissertation
Will your dissertation be placed in an online repository?	Yes
Author	Nele Mareike Wenck
Language	English
Title of dissertation/thesis	The Impact of Capillary Heterogeneity on Subsurface Carbon Dioxide Storage
University or institution	Imperial College London
Unlimited circulation?	Yes

Rights Granted

Exclusivity:	Non-Exclusive
Format:	Thesis or Dissertation
Language:	English
Territory:	World
Duration:	Lifetime of Licensee's Edition
Maximum Circulation:	Unlimited

GENERAL TERMS AND CONDITIONS

1. Definitions and Interpretation

1.1 Capitalised words and expressions in these General Terms and Conditions have the meanings given to them in the Licence Cover Sheet.

1.2 In this Licence any references (express or implied) to statutes or provisions are references to those statutes or provisions as amended or re-enacted from time to time. The term including will be construed as illustrative, without limiting the sense or scope of the words preceding it. A reference to in writing or written includes faxes and email. The singular includes the plural and vice versa.

2. Grant of Rights

2.1 The Licensor grants to Licensee the non-exclusive right to use the Licensed Material as specified in the Licence Cover Sheet.

2.2 The rights licensed to Licensee under this Licence do not include the right to use any third party copyright material incorporated in the Licensed Material. Licensee should check the Licensed Material carefully and seek permission for the use of any such third party copyright material from the relevant copyright owner(s).

2.3 Unless otherwise stated in the Licence Cover Sheet, the Licensed Material may be:

2.3.1 subjected to minor editing, including for the purposes of creating alternative formats to provide access for a beneficiary person (provided that any such editing does not amount to derogatory treatment); and/or

2.3.2 used for incidental promotional use (such as online retail providers' search facilities).

2.4 Save as expressly permitted in this Licence or as otherwise permitted by law, no use or modification of the Licensed Material may be made by Licensee without Licensor's prior written permission.

3. Copyright Notice and Acknowledgement

3.1 Licensee must ensure that the following notices and acknowledgements are reproduced prominently alongside each reproduction by Licensee of the Licensed Material:

3.1.1 the title and author of the Licensed Material;

3.1.2 the copyright notice included in the Licensed Material; and

3.1.3 the statement "Reproduced with permission of The Licensor through PLSclear."

4. Reversion of Rights

4.1 The rights licensed to Licensee under this Licence will terminate immediately and automatically upon the earliest of the following events to occur:

4.1.1 the Licensed Material not being used by Licensee within 18 months of the Licence Date;

4.1.2 expiry of the Licence Duration; or

4.1.3 the Maximum Circulation being reached.

5. Miscellaneous

5.1 By using the Licensed Material, Licensee will be deemed to have accepted all the terms and conditions contained in this Licence.

5.2 This Licence contains the entire understanding and agreement of the parties relating to its subject matter and supersedes in all respects any previous or other existing arrangements, agreements or understandings between the parties whether oral or written in relation to its subject matter.

5.3 Licensee may not assign this Licence or any of its rights or obligations hereunder to any third party without Licensor's prior written consent.

5.4 This Licence is governed by and shall be construed in accordance with the laws of England and Wales and the parties hereby irrevocably submit to the non-exclusive jurisdiction of the Courts of England and Wales as regards any claim, dispute or matter arising under or in relation to this Licence.

SPRINGER NATURE LICENSE
TERMS AND CONDITIONS

Aug 05, 2023

This Agreement between Imperial College London -- Nele Wenck ("You") and Springer Nature ("Springer Nature") consists of your license details and the terms and conditions provided by Springer Nature and Copyright Clearance Center.

License Number	5602450140379
License date	Aug 05, 2023
Licensed Content Publisher	Springer Nature
Licensed Content Publication	Mathematical Geosciences
Licensed Content Title	Identifying the Representative Elementary Volume for Permeability in Heterolithic Deposits Using Numerical Rock Models
Licensed Content Author	Kjetil Nordahl et al
Licensed Content Date	Aug 7, 2008
Type of Use	Thesis/Dissertation
Requestor type	academic/university or research institute
Format	electronic
Portion	figures/tables/illustrations

Number of figures/tables /illustrations	1
Will you be translating?	no
Circulation/distribution	1 - 29
Author of this Springer Nature content	no
Title	The Impact of Capillary Heterogeneity on Subsurface Carbon Dioxide Storage
Institution name	Imperial College London
Expected presentation date	Nov 2023
Portions	Figure 1
Requestor Location	Imperial College London United Kingdom Attn: Imperial College London
Total	0.00 USD

Terms and Conditions

Springer Nature Customer Service Centre GmbH Terms and Conditions

The following terms and conditions ("Terms and Conditions") together with the terms specified in your [RightsLink] constitute the License ("License") between you as Licensee and Springer Nature Customer Service Centre GmbH as Licensor. By clicking 'accept' and completing the transaction for your use of the material ("Licensed Material"), you confirm your acceptance of and obligation to be bound by these Terms and Conditions.

1. Grant and Scope of License

1. 1. The Licensor grants you a personal, non-exclusive, non-transferable, non-sublicensable, revocable, world-wide License to reproduce, distribute, communicate to the public, make available, broadcast, electronically transmit or create derivative works using the Licensed Material for the purpose(s) specified in your RightsLink Licence Details only. Licenses are granted for the specific use requested in the order and for no other use, subject to these Terms and Conditions. You acknowledge and agree that the rights granted to you under this License do not include the right to modify, edit, translate, include in collective works, or create derivative works of the Licensed Material in whole or in part unless expressly stated in your RightsLink Licence Details. You may use the Licensed Material only as permitted under this Agreement and will not reproduce, distribute, display, perform, or otherwise use or exploit any Licensed Material in any way, in whole or in part, except as expressly permitted by this License.

1. 2. You may only use the Licensed Content in the manner and to the extent permitted by these Terms and Conditions, by your RightsLink Licence Details and by any applicable laws.

1. 3. A separate license may be required for any additional use of the Licensed Material, e.g. where a license has been purchased for print use only, separate permission must be obtained for electronic re-use. Similarly, a License is only valid in the language selected and does not apply for editions in other languages unless additional translation rights have been granted separately in the License.

1. 4. Any content within the Licensed Material that is owned by third parties is expressly excluded from the License.

1. 5. Rights for additional reuses such as custom editions, computer/mobile applications, film or TV reuses and/or any other derivative rights requests require additional permission and may be subject to an additional fee. Please apply to journalpermissions@springernature.com or bookpermissions@springernature.com for these rights.

2. Reservation of Rights

Licensor reserves all rights not expressly granted to you under this License. You acknowledge and agree that nothing in this License limits or restricts Licensor's rights in or use of the Licensed Material in any way. Neither this License, nor any act, omission, or statement by Licensor or you, conveys any ownership right to you in any Licensed Material, or to any element or portion thereof. As between Licensor and you, Licensor owns and retains all right, title, and interest in and to the Licensed Material subject to the license granted in Section 1.1. Your permission to use the Licensed Material is expressly conditioned on you not impairing Licensor's or the applicable copyright owner's rights in the Licensed Material in any way.

3. Restrictions on use

3. 1. Minor editing privileges are allowed for adaptations for stylistic purposes or formatting purposes provided such alterations do not alter the original meaning or intention of the Licensed Material and the new figure(s) are still accurate and representative of the Licensed Material. Any other changes including but not limited to, cropping, adapting, and/or omitting material that affect the meaning, intention or moral rights of the author(s) are strictly prohibited.

3. 2. You must not use any Licensed Material as part of any design or trademark.

3. 3. Licensed Material may be used in Open Access Publications (OAP), but any such reuse must include a clear acknowledgment of this permission visible at the same time as the figures/tables/illustration or abstract and which must indicate that the Licensed Material is not part of the governing OA license but has been reproduced with permission. This may be indicated according to any standard referencing system but must include at a minimum 'Book/Journal title, Author, Journal Name (if applicable), Volume (if applicable), Publisher, Year, reproduced with permission from SNCSC'.

4. STM Permission Guidelines

4. 1. An alternative scope of license may apply to signatories of the STM Permissions Guidelines ("STM PG") as amended from time to time and made available at https://www.stm-assoc.org/intellectual-property/permissions/permissions-guidelines/.

4. 2. For content reuse requests that qualify for permission under the STM PG, and which may be updated from time to time, the STM PG supersede the terms and conditions contained in this License.

4. 3. If a License has been granted under the STM PG, but the STM PG no longer apply at the time of publication, further permission must be sought from the Rightsholder. Contact journalpermissions@springernature.com or bookpermissions@springernature.com for these rights.

5. Duration of License

5. 1. Unless otherwise indicated on your License, a License is valid from the date of purchase ("License Date") until the end of the relevant period in the below table:

Reuse in a medical communications project	Reuse up to distribution or time period indicated in License
Reuse in a dissertation/thesis	Lifetime of thesis
Reuse in a journal/magazine	Lifetime of journal/magazine
Reuse in a book/textbook	Lifetime of edition
Reuse on a website	1 year unless otherwise specified in the License
Reuse in a presentation/slide kit/poster	Lifetime of presentation/slide kit/poster. Note: publication whether electronic or in print of presentation/slide kit/poster may require further permission.

Reuse in conference proceedings	Lifetime of conference proceedings
Reuse in an annual report	Lifetime of annual report
Reuse in training/CME materials	Reuse up to distribution or time period indicated in License
Reuse in newsmedia	Lifetime of newsmedia
Reuse in coursepack/classroom materials	Reuse up to distribution and/or time period indicated in license

6. Acknowledgement

6. 1. The Licensor's permission must be acknowledged next to the Licensed Material in print. In electronic form, this acknowledgement must be visible at the same time as the figures/tables/illustrations or abstract and must be hyperlinked to the journal/book's homepage.

6. 2. Acknowledgement may be provided according to any standard referencing system and at a minimum should include "Author, Article/Book Title, Journal name/Book imprint, volume, page number, year, Springer Nature".

7. Reuse in a dissertation or thesis

7. 1. Where 'reuse in a dissertation/thesis' has been selected, the following terms apply: Print rights of the Version of Record are provided for; electronic rights for use only on institutional repository as defined by the Sherpa guideline (www.sherpa.ac.uk/romeo/) and only up to what is required by the awarding institution.

7. 2. For theses published under an ISBN or ISSN, separate permission is required. Please contact journalpermissions@springernature.com or bookpermissions@springernature.com for these rights.

7. 3. Authors must properly cite the published manuscript in their thesis according to current citation standards and include the following acknowledgement: '*Reproduced with permission from Springer Nature*'.

8. License Fee

You must pay the fee set forth in the License Agreement (the "License Fees"). All amounts payable by you under this License are exclusive of any sales, use, withholding, value added or similar taxes, government fees or levies or other assessments. Collection and/or remittance of such taxes to the relevant tax authority shall be the responsibility of the party who has the legal obligation to do so.

9. Warranty

9. 1. The Licensor warrants that it has, to the best of its knowledge, the rights to license reuse of the Licensed Material. **You are solely responsible for ensuring that**

the material you wish to license is original to the Licensor and does not carry the copyright of another entity or third party (as credited in the published version). If the credit line on any part of the Licensed Material indicates that it was reprinted or adapted with permission from another source, then you should seek additional permission from that source to reuse the material.

9. 2. EXCEPT FOR THE EXPRESS WARRANTY STATED HEREIN AND TO THE EXTENT PERMITTED BY APPLICABLE LAW, LICENSOR PROVIDES THE LICENSED MATERIAL "AS IS" AND MAKES NO OTHER REPRESENTATION OR WARRANTY. LICENSOR EXPRESSLY DISCLAIMS ANY LIABILITY FOR ANY CLAIM ARISING FROM OR OUT OF THE CONTENT, INCLUDING BUT NOT LIMITED TO ANY ERRORS, INACCURACIES, OMISSIONS, OR DEFECTS CONTAINED THEREIN, AND ANY IMPLIED OR EXPRESS WARRANTY AS TO MERCHANTABILITY OR FITNESS FOR A PARTICULAR PURPOSE. IN NO EVENT SHALL LICENSOR BE LIABLE TO YOU OR ANY OTHER PARTY OR ANY OTHER PERSON OR FOR ANY SPECIAL, CONSEQUENTIAL, INCIDENTAL, INDIRECT, PUNITIVE, OR EXEMPLARY DAMAGES, HOWEVER CAUSED, ARISING OUT OF OR IN CONNECTION WITH THE DOWNLOADING, VIEWING OR USE OF THE LICENSED MATERIAL REGARDLESS OF THE FORM OF ACTION, WHETHER FOR BREACH OF CONTRACT, BREACH OF WARRANTY, TORT, NEGLIGENCE, INFRINGEMENT OR OTHERWISE (INCLUDING, WITHOUT LIMITATION, DAMAGES BASED ON LOSS OF PROFITS, DATA, FILES, USE, BUSINESS OPPORTUNITY OR CLAIMS OF THIRD PARTIES), AND WHETHER OR NOT THE PARTY HAS BEEN ADVISED OF THE POSSIBILITY OF SUCH DAMAGES. THIS LIMITATION APPLIES NOTWITHSTANDING ANY FAILURE OF ESSENTIAL PURPOSE OF ANY LIMITED REMEDY PROVIDED HEREIN.

10. Termination and Cancellation

10. 1. The License and all rights granted hereunder will continue until the end of the applicable period shown in Clause 5.1 above. Thereafter, this license will be terminated and all rights granted hereunder will cease.

10. 2. Licensor reserves the right to terminate the License in the event that payment is not received in full or if you breach the terms of this License.

11. General

11. 1. The License and the rights and obligations of the parties hereto shall be construed, interpreted and determined in accordance with the laws of the Federal Republic of Germany without reference to the stipulations of the CISG (United Nations Convention on Contracts for the International Sale of Goods) or to Germany´s choice-of-law principle.

11. 2. The parties acknowledge and agree that any controversies and disputes arising out of this License shall be decided exclusively by the courts of or having jurisdiction for Heidelberg, Germany, as far as legally permissible.

11. 3. This License is solely for Licensor's and Licensee's benefit. It is not for the

benefit of any other person or entity.

Questions? For questions on Copyright Clearance Center accounts or website issues please contact springernaturesupport@copyright.com or +1-855-239-3415 (toll free in the US) or +1-978-646-2777. For questions on Springer Nature licensing please visit https://www.springernature.com/gp/partners/rights-permissions-third-party-distribution

Other Conditions:

Version 1.4 - Dec 2022

Questions? customercare@copyright.com.

ELSEVIER LICENSE
TERMS AND CONDITIONS

Aug 04, 2023

This Agreement between Imperial College London -- Nele Wenck ("You") and Elsevier ("Elsevier") consists of your license details and the terms and conditions provided by Elsevier and Copyright Clearance Center.

License Number	5602160443656
License date	Aug 04, 2023
Licensed Content Publisher	Elsevier
Licensed Content Publication	International Journal of Greenhouse Gas Control
Licensed Content Title	Recent advances in risk assessment and risk management of geologic CO2 storage
Licensed Content Author	Rajesh J. Pawar,Grant S. Bromhal,J. William Carey,William Foxall,Anna Korre,Philip S. Ringrose,Owain Tucker,Maxwell N. Watson,Joshua A. White
Licensed Content Date	Sep 1, 2015
Licensed Content Volume	40
Licensed Content Issue	n/a
Licensed Content Pages	20

Start Page	292
End Page	311
Type of Use	reuse in a thesis/dissertation
Portion	figures/tables/illustrations
Number of figures/tables/illustrations	1
Format	electronic
Are you the author of this Elsevier article?	No
Will you be translating?	No
Title	The Impact of Capillary Heterogeneity on Subsurface Carbon Dioxide Storage
Institution name	Imperial College London
Expected presentation date	Nov 2023
Portions	Figure 9 on page 304
Requestor Location	Imperial College London United Kingdom Attn: Imperial College London
Publisher Tax ID	GB 494 6272 12

Total 0.00 GBP

Terms and Conditions

INTRODUCTION

1. The publisher for this copyrighted material is Elsevier. By clicking "accept" in connection with completing this licensing transaction, you agree that the following terms and conditions apply to this transaction (along with the Billing and Payment terms and conditions established by Copyright Clearance Center, Inc. ("CCC"), at the time that you opened your RightsLink account and that are available at any time at https://myaccount.copyright.com).

GENERAL TERMS

2. Elsevier hereby grants you permission to reproduce the aforementioned material subject to the terms and conditions indicated.

3. Acknowledgement: If any part of the material to be used (for example, figures) has appeared in our publication with credit or acknowledgement to another source, permission must also be sought from that source. If such permission is not obtained then that material may not be included in your publication/copies. Suitable acknowledgement to the source must be made, either as a footnote or in a reference list at the end of your publication, as follows:

"Reprinted from Publication title, Vol /edition number, Author(s), Title of article / title of chapter, Pages No., Copyright (Year), with permission from Elsevier [OR APPLICABLE SOCIETY COPYRIGHT OWNER]." Also Lancet special credit - "Reprinted from The Lancet, Vol. number, Author(s), Title of article, Pages No., Copyright (Year), with permission from Elsevier."

4. Reproduction of this material is confined to the purpose and/or media for which permission is hereby given. The material may not be reproduced or used in any other way, including use in combination with an artificial intelligence tool (including to train an algorithm, test, process, analyse, generate output and/or develop any form of artificial intelligence tool), or to create any derivative work and/or service (including resulting from the use of artificial intelligence tools).

5. Altering/Modifying Material: Not Permitted. However figures and illustrations may be altered/adapted minimally to serve your work. Any other abbreviations, additions, deletions and/or any other alterations shall be made only with prior written authorization of Elsevier Ltd. (Please contact Elsevier's permissions helpdesk here). No modifications can be made to any Lancet figures/tables and they must be reproduced in full.

6. If the permission fee for the requested use of our material is waived in this instance, please be advised that your future requests for Elsevier materials may attract a fee.

7. Reservation of Rights: Publisher reserves all rights not specifically granted in the

combination of (i) the license details provided by you and accepted in the course of this licensing transaction, (ii) these terms and conditions and (iii) CCC's Billing and Payment terms and conditions.

8. License Contingent Upon Payment: While you may exercise the rights licensed immediately upon issuance of the license at the end of the licensing process for the transaction, provided that you have disclosed complete and accurate details of your proposed use, no license is finally effective unless and until full payment is received from you (either by publisher or by CCC) as provided in CCC's Billing and Payment terms and conditions. If full payment is not received on a timely basis, then any license preliminarily granted shall be deemed automatically revoked and shall be void as if never granted. Further, in the event that you breach any of these terms and conditions or any of CCC's Billing and Payment terms and conditions, the license is automatically revoked and shall be void as if never granted. Use of materials as described in a revoked license, as well as any use of the materials beyond the scope of an unrevoked license, may constitute copyright infringement and publisher reserves the right to take any and all action to protect its copyright in the materials.

9. Warranties: Publisher makes no representations or warranties with respect to the licensed material.

10. Indemnity: You hereby indemnify and agree to hold harmless publisher and CCC, and their respective officers, directors, employees and agents, from and against any and all claims arising out of your use of the licensed material other than as specifically authorized pursuant to this license.

11. No Transfer of License: This license is personal to you and may not be sublicensed, assigned, or transferred by you to any other person without publisher's written permission.

12. No Amendment Except in Writing: This license may not be amended except in a writing signed by both parties (or, in the case of publisher, by CCC on publisher's behalf).

13. Objection to Contrary Terms: Publisher hereby objects to any terms contained in any purchase order, acknowledgment, check endorsement or other writing prepared by you, which terms are inconsistent with these terms and conditions or CCC's Billing and Payment terms and conditions. These terms and conditions, together with CCC's Billing and Payment terms and conditions (which are incorporated herein), comprise the entire agreement between you and publisher (and CCC) concerning this licensing transaction. In the event of any conflict between your obligations established by these terms and conditions and those established by CCC's Billing and Payment terms and conditions, these terms and conditions shall control.

14. Revocation: Elsevier or Copyright Clearance Center may deny the permissions described in this License at their sole discretion, for any reason or no reason, with a full refund payable to you. Notice of such denial will be made using the contact information provided by you. Failure to receive such notice will not alter or invalidate the denial. In no event will Elsevier or Copyright Clearance Center be responsible or liable for any costs, expenses or damage incurred by you as a result of a denial of your permission request, other than a refund of the amount(s) paid by you to Elsevier and/or Copyright Clearance Center for denied permissions.

LIMITED LICENSE

The following terms and conditions apply only to specific license types:

15. **Translation**: This permission is granted for non-exclusive world **English** rights only unless your license was granted for translation rights. If you licensed translation rights you may only translate this content into the languages you requested. A professional translator must perform all translations and reproduce the content word for word preserving the integrity of the article.

16. **Posting licensed content on any Website**: The following terms and conditions apply as follows: Licensing material from an Elsevier journal: All content posted to the web site must maintain the copyright information line on the bottom of each image; A hyper-text must be included to the Homepage of the journal from which you are licensing at http://www.sciencedirect.com/science/journal/xxxxx or the Elsevier homepage for books at http://www.elsevier.com; Central Storage: This license does not include permission for a scanned version of the material to be stored in a central repository such as that provided by Heron/XanEdu.

Licensing material from an Elsevier book: A hyper-text link must be included to the Elsevier homepage at http://www.elsevier.com . All content posted to the web site must maintain the copyright information line on the bottom of each image.

Posting licensed content on Electronic reserve: In addition to the above the following clauses are applicable: The web site must be password-protected and made available only to bona fide students registered on a relevant course. This permission is granted for 1 year only. You may obtain a new license for future website posting.

17. **For journal authors:** the following clauses are applicable in addition to the above:

Preprints:

A preprint is an author's own write-up of research results and analysis, it has not been peer-reviewed, nor has it had any other value added to it by a publisher (such as formatting, copyright, technical enhancement etc.).

Authors can share their preprints anywhere at any time. Preprints should not be added to or enhanced in any way in order to appear more like, or to substitute for, the final versions of articles however authors can update their preprints on arXiv or RePEc with their Accepted Author Manuscript (see below).

If accepted for publication, we encourage authors to link from the preprint to their formal publication via its DOI. Millions of researchers have access to the formal publications on ScienceDirect, and so links will help users to find, access, cite and use the best available version. Please note that Cell Press, The Lancet and some society-owned have different preprint policies. Information on these policies is available on the journal homepage.

Accepted Author Manuscripts: An accepted author manuscript is the manuscript of an article that has been accepted for publication and which typically includes author-incorporated changes suggested during submission, peer review and editor-author communications.

Authors can share their accepted author manuscript:

- immediately
  - via their non-commercial person homepage or blog
  - by updating a preprint in arXiv or RePEc with the accepted manuscript
  - via their research institute or institutional repository for internal institutional uses or as part of an invitation-only research collaboration work-group
  - directly by providing copies to their students or to research collaborators for their personal use
  - for private scholarly sharing as part of an invitation-only work group on commercial sites with which Elsevier has an agreement
- After the embargo period
  - via non-commercial hosting platforms such as their institutional repository
  - via commercial sites with which Elsevier has an agreement

In all cases accepted manuscripts should:

- link to the formal publication via its DOI
- bear a CC-BY-NC-ND license - this is easy to do
- if aggregated with other manuscripts, for example in a repository or other site, be shared in alignment with our hosting policy not be added to or enhanced in any way to appear more like, or to substitute for, the published journal article.

Published journal article (JPA): A published journal article (PJA) is the definitive final record of published research that appears or will appear in the journal and embodies all value-adding publishing activities including peer review co-ordination, copy-editing, formatting, (if relevant) pagination and online enrichment.

Policies for sharing publishing journal articles differ for subscription and gold open access articles:

Subscription Articles: If you are an author, please share a link to your article rather than the full-text. Millions of researchers have access to the formal publications on ScienceDirect, and so links will help your users to find, access, cite, and use the best available version.

Theses and dissertations which contain embedded PJAs as part of the formal submission can be posted publicly by the awarding institution with DOI links back to the formal publications on ScienceDirect.

If you are affiliated with a library that subscribes to ScienceDirect you have additional private sharing rights for others' research accessed under that agreement. This includes use for classroom teaching and internal training at the institution (including use in course packs and courseware programs), and inclusion of the article for grant funding purposes.

Gold Open Access Articles: May be shared according to the author-selected end-user license and should contain a CrossMark logo, the end user license, and a DOI link to the formal publication on ScienceDirect.

Please refer to Elsevier's posting policy for further information.

18. **For book authors** the following clauses are applicable in addition to the above: Authors are permitted to place a brief summary of their work online only. You are not

allowed to download and post the published electronic version of your chapter, nor may you scan the printed edition to create an electronic version. **Posting to a repository:** Authors are permitted to post a summary of their chapter only in their institution's repository.

19. **Thesis/Dissertation**: If your license is for use in a thesis/dissertation your thesis may be submitted to your institution in either print or electronic form. Should your thesis be published commercially, please reapply for permission. These requirements include permission for the Library and Archives of Canada to supply single copies, on demand, of the complete thesis and include permission for Proquest/UMI to supply single copies, on demand, of the complete thesis. Should your thesis be published commercially, please reapply for permission. Theses and dissertations which contain embedded PJAs as part of the formal submission can be posted publicly by the awarding institution with DOI links back to the formal publications on ScienceDirect.

Elsevier Open Access Terms and Conditions

You can publish open access with Elsevier in hundreds of open access journals or in nearly 2000 established subscription journals that support open access publishing. Permitted third party re-use of these open access articles is defined by the author's choice of Creative Commons user license. See our open access license policy for more information.

Terms & Conditions applicable to all Open Access articles published with Elsevier:

Any reuse of the article must not represent the author as endorsing the adaptation of the article nor should the article be modified in such a way as to damage the author's honour or reputation. If any changes have been made, such changes must be clearly indicated.

The author(s) must be appropriately credited and we ask that you include the end user license and a DOI link to the formal publication on ScienceDirect.

If any part of the material to be used (for example, figures) has appeared in our publication with credit or acknowledgement to another source it is the responsibility of the user to ensure their reuse complies with the terms and conditions determined by the rights holder.

Additional Terms & Conditions applicable to each Creative Commons user license:

CC BY: The CC-BY license allows users to copy, to create extracts, abstracts and new works from the Article, to alter and revise the Article and to make commercial use of the Article (including reuse and/or resale of the Article by commercial entities), provided the user gives appropriate credit (with a link to the formal publication through the relevant DOI), provides a link to the license, indicates if changes were made and the licensor is not represented as endorsing the use made of the work. The full details of the license are available at http://creativecommons.org/licenses/by/4.0.

CC BY NC SA: The CC BY-NC-SA license allows users to copy, to create extracts, abstracts and new works from the Article, to alter and revise the Article, provided this is not done for commercial purposes, and that the user gives appropriate credit (with a link to the formal publication through the relevant DOI), provides a link to the license, indicates if changes were made and the licensor is not represented as endorsing the use made of the work. Further, any new works must be made available on the same conditions. The full

details of the license are available at http://creativecommons.org/licenses/by-nc-sa/4.0.

CC BY NC ND: The CC BY-NC-ND license allows users to copy and distribute the Article, provided this is not done for commercial purposes and further does not permit distribution of the Article if it is changed or edited in any way, and provided the user gives appropriate credit (with a link to the formal publication through the relevant DOI), provides a link to the license, and that the licensor is not represented as endorsing the use made of the work. The full details of the license are available at http://creativecommons.org/licenses/by-nc-nd/4.0. Any commercial reuse of Open Access articles published with a CC BY NC SA or CC BY NC ND license requires permission from Elsevier and will be subject to a fee.

Commercial reuse includes:

- Associating advertising with the full text of the Article
- Charging fees for document delivery or access
- Article aggregation
- Systematic distribution via e-mail lists or share buttons

Posting or linking by commercial companies for use by customers of those companies.

20. **Other Conditions**:

v1.10

Questions? customercare@copyright.com.